SIMULATING NORMAL AND ARRHYTHMIC DYNAMICS: FROM SUB-CELLULAR TO TISSUE AND ORGAN LEVEL

EDITED BY: Hans Dierckx, Flavio H. Fenton, Simonetta Filippi, Alain Pumir and S. Sridhar
PUBLISHED IN: Frontiers in Physics and Frontiers in Physiology

frontiers Research Topics

ISSN 1664-8714
ISBN 978-2-88963-067-7
DOI 10.3389/978-2-88963-067-7

About Frontiers

Frontiers is more than just an open-access publisher of scholarly articles: it is a pioneering approach to the world of academia, radically improving the way scholarly research is managed. The grand vision of Frontiers is a world where all people have an equal opportunity to seek, share and generate knowledge. Frontiers provides immediate and permanent online open access to all its publications, but this alone is not enough to realize our grand goals.

Frontiers Journal Series

The Frontiers Journal Series is a multi-tier and interdisciplinary set of open-access, online journals, promising a paradigm shift from the current review, selection and dissemination processes in academic publishing. All Frontiers journals are driven by researchers for researchers; therefore, they constitute a service to the scholarly community. At the same time, the Frontiers Journal Series operates on a revolutionary invention, the tiered publishing system, initially addressing specific communities of scholars, and gradually climbing up to broader public understanding, thus serving the interests of the lay society, too.

Dedication to Quality

Each Frontiers article is a landmark of the highest quality, thanks to genuinely collaborative interactions between authors and review editors, who include some of the world's best academicians. Research must be certified by peers before entering a stream of knowledge that may eventually reach the public - and shape society; therefore, Frontiers only applies the most rigorous and unbiased reviews.
Frontiers revolutionizes research publishing by freely delivering the most outstanding research, evaluated with no bias from both the academic and social point of view. By applying the most advanced information technologies, Frontiers is catapulting scholarly publishing into a new generation.

What are Frontiers Research Topics?

Frontiers Research Topics are very popular trademarks of the Frontiers Journals Series: they are collections of at least ten articles, all centered on a particular subject. With their unique mix of varied contributions from Original Research to Review Articles, Frontiers Research Topics unify the most influential researchers, the latest key findings and historical advances in a hot research area! Find out more on how to host your own Frontiers Research Topic or contribute to one as an author by contacting the Frontiers Editorial Office: researchtopics@frontiersin.org

SIMULATING NORMAL AND ARRHYTHMIC DYNAMICS: FROM SUB-CELLULAR TO TISSUE AND ORGAN LEVEL

Topic Editors:
Hans Dierckx, Ghent University, Belgium
Flavio H. Fenton, Georgia Institute of Technology, United States
Simonetta Filippi, Campus Bio-Medico University, Italy
Alain Pumir, Université Claude Bernard, CNRS, Laboratoire de Physique, France
S. Sridhar, Indian Institute of Science, India

Citation: H., Dierckx, Fenton, F. H., Filippi, S., Pumir, A., Sridhar, S., eds. (2019). Simulating Normal and Arrhythmic Dynamics: From Sub-Cellular to Tissue and Organ Level. Lausanne: Frontiers Media. doi: 10.3389/978-2-88963-067-7

Table of Contents

05 ***Editorial: Simulating Normal and Arrhythmic Dynamics: From Sub-cellular to Tissue and Organ Level***
Hans Dierckx, Flavio H. Fenton, Simonetta Filippi, Alain Pumir and S. Sridhar

08 ***V241F KCNQ1 Mutation Shortens Electrical Wavelength and Reduces Ventricular Pumping Capabilities: A Simulation Study With an Electro-Mechanical Model***
Aulia Khamas Heikhmakhtiar, Fakhmi Adi Rasyidin and Ki Moo Lim

18 ***Computational Model of Calcium Signaling in Cardiac Atrial Cells at the Submicron Scale***
Miquel Marchena and Blas Echebarria

32 ***Marker-Free Tracking for Motion Artifact Compensation and Deformation Measurements in Optical Mapping Videos of Contracting Hearts***
Jan Christoph and Stefan Luther

53 ***Mathematical Analysis of the Role of Heterogeneous Distribution of Excitable and Non-excitable Cells on Early Afterdepolarizations***
Seunghyun Kim and Daisuke Sato

64 ***Investigation of the Syncytial Nature of Detrusor Smooth Muscle as a Determinant of Action Potential Shape***
Shailesh Appukuttan, Mithun Padmakumar, John S. Young, Keith L. Brain and Rohit Manchanda

77 ***Slow Recovery of Excitability Increases Ventricular Fibrillation Risk as Identified by Emulation***
Brodie A. Lawson, Kevin Burrage, Pamela Burrage, Christopher C. Drovandi and Alfonso Bueno-Orovio

96 ***Killing Many Birds With Two Stones: Hypoxia and Fibrosis can Generate Ectopic Beats in a Human Ventricular Model***
Rafael Sachetto, Sergio Alonso and Rodrigo Weber dos Santos

108 ***Synchronization of Pacemaking in the Sinoatrial Node: A Mathematical Modeling Study***
Daniel Gratz, Birce Onal, Alyssa Dalic and Thomas J. Hund

119 ***Microscopic Isthmuses and Fibrosis Within the Border Zone of Infarcted Hearts Promote Calcium-Mediated Ectopy and Conduction Block***
Fernando O. Campos, Yohannes Shiferaw, Rodrigo Weber dos Santos, Gernot Plank and Martin J. Bishop

133 ***A Minimal Model Approach for Analyzing Continuous Glucose Monitoring in Type 2 Diabetes***
Pranay Goel, Durga Parkhi, Amlan Barua, Mita Shah and Saroj Ghaskadbi

141 ***Spatiotemporal Permutation Entropy as a Measure for Complexity of Cardiac Arrhythmia***
Alexander Schlemmer, Sebastian Berg, Thomas Lilienkamp, Stefan Luther and Ulrich Parlitz

154 ***Causal Scale of Rotors in a Cardiac System***
Hiroshi Ashikaga, Francisco Prieto-Castrillo, Mari Kawakatsu and Nima Dehghani

167 ***Modeling the Electrophysiological Properties of the Infarct Border Zone***
Caroline Mendonca Costa, Gernot Plank, Christopher A. Rinaldi, Steven A. Niederer and Martin J. Bishop

181 ***Confocal Microscopy-Based Estimation of Parameters for Computational Modeling of Electrical Conduction in the Normal and Infarcted Heart***
Joachim Greiner, Aparna C. Sankarankutty, Gunnar Seemann, Thomas Seidel and Frank B. Sachse

196 ***Cardiac Re-entry Dynamics and Self-termination in DT-MRI Based Model of Human Fetal Heart***
Irina V. Biktasheva, Richard A. Anderson, Arun V. Holden, Eleftheria Pervolaraki and Fen Cai Wen

214 ***Validation and Trustworthiness of Multiscale Models of Cardiac Electrophysiology***
Pras Pathmanathan and Richard A. Gray

233 ***Initiation of Rotors by Fast Propagation Regions in Excitable Media: A Theoretical Study***
Xiang Gao, Alexei Krekhov, Vladimir Zykov and Eberhard Bodenschatz

243 ***Progress in Mathematical Modeling of Gastrointestinal Slow Wave Abnormalities***
Peng Du, Stefan Calder, Timothy R. Angeli, Shameer Sathar, Niranchan Paskaranandavadivel, Gregory O'Grady and Leo K. Cheng

257 ***A Cell-Based Framework for Numerical Modeling of Electrical Conduction in Cardiac Tissue***
Aslak Tveito, Karoline H. Jæger, Miroslav Kuchta, Kent-Andre Mardal and Marie E. Rognes

frontiers in Physics

EDITORIAL
published: 18 June 2019
doi: 10.3389/fphy.2019.00089

Editorial: Simulating Normal and Arrhythmic Dynamics: From Sub-cellular to Tissue and Organ Level

Hans Dierckx[1], *Flavio H. Fenton*[2], *Simonetta Filippi*[3], *Alain Pumir*[4] *and S. Sridhar*[5]*

[1] Department of Physics and Astronomy, Ghent University, Gent, Belgium, [2] School of Physics, Georgia Institute of Technology, Atlanta, GA, United States, [3] Nonlinear Physics and Mathematical Modelling Unit, Campus Bio-Medico University, Rome, Italy, [4] Université de Lyon, ENS de Lyon, Université Claude Bernard, CNRS, Laboratoire de Physique, Lyon, France, [5] Robert Bosch Centre for Cyber-Physical Systems, Indian Institute of Science, Bengaluru, India

Keywords: arrhythmia (heart rhythm disorders), computational cardiology, physiological rhythms, excitable media, multiscale modeling and simulation

Editorial on the Research Topic

Simulating Normal and Arrhythmic Dynamics: From Sub-Cellular to Tissue and Organ Level

How physiological organs function as aggregates of individual cells is in many ways a challenging problem, involving several temporal and spatial scales that lead to complex emergent behavior. In fact, organs and tissues, which are typically a few centimeters in size, consist of cells in the order $\sim 10 - 100\mu m$. Cell functions are in turn regulated by proteins, with typical sizes of $\sim$ 10nm. Temporally, the response of the cells to external signals range from a few milliseconds (influx of Sodium ions through specialized ion channels) to a fractions of seconds (cell repolarization), or even longer when cells remodel due to a change in the environment or disease. Decades of careful exploration have shown the importance of specialized proteins (such as ion channels), as well as many regulatory pathways which endow tissues and organs with their unique properties. In this context, developing mathematical models that are realistic enough to study how organs function, is a serious challenge. Further, we stress that mathematical models not only have to reproduce the experimental data they are based on, but they should also lead to predictions. In the present problem, the issue is to elucidate the complex, collective behavior of an assembly of cells, in order to understand how organs function.

Thanks in part to the progress in mathematical modeling and simulations of molecular and other sub-cellular processes, it is now possible to understand how cells, coupled together in a tissue, collectively give rise to the behavior observed in a complex organ. Furthermore, the remarkable development of medical imaging now makes it possible to obtain high quality data, which can be used as an input to the models, and also as a point of comparison for predictions. As a result, the simulation approach can be successful not only in understanding the normal functioning of organs, but also during diseases. The heart is certainly the most-studied and the best example of such an approach.

This research topic consists of 19 research articles with emphasis on the development of new methods and models for the study and understanding of cardiac function and other similar electrophysiological systems such as the gastrointestinal complex and urinary bladder. These studies focus mostly on normal cardiac function and some of the pathological/disease states that can lead to deadly arrhythmias such as tachycardia and fibrillation, which remain as one of the leading causes of death in the industrialized world.

Edited and reviewed by:
Thomas Beyer,
Medical University of Vienna, Austria

***Correspondence:**
S. Sridhar
dharmails@gmail.com;
sridhars@iisc.ac.in

Specialty section:
This article was submitted to Medical Physics and Imaging, a section of the journal Frontiers in Physics

Received: *24 April 2019*
Accepted: *29 May 2019*
Published: *18 June 2019*

Citation:
Dierckx H, Fenton FH, Filippi S, Pumir A and Sridhar S (2019) Editorial: Simulating Normal and Arrhythmic Dynamics: From Sub-cellular to Tissue and Organ Level. Front. Phys. 7:89. doi: 10.3389/fphy.2019.00089

1. IMAGING METHODS AND IMPLICATIONS FOR SIMULATIONS

From a methodological point of view, imaging techniques have remarkably improved in the past few years, providing us access to many properties of the tissue. As reported by Christoph and Luther, this allows us to track reliably the motion of the heart, especially during contraction. Another use of imaging techniques is proposed by Greiner et al.. Using confocal microscopy imaging, they managed to extract important parameters, essential to describe better the properties, not only of healthy heart, but also of infarcted organs. These are essential properties that any reliable model has to necessarily take into account. An interesting interaction between imaging and modeling is provided by the work of Biktasheva et al., wherein they determine the role of fiber orientation and other geometric factors that affect the dynamics and termination of re-entries in fetal hearts.

2. PHYSICS-BASED APPROACHES

While studying organs and tissues, it is highly desirable to supplement the fantastic investigation techniques provided by imaging methods with new theoretical tools. Physics-inspired techniques certainly play an important role in this context. They have also been employed, in particular in the context of cardiac dynamics, to analyse both normal and arrhythmic states. Schlemmer et al. have focused on the permutation entropy measure to quantify simultaneously both spatial structures and temporal complexity during cardiac arrhythmia in both 2D and 3D cases. Ashikaga et al., used information theory metrics to determine the causal relationship between rotors and spiral waves. Their results suggest that rotors may not be the mechanism that supports spiral waves at all the spatiotemporal scales in heart.

In the sinoatrial node (SA) the physical mechanisms underlying the spatial and temporal synchronization of the pacemaker cells have been investigated using models of coupled oscillators. Gratz et al. use advanced simulation tools to explore the role of coupling on spontaneous action potential dynamics and the spatiotemporal synchronization of pacemaking cells. The authors identify distinct cellular coupling regimes that promote spiral waves and synchronous activation respectively. They also characterize the synchronization of spatially proximal cells via a synchrony factor that is observed to vary non-linearly with coupling.

3. USING SIMULATIONS TO STUDY CARDIAC ARRHYTHMIAS

In the heart, numerous causes have been identified, that may lead to the initiation of cardiac pathologies. This is a subject of primary concern in a number of biological and medical investigations, which is also amply reflected in this research topic. The efficient pumping function of the heart may be affected due to the presence of electrophysiological anomalies at different scales. A case in point is the recently discovered mutation in the slow delayed rectified potassium channel. In this spirit, the contribution of Heikhmakhtiar et al. presents a comprehensive modeling study of the influence of this mutation on the pumping capabilities of the heart. This is one of the first major studies that combine electrophysiological dynamics of a complex human ventricular model with that of a contraction model via the Calcium dynamics in a 3D ventricular tissue. The main results from the simulations, indicate that this mutation not only decreases the action potential duration but during arrhythmias it can lead to very high volume of the left ventricle with corresponding very low pressure.

Several cardiac arrhythmias have been know for a very long time to be related to the presence of fast waves of electrical activity, organized as "rotors." Modeling studies can lead to a better understanding of the underlying conditions that result in the generation of such "rotors." For example, Gao et al. provide a two-dimensional theoretical analysis of how the geometrical features of localized heterogeneities (curvature, shape, and size) can affect rotor initiation.

Similarly, variability in cell dynamics has also been linked to the generation of arrhythmic waves when connected in tissue as shown by Kim and Sato. They show that reactivation of the L-type calcium channels can spontaneously release Ca^{2+} producing Early After Depolarizations (EADs) which can trigger action potentials in neighboring cells under certain conditions. Using a rabbit ventricular cell model they show that EADs can lead to new propagating waves only when there is an heterogeneity in cell coupling with small regions of non-excitable cells. This study thus connects the effect of ischemia and tissue decoupling with the generation of EADs and arrhythmia initiation via reentrant waves. Similarly Sachetto et al. show how reentrant waves can be generated by ectopic beats, not generated by EADs but via pure fibrosis effects. The effect of tissue damage by fibrosis and hypoxia is studied using a human ventricular model. Their results show that micro-reentries are formed inside sections of damaged tissue and can act as focal regions of re-excitation.

The proarrhythmic effect of damaged tissue during infarct is also investigated by Campos et al.. They describe the role of macroscopic and microscopic anatomical properties of the infarct tissue border zone in creating a calcium mediated substrate for arrhythmia initiation by ectopy and conduction block. In a similar vein, Costa et al. compare *in silico* experimental data available in the literature, and identify ionic remodeling as the most prominent property influencing the pro-arrhythmic nature of the infarct tissue in the early stages and structural remodeling during the chronic stages.

It is difficult to account using a single model, all the electrophysiological variability that comes from the complex ion-channel dynamics and the multi-scale nature of the heart tissue. Therefore, studies such as the ones presented by Lawson et al. are necessary to understand drug effects on electrophysiological cell variability. In this study a novel emulation approach, based on Gaussian process regression augmented with machine learning, is used along with more than 5000 monodomain simulations of long-lasting arrhythmic episodes along with enriched emulations to 80 million different electrophysiological scenarios. This multivariate analysis allows to explain the

role and increased arrhythmic risk of incomplete activation of slow inward currents in mediating tissue rate-dependence and dispersion of repolarization, and the emergence of slow recovery of excitability. Pathmanathan and Gray also address the complexity and multi-scale nature of cardiac models and the difficulties in evaluating them for validation and prediction. They present methodologies that are currently being developed by the medical device community, to further categorize credibility of physiological models with respect to experiments.

4. INCLUDING SUBCELLULAR LEVEL IN THE DESCRIPTION OF THE HEART

As already mentioned, the dynamics of organs is intrinsically a multiscale problem. Since pathological cells in a tissue may result in a disease, it is important to develop a description that includes sub-cellular details. Thus, depending on the problem, the tissue-scale approach has to be improved, to take into account the properties of specific cells. In the case of cardiac arrhythmias, the standard approach at the tissue level, the mono- and bidomain formulations for the heart, may need to be extended by representing processes at the cellular level. In this issue, Tveito et al. propose a method to model many cells together in the microdomain, which allows them to handle non-uniform distribution of ion channels along the cell membrane. Marchena and Echebarria present a homogenized model of the intracellular Ca handling, taking into account the spatial organization of RyR clusters.

5. OTHER ORGANS

In addition to the heart, other organs with similar electrophysiology such as the urinary bladder and uterine myometrium also exhibit regular rhythms during their normal functioning and deviate from them under pathological conditions. Spatial patterns of electrical activity including spiral waves have been observed in the smooth muscles of the gastrointestinal (GI) systems. These slow waves are generated from a single pacemaker in the proximal end of the stomach and serve to regulate cyclic muscular contractions that enable breaking down and transit of ingested food along the GI tract. Du et al. have reviewed recent advances in the mathematical modeling of both normal and abnormal slow waves.

Appukuttan et al. combine computational models and experimental data to propose a plausible mechanism to explain the occurrence of a diversity of action potentials at the level of a single cell in the urinary bladder wall (detrusor). The authors study the role of passive signals such as spontaneous excitatory junction potentials (sEJPs) on modulating the shape of the action potentials. They map the action potential shape and the syncytial properties of the tissue in order to characterize changes occurring during pathological conditions such as overactive bladder.

Insulin regulation is another physiological process showing rhythmic variations, with the blood glucose levels varying over a duration of hours. These rhythms are different for healthy and diabetic people respectively and can be tracked via Continuous Glucose Monitoring (CGM), providing insight into dietary habits of individuals and suitable clinical interventions. In their study Goel et al. have built a minimal model for tracking blood sugar level during type 2 diabetes in the process providing a plausible strategy toward personalized analysis of CGM.

6. FUTURE OF SIMULATION STUDIES OF NORMAL AND ABNORMAL PHYSIOLOGICAL DYNAMICS

The progress in developing quantitatively accurate multiscale simulations of organs, as presented in this Research Topic, now make it possible to develop methods that would be useful in clinics. This is particularly important for the case of cardiac arrhythmia, wherein advances in multiscale simulations are aimed at helping clinicians improve personalized treatment for patients. The papers presented in this research topic show how imaging techniques complement simulations and are necessary, to both develop better physics-based models across scales (from sub-cellular to organ-level) and to investigate arrhythmia. Moreover, many of these techniques are found to be applicable to other biological and physiological fields.

AUTHOR CONTRIBUTIONS

All authors listed have made a substantial, direct and intellectual contribution to the work, and approved it for publication.

FUNDING

This work has received funding in part from NSF DCSD #1762553 (FHF).

ACKNOWLEDGMENTS

We thank all authors, reviewers, and editors that have contributed to this Research Topic.

Conflict of Interest Statement: The authors declare that the research was conducted in the absence of any commercial or financial relationships that could be construed as a potential conflict of interest.

frontiers in Physics

ORIGINAL RESEARCH
published: 18 December 2018
doi: 10.3389/fphy.2018.00147

V241F KCNQ1 Mutation Shortens Electrical Wavelength and Reduces Ventricular Pumping Capabilities: A Simulation Study With an Electro-Mechanical Model

Aulia Khamas Heikhmakhtiar[1], *Fakhmi Adi Rasyidin*[2] *and Ki Moo Lim*[1]*

[1] Computational Medicine Lab, Department of IT Convergence Engineering, Kumoh National Institute of Technology, Gumi, South Korea, [2] Computational Medicine Lab, Department of Industrial Engineering, Kumoh National Institute of Technology, Gumi, South Korea

Death due to ventricular fibrillation (VF) can occur over a relatively short time period. During the first stage, an irregular heartbeat or arrhythmia of the heart may occur. Therefore, studying arrhythmia could reveal important insights relevant to the prevention of VF. One of the factors known to cause arrhythmia is the generation of mutations in the ion channels of myocytes. The current experimental methods to monitor and observe subjects with arrhythmia are invasive, and could possibly harm the subject with no guarantee of obtaining good results. These limitations could be overcome by using an extensively validated computational simulation study. This study aims to enhance our understanding of the effect of the V241F mutation on electromechanical behavior in the heart. We simulated three conditions; wild-type (WT), heterozygous/intermediate V241F, and pure V241F conditions in an electrophysiological single cell model and three-dimensional electro-mechanics ventricular model. The electro-mechanics model is a one-way coupling of the electrical compartment to the mechanical compartment by Ca^{2+} transient concentration. Consistent with a previous study, the V241F mutation significantly shortened the action potential duration at 90% repolarization (APD_{90}) under pure V241F mutation conditions, due to the gain of function of the slow delayed rectifier potassium (I_{Ks}) channel. This APD_{90} shortening is associated with a short electrical wavelength, which shortens the Ca^{2+} activation time as well. The hemodynamic responses showed that the V241F mutation lowered ventricular contraction under normal sinus rhythm conditions by decreasing the stroke volume, stroke work, and ejection fraction. During reentry, the V241F mutation significantly reduced the ventricular contractility compared with the WT condition. In conclusions, the effect of the two variants of V241F (intermediate and pure) mutation not only disturbed the electrophysiological events but also affected the mechanical behavior significantly. The result of this study can be used as a reference for the cardiovascular expert to decide the appropriate pharmacology of I_{Ks} conductance block for the patient.

Keywords: V241F KCNQ1 mutation, electromechanical model, sinus rhythm, ventricular fibrillation, computational model

OPEN ACCESS

Edited by:
Hans Dierckx,
Ghent University, Belgium

Reviewed by:
Winfried Mayr,
Medical University of Vienna, Austria
Jieyun Bai,
The University of Auckland, New Zealand

***Correspondence:**
Ki Moo Lim
kmlim@kumoh.ac.kr

Specialty section:
This article was submitted to Biomedical Physics, a section of the journal Frontiers in Physics

Received: *15 December 2017*
Accepted: *04 December 2018*
Published: *18 December 2018*

Citation:
Heikhmakhtiar AK, Rasyidin FA and Lim KM (2018) V241F KCNQ1 Mutation Shortens Electrical Wavelength and Reduces Ventricular Pumping Capabilities: A Simulation Study With an Electro-Mechanical Model. Front. Phys. 6:147. doi: 10.3389/fphy.2018.00147

INTRODUCTION

Recent data from the American Heart Association showed that cardiovascular diseases are the primary causes of death worldwide [1]. Sudden cardiac death and ventricular fibrillation (VF) are associated with a <11% chance of survival. VF occurs when the heart quivers instead of performing a normal contraction. This results in a reduction of blood distribution within the circulatory system [2]. VF causes death within a short period (<1 h) in the absence of any observable symptoms [3]. In the last two decades, the number of deaths from VF worldwide has reached 300,000 per year [3–5]. Since VF is initiated by ventricular arrhythmia [5–7], the study of arrhythmia is of great of importance. Over the last few decades, researchers have found that disturbance in the electrical activity of the heart is due to ion channel mutations, also known as ion channelopathies [8, 9].

Ion channels are protein complexes that act as gates in the cardiomyocytes membrane and sarcolemma, regulating the permeability of specific ions through the membrane [10]. The ion channels in myocytes dynamically control the ionic currents that orchestrate action potentials (APs). Changes in the electrical properties of myocytes directly affect their mechanical activation [11]. Hence, changes in the properties of ion channels due to mutations will presumably change the AP shape, as well as alter the myocytes. In addition, mechanical activation of the myocytes will also affect the electrophysiological events related to stretch-activated channels (mechano-electric feedback) [12]. Understanding the mechanism of electrical disturbance in the early stages of VF could help clinicians make decisions regarding the optimal therapies.

In 2014, a novel mutation in the slow delayed rectifier potassium (K^+) channel (I_{Ks}) was found. The mutation p.Val241phe (V241F) occurs in the S4 transmembrane domain of the KCNQ1 gene in Korean families with a history of atrial fibrillation and bradycardia [13]. I_{Ks} are composed of both KCNQ1 (K_VLQT1) channel subunits and KCNE1 (minK) subunits in myocytes and are involved in the repolarization of the AP during the plateau phase and refractory period [14]. V241F is a gain of function mutation of KCNQ1 that abbreviates the action potential duration at 90% repolarization (APD_{90}). A short APD_{90} results in short QT syndrome and is one of the primary causes of VF [15]. Our previous study enhanced understanding of the electrophysiological activity of the V241F mutation by using an image-based three-dimensional (3D) cardiac model [16]. In this study, we observed the contribution of the V241F mutation to ventricular pumping of the heart by using a 3D electro-mechanic ventricular model.

The goal of this study was to computationally predict the electrical activity and mechanical responses of human ventricles with the V241F mutation under conditions of normal sinus rhythm and VF. The experimental study of arrhythmia has many limitations because it is difficult to measure the electrical and mechanical activity of the heart non-invasively; furthermore, only the surface can be observed. Hence, we used an extensively validated computational model as an alternative to uncover the effect of the V241F mutation on the electrical and mechanical activity of the heart. To the best of our knowledge, no study has observed the contribution of the V241F mutation to the electrophysiological activity of the heart and the mechanical responses of the ventricle. Here, we simulated an electrophysiological single cell model, and a 3D electromechanical model of a failing ventricle under wild-type (WT), intermediate V241F, and pure V241F mutation conditions.

MATERIALS AND METHODS

In this study, we used an electromechanical model of failing ventricle based on magnetic resonance imaging with finite element combined with the lumped-parameter model, similar to our previous study [17]. The methods for the electromechanical coupling we used in this study are based on those described by Gurev et al. [18, 19]. The present electromechanical model consists of electrical and mechanical properties that were weakly coupled by intracellular calcium (Ca^{2+}) transient. Physiologically, the electrical propagation in the ventricular tissue represents depolarization of each cell throughout the ventricle. The depolarization in the myocytes activates the Ca^{2+} channel of the sarcoplasmic reticulum, releasing Ca^{2+} into the cytosol. The Ca^{2+} then binds to troponin C, causing myofilament sliding to occur. This event also called cross-bridge contraction, which generates active tension resulting in deformation of the ventricles. The intracellular Ca^{2+} transient acts as the trigger to convert the electrical activation into a mechanical phenomenon. In our simulation, we obtained the Ca^{2+} information from the electrophysiological model from each myocardial cell and input it into the contractile myofilament dynamics model.

Electrical Model

The electrical mesh consists of 241,725 nodes with 1,298,751 elements forming in a tetrahedral shape. The mesh was embedded with Purkinje networks model, based on the study of Berenfeld and Jalife, on the endocardial boundary [20]. The Purkinje fiber was constructed from 2D line mesh, which then mapped onto the endocardial surface of the 3D ventricular mesh. The attachment of the Purkinje network was used only in the simulation under normal sinus rhythm condition. The electrical simulation includes multi-level electrophysiological activity: single cell activation and the propagation of the electrical signal in the ventricle tissue. The electrical propagation is expressed by solving a mono-domain partial differential equation which presented the current flow in the ventricles composed of myocytes connected by gap junctions. The single cell activation is expressed by solving a set of the ordinary differential equation which expressed the current flow through ion channels, pumps, and exchanger in the membrane and the sarcoplasmic reticulum. The electrophysiological cell model incorporated into our model was based on the work of ten Tusscher et al. [21] which includes epicardium, M-cell, and endocardium elements. The cell membrane is represented as a capacitor, and the ion channels are represented as the resistance. Ions traversing the cell membrane are represented as an electrical current passing through the capacitor and resistors. The electrophysiological behavior of this model can be described using the following differential equation

from Hodgkin and Huxley [22]:

$$C_m \frac{dV_m}{dt} = -(I_{ion} + I_{stim})$$

Where V is voltage, t is time, I_{ion} is the sum of all transmembrane ionic currents, I_{stim} is the external current stimulus, and C_m is the cell capacitance per unit surface area. The total ionic current I_{ion} is represented by:

$$I_{ion} = I_{Na} + I_{K1} + I_{to} + I_{Kr} + I_{Ks} + I_{Ca,L} + I_{Na,Ca} + I_{Na,K} + I_{p,Ca} + I_{p,K} + I_{b,Ca} + I_{b,Na}$$

Where I_{Na} is the fast sodium current, I_{K1} is the inward rectifier potassium current, I_{to} is the transient outward potassium current, I_{Kr} and I_{Ks} are rapid delayed rectifier and slow delayed rectifier potassium current, respectively, I_{CaL} is the L-type inward calcium current, I_{NaCa} is the sodium-calcium exchanger current, I_{NaK} is the sodium-potassium pump current, I_{pCa} is the plateau calcium current, I_{pK} is the plateau potassium current, I_{bCa} is the background calcium current, and I_{bNa} is the background sodium current. Based on the single cell model, the equation was modified to model the electrophysiological phenomena in 3D space. The 3D electrical propagation phenomenon can be described with the following partial differential equation:

$$\frac{dV}{dt} = -\frac{I_{ion} + I_{stim}}{C_m} + \frac{1}{\rho_x S C_m}\frac{\partial^2 V}{\partial x^2} + \frac{1}{\rho_y S C_m}\frac{\partial^2 V}{\partial y^2} + \frac{1}{\rho_z S C_m}\frac{\partial^2 V}{\partial z^2}$$

where ρ is the cellular resistivity with respect to the x, y, and z directions, and S is surface to volume.

To implement the properties of the V241F mutation into the signal cell and three-dimensional electrophysiological model, we modified the I_{Ks} of the ten Tusscher cell model with the equation of V241F mutation. We implemented the V241F mutation equation by Ki et al. which has been validated with experimental data [13].

Mechanical Model

The contraction and deformation of the ventricles were simulated according to the mechanical properties. To initiate myocytes contraction, Ca^{+2} arising from the electrical simulation under the V241F mutation was used as the input. Contraction of the ventricle was the result of active tension, as represented by the myofilament dynamics model of Rice et al. [23]. Ventricular deformation is described by the stress equilibrium equations of passive cardiac mechanics, with the myocardium assumed to be an orthotropic, incompressible, and hyperelastic material that has passive properties defined by an exponential strain energy function [24]. The mechanical mesh consists of 356 nodes with 172 Hermite (non-linear) elements. The ventricular contraction was calculated by solving the active myofilament model equations simultaneously with passive cardiac mechanics equation on each node of the finite-element mesh. The Rice et al. model is well-known to have a very good understanding describing excitation-contraction coupling phenomenon. The mechanical ventricular model was integrated with the lumped parameter model. The lumped model represented the systemic and pulmonic circulatory system based on a study by Kerckhoffs et al. [25]. The ATP consumption presented here is based on the rates of ATP consumed for myofilament contraction. The ATP consumption rate (E) is the outcome of cross-bridge detachment rate (g_{xbT}) and the single overlap fraction of thick filaments ($SOVF_{Thick}$):

$$E = g_{xbT} \times SOVF_{Thick}$$

Simulation Protocol

For the single cell simulation model, we applied a stimulus to the cell 30 times with a basic cycle length (BCL) of 1 s. The strength of the stimulus was 52 pA/pF and it was applied for 0.2 ms. After the cell reached a steady-state condition, we obtain the APD_{90}, I_{Ks} current, and APD restitution curve toward BCL and diastolic interval (DI) under WT, intermediate V241F, and pure V241F mutation conditions. APD_{90} was defined as the interval between the depolarization and repolarization at 90% of the AP upstroke, measured from the top.

Using a 3D electromechanical model, we analyzed the electrical propagation wave under two conditions: normal sinus rhythm and reentry/arrhythmia. We decreased the CV of the electrical propagation to 60 cm/s, and in the finite element model, we multiplied the constant of passive scaling level by 5 in the strain energy function to increase the stiffness of the myocardium tissue. During normal sinus pacing, the electrical stimulation was applied using a Purkinje network model with BCL of 600 ms for all three cases. The electrical signal propagation comes from the Purkinje networks is expressed by solving one-dimensional wave propagation equation which triggered the ventricle tissue activation. The simulation lasted for 42 s in order to reach a steady state was reached.

To simulate the reentry condition in 3D ventricular model, we used the standard S1-S2 protocol. S1 is an electrical stimulus which applied three times at the apex with 600 ms BCL. The S1 stimulus generated three planar wave-forms toward the base of the ventricle. The S2 is the protocol which reset the membrane potential in half of the ventricular medium to resting state. The S2 was applied just before the head of the third planar wave reach the base area. This protocol will allow the reentry to be generated toward the resting potential state nodes. The simulation time for the reentry condition was 10 s under the WT, intermediate V241F, and pure V241F mutation conditions.

Next, we coupled the transient Ca^{2+} data from the electrical simulation with those of the mechanical simulation. The mechanical simulation results for the normal sinus rhythm condition was taken from the last cycle of the simulation/steady-state. For the reentry, we used all 10 s data to compare the mechanical responses among the WT, intermediate V241F, and pure V214F mutation conditions during reentry. See the **Supplementary Material** regarding the electro-mechanical coupling technics.

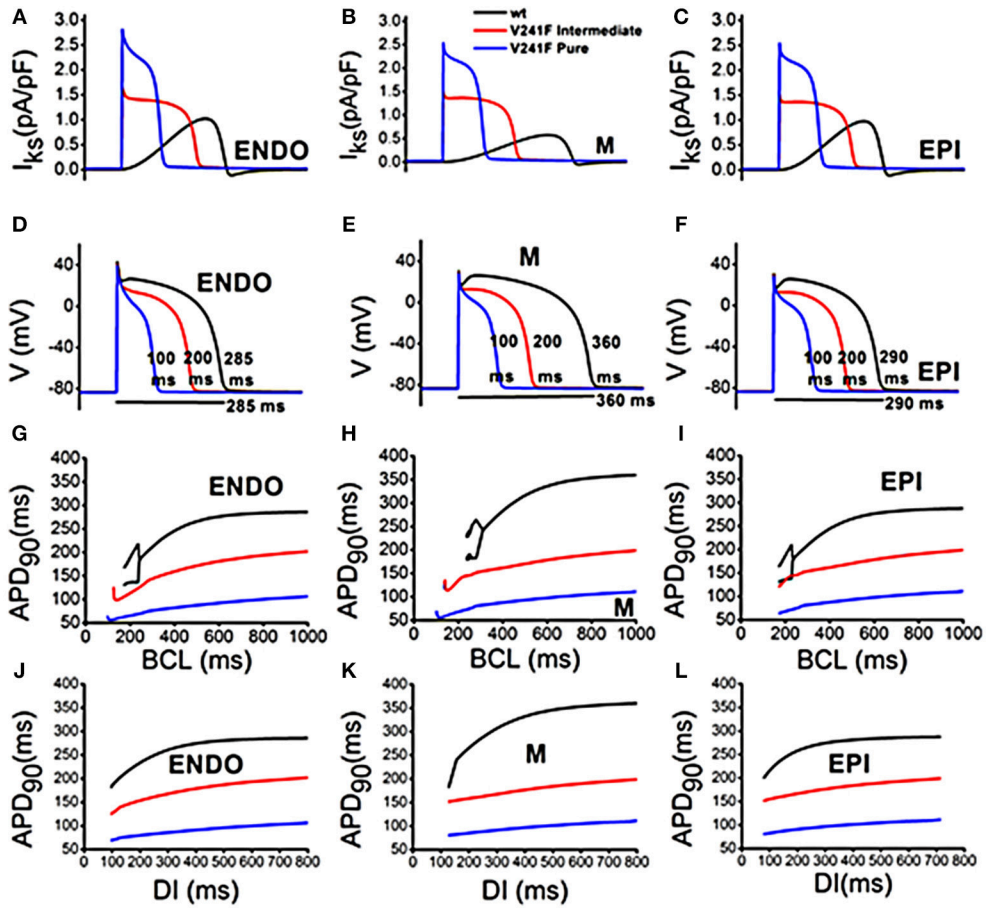

FIGURE 1 | Cardiac single cell response of WT and variants of intermediate and pure V241F mutation condition in 3 type of cell: **(A)** Slow delayed rectifier K^+ current (I_{Ks}) in endocardial cell **(B)** Slow delayed rectifier K^+ current (I_{Ks}) in mid-myocardial cell **(C)** Slow delayed rectifier K^+ current (I_{Ks}) in epicardial cell **(D)** APD profile in endocardial cell **(E)** APD profile in mid-myocardial cell **(F)** APD profile in epicardial cell **(G)** APD according to BCL in endocardial cell **(H)** APD according to BCL in mid-myocardial cell **(I)** APD according to BCL in epicardial cell **(J)** APD according to DI in endocardial cell **(K)** APD according to DI in mid myocardial cell **(L)** APD according to DI in epicardial cell.

Under the reentry condition, the spiral wave will be induced to the ventricular tissue. The altered activation of the electrical signal desynchronized the contractility of the ventricle. Hence the chaotic condition was exhibited, and quivering of the heart altered the LV pressure, aortic pressure, blood volume in the ventricles, and ATP consumption rates.

RESULTS

Single Cell Responses

Figure 1 compares cellular responses among the WT, V241F intermediate V241F, and pure V241F mutation conditions including I_{Ks} (**Figures 1A–C**), AP shape (**Figures 1D,E**), APD toward BCL (**Figures 1D,E**), and APD toward Di (**Figures 1J–L**). **Figures 1A–C** shows that V241F pure mutation has the highest I_{Ks} density compared to intermediate and WT conditions. Notice that the I_{Ks} current was activated during the depolarization for both intermediate and pure V241F conditions. This early activation of the I_{Ks} is consistent with the findings of Ki et al. in the atrium cell endowed with the V241F mutation [13]. Normally the I_{Ks} activated during repolarization. The pure V241F current was deactivated earlier compared to that under the intermediate and WT conditions. **Figures 1D–F** shows that the APD_{90} of the pure mutation was 100 and 200 ms under the intermediate conditions in endo, M-cell, and epicedial cell, respectively. In the ten Tusscher model, they differentiate the conductance of I_{Ks} and I_{to} to generate the AP shape for endo, M, and epicardium cell. Under the intermediate and pure V241F conditions, the I_{Ks} was activated in the earlier phase of AP, leaving its role at the repolarization time. As the result, the shape of AP for endo, M, and epicardium under intermediate and pure V241F become uniform. This means that the I_{Ks} has more significant impact than the I_{to} to compose the endo, M, and epi AP shape. In the comparison of APD toward the BCL, the alternant was observed in the M-cell under intermediate and V241F pure mutation at the 150 and 175 ms BCL, respectively.

Figure 2 shows the CV restitution curves under WT, intermediate and pure V241F mutation conditions. At BCL 700,

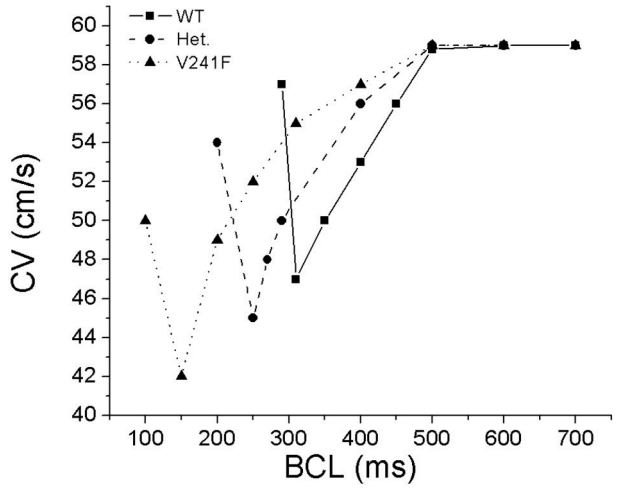

FIGURE 2 | Conduction velocity restitution curves obtained from a cable shape mesh by pacing at the left side of the mesh for 100 time under WT, intermediate (notified by Het.), and pure V241F mutation conditions.

600, and 500, the CV was all the same for the three conditions, 59 cm/s. The CV of the pure V241F mutation was decreased to 42 cm/s until BCL 150 ms. The CV of the pure V241F mutation was unstable at BCL 100 ms. The CV of the intermediate was remained to decrease until BCL 250 ms. However, the CV of the intermediate was increased at BCL 200. The CV of the WT was decreased steadily until BCL 300 ms. The CV was increased at BCL 290 ms. The increased BCL at the last point was due to alternant during the stimulation. The cell failed to generate action potential at the even stimuli. In results, the AP generation was skipped one cycle and exhibiting double BCL from what it is supposed to.

Three-Dimensional Ventricular Responses During Normal Sinus Rhythm

Figure 3 represents the transmembrane potential propagation in the 3D ventricular model during one cycle (600 ms) of sinus pacing. Even though all stimulations started at the same time, the pure V241F mutation condition showed a faster repolarization phase compared with the intermediate V241F and WT conditions. After the Purkinje firing the electrical signal to the ventricular tissue, under the V241F pure mutation condition, the membrane potential already in the repolarization phase at 140 ms indicated by the yellow color. Under the intermediate condition, the wavelength completely gone at the 340 ms. Under the WT condition, the wavelength was sustained to more than 340 ms.

Figure 4 shows the electrical activation time (EAT) that was put into our electromechanical model of ventricular heart failure (**Figure 4A**) and electrical deactivation time (EDT) (**Figure 4B**) for WT, V241F intermediate and pure mutation during one cycle of sinus rhythm. The EAT was the same under all three conditions (see **Figure 4A**). However, the EDT under the WT condition was longer compared with that of the intermediate V241F and pure V241F mutation conditions (**Figure 4B**). The pure V241F mutation condition had the lowest EDT which is associated with the short wavelength. The EDT results indicated that the pure V241F mutation had faster repolarization than the intermediate V241F and WT conditions. The maximum and minimum EAT and EDT values for all three conditions are given in **Figure 4C**.

Table 1 shows the ventricular mechanical responses during normal sinus pacing (one cycle) under the WT, intermediate V241F, and pure V241F mutation conditions. The stroke volume (SV), stroke work (SW), and ejection fraction (EF) were decreased under intermediate V241F mutation condition and further decreased under the pure V241F mutation condition. The SV reach 44 mL under the WT condition, and 36 and 32 mL under the intermediate V241F and the pure V241F mutation conditions, respectively. SW indicates the performance of ventricle during contraction. The SW of WT condition was 4,566 mmHg mL. In the case of pure V241F mutation, the SW indicated the lowest performance, having a value of 3,315 mmHg mL. The contractile adenosine three phosphate (ATP) consumption rates under the intermediate V241F mutation and WT conditions were 92 and 166 s^{-1}, respectively. Under the pure mutation condition, the ATP consumption rate dropped to 84 s^{-1}.

Three-Dimensional Ventricular Responses During Reentry

Figure 5A shows the snapshot view of arrhythmia under the WT, intermediate V241F, and pure V241F mutation conditions. In our simulation, the reentry wave was sustained until the end of simulation for all three condition. Nevertheless, the center of rotation of the spiral wave appeared in a different place for each conditions. However, from the snapshot, we can see that pure V241F mutation condition had the shortest wavelength among all three conditions. This accorded with the APD_{90} of the pure V241F mutation also being the shortest APD_{90} (**Figure 5B**).

Figure 6 illustrates the mechanical responses, including the LV pressures (**Figure 6A**), the LV volume (**Figure 6B**), LV pressure-volume relation (**Figure 6C**), and contractile ATP consumption rates (**Figure 6D**) during 10 s of reentry under the WT, intermediate V241F, and pure V241F mutation conditions. The figures on the right-hand side correspond to the last 1 s of the mechanical responses, i.e., the steady state condition. According to the LV pressure data, the peak ventricular pressure was 30 mmHg for the pure V241F mutation, 35 mmHg for the intermediate V241F condition, and 42 mmHg for the WT condition. The short APD_{90} under the mutation conditions resulted in reduced calcium activation in the myocytes; thus, the mutation conditions showed poorer contractility. A short wavelength under the mutation conditions caused faster reentry and increased the electrical activation rate, thus producing a more chaotic condition. We can see from the LV pressure graph that the pure V241F mutation condition had the highest ventricular beating frequency over 1 s (right side of **Figure 6**). The ventricular beat rate was 420 bpm for the pure V241F mutation, 300 bpm for the intermediate V241F mutation, and 240 bpm for the WT condition.

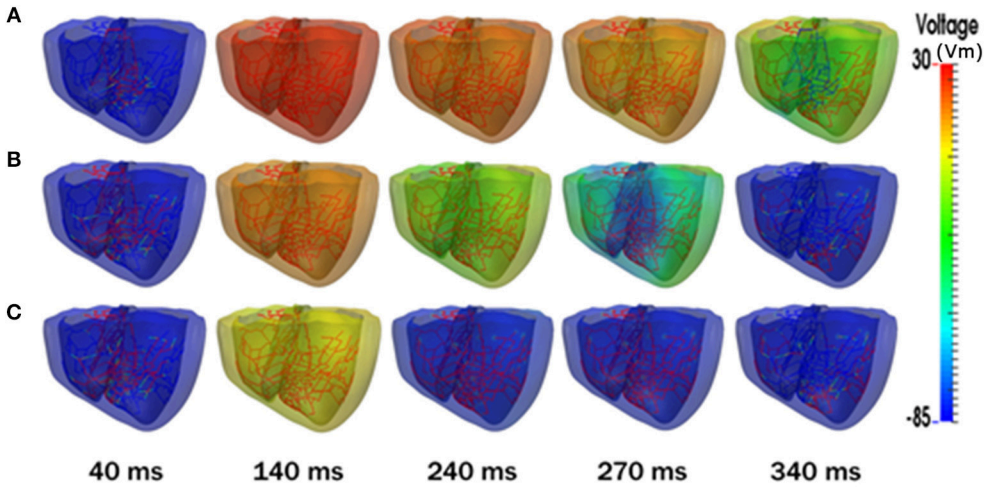

FIGURE 3 | Snapshots of transmural distribution of membrane potential during one cycle of sinus pacing. **(A)** WT, **(B)** V241F Intermediate, **(C)** V241F Pure conditions in the 3D ventricular tissue model.

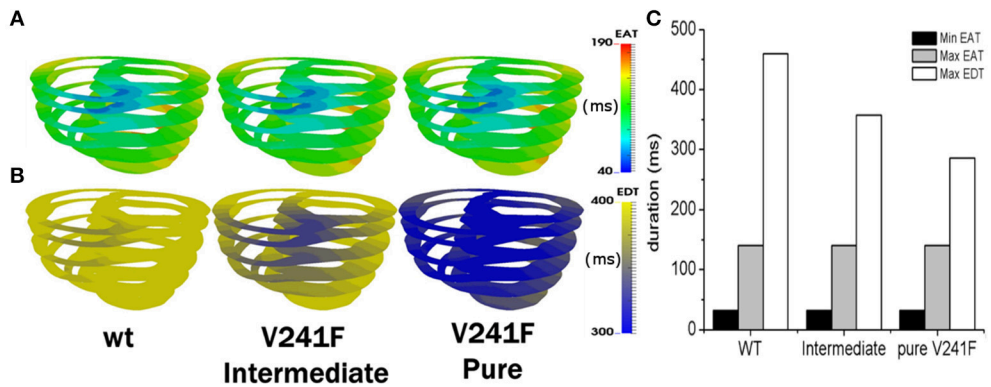

FIGURE 4 | EAT during one cycle of sinus pacing for WT, V241F intermediate and Pure Condition. **(A)** EAT mapped on ventricle model, **(B)** EDT mapped on ventricle model. **(C)** Comparison graph of minimum EAT, maximum EAT, and maximum EDT.

According to LV volume graph (**Figure 6B**), the pure V241F mutation had the highest blood volume in the LV. The pure V241F mutation had a blood volume of 55 mL when it reached the steady-state of reentry. However, the intermediate V241F and WT conditions had similar steady state blood volumes of 34 and 33 mL, respectively. The larger volume in the pure V241F mutation condition was related to the LV pressure (**Figure 6A**); under this condition, the ventricle had the lowest contractility, which was insufficient for ejecting the blood.

Figure 6C shows the LV pressure-volume relation under reentry condition for all three cases. As the figure shows, the pure V241F mutation condition had the highest volume, while its LV pressure was the lowest compared to the intermediate V241F mutation and WT conditions, representing a very weak contraction. Thus, under a steady state of reentry condition (**Figure 6C** right side), it shows that the pure mutation has the smallest amount of SV and SW. The LV pressure under the intermediate V241F mutation condition ranged at 24–35 mmHg with LV volume ranged at 32–34 mL. Under the WT condition, the LV pressure ranged at 21–42 mmHg with the LV volume ranged at 31–33 mmHg.

Figure 6D shows the ATP consumption rate for all three cases during reentry. The contractile ATP consumption rate for the pure V241F mutation was the lowest, which accord with the PV curves results (see **Figure 6C**) showing that, because of pure mutation condition relatively little energy could be consumed, the pressure of the ventricle was insufficient to pump the blood efficiently.

During reentry or fibrillation, because of the chaotic electrical events, the hemodynamics of the heart was seriously altered under the WT, intermediate, and pure V241F mutation conditions (**Figure 6**). All three conditions showed poor pumping contraction capabilities with the pure V241F being the worst condition. The frequency of the LV pressure was very high with the blood remaining steady in the LV.

DISCUSSION

Using a single cell and three-dimensional electromechanical model of human ventricle, this study investigated the effect of the V241F *KCNQ1* mutation during normal sinus rhythm and reentry using a computational method. The method to couple the electrical and the mechanical compartment as well as the lumped circulatory model is based on the study of Gurev et al. [18, 19]. This is the first study to implement a finite element-based electromechanical model for the heart to investigate cardiac electrophysiology and the mechanism underlying the V241F KCNQ1 mutation. The major findings of our research are as follows:

1. Similarly to the atrial cell by Ki et al. [13], in a single cell simulation that was applied to three types of ventricle cellular model (endo, M-cell, epi), V241F mutation activates the I_{Ks} channel during depolarization phase (activated early) and it increased the I_{Ks} density (**Figures 1A–C**). This is the caused for the short APD_{90}.
2. Under the 3D model of normal sinus rhythm condition, repolarization showed faster acceleration during sinus pacing under the V241F pure mutation condition compared with the intermediate V241F mutation and WT conditions (**Figure 3**). With the same CV, the EAT of the three cases were the same except for the EDT (**Figure 4**). The SV, SW, and EF under sinus rhythm were lowered under the intermediate condition, even worst under that V241F pure mutation condition (**Table 1**).
3. During the reentry phase, the pure V241F mutation generated the shortest membrane potential propagation wave (**Figure 5A**) among all three conditions.
4. The mechanical response of pure V241F mutation has the lowest LV pressure, highest LV volume, and lowest ATP consumption rates during reentry.

TABLE 1 | Ventricular mechanical responses during sinus rhythm under WT, V241F intermediate, and V241F pure mutation conditions.

Variant type	WT	V241F intermediate	V241F pure
End diastolic volume (mL)	76	83	85
End systolic volume (mL)	32	47	53
Stroke volume (mL)	44	36	32
LV systolic pressure (mmHg)	125	127	127
Stroke work (mmHg mL)	4,566	3,693	3,315
ATP consumption rate (s^{-1})	163	92	84
Mean left atrial pressure (mmHg)	14	13	15
Mean aortic pressure (mmHg)	99	99	102
Ejection fraction (%)	58	43	38

The single cell electrophysiological responses showed that the KCNQ1 mutation activates the I_{Ks} channel during depolarization time with a high density of current. This early activation force the vast amount of positive ions to leave early out of the myocytes abbreviated the APD during repolarization time significantly (**Figure 1**). These results are consistent with the study by Ki et al. which of the mutation was occurred in the atrium cell [13]. The APD_{90} shortening due to the V214F mutation makes the short wavelength hence short QT wave. This increases the fatal effect since the short QT syndrome is associated with VF which could lead to sudden cardiac death [15]. The wavelength shortening owing to the mutation was observed under normal sinus rhythm and reentry conditions (**Figures 3**, **5**).

The low performance of ventricular contractility under sinus rhythm condition is described in **Table 1**. The pure V241F mutation showed the lowest SV, SW, EF, and ATP consumption

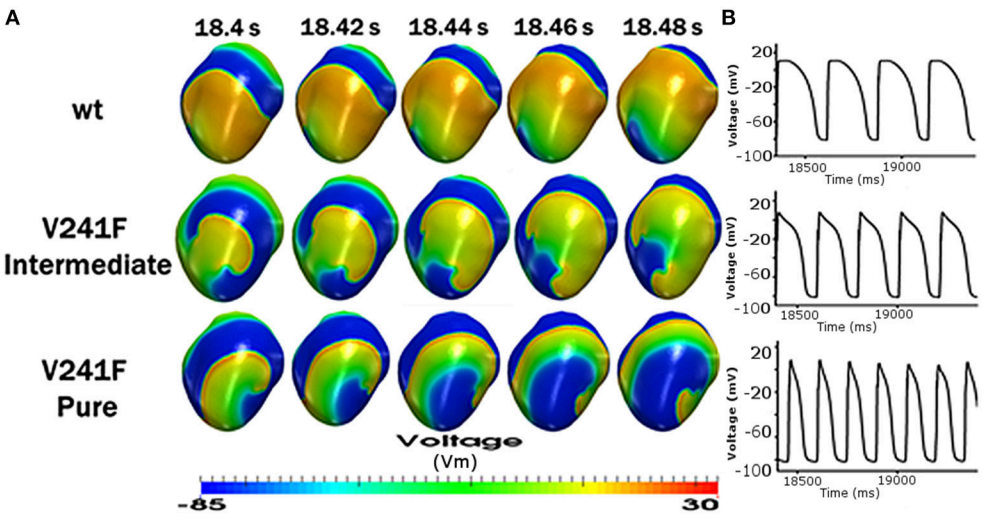

FIGURE 5 | Reentrant dynamics wave in the 3D ventricular tissue model for WT and V241F mutation conditions. **(A)** Snapshot of trans mural distribution of wt condition (top), Snapshot of trans mural distribution of V241F Intermediate (center), Snapshot of trans mural distribution of V241F Pure (bottom) of membrane potential; and **(B)** time traces of action potentials (AP) in 1 s.

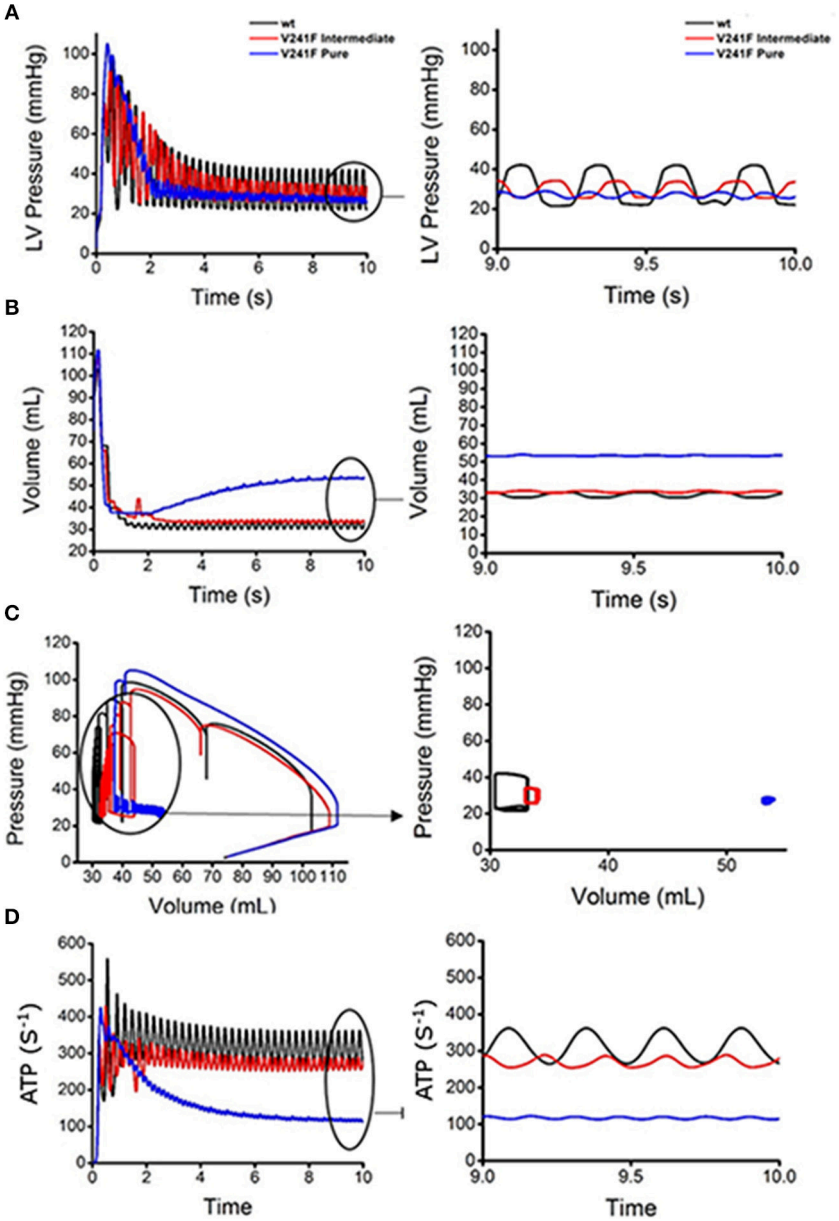

FIGURE 6 | Ventricular mechanical responses of reentrant dynamics wave in the 3D ventricular tissue model for WT, V241F intermediate and pure condition. **(A)** LV pressure waveforms, **(B)** LV volume waveforms, **(C)** LV pressure-volume curves and **(D)** ATP curves for WT, V241F Intermediate, and Pure mutation conditions.

rates compared to the intermediate V241F mutation and WT conditions. The poor activation of the mechanical responses is related to the APD abbreviation. Short APD means the time for Ca^{+2} activation was also decreased. Since the Ca^{+2} is the trigger for myofilament sliding or cross-bridge activation, short Ca^{+2} activation time would decrease the ventricular pumping efficacy.

During reentry, the V241F mutations (intermediate and pure) shortened the electrical propagation wavelength (**Figure 5A**) and increased the frequency of the electrical activation especially to the nodes close to the center of the rotor (**Figure 5B**). Under the WT condition, the wavelength was two times longer to that under pure mutation condition. The AP shape and the frequency of the activation at specific node were aligned in **Figure 5**.

To compare the hemodynamic responses under the WT, intermediate, and pure V241F mutation during reentry, we present the LV pressure waveform, LV volume waveform, LV Pressure-Volume (PV) curve, and contractile ATP consumption rate. Our results showed that the V241F mutation (intermediate and pure) decreased the LV pressure (**Figure 6A**) and ATP consumption rate (**Figure 6D**) during reentry. Because the pressure of the LV was low, there was insufficient strength to pump the blood out of the ventricles, resulting in the

accumulation of blood inside the ventricles (**Figure 6B**). The relationship between the pressure and volume waveforms of the LV is described by the PV curve. The pure V241F mutation condition showed the smallest loop during reentry (**Figure 6C**). The pressure's waveforms vary with the ATP consumption rate among all three conditions (**Figure 6D**).

Our results show that the electrophysiological activation is strongly related to the ventricular pumping under both sinus rhythm contraction and reentry scenarios under WT, intermediate, and V241F pure mutation conditions. The alteration to the electrical activation would cause abnormality of the hemodynamics of the heart. In this case, the shortening of APD_{90} due to the V241F mutation lowered the pumping performance of that under the intermediate condition and even more with that under pure mutation condition.

This study demonstrated mechanistically the effect of the V241F mutation on the electrical activation and also mechanical pumping behavior under sinus rhythm and reentry condition. The gain of function of the I_{Ks} channel lowers the pumping efficacy by altering the APD_{90}, thus shortened the electrical activation wavelength. The clinical impact of this study is that the ratio of the APD_{90} shortening in the myocytes by the V241F mutation can be used as a reference for the cardiologist expert to decide the appropriate pharmacology of I_{Ks} conductance block for the patient. Previous studies indexed pharmacological substances related to voltage-gated potassium channels [26, 27]. Although further investigation, such as *in vivo* or *in vitro* test should be conducted.

LIMITATIONS

There were several limitations to this study that should be addressed. We used isotropic conductivity for the electrical propagation through tissue. The electromechanical model we used is a one-directional coupling model. We coupled the electrical activation to the mechanical contraction by giving the mechanical model the information of the Ca^{2+} transient from the electrical simulation. The mechano-electrical feedback was not considered in this study. For example, stretch-activated channel [28] was not implemented and the information of contractile energy consumption was not fed back to the electrical model. The energy consumption was calculated to quantify the mechanical activity of the ventricle. The experimental study about the V241F mutation on the ventricle, to our best knowledge, is not available yet. Hence it becomes a constraint to explicitly validate this computational prediction.

In conclusions, the effect of the two variants of V241F (intermediate and pure) mutation not only disturbed the electrophysiological events but also affected the mechanical behavior significantly. Within a single cell, the pure V241F mutation shortened the ventricular APD_{90} of M-cell by 73 and 45% under the pure and intermediate V241F mutations, respectively. In the 3D electrical model of normal sinus rhythm and reentry, the APD of the intermediate and pure V241F mutation conditions was significantly shortened vs. the WT, which prone to VF situation. As a result, the mechanical responses associated with a normal sinus rhythm under the V241F mutation conditions consumed less ATP, and showed a decreased EF, SV, and SW. Hemodynamic function during reentry was impaired by the V241F mutation, resulting in very weak heart contractility and an accumulation of blood in the LV.

AUTHOR CONTRIBUTIONS

AH ran the simulation, organized the results, and constructed and wrote the manuscript according to the theory and the results of the study. FR ran parts of the simulation of this study. KL guided and supervised the authors starting from the theoretical study, simulation, and finalization of the paper.

ACKNOWLEDGMENTS

This research was partially supported by the MSIT (Ministry of Science, ICT), under the ITRC (Information Technology Research Center) support program (IITP-2018-2014-0-00639) supervised by the IITP, and NRF (National Research Foundation) under basic engineering research project (2016R1D1A1B0101440) and the EDISON (NRF-2011-0020576) Programs.

SUPPLEMENTARY MATERIAL

The Supplementary Material for this article can be found online at: https://www.frontiersin.org/articles/10.3389/fphy.2018.00147/full#supplementary-material

REFERENCES

1. Benjamin EJ, Blaha MJ, Chiuve SE, Cushman M, Das SR, Deo R, et al. Heart disease and stroke statistics—2017 update: a report from the American Heart Association. *Circulation* (2017) 135:e146–603. doi: 10.1161/CIR.0000000000000485
2. Jalife J. Ventricular fibrillation: mechanisms of initiation and maintenance. *Ann Rev Physiol.* (2000) 62:25–50. doi: 10.1146/annurev.physiol.62.1.25
3. Zipes DP, Wellens HJ. Sudden cardiac death. *Circulation* (1998) 98:2334–51. doi: 10.1161/01.CIR.98.21.2334
4. Myerburg R, Kessler K, Interian A Jr., Fernandez P, Kimura S, Kozlovskis P, et al. Clinical and experimental pathophysiology of sudden cardiac death. In: *Cardiac Electrophysiology: From Cell to Bedside, 1st Edn.* Philadelphia, PA: WB Saunders Co (1990). p. 666–78.
5. Weiss JN, Garfinkel A, Karagueuzian HS, Qu Z, Chen P-S. Chaos and the transition to ventricular fibrillation. *Circulation* (1999) 99:2819–26. doi: 10.1161/01.CIR.99.21.2819
6. Chen PS, Garfinkel A, Weiss JN, Karagueuzian HS. Spirals, chaos, and new mechanisms of wave propagation. *Pacing Clin Electrophysiol.* (1997) 20:414–21. doi: 10.1111/j.1540-8159.1997.tb06200.x
7. Karma A. Electrical alternans and spiral wave breakup in cardiac tissue. *Chaos* (1994) 4:461–72. doi: 10.1063/1.166024
8. Hsiao P-Y, Tien H-C, Lo C-P, Juang J-MJ, Wang Y-H, Sung RJ. Gene mutations in cardiac arrhythmias: a review of recent evidence in ion channelopathies. *Appl Clin Genet.* (2013) 6:1–13. doi: 10.2147/TACG.S29676
9. Wilde AA, Bezzina CR. Genetics of cardiac arrhythmias. *Heart* (2005) 91:1352–8. doi: 10.1136/hrt.2004.046334

10. Roden DM, Balser JR, George AL Jr, Anderson ME. Cardiac ion channels. *Ann Rev Physiol.* (2002) 64:431–75. doi: 10.1146/annurev.physiol.64.083101.145105
11. Shih H-T. Anatomy of the action potential in the heart. *Tex Heart Inst J.* (1994) 21:30–41.
12. Hu H, Sachs F. Stretch-activated ion channels in the heart. *J Mol Cell Cardiol.* (1997) 29:1511–23. doi: 10.1006/jmcc.1997.0392
13. Ki C-S, Jung CL, Kim H-j, Baek K-H, Park SJ, On YK, et al. A KCNQ1 mutation causes age-dependant bradycardia and persistent atrial fibrillation. *Pflügers Arch.* (2014) 466:529–40. doi: 10.1007/s00424-013-1337-6
14. Sanguinetti M, Curran M, Zou A, Shen J, Specter P, Atkinson D, et al. Coassembly of KvLQT1 and minK (IsK) proteins to form cardiac IKs potassium channel. *Nature* (1996) 384:80–3. doi: 10.1038/384080a0
15. Gussak I, Brugada P, Brugada J, Wright RS, Kopecky SL, Chaitman BR, et al. Idiopathic short QT interval: a new clinical syndrome? *Cardiology* (2000) 94:99–102. doi: 10.1159/000047299
16. Imaniastuti R, Lee HS, Kim N, Youm JB, Shim EB, Lim KM. Computational prediction of proarrhythmogenic effect of the V241F KCNQ1 mutation in human atrium. *Prog Biophys Mol Biol.* (2014) 116:70–5. doi: 10.1016/j.pbiomolbio.2014.09.001
17. Lim KM, Constantino J, Gurev V, Zhu R, Shim EB, Trayanova NA. Comparison of the effects of continuous and pulsatile left ventricular-assist devices on ventricular unloading using a cardiac electromechanics model. *J Physiol Sci.* (2012) 62:11–9. doi: 10.1007/s12576-011-0180-9
18. Gurev V, Constantino J, Rice J, Trayanova N. Distribution of electromechanical delay in the heart: insights from a three-dimensional electromechanical model. *Biophys J.* (2010) 99:745–54. doi: 10.1016/j.bpj.2010.05.028
19. Gurev V, Lee T, Constantino J, Arevalo H, Trayanova NA. Models of cardiac electromechanics based on individual hearts imaging data. *Biomech Model Mechanobiol.* (2011) 10:295–306. doi: 10.1007/s10237-010-0235-5
20. Berenfeld O, Jalife J. Purkinje-muscle reentry as a mechanism of polymorphic ventricular arrhythmias in a 3-dimensional model of the ventricles. *Circ Res.* (1998) 82:1063–77. doi: 10.1161/01.RES.82.10.1063
21. Ten Tusscher KH, Panfilov AV. Alternans and spiral breakup in a human ventricular tissue model. *Am J Physiol Heart Circ Physiol.* (2006) 291:H1088–100. doi: 10.1152/ajpheart.00109.2006
22. Hodgkin AL, Huxley AF. A quantitative description of membrane current and its application to conduction and excitation in nerve. *J Physiol.* (1952) 117:500–44. doi: 10.1113/jphysiol.1952.sp004764
23. Rice JJ, Wang F, Bers DM, De Tombe PP. Approximate model of cooperative activation and crossbridge cycling in cardiac muscle using ordinary differential equations. *Biophys J.* (2008) 95:2368–90. doi: 10.1529/biophysj.107.119487
24. Holzapfel GA, Ogden RW. Constitutive modelling of passive myocardium: a structurally based framework for material characterization. *Philos Trans R Soc Lond A* (2009) 367:3445–75. doi: 10.1098/rsta.2009.0091
25. Kerckhoffs RC, Neal ML, Gu Q, Bassingthwaighte JB, Omens JH, McCulloch AD. Coupling of a 3D finite element model of cardiac ventricular mechanics to lumped systems models of the systemic and pulmonic circulation. *Ann Biomed Eng.* (2007) 35:1–18. doi: 10.1007/s10439-006-9212-7
26. Li G-R, Dong M-Q. Pharmacology of cardiac potassium channels. *Adv Pharmacol.* (2010) 59. 93–134. doi: 10.1016/S1054-3589(10)59004-5
27. Tamargo J, Caballero R, Gómez R, Valenzuela C, Delpón E. Pharmacology of cardiac potassium channels. *Cardiovasc Res.* (2004) 62:9–33. doi: 10.1016/j.cardiores.2003.12.026
28. Hu Y, Gurev V, Constantino J, Bayer JD, Trayanova NA. Effects of mechano-electric feedback on scroll wave stability in human ventricular fibrillation. *PLoS ONE* (2013) 8:e60287. doi: 10.1371/journal.pone.0060287

Conflict of Interest Statement: The authors declare that the research was conducted in the absence of any commercial or financial relationships that could be construed as a potential conflict of interest.

frontiers in Physiology

ORIGINAL RESEARCH
published: 10 December 2018
doi: 10.3389/fphys.2018.01760

Computational Model of Calcium Signaling in Cardiac Atrial Cells at the Submicron Scale

*Miquel Marchena and Blas Echebarria**

Departament de Física, Universitat Politècnica de Catalunya, Barcelona, Spain

In cardiac cells, calcium is the mediator of excitation-contraction coupling. Dysfunctions in calcium handling have been identified as the origin of some cardiac arrhythmias. In the particular case of atrial myocytes, recent available experimental data has found links between these dysfunctions and structural changes in the calcium handling machinery (ryanodine cluster size and distribution, t-tubular network, etc). To address this issue, we have developed a computational model of an atrial myocyte that takes into account the detailed intracellular structure. The homogenized macroscopic behavior is described with a two-concentration field model, using effective diffusion coefficients of calcium in the sarcoplasmic reticulum (SR) and in the cytoplasm. The model reproduces the right calcium transients and dependence with pacing frequency. Under basal conditions, the calcium rise is mostly restricted to the periphery of the cell, with a large concentration ratio between the periphery and the interior. We have then studied the dependence of the speed of the calcium wave on cytosolic and SR diffusion coefficients, finding an almost linear relation with the former, in agreement with a diffusive and fire mechanism of propagation, and little dependence on the latter. Finally, we have studied the effect of a change in RyR cluster microstructure. We find that, under resting conditions, the spark frequency decreases slightly with RyR cluster spatial dispersion, but markedly increases when the RyRs are distributed in clusters of larger size, stressing the importance of RyR cluster organization to understand atrial arrhythmias, as recent experimental results suggest (Macquaide et al., 2015).

Keywords: calcium modeling, atrial cells, local calcium signaling, calcium release unit, ryanodine receptor

OPEN ACCESS

Edited by:
Simonetta Filippi,
Università Campus Bio-Medico, Italy

Reviewed by:
Sonia Cortassa,
National Institutes of Health (NIH), United States
Sanjay Ram Kharche,
University of Western Ontario, Canada

****Correspondence:***
Blas Echebarria
blas.echebarria@upc.edu

Specialty section:
This article was submitted to Computational Physiology and Medicine, a section of the journal Frontiers in Physiology

Received: *05 December 2018*
Accepted: *21 November 2018*
Published: *10 December 2018*

Citation:
Marchena M and Echebarria B (2018) Computational Model of Calcium Signaling in Cardiac Atrial Cells at the Submicron Scale. Front. Physiol. 9:1760. doi: 10.3389/fphys.2018.01760

1. INTRODUCTION

Calcium is one of the most important intracellular messengers, and thus the mechanisms that control the intracellular free calcium concentration are of fundamental physiological importance (Berridge, 1997). For instance, Ca^{2+} takes part in oocyte activation at fertilization (Poenie et al., 1985), axonal growth (Bixby and Harris, 1991), cell migration (Huttenlocher et al., 1997), gene expression (Bading et al., 1993), formation of nodules in plant root hairs (Ehrhardt et al., 1996), development of muscle (Ford and Podolsky, 1972), release of cytokines from epithelial cells (Kaufman and Roizman, 1989), cell death (Schanne et al., 1979; Farber, 1981), and excitation-contraction coupling in muscle cells (Fabiato and Fabiato, 1979).

In cardiac cells, calcium dysregulation has been related to the appearance of arrhythmias and sudden cardiac death. A life-threatening arrhythmia, fibrillation, results when an electrical wavebreak induces reentry and triggers a cascade of new wavebreaks. Ventricular fibrillation (VF) is the most common cause of sudden death, whereas atrial fibrillation (AF), the most prevalent clinical arrhythmia, accounts for nearly one third of strokes in the elderly (Weiss et al., 2005). Clinically, AF duplicates the mortality rate and increases the risk of ictus (in which poor blood flow to the brain results in cell death) 5-fold. In spite of this the treatment of AF remains deficient or inefficient, because of the incomplete knowledge of the complex pathophysiology of this disease. Often, AF has been linked to a dysregulation in the dynamics of intracellular calcium, thus the importance of a good knowledge of calcium handling dynamics in the cell. On the other hand, in the last ten years, the refinement of the experimental techniques, such as STED and dSTORM (Hell and Wichmann, 1994; Izu et al., 2006; Soeller and Baddeley, 2013) has provided, for instance, a link between the calcium handling microstructure and the occurrence of cardiac diseases, as AF (Macquaide et al., 2015), prompting the quest for more detailed models of calcium handling, able to mechanistically explain this relation.

Inside cardiac cells, most intracellular calcium is stored in a complex structure called sarcoplasmic reticulum (SR), see **Figure 1**. Ca^{2+} is released from this internal network via the Ryanodine Receptors (RyR, Franzini-Armstrong and Protasi, 1997) when a threshold calcium concentration in the cytoplasm is achieved. This happens due to a small influx of calcium through the L-type calcium channels (LCC) during the cardiac action potential. This current triggers calcium release from the SR by activating the RyRs. RyRs open and close collectively in clusters forming functional units known as Calcium Release Units (CaRU), which are often confronted to a cluster of LCCs. In each CaRU the number of RyR and LCC is small (of the order of 10–100 of the former and 5–10 of the latter), thus its dynamics is intrinsically stochastic. CaRUs are distributed inside the cell, resulting in random and discrete Ca^{2+} release events, known as Ca^{2+} sparks (Cheng et al., 1994). A Ca^{2+} spark has been considered as the unitary dynamical element which produces the cellular Ca^{2+} dynamics, such as Ca^{2+} waves and oscillations (Falcke, 2003). The (seemingly deterministic) global calcium signal appears from the coordination of several tens of thousands of these CaRUs.

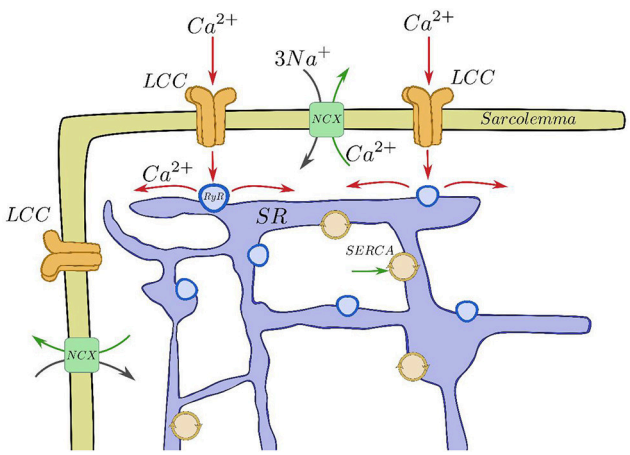

FIGURE 1 | Basic components of the CICR process. Calcium enters through the LCCs, stimulating release from the RyRs, that then is reuptaken into the SR by SERCA and taken out of the cell by the sodium-calcium exchanger.

After the excitation process, Ca^{2+} removal allows relaxation of the cardiac muscle. This requires Ca^{2+} transport out of the cytoplasm by several pathways. The concentration in the SR is recovered by the active pumping of calcium from the cytoplasm to the SR carried out by the Sarcoplasmic Reticulum Ca^{2+}-ATPase (SERCA). Moreover, the Na-Ca exchanger pumps Ca^{2+} out of the cell. The whole process described is called calcium-induced calcium release (CICR, Berridge, 1993; Clapham, 1995). CaRUs not just couple SR and cytoplasm Ca^{2+} concentrations via Ca^{2+} release but they are also correlated due to the Ca^{2+} diffusion in both domains. Therefore, the behavior of a single CaRU depends on the behaviors of the neighboring CaRUs.

Even though the same mechanism (CICR) triggers the transient elevation of Ca^{2+} in both ventricular and atrial myocytes, there are substantial differences in the intracellular structures. The absence of transversal tubules (t-tubules) in atrial myocytes produces inhomogeneous spatio-temporal calcium patterns when the CICR occurs. In particular, the excitation starts at the cell membrane and then propagates inward, resulting in a delay in activation time between the subsarcolemma and the cell interior. This is a key difference between atrial and ventricular cells. In the latter, the opening of LCC channels along the t-tubules triggers the release of calcium from the SR, resulting in a homogenized calcium pattern. In the former, this trigger is due to the inward wave.

Detailed models of calcium handling have been first developed for ventricular cells, including the stochastic modeling of each individual CaRU, coupled then by diffusion. In this framework, each CaRU is typically divided into different subcompartments, in which the calcium concentration is assumed to be homogeneous (Restrepo et al., 2008; Rovetti et al., 2010), although some recent models consider also calcium diffusion within the CaRU (Nivala M. et al., 2012). These models have been very successful in reproducing several calcium dysfunctions, such as calcium alternans (Restrepo et al., 2008; Rovetti et al., 2010; Alvarez-Lacalle et al., 2015) or spontaneous calcium release induced delayed afterdepolarizations (Song et al., 2015). Current advances in microscopy have allowed the development of very detailed models of calcium release at the level of the CaRU, including realistic shape of the SR, the RyR cluster, myofibrils and the mitochondria (Kekenes-Huskey et al., 2012; Hatano et al., 2013; Hake et al., 2014; Rajagopal et al., 2015).

Modeling is less developed for the case of atrial cells (Heijman et al., 2016). Common pool models, in which calcium concentration is considered to be homogeneous in each of several compartments (SR, cytosol, dyadic space, etc) have been developed for rabbit (Lindblad et al., 1996), dog (Ramirez et al., 2000), mouse (Davies et al., 2014), and human (Courtemanche et al., 1998; Nygren et al., 1998; Grandi et al., 2011; Lugo

et al., 2014). One of the first models that took into account inward wave propagation was by Koivumäki et al. (2011), where the bulk cytoplasm and SR spaces were divided into several compartments, being thus a one-dimensional model, allowing for centripetal but not lateral diffusion. A similar model was also used by Li et al. (2012), showing the presence of alternans. A model allowing for both centripetal and lateral diffusion, as well as stochastic RyR gating was developed by Voigt et al. (2013), in order to study the mechanisms of after-depolarizations and triggered activity in paroxysmal atrial fibrillation. Calcium wave initiation and propagation has been considered by Thul et al. (2012) in a three-dimensional geometry, assuming a diffuse and fire model for calcium release. Finally, Macquaide et al. (2015) developed a detailed three-dimensional bidomain model of calcium propagation to study intra-CaRU cluster interactions, supporting the idea that cluster fragmentation and redistribution sustains atrial fibrillation through the enhancement of calcium release.

Still, there are several open questions regarding CICR in atrial cells. To name some: (1) the role of buffers, RyR sensitivity and the level of cytosolic calcium in calcium wave propagation; (2) the effect of the RyR cluster spatial structure and size distribution; (3) the role of t-tubules (if present). Most subcellular ventricular and atrial models (Restrepo et al., 2008; Rovetti et al., 2010; Voigt et al., 2013) consider the cell divided into several thousands of functional units (CaRUs). Each CaRU is then divided into different compartments, replicating at the subcellular scale the structure of common pool models. Despite the success of such models to replicate calcium transients and spark characteristics, they are not well-suited to study the effects of changes in the microstructure (position of the RyR clusters, inhomogeneities, etc). Rather, to study the effect of RyR cluster distribution on wave propagation, continuum models of calcium diffusion with point release sites have been considered, although often with simplified release dynamics (Izu et al., 2006; Thul et al., 2012, 2015; Øyehaug et al., 2013). On the other hand, very detailed models at the level of the CaRU (Hake et al., 2014) are very demanding computationally, and typically not well-suited to study effects that require of long simulation times, as calcium homeostasis or spark rates. With that in mind, we present a subcellular calcium atrial model where the homogenized local behavior is described with a two-concentration field model, using effective diffusion coefficients of calcium in the SR and in the cytoplasm, with stochastic gating of the RyRs and LCCs. This model follows the spirit of earlier bidomain models (Jafri and Keizer, 1995; Keener and Sneyd, 1998), defining at each point in space cytosolic and SR calcium concentrations, with given volume fractions (Keizer and De Young, 1992). The model presents some important characteristics: (1) a very fine discretization, making it possible to describe (even if coarsely) the RyR cluster structure; (2) incorporation of the cell structure with distinction between z-lines and normal cytosol in terms of the volume ratio of SR and cytosolic volumes, diffusion constants and presence of buffers; (3) freedom to set the center of the RyR clusters arbitrarily, that do not need to be disposed in an homogeneous regular grid. In this paper, we focus on the effect of CaRU spatial structure and distribution, and find that a more disordered distribution of the CaRUs presents a lower frequency of sparks in resting conditions. On the contrary, when the spatial distribution is maintained constant, but the RyRs are distributed in a smaller number of larger CaRUs (so the total number of RyRs remains constant), the spark frequency increases, in accordance with experimental results in cells presenting AF (Macquaide et al., 2015).

2. METHODS

Our computational model performs single cell simulations and is based on homogenization (Goel et al., 2006). Although it is well-known that the SR forms a branching network (largely interconnected), with an interior that is distinct from the cell cytoplasm, this fact has largely been ignored, with most models making the a priori assumption that a Ca^{2+} concentration for both the SR and the cytoplasm can be defined at each point in space. So that, the cytoplasm and the SR are assumed to coexist at every point in space. For this reason, a fraction of each volume is occupied by the cytoplasm (ν_i) and the complementary fraction by the SR (ν_{sr}), given that $\nu_i + \nu_{sr} = 1$.

We define c_i, c_{sr}, and c_{bi} as the concentration of calcium in the cytoplasm, the SR, and the concentration of calcium bound to buffers. This description assumes that there exist effective diffusion coefficients $D_i = D_i(\nu_i)$ and $D_{sr} = D_{sr}(\nu_{sr})$ that, in an average sense, incorporate the effect of that complex geometry. Although in principle these coefficients could be calculated knowing the SR structure (Goel et al., 2006), we will take the functional forms used in Goel et al. (2006). Since both fractions, ν_i and ν_{sr}, vary in different parts of the cell, it implies that both diffusion coefficients are functions of the position, $D_i = D_i(\mathbf{r})$ and $D_{sr} = D_{sr}(\mathbf{r})$. In our simulations we take the values $D_i \sim 250$ $\mu m^2/s$ and $D_{sr} \sim 90$ $\mu m^2/s$, that are within the upper range considered in the literature (Louch et al., 2010; Bers and Shannon, 2013).

The cardiac cell is modeled as a two dimensional domain with $L_x = 100$ μm and $L_y = 15$ μm. The spatial grid belongs to the submicron scale and it is defined as $dx = dy = 0.1\mu$m. There are points of the grid with and without RyRs. A typical RyR has a size of 30 x 30 nm. The RyRs are transmembrane proteins located at the surface of the SR, so they form a 2D grid. Thus in each of our grid points we locate a maximum of 10 RyRs.

A collection of grid points presenting RyRs form a cluster, i.e., a CaRU. In atrial cells, CaRUs are arranged periodically in the longitudinal and transversal directions, with some—seemingly Gaussian—dispersion (Chen-Izu et al., 2006). In our model, we place the centers of the clusters on the perimeter following an exact periodic distribution with a period $\bar{T}_x = \bar{T}_y = 0.5$ μm (see **Figure 2**). In front of all these exterior CaRUs there are LCC groups. Inside the cell, CaRUs are placed following a Gaussian distribution centered at the z-lines and with a fixed dispersion σ. We take $\sigma = 0.4$ μm as standard value. The average distance between CaRUs is $T_x = 1.6$ μm and $T_y = 0.5$ μm. Experimental data shows that the SR domain coincides with these z-lines (Soeller et al., 2007). In this sense, we identify the z-lines with periodic narrow strips (0.3 μm width) with a predefined period

(T_x). Let be Ω_c the sarcomere domain, that is, the zone between z-lines and let be Ω_{sr} the zone contained in z-lines and all the contour ($\partial\Omega$). Notice that $\Omega_c \cap \Omega_{sr} = \emptyset$. Besides, we consider the presence of Ca^{2+} buffers: troponin (TnC), Calmodulin (CaM), and SR Ca-binding sites. The TnC buffer affects the cytoplasmic concentration of calcium in the Ω_c domain. The other buffers, calmodulin and SR, affect also c_i but in all the cell, $\Omega_c \cup \Omega_{sr}$. We assume that all the buffers are immobile.

Because of the homogenization coarse grain, we define $c_i(\mathbf{r}, t)$ (free calcium concentration), $c_{sr}(\mathbf{r}, t)$ (calcium concentration in the SR), and $c_{bi}(\mathbf{r}, t)$ (calcium attached to buffers: TnC, CaM, and SR buffer) in all points. Therefore, we state the problem with the following set of partial differential equations (PDEs).

$$\frac{\partial c_i(\mathbf{r},t)}{\partial t} = J_i(\mathbf{r},t) + \nabla\cdot\left[D_i(\mathbf{r})\nabla c_i(\mathbf{r},t)\right] - J_{bi}(\mathbf{r},t) \quad (1)$$

$$\frac{\partial c_{sr}(\mathbf{r},t)}{\partial t} = \frac{v_i(\mathbf{r})}{v_{sr}(\mathbf{r})}J_{sr}(\mathbf{r},t) + \nabla\cdot\left[D_{sr}(\mathbf{r})\nabla c_{sr}(\mathbf{r},t)\right], \quad (2)$$

$$\frac{\partial c_{bi}(\mathbf{r},t)}{\partial t} = J_{bi}(\mathbf{r},t), \quad (3)$$

where J_i and J_{sr} are the fluxes into the cytosol and the SR spaces, respectively, J_{bi} accounts for the binding of free calcium to the different buffers. In order to relate the fluxes between the cytoplasm and the SR we have multiplied by the volume fraction v_i/v_{sr}, that depends on $\mathbf{r}$, that is, on the domain Ω_c and Ω_{sr}. In addition, each point could have different components (RyR or not, LCC or not) and could belong to the membrane or not. The fluxes that may contribute to the total flux into the cytosol J_i are the SR release flux J_{rel}, the SERCA pump J_{up}, the L-type calcium flux J_{CaL} and the sodium-calcium exchanger flux J_{NaCa}. The release flux J_{rel} carries Ca^{2+} ions from the SR to the cytoplasm through the RyRs. Thus, it exists only on those points that have a CaRU, indicated by a red dot in **Figure 2**. J_{up} pumps calcium from the cytoplasm to the SR and it is present in all cell domain ($\Omega_c \cup \Omega_{sr}$). The sum of these two fluxes (when appropriate) constitute the total flux from the SR. Then, J_{CaL}, the inward L-type calcium flux, depends on the LCC clusters, so that it will act on those points that contain this channel, indicated by a cross in **Figure 2**. Indeed, LCCs appear only in some points of the cell membrane, $\partial\Omega$ (those that also have a CaRU). Finally, the NaCa exchanger, J_{NaCa}, acts along all the perimeter $\partial\Omega$.

A detailed description of all the fluxes can be found in the **Supplementary Material**. Below we present some details of the release and L-type calcium fluxes.

2.1. Release Flux

As shown in **Figure 2**, we consider each CaRU formed by several grid points containing RyRs. As standard for a CaRU, we consider one containing 36 RyRs, divided equally among 4 grid points, each one containing 9 RyRs. We will change this configuration in section 3.4 to consider larger CaRUs, maintaining fixed the total number of RyRs in the cell. This resembles the situation found in cells presenting AF (Macquaide et al., 2015).

Following Stern et al. (1999) each RyR can be in one of four different states: close C, open O, and two inactivated states I_1, I_2 (**Figure 3**). Calcium release from the SR to the cytoplasm is taken to be proportional to the concentration difference and the number of RyR in the open state, O_{RyR},

$$J_{rel} = g_{rel}O_{RyR}(c_{sr} - c_i). \quad (4)$$

This flux is only present in those points that present RyRs (highlighted in red in **Figure 2**).

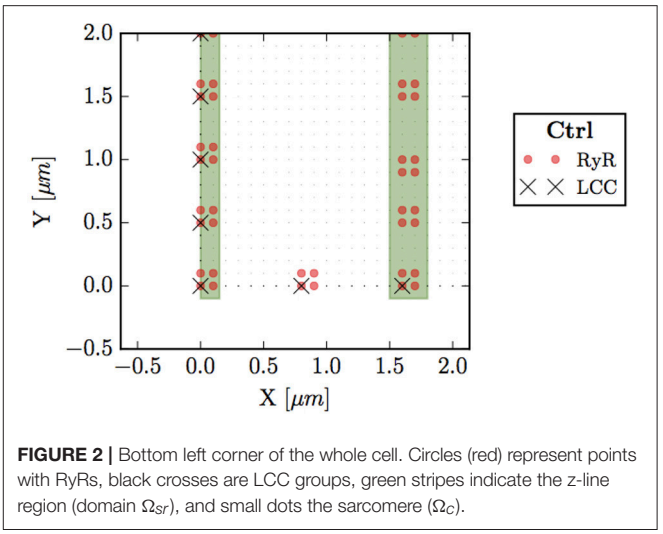

FIGURE 2 | Bottom left corner of the whole cell. Circles (red) represent points with RyRs, black crosses are LCC groups, green stripes indicate the z-line region (domain Ω_{sr}), and small dots the sarcomere (Ω_c).

2.2. L-Type Calcium Flux

The inward current of calcium from the extracellular medium toward each CaRU is dependent on the number of LCC channels in the open state O_{LCC}, the voltage, and the local calcium concentration in these points, which are close to the membrane, according to

$$I_{CaL} = g_{CaL}O_{LCC}4z_m\frac{e^{2z}c_i - [Ca]_0}{e^{2z} - 1}, \quad (5)$$

where $z = VF/(RT)$ and $z_m = 0.341zF$. The current I_{CaL} is converted to the flux J_{CaL} , with units of μ M/ms, through:

$$J_{CaL} = \frac{I_{CaL}}{2Fv_{myo}}, \quad (6)$$

where v_{myo} is the volume of the cytosol.

We have used the LCC model described in Mahajan et al. (2008) with some changes in the parameters as in Alvarez-Lacalle et al. (2015). We consider the presence of 5 LCC channels in each CaRU (located all in the same grid point) with five possible states (**Figure 3**): two closed states (C_1 and C_2), two inactivated states (I_1 and I_2) and one open state (O). The stochastic dynamics of the transitions is implemented using a time-adaptive Gillespie's method (Nivala J. et al., 2012). The transition rates a_{ij} are described in the **Supplementary Material**.

2.3. Other Fluxes

There are extra fluxes that appear on the model. The Na-Ca exchanger and the SERCA pump are both explained in the **Supplementary Material**.

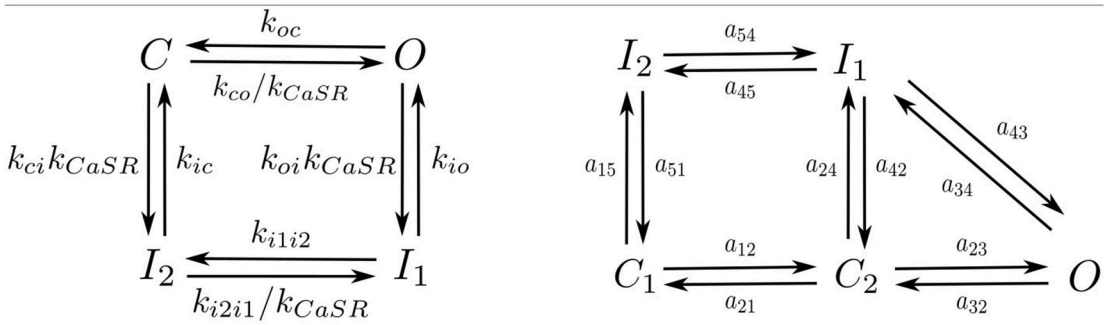

FIGURE 3 | Markov models of the RyR **(Left)** and LCC channels **(Right)**.

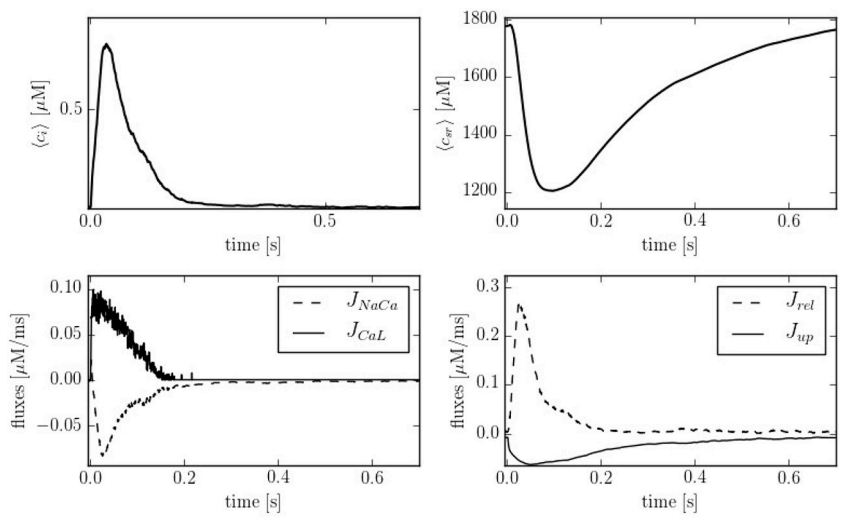

FIGURE 4 | (Top) Temporal profiles of [Ca^{2+}] for both domains, cytoplasm and SR. **(Bottom left)** Inward and outward cell currents of J_{NaCa} (dashed line) and J_{CaL} (solid line). **(Bottom right)** SERCA pump flux (solid line) and release flux (dashed line) in the cytoplasm at a pacing period of 800 ms.

3. RESULTS

3.1. Calcium Handling Characteristics

The calcium trace results from the sum of calcium at different sites. Since in our model the volume fraction changes from site to site, we have to define the average calcium concentrations as:

$$\langle c_i \rangle = \frac{\sum_{\mathbf{r}} \nu_i(\mathbf{r}) c_i(\mathbf{r},t)}{\sum_{\mathbf{r}} \nu_i(\mathbf{r})}, \quad \langle c_{sr} \rangle = \frac{\sum_{\mathbf{r}} \nu_{sr}(\mathbf{r}) c_{sr}(\mathbf{r},t)}{\sum_{\mathbf{r}} \nu_{sr}(\mathbf{r})} \tag{7}$$

Figure 4 shows typical traces during one beat of the average calcium over all the cell in both domains: cytoplasm and SR. The calcium peak, of ∼700–800 nM, agrees well with experimental observations (Mackenzie et al., 2004). The calcium concentration in the SR, though, is larger than observed in experiments due to the lack of the SR buffer calsequestrin (CSQN) in our model. We also show in **Figure 4** the four cytoplasmic fluxes, corresponding to the sodium-calcium exchanger (J_{NaCa}), the L-type calcium flux (J_{CaL}), SR release (J_{rel}), and SERCA (J_{up}). Due to the small number of LCC channels, the L-type calcium flux is particularly stochastic.

Depending on the pacing period, the model shows different behaviors. We have quantified this effect by calculating the calcium peak and the calcium diastolic level in the cytoplasm and in the SR domain (**Figure 5**). To assure that the system is close to the steady state, we have paced the cell for 50 s at each pacing period, and then taken the average over the next 20 stimulations. As the pacing period decreases, the cytosolic calcium peak increases moderately, up to a pacing period period of ∼200-300 ms, beyond which it decreases, due to the decrease in SR calcium content and fractional release. This behavior agrees qualitatively with the observed change in the contractile force as a function of pacing period observed in atrial cells (Maier et al., 2000; Schotten et al., 2002), that shows a peak at a period of ∼500 ms, beyond which it decreases.

3.2. Inward Calcium Wave Propagation

In order to compare the spatial heterogeneities within the cell, we have considered longitudinal sections at the central and peripheral regions, averaged over a 1 μm width. The complete CaRU distribution is shown in **Figure 6**, where the longitudinal

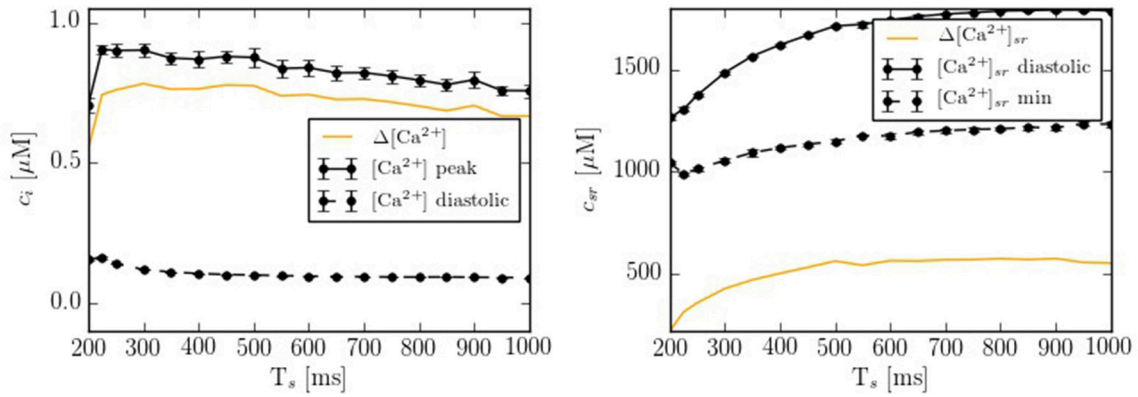

FIGURE 5 | Ca^{2+} peak and Ca^{2+} basal level as function of the pacing period (T_S) in both domains: cytoplasm and SR. Each point has been averaged over 10 beats in steady state.

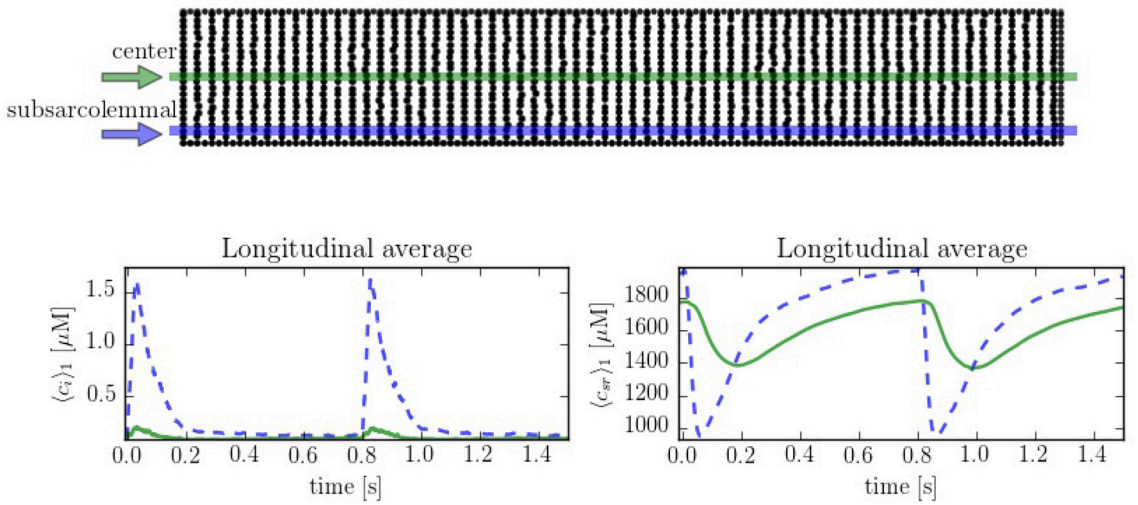

FIGURE 6 | (Top) Spatial distribution of the CaRU. Black dots show the position of the CaRUs. The green and blue lines indicate longitudinal lines at the cell center and periphery. **(Down)** Local Ca^{2+} measured in the subsarcolemmal space (blue dashed lines) and the center of the cell (solid lines) for both cytoplasm and SR domains at a pacing period of 800 ms. All traces have been averaged over a longitudinal section of 1 μm width.

sections are plotted in green and blue. Simulations suggest strong differences between calcium levels in the subsarcolemmal space and the center of the cell (see **Figure 6**), as well as a delay between release at the peripheral and central regions.

The spatio-temporal and local correlation between c_i and c_{sr} calcium is shown in the line scan profiles on **Figure 7**. The four profiles correspond to the same beat. In the subsarcolemmal region the presence of LCCs and CaRUs results in an important release activity causing a relevant SR depletion. On the other hand, in the central region, calcium does not penetrate, and the local activity is scarce. Still, there is a depletion of the SR content (visible also in **Figure 6**) due, not so much to release, almost negligible at the central region, but to diffusion of SR calcium to the periphery.

The spatio-temporal Ca^{2+} dynamics in the cytoplasm allows us to clearly understand how the standard inward wave propagation occurs. **Figure 8** shows spatial profiles at different times during a single beat. Under normal conditions, the calcium wave starts on the cell membrane and propagates to the center but this propagation does not reach the central region. This situation is observed more clearly averaging the calcium concentration over the longitudinal direction, so we can observe the average inward propagation of the calcium wave (**Figure 9**) Typically, the inward wave propagates 4 or 5 μm in the transversal direction. From the figure, we can estimate an inward wave velocity of roughly 150 μm/s, that agrees well with typical observed calcium wave velocities of $\sim$100 μm/s (Izu et al., 2013).

Intracellular waves are Ca^{2+} release events that propagate across the cell at a constant velocity. To have a better control of the calcium wave and be able to study its speed and dependence on different parameters, we have created a new geometry with 10

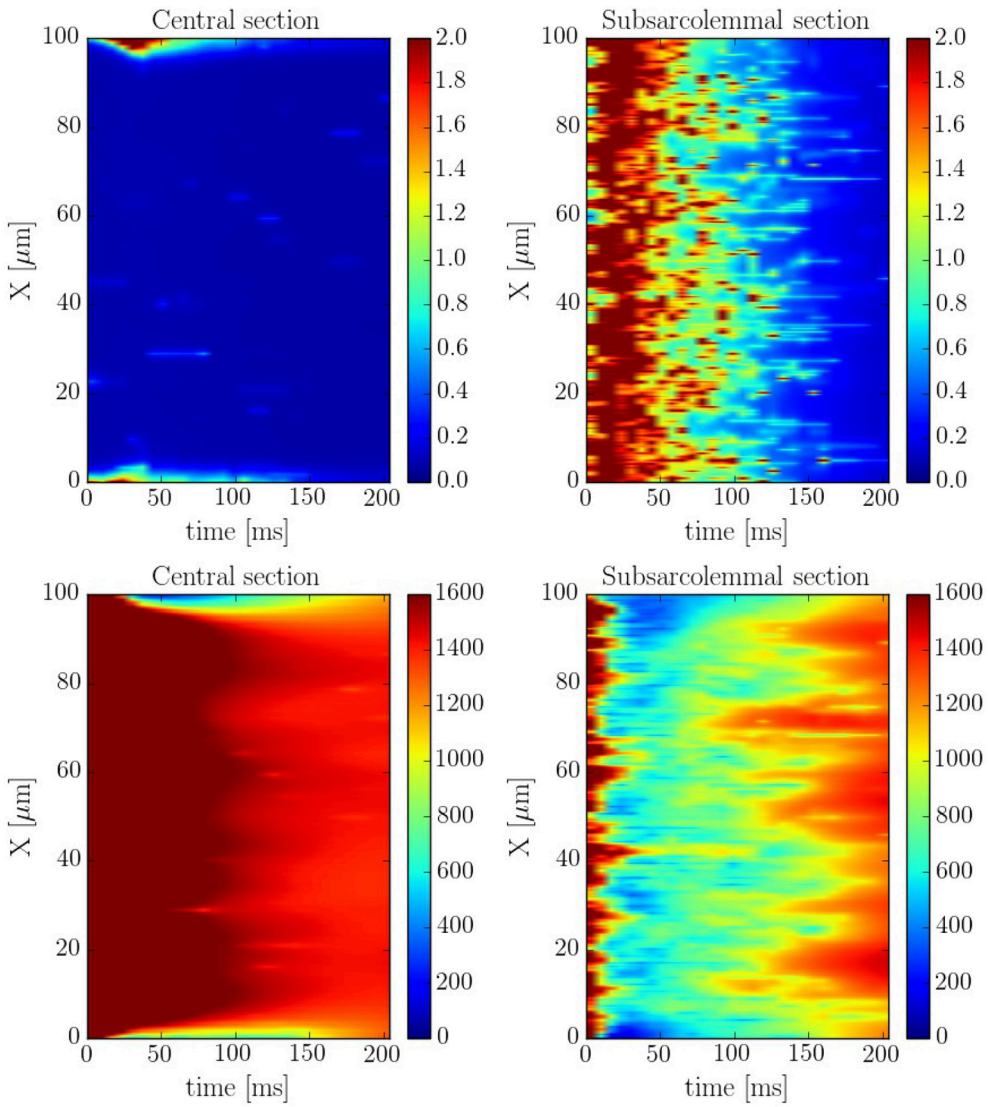

FIGURE 7 | Longitudinal line scan during a single beat on the subsarcolemmal and the central region at a pacing period of 800 ms for cytosolic **(Top)** and SR **(Bottom)** calcium. The colorbar corresponds to calcium concentration in μM.

equidistant z-lines (see **Figure S2**, in Supplementary Material). The distance between two z-lines is 1.5 μm. Initially, cytosolic calcium at the first z-line is increased and then the system let to evolve without being forced. The wave front is monitored and the wave front velocity calculated. This way we determine the wave velocity as a function of different parameters. The typical wave velocity is of the order of 200 − 300 μm/s, that agrees well with a diffusive process within z-lines, that would give a speed of $v \sim 2D/d \sim 2 \cdot 200\ \mu m^2 s^{-1}/1.5\ \mu m \sim 260\ \mu m/s$. This velocity increases slightly with the calcium SR load (**Figure 10**). The dependence on intracellular calcium diffusion D_i is roughly linear, as one would expect in saltatory dynamics (Dawson et al., 1999). The dependence on SR calcium diffusion D_{sr}, on the other hand, is not so pronounced.

3.3. Effect of the Cell Structure

It is interesting to compare also the calcium dynamics at the z-lines and in the space within z-lines, where no CaRUs are present. To this end we have performed transversal section measurements, as shown in **Figure 11**, in a situation when the cell is at rest, without external stimulation. The sarcomere measurement corresponds to the space between the z-lines. It is important to notice that, because of the proximity between the measurements, there exists a correlation between the resulting profiles. For instance, at $t = 0.6$ s there is a spark that starts in the first z-line, it propagates to the sarcomere region and, then, to the second z-line. The second thing to notice is that, due to the presence of random Ca^{2+} releases associated to the position of the RyRs, at the z-lines the calcium trace is more stochastic (**Figure 11**).

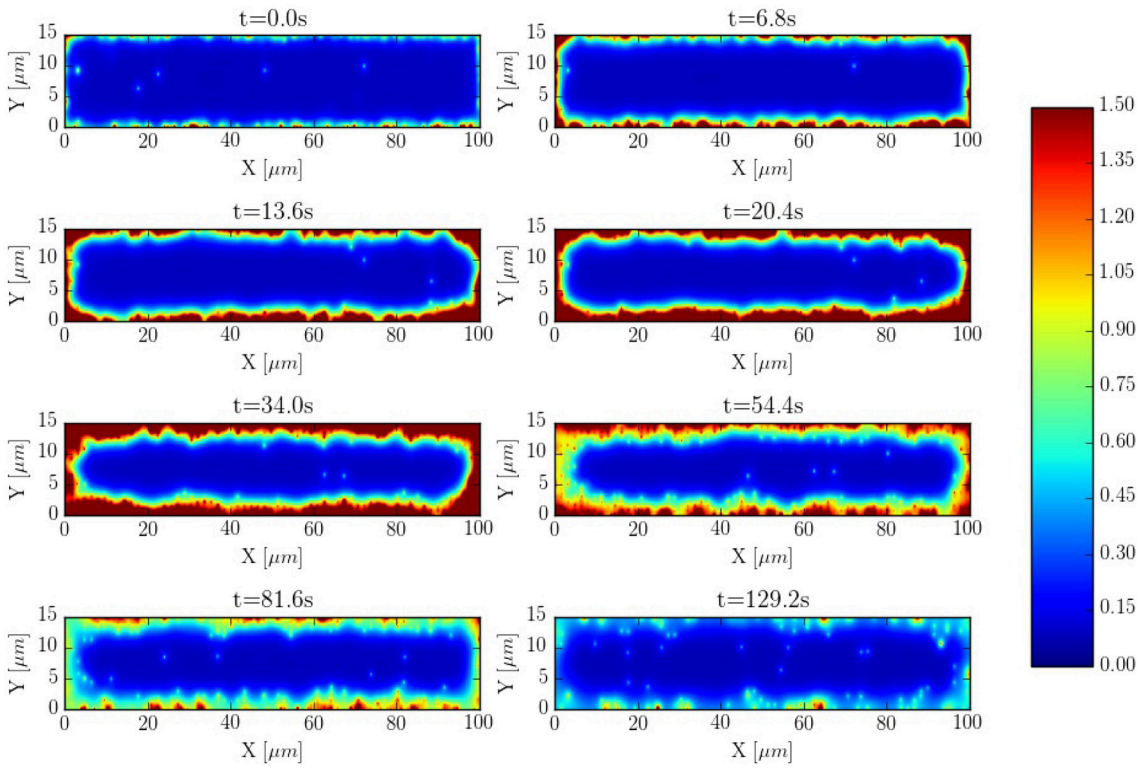

FIGURE 8 | Inward wave propagation at a pacing period of 800 ms. The colorbar corresponds to calcium concentration in μM.

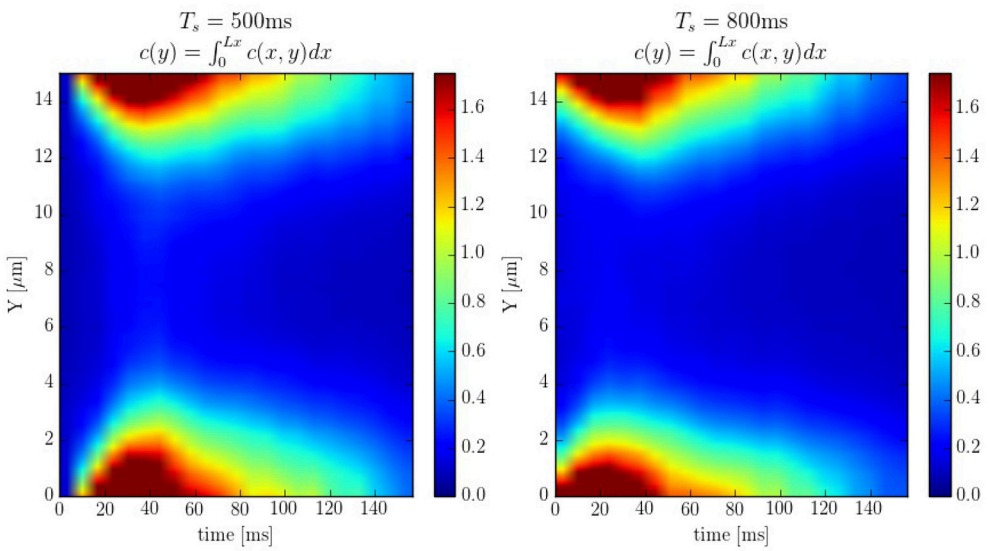

FIGURE 9 | Line scans averaged over the longitudinal direction at pacing periods of 500 and 800ms. The colorbar corresponds to calcium concentration in μM.

3.4. RyR Cluster Structure and Distribution

Calcium sparks are the basic calcium release events. A good understanding of their characteristics (size, amplitude, and frequency) is thus very important to properly characterize the process of CICR. Due to the fine discretization of our model, we can observe their detailed spatio-temporal profiles. **Figure 12** shows, for instance, the standard time evolution of a spark. We have also studied the effect of the microstructure in the frequency

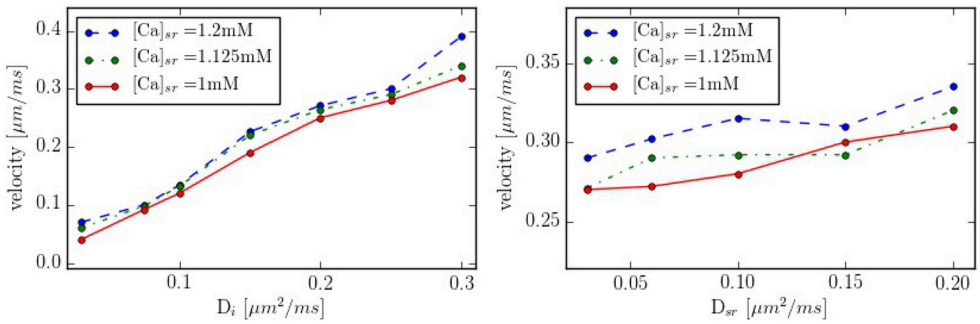

FIGURE 10 | Propagation velocity as function of the diffusion constants D_i and D_{Sr} for different values of the SR calcium load. As standard values we take $D_i = 0.25$ μm^2/ms and $D_{Sr} = 0.09$ μm^2/ms in the zone between z-lines.

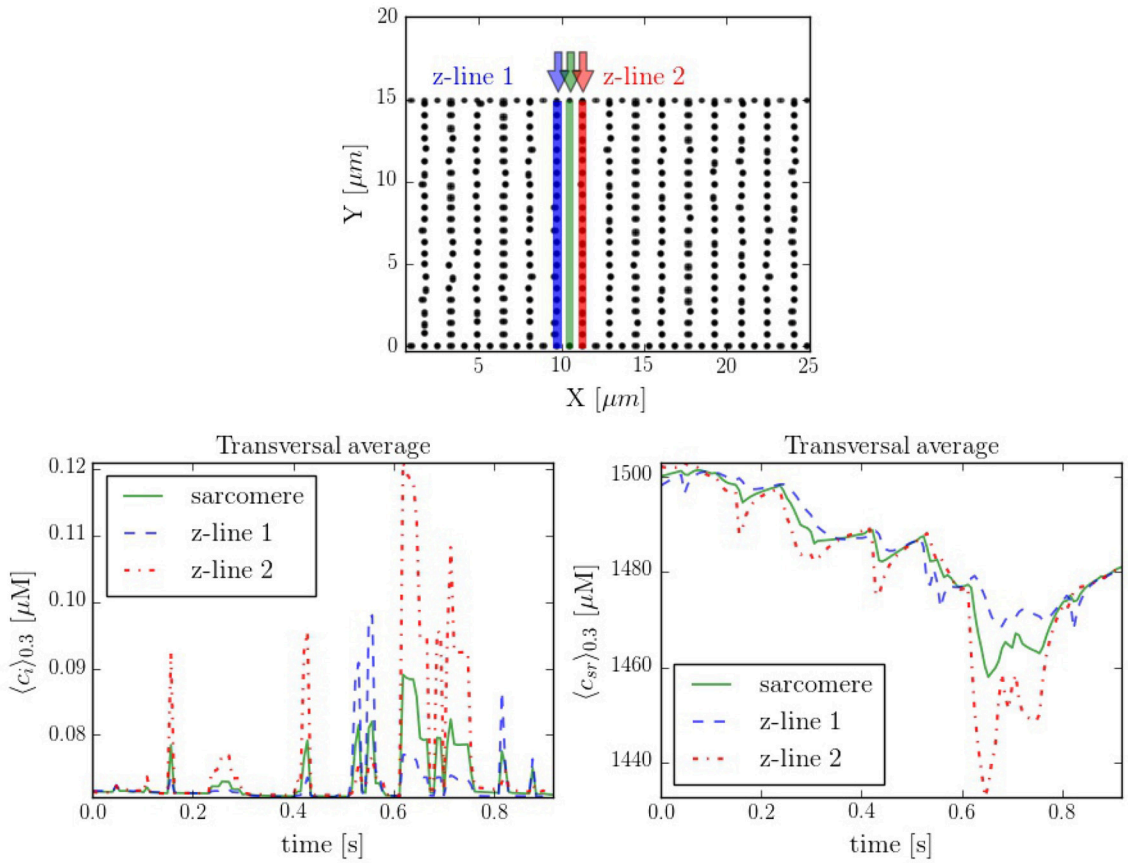

FIGURE 11 | (Top) Spatial distribution of the CaRUs. Black dots show the position of the CaRUs. The blue and red lines indicate two transversal lines within neighboring z-lines. The green line a transversal line within those two z-lines. **(Down)** Local Ca^{2+} measured in the three transversal lines in post-rest potential conditions. All traces have been averaged over a transversal section of 0.3 μm width.

of sparks. We have modified the microstructure, changing the size and distribution of the CaRUs. This is particularly important since it has been observed that the RyR distribution changes in a particular way under conditions of AF (Macquaide et al., 2015). We have then calculated the spark frequency under resting conditions for different configurations defined by the Gaussian distribution of position sites and size of the CaRUs. For the standard size of the CaRU (36 RyRs divided equally among 4 grid points, each one containing 9 RyRs), we have considered three values of the dispersion in the Gaussian distribution, the standard value of $\sigma = 0.4$ μm, and two cases with larger dispersion of $\sigma = 2$ and 3.6 μm, see **Figure 13**. Besides, we also consider the

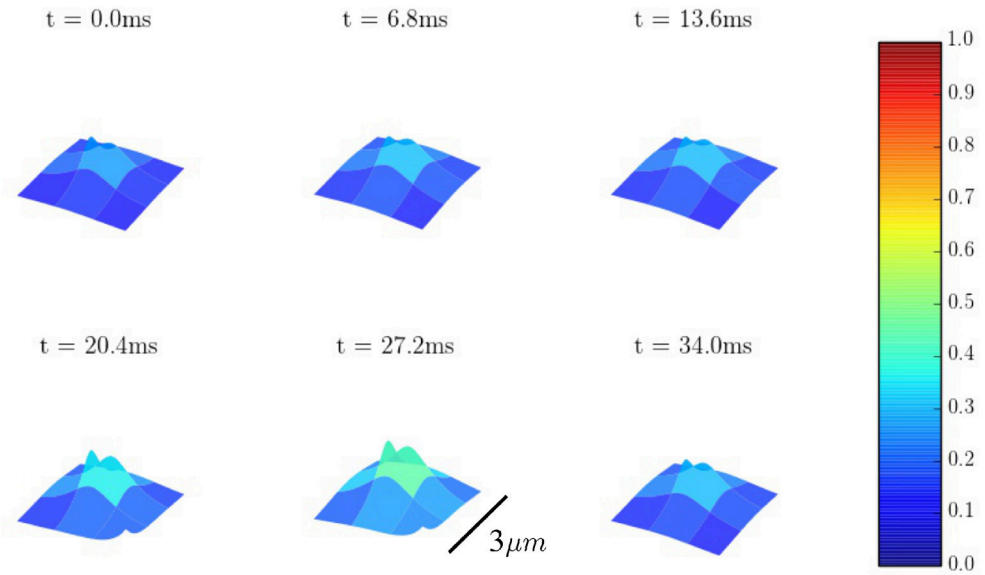

FIGURE 12 | Spatial profiles of a Ca^{2+} spark.

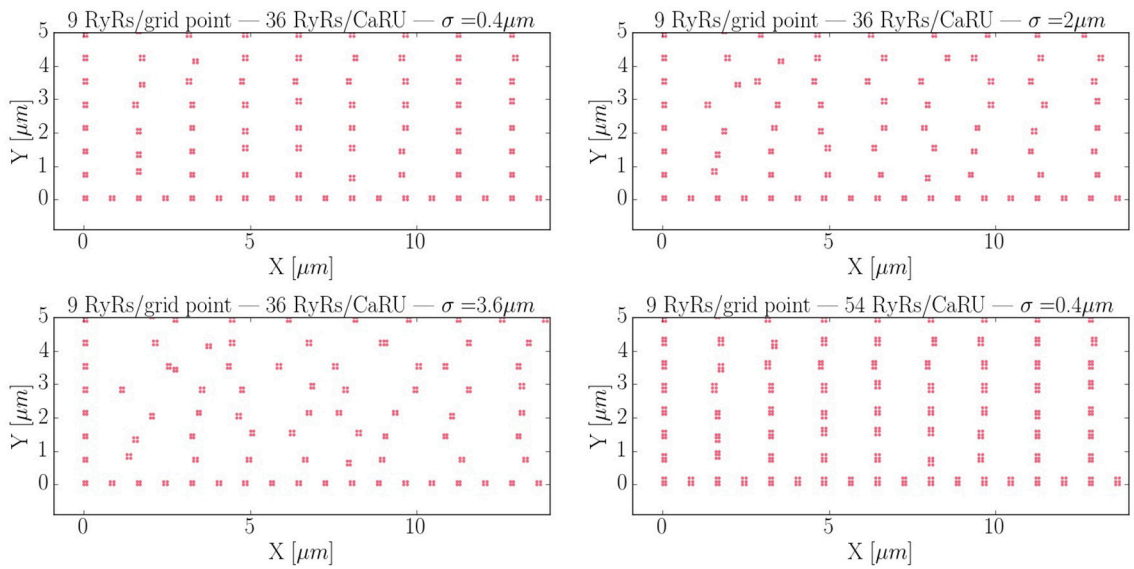

FIGURE 13 | Different RyR distributions considered in the text. The bottom left corner of the whole cell is displayed. The red dots represent grid points with RyRs. First: control configuration, with standard dispersion in the position of the RyRs $\sigma = 0.4$ μm. Second: increased the dispersion of σ to 2 μm. Third: $\sigma = 3.6$ μm. Fourth: New structure configuration, where each grid point contains 9 RyRs and a CaRU is formed by 6 grid points, so that, each CaRU represents 54 RyRs. The total number of RyRs remains constant but now, in the new structure, they are more grouped, that is, the CaRUs are bigger. The dispersion is the same as in the standard case: $\sigma = 0.4$ μm.

effect of a change in the CaRU size, considering CaRUs with 54 RyRs, divided equally among 6 grid points, each one containing 9 RyRs (**Figure 13** down right), but maintaining fixed the total number of RyRs in the cell. Since the total number of RyRs is the same, this means that there are larger, but less CaRUs in the cell.

In **Figure 14A** the average mean CaRU size is shown. To define the size of a CaRU, we follow the results by Macquaide et al. (2015), that showed using a computational model that clusters closer than 150 nm triggered together functionally as a single cluster. We thus assume that a group of clusters belong to the same CaRU if they are separated, at most, by 0.15 μm edge to edge from each other. By definition, there is a random component in the structure, so that, there is a non-zero dispersion on the distance with respect to the z-line

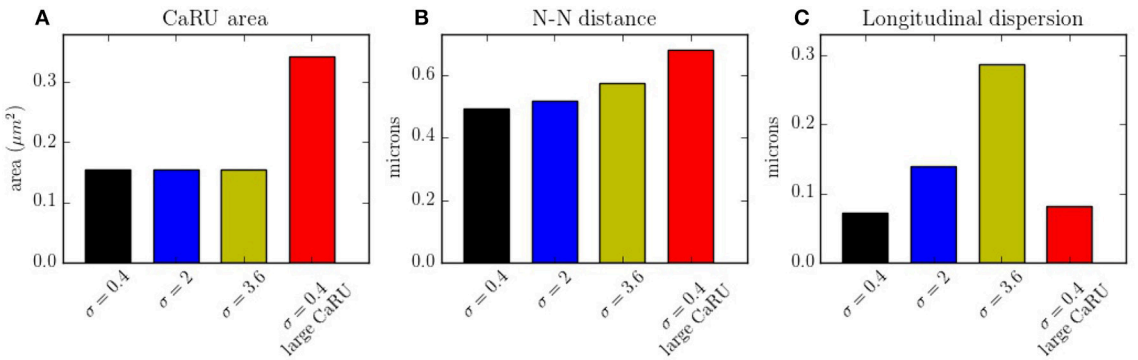

FIGURE 14 | (A) Mean area occupied by a CaRU. **(B)** Nearest-neighbor distance among CaRUs, measured from the center of each CaRU. **(C)** Longitudinal dispersion, measured as the mean distance between the RyRs and the center of the z-line. All calculations have been averaged over 35 configurations.

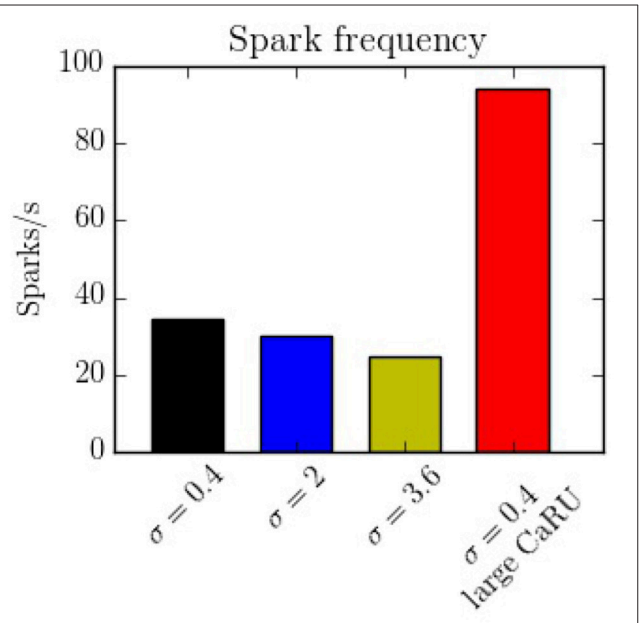

FIGURE 15 | Spark frequency for the four different configurations. The spark frequency decreases with nearest-neighbor distance but increases with the size of the CaRU.

(**Figure 14C**). Finally, the mean nearest neighbor distance is shown in **Figure 14B**. In the new structure, since the RyRs are more grouped, the total number of CaRUs is smaller, such that the mean distance among them increases.

The spark frequency is one of the most important indicators of the stochastic activity during a post-rest potential period. The total number of spontaneous calcium sparks has been recorded. In order to consider the sparks, we have counted all the calcium release events greater than a certain spatial radial threshold of 1.6 μm. As shown in **Figure 15**, we observe that the frequency decreases with the longitudinal dispersion meaning that the cluster-cluster communication plays an important role in stochastic activity. On the other hand, when the CaRUs are bigger (structure configuration) this probability increases.

4. DISCUSSION AND CONCLUSIONS

In this work we present a novel model to fully simulate a 2D longitudinal plane of a cardiac atrial cell. By modeling the intracellular calcium dynamics and solving the spatio-temporal Ca^{2+} reaction-diffusion equations, both local and global behavior have been recorded. Because of the high spatial resolution, the model allows us to study in detail the dynamics in the surroundings of the CaRUs, that is, the local calcium concentrations and the spark activity. It is also well-suited to study the effect of changes in the spatial distribution and form of CaRUs. In this regard, important differences have been noticed using different spatial configurations of RyRs, showing that the resulting calcium dynamics is highly dependent on the spatial distribution. We observe, for instance, a decrease in spark frequency with CaRU spatial dispersion (**Figure 15**). This is correlated with an increase in CaRU nearest-neighbor distance, suggesting that cooperativity among local release events at nearby CaRUs could play an important role in the generation of sparks. In fact, sparks (or macrosparks) encompassing several CaRUs have also been observed experimentally (Kockskämper et al., 2001). When the same total number of RyRs of the cell are distributed in larger CaRUs, we observe an increase in spark frequency (**Figure 15**). These larger CaRUs are obtained increasing their size, but maintaining the density of RyRs, similar to what is observed in atrial cells presenting AF (Macquaide et al., 2015). Due to the larger number of RyRs per CaRU, an increase in the spark probability of each individual CaRU is expected, but, since the number of CaRUs is decreased, the increase in spark frequency per CaRU must be non-linear with size. In this case, the increase in nearest-neighbor distance (**Figure 14**) does not result in a decrease in spark rate. However, it should be noted that we have measured the nearest-neighbor distance from the centers of the CaRUs, but since their size is larger, the distance between the edges of the CaRUs could actually be similar, or smaller. A more detailed study of the influence of the CaRU structure in spark frequency, the appearance of macrosparks, and the transition to waves is deferred to a future study.

In our simulations, the opening of the L-type calcium channels induce a calcium increase in the periphery of the cell, that hardly

reaches the interior (**Figure 6**). This result agrees with what is observed in atrial cells without t-tubules where, under basal conditions, calcium signals are restricted to subsarcolemmal regions (Mackenzie et al., 2004). The observed values of the calcium transients, slightly over 1 μM at the periphery and 0.2–0.3 μM at the center are similar to what we obtain in our simulations (**Figure 6**). As observed in previous works (Dawson et al., 1999), the speed of the wave varies roughly linearly with the diffusion coefficient in the cytosol. Although we have not changed the distance among z-planes in this work, the fact that this linear relation continues at low values of the diffusion constant, seems to indicate the lack of a threshold for propagation in the model. This contrasts with results by Izu et al. (2006) and Hoang-Trong et al. (2015) that found a strong dependence on wave initiation with the distance among CaRUs. However, one should notice that, for the calculation of wave propagation (**Figure 10**), we have considered an increased strength of the L-type calcium current, probably pushing the threshold to smaller values of the diffusion constant than we have considered. In our simulations, calcium waves are obtained at transients larger than in experiments and with diffusion and RyR cluster spacing in the upper and lower ranges, respectively, allowing for diffuse and fire behavior. However, one should mention the difficulty to reconciliate calcium wave propagation at low calcium concentrations with a stochastic description of the RyR cluster (Izu et al., 2013). Recent studies suggest also an important role of SR calcium diffusion for the propagation of the calcium wave, through junctional SR calcium depletion and sensitization of the RyRs (Keller et al., 2007). We find that the dependence with diffusion in the SR is not so pronounced (**Figure 10**), seemingly ruling out an important role of SR Ca diffusion in wave propagation. This effect, however, should be studied in more detail, as well as the role of buffers, RyR sensitivity and the level of cytosolic calcium in calcium wave propagation.

The present study presents several limitations. To cite some, that we consider a two-dimensional geometry, a voltage clamp protocol, isotropic diffusion, or immobile buffers. The main reason to use a two-dimensional geometry was computational cost. A generalization to three-dimensions is straight-forward and we are implementing it to study some of the questions posed in this article in more detail. The dynamics of transmembrane voltage can be also readily incorporated into the model, and could be used to study the arrhythmogenic effect of spontaneous calcium release events, for instance. The correct characterization of calcium diffusion in the cell represents a harder challenge. We have considered typical values of the diffusion coefficients in the cytosol and SR and assumed that they depend linearly on the cytosolic/SR volume fractions, as suggested by homogenization (Goel et al., 2006). However, diffusion (particularly in the SR) is most likely to be anisotropic, and this could importantly affect wave characteristics. A better knowledge of the SR microstructure could help to estimate these diffusion coefficients and give a better representation of calcium wave propagation. An important addition would be to incorporate a (partial) network of t-tubules. The presence of t-tubules in atrial cells has been found to depend on the species, and there is evidence of their presence in large mammals' atrial cells (Richards et al., 2011). Besides transversal, axial tubules have also been found to contribute to rapid activation of the atrial cell (Brandenburg et al., 2016). In heart disease, including human heart failure (HF), there is extensive remodeling, resulting in loss and disorganization of t-tubules (Dibb et al., 2013). Besides, there are other important factors that may affect calcium transients. For instance, the presence of IP_3R may affect the form of Ca^{2+} sparks, leading to a difference between calcium handling at the peripheral and central regions (Mackenzie et al., 2004; Kim et al., 2010). Another important effect, not included in our model, is the presence of mitochondria. In venticular myocytes, there is evidence suggesting that the mitochondrial outer membrane is linked to t-tubules (Hayashi et al., 2009). Models of excitation-contraction coupling, including mitochondrial calcium handling have been developed for ventricular myocytes (Cortassa et al., 2003, 2006; Matsuoka et al., 2004; Maack and O'rourke, 2007; Hatano et al., 2011) and used, to study, for instance, the influence of the distance between mitochondria and Ca^{2+} release sites (Hatano et al., 2013). In the atria, the mitochondria has been suggested to act as a buffer that prevents inward calcium propagation (Mackenzie et al., 2004). The effect of these structural factors on wave propagation is an important matter for future work.

AUTHOR CONTRIBUTIONS

MM assisted with the design of the work, performed the simulations, analyzed the data and prepared the manuscript. BE obtained funds, designed the work and revised and edited the manuscript. All authors approved the final manuscript.

FUNDING

Financial support was provided by the Fundació La Marató de TV3, under grant number 20151110, and from the Spanish Ministerio de Economía y Competitividad (MINECO) under grant number SAF2014-58286-C2-2-R.

ACKNOWLEDGMENTS

We thank L. Hove-Madsen and E. Alvarez-Lacalle for fruitful discussions.

SUPPLEMENTARY MATERIAL

The Supplementary Material for this article can be found online at: https://www.frontiersin.org/articles/10.3389/fphys.2018.01760/full#supplementary-material

REFERENCES

Alvarez-Lacalle, E., Echebarria, B., Spalding, J., and Shiferaw, Y. (2015). Calcium alternans is due to an order-disorder phase transition in cardiac cells. *Phys. Rev. Lett.* 114:108101. doi: 10.1103/PhysRevLett.114.108101

Bading, H., Ginty, D. D., and Greenberg, M. E. (1993). Regulation of gene expression in hippocampal neurons by distinct calcium signaling pathways. *Science* 260:181. doi: 10.1126/science.8097060

Berridge, M. J. (1993). Inositol triphosphate and calcium signalling. *Cell* 361, 315–325.

Berridge, M. J. (1997). Elementary and global aspects of calcium signalling. *J. Physiol.* 499, 291–306. doi: 10.1113/jphysiol.1997.sp021927

Bers, D. M., and Shannon, T. R. (2013). Calcium movements inside the sarcoplasmic reticulum of cardiac myocytes. *J. Mol. Cell. Cardiol.* 58, 59–66. doi: 10.1016/j.yjmcc.2013.01.002

Bixby, J. L., and Harris, W. A. (1991). Molecular mechanisms of axon growth and guidance. *Annu. Rev. Cell Biol.* 7, 117–159. doi: 10.1146/annurev.cb.07.110191.001001

Brandenburg, S., Kohl, T., Williams, G. S., Gusev, K., Wagner, E., Rog-Zielinska, E. A., et al. (2016). Axial tubule junctions control rapid calcium signaling in atria. *J. Clin. Invest.* 126:3999. doi: 10.1172/JCI88241

Cheng, H., Lederer, W., and Cannell, M. B. (1994). *Calcium Sparks: Elementary Events Underlying Excitation-Contraction Coupling in Heart Muscle*. PhD thesis, University of Maryland.

Chen-Izu, Y., McCulle, S. L., Ward, C. W., Soeller, C., Allen, B. M., Rabang, C., et al. (2006). Three-dimensional distribution of ryanodine receptor clusters in cardiac myocytes. *Biophys. J.* 91, 1–13. doi: 10.1529/biophysj.105.077180

Clapham, D. E. (1995). Calcium signalling. *Cell* 80, 259–268. doi: 10.1016/0092-8674(95)90408-5

Cortassa, S., Aon, M. A., Marbán, E., Winslow, R. L., and O'Rourke, B. (2003). An integrated model of cardiac mitochondrial energy metabolism and calcium dynamics. *Biophys. J.* 84, 2734–2755. doi: 10.1016/S0006-3495(03)75079-6

Cortassa, S., Aon, M. A., O'Rourke, B., Jacques, R., Tseng, H. J., Marbán, E., et al. (2006). A computational model integrating electrophysiology, contraction, and mitochondrial bioenergetics in the ventricular myocyte. *Biophys. J.* 91, 1564–1589. doi: 10.1529/biophysj.105.076174

Courtemanche, M., Ramirez, R. J., and Nattel, S. (1998). Ionic mechanisms underlying human atrial action potential properties: insights from a mathematical model. *Am. J. Physiol. Heart Circ. Physiol.* 275, H301–H321. doi: 10.1152/ajpheart.1998.275.1.H301

Davies, L., Jin, J., Shen, W., Tsui, H., Shi, Y., Wang, Y., et al. (2014). Mkk4 is a negative regulator of the transforming growth factor beta 1 signaling associated with atrial remodeling and arrhythmogenesis with age. *J. Am. Heart Assoc.* 3:e000340. doi: 10.1161/JAHA.113.000340

Dawson, S. P., Keizer, J., and Pearson, J. E. (1999). Fire–diffuse–fire model of dynamics of intracellular calcium waves. *Proc. Natl. Acad. Sci. U.S.A.* 96, 6060–6063. doi: 10.1073/pnas.96.11.6060

Dibb, K. M., Clarke, J. D., Eisner, D. A., Richards, M. A., and Trafford, A. W. (2013). A functional role for transverse (t-) tubules in the atria. *J. Mol. Cell. Cardiol.* 58, 84–91. doi: 10.1016/j.yjmcc.2012.11.001

Ehrhardt, D. W., Wais, R., and Long, S. R. (1996). Calcium spiking in plant root hairs responding to rhizobium nodulation signals. *Cell* 85, 673–681. doi: 10.1016/S0092-8674(00)81234-9

Fabiato, A., and Fabiato, F. (1979). Calcium and cardiac excitation-contraction coupling. *Annu. Rev. Physiol.* 41, 473–484. doi: 10.1146/annurev.ph.41.030179.002353

Falcke, M. (2003). On the role of stochastic channel behavior in intracellular ca 2+ dynamics. *Biophys. J.* 84, 42–56. doi: 10.1016/S0006-3495(03)74831-0

Farber, J. L. (1981). The role of calcium in cell death. *Life sci.* 29, 1289–1295. doi: 10.1016/0024-3205(81)90670-6

Ford, L. E., and Podolsky, R. J. (1972). Calcium uptake and force development by skinned muscle fibres in egta buffered solutions. *J. Physiol.* 223:1. doi: 10.1113/jphysiol.1972.sp009830

Franzini-Armstrong, C., and Protasi, F. (1997). Ryanodine receptors of striated muscles: a complex channel capable of multiple interactions. *Physiol. Rev.* 77, 699–729. doi: 10.1152/physrev.1997.77.3.699

Goel, P., Sneyd, J., and Friedman, A. (2006). Homogenization of the cell cytoplasm: the calcium bidomain equations. *Multiscale Model. Simul.* 5, 1045–1062. doi: 10.1137/060660783

Grandi, E., Pandit, S. V., Voigt, N., Workman, A. J., Dobrev, D., Jalife, J., et al. (2011). Human atrial action potential and ca2+ model: sinus rhythm and chronic atrial fibrillation. *Circ. Res.* 109, 1055–1066. doi: 10.1161/CIRCRESAHA.111.253955

Hake, J., Kekenes-Huskey, P. M., and McCulloch, A. D. (2014). Computational modeling of subcellular transport and signaling. *Curr. Opin. Struct. Biol.* 25, 92–97. doi: 10.1016/j.sbi.2014.01.006

Hatano, A., Okada, J., Washio, T., Hisada, T., and Sugiura, S. (2011). A three-dimensional simulation model of cardiomyocyte integrating excitation-contraction coupling and metabolism. *Biophys. J.* 101, 2601–2610. doi: 10.1016/j.bpj.2011.10.020

Hatano, A., Okada, J.-I., Washio, T., Hisada, T., and Sugiura, S. (2013). Mitochondrial colocalization with ca2+ release sites is crucial to cardiac metabolism. *Biophys. J.* 104, 496–504. doi: 10.1016/j.bpj.2012.12.004

Hayashi, T., Martone, M. E., Yu, Z., Thor, A., Doi, M., Holst, M. J., et al. (2009). Three-dimensional electron microscopy reveals new details of membrane systems for ca2+ signaling in the heart. *J. Cell Sci.* 122, 1005–1013. doi: 10.1242/jcs.028175

Heijman, J., Erfanian Abdoust, P., Voigt, N., Nattel, S., and Dobrev, D. (2016). Computational models of atrial cellular electrophysiology and calcium handling, and their role in atrial fibrillation. *J. Physiol.* 594, 537–553. doi: 10.1113/JP271404

Hell, S. W., and Wichmann, J. (1994). Breaking the diffraction resolution limit by stimulated emission: stimulated-emission-depletion fluorescence microscopy. *Opt. Lett.* 19, 780–782. doi: 10.1364/OL.19.000780

Hoang-Trong, T. M., Ullah, A., and Jafri, M. S. (2015). Calcium sparks in the heart: dynamics and regulation. *Res. Rep. Biol.* 6, 203–214. 10.2147/RRB.S61495

Huttenlocher, A., Palecek, S. P., Lu, Q., Zhang, W., Mellgren, R. L., Lauffenburger, D. A., et al. (1997). Regulation of cell migration by the calcium-dependent protease calpain. *J. Biol. Chem.* 272, 32719–32722. doi: 10.1074/jbc.272.52.32719

Izu, L. T., Means, S. A., Shadid, J. N., Chen-Izu, Y., and Balke, C. W. (2006). Interplay of ryanodine receptor distribution and calcium dynamics. *Biophys. J.* 91, 95–112. doi: 10.1529/biophysj.105.077214

Izu, L. T., Xie, Y., Sato, D., Bányász, T., and Chen-Izu, Y. (2013). Ca2+ waves in the heart. *J. Mol. Cell. Cardiol.* 58, 118–124. doi: 10.1016/j.yjmcc.2012.11.014

Jafri, M. S., and Keizer, J. (1995). On the roles of ca2+ diffusion, ca2+ buffers, and the endoplasmic reticulum in ip3-induced ca2+ waves. *Biophys. J.* 69, 2139–2153. doi: 10.1016/S0006-3495(95)80088-3

Kaufman, M. T., and Roizman, B. (1989). Calcium mobilization and exocyt osis after one. *Virology* 172:435.

Keener, J. P., and Sneyd, J. (1998). *Mathematical Physiology, Vol. 1*. New York, NY: Springer.

Keizer, J., and De Young, G. W. (1992). Two roles of ca2+ in agonist stimulated ca2+ oscillations. *Biophys. J.* 61, 649–660. doi: 10.1016/S0006-3495(92)81870-2

Kekenes-Huskey, P. M., Cheng, Y., Hake, J. E., Sachse, F. B., Bridge, J. H., Holst, M. J., et al. (2012). Modeling effects of l-type ca2+ current and na+-ca2+ exchanger on ca2+ trigger flux in rabbit myocytes with realistic t-tubule geometries. *Front. Physiol.* 3:351. doi: 10.3389/fphys.2012.00351

Keller, M., Kao, J. P., Egger, M., and Niggli, E. (2007). Calcium waves driven by "sensitization" wave-fronts. *Cardiovasc. Res.* 74, 39–45. doi: 10.1016/j.cardiores.2007.02.006

Kim, J.-C., Son, M.-J., Subedi, K. P., Li, Y., Ahn, J. R., and Woo, S.-H. (2010). Atrial local ca2+ signaling and inositol 1, 4, 5-trisphosphate receptors. *Prog. Biophys. Mol. Biol.* 103, 59–70. doi: 10.1016/j.pbiomolbio.2010.02.002

Kockskämper, J., Sheehan, K. A., Bare, D. J., Lipsius, S. L., Mignery, G. A., and Blatter, L. A. (2001). Activation and propagation of ca 2+ release during excitation-contraction coupling in atrial myocytes. *Biophys. J.* 81, 2590–2605. doi: 10.1016/S0006-3495(01)75903-6

Koivumäki, J. T., Korhonen, T., and Tavi, P. (2011). Impact of sarcoplasmic reticulum calcium release on calcium dynamics and action potential morphology in human atrial myocytes: a computational study. *PLoS Comput. Biol.* 7:e1001067. doi: 10.1371/journal.pcbi.1001067

Li, Q., O'Neill, S. C., Tao, T., Li, Y., Eisner, D., and Zhang, H. (2012). Mechanisms by which cytoplasmic calcium wave propagation and alternans are generated

in cardiac atrial myocytes lacking t-tubules-insights from a simulation study. *Biophys. J.* 102, 1471–1482. doi: 10.1016/j.bpj.2012.03.007

Lindblad, D. S., Murphey, C. R., Clark, J. W., and Giles, W. R. (1996). A model of the action potential and underlying membrane currents in a rabbit atrial cell. *Am. J. Physiol. Heart Circ. Physiol.* 271, H1666–H1696. doi: 10.1152/ajpheart.1996.271.4.H1666

Louch, W. E., Hake, J., Jølle, G. F., Mørk, H. K., Sjaastad, I., Lines, G. T., et al. (2010). Control of ca2+ release by action potential configuration in normal and failing murine cardiomyocytes. *Biophys. J.* 99, 1377–1386. doi: 10.1016/j.bpj.2010.06.055

Lugo, C. A., Cantalapiedra, I. R., Peñaranda, A., Hove-Madsen, L., and Echebarria, B. (2014). Are sr ca content fluctuations or sr refractoriness the key to atrial cardiac alternans?: insights from a human atrial model. *Am. J. Physiol. Heart Circ. Physiol.* 306, H1540–H1552. doi: 10.1152/ajpheart.00515.2013

Maack, C., and O'rourke, B. (2007). Excitation-contraction coupling and mitochondrial energetics. *Basic Res. Cardiol.* 102, 369–392. doi: 10.1007/s00395-007-0666-z

Mackenzie, L., Roderick, H. L., Berridge, M. J., Conway, S. J., and Bootman, M. D. (2004). The spatial pattern of atrial cardiomyocyte calcium signalling modulates contraction. *J. Cell Sci.* 117, 6327–6337. doi: 10.1242/jcs.01559

Macquaide, N., Tuan, H.-T., Hotta, J., Sempels, W., Lenaerts, I., Holemans, P., et al. (2015). Ryanodine receptor cluster fragmentation and redistribution in persistent atrial fibrillation enhance calcium release. *Cardiovasc. Res.* 108, 387–398. doi: 10.1093/cvr/cvv231

Mahajan, A., Shiferaw, Y., Sato, D., Baher, A., Olcese, R., Xie, L.-H., et al. (2008). A rabbit ventricular action potential model replicating cardiac dynamics at rapid heart rates. *Biophys. J.* 94, 392–410. doi: 10.1529/biophysj.106.98160

Maier, L. S., Barckhausen, P., Weisser, J., Aleksic, I., Baryalei, M., and Pieske, B. (2000). Ca2+ handling in isolated human atrial myocardium. *Am. J. Physiol. Heart Circ. Physiol.* 279, H952–H958. doi: 10.1152/ajpheart.2000.279.3.H952

Matsuoka, S., Sarai, N., Jo, H., and Noma, A. (2004). Simulation of atp metabolism in cardiac excitation–contraction coupling. *Prog. Biophys. Mol. Biol.* 85, 279–299. doi: 10.1016/j.pbiomolbio.2004.01.006

Nivala, J., Knowles, P., Dotro, G., García, J., and Wallace, S. (2012). Clogging in subsurface-flow treatment wetlands: measurement, modeling and management. *Water Res.* 46, 1625–1640. doi: 10.1016/j.watres.2011.12.051

Nivala, M., de Lange, E., Rovetti, R., and Qu, Z. (2012). Computational modeling and numerical methods for spatiotemporal calcium cycling in ventricular myocytes. *Front. Physiol.* 3:114. doi: 10.3389/fphys.2012.00114

Nygren, A., Fiset, C., Firek, L., Clark, J. W., Lindblad, D. S., Clark, R.B., et al. (1998). Mathematical model of an adult human atrial cell: the role of k+ currents in repolarization. *Circ. Res.* 82, 63–81.

Øyehaug, L., Loose, K. Ø., Jølle, G. F., Røe, Å. T., Sjaastad, I., Christensen, G., et al. (2013). Synchrony of cardiomyocyte ca2+ release is controlled by t-tubule organization, sr ca2+ content, and ryanodine receptor ca2+ sensitivity. *Biophys. J.* 104, 1685–1697. doi: 10.1016/j.bpj.2013.03.022

Poenie, M., Alderton, J., Tsien, R. Y., and Steinhardt, R. A. (1985). Changes of free calcium levels with stages of the cell division cycle. *Nature* 315, 147–149. doi: 10.1038/315147a0

Rajagopal, V., Bass, G., Walker, C. G., Crossman, D. J., Petzer, A., Hickey, A., et al. (2015). Examination of the effects of heterogeneous organization of ryr clusters, myofibrils and mitochondria on ca2+ release patterns in cardiomyocytes. *PLoS Comput. Biol.* 11:e1004417. doi: 10.1371/journal.pcbi.1004417

Ramirez, R. J., Nattel, S., and Courtemanche, M. (2000). Mathematical analysis of canine atrial action potentials: rate, regional factors, and electrical remodeling. *Am. J. Physiol. Heart Circ. Physiol.* 279, H1767–H1785. doi: 10.1152/ajpheart.2000.279.4.H1767

Restrepo, J. G., Weiss, J. N., and Karma, A. (2008). Calsequestrin-mediated mechanism for cellular calcium transient alternans. *Biophys. J.* 95, 3767–3789. doi: 10.1529/biophysj.108.130419

Richards, M. A., Clarke, J. D., Saravanan, P., Voigt, N., Dobrev, D., Eisner, D. A., et al. (2011). Transverse tubules are a common feature in large mammalian atrial myocytes including human. *Am. J. Physiol. Heart Circ. Physiol.* 301, H1996–H2005. doi: 10.1152/ajpheart.00284.2011

Rovetti, R., Cui, X., Garfinkel, A., Weiss, J. N., and Qu, Z. (2010). Spark-induced sparks as a mechanism of intracellular calcium alternans in cardiac myocytes. *Circ. Res.* 106, 1582–1591. doi: 10.1161/CIRCRESAHA.109.213975

Schanne, F. A., Kane, A. B., Young, E. E., and Farber, J. L. (1979). Calcium dependence of toxic cell death: a final common pathway. *Science* 206, 700–702. doi: 10.1126/science.386513

Schotten, U., Greiser, M., Benke, D., Buerkel, K., Ehrenteidt, B., Stellbrink, C., et al. (2002). Atrial fibrillation-induced atrial contractile dysfunction: a tachycardiomyopathy of a different sort. *Cardiovasc. Res.* 53, 192–201. doi: 10.1016/S0008-6363(01)00453-9

Soeller, C., and Baddeley, D. (2013). Super-resolution imaging of ec coupling protein distribution in the heart. *J. Mol. Cell. Cardiol.* 58, 32–40. doi: 10.1016/j.yjmcc.2012.11.004

Soeller, C., Crossman, D., Gilbert, R., and Cannell, M. B. (2007). Analysis of ryanodine receptor clusters in rat and human cardiac myocytes. *Proc. Natl. Acad. Sci. U.S.A.* 104, 14958–14963. doi: 10.1073/pnas.0703016104

Song, Z., Ko, C. Y., Nivala, M., Weiss, J. N., and Qu, Z. (2015). Calcium-voltage coupling in the genesis of early and delayed afterdepolarizations in cardiac myocytes. *Biophys. J.* 108, 1908–1921. doi: 10.1016/j.bpj.2015.03.011

Stern, M. D., Song, L.-S., Cheng, H., Sham, J. S., Yang, H. T., Boheler, K. R., et al. (1999). Local control models of cardiac excitation–contraction coupling: a possible role for allosteric interactions between ryanodine receptors. *J. Gen. Physiol.* 113, 469–489. doi: 10.1085/jgp.113.3.469

Thul, R., Coombes, S., Roderick, H. L., and Bootman, M. D. (2012). Subcellular calcium dynamics in a whole-cell model of an atrial myocyte. *Proc. Natl. Acad. Sci. U.S.A.* 109, 2150–2155. doi: 10.1073/pnas.11158 55109

Thul, R., Rietdorf, K., Bootman, M. D., and Coombes, S. (2015). Unifying principles of calcium wave propagation-insights from a three-dimensional model for atrial myocytes. *Biochim. Biophys. Acta*, 1853, 2131–2143. doi: 10.1016/j.bbamcr.2015.02.019

Voigt, N., Heijman, J., Wang, Q., Chiang, D. Y., Li, N., Karck, M., et al. (2013). Cellular and molecular mechanisms of atrial arrhythmogenesis in patients with paroxysmal atrial fibrillation. *Circulation* 129, 145–156. doi: 10.1161/CIRCULATIONAHA.113.006641

Weiss, J. N., Qu, Z., Chen, P.-S., Lin, S.-F., Karagueuzian, H. S., Hayashi, H., et al. (2005). The dynamics of cardiac fibrillation. *Circulation* 112, 1232–1240. doi: 10.1161/CIRCULATIONAHA.104.529545

Conflict of Interest Statement: The authors declare that the research was conducted in the absence of any commercial or financial relationships that could be construed as a potential conflict of interest.

frontiers in Physiology

METHODS
published: 02 November 2018
doi: 10.3389/fphys.2018.01483

Marker-Free Tracking for Motion Artifact Compensation and Deformation Measurements in Optical Mapping Videos of Contracting Hearts

Jan Christoph [1,2,3]* *and Stefan Luther* [1,2,3,4]

[1] *Biomedical Physics Group, Max Planck Institute for Dynamics and Self-Organization, Göttingen, Germany,* [2] *German Center for Cardiovascular Research, Göttingen, Germany,* [3] *Institute for Nonlinear Dynamics, University of Göttingen, Göttingen, Germany,* [4] *Department of Pharmacology, University Medical Center, University of Göttingen, Göttingen, Germany*

Optical mapping is a high-resolution fluorescence imaging technique, which provides highly detailed visualizations of the electrophysiological wave phenomena, which trigger the beating of the heart. Recent advancements in optical mapping have demonstrated that the technique can now be performed with moving and contracting hearts and that motion and motion artifacts, once a major limitation, can now be overcome by numerically tracking and stabilizing the heart's motion. As a result, the optical measurement of electrical activity can be obtained from the moving heart surface in a co-moving frame of reference and motion artifacts can be reduced substantially. The aim of this study is to assess and validate the performance of a 2D marker-free motion tracking algorithm, which tracks motion and non-rigid deformations in video images. Because the tracking algorithm does not require markers to be attached to the tissue, it is necessary to verify that it accurately tracks the displacements of the cardiac tissue surface, which not only contracts and deforms, but also fluoresces and exhibits spatio-temporal physiology-related intensity changes. We used computer simulations to generate synthetic optical mapping videos, which show the contracting and fluorescing ventricular heart surface. The synthetic data reproduces experimental data as closely as possible and shows electrical waves propagating across the deforming tissue surface, as seen during voltage-sensitive imaging. We then tested the motion tracking and motion-stabilization algorithm on the synthetic as well as on experimental data. The motion tracking and motion-stabilization algorithm decreases motion artifacts approximately by 80% and achieves sub-pixel precision when tracking motion of 1–10 pixels (in a video image with 100 by 100 pixels), effectively inhibiting motion such that little residual motion remains after tracking and motion-stabilization. To demonstrate the performance of the algorithm, we present optical maps with a substantial reduction in motion artifacts showing action potential waves propagating across the moving and strongly deforming ventricular heart surface. The tracking algorithm reliably tracks motion if the tissue surface is illuminated homogeneously and shows sufficient contrast or texture which can be tracked or if the contrast is artificially or numerically enhanced. In this study, we also show how a reduction

OPEN ACCESS

Edited by:
Ewald Moser,
Medizinische Universität Wien, Austria

Reviewed by:
Sean Parsons,
McMaster University, Canada
Elisabetta Cerbai,
Università degli Studi di Firenze, Italy

***Correspondence:**
Jan Christoph
jan.christoph@ds.mpg.de

Specialty section:
This article was submitted to Biomedical Physics, a section of the journal Frontiers in Physiology

Received: *24 February 2018*
Accepted: *01 October 2018*
Published: *02 November 2018*

Citation:
Christoph J and Luther S (2018) Marker-Free Tracking for Motion Artifact Compensation and Deformation Measurements in Optical Mapping Videos of Contracting Hearts. Front. Physiol. 9:1483. doi: 10.3389/fphys.2018.01483

in dissociation-related motion artifacts can be quantified and linked to tracking precision. Our results can be used to advance optical mapping techniques, enabling them to image contracting hearts, with the ultimate goal of studying the mutual coupling of electrical and mechanical phenomena in healthy and diseased hearts.

Keywords: fluorescence imaging, optical mapping, motion tracking, computer vision, cardiac arrhythmias, ventricular fibrillation, atrial fibrillation, heart rhythm disorders

1. INTRODUCTION

Optical mapping is a high-resolution fluorescence imaging technique, which is widely used in basic cardiovascular science (Herron et al., 2012). It employs optical probes or fluorophores, excitation light, high-speed cameras and filtering equipment and is typically used to image the electrophysiological activity that triggers the beating of the heart. With voltage- and calcium-sensitive dyes, for instance, it is possible to image action potential and calcium waves propagating across the heart surface in great detail and at very high speeds. To avoid undesired motion artifacts during such highly sensitive measurements, it has been necessary to suppress the beating of the heart during optical mapping by using pharmacological excitation-contraction uncoupling substances such as Blebbistatin (Fedorov et al., 2007) or DAM. Recent developments, however, have demonstrated that action potential and calcium waves can also be imaged as they propagate across the strongly contracting and deforming heart surface (Zhang et al., 2016; Christoph et al., 2017, 2018). In combining optical mapping with computer vision techniques and numerically tracking the heart's motion, the optical imaging of electrical activity during heart contraction is possible. The tracking inherently also allows the measurement of the cardiac deformation and thus the mechanical activity. The simultaneous imaging of both the heart's contractile motion and the electrochemical processes that generate the heart's contractions is pivotal for a better understanding of the heart's electrophysiology and mechanics and their mutual coupling.

In this work, we validate and discuss the performance of a 2D numerical motion tracking and motion compensation algorithm, which reliably tracks both the heart's rigid and non-rigid body motion and planar movements within video images obtained with a single camera during optical mapping. In previous studies, we used the algorithm to map action potential waves during sinus rhythm on the contracting three-dimensional heart surface using multiple cameras (Christoph et al., 2017) and to map arrhythmic action potential and calcium vortex waves during ventricular tachycardia and fibrillation on the surface of contracting rabbit and pig hearts (Christoph et al., 2018). Processing various optical mapping recordings obtained with different species and sensitivities (Di-4-ANEPPS, Di-4-ANBDQPQ, Rhod-2AM), we were able to retrieve motion-stabilized optical maps and co-moving optical traces, in which the fluorescent signals could be measured along a trajectory describing the movement of the tissue through the video image. After motion-stabilization, we were able to measure sequences of action potentials and calcium transients and their spatio-temporal evolution across the moving heart surface with a substantial reduction in dissociation-related motion artifacts. Dissociation-related motion artifacts occur due to a loss of the correspondence between a particular pixel of the camera sensor and a particular piece of cardiac tissue that is imaged with the pixel when the tissue moves. Furthermore, using the tracking data, we were able to measure and analyze the rapid mechanical deformations that the ventricular cardiac muscle exhibits during fibrillation, and were able to relate elasto-mechanical patterns arising in the heart wall to the turbulent electrical activity that causes the heart's fibrillatory contractions (Christoph et al., 2018). While the aim of our previous multi-camera study (Christoph et al., 2017) was to provide a proof-of-concept that three-dimensional electromechanical optical mapping is possible, our aim in the present study is to discuss the performance of the 2D tracking itself. In this study, we carefully assess and demonstrate the algorithm's efficacy and robustness in reliably detecting shifts of the tissue in the video images using both experimental and synthetic optical mapping data generated with computer simulations. In particular, the synthetic optical mapping data allows the comparison of the tracking outcomes to ground-truth data, as it becomes possible to precisely measure mismatches between the simulated and tracked tissue configurations. We reproduced experimental data as closely as possible and used the electromechanical computer simulations to mimic key video properties such as different contraction strengths, image contrasts and fractional intensity changes of the fluorescence. We then used the simulations to systematically generate optical mapping videos containing motion and motion artifacts and applied the tracking algorithm to track and stabilize the motion and remove the motion artifacts under various conditions.

2. MATERIALS AND METHODS

Experimental and synthetic optical mapping video data was generated and analyzed, the video data showing the contracting and fluorescing heart surface filmed through a monocular imaging setup with one camera. In particular, video data with varying amplitudes of motion and fluorescent signal strengths was analyzed.

2.1. Experimental Setup and Imaging Protocol

Contracting isolated Langendorff-perfused rabbit hearts ($N = 2$) were filmed during regular rhythm and ventricular arrhythmias using a single-camera optical mapping system, see **Figure 1**. Pharmacological excitation-contraction uncoupling agents such as Blebbistatin were intentionally not administered. Any other

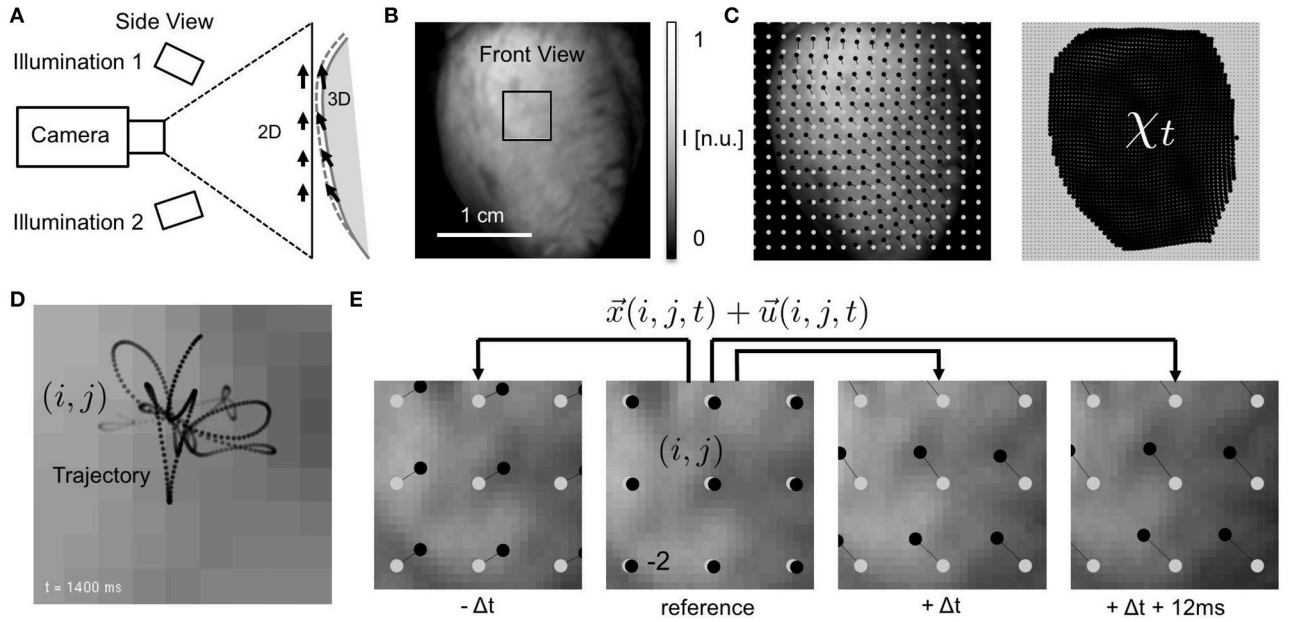

FIGURE 1 | Electromechanical optical mapping with beating, strongly deforming and fluorescing hearts. **(A)** Schematic drawing of experimental setup with single high-speed camera filming ventricular surface of rabbit heart (side view). Tracking of motion is possible only within the image plane (2D). **(B)** Raw video image (128 × 128 pixels) showing heart surface during optical mapping with voltage-sensitive staining (front view). ROI see **(E)**. **(C)** Tracked displacements and mechanical configuration χ_t at time *t* (left: every 8*th* vector, right: every 2*nd* vector). Points (black) indicating displacements of single tissue segment with respect to reference position (gray). See also **Supplementary Video 1**. **(D)** Trajectory of tracked tissue segment moving during ventricular fibrillation through pixel plane. Motion amplitudes are in the order of a few pixels (maximal 3–4 pixels from initial position, 2 ms temporal resolution). **(E)** Tracking of tissue movements during pacing with displacement amplitudes in the order of $|\vec{u}| \approx 10.0$ pixels. Points (black) indicating movements of single tissue segment (i,j) with respect to reference position (gray) in reference video image I_r (shown is every 10*th* segment or vector for illustration purposes).

mechanical constraints were avoided to let the heart beat freely. The optical mapping system consisted of a single EMCCD camera (Evolve 128, Photometrics Inc., 128 × 128 pixels, 16 bit dynamic range), using a high-aperture lens (objective Fujinon 1.4/9 *mm*, approx. 2 × 2 *cm* field of view, Fujifilm Corp.) and long-pass filtering (Edmund Optics, transmission > 610 *nm*) to filter the fluorescent light emitted from the heart surface. Hearts were stained with voltage-sensitive dye (Di-4-ANEPPS, 20 *ml* of 1 $mMol/l$ concentrated dye-Tyrode solution, 605 *nm* emission peak, bolus injection, recirculated). The dye was excited using four light-emitting diodes operating at wavelengths of 532 *nm*, powered by batteries (12 *V*, 26 *Ah*, rechargeable) to maintain constant, low-noise illumination. The diodes were positioned close to and around the camera lens and directed onto the central part of the ventricular wall, to establish a homogeneous illumination. For even distribution of the dye in the tissue, filming was started not earlier than 5 min after the dye was administered. Camera triggers were provided from an external triggering source (wave form generator, 33220A, Agilent) and recordings were obtained at a frame rate of $fps = 500Hz$. Hearts were excised from anesthetized New Zealand white rabbits ($N = 2$, female, 6–12 months, $2.5 - 3.5kg$) and inserted into cardioplegic solution for temporary cessation of cardiac activity. This study was carried out in accordance with German animal welfare laws and the recommendations of the Lower Saxony State Office for Customer Protection and Food Safety (LAVES) and the Federation of European Laboratory Animal Science Associations (FELASA). The protocol was approved by the Lower Saxony State Office for Customer Protection and Food Safety (LAVES). The hearts were positioned at the center of a 8-sided, glass-walled bath filled with oxygenated 37° warm Tyrode solution (95% O_2, 5% CO_2) and connected to a retrograde Langendorff-perfusion system (Hugo-Sachs Apparatus, March-Hugstetten, Germany). The flow rate of the perfusate was $30ml\,min^{-1}$ at a perfusion pressure of 50 $mmHg \pm 5\,mmHg$. The Tyrode solution was kept at a constant temperature of $37°C \pm 0.5°C$ (custom-made temperature control, Max Planck Institute for Dynamics and Self-Organization, Göttingen, Germany) and was constantly reperfused. Hearts were attached at the aorta to the retrograde perfusion outflow, hanging vertically from the aortic block, the apex facing the bottom of the bath. The camera was positioned at heart level and filmed the epicardial ventricular surface through one of the glass walls of the bath. Filming was performed at working distances of approximately $d = 30\,cm$. Hearts were filmed with their ventricular surface facing the camera, see **Figure 1A**. Mechanical pressure on the hearts was carefully avoided to prevent compression of the coronary arteries. Electrocardiograms were recorded using a data acquisition system (MP150, Biopac Systems Inc., Goleta, USA), acquiring data at a sampling rate of 2.0 *kHz* throughout the entire duration of the experiment.

2.2. Synthetic Optical Mapping Videos Generated With Computer Simulations

To be able to assess the efficacy of motion tracking and motion artifact compensation algorithms systematically, synthetic optical mapping video data was generated using computer simulations. A modified two-dimensional numerical reaction-diffusion mechanics model (Weise et al., 2011; Christoph, 2015) was used to create maps of electrical action potential wave patterns on a correspondingly contracting and deforming two-dimensional elastic surface, see section 2.2.1. The simulation data was used to deform a video image showing the heart surface during an optical mapping experiment with voltage-sensitive staining (Di-4-ANEPPS), and to modulate its pixel intensities according to the model's transmembrane voltage or electrical wave pattern, see section 2.2.2. Tracking and motion compensation was then applied to the synthetically generated optical mapping video data.

2.2.1. Numerical Model

A two-dimensional elastic excitable medium with tunable muscle fiber anisotropy was used to produce nonlinear waves of excitation propagating in a correspondingly deforming two-dimensional elastic medium, see **Figures 2A,B**. The elastic excitable medium consists of two numerical models, an electrical and an elastic model, coupled using forward electromechanical coupling. The electrical model allows the simulation of electrical impulse propagation, such as planar or target wave patterns, and also produces spiral wave patterns or chaotic wave activity composed of multiple spiral waves, as similarly observed in optical mapping experiments on the heart surface during arrhythmias. Due to the forward electromechanical coupling the electrical wave patterns cause local contractions and deformations of the elastic medium.

The electrical part of the model was simulated using the phenomenological, two-variable Aliev-Panfilov model (Aliev and Panfilov, 1996) comprised of two coupled partial differential equations with dynamic state variables u and v:

$$\dot{u} = \nabla^2 u - ku(u-a)(u-1) - uv \quad (1)$$

$$\dot{v} = \varepsilon(u)(ku - v) \quad (2)$$

where u and v are dimensionless normalized representations of the transmembrane potential and the conductance of a slow repolarizing current, or excitatory and refractory dynamics, respectively. Note that the range of u is within the interval [0,1]. The value of u is used to modulate the video images, see section 2.2.2. The diffusion term $\nabla^2 u$ provides the diffusive coupling between neighboring cells of the electrical lattice and leads to spreading waves of electrical excitation through the excitable medium. k, a, and $\varepsilon(u)$ are model parameters. The generation of active stress T_a due to excitation is modeled using a third partial differential equation that depends on the excitatory variable u as described previously (Nash and Panfilov, 2004):

$$\dot{T}_a = \varepsilon(u)(k_T u - v) \quad (3)$$

The equation simulates immediate and homogeneous active stress generation in response to electrical stimulation and simulates excitation-contraction coupling (Bers, 2002). The parameter k_T determines the magnitude of the active stress build-up in each cell of the model and defines the strength of the contractions occurring in the medium, see **Figure 2E**.

The elasto-mechanical model consists of a mass-spring damper system with controllable, tunable linearly transverse muscle fiber anisotropy (Bourguignon and Cani, 2000; Christoph, 2015). **Figure 2B** illustrates the lattice structure of the mass-spring damper system. The system consists of a regular lattice with cells defined by four vertices of the lattice and the cells containing sets of perpendicular springs attached to the barycenter and to the edges of the cells. The sets of springs can be oriented arbitrarily in the two-dimensional plane and introduce preferred orientations and anisotropy to the elastic system. One of the springs is set to be the active spring along which contractions occur upon electrical excitation, representing the fiber orientation. The springs rest lengths are modulated by the active stress variable T_a, which is in turn dependent on the excitation u, the active stress inducing a shortening of the active springs, which results in the contraction of the cell. As a result, the tissue exhibits contractions and large deformations with length changes in the order of up to 10%. The cells at the boundaries of the elastic medium are connected to additional springs, which are fixed with one of their ends in space, mimicking an elastic interface with its surrounding.

Each cell of the elastic model corresponds to one cell of the electrical model. The model was solved using finite differences numerical integration schemes. The electrical model was solved using forward Euler integration and the elastic model was solved using Verlet integration. During integration, both models were updated simultaneously.

Figure 2E shows how the contraction strength and overall amount of deformation of the model can be varied with the parameter k_T from Equation (3). Typical values for the parameter k_T used in this study were $k_T = [0.001, 0.005, 0.01, 0.1, 0.2, ..., 3.0]$. The graph shows that magnitudes of the displacements $|\vec{u}|$ exhibited by the nodes of the simulation grow rapidly with increasing k_T for very small k_T and less rapidly for larger k_T. The graph shows the average displacements $< |\vec{u}| >$, which were computed from the maximal separation of the positions $|\vec{x}_{xy}(t) - \vec{x}_{xy}(t')|$ of one vertex (x, y) of the simulation grid over the entire time course of the simulation and averaging over all vertices.

2.2.2. Synthetic Video Generation

The electrical patterns and deformations exhibited by the numerical model were used to create videos showing a deforming grayscale texture image, being locally superimposed by intensity modulations in locations where the tissue is electrically activated, see **Figure 2**. The video image is a video frame from one of the recordings obtained during the optical mapping experiments. The size of the video image of 100 × 100 pixels (slightly cropped) matches the grid size of the simulation. Therefore, in terms of spatial units, one cellular unit of the simulation domain corresponds to one pixel in the video data. **Figure 2E** correspondingly shows by how many pixels (approximately) the nodes of the mechanical grid move through the image plane

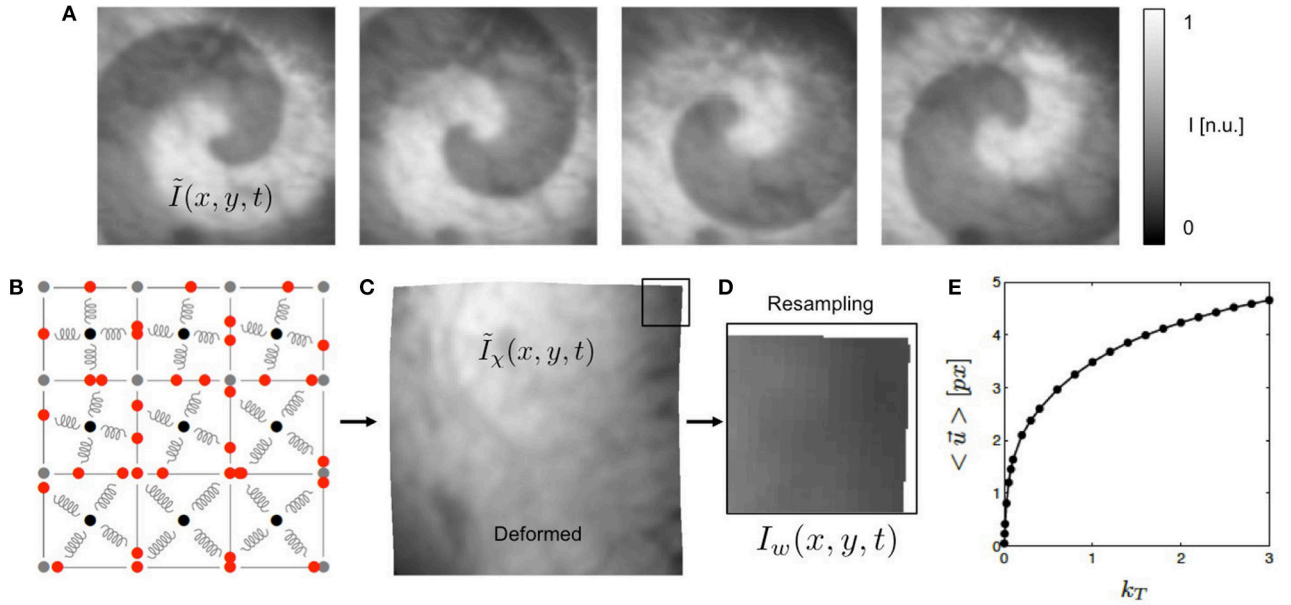

FIGURE 2 | Generation of synthetic optical maps using computer simulations. **(A)** Original optical mapping image (100 × 100 pixels) cropped from video still frame showing heart surface of rabbit heart superimposed by simulated spiral wave pattern (exaggerated) generated using reaction-diffusion excitable dynamics model. Simulated fluorescence intensity drop during depolarization of action potential (exaggerated). **(B)** Deformable elastic medium simulated with mass-spring damper lattice model (here consisting of only 3 × 3 cells for illustration purposes, system used in study consists of 100 × 100 cells). Each pixel in **(A)** corresponds to one cell. **(C)** Deformed video image $\tilde{I}_\chi(x,y)$ containing fluorescent signal ($\Delta F/F < 5\%$, not visible in a still frame), deformation caused by spiral dynamics. See also **Supplementary Video 3**. **(D)** Deformed and resampled part of video image $I(x,y)$. **(E)** Overall displacements of simulation in pixels depending on simulation parameter k_T to modulate contraction strength of springs.

$(0.5 - 5.0$ pixels). We found that for the chosen values for the parameter k_T we obtained similar magnitudes of motion as seen during the experiments. The intensity values of the video image were normalized $I \in [0,1]$ (dark cropped areas corresponding to values < 0.1).

First, the simulation output of the electrical model was used to create videos showing an optical mapping grayscale image of the heart surface superimposed by a rotating spiral wave pattern, the pixels' intensities decreased by a fraction of the value of the excitatory variable u, as shown in **Figure 2A**. Because each pixel of the original undeformed video image corresponds to a discrete cell of the simulation, there is a one-to-one correspondence between the pixel's original intensity value and the cell's value for u. More specifically, the time-varying two-dimensional maps of the electrical variable $u(x,y,t)$ were used to decrease the otherwise static pixel intensity of the texture image $I_{texture}(x,y)$. The intensity value I in each pixel (x,y) was modulated linearly as follows:

$$\tilde{I}(x,y,t) = I_{texture}(x,y) + f \cdot u(x,y,t) + \xi \qquad (4)$$

where $|f| \in [0,1]$ is a scaling factor and represents the maximal intensity change of the fluorescence-induced intensity modulations or fractional change in fluorescence in normalized units and ξ corresponds to noise. Typical values used in this study for the parameters were $f = [-0.01, -0.03, -0.06, -0.12]$ and $\xi = [0.005, 0.01, 0.03]$. While in this study we only simulated a decrease in the signal with $f < 0$, mimicking the behavior of typical voltage-sensitive dyes, it would also be possible to simulate an increase in fluorescence with $f > 0$ as seen during calcium-sensitive imaging. The normalized fractional change in fluorescence f represents the fractional change in fluorescence $\Delta F/F$ exhibited by fluorescent dyes in optical mapping experiments. The texture image $I_{texture}(x,y)$ was normalized with all its intensity values in the range $I \in [0,1]$. The histogram of grayvalues $\rho(I)$ of the texture image could be scaled such that the image properties fulfilled specific criteria; for instance, the video images contrast matching a predefined local image contrast c with its corresponding contrast distribution, see **Figure 8C** and section 3.2.

The image frames of the resulting video sequence $\tilde{I}(x,y,t)$ were then deformed within the two-dimensional image plane according to the deformed geometry or time-varying mechanical configuration $\chi(t)$ of the simulation grid, adding the displacements $\vec{u}(x,y,t)$ to the vertices defining each pixel, yielding a deformed, intensity modulated video $\tilde{I}_\chi(x,y,t)$, see **Figure 2C**. The magnitudes of the deformations could be tuned using the parameter k_T from Equation (3). The average displacement strengths given in pixels achieved for various values for k_T are shown in **Figure 2E**. To obtain videos showing the moving, deformed texture $\tilde{I}(x,y,t)$ in a static laboratory camera view frame, the video data was then resampled, redistributing the pixel intensity values of $\tilde{I}(x,y,t)$ into a regular undeformed pixel grid, yielding resampled video sequences $I(x,y,t)$, see **Figure 2D**. Resampling was performed using polygon clipping algorithms. The simulations

typically included $N_t = 50,000$ time steps, from which every $10th$ time step was extracted, the resulting image sequences then consisting of 5,000 frames, showing about 10 spiral rotations.

2.3. Motion Tracking

Motion tracking was performed with both the experimental and the synthetic optical mapping videos to obtain two-dimensional in-plane displacement vector fields $\vec{u}(x, y, t)$, the displacement vectors indicating planar local shifts of tissue segments in the video images. Motion tracking was performed using a Lucas-Kanade optical flow estimation algorithm (Periaswamy et al., 2000, see also Christoph et al., 2017, 2018). Generally, the motion tracking algorithm is able to track rigid and non-rigid body motion, affine deformations as well as translational and rotational motion in images at a sub-pixel resolution. The motion tracking algorithm does not require any visible characteristic features, landmarks or markers attached to the heart surface to facilitate or assist the motion tracking. Instead it estimates optical flow that occurs in between two images. We found that simply the visible anatomical texture of the heart surface is sufficient to associate two local tissue segments in between two frames with each other. Nevertheless, we enhanced the anatomic texture and the visible features on the heart surface numerically to increase the accuracy and robustness of the motion tracking algorithm, see **Figure 4** and section 3.3.

When tracking experimental data, short video sequences with durations of $1.0 - 10.0\,s$ ($500 - 5,000$ frames, $500\,Hz$) of the optical mapping recordings were extracted and stored as normalized videos containing intensity values $I \in [0, 1]$ with floating point precision, the intensity values normalized by the maximal and minimal values found in the entire video sequence v_s, see also **Figure 1B**:

$$I(x, y, t) = (v_s(x, y, t) - \min(v_s))/(\max(v_s) - \min(v_s)) \quad (5)$$

such that the experimental and the synthetic video data were stored in the same format. Next, in both the experimental and the synthetic data, the motion was tracked throughout the sequence of video images, comparing each video frame to one predefined reference frame $I_r(x, y, t)$ out of the sequence ($t \in [1, ..., N]$ frames), registering the shifts of the tissue in between the two frames in each pixel. For data showing periodic cardiac activity, a reference frame showing the undeformed, non-contracted heart shortly before ($25\,ms \pm 5\,ms$) the electrical activation (depolarization) of the tissue was selected. For data showing arrhythmic cardiac activity, an arbitrary frame or a frame in the

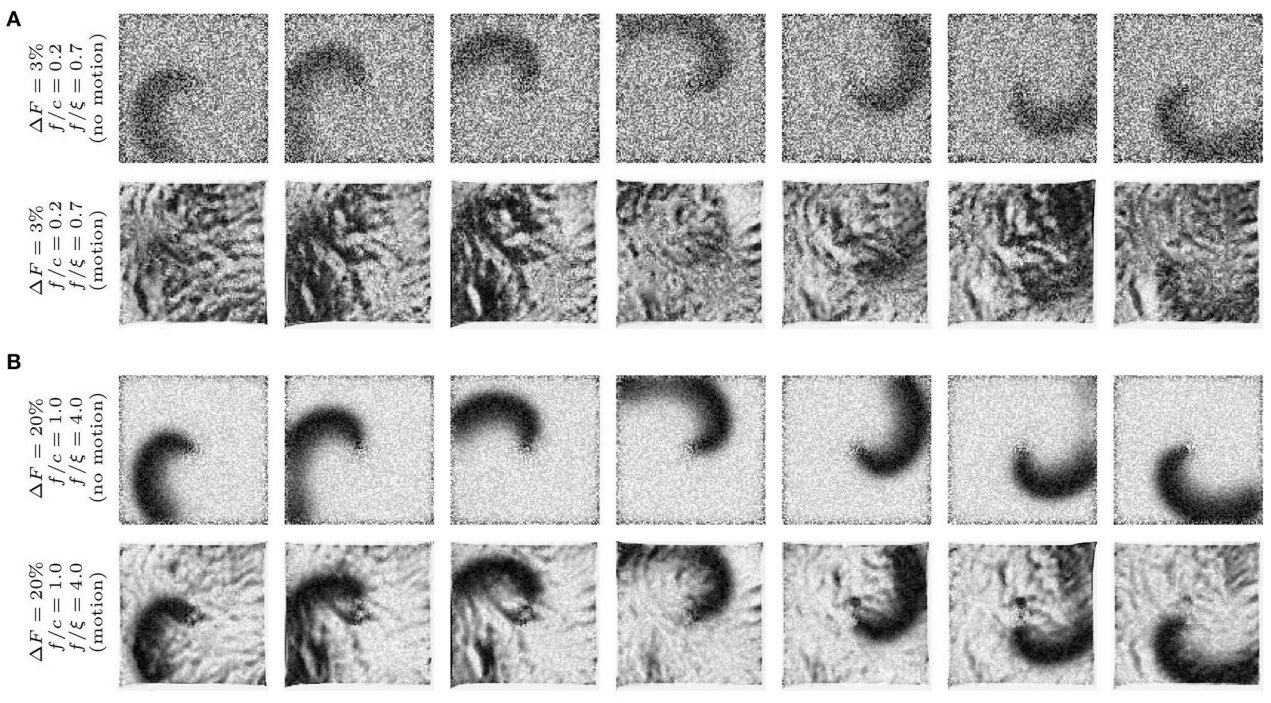

FIGURE 3 | Synthetic optical mapping videos (pixel-wise normalized) with simulated spiral waves on a deforming heart surface. The spiral wave pattern is caused by electrical activity and displayed as an intensity decrease which is typically seen during voltage-sensitive optical mapping. Clockwise rotating spiral wave with two different signal strengths f: **(A)** weak signal ($\Delta F/F = 3\%$) and **(B)** strong signal ($\Delta F/F = 20\%$) on non-deforming (top sequence) and deforming (bottom sequence) heart surface. The noise ξ is constant in all image sequences ($\xi = 0.03$) even though it appears to be stronger in **(A)** due to the pixel-wise normalization (pixel intensities $I \in [0, 1]$ dimensionless normalized units, n.u.). The amplitude of motion is the same in all image sequences ($|\vec{u}| \approx 3 - 5$ pixels). On the deforming surface the spiral wave pattern is superimposed by motion artifacts. **(B)** Due to the large signal strength f, the spiral wave is still visible on the deforming medium and motion artifacts are comparatively low. The amount of motion artifacts depends on the signal-to-contrast ratio $f_C = |f|/c$, the ratio of fluorescence signal strength f to the strength of the local contrast c or short-scale intensity gradients in the image (c constant in all images).

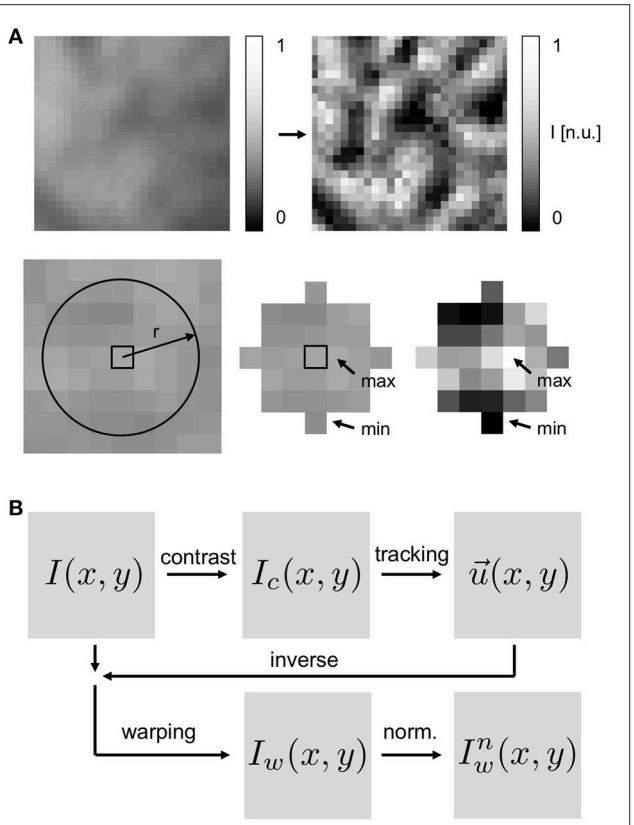

FIGURE 4 | Motion tracking using contrast-enhanced video images: **(A)** Top left image: original, raw video image with pixel intensities normalized to minimal and maximal values in entire video ($I(x,y) \in [0,1]$). Top right image: contrast-enhanced video image used for motion tracking ($I_C(x,y) \in [0,1]$) with pixel intensities normalized by minimal and maximal value in local neighborhood (disk-shaped region $\mathcal{S}_{xy}$) around each pixel. Resulting contrast-enhanced images show maximally intensified short-scale image gradients and suppressed large-scale image gradients. **(B)** Schematic of motion tracking procedure with tracking of contrast-enhanced images I_C. The original video images I are deformed using the inverse tracking data $-\vec{u}$ to obtain motion-stabilized or warped videos $I_W(x,y,t)$, which are then further post-processed, i.e., pixel-wise normalized (I_W^n).

middle of the image sequence was selected as the reference frame. The motion was tracked either in the original normalized videos $I(x,y,t)$, as derived in Equation (5), or in contrast-enhanced videos $I_c(x,y,t)$, see below, which show the maximally intensified contrast of the tissue, see **Figure 4**. To obtain contrast-enhanced videos, each pixel's intensity value $I(x,y,t)$ was renormalized by the maximal and minimal intensity values found within a small disk-shaped sub-region $\mathcal{S}_{x,y}$ around the pixel:

$$I_c(x,y,t) = (I(x,y,t) - \min(\mathcal{S}))/(\max(\mathcal{S}) - \min(\mathcal{S})) \qquad (6)$$

the sub-region $\mathcal{S}_{x,y}$ typically retaining a diameter of 5–7 pixels and renormalizing all pixels in each video frame individually. The conversion produced video sequences, in which the local tissue contrast is maximally intensified and the tissues' features and its unique local texture become very pronounced, see **Figure 4A**. The conversion also caused larger-scale intensity gradients across the images to vanish. Motion was then tracked in either the resulting contrast-enhanced videos $I_c(x,y,t)$ or the original simply normalized videos $I(x,y,t)$ to compare the different outputs. The typical frequency of the detectable features in the video images is a few pixels (5–10), see section 3.2, and given by the granular, tile-shaped texture of the tissue. Two-dimensional in-plane displacements $\vec{u}(x,y,t) \in \mathbb{R}^2$ were determined for each pixel (x,y) in every frame $I(x,y,t)$ or $I_c(x,y,t)$ throughout the normal or contrast-enhanced video image sequences. The displacement fields $\vec{u}(x,y,t)$ were stored for further analysis. Video data in which the heart deformed excessively or rotated, such that parts of the heart turned away from the camera or moved out of its field of view was discarded. Motion tracking (Matlab), warping and resampling (custom C++ code) and other processing requires approximately 1–3 min of computation time per video image (in the order 100×100 pixels) on a single CPU.

2.4. Motion Stabilization and Motion Artifact Removal

Using the displacement data obtained during the motion tracking procedure, we processed the original videos and produced warped or motion-stabilized videos in which motion appears to be absent or significantly reduced, see also **Supplementary Video 3**. The tracked displacements were used to deform each video image to match the image in the reference frame. More precisely, motion-stabilized or warped video images $I_w(x,y)$ were obtained by deforming the original video images $I(x,y)$ using the inverse tracked displacements $-\vec{u}(x,y)$ to shift and deform each pixel accordingly, see **Figure 4B**. The deformed video image was then resampled in the image plane using the regular cartesian pixel grid yielding a deformed, resampled and motion-stabilized video image $I_w(x,y)$, see **Figures 2D**, **4B**. The resulting frames showed a similarly deformed tissue configuration χ_r as shown in the reference frame I_r throughout the sequence of video images. For synthetic video data containing motion, the successfully tracked and warped video images $I_w(x,y,t)$ were very similar to the original undeformed video images $\tilde{I}(x,y,t)$ containing only fluorescent activity.

2.5. Post-processing

Post-processing for the visualization of electrical waves was performed equally for both experimental and synthetic optical mapping data. Experimental video data was stored as unsigned (16 bit) integer valued-data and converted into floating-point valued data after normalizing each pixel by the minimal and maximal pixel value in the entire video, yielding normalized dimensionless pixel intensity values $I(x,y,t) \in [0,1]$ as described by Equation (5). The simulation data was stored as normalized data with all pixel values normalized $I(x,y,t) \in [0,1]$. To visualize wave activity the video data was normalized pixel-wise, meaning that each time-series $I_{xy}(t)$ in each pixel was normalized individually by its minimal $I_{\min} = \min(I_{xy}(t))$ and maximal $I_{\max} = \max(I_{xy}(t))$ intensity value respectively, see also (Laughner et al., 2012):

$$I_n(x,y,t) = (I(x,y,t) - I_{\min})/(I_{\max} - I_{\min}) \qquad (7)$$

Alternatively, the video data was normalized pixel-wise using a sliding-window normalization, meaning that each time-series $I_{xy}(t)$ in each pixel was normalized individually by the minimal $I_{\min} = \min(I_{xy}(t))$ and maximal $I_{\max} = \max(I_{xy}(t))$ intensity value found within a temporal window of size $t \pm w$, respectively, the window size being at least one cycle length of the wave activity (e.g., approx. 100 *ms* during ventricular fibrillation). Both normalizations equally amplify temporal intensity fluctuations in each pixel (cf. **Figure 7**) and they are typically used to visualize action potentials or calcium cycling. However, both normalizations can also amplify intensity fluctuations that are not produced by electrical activity but instead by optical flow or in other words motion artifacts.

In the synthetic data, motion artifact strengths $\tilde{m}(x, y, t)$ were computed by calculating the absolute difference between the motion-stabilized video, which was obtained in an exact co-moving frame, and the video obtained in a static camera view or lab frame before or after tracking. The exact co-moving video corresponds to an idealized measurement, in which the amplified, normalized fluorescent signal can be measured precisely in each tissue coordinate. This video is not available in experiments because motion tracking algorithms are imperfect and the tracked tissue configuration is only an approximation of the real tissue configuration. In simulations, however, the real tissue configuration is available. Motion artifact strengths $\tilde{m}$ were computed using the pixel-wise normalized videos:

$$\tilde{m} = \sum_{x,y,t} (|\tilde{I}_n(x, y, t)| - |I_n(x, y, t)|) \tag{8}$$

summing the absolute differences of the two videos' pixel intensities over all pixels and video frames. The video $\tilde{I}_n(x, y, t)$ that was obtained in the exact co-moving frame was first pixel-wise normalized, then deformed and finally resampled. The video $I_n(x, y, t)$ that was obtained in a static camera view frame with pixel-based video-processing was first deformed, then resampled and finally pixel-wise normalized. The first video will never contain motion artifacts and the latter video may contain motion artifacts.

3. RESULTS

3.1. Efficacy of Motion Artifact Removal in Experimental Data

Figure 5 shows a quasi-planar action potential wave propagating across the contracting ventricular surface of a rabbit heart, see also **Supplementary Video 2**. The wave was elicited after the application of a pacing stimulus on the endocardial wall close to the apex of the heart using a MAP-catheter electrode. As a result, the wave propagated upwards from the apex toward the base of the heart. Due to the voltage-sensitive staining and long-pass emission filtering, the fluorescent intensity decreases on the detector during the depolarization of the action potential. Correspondingly, activated or depolarized tissue corresponds to dark regions, whereas undepolarized tissue during the diastolic interval corresponds to bright regions in the image. The video data was normalized using a pixel-wise sliding-window normalization, see section 2.5. Other post-processing such as smoothing was not performed. The upper image series shows the action potential wave visualized after tracking and motion stabilization in the co-moving frame, in which motion artifacts appear to be absent or at least substantially reduced. The action potential propagates across the ventricular surface

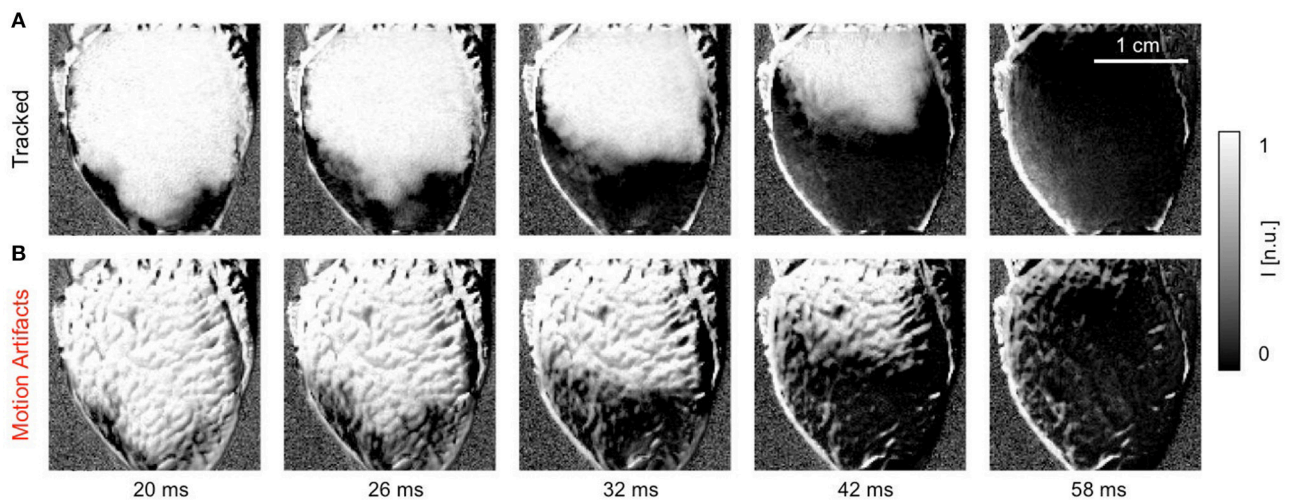

FIGURE 5 | Efficacy of motion tracking and motion artifact compensation during electromechanical optical mapping: planar action potential wave propagating upwards across ventricular surface of a rabbit heart as the heart contracts (dark areas correspond to depolarized tissue and bright areas correspond to undepolarized tissue, staining Di-4-ANEPPS, pixel-wise sliding-window normalization [n.u.]). See also **Supplementary Video 2**. **(A)** Motion-stabilized image sequence with substantial reduction in dissociation-related motion artifacts after motion tracking and numerical motion-stabilization. **(B)** The same image sequence without motion tracking and stabilization. Motion artifacts appear as a high-frequency, network-like spatial pattern with black-and-white deflections superimposing and distorting the action potential wave pattern. Both image series were processed in the same way before and after motion tracking.

as the heart contracts. Depolarized and undepolarized tissue areas correspond to two clearly distinguishable, homogeneous areas with low and high light intensities due to the pixel-wise normalization of the data, see Equation (5). For comparison, the lower image series shows the same image sequence without motion tracking and motion stabilization. Due to the shifts of the tissue and a deallocation or dissociation of tissue regions and their corresponding pixel on the camera sensor measuring the tissue region during this pixel-based measurement, the video contains dissociation-related motion artifacts. Such dissociation motion artifacts appear as a network-like, tile-shaped spatial pattern with black-and-white deflections superimposing and distorting the action potential wave pattern, which can be seen in the upper image sequence. Note that both image series were processed in the same way, normalizing the optical traces obtained in each pixel using a sliding-window normalization, see Equation (5). However, the motion that is still present in the lower image series causes the undesired high-frequency spatial motion artifact patterns. In contrast, because the motion was tracked and stabilized in the upper image sequence before the post-processing, the high-frequency spatial motion artifact pattern vanished.

Further analysis of the motion-stabilized video data shows that it is possible to improve the robustness and accuracy of measurements, such as activation time or action potential duration measurements. **Figure 6A** shows activation maps

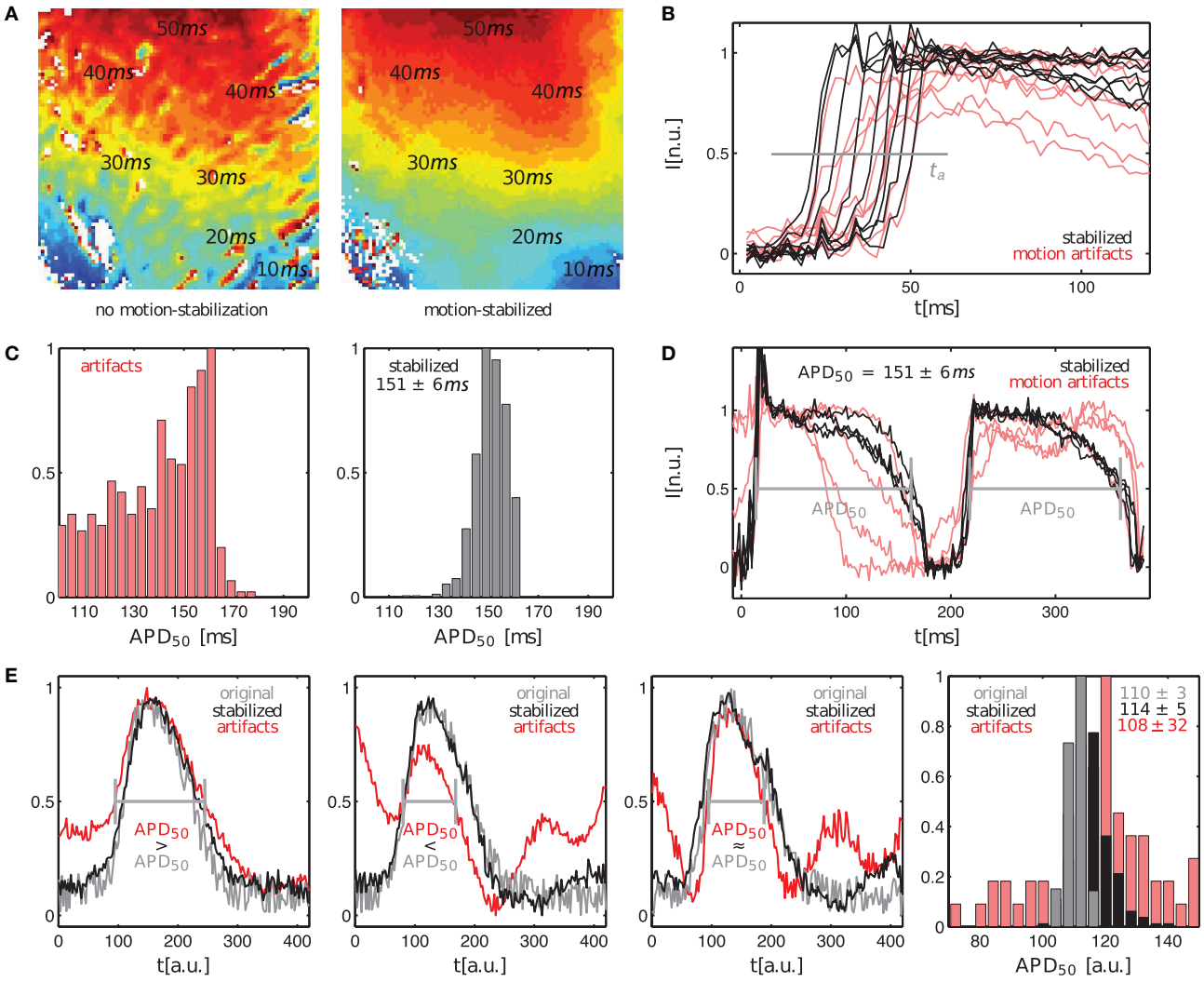

FIGURE 6 | Comparison of activation time and action potential duration measurements in optical maps with and without motion artifacts. **(A)** Activation maps showing quasi-planar action potential wave propagation on left ventricular surface of contracting rabbit heart before tracking and without motion-stabilization (left) and after tracking and with motion-stabilization and motion artifact compensation (right). **(B)** Upstroke detection (at 0.5) for computation of activation maps in **(A)**. **(C,D)** Action potential duration measurements of $< APD_{50} >= 151\,ms \pm 6\,ms$ for motion-stabilized video data. Variance in action potential duration due to motion decreases with motion compensation. **(E)** Comparison of uncertainty in action potential duration measurements in original artifact-free data ($APD_{50} = 110 \pm 3 a.u.$) and tracked, motion-stabilized synthetic video data ($APD_{50} = 114 \pm 5\,a.u.$). Uncertainties without motion or motion compensation are both $\sigma_{APD} < 5\%$ and are much larger with motion.

computed for the quasi-planar action potential wave shown in **Figure 5**. The activation map on the left was computed from the raw, non-tracked video data including motion artifacts. The activation map on the right was computed from the tracked, motion-stabilized video data. Both maps exhibit a global gradient from short (blue: $t^a < 10\,ms$) to long activation times (red: $t^a > 40\,ms$), beginning with short activation times close to the apex and large activation times further up on the ventricular surface. The gradients in each of the activation maps reflect the situation in **Figure 5**, in which a wave travels across the ventricular wall starting from the apex toward the base of the heart. However, one can observe strong artifacts in the raw activation map containing motion. In about 15% of the pixels the activation times deviate strongly ($> 10\%$) from the activation times in the tracked map. It seems that the motion artifacts seen in the normalized video sequence (lower sequence) in **Figure 5** similarly manifest in the activation maps. Otherwise, the high similarity of both activation maps suggests that activation times and activation maps can, at least to a certain extent, be computed from unprocessed video data. The maximal activation time, that is the time which was required for the wave to traverse the entire field of view, is equal in both untracked and tracked maps with $t^a_{max} = 52\,ms \pm 2\,ms$. We frequently found that in the uncompensated, raw video data with large fluorescent signals (here $\Delta F/F \approx 6 - 8\%$) and moderate motion, simply the upstroke of the action potential can be sufficient for the computation of activation times, provided it can be detected appropriately. However, note that without motion tracking, the measurement of activation times is nevertheless inaccurate because in a non-co-moving frame of reference the spatial correspondence is lost. **Figure 6B** shows exemplary traces of the action potential upstrokes obtained from both the raw and the motion-compensated videos for comparison. In the uncompensated optical maps, the action potential upstrokes are in some cases not as steep or pronounced as in the motion-stabilized optical maps. This is the probable cause of the artifact patterns seen in the raw activation map (left) in **Figure 6A**.

Figures 6C,D shows action potential duration measurements obtained from the same data set shown in **Figure 5**. The action potential duration (APD) of the 2 subsequent action potentials shown in **Figure 6B** was measured in approximately 500 traces obtained from the tracked, motion-stabilized video data by computing the delay between the upstroke and repolarization times at 50% of the height of the action potentials (APD_{50}), or at a value of 0.5 in the normalized videos. **Figure 6C** shows histograms with the distributions of action potential durations for the raw, untracked video data including motion artifacts and the tracked, motion-stabilized video data. In case of the raw data without motion-stabilization, the histogram exhibits a broad distribution of APDs, which prohibits the unique identification of a dominant action potential duration. With motion-stabilization, the histogram exhibits a narrow distribution from which it is possible to determine a mean action potential duration of $APD_{50} = 151 \pm 6\,ms$. A similar drastic decrease in APD measurement uncertainty after tracking is also found by Khwaounjoo et al. (2015).

Figure 6E shows the variability and uncertainty in the action potential duration measurement in synthetic video data with motion. Three exemplary plots obtained from three adjacent sites show the original artifact-free course of the simulated action potential (gray) together with the tracked, motion-stablized curves (black) and the curves including motion-artifacts (red) for average maximal displacements of $< |\vec{u}_{max}| >= 3.2$ pixels. The original and the motion-stabilized curves (gray and black) can barely be distinguished from each other given the pronounced amount of noise, while the curves including motion artifacts (red) deviate strongly from both the original and motion-stabilized curves. The right panel in **Figure 6E** shows the histogram with the three respective distributions of action potential durations (computed with the video data smoothed with kernel sizes $k_x = k_y = 3$ pixels and $k_t = 11$ time steps; the smoothing provides more robust upstroke and repolarization time detections). As for the experimental data, the distribution of measured action potential durations with motion artifacts is very broad with a high variability in action potential durations. The histogram's maximum indicates an $APD_{50} \approx 120 a.u.$, which deviates by about 17% from the actual value. The average ($APD_{50} = 108 \pm 32 a.u.$) only deviates by about 2% from the true value, but the distribution is very broad and has a large uncertainty of 30%. Both the original and the motion-stabilized distributions are narrow and very distinctly exhibit a peak, which we used to compute the average action potential durations of $APD_{50} = 110 \pm 3 a.u.$ and $APD_{50} = 114 \pm 5 a.u.$, respectively. The tracked, motion-stabilized data deviates by 3.6% from the original data and exhibits a slightly higher uncertainty of $\sigma_{APD} = 4.5\%$ (about 1.7 times as large as the uncertainty for the original data with $\sigma_{APD} = 2.7\%$).

The efficacy of the tracking algorithm in inhibiting motion artifacts during arrhythmias is demonstrated in **Figure 7**. The image sequences in **Figure 7A** show chaotic action potential vortex wave activity mapped on the contracting rabbit heart surface during ventricular fibrillation. Just as in **Figure 5**, motion artifact patterns have decreased drastically due to the motion tracking. Instead of heavy motion artifacts (B,D) one immediately observes action potential wave patterns (A,C). Again, due to the voltage-sensitive imaging, depolarized tissue corresponds to dark and repolarized or inactivated tissue to white areas. For comparison, we show the same data for two different normalizations [A,B: pixel-wise as in Equation (5); C,D: pixel-wise within sliding-window with $\tau = 140 - 160\,ms$]. The two different normalizations show that the motion artifact pattern and the reduction in motion artifacts is independent from other processing steps and the particular visualization of the wave pattern. In both uncompensated optical maps that are obscured with motion artifacts one can observe the typical high-frequency spatial motion artifact patterns, as observed in **Figure 5**.

In summary, **Figures 5–7** demonstrate that it is possible to perform optical mapping experiments with beating isolated hearts and to reliably retrieve optical maps with substantially reduced motion artifacts from the moving, contracting heart surface during regular and irregular cardiac rhythms. The differences between the raw and motion-stabilized video data are substantial and can immediately be identified in the optical maps. Motion artifacts correspond to high-frequency, short-scale

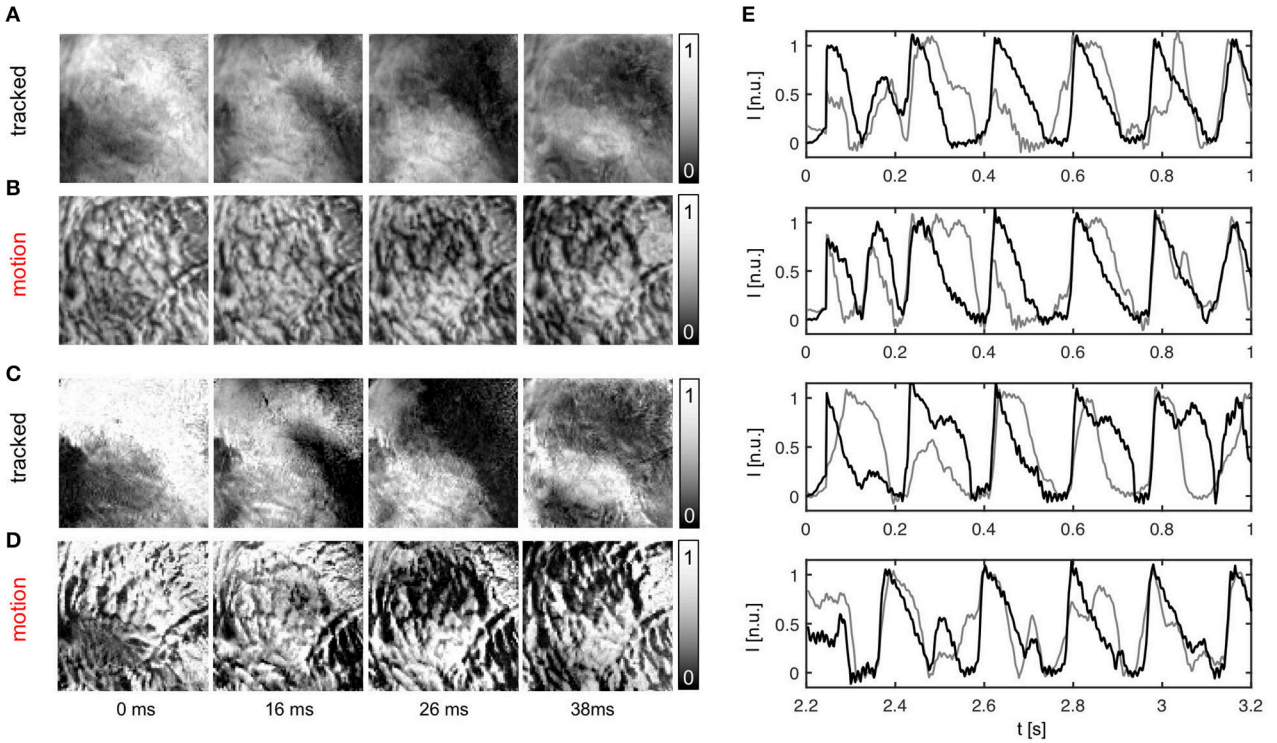

FIGURE 7 | Action potential vortex waves mapped on contracting left ventricular surface of rabbit heart during ventricular fibrillation. Electromechanical optical mapping was performed with voltage-sensitive staining (Di-4-ANEPPS, 128 × 128 pixels, 500 fps, approx. 1 × 1 cm field of view). **(A,C)** Maps with substantially inhibited motion artifacts after tracking and motion-stabilization showing action potential waves. **(B,D)** Action potential wave maps without tracking and motion stabilization. Maps exhibit strong motion artifacts. In **(A,B)** and **(C,D)** the same activity is shown with two different normalizations, see main text. **(E)** Exemplary time-series obtained from optical maps with motion before (gray) and after tracking and numerical motion-stabilization (black).

spatial patterns, which are absent in the registered, co-moving maps.

3.2. Characterization and Quantification of Motion Artifacts

Here, we introduce a framework for characterizing and quantifying motion artifacts, analyzing their spatial characteristics and appearance in optical maps. As can be seen in **Figures 3**, **5B**, **7B,D**, motion produces a very characteristic network-like, tile-shaped dark-bright spatial pattern of pixel intensities in normalized optical maps. We reproduced this characteristic motion artifact pattern in synthetic optical maps and systematically varied important video properties, such as displacement or contraction strength and fluorescent signal strength (ΔF or f), to determine their contribution to the emergence of this spatial motion artifact pattern. Next, we related the data to motion artifact patterns found in experiments, see **Figures 8**–**10**. **Figure 8A** shows how motion artifacts $\tilde{m}$ increase with increasing amplitudes of motion (here for given values of signal strength f and image contrast c, see below) in the synthetic data. The overall amplitude of motion is given as the average of maximal displacements $< |\vec{u}_{max}| >$, computed by averaging the magnitudes of the maximal shifts $|\vec{u}_{max}(x,y)| = \max|\vec{x}_i - \vec{x}_j|$ that each vertex (x,y) underwent throughout the simulation. The maximal shifts are the maximal distances measured in pixels between a vertex at time t_i and the same vertex at time t_j. Motion artifacts occur even with slight tissue movement (finite and quickly increasing $\tilde{m}$ for < 1 pixel), which underscores the sensitivity of optical mapping to motion. The graph also shows that the strength of motion artifacts $\tilde{m}$ increases less quickly for shifts larger than $\sim 3-5$ pixels, indicating an involvement of other mechanisms in the emergence and development of motion artifacts, see **Figure 8A**. Next, **Figures 8B,C** show that the strength of motion artifacts does not only depend on the strength of the contraction and amplitude of the motion, but also depends on the signal strength f, as well as on the local image contrast c and their relative magnitudes with respect to each other. The signal strength f is the strength or amplitude of the fluorescent signal in the raw, normalized synthetic video data. In the experiments it would correspond to the fractional change in fluorescence $\Delta F/F$. The local image contrast c is a measure for the maximal intensity differences that can be found in a small sub-region $\mathcal{S}_{xy}$ around each pixel, see Equation (10). The image contrast c expresses the likeliness of such intensity differences to cause dissociation-related motion artifacts. Dissociation-related motion artifacts occur due to a loss of the sensor-tissue correspondence and are consequently produced by optical flow on the camera sensor caused by the tissue's movements through the video image. Considering these key determinants of motion artifacts, we created synthetic optical mapping videos

for various values of the fluorescent signal strength f, the local image contrast c and varying amplitudes of motion $< |\vec{u}_{max}| >$. In the following, the fluorescent signal strength f and image contrast c are given as normalized units, where $f \in [0,1]$ represents a normalized unit of maximal fractional change in fluorescence intensity and $c \in [0,1]$ represents a normalized unit of image contrast. **Figure 8B** shows how motion artifacts remain small for large simulated fluorescent signals f, i.e., they are less noticeable, and increase with decreasing signal strength and saturate at a stationary value ($\sim$ 0.15) with vanishing signal f. More importantly, the graph demonstrates that increasing local image contrast c promotes the emergence of motion artifacts. With fixed fluorescent signal strength f and increasing image contrast c, i.e., the intensity of structures and features visible in the image, motion artifacts become larger. Motion artifacts are thus a relative measure. With little or no fluorescent signal ($f = 0$) or very large image contrast compared to the signal strength ($f/c << 1$) one obtains in large parts only motion artifacts during an optical mapping measurement.

Accordingly, **Figure 3** illustrates how motion artifacts emerge under various conditions in synthetically generated optical maps. In particular, it highlights how motion artifact strength $\tilde{m}$ varies greatly with differing signal strengths f. The image series show a clockwise rotating action potential spiral wave, which induces a dark spiral wave pattern on an otherwise brighter background in the synthetic video data. In real optical mapping experiments, such data would be obtained with voltage-sensitive staining (for instance using Di-4-ANEPPS). The strength of the motion is the same in all images. The video data was normalized pixel-wise, as described by Equation (5) and equally as shown in **Figure 5A**, to facilitate viewing of the intensity fluctuations caused by the electrical wave activity. The image series in **Figure 3A** show a spiral with low signal strength ($f = -0.02$) on a non-deforming vs. a deforming heart surface, respectively. The image series in **Figure 3B** show a spiral with larger signal strength ($f = -0.12$) on a non-deforming vs. a deforming heart surface, respectively. Due to the absence of motion in the upper image series in each of the two panels, the spiral wave patterns are not obscured by motion artifacts, they are artifact-free. In contrast, the same spiral wave patterns shown in the lower image series in each panel are obscured by motion artifacts. It is important to note that the noise level ($\xi = 0.03$) and the local image contrast ($c = 0.055$), as well as the amplitude of the contraction and motion ($< |\vec{u}_{max}| > \approx 3 - 5$ pixel), are the same in all four image sequences. Due to the pixel-wise normalization, which normalizes all activity including noise and eliminates differences in absolute signal strength (baseline), all relative signal intensity changes become amplified to the same level. Therefore, the spiral wave in the upper image sequence in **Figure 3A** is superimposed by stronger noise and is perceived weaker in comparison to the upper image sequence in **Figure 3B**, which contains a stronger signal in comparison to the noise level ($\xi_1 = \xi_2 = 0.03$). Comparing the two image series with motion shown in **Figures 3A,B**, one notices that the deformed image sequence with low signal strength f is heavily distorted and obscured by motion artifact patterns, while the deformed image sequence with high signal strength f is less affected by motion artifacts. The spiral wave pattern is nevertheless visible. Were the image contrast in the upper image sequence larger ($c_1 > c_2$) and the two signal strengths of both spirals the same ($f_1 = f_2$), one would obtain a very similar outcome. The figure illustrates that with increasing fluorescent signal strength f or decreasing image contrast c motion artifacts become less severe. Therefore, we suggest defining the signal-to-contrast ratio:

$$f_c = \frac{f}{c} \tag{9}$$

which indicates the relative signal strength f in comparison to the local image contrast c and gives an estimate for the likeliness of motion artifacts to be visible in optical mapping data. Both values f and c can be determined in experimental data, see **Figures 9D,E** and below. The situation in the image sequence shown in **Figure 3A** ($f_c = |f|/c = 0.02/0.055 = 0.36$) would be observed during voltage-sensitive imaging with Di-4-ANEPPS with fractional changes in fluorescence intensity typically ranging in the order of $\Delta F/F \approx -3\%$ to -8%. Strong signal strengths f as shown in the image sequence in **Figure 3B** ($f_c = |f|/c = 0.12/0.055 = 2.2$) are typically encountered, for instance, during calcium-sensitive imaging with Rhod2-AM with fractional changes in fluorescence intensity typically ranging in the order of $\Delta F/F \approx 10 - 30\%$. Note that the synthetic videos in **Figure 3** were generated by deforming a video image that was obtained in an optical mapping experiment with voltage-sensitive staining (Di-4-ANEPPS). The image shows the typical granular texture of the ventricular surface of a rabbit heart, which one similarly encounters with other fluorescent dyes (Rhod-2 AM, Di-4-ANBDQPQ) and other species.

The image contrast c in both the synthetic and experimental video images was determined to be the peak of distribution of local image contrasts, which were computed for every pixel (x, y) showing the heart surface in the raw, normalized video image, see **Figure 9E**. The histogram in **Figure 9E** shows the distribution of image contrasts computed for the original raw video image $I(x, y)$ shown in the upper left subpanel of **Figure 9B**. This is the same image used to create the synthetic optical maps shown in **Figure 3**. The image in the lower left subpanel is the resulting contrast image $I_c(x, y)$. The image contrast c in each pixel (x, y) of that contrast image was computed within a small disk-shaped sub-region $\mathcal{S}_{xy}$ around the pixel:

$$I_c(x, y) = max(\mathcal{S}_d(x, y)) - min(\mathcal{S}_d(x, y)) \tag{10}$$

The diameter d of the sub-region $\mathcal{S}_{xy}$ was typically chosen to range in the order of $d = 5 - 7$ pixels. Note that while the raw video image $I(x, y)$ contains values between $I \in [0, 1]$, the contrast image $I_c(x, y)$ only contains values between approximately $I_c \in [0, 0.2]$. These are the magnitudes of image intensity differences that can typically be found within short length scales of a few pixels in the normalized and otherwise unprocessed video data. This length scale is significant because the amplitudes of the motion may occur on a similar length scale. In this case the intensity differences would create optical flow that may ultimately lead to motion artifacts, see below. How such local intensity gradients in the video images can

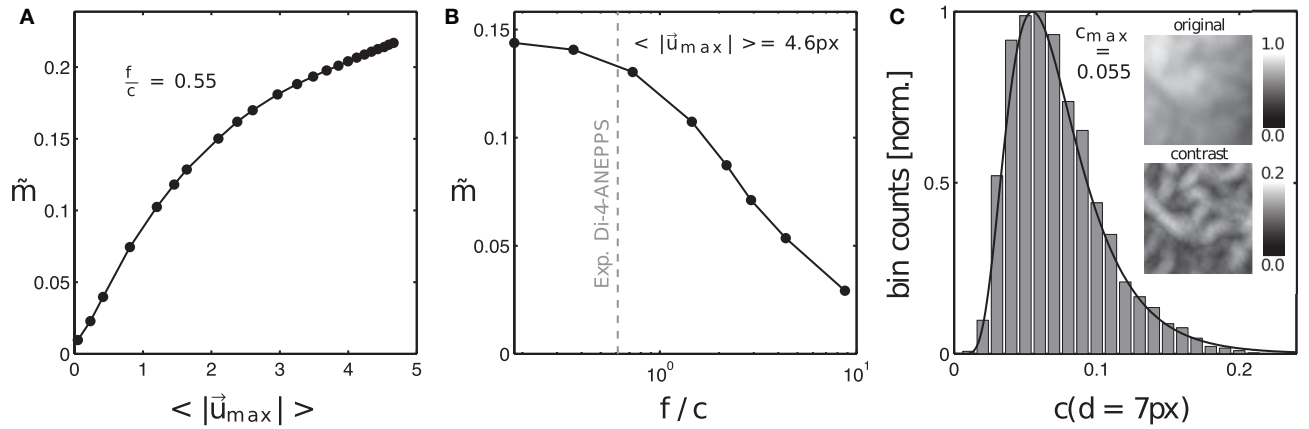

FIGURE 8 | Motion artifact strength $\tilde{m}$ generated systematically in synthetic optical mapping videos, see also **Figure 3**. **(A)** Increase in motion artifact strength $\tilde{m}$ with increasing amplitudes of motion $|\vec{u}|$. **(B)** Decrease in motion artifact strength $\tilde{m}$ with increasing fluorescent signal strength f or decreasing local tissue contrast c. The strength of motion artifacts depends on the relative signal-to-contrast ratio f/c. **(C)** Distribution of image contrast in optical mapping video frame used to generate synthetic optical mapping video. Top image: original texture, normalized to [0, 1]. Bottom image: contrast image. Image contrast c is the maximal absolute intensity difference that is found around a pixel (x, y) within a disk-shaped region $\mathcal{S}_{xy}$ with diameter d (here typically $5 - 7$ pixels).

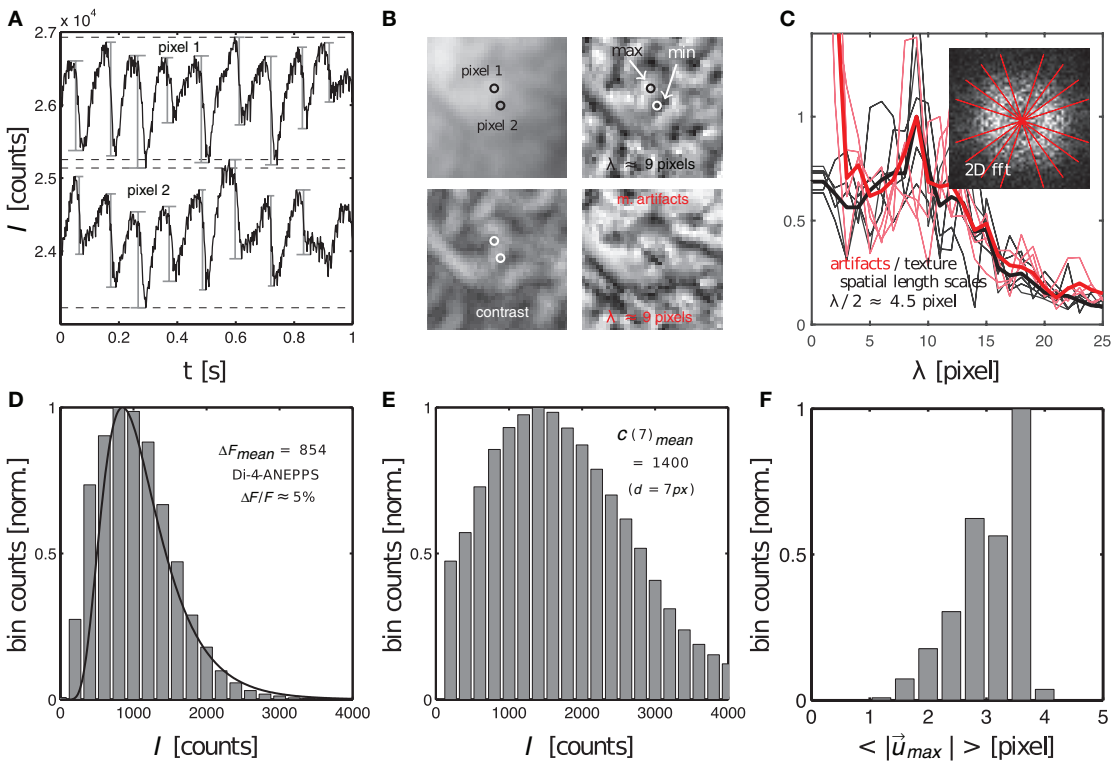

FIGURE 9 | Characterization of dissociation-related motion artifacts in optical mapping videos showing the contracting, fluorescing heart surface. Measurements of important quantifiers: fluorescent signal strength f, image contrast c, amplitude of motion $|\vec{u}|$ and characteristic length scales λ of short-scale image gradients. **(A)** Action potentials measured during ventricular fibrillation in two close by pixels (see **B**) on the surface of a mildly contracting rabbit heart [graph reproduced from Christoph et al. (2017)]. Difference in baseline reflects different pixel intensities. **(B)** Raw optical mapping video image (top left), contrast image (bottom left), contrast image normalized to local minima and maxima (top right) and motion artifacts (bottom right). All images have the same characteristic texture with the same characteristic length scale or dominant spatial frequency ($\lambda \approx 9$ pixels). **(C)** Radial profiles (fat lines: average) within 2D power spectra of spatial patterns (contrast image and motion artifacts) indicate dominant frequency of $\lambda \approx 9$ pixels (see two overlapping peaks). **(D)** Fluorescent signal strength or fractional change in fluorescence ΔF (given as intensity counts I) measured from sequences of action potentials, see **(A)**, with the peak of the distribution at $\Delta F = 854$ intensity counts in 16-bit video image. **(E)** Image contrast (given as intensity counts I) with peak at $C = 1400$ in 16-bit video image. **(F)** Amplitudes of motion during ventricular fibrillation ($2 - 4$ pixels, 128×128 pixel sensor size).

easily obscure action potential signals is illustrated in **Figure 9A**, which shows two time-series of a sequence of action potentials measured on the ventricular surface of a moderately contracting rabbit heart during ventricular fibrillation (graph reproduced from Christoph et al., 2017). The two time-series were extracted from two nearby sites (pixel 1 and pixel 2) only a few pixels apart in the pixel plane and only a few hundred micrometers apart on the surface of the heart, see **Figure 9B**. Both time-series in **Figure 9A** possess different baselines, about 2,000 intensity counts apart from each other, and exhibit slight motion artifacts, which become apparent as modulations of the traces around the baseline. The magnitude of the downstrokes (upstrokes of each action potential) are in the order of 1,000 counts (ΔF), see **Figure 9D**, and are smaller than the difference in baseline. Hence, if both sites were to move toward each other or to switch their positions, the potential difference in baseline, i.e., the difference in local intensity or image contrast, could easily override the fluorescent signal ΔF, which is much smaller. The signal-to-contrast ratio in this recording is $f_c < 1$.

Next to the fluorescent signal and image contrast strengths, it is also important to consider the spatial length scales of image gradients and the magnitude of the displacements or motion seen in the video images. **Figure 10B** displays the original video image (top left) used in the simulations, its contrast image (bottom left) computed using the formula given in Equation (10), a contrast-enhanced locally normalized version of the original image (top right) computed using the formula given in Equation (8), and resulting motion artifacts appearing in this region without or with very little fluorescent signal $f_c << 1$ (bottom right). One can see that all four images retain similar spatial frequency components. In particular, the image showing the local image contrast (lower left) and the image showing the motion artifacts (lower right) exhibit analogous spatial patterns with similar frequency components. The comparison illustrates how the loss of correspondence and dissociation in an optical mapping experiment leads to dissociation-related motion artifacts and links the phenomenon to the image contrast. **Figure 10C** shows that the dominant spatial frequency components measured from the two-dimensional Fourier-transforms of both the contrast-enhanced, locally normalized image (upper right) and the motion artifact patterns (lower right) in **Figure 10B** are equal at $\lambda = 9 \pm 1$ pixels (peaks in red and black curves). This means that the distances between local maxima and minima in the video images are on average $\lambda/2 \approx 4.5$ pixels and that these length scales match with the length scales appearing in the motion artifact patterns. The graph highlights that motion artifacts can quickly emerge even with slight movement over only a few pixels, c.f. **Figure 9A**. It also highlights the necessity to be able to track movements with sub-pixel precision. Furthermore, the graph highlights that it is important to take spatial length scales into consideration when studying the emergence of motion artifacts. Therefore, we suggest defining a factor, which expresses the strength of the motion in optical mapping videos in comparison to the frequency of contrast or features in the image:

$$u_\lambda = \frac{< |\vec{u}| >}{\lambda_c} \tag{11}$$

Here the frequency of visible features is given as the inverse characteristic length scale λ_c, as computed via the two-dimensional spectral analysis shown in **Figure 10C**. If $u_\lambda \approx 1$, then the motion is so large that it will create strong dissociation-related motion artifacts, given that the image contrast c is sufficiently high.

Lastly, the quantities f and c can be extracted from experimental data and used to estimate how likely it is that the video data contains weak or strong motion artifacts. **Figures 9D–F** show the distributions of the fluorescent signal strengths $\rho(\Delta F)$, the local contrast $\rho(C)$ and the motion strength $\rho(|\vec{u}_{max}|)$ in the experimental data set shown in **Figure 9A**. The peaks of the distributions ($\Delta F_{mean} = 854$ counts, $C_{mean} = 1,400$ counts, $< |\vec{u}_{max}| >= 3.5$ pixels) were used to determine the signal-to-contrast ratio f_c and the relative motion factor u_λ for the data set. The likeliness for motion artifacts to occur in this data set is large as $f_c < 1$ or $\Delta F < C$ and $u_\lambda \approx 1$ or $< |\vec{u}_{max}| >\approx \lambda/2$. Note, that the overall motion in the original recording is moderate ($< |\vec{u}_{max}| >\approx 5$ pixels) as it shows the rapidly contracting heart surface during fibrillation. The short distances in the network-like spatial patterns on the surface of the heart can easily generate motion artifacts even when the motion is moderate and in the order of a few pixels (the diameter of the heart being in the order of 100 pixels in our data).

3.2.1. Measuring Motion Artifact Strength Based on Frequency Components in Optical Mapping Video Images

As the absolute strength of motion artifacts can not be extracted from experimental data *per se*, we compared motion artifacts appearing in experimental data to synthetic data, which resembled the experimental data as closely as possible, and for which we could compute the absolute values $|\vec{u}|$, f, c and λ as described above. **Figure 10A** shows four normalized synthetic video images depicting a spiral wave pattern (c.f. **Figure 3**), where the first three images show the electrical pattern being obscured by motion artifacts for different and increasing amplitudes of motion ($< |\vec{u}| >= 0.4, 0.8, 4.8$ pixels) and the last image shows the corresponding tracked and motion-stabilized image with a substantial reduction in motion artifacts (3*rd* image: $< |\vec{u}| >= 4.8$ pixels). The synthetic data reproduced the specific signal-to-contrast ratio f_c, amplitude of motion $|\vec{u}|$ or relativ motion u_λ, and texture of the respective experimental data set, see **Figure 10C**. The lower image sequence shows the spatial frequency contents in the corresponding two-dimensional power spectra. These spectra were computed as averages from all images in each video sequence. The spectra show that with increasing motion and accordingly with increasing motion artifacts, as seen in the upper sequence, the spectral power increases in magnitude for higher frequency components. Comparing both the upper right and lower right images in **Figure 10A** one finds that the tracking and motion compensation equally reduced motion artifacts and the high-frequency components in the power spectrum. **Figure 10B** shows the frequency components sampled and averaged along the radial direction within the two-dimensional power spectra (red lines forming a star in sub-image). The graph shows the mean radial profiles $P^*(\lambda)$ (averaged

from $N = 8$ lines) for different amplitudes of motion ($< |\vec{u}_{max}| >= 0.1 - 4.8$ pixels). One can see that the height of the profiles continuously increases with increasing motion strength (light gray: little motion, dark gray or black: up to 5 pixels motion), indicating that higher frequency content becomes larger with increasing motion artifact strengths. For motion above 0.5 pixels each profile exhibits a peak at the characteristic length scale λ, see also **Figure 9C**. Computing the integral values $r = \int P^*(\lambda)d\lambda$ for each profile and plotting the values of r over the amplitude of motion $< |\vec{u}_{max}| >$ yields the upper curve in **Figure 10D**. The curve shows a continuous, monotonous increase in r that retains a similar shape as the curve in **Figure 8B**, which indicates that motion artifact strength $\tilde{m}$ depends similarly on the amplitude of motion $|\vec{u}|$. The graph shown in **Figure 10E** further emphasizes this dependency, illustrating that the strength of motion artifacts $\tilde{m}$ increases linearly with r, suggesting that r is a valid measure for the estimation of the magnitude of motion artifacts. This means, that the strength of motion artifacts occurring in experimental data can be estimated by comparing the magnitudes of the frequency content of the spatial motion artifact patterns of synthetic and experimental data with each other. **Figure 10D** includes two data points (gray dots) computed for the experimental data sets shown in **Figure 10C** matching the synthetic values (black dots) computed for the same image texture, amount of motion, f_c and u_λ. Comparing the amount of distortion and motion artifacts in the upper left image (motion $< |\vec{u}| >= 0.4$ pixels) and the upper right image (after tracking and stabilization, initial motion $< |\vec{u}| >= 4.8$ pixels) in **Figure 9A**, one can conclude that the tracking and motion-stabilization yields optical maps, which still include residual motion artifacts comparable in strength to optical maps containing slight motion ($< |\vec{u}| >= 0.4$ pixels). The spectral profiles in **Figure 10B**

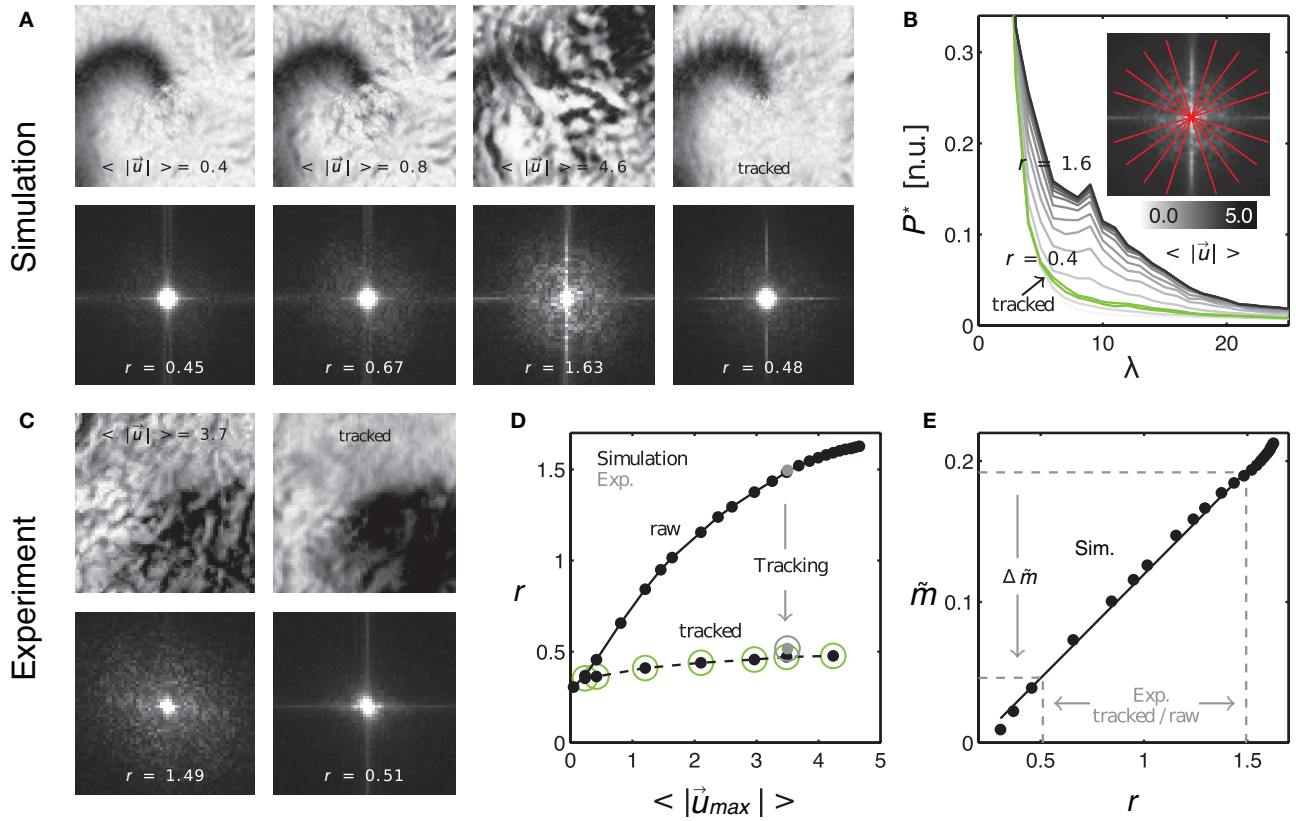

FIGURE 10 | Evaluating tracking performance and residual motion artifacts by comparing synthetic to experimental data. **(A)** Synthetic optical maps before (panels 1–3) and after (panel 4) tracking. Increasing amplitudes of motion (panels 1–3: 0.4, 0.8, and 4.6 pixel) cause an increase in motion artifacts. Tracking and motion stabilization (panel 4) inhibits (residual) motion artifacts to levels found at 0.4–0.8 pixels of motion before tracking. Spectral maps obtained from the optical maps (bottom) show an increase in high-frequency spectral components with increasing motion. Tracking and motion compensation decreases the high-frequency spectral components to a level comparable to the left image ($r = 0.45$) with low amounts of motion (0.4 pixels). **(B)** Radial profiles of normalized spectral maps indicating an increase in width of the profiles (color-coded from gray to black, $r = 0.4$ to 1.6) with increasing motion and decrease in width after tracking (green curve). **(C)** Comparison with experimental data. Tracking and motion-stabilization reduces motion artifacts and radial profile width r (pre-tracking $r = 1.49$, post-tracking $r = 0.51$). **(D)** Profile width r over magnitude of motion $< |\vec{u}| >$ for raw and tracked (circles) simulated (black dots) and experimental data (gray dots). **(E)** Linear increase of motion artifact strength $\tilde{m}$ with spectral profile width r. Motion artifact reduction $\Delta\tilde{m}$ calculated for experimental data via the linear relationship between motion artifact strength (obtained in simulations mimicking experimental data) and spatial high-frequency components in optical maps (quantifiable by r with both experimental and simulation data).

confirm this conclusion. The profile obtained for the tracked and motion-stabilized data (green, $r = 0.4$) closely aligns with the profile obtained for very slight motion (light gray, $< |\vec{u}| >= 0.2$ pixels). Also, in **Figure 10D** all values of r for the tracked and motion-stabilized data points (circles) are below $r < 0.5$. This value for r is also obtained for data sets with motion smaller than 0.5 pixels (c.f. **Figure 10A**), lower left image, $r = 0.45$). The data demonstrates that analyzing the spatial frequency content of motion artifact patterns in optical maps, can provide both an estimate for the amount of residual motion artifacts $\tilde{m}^*$ that are left in motion-stabilized videos after motion tracking, and an evaluation of the accuracy of the tracking, see following section 3.3.

3.3. Evaluating Motion Tracking and Motion Compensation Performance

To evaluate the performance of the motion tracking and motion compensation algorithm, we assessed how well the algorithm tracks simulated movements of cardiac tissue in the synthetic optical maps, see **Figure 11**. The efficacy of the motion tracking and motion-stabilization is also demonstrated in **Supplementary Video 3**. As discussed earlier in this paper, and in the discussion, it is crucial to take into consideration the fluorescent signal when tracking motion in optical mapping videos, as the motion tracking algorithm may confuse the signal with motion-related optical flow and may accidentally track electrical activity instead of motion and deformation. Here we show that with strong fluorescent signal strengths f larger than the local image contrast c (or large signal-to-contrast ratios $f_c > 1$), the tracking algorithm may accidentally track the electrical wave phenomena propagating across the heart surface instead of the motion itself. To inhibit such phenomena, we introduced a pre-processing step in our motion tracking scheme, see **Figure 4**. Using Equation (8), we created locally normalized, contrast-enhanced videos $I_c(x, y, t)$, in which each pixel is normalized to the maximal and minimal intensity values found within a small disk-shaped sub-region $\mathcal{S}_{x,y}$ around the pixel (x, y). As a result, the tissue texture or image contrast was maximally intensified, see **Figure 4A**, and intensity fluctuations caused by the electrical activity were suppressed (see also Figure 4 in Christoph et al., 2017). We tracked both the original video data $I(x, y, t)$, as well as the contrast-enhanced video data, $I_c(x, y, t)$ and compared and evaluated the outcome of the tracking in terms of accuracy and robustness. **Figure 11** shows how tracking the contrast-enhanced videos outperforms tracking the raw videos and yields good tracking performance for both small and large fluorescent signals. **Figure 11A** shows the untracked video including heavy motion artifacts (for a signal-to-contrast ratio of $f_c = 0.6$). In contrast, **Figure 11B** shows tracked and motion-stabilized optical maps of the same video as shown in **Figure 11A**, the tracking performed on the raw video $I(x, y, t)$ without contrast-enhancement. Because of the tracking and motion-stabilization, motion artifacts are substantially reduced and do no longer obscure the electrical wave pattern as seen **Figure 11A**. Instead, the electrical wave pattern is visible. However, while in the first image sequence with low signal strength ($f_c = 0.6$) the tracking is accurate, the red arrows indicate the mismatches between the simulated and the tracked tissue configuration, in the two lower image sequences the tracking becomes inaccurate because they contain larger fluorescent signal strengths (2*nd*: $f_c = 2.8$, 3*rd*: $f_c = 3.8$). In the bottom most (3*rd*) image sequence the mismatches (red arrows) are not shown. Instead the warped, motion-stabilized images are shown to highlight the distortions that are introduced when warping the original video images using the inaccurate tracking results, see also **Supplementary Video 4**. In the first image sequence, the tracking was still able to reliably associate tissue regions with each other throughout the image sequence, because the fluorescent signal strength was smaller than the local tissue contrast ($f < c$). Mismatches occur only close to the boundaries of the image (cf. **Figure 12A**). Only mild motion artifacts are recognizable (cf. **Figure 8**). In the central image sequence (2*nd*) the mismatches (red vectors) between the simulated and tracked tissue configuration are significantly larger than in the first image sequence and occur particularly close to the action potential, suggesting that the algorithm accidentally tracks the electrical wave pattern. The fluorescent signal is significantly larger than the local tissue contrast ($f_c = 2.8$) and the algorithm is no longer able to associate a tissue region with its own systolic/diastolic or darker/brighter rendition altered through the fluorescence. Even though motion artifacts do not appear to be stronger than in the first image sequence due to the larger relative signal strength, the tracked tissue configuration does not correspond to the real tissue configuration, which consequently makes a mechanical measurement inaccurate. Furthermore, the inaccurate tracking results cause distortions in warped image sequences, as comparably shown in the lower image sequence ($f_c = 3.8$), when aiming at stabilizing the motion numerically. However, accidental tracking of the electrical wave pattern can be overcome when the tracking is not performed with the original videos $I(x, y, t)$, but instead with contrast-enhanced videos $I_c(x, y, t)$, see **Figure 11C**. For the same video data and signal-to-contrast ratio ($f_c = 2.8$), as shown in the central image sequence in **Figure 11B**, the accuracy and robustness of the tracking becomes significantly improved. The mismatches or tracking errors close to the action potential vanish and the mismatches overall are comparably small, just as with small signal-to-contrast ratios, ($f_c = 0.6$ cf. **Figure 11A**). All videos in **Figure 11** contained the same motion before tracking (initial motion $< |\vec{u}| >= 4.7$ pixels).

Contrast-enhanced tracking (LK_c) is accurate and robust and yields small tracking errors for any given signal-to-contrast ratio, see **Figure 12B**. While without contrast-enhancement (LK) the tracking error η grows exponentially with increasing signal strength or signal-to-contrast ratio, it stays small ($\eta = 0.1 - 0.4$ pixels) with contrast enhancement for all signal strengths or signal-to-contrast ratios. Without contrast-enhancement, the tracking does not achieve sub-pixel accuracy ($\eta > 1$ pixel) when the fluorescent signal f becomes twice as large as the image contrast c. The tracking error corresponds to the mismatches between the simulated and the tracked configuration (red vectors, see **Figure 11** averaged over all images in the video. Shifts or motion can be tracked with a precision of $0.1 - 0.4$ pixels, while the amplitudes of motion were about $10 - 50$ times

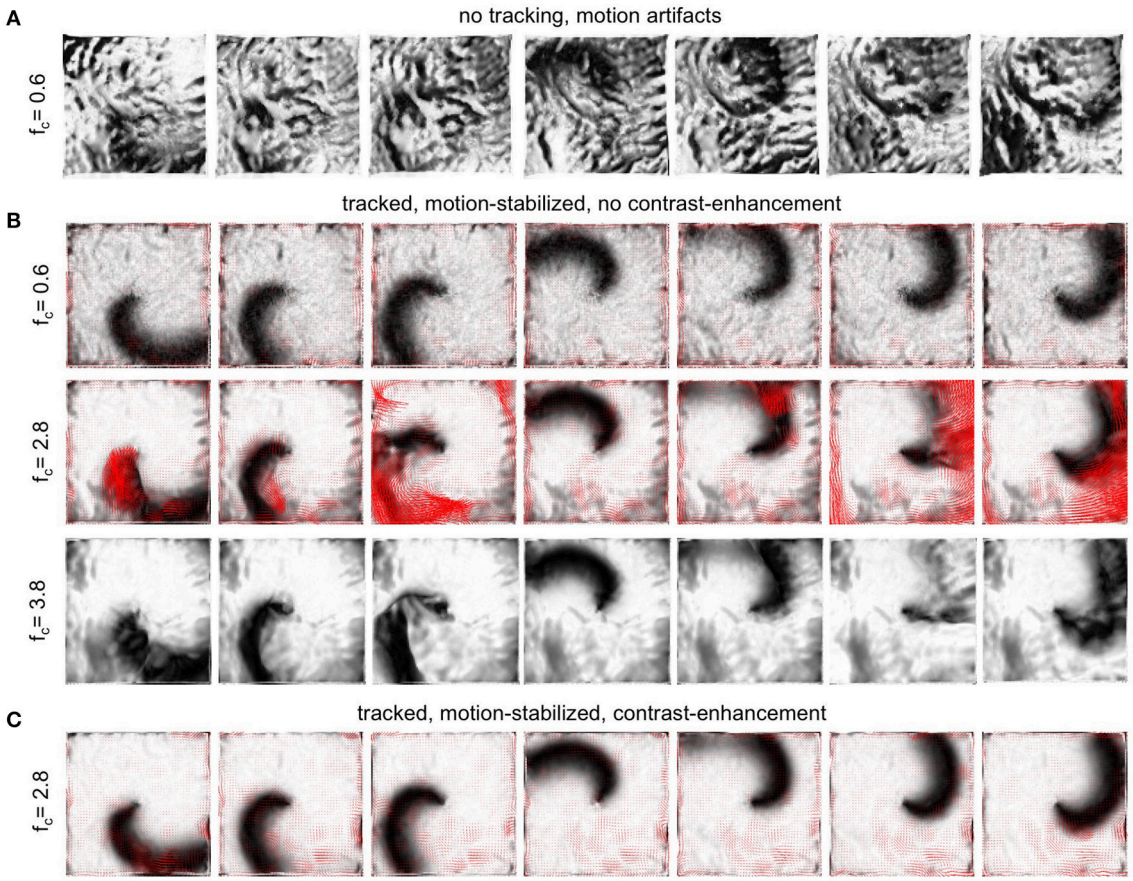

FIGURE 11 | Efficacy of motion compensation and tracking error determined with synthetic optical maps showing contracting, fluorescing cardiac tissue. See also **Supplementary Videos 3** and **4**. **(A)** Deformed, non-tracked optical maps obscured by motion artifacts for weak to moderate signal strength ($f_C = 0.6$). **(B)** Motion-stabilized optical maps with substantial artifact reduction for various signal-to-contrast ratios $f_C = 0.6$, $f_C = 2.8$, $f_C = 3.8$ (increasing signal strength) after tracking and warping. Red vectors (row 1 & 2) indicate tracking errors, calculated as mismatches between the tracked and actual simulated tissue configuration. While tracking is sufficiently accurate for small fluorescent signal strengths ($f < c$, here $f_C < 0.6$), the tracking error increases with increasing signal strengths, with mismatches emerging particularly close to the wave front. For very strong signals ($f > c$, here $f_C = 3.8$) the warped, motion-stabilized images become visibly distorted as a result of the erroneous tracking. **(C)** Substantial reduction of tracking errors by introducing contrast-enhancement, amplifying local image gradients to minimize accidental tracking of the electrical wave and the related intensity modulations it causes in the video images. Contrast-enhancement improves the accuracy of the tracking and maintains robust and sufficiently accurate tracking with larger signal strengths ($f_C > 2.8$), see also **Figure 12**. All optical maps are pixel-wise normalized over time.

larger in the order of about 5 pixels. We typically observed such amplitudes of motion during arrhythmias and pacing in the experimental data sets (with a sensor size of 128 pixels and the diameter of the ventricle in the order of 100 pixels). As shown in **Figure 12A**, the tracking error remains small ($\eta < 0.5$ pixels) within the entire video image and becomes only larger ($\eta > 2$ pixels) close to the boundaries (within ~ 5 pixels) of the video image. Just as in **Figure 11** all tracked and analyzed videos in **Figure 12B** contained the same motion before tracking (initial motion $< |\vec{u}| >= 4.7$ pixels). Nevertheless, the accuracy of the tracking algorithm does not diminish with increasing and stronger motion. **Figure 12C** shows that the strength of residual motion artifacts $\tilde{m}^*$ after tracking and motion-stabilization remains constantly small for displacements ranging from $0-5$ pixels, and the algorithm has demonstrated to reliably detect shifts with larger magnitudes (~ 10 pixels in video image of size 128×128 pixels), see experimental data set shown in **Figures 1C,E**.

Finally, comparing the experimental and synthetic video data to each other, as shown in **Figures 10C–E**, it is possible to estimate the accuracy of the tracking in the experiments. **Figure 10C** shows a substantial reduction in motion artifacts comparing the simulated pre- and post-tracking data. After tracking, the spatial high-frequency content in the optical maps decreased substantially and it is possible to relate this reduction to a reduction in dissociation-related motion artifacts, as shown in **Figure 10C**, and to consider it as a measure for the precision of the tracking, see also section 3.2.1. In the synthetic data, which matches the experimental data in terms of fluorescent signal and contraction strengths and image contrast, both the amount of motion artifacts $\tilde{m}$ that results with small sub-pixel shifts of the tissue ($|\vec{u}| = 0.4$ pixel) and the amount of residual motion

artifacts $\tilde{m}^*$ that is seen after tracking corresponds to the amount of residual motion artifacts $\tilde{m}^*$ found in the experimental data after tracking. From **Figure 10E** it is consequently possible to conclude that for the particular data set shown in **Figure 10C** motion artifacts were reduced by about $75 - 80\%$ ($\Delta\tilde{m} \approx 1 - 0.04/0.2 = 0.8$). Furthermore, it can be concluded that the motion tracking algorithm is able to detect shifts with sub-pixel accuracy ($< |\vec{u}| >= 0.4$ pixel) in the experimental data set shown in **Figure 10C**. **Figure 12C** shows that residual motion artifacts $\tilde{m}^*$ remain small for both small and large amplitudes of motion, suggesting that similar results could be obtained with other experimental data sets. **Figure 12D** demonstrates that with varying signal-to-contrast ratios there is an optimum around $f_c = 1$ for which residual motion artifacts $\tilde{m}^*$ become minimized after tracking. The graph suggests that for small signal strengths f residual motion artifacts become larger simply because with vanishing signal ($f_c << 1$) and imperfect tracking it becomes more likely to measure optical flow instead of signal. Likewise, with large signals slight mismatches or tracking errors may lead to an overly strong contribution of the signal to motion artifacts. The regime in which we found the minimum in residual motion artifacts $\tilde{m}^*$ for signal-to-contrast ratios of $f_c = 0.2 - 2.0$ is often faced in experimental data sets, for example Di-4-ANEPPS ($f_c \approx 0.5 - 1.0$, see for instance Rohde et al., 2005 with $f_c \approx 0.5$) or Rhod-2 AM ($f_c \approx 1.0 - 2.0$), cf. **Figures 9D–F**.

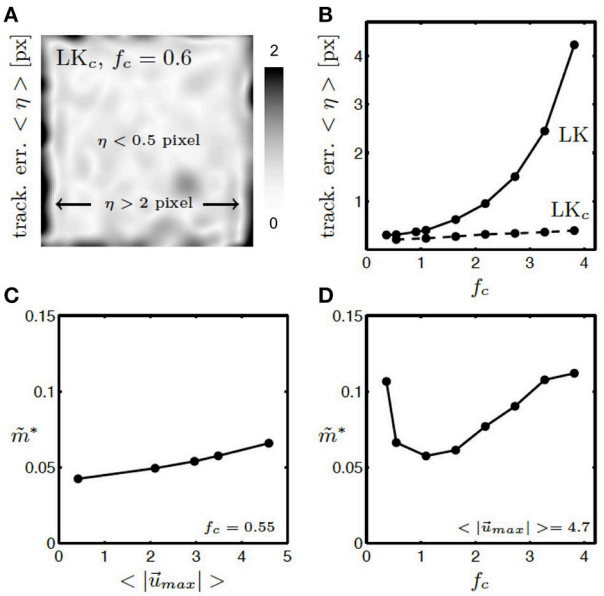

FIGURE 12 | Tracking error η and residual motion artifacts $\tilde{m}^*$ in synthetic, tracked and motion-stabilized optical maps with various amplitudes of motion and relative signal strengths. **(A)** Tracking error η within video image averaged over all video frames with contrast-enhancement (LK_C). Within the video image errors are acceptable (< 0.5 pixel), toward the boundaries errors can become large ($\eta > 2$ pixel). Video image is 100×100 pixel in size. See also **Supplementary Video 4**. **(B)** Tracking error η with (LK_C) and without (LK) contrast-enhancement. Tracking error grows exponentially with increasing signal-to-contrast ratio f_C without image contrast-enhancement (LK) and remains small with image contrast-enhancement (LK_C) for all signal-to-contrast ratios f_C. **(C)** Residual motion artifacts $\tilde{m}^*$ are equally small (cf. **Figure 10E**) for small and large amplitudes of motion in the original videos. **(D)** Residual motion artifacts $\tilde{m}^*$ are minimal for relative signal strengths in the range of $f_C = 0.5 - 2.0$ or when $f \approx c$.

4. DISCUSSION

In this study, we validated the robustness and accuracy of a 2D marker-free motion tracking and motion stabilization algorithm for performing electromechanical optical mapping studies with beating, fluorescing hearts. Using experimental and synthetically generated optical mapping videos, we compared the tracked data to simulated ground-truth data and found that the algorithm reduces motion artifacts substantially by about $75 - 80\%$ and achieves sub-pixel accuracy (< 0.5 pixels, $\sim 0.2 - 0.4$ pixels, see lower curve in **Figure 12B**) when tracking motion with amplitudes in the range of $1 - 10$ pixels (in video images that are in the order of 100×100 pixels in size, the heart filling the entire field of view). We further found that the motion tracking algorithm is robust against fluorescence intensity fluctuations which are caused by electrical activity. One of the most important issues in tracking motion in optical mapping videos is the careful disentanglement of motion from fluorescent activity, particularly when using marker-free tracking approaches as in this study. Unlike other tracking algorithms (Seo et al., 2010; Bourgeois et al., 2011; Zhang et al., 2016), the motion tracking algorithm discussed in this paper does not require markers attached to the tissue surface to facilitate the tracking. It instead analyzes and compares anatomical features or landmarks that are visible on the heart surface. With such a marker-free tracking approach, it is important to identify and eliminate factors that could possibly mislead or irritate the tracking and lead to falsely detected shifts or displacements. Such an assessment is particularly important because optical mapping videos, which show fluorescing and contracting cardiac tissue, do not only contain intensity changes that can be attributed to motion (optical flow) alone, but also contain fluorescence intensity fluctuations that are caused by electrical activity, i.e., intensity drops during action potential depolarization or intensity increases during calcium cycling. The motion and fluorescence appear as two superimposed spatio-temporal dark-bright patterns, both of which can be detected by the tracking and therefore need to be disentangled from each other. In the worst case, if the fluorescent signal is large enough, the tracking algorithm may be unable to associate two corresponding image regions between two frames, for example when one video frame shows the tissue during diastole and the other during systole. Even with weak fluorescent signals, such superposition phenomena can lead to tracking errors, which may not be visually evident, see **Figures 11**, **12**. To reconcile this problem, we introduced and applied a contrast-enhancement pre-processing procedure, which intensifies short-scale gradients in video images and suppresses intensity fluctuations caused by electrical activity (Christoph et al., 2017). In this study, we validated that this contrast-enhancement, see **Figure 4**, creates a unique and robust spatial pattern or texture that can be reliably identified and tracked through video images in the presence of fluorescent signals, just like artificial markers attached to the

heart surface. In **Figure 11** it is shown that strong fluorescent signals ($f > c$) can lead to tracking artifacts, if the tracking is performed without contrast-enhancement. The tracking artifacts may arise when the original, unprocessed video image is tracked and the algorithm uses the local grayscale pattern to uniquely identify a particular tissue segment and follow its motion through the image plane. However, this original spatial intensity pattern is superimposed or modulated by fluorescence intensity changes that typically occur when the tissue is loaded and imaged, for instance, with voltage- or calcium-sensitive dyes. In **Figures 11**, **12B**, we show that if these modulations become large, they can alter the image in a way that the algorithm — without further precautions—is unable to match the local spatial intensity pattern associated with one tissue region with its corresponding deformed spatial pattern in a different video frame. As a result, the algorithm produces tracking errors with increasing fluorescent signal strengths ($\Delta F/F$). In the worst case, with very strong fluorescent signals, the tracking algorithm could accidentally track the movements of action potential or calcium waves across the surface instead of motion, as demonstrated in **Figure 11B**. Using synthetic data, we verified that with contrast-enhancement the tracking achieves sub-pixel precision for arbitrary fluorescent signal strengths f, see **Figure 12A** and lower curve in **Figure 12B**. Tracking the contrast-enhanced videos, we were able to image strongly beating and contracting hearts stained with voltage-sensitive dye (Di-4-ANEPPS) and obtain co-moving optical maps showing action potential waves propagating across the heart surface with substantially inhibited motion artifacts. At the same time, we were able to ensure that we performed an accurate measurement of the time-varying mechanical configuration $\chi(t)$ of the tissue surface visible within the video images as we verified that tracking errors remain low, see **Figure 12B**.

The main advantage of our method is that we can image the beating heart without having to attach markers to its surface. At the same time, the algorithm is fully automatic and does not require any manual supervision, i.e., manual selection of markers or image features to initiate or enable the tracking is not necessary. Motion tracking (Matlab), warping and resampling and other processing (custom C++ code) requires approximately 1 min of computation time per video image on a single CPU. We do, however, anticipate that the tracking and motion-stabilization could also be performed much faster (in the order of seconds or even milliseconds per video frame) using parallel computing and streamlining the procedures. In this study, we analyzed relatively small video images with sizes of 100×100 or 128×128 pixels. Videos with such sizes are produced by state-of-the-art cameras (MiCAM ULTIMA camera, SciMedia, Japan: 100×100 pixels; Evolve 128 camera, Photometrics Inc., USA: 128×128 pixels). The tracking can also be performed with video data recorded with cameras with much larger sensors, given that the video properties (noise level, image gradients, density or length scales of image features) are comparable and do simply scale with the size of the video image. Note thus that the different amplitudes of motion, which we observed during fibrillation (approximately $1 - 5$ pixels), tachycardia or pacing (approximately $5 - 15$ pixels), and sinus rhythm (approximately $10 - 30$ pixels) would scale with the image sensor size if the heart filled the field of view and could be stated in calibrated units (mm). The tracking is also generally applicable to other data obtained with different setups, species (we successfully applied the algorithm to data obtained with rabbit, pig, mouse and alligator hearts) or dyes (we used Di-4-ANEPPS, Di-4-ANBDQPQ, Rhod2-AM, Fluo-3). Due to the single-camera imaging setup, we were only able to image planar movements within the video images, see **Figures 1A,B**. However, using the same tracking algorithm and a multi-camera setup, we previously demonstrated that the three-dimensional motion and deformation of the heart surface can also be captured and that action potential waves can be mapped on large (180°) and strongly curved parts of the deforming ventricular walls (Christoph et al., 2017). As in the present study, the 2D motion tracking algorithm was used to detect two-dimensional displacements in the video images, and afterwards the 2D data was used to compute three-dimensional displacements combining the data from multiple cameras. While the aim in the multi-camera study was to provide a proof-of-concept that three-dimensional electromechanical optical mapping is possible, our aim in the present study is to discuss the performance of the two-dimensional tracking itself. We verified, with the aid of synthetic video data, that the tracking of the tissue's mechanical configuration is accurate and robust. The robustness is demonstrated in the tracking's ability to produce displacement vector fields, which describes a smooth and continuous movement of the tissue through space, even though each video frame was registered individually and independently. This has implications for both 2D and 3D imaging alike, as the 2D tracking data is the basis for the 3D reconstruction discussed in Christoph et al. (2017).

Motion artifacts can be reduced substantially using numerical motion tracking and motion compensation techniques, as shown in this and in previous studies (Christoph, 2015; Zhang et al., 2016; Christoph et al., 2017, 2018). However, judging from the outcome of the motion tracking and motion compensation alone, it is not immediately apparent how accurate the motion was tracked. Furthermore, it is difficult to quantify the amount of residual motion that may still be present in motion-stabilized videos or to determine to what extent motion artifacts were reduced. Motion artifacts are well known to manifest as distortions or deflections in optical traces (Rohde et al., 2005; Christoph, 2015; Christoph et al., 2017) and become immediately apparent particularly during sinus rhythm, as during sinus rhythm motion alters the very characteristic shape of the action potential. A quantitative assessment of motion artifacts and potential deviations of the optical traces from the true action potential remains difficult, as ground-truth data is unknown. In particular during arrhythmias, the identification of motion artifacts is not trivial because action potentials can take on various and less specific shapes than during sinus rhythm. To better understand the origins of motion artifacts, we generated synthetic motion artifact patterns and studied their properties and dependence on motion and other features of the video data. We found that a spectral analysis of motion artifact patterns in optical maps can be used to estimate the residual error of the tracking and the amount of residual motion and

motion artifacts. We also found that the strength of dissociation-related motion artifacts are mainly determined by the ratio of the fluorescent signal strength f in comparison to the local image contrast c and the ratio of the amplitude of motion $|\vec{u}|$ in comparison to the length scales λ of image features. In determining these video properties alongside a spectral analysis of motion artifacts, one can evaluate the efficacy of motion-stabilization and motion artifact compensation algorithms. In the synthetic data, the amount of residual motion artifacts is a direct measure for the accuracy of the tracking, see **Figure 10E**. Using a simplistic computer model, we were able to create optical maps, which reproduced the most essential aspects of an optical mapping video. In future work, it may be necessary to simulate the full three-dimensional heart together with a three-dimensional imaging scene and the positioning of different light sources within that scene. Taking into account a more realistic imaging situation is necessary in order to simulate the generation of illumination-related motion artifacts caused by movements of the heart inside an inhomogeneously illuminated scene. Inhomogeneous illumination or, more precisely, relative motion between the heart and light sources can cause illumination-related motion artifacts, which add to dissociation-related motion artifacts. Illumination-related motion artifacts can not be overcome by tracking, but can be compensated by ratiometric imaging (Brandes et al., 1992; Knisley et al., 2000; Hooks et al., 2001; Tai et al., 2004; Bachtel et al., 2011; Bourgeois et al., 2011; Zhang et al., 2016) or numerical light-field correction techniques (introduced in Christoph et al., 2017). Here, we neglected illumination-related motion artifacts, because in the experiments we typically illuminated the hearts "flat", meaning that we avoided larger intensity gradients across the images and tried to illuminate the heart surface as evenly as possible with multiple LEDs from all sides. We experienced that with flat illumination and small amplitudes of motion ($1 - 10$ pixels) illumination changes do not pose greater issues. Nevertheless, in future work, illumination-related motion artifacts will have to be considered more carefully.

Performing optical mapping experiments with beating hearts requires careful handling of the tissue preparations. For instance, it is very important, and much more so than during conventional optical mapping without motion, to avoid dust or Tyrode stains on the glass walls through which the imaging is performed. The avoidance of particles or bubbles flowing inside the bath is also necessary. Both dust or stains on the glass walls and particles and bubbles moving through the field of view may accidentally be tracked or may compromise tracking. Imaging the heart from the top through the surface of the Tyrode solution may be prohibited by ripples that form on the water surface when the heart contracts. The tracking may also pick up the flickering of instable light sources. Strongly contracting tissue preparations may require mechanical fixation to inhibit excessive motion. Especially during sinus rhythm, the heart may rotate or move out of the field of view such that its motion can not be captured with a single camera. At the same time, one needs to be very careful when trying to fix it in one location. Subjecting the heart wall to mechanical pressure or bringing it in mechanical contact with instrumentation could lead to blockage of its vascular system and improper perfusion and ischemia. We experimented with molds and flexible holders to mechanically restrict the hearts, but, due to repeated complications with proper perfusion, have resorted to freely moving hearts, which are simply attached to the perfusion outflow.

5. CONCLUSIONS

We demonstrated that optical mapping can be performed with strongly contracting isolated hearts using computer vision techniques. Without using artificial markers attached to the heart surface, we tracked and numerically stabilized the motion of the beating heart to measure electrophysiological wave phenomena propagating across the contracting heart surface in a co-moving frame of reference. We validated the robustness and accuracy of the marker-free motion tracking and motion compensation algorithm using synthetically generated optical mapping videos and found that the algorithm achieves sub-pixel accuracy, reduces motion artifacts substantially and is unaffected by intensity modulations in the video images caused by electrical activity. As a result, it becomes possible to perform electromechanical optical mapping with beating hearts without having to attach markers to the heart. Furthermore, we found that (residual) motion artifacts can be used as a direct measure for the accuracy of the tracking.

DATA AVAILABILITY STATEMENT

The datasets generated and analyzed for this study are available from the corresponding author upon reasonable request.

AUTHOR CONTRIBUTIONS

JC and SL designed the research. JC designed, implemented and conducted the simulations and analyzed all numerical data. JC conducted the experiments and analyzed all data. JC wrote and revised the manuscript. Both authors read and approved the submitted version.

FUNDING

The research has received funding from the German Research Foundation (to SL), the Collaborative Research Center SFB 1002 Modulatory Units in Heart Failure (to SL and JC), the Collaborative Research Center SFB 937 Collective Behavior of Soft and Biological Matter (to SL and JC), the German Center for Cardiovascular Research (DZHK e.V., partnersite Göttingen) (to SL and JC), and the Max Planck Society (to SL). This research was supported in part by the National Science Foundation Grant No. NSF PHY-1748958, NIH Grant No. R25GM067110, and the Gordon and Betty Moore Foundation Grant No. 2919.01 (to SL and JC).

ACKNOWLEDGMENTS

We would like to thank M. Kunze for technical assistance.

SUPPLEMENTARY MATERIAL

The Supplementary Material for this article can be found online at: https://www.frontiersin.org/articles/10.3389/fphys.2018.01483/full#supplementary-material

Supplementary Video 1 | Tracking of contracting and deforming left ventricular heart surface of a rabbit heart during pacing and the onset of ventricular fibrillation. Points (black) indicating in-plane displacements of single tissue segment with respect to reference position (gray).

Supplementary Video 2 | Action potential wave propagating across contracting and deforming left ventricular surface of a rabbit heart.

Supplementary Video 3 | Synthetic optical maps showing action potential spiral wave ($\Delta F/F > 10\%$, exaggerated) on contracting tissue before and after tracking and motion-stabilization.

Supplementary Video 4 | Tracking errors in synthetic optical maps without and with contrast-enhancement for a signal-to-contrast ratio of $fc = 2.8$, c.f. **Figure 11.** Without contrast-enhancement the tracking and motion-stabilized videos contain errors and heavy distortions respectively. Contrast-enhancement reduces mismatches between real simulated and tracked tissue configurations (red vectors) significantly.

REFERENCES

Aliev, R., and Panfilov, A. (1996). A simple two-variable model of cardiac excitation. *Chaos Solit. Fract.* 7, 293–301. doi: 10.1016/0960-0779(95)00089-5

Bachtel, A. D., Gray, R. A., and Rogers, J. M. (2011). A novel approach to dual excitation ratiometric optical mapping of cardiac action potentials with di-4-anepps using pulsed led excitation. *IEEE Trans. Biomed. Eng.* 58, 2120–2126. doi: 10.1109/TBME.2011.2148719

Bers, D. M. (2002). Cardiac excitation-contraction coupling. *Nature* 415, 198–205. doi: 10.1038/415198a

Bourgeois, E. B., Bachtel, A. D., Huang, J., Walcott, G. P., and Rogers, J. M. (2011). Simultaneous optical mapping of transmembrane potential and wall motion in isolated, perfused whole hearts. *J. Biomed. Opt.* 16:096020. doi: 10.1117/1.3630115

Bourguignon, D., and Cani M. (2000). "Controlling anisotropy in mass-spring systems," in *Computer Animation and Simulation* (Vienna: Springer), 113–123.

Brandes, R., Figueredo, V. M., Comacho, S. A., Masie, B. M., and Weiner, W. M. (1992). Suppression of motion artifacts in fluorescence spectroscopy of perfused hearts. *Am. J. Physiol. Heart Circ. Physiol.* 263, 972–980. doi: 10.1152/ajpheart.1992.263.3.H972

Christoph, J. (2015). *Intramural Visualization of Scroll Waves in the Heart*. Göttingen: Georg-August-University Göttingen. Available online at: http://hdl.handle.net/11858/00-1735-0000-0023-9642-D

Christoph, J., Chebbok, M., Richter, C., Schröder-Schetelig, J., Bittihn, P., Uzelac, I., et al. (2018). Electromechanical vortex filaments during cardiac fibrillation. *Nature* 555, 667–672. doi: 10.1038/nature26001

Christoph, J., Schröder-Schetelig, J., and Luther, S. (2017). Electromechanical optical mapping. *Prog. Biophys. Mol. Biol.* 130, 150–169. doi: 10.1016/j.pbiomolbio.2017.09.015

Fedorov, V. V., Lozinsky, I. T., Sosunov, E. A., Anyukhovsky, E. P., Rosen, M. R., Balke, C. W., et al. (2007). Application of blebbistatin as an excitation-contraction uncoupler for electrophysiologic study of rat and rabbit hearts. *Heart Rhythm* 4, 619–626, doi: 10.1016/j.hrthm.2006.12.047

Herron, T. J., Lee, P., and Jalife, J. (2012). Optical imaging of voltage and calcium in cardiac cells and tissues. *Circ. Res.* 110, 609–623. doi: 10.1161/CIRCRESAHA.111.247494

Hooks, D. A., LeGrice, I. J., Harvey, J. D., and Smaill, B. H. (2001). Intramural multisite recording of transmembrane potential in the heart. *Biophys. J.* 81, 2671–2680. doi: 10.1016/S0006-3495(01)75910-3

Khwaounjoo, P., Rutherford, S. L., Svrcek, M., LeGriece, I. J., Trew, M. L., and Smaill, B. H. (2015). Image-based motion correction for optical mapping of cardiac electrical activity. *Ann. Biomed. Eng.* 43, 1235–1246. doi: 10.1007/s10439-014-1172-8

Knisley, S. B., Justice, R. K., Kong, W., and Johnson, P. L. (2000). Ratiometry of transmembrane voltage-sensitive fluorescent dye emission in hearts. *Am. J. Physiol. Heart Circul. Physiol.* 279, 1421–1433. doi: 10.1152/ajpheart.2000.279.3.H1421

Laughner, J. I., Ng, F. S., Sulkin, M. S., Arthur, R. M., and Efimov, I. R. (2012). Processing and analysis of cardiac optical mapping data obtained with potentiometric dyes. *Am. J. Physiol. Heart. Circ. Physiol.* 303, 753–765. doi: 10.1152/ajpheart.00404.2012

Nash, M., and Panfilov, A. (2004). Electromechanical model of excitable tissue to study reentrant cardiac arrhythmias. *Prog. Biophys. Mol. Biol.* 85, 501–522. doi: 10.1016/j.pbiomolbio.2004.01.016

Periaswamy, S., Weaver, J., Healy, D., Rockmore, P., Kostelec., and Farid, H. (2000). "Differential affine motion estimation for medical image registration," in *Wavelet Applications in Signal and Image Processing VIII, International Symposium on Optical Science and Technology* (San Diego, CA). doi: 10.1117/12.408594

Rohde, G. K., Benoit, B. M., and Lin, S. (2005). Corrections of motion artifacts in cardiac optical mapping using image registration. *IEEE Trans. Biomed. Eng.* 52, 338–341. doi: 10.1109/TBME.2004.840464

Seo, K., Inagaki, M., Nishimura, S., Hidaka, I., Sugimachi, M., Hisada, T., et al. (2010). Structural heterogeneity in the ventricular wall plays a significant role in the initiation of stretch-induced arrhythmias in perfused rabbit right ventricular tissues and whole heart preparations. *Circ. Res.* 106, 176–184. doi: 10.1161/CIRCRESAHA.109.203828

Tai, D. C.-S., Caldwell, B. J., LeGrice, I. J., Hooks, D. A., Pullan, A. J., and Smaill, B. H. (2004). Correction of motion artifact in transmembrane voltage-sensitive fluorescent dye emission in hearts. *Am. J. Physiol. Heart Circ. Physiol.* 287, 985–993. doi: 10.1152/ajpheart.00574.2003

Weise, L. D., Nash, M. P., and Panfilov, A. V. (2011). A discrete model to study reaction-diffusion mechanics systems. *PLoS ONE* 6:e21934. doi: 10.1371/journal.pone.0021934

Zhang, H., Iijima, K., Huang, J., Walcott, G. P., and Rogers, J. M. (2016). Optical mapping of membrane potential and epicardial deformation in beating hearts. *Biophys. J.* 111, 438–451. doi: 10.1016/j.bpj.2016.03.043

Conflict of Interest Statement: The authors declare that the research was conducted in the absence of any commercial or financial relationships that could be construed as a potential conflict of interest.

frontiers in Physics

ORIGINAL RESEARCH
published: 12 October 2018
doi: 10.3389/fphy.2018.00117

Mathematical Analysis of the Role of Heterogeneous Distribution of Excitable and Non-excitable Cells on Early Afterdepolarizations

Seunghyun Kim[1†] *and Daisuke Sato*[2*]

[1] Department of Mathematics, University of California, Davis, Davis, CA, United States, [2] Department of Pharmacology, University of California, Davis, Davis, CA, United States

OPEN ACCESS

Edited by:
S. Sridhar,
Robert Bosch Centre for Cyber-Physical Systems, Indian Institute of Science, India

Reviewed by:
Fei Geng,
McMaster University, Canada
Alok Ranjan Nayak,
International Institute of Information Technology, India

***Correspondence:**
Daisuke Sato
dsato@ucdavis.edu

†Present Address:
Seunghyun Kim,
Department of Mathematics, University of California, Los Angeles, Los Angeles, CA, United States

Specialty section:
This article was submitted to Biomedical Physics, a section of the journal Frontiers in Physics

Received: 16 January 2018
Accepted: 20 September 2018
Published: 12 October 2018

Citation:
Kim S and Sato D (2018) Mathematical Analysis of the Role of Heterogeneous Distribution of Excitable and Non-excitable Cells on Early Afterdepolarizations. Front. Phys. 6:117. doi: 10.3389/fphy.2018.00117

Early afterdepolarizations (EADs) are abnormal oscillations during the plateau phase of the cardiac action potential and have been linked to cardiac arrhythmias. At the cellular level, EADs can be caused by reactivation of the L-type calcium (Ca^{2+}) channels, spontaneous Ca^{2+} releases from the sarcoplasmic reticulum, or both. In tissue, these EADs can trigger action potentials in neighboring cells, which may propagate as a nonlinear wave. In this scenario, EADs are attributed to cellular/subcellular/channel properties. In this study, we show a novel mechanism of EADs due to heterogeneous distribution of excitable and non-excitable cells in tissue, using a physiologically detailed computational model and mathematical analysis. In tissue, excitability of cells depends on the cell type and physiological and pathological conditions. Non-excitable cells create a non-excitable gap in tissue, which has been thought to be a cause of slow waves and reflected waves. Here, we show that the non-excitable gap also can be responsible for EAD generation. However, EADs occur only when the non-excitable gap size is optimal. If the gap size is too small, no EADs occur. If the gap size is too large, the action potential wave cannot propagate through the gap region. We also demonstrate that EADs caused by the non-excitable gap can initiate reentry in tissue, which has been linked to ventricular tachycardia and fibrillation. Thus, the non-excitable gap can lead to both focal and reentrant arrhythmias. EADs shown in this study are spatial phenomena and require tissue heterogeneity. Our study sheds light on the role of tissue heterogeneity on focal and reentrant arrhythmias.

Keywords: early afterdepolarizations, heterogeneity, reflection, excitable media, reentry, arrhythmias, non-excitable gap, cardiac tissue

INTRODUCTION

Sudden cardiac death is one of the major causes of death in the world [1]. Sudden cardiac death is most often caused by arrhythmias. Under normal conditions, action potential waves propagate smoothly in the heart. During arrhythmias, in contrast, action potential waves are less organized and often show spatiotemporally chaotic behaviors. However, it is not clear how regular sinus rhythm becomes irregular arrhythmias.

Cardiac myocytes are excitable cells. These cells are coupled by gap junctions in tissue. The membrane excitability and gap junction coupling are highly heterogeneous in the heart [2, 3]. These heterogeneities are especially amplified under pathological conditions such as heart failure and myocardial infarction [4–9].

Early afterdepolarizations (EADs) are abnormal oscillations of the membrane potential during the plateau phase of the action potential. EADs can be caused by reactivation of the Ca^{2+} and/or Na^{+} channels or spontaneous Ca^{2+} releases from the sarcoplasmic reticulum, or both [10–15]. These abnormal oscillations can re-excite surrounding tissue and cause triggered activities if they overcome the source-sink mismatch [16–20].

Cardiac myocytes are electrotonically coupled via gap junctions in tissue. When some cells are excited in tissue, currents flow from excited cells to neighboring cells via gap junctions and excite the neighboring cells. The propagation excitation forms the action potential wave. Under pathological conditions such as ischemia and myocardial infarction, cells can be less excitable or non-excitable [21, 22]. If one cell is non-excitable, the membrane potential of the cell is passively changed by the membrane potential of surrounding cells. Generally, one or few non-excitable cells do not cause a problem since the action potential wave can pass through these cells. However, as the number of non-excitable cells increases, the action potential wave slows down in this region, and eventually fails to propagate when the number of non-excitable cells exceeds a certain threshold. In addition to propagation failure, non-excitable cells in tissue also can cause retrograde waves, which may lead to focal arrhythmias. This phenomenon is known as "reflection" and shown in experiments using the ventricular tissue, atrial tissue, and Purkinje fiber [23–29]. These reflected waves have been also shown in computer simulations [30–35]. The simplified mathematical model of cardiac tissue showed the mechanisms of reflected waves and the role of the non-excitable region [31]. The detailed analysis using 1- and 2-variable models has shown that the number of reflected waves is highly sensitive to the size of the non-excitable region [33, 35].

In this study, we show how non-excitable cells in excitable tissue affect EAD formation due to reactivation of the Ca^{2+} channels using computational models and mathematical analysis. The key finding in this study is that a small region (1∼2 mm) of non-excitable tissue can lead to EADs and promote arrhythmias. Thus, tissue properties are critical for EAD formation as well as cellular properties. Such heterogeneous distribution of non-excitable and excitable cells in tissue, as in pathological conditions such as ischemia, can lead to the onset of ventricular tachycardia and fibrillation.

MATERIALS AND METHODS

Physiological Model

We used a physiologically detailed model of the rabbit ventricular action potential model used in our previous studies [19, 36–38]. The membrane potential is governed by

$$\frac{\partial V(x,t)}{\partial t} = -s(x) \cdot \frac{I_{ion}(x,t)}{C_m} + \nabla \cdot D\nabla V(x,t),$$

where V is the membrane potential, I_{ion} is the total transmembrane current, C_m is the cell membrane capacitance, D is the effective diffusion constant of the voltage due to currents from neighboring cells through gap junctions, x represents position in space and t is time. In this study, we introduced the variable $s(x)$ to control excitability in tissue as follows (**Figure 1A**).

$$\begin{cases} s(x) = 0 & \text{for non} - \text{excitable cells} \\ s(x) = 1 & \text{for excitable cells} \end{cases}$$

Since the original parameters of this model were built based on the healthy rabbit cell data [37], EADs do not occur even at slow heart rates. In order to promote EAD formation at the cellular level, we modified parameters to reduce repolarization reserve by increasing inward current (I_{CaL}) and reducing K currents. We note that even with these modifications, EADs do not occur without the non-excitable gap. EADs occur only when the non-excitable gap is inserted in tissue and/or repolarization reserve is further reduced by increasing I_{CaL} (or decreasing K current). Parameters and equations used in this study are shown in the **Supplementary Material**.

Computer Simulation

A one-dimensional cable (9 cm) was paced at one end. To ensure propagation, the leftmost five cells were paced in a one-dimensional cable. Non-excitable cells were inserted in the middle of the cable as shown in **Figure 1A.** The two-dimensional

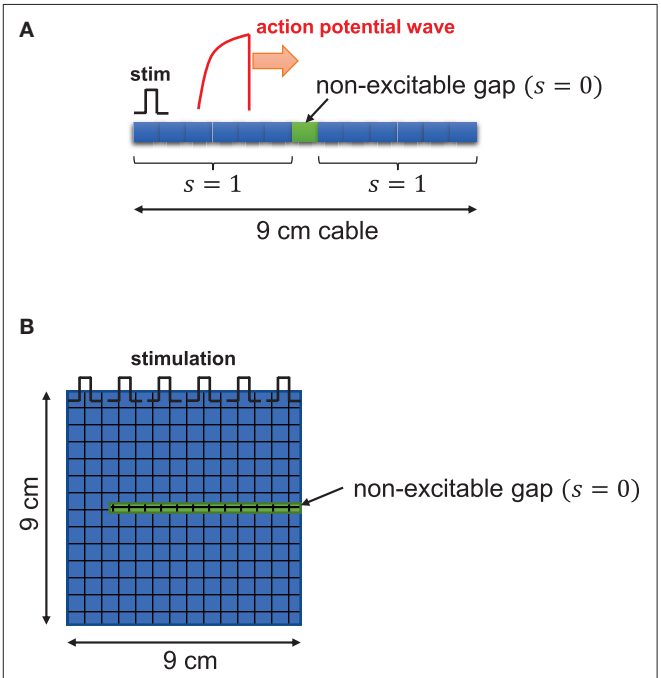

FIGURE 1 | Schematic illustration. One dimensional tissue was paced with stimuli applied uniformly at the left edge of the tissue. The cable length is 9 cm. **(A)** In the cable, s(x), function of excitability with respect to position in tissue, is 1 for excitable cells and 0 for non-excitable cells. **(B)** In two-dimensional tissue, the non-excitable gap was inserted in the middle of the tissue.

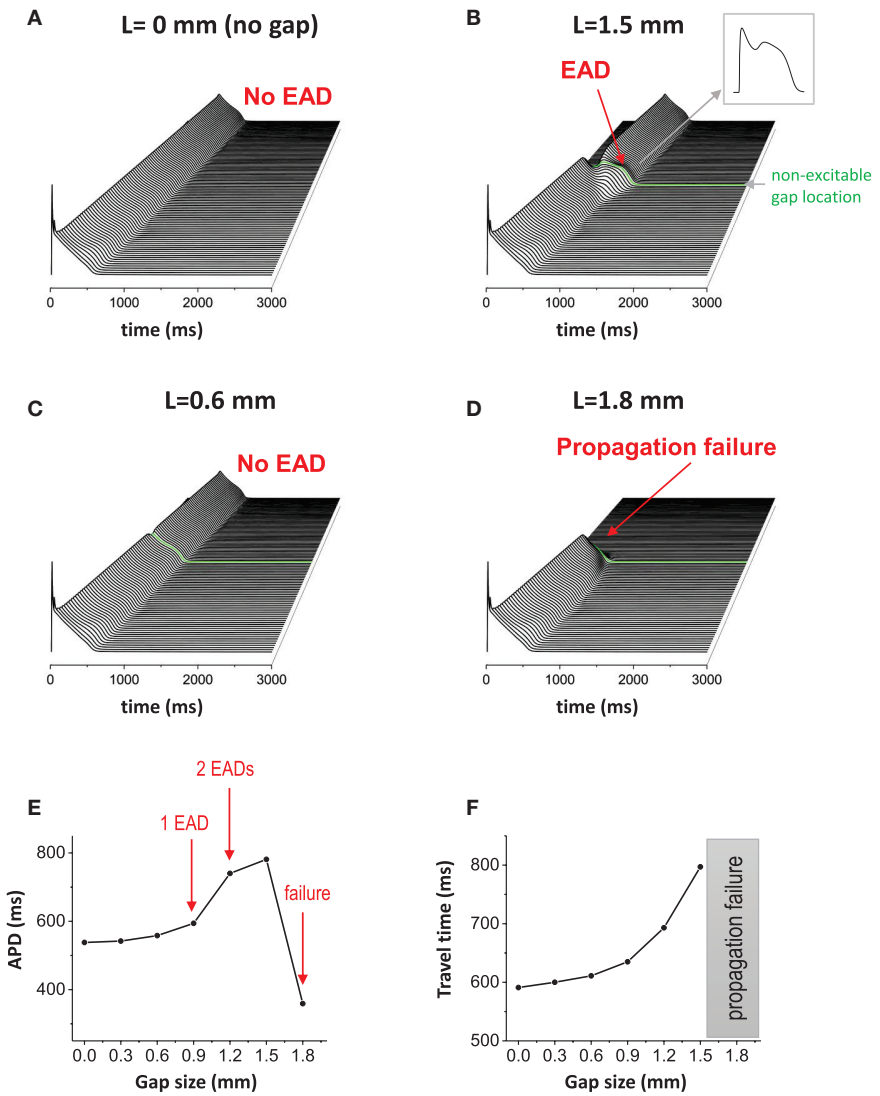

FIGURE 2 | Non-excitable gap causes EADs. **(A)** Without non-excitable gap, the action potential wave propagates without causing EADs in 1D tissue. Space-time plot. **(B)** When non-excitable gap is inserted, EADs occurred around the non-excitable gap region. The maximum APD is 781 ms. The gap size is 1.5 mm. **(C)** If the gap size is too small (0.6 mm), no EADs occurred. **(D)** If the gap size is too large (1.8 mm), propagation failed at the gap region. **(E)** APD vs. the gap size. **(F)** The travel time of action potential wave vs. gap size.

tissue (9×9 cm) was paced from the top and non-excitable cells were inserted as shown in **Figure 1B.** We solve this equation using the operator splitting method [39]. We use the Euler method with the variable time step of 0.01∼0.1 ms to compute the single cell action potential. The space step (Δx) is 150 μm, which is similar to the length of the cardiac myocyte. For the numerical accuracy, we used double precision in our simulations and checked the results using smaller time steps. All codes are written in C/C++. We used the 25-node high-performance computing cluster.

Simplified Model

In order to understand the dynamical mechanisms of EADs due to non-excitable gap, we also constructed the reduced mathematical model of EADs. The basic structure of the model is the same as our previous studies [40]. This model has three variables: membrane voltage (v), and gating variables (f and x). These variables are governed by

$$C_m \frac{dv}{dt} = -(i_{Ca} + i_K) + g_{gap}(v_2 - v),$$
$$\frac{df}{dt} = \frac{f_\infty - f}{\tau_f},$$
$$\frac{dx}{dt} = \frac{x_\infty - x}{\tau_x},$$

where i_{Ca} is the simplified L-type Ca^{2+} current and i_K is the generic K current, g_{gap} is the effective conductance between

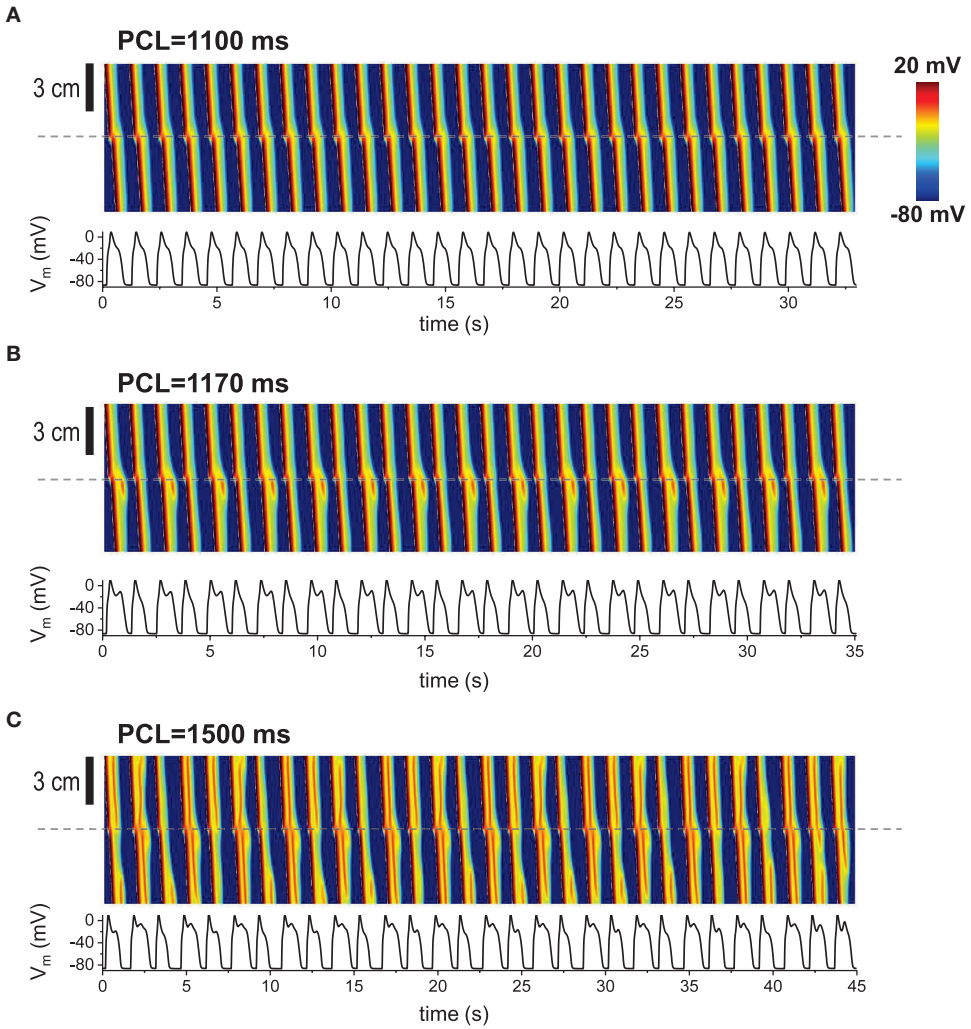

FIGURE 3 | Repetitive pacing When 1D cable was paced repetitively, various patterns appeared. Top: Space-time plot. The AP traces (bottom) were taken at the middle of the cable (indicated by dashed lines). The gap size is 1.5 mm. The tissue was paced 200 times. Last 30 beats are shown here. **(A)** Periodic (period-1) pattern. No EADs at the gap region. **(B)** Period-2. EADs occur every other beat. **(C)** Complex pattern. Spatiotemporal chaos.

proximal and distal regions. v_2 is the membrane potential in the distal region. Due to the large delay at the gap region, the action potential in the distal region remains the plateau phase when the membrane potential in the proximal region is repolarizing. Thus, the membrane potential in the distal region was assumed to be constant. f and x are gating variables of the Ca^{2+} current and the generic K current, respectively. f_∞ and x_∞ are steady state values of f and x gates, respectively. τ_f and τ_x are time constants of f and x gates, respectively. The simplified L-type Ca^{2+} current and the generic K current are

$$\begin{aligned} i_{Ca} &= g_{Ca} d_\infty f\,(v - e_{Ca})\,, \\ i_K &= g_k \cdot x \cdot (v - e_k)\,, \end{aligned}$$

where g_{Ca} is the maximum conductance of i_{Ca}, g_k is the maximum conductance of i_k, d_∞ is the instantaneous activation gate of the Ca^{2+} channel, e_{Ca} is the reversal potential of i_{Ca}, e_k is the reversal potential of i_k. Steady state values, d_∞, f_∞ and x_∞ are voltage dependent and governed by

$$\begin{aligned} d_\infty &= \frac{1}{1 + \exp\left(-\frac{v+32}{6.24}\right)}, \\ f_\infty &= \frac{1}{1 + \exp\left(\frac{v+21}{8.6}\right)}, \\ x_\infty &= \frac{1}{1 + \exp\left(-\frac{v+35}{5}\right)}. \end{aligned}$$

We use the Euler method with the variable time step of 0.1 ms to solve the simplified model.

RESULTS

One-dimensional cable was paced at one end. In this study, the cable length is 9 cm, which is longer than the typical human

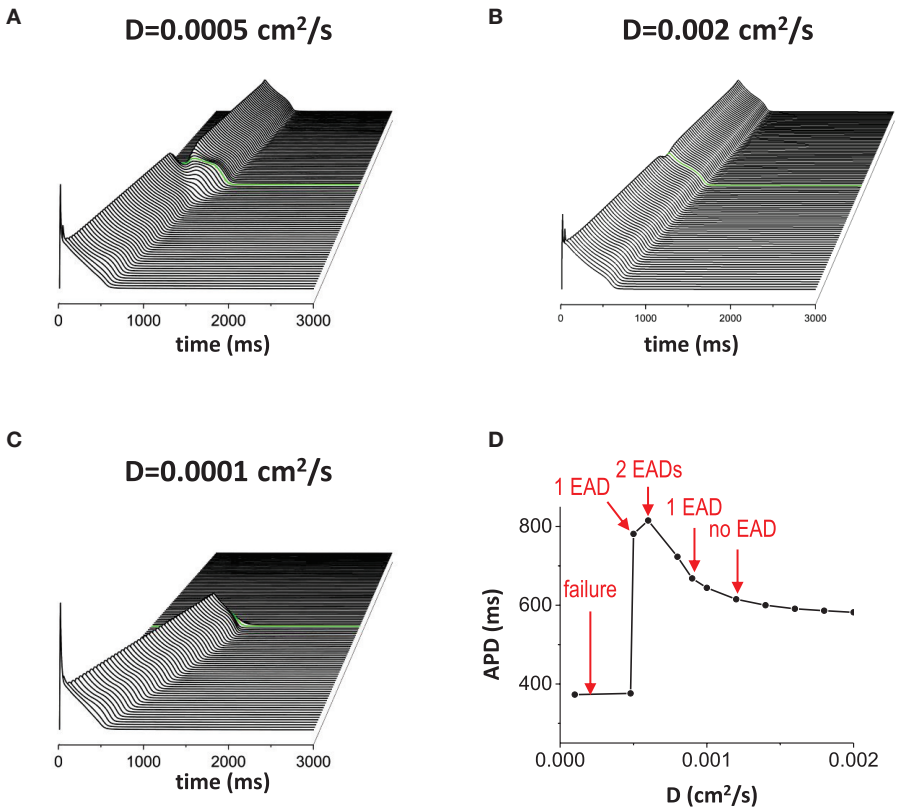

FIGURE 4 | Gap junction conductance affects EAD formation. The diffusive current between cells also affects EAD formation. In this figure, the gap size was fixed at 1.5 mm. **(A)** normal D. D = 0.0005 cm^2/s. **(B)** large D. D = 0.002 cm^2/s. **(C)** small D. D = 0.00001 cm^2/s. **(D)** APD vs. *D*.

heart size, to avoid unnecessary boundary effects. When cells are well connected via gap junctions without a non-excitable gap, the action potential wave propagates smoothly without EADs in the cable (**Figure 2A**). Hereafter, we refer to this case as the "control" case. The maximum action potential duration (APD) in the cable was 538 ms in the control case. The travel time of the action potential wave from one end to the other end totaling 9 cm was 591 ms. When a non-excitable gap of 1.5 mm (= 10 cells) is inserted in the middle of the cable (**Figures 1**, **2B** green line), the propagation speed of the action potential slows down at the gap region. In this case, the travel time of the action potential wave propagated from one end to the other end was 797 ms. Therefore, the delay of the propagation at the gap region is 259 ms. In addition, EADs occur near the gap region (**Figure 2B**). In this case, the maximum APD in the cable was 781 ms. The gap size is critical for the formation of EADs. If the gap size is too small, EADs do not occur (**Figure 2C**). EADs occurred only when the gap size reaches 1.5 mm. On the other hand, if the gap size is too large (gap size greater than or equal to 1.8 mm), the action potential wave cannot propagate due to non-excitability in the gap (**Figure 2D**). **Figure 2E** shows a graph of APD vs. gap size, and the number of EADs with different gap sizes. Additionally, the travel time of action potential wave is depicted against the gap size (**Figure 2F**). Note that the action potential fails to propagate if the gap size is larger than 1.8 mm.

In our previous studies, we have shown that EADs can be periodic and chaotic due to nonlinearity of EAD dynamics [15, 19, 40–42]. When the 1D cable was paced repetitively, various patterns appeared such as periodic (period-1), period-2 and even spatiotemporally chaotic patterns (**Figures 3A–C**). These patterns appear only when non-excitable cells exist in tissue.

When the non-excitable gap exists, changing the gap junction conductance also has the similar effects to the gap size since the effective gap size is proportional to $1/\sqrt{D}$. In other words, the diffusion coefficient D rescales the length of the gap. Thus, although changing the size and changing the gap junction conductance are physiologically different, mathematically, we expect similar results. We used a fixed gap size = 1.5 mm for all simulations in **Figure 4**. When D is normal value (D = 0.0005 cm^2/s), 1 EAD was observed near the gap region (**Figure 4A**). If D becomes larger (D = 0.002 cm^2/s), the effective gap size becomes smaller and no EADs occurred (**Figure 4B**). If D is too small (D = 0.00001 cm^2/s), the action potential wave could not cross the gap region due to the large effective gap (**Figure 4C**). **Figure 4D** shows how diffusive coupling impacts EAD formation. There is an optimal window for EAD formation.

Reducing repolarization reserve by increasing inward currents such as I_{CaL} and/or reducing outward currents such as I_{Kr} and I_{Ks}, promotes EAD generation. When I_{CaL} is increased (**Figure 5A**), APD was prolonged (APD = 1816 ms) and the

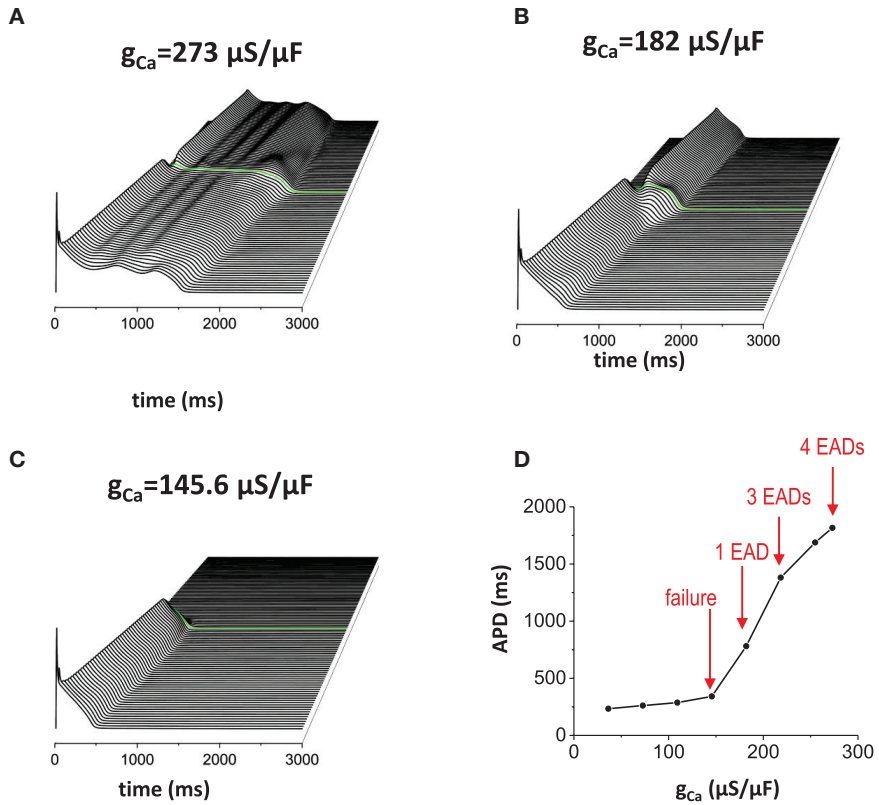

FIGURE 5 | Effects of the inward current. When inward current (I_{CaL}) is increased, EADs occur without the non-excitable gap region. In addition, non-excitable gap promotes EADs further **(A)**. $g_{Ca} = 273$ μA/μF. Without the non-excitable gap region, 3 EADs were observed. Near the gap region, 4 EADs were observed. The maximum APD is 1816 ms. **(B)** $g_{Ca} = 182$ μA/μF. Control. The maximum APD is 781 ms. **(C)** $g_{Ca} = 145.6$ μA/μF. The maximum APD is 341 ms. **(D)** a graph of APD vs. g_{Ca}.

action potential wave has EADs without the non-excitable gap. When the non-excitable gap is inserted, it promoted EADs further if the gap size optimal (the gap size is 1.5 mm in **Figure 5**). Near the gap region, four EADs occurred whereas only three EADs occurred in the other regions. **Figure 5B** is the control model for comparison. If the inward current is too small, the action potential is too short to provide enough source current to initiate new action potential in the distal region even if the gap size is optimal for the control model (**Figure 5C**). **Figure 5D** is a graph of APD vs. conductance of the inward current (g_{Ca}), summarizing our observation that EADs occur when the inward current increases.

Reducing outward current also has the same effects (**Figures 6A–D**). When the outward current became smaller (in this case, we reduced I_{NaK}), more EADs occurred (**Figure 6A**). **Figure 6B** is the control model for comparison. Then, when the outward current became too large, the action potential wave failed to propagate (**Figure 6C**). To summarize these results, we plotted a graph of APD against conductance of the outward current (g_{NaK}; **Figure 6D**).

To understand the dynamical mechanisms of EADs due to the non-excitable gap, we analyzed using a simplified mathematical model of EADs (see Material and Methods). In this model, v is the membrane potential of the cell in the proximal region near the gap. We assessed how current from the distal region promotes EAD generation. We assume the membrane potential of the cell in the distal region (v_2) remains in the plateau phase due to the large delay (>200 ms) of the propagation at the gap region. Since x is the slowest variable in this system, we take it as a parameter. Then, the 2-variable system can be written as

$$\begin{aligned}\frac{dv}{dt} &= F(v,f) = -(g_{Ca} d_\infty f\,(v - e_{Ca}) + g_k \cdot x \cdot (v - e_k)) \\ &\quad + g_{gap}(v_2 - v), \\ \frac{df}{dt} &= G(v,f) = \frac{f_\infty - f}{\tau_f},\end{aligned}$$

where

$$\begin{aligned}d_\infty &= \frac{1}{1 + \exp\left(-\frac{v+32}{6.24}\right)}, \\ f_\infty &= \frac{1}{1 + \exp\left(\frac{v+21}{8.6}\right)}.\end{aligned}$$

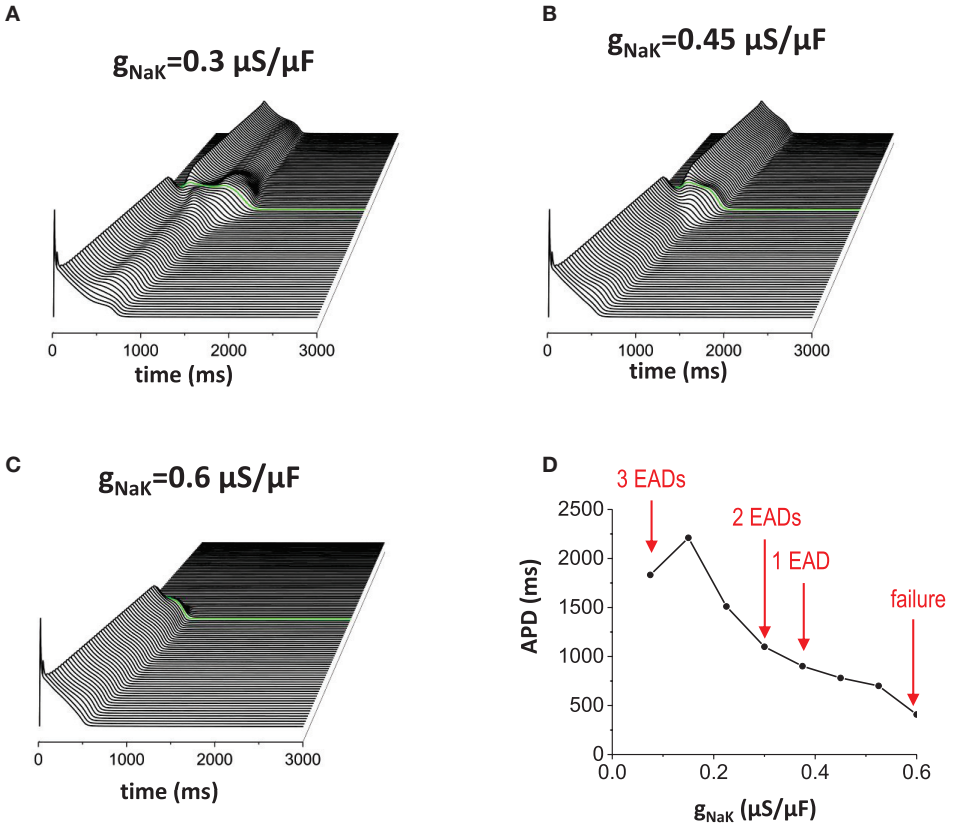

FIGURE 6 | Effects of the outward current. Reducing outward current (I_{NaK}) also has similar effects of increasing inward current. **(A)** When the outward current was reduced (g_{NaK} = 0.3 μA/μF), EADs occured without the non-excitable gap region. Near the gap region, more EADs were observed (2 EADs). **(B)** g_{NaK} = 0.45 μA/μF. Control. **(C)** g_{NaK} = 0.6 μA/μF. Large outward current reduces APD. Since APD is shorter, the action potential in the proximal region cannot provide enough source current to excite cells in the distal region. **(D)** APD vs. g_{NaK}.

Thus, the matrix to compute the stability of the system is

$$M = \begin{pmatrix} F_v & F_f \\ G_v & G_f \end{pmatrix} = \begin{pmatrix} -g_{Ca}d'_\infty fv - g_{Ca}d_\infty f - g_k x + g_{gap} & -g_{Ca}d_\infty v \\ f'_\infty/\tau_f & -1/\tau_f \end{pmatrix}$$

Figures 7A–C show the effects of the current from the distal region. As the gap junction conductance is increased (from g_{gap}=0 to g_{gap}=0.009 μA/μF), the attractor region (blue part in **Figure 7A**) was extended and repeller (green part in **Figure 7A**) became attractor (unstable focus → stable focus). We varied the distal membrane potential from +30 mV to −30 mV (**Figures 7B,C**). In all cases, the current from the distal region promoted oscillatory attractors. We note that if the distal membrane potential becomes lower than ∼−30 mV, the current from the distal region suppresses EADs. We also computed basins of attraction (**Figures 7D–F**). In all cases, the basin of attraction was increased as the gap junction conductance was increased. However, as the distal membrane potential becomes lower, larger conductance was required to extend the basin of attraction (**Figure 7E** vs. **Figure 7F**). On the other hand, the current from the distal region has little effect on fix points (red dots in **Figure 7**) and EAD oscillations always occur near −20 mV.

When non-excitable cells are inserted in 2-dimensional tissue, EADs caused by the non-excitable gap region can initiate reentry, which has been associated with ventricular tachycardia. Without non-excitable gap, the action potential wave propagates smoothly. When non-excitable gap is inserted (**Figure 1C**), EADs occur near this region. EADs prolong APD. Thus, if cells in this region cannot recover by the time the next wave arrives, the wave cannot propagate in this region. This large dispersion of refractoriness and regional block of the wave can cause reentry (**Figure 8A**, **Supplemental Movie 1**). If the gap size is too small to cause EADs, although there is a small delay of the propagation at the gap region, dispersion of refractoriness is much smaller and rarely causes reentry (**Figure 8B**, **Supplemental Movie 2**). If the gap size is too large, any waves cannot propagate in this region and waves go around this region (**Figure 8C** , **Supplemental Movie 3**). These results demonstrate that non-excitability in tissue can lead to large dispersion of refractoriness and may cause arrhythmias.

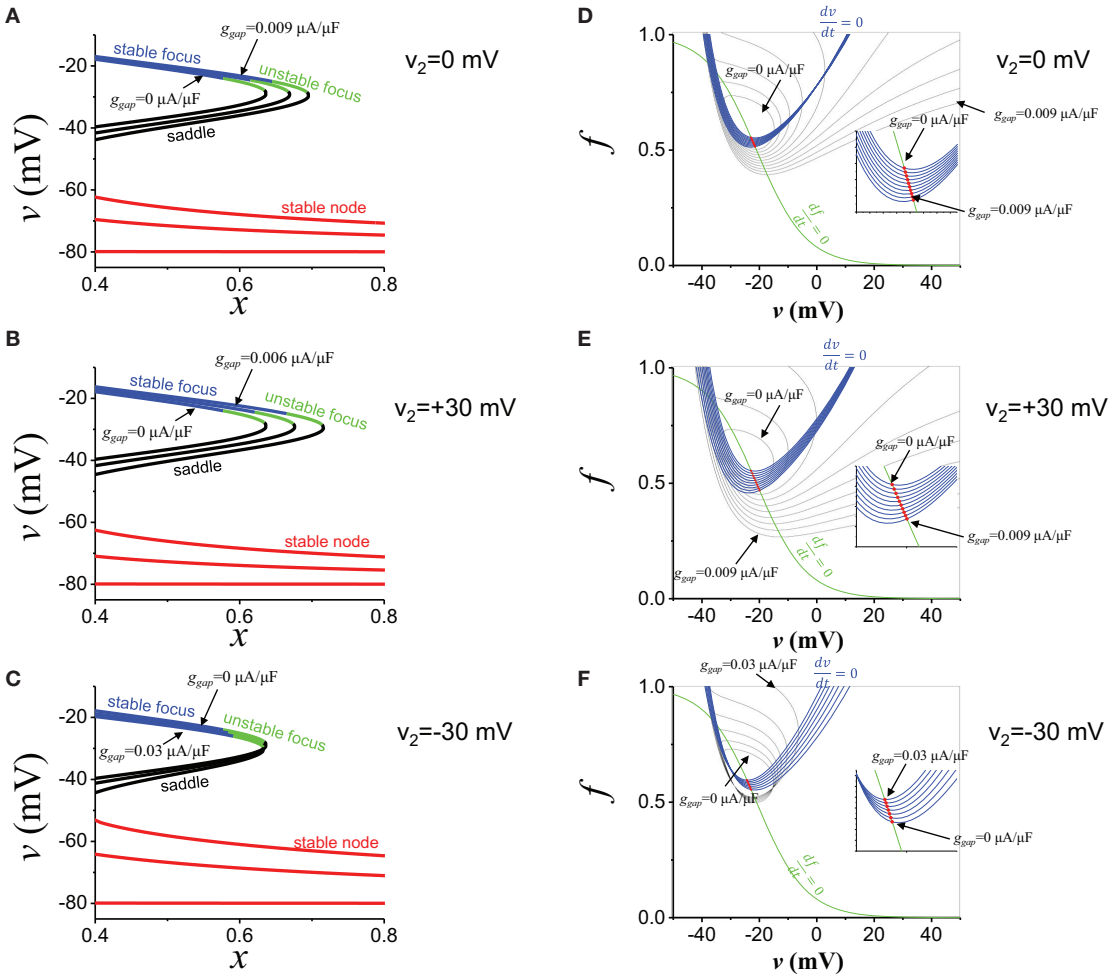

FIGURE 7 | EAD mechanisms. **(A)** The stability of the fats subsystem (*v,f*). *x* is the parameter. Blue: stable focus. Green: unstable focus. Black: saddle. Red: stable node. g_{gap} values are 0, 0.0045, and 0.009 μA/μF. v_2 is 0 mV. **(B)** The same as **(A)**, but v_2 is +30 mV. g_{gap} values are 0, 0.003, and 0.006 μA/μF. **(C)** The same as **(A)**, but v_2 is −30 mV. g_{gap} values are 0, 0.015, and 0.03 μA/μF. **(D)** Basin of attraction. g_{gap} value was varied from 0 to 0.009 μA/μF. v_2 is 0 mV. Red dots indicate fixed points. Blue and green lines are nuclines. **(E)** The same as **(D),** but v_2 is +30 mV. g_{gap} value was varied from 0 to 0.009 μA/μF. **(F)** The same as **(D)**, but v_2 is −30 mV. g_{gap} value was varied from 0 to 0.03 μA/μF.

DISCUSSION

Tissue heterogeneity has been thought to be one of the contributing factors of arrhythmias [43–47]. In this study, we investigated how non-excitable cells in excitable tissue promote EADs and thus arrhythmias.

EADs can be caused by reactivation of the Ca^{2+} channels, spontaneous Ca^{2+} releases from the SR, or both [10–15]. In addition, recent studies have shown that reactivation of the Na^{+} channels can also lead to EADs [15, 48]. In this study, we showed the mechanism of Ca^{2+} channel-mediated EADs due to heterogeneously distributed excitable and non-excitable cells, and demonstrated reentrant arrhythmias in 2D tissue using physiologically detailed computational models. It has been well-studied how non-excitable cells in excitable tissue can lead to reflected waves [23–29]. In these studies, the key to the reflected waves was reactivation of the Na^{+} channels. In this study, we showed the reflection occurs at the plateau voltage due to reactivation of the Ca^{2+} channels. In our simulations, EADs did not cause a retrograde wave since the amplitude of EADs was too small but prolonged APDs.

The number of EADs is sensitive to the gap size (**Figure 2**). The detailed analysis using a two-variable model has shown that there are infinite patterns of reflected waves (1 reflected wave, 2 reflected waves, 3 reflected waves … infinite reflected waves) between normal propagation (no reflected waves) and propagation failure when the gap size is varied [33]. In our study, we did not observe these patterns even when the gap size is finely tuned. This is probably because the memory effect in the model interfered the patterns.

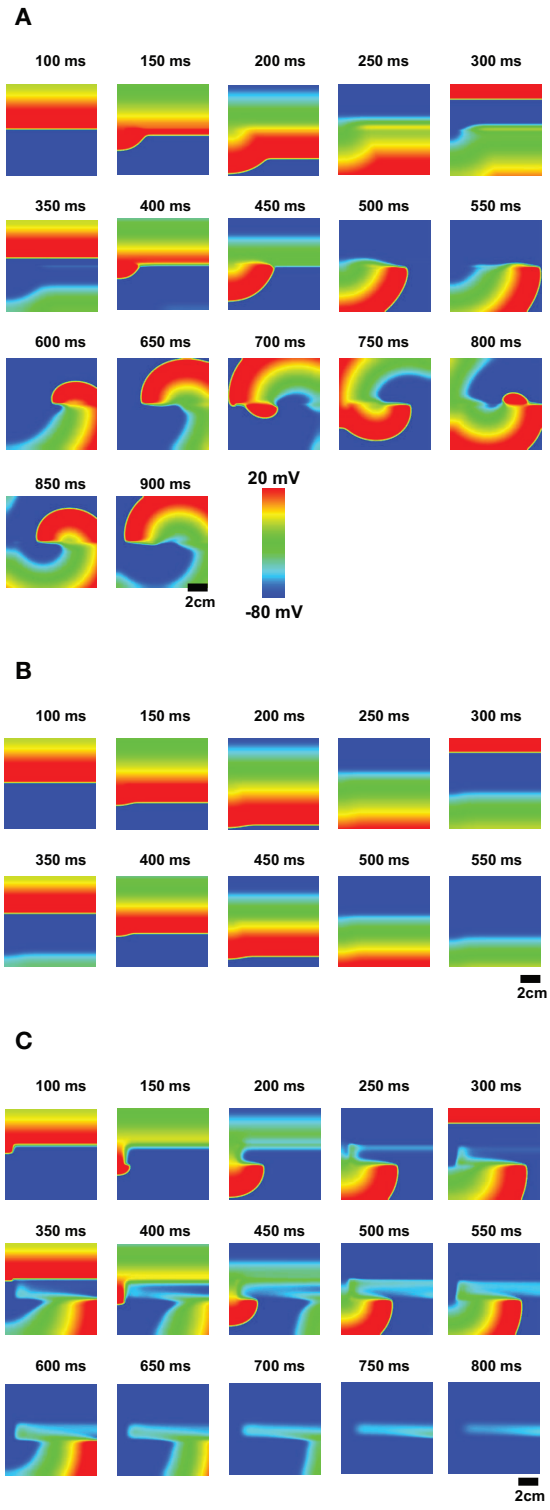

FIGURE 8 | EADs due to the non-excitable gap region cause reentry**. (A)** The optimal non-excitable gap region (1.2 mm) cause EADs. These EADs block the next action potential wave and cause reentry. The tissue size is 9 × 9 cm. (**Supplemental Movie 1**; **B)** If the gap size is too small, EADs will not occur although there is a delay at the gap region. (**Supplemental Movie 2**; **C)** If the gap size is too large, the action potential wave cannot propagate and the wave avoids this region (**Supplemental Movie 3**).

In tissue, large dispersion of refractoriness can initiate reentry [49]. When non-excitable cells are inserted in 2D tissue, dispersion of refractoriness can be observed without EADs (**Figure 8B**, **Supplemental Movie 2**). However, the dispersion is small in this case. When EADs occur, the dispersion becomes large enough to initiate reentry (**Figure 8A**, **Supplemental Movie 1**). The non-excitable gap also becomes an anchor of the spiral waves (**Supplemental Movie 1**). But no EADs were observed since the cycle of the rotation of the spiral wave was too fast for EADs. If the gap size is too large, the gap region blocks action potential waves (**Figure 8C**, **Supplemental Movie 3**). It is known that obstacles in tissue can lead to reentry [50, 51]. Thus, the large gap region can also initiate reentry by different mechanisms.

It is known that tissue geometry is also an important factor for reflected waves [32]. When an action potential wave propagates from a narrow path to a wide path, the propagation speed slows down due to the source-sink mismatch. This delay can re-excite the cells in the narrow path and cause a retrograde wave. Thus, propagation delay due to tissue geometry may be able to initiate EADs. This possibility needs to be investigated.

Reflected waves have been observed and investigated in various systems such as cardiac tissue and neurons. The cardiac subcellular Ca^{2+} system is also an excitable system. Under normal conditions, Ca^{2+} release from the sarcoplasmic reticulum (SR) forms a spark. However, when Ca^{2+} sparks recruit new Ca^{2+} sparks in neighboring Ca^{2+} release units, Ca^{2+} sparks propagate as a wave [52, 53]. Each Ca^{2+} release unit contains a few to several hundred ryanodine receptors [54–58] and the number of ryanodine receptors affects the positive feedback process known as Ca^{2+}-induced Ca^{2+} release [58, 59]. In addition, the subcellular structure is very complex. These subcellular heterogeneities may lead to reflection and form complex patterns in Ca^{2+} waves.

In this paper, we showed only mathematical and computational results. These results should be verified in experiments. Reflected waves have been observed in many wet experiments. We expect that we can use the same experimental setup for EADs due to non-excitable cells. However, to observe EADs, repolarization reserve needs to be reduced.

CONCLUSIONS

Cellular mechanisms of EADs have been widely studied. In this study, we showed that tissue properties are also critical for initiation and promotion of EADs. Non-excitable gap in tissue can promote EADs and prolonged action potentials due to EADs can cause conduction block and reentry of the action potential wave.

The limitation of this study is that we considered only Ca^{2+} channel reactivation. Retrograde waves propagate when the Na^{+} channels are reactivated. If both cases are considered, focal and reentrant arrhythmias can coexist and the dynamics will become much more complex.

Ablation creates non-excitable tissue. The border zone of myocardial infarction is also mixture of

excitable and non-excitable cells. Our study implies that EADs can be promoted in these regions due to tissue heterogeneity. This study sheds light on the role of tissue heterogeneity on EAD generation and initiation of reentrant arrhythmias.

AUTHOR CONTRIBUTIONS

All authors SK and DS contributed ideas and discussion. All authors performed computer simulations and mathematical analysis, wrote the manuscript, approved the final version of the manuscript and agree to be accountable for all aspects of the work.

FUNDING

This work was supported by National Institutes of Health grant R00-HL111334, American Heart Association Grant-in-Aid 16GRNT31300018, and Amazon AWS Cloud Credits for Research (DS).

ACKNOWLEDGMENTS

The authors wish to thank Dr. Timothy J. Lewis for a critical reading of the manuscript, and his comments and suggestions.

SUPPLEMENTARY MATERIAL

The Supplementary Material for this article can be found online at: https://www.frontiersin.org/articles/10.3389/fphy.2018.00117/full#supplementary-material

Supplemental Movie 1 | Movie of **Figure 8A.**

Supplemental Movie 2 | Movie of **Figure 8B.**

Supplemental Movie 3 | Movie of **Figure 8C.**

REFERENCES

1. Zipes DP, Wellens HJJ. Sudden cardiac death. *Circulation* (1998) **98**:2334–51.
2. Roberts-Thomson KC, Lau DH, Sanders P. The diagnosis and management of ventricular arrhythmias. *Nat Rev Cardiol.* (2011) **8**:311–21. doi: 10.1038/nrcardio.2011.15
3. Burchfield JS, Xie M, Hill JA. Pathological ventricular remodeling: mechanisms: part 1 of 2. *Circulation* (2013) **128**:388–400. doi: 10.1161/circulationaha.113.001878
4. Peters NS. Myocardial gap junction organization in ischemia and infarction. *Microsc Res Tech.* (1995) **31**:375–86. doi: 10.1002/jemt.10703 10507
5. Saffitz JE, Schuessler RB, Yamada KA. Mechanisms of remodeling of gap junction distributions and the development of anatomic substrates of arrhythmias. *Cardiovasc Res.* (1999) **42**:309–17.
6. Jongsma HJ, Wilders R. Gap junctions in cardiovascular disease. *Circ Res.* (2000) **86**:1193–7. doi: 10.1161/01.RES.86.12.1193
7. Severs NJ. Gap junction remodeling in heart failure. *J Card Fail* (2002) **8**:S293–9. doi: 10.1054/jcaf.2002.129255
8. Severs NJ, Coppen SR, Dupont E, Yeh HI, Ko YS, Matsushita T. Gap junction alterations in human cardiac disease. *Cardiovasc Res.* (2004) **62**:368–77. doi: 10.1016/j.cardiores.2003.12.007
9. Bruce AF, Rothery S, Dupont E, Severs NJ. Gap junction remodelling in human heart failure is associated with increased interaction of connexin43 with ZO-1. *Cardiovas Res.* (2008) **77**:757–65. doi: 10.1093/cvr/cvm083
10. January C, Riddle J. Early afterdepolarizations: mechanism of induction and block. A role for L-type Ca2+ current. *Circ Res.* (1989) **64**:977–90.
11. January CT, Moscucci A. Cellular mechanisms of early afterdepolarizationsa. *Ann N Y Acad Sci.* (1992) **644**:23–32. doi: 10.1111/j.1749-6632.1992.tb30999.x
12. Zeng J, Rudy Y. Early afterdepolarizations in cardiac myocytes: mechanism and rate dependence. *Biophys J.* (1995) **68**:949–64. doi: 10.1016/s0006-3495(95)80271-7
13. Viswanathan PC, Rudy Y. Pause induced early afterdepolarizations in the long QT syndrome: a simulation study. *Cardiovas Res.* (1999) **42**:530–42. doi: 10.1016/s0008-6363(99)00035-8
14. Volders PGA, Vos MA, Szabo B, Sipido KR, de Groot SHM, Gorgels APM, et al. Progress in the understanding of cardiac early afterdepolarizations and torsades de pointes: time to revise current concepts. *Cardiovas Res.* (2000) **46**:376–92. doi: 10.1016/s0008-6363(00)00022-5
15. Sato D, Clancy CE, Bers DM. Dynamics of sodium current mediated early afterdepolarizations. *Heliyon* (2017) **3**:e00388. doi: 10.1016/j.heliyon.2017.e00388
16. Gilmour RF, Moïse S. Triggered activity as a mechanism for inherited ventricular arrhythmias in German shepherd dogs. *J Am Coll Cardiol.* (1996) **27**:1526–33. doi: 10.1016/0735-1097(95)00618-4
17. Burashnikov A, Antzelevitch C. Reinduction of atrial fibrillation immediately after termination of the arrhythmia is mediated by late phase 3 early afterdepolarization-induced triggered activity. *Circulation* (2003) **107**:2355–60. doi: 10.1161/01.cir.0000065578.00869.7c
18. Patterson E, Jackman WM, Beckman KJ, Lazzara R, Lockwood D, Scherlag BJ, et al. Spontaneous pulmonary vein firing in man: relationship to tachycardia-pause early afterdepolarizations and triggered arrhythmia in canine pulmonary veins *in vitro*. *J Cardiovas Electrophysiol.* (2007) **18**:1067–75. doi: 10.1111/j.1540-8167.2007.00909.x
19. Sato D, Xie LH, Sovari AA, Tran DX, Morita N, Xie F, et al. Synchronization of chaotic early afterdepolarizations in the genesis of cardiac arrhythmias. *Proc Natl Acad Sci USA.* (2009) **106**:2983–8. doi: 10.1073/pnas.0809148106
20. Xie Y, Sato D, Garfinkel A, Qu Z, Weiss JN. So little source, so much sink: requirements for afterdepolarizations to propagate in tissue. *Biophys J.* (2010) **99**:1408–15. doi: 10.1016/j.bpj.2010.06.042
21. Janse MJ, Wit AL. Electrophysiological mechanisms of ventricular arrhythmias resulting from myocardial ischemia and infarction. *Physiol Rev.* (1989) **69**:1049–169. doi: 10.1152/physrev.1989.69.4.1049
22. RodrÍGuez B, Trayanova N, Noble D. Modeling cardiac ischemia. *Ann N Y Acad Sci.* (2006) **1080**:395–414. doi: 10.1196/annals.1380.029
23. Antzelevitch C, Jalife J, Moe GK. Characteristics of reflection as a mechanism of reentrant arrhythmias and its relationship to parasystole. *Circulation* (1980) **61**:182–91.
24. Antzelevitch C, Moe GK. Electrotonically mediated delayed conduction and reentry in relation to "slow responses" in mammalian ventricular conducting tissue. *Circ Res.* (1981) **49**:1129–39.
25. Jalife J, Moe GK. Excitation, conduction, and reflection of impulses in isolated bovine and serum cardiac purkinje fibers. *Circ Res.* (1981) **49**:233–47.
26. Antzelevitch C, Bernstein MJ, Feldman HN, Moe GK. Parasystole, reentry, and tachycardia: a canine preparation of cardiac arrhythmias occurring across inexcitable segments of tissue. *Circulation* (1983) **68**:1101–15.
27. Rozanski GJ, Jalife J, Moe GK. Reflected reentry in nonhomogeneous ventricular muscle as a mechanism of cardiac arrhythmias. *Circulation* (1984) **69**:163–73.
28. Lukas A, Antzelevitch C. Reflected reentry, delayed conduction, and electrotonic inhibition in segmentally depressed atrial tissues. *Can J Physiol Pharmacol.* (1989) **67**:757–64.
29. Auerbach DS, Grz?da KR, Furspan PB, Sato PY, Mironov S, Jalife J. Structural heterogeneity promotes triggered activity, reflection and

arrhythmogenesis in cardiomyocyte monolayers. *J Physiol.* (2011) ***589***:2363–81. doi: 10.1113/jphysiol.2010.200576
30. Goldstein SS, Rall W. Changes of action potential shape and velocity for changing core conductor geometry. *Biophys J.* (1974) **14**:731–57. doi: 10.1016/s0006-3495(74)85947-3
31. Cabo C, Barr RC. Reflection after delayed excitation in a computer model of a single fiber. *Circ Res.* (1992) **71**:260–70.
32. Zhou Y, Bell J. Study of propagation along nonuniform excitable fibers. *Math Biosci.* (1994) **119**:169–203.
33. Lewis TJ. *The Effects of Nonexcitable Regions on Signal Propagation in ExcitableMedia: Propagation Failure and Reflection*. Ph.D. Thesis, University of Utah, Salt Lake City, UT (1998).
34. Keener JP, Lewis TJ. Wave-block in excitable media due to regions of depressed excitability. *SIAM J Appl Math.* (2000) **61**:293–316. doi: 10.1137/s0036139998349298
35. Cytrynbaum EN, Lewis TJ. A global bifurcation and the appearance of a one-dimensional spiral wave in excitable media. *SIAM J Appl Dynam Syst.* (2009) **8**:348–70. doi: 10.1137/080722254
36. Mahajan A, Sato D, Shiferaw Y, Baher A, Xie LH, Peralta R, et al. Modifying L-type calcium current kinetics: consequences for cardiac excitation and arrhythmia dynamics. *Biophys J.* (2008) **94**:411–23. doi: 10.1529/biophysj.106.98590
37. Mahajan A, Shiferaw Y, Sato D, Baher A, Olcese R, Xie LH, et al. A rabbit ventricular action potential model replicating cardiac dynamics at rapid heart rates. *Biophys J.* (2008) **94**:392–410. doi: 10.1529/biophysj.106.98160
38. Xie Y, Grandi E, Bers DM, Sato D. How does beta-adrenergic signalling affect the transitions from ventricular tachycardia to ventricular fibrillation? *Europace* (2014) **16**:452–7. doi: 10.1093/europace/eut412
39. Qu Z, Garfinkel A. An advanced algorithm for solving partial differential equation in cardiac conduction. *IEEE Trans Biomed Eng.* (1999) **46**:1166–8.
40. Xie Y, Izu LT, Bers DM, Sato D. Arrhythmogenic transient dynamics in cardiac myocytes. *Biophys J.* (2014) **106**:1391–7. doi: 10.1016/j.bpj.2013.12.050
41. Tran DX, Sato D, Yochelis A, Weiss JN, Garfinkel A, Qu Z. Bifurcation and chaos in a model of cardiac early afterdepolarizations. *Phys Rev Lett.* (2009) **102**:258103. doi: 10.1103/PhysRevLett.102.258103
42. Sato D, Xie LH, Nguyen TP, Weiss JN, Qu Z. Irregularly appearing early afterdepolarizations in cardiac myocytes: random fluctuations or dynamical chaos? *Biophys J.* (2010) **99**:765–73. doi: 10.1016/j.bpj.2010.05.019
43. Schmidt A, Azevedo CF, Cheng A, Gupta SN, Bluemke DA, Foo TK, et al. Infarct tissue heterogeneity by magnetic resonance imaging identifies enhanced cardiac arrhythmia susceptibility in patients with left ventricular dysfunction. *Circulation* (2007) **115**:2006–14. doi: 10.1161/circulationaha.106.653568
44. Bishop MJ, Connolly A, Plank G. Structural heterogeneity modulates effective refractory period: a mechanism of focal arrhythmia initiation. *PLoS ONE* (2014) **9**:e109754. doi: 10.1371/journal.pone.0109754
45. Qu Z, Weiss JN. Mechanisms of ventricular arrhythmias: from molecular fluctuations to electrical turbulence. *Annu Rev Physiol.* (2015) **77**:29–55. doi: 10.1146/annurev-physiol-021014-071622
46. Kazbanov IV, ten Tusscher KH, Panfilov AV. Effects of heterogeneous diffuse fibrosis on arrhythmia dynamics and mechanism. *Sci Rep*. (2016) **6**:20835. doi: 10.1038/srep20835
47. Varela M, Colman MA, Hancox JC, Aslanidi OV. Atrial heterogeneity generates re-entrant substrate during atrial fibrillation and anti-arrhythmic drug action: mechanistic insights from canine atrial models. *PLoS Comput Biol.* (2016) **12**:e1005245. doi: 10.1371/journal.pcbi.1005245
48. Edwards AG, Grandi E, Hake JE, Patel S, Li P, Miyamoto S, et al. Nonequilibrium reactivation of Na+ current drives early afterdepolarizations in mouse ventricle. *Circ Arrhythm Electrophysiol.* (2014) **7**:1205–13. doi: 10.1161/circep.113.001666
49. Weiss JN, Karma A, Shiferaw Y, Chen PS, Garfinkel A, Qu Z. From pulsus to pulseless: the saga of cardiac alternans. *Circ Res.* (2006) **98**:1244–53. doi: 10.1161/01.RES.0000224540.97431.f0
50. Panfilov AV, Keener JP. Effects of high frequency stimulation on cardiac tissue with an inexcitable obstacle. *J Theor Biol.* (1993) **163**:439–48. doi: 10.1006/jtbi.1993.1129
51. Spector PS, Habel N, Sobel BE, Bates JH. Emergence of complex behavior: an interactive model of cardiac excitation provides a powerful tool for understanding electric propagation. *Circ Arrhythm Electrophysiol.* (2011) **4**:586–91. doi: 10.1161/circep.110.961524
52. Dawson SP, Keizer J, Pearson JE. Fire-diffuse-fire model of dynamics of intracellular calcium waves. *Proc Natl Acad Sci USA*. (1999) **96**:6060–3.
53. Izu LT, Wier WG, Balke CW. Evolution of cardiac calcium waves from stochastic calcium sparks. *Biophys J.* (2001) **80**:103–20. doi: 10.1016/s0006-3495(01)75998-x
54. Franzini-Armstrong C, Protasi F, Ramesh V. Shape, size, and distribution of Ca2+ release units and couplons in skeletal and cardiac muscles. *Biophys J.* (1999) **77**:1528–39. doi: 10.1016/S0006-3495(99)77000-1
55. Soeller C, Crossman D, Gilbert R, Cannell MB. Analysis of ryanodine receptor clusters in rat and human cardiac myocytes. *Proc Natl Acad Sci. USA.* (2007) **104**:14958–63. doi: 10.1073/pnas.0703016104
56. Baddeley D, Jayasinghe ID, Lam L, Rossberger S, Cannell MB, Soeller C. Optical single-channel resolution imaging of the ryanodine receptor distribution in rat cardiac myocytes. *Proc Natl Acad Sci. USA.* (2009) **106**:22275–80. doi: 10.1073/pnas.0908971106
57. Soeller C, Jayasinghe ID, Li P, Holden AV, Cannell MB. Three-dimensional high-resolution imaging of cardiac proteins to construct models of intracellular Ca2+ signalling in rat ventricular myocytes. *Exp Physiol.* (2009) **94**:496–508. doi: 10.1113/expphysiol.2008.043976
58. Galice S, Xie Y, Yang Y, Sato D, Bers DM. Size matters: ryanodine receptor cluster size affects arrhythmogenic sarcoplasmic reticulum calcium release. *J Am Heart Assoc.* (2018) **7**:e008724. doi: 10.1161/jaha.118.008724
59. Sobie EA, Dilly KW, dos Santos Cruz J, Lederer WJ, Jafri MS. Termination of cardiac Ca(2+) sparks: an investigative mathematical model of calcium-induced calcium release. *Biophys J.* (2002) **83**:59–78. doi: 10.1016/S0006-3495(02)75149-7

Conflict of Interest Statement: The authors declare that the research was conducted in the absence of any commercial or financial relationships that could be construed as a potential conflict of interest.

frontiers in Physiology

ORIGINAL RESEARCH
published: 20 September 2018
doi: 10.3389/fphys.2018.01300

Investigation of the Syncytial Nature of Detrusor Smooth Muscle as a Determinant of Action Potential Shape

Shailesh Appukuttan[1†], *Mithun Padmakumar*[1†], *John S. Young*[2], *Keith L. Brain*[3,4] *and Rohit Manchanda*[1*]

[1] Computational Neurophysiology Lab, Department of Biosciences and Bioengineering, Indian Institute of Technology Bombay, Mumbai, India, [2] School of Pharmacy and Biomedical Sciences, University of Portsmouth, Portsmouth, United Kingdom, [3] Institute of Clinical Sciences, College of Medical and Dental Sciences, University of Birmingham, Birmingham, United Kingdom, [4] Christ Church, University of Oxford, Oxford, United Kingdom

OPEN ACCESS

Edited by:
S. Sridhar,
Robert Bosch Centre for Cyber-Physical Systems, Indian Institute of Science, India

Reviewed by:
Nick Spencer,
Flinders University, Australia
Satish S. Nair,
University of Missouri, United States

***Correspondence:**
Rohit Manchanda
rmanch@iitb.ac.in

[†]These authors have contributed equally to this work

Specialty section:
This article was submitted to Biophysics, a section of the journal Frontiers in Physiology

Received: 29 May 2018
Accepted: 29 August 2018
Published: 20 September 2018

Citation:
Appukuttan S, Padmakumar M, Young JS, Brain KL and Manchanda R (2018) Investigation of the Syncytial Nature of Detrusor Smooth Muscle as a Determinant of Action Potential Shape. Front. Physiol. 9:1300. doi: 10.3389/fphys.2018.01300

Unlike most excitable cells, certain syncytial smooth muscle cells are known to exhibit spontaneous action potentials of varying shapes and sizes. These differences in shape are observed even in electrophysiological recordings obtained from a single cell. The origin and physiological relevance of this phenomenon are currently unclear. The study presented here aims to test the hypothesis that the syncytial nature of the detrusor smooth muscle tissue contributes to the variations in the action potential profile by influencing the superposition of the passive and active signals. Data extracted from experimental recordings have been compared with those obtained through simulations. The feature correlation studies on action potentials obtained from the experimental recordings suggest the underlying presence of passive signals, called spontaneous excitatory junction potentials (sEJPs). Through simulations, we are able to demonstrate that the syncytial organization of the cells, and the variable superposition of the sEJPs with the "native action potential", contribute to the diversity in the action potential profiles exhibited. It could also be inferred that the fraction of the propagated action potentials is very low in the detrusor. It is proposed that objective measurements of spontaneous action potential profiles can lead to a better understanding of bladder physiology and pathology.

Keywords: urinary bladder, smooth muscle, detrusor, syncytium, action potential shape, feature correlation, neuron model

1. INTRODUCTION

Excitable cells exhibit a variety of action potential (AP) shapes but, generally, individual cells from the same tissue, or region of tissue, tend to display a common AP shape, characteristic of that cell type. The smooth muscle layer of the urinary bladder wall (detrusor) contrasts in this regard; it is found to exhibit APs of widely varying temporal profiles (Meng et al., 2008). Remarkably, these variations in AP shapes are observed even in electrophysiological recordings obtained from a single cell. The physiological basis for this diversity is currently not understood, and calls for a deeper analysis, as it could pave the way toward a better understanding of bladder

electrophysiology and its contribution to downstream events, e.g., Ca^{2+} dynamics and contraction. Intuitively, there could be only two possibilities for obtaining APs of different profiles: (i) multiple AP generation mechanisms, i.e., differences in ion channel compositions between cells, or (ii) a single AP generation mechanism with variable modulation due to factors linked to syncytial function, including innervation. A preliminary study demonstrated the origin of different AP shapes from a single basic underlying mechanism (Appukuttan et al., 2015a).

Generally, the focus of investigation when analyzing APs principally lies in the frequency of spiking, and the characteristics of the individual APs are often overlooked. Both are emergent properties of the tissue depending upon a wide range of parameters and mechanisms, and in the case of detrusor smooth muscle (DSM), also involving the complex cellular environment. Changes in the underlying factors could potentially result in pathology such as the overactive bladder (Fry et al., 2002). Though analysis of AP frequency could assist in identifying abnormalities arising in pathology, we believe that the individual AP features potentially offer greater insight into changes in any of the underlying factors, such as ionic mechanisms and syncytial interactions.

Prior studies have shown that the DSM cells are electrically coupled to one another via low-resistance electrical pathways formed by gap junctions, thereby resulting in a three-dimensional electrical syncytium (Fry et al., 2004). This implies that the electrical activity recorded from a particular cell in the syncytium need not necessarily have been initiated in that cell, but may have originated at any other cell within its electrical "reach". This also entails that the response of the cell is determined not just by the biophysical properties of that particular cell, but also by the properties and location of other cells in the syncytium. Past studies have demonstrated that the excitability of individually identical cells differ based on the size of the syncytium, their location within it, and the extent of gap junctional coupling between neighboring cells (Appukuttan et al., 2017a). Further, the electrical syncytium itself can be partitioned into sub-syncytia, representing smaller muscle bundles that are internally well-coupled, whereas coupling between bundles is comparatively poor, as reported for the detrusor (Bramich and Brading, 1996) and colonic smooth muscle (Spencer et al., 2002). The pattern of innervation further complicates the biophysical setting. In the case of the detrusor, a single nerve terminal could innervate multiple DSM cells and each DSM cell could potentially receive inputs from multiple nerve terminals, resulting in a complex many-to-many mapping between muscle and nerve. These considerations make the interpretation of DSM electrophysiological signals problematic.

In view of the above, a computational approach might assist in unraveling how DSM action potential profiles are determined. We employed a previously established passive model of the detrusor, developed using the compartmental modeling technique (Appukuttan et al., 2015b), and incorporated an identical action potential generation mechanism in each DSM cell in order to study the initiation, propagation, and modulation of AP shapes in the detrusor. The detrusor has not been found to follow any single AP template, and the DSM cells are known to possess an array of nine or more active channels contributing to their generation (Brading, 2006; Steers and Tuttle, 2009; Brading and Brain, 2011; Petkov, 2011). Models for the detrusor specific AP that satisfactorily emulate this ensemble of ion channels are yet to be developed. The purpose of the present study has been to obtain a better understanding of their syncytial nature and gather insights into their role toward the diversity in AP shapes. It was deemed appropriate to employ a "standard" AP shape for such an investigation so as to delineate the contributions arising from the syncytial organization of the cells. The classical Hodgkin-Huxley (HH) model, being a well–understood AP model, was therefore employed to explore this computationally.

The urinary bladder regulates both the storage and voiding of urine. Localized contractions help the bladder maintain tone during the storage phase as the bladder increases in volume with the accumulation of urine (Drake et al., 2003; Andersson, 2010, 2011). Whereas, coordinated contractions along the bladder wall, along with relaxation of the urethra, result in emptying the bladder during the voiding phase. Experimental studies in the past have suggested that spontaneous spiking of the cells causes the localized contractions, while the coordinated contractions are the concerted outcome of nerve-evoked APs (Andersson, 2011). Overactive bladder is an example of bladder pathology, more prevalent amongst the elderly population, which severely debilitates the affected. It is characterized by a frequent urge to urinate, with often an inability to control the urge, thereby hampering lifestyle (Milsom et al., 2001; Chapple et al., 2005). The etiology is often associated with detrusor overactivity wherein the detrusor undergoes unsolicited contractions arising from aberrant spiking. We believe that the undesirable spread of originally localized contractions, via the propagation of spontaneous APs owing to changes in the underlying syncytial features, could play an important role under such pathlogical conditions.

The detrusor is known to exhibit spontaneously occurring action potentials (Meng et al., 2008). The spontaneity of the action potentials is believed to have both a myogenic and neurogenic origin. While non-smooth muscle pace-making cells, such as Interstitial Cells (ICs), present in the urinary bladder wall are reported to be responsible for myogenic APs (McCloskey and Gurney, 2002; Hashitani et al., 2004; Kubota et al., 2006; Shen et al., 2008), the spontaneous asynchronous release of neurotransmitter packets from the nerve terminals causes the neurogenic APs (Young et al., 2008). These monoquantal events are termed as spontaneous excitatory junction potentials (sEJPs) as they are not elicited by an AP on the presynaptic nerve terminal. This is evidenced by the inability to abolish them using TTX, a blocker of Na^{+} channels (Young et al., 2008). This is in contrast to excitatory junction potentials (EJPs) which involve the synchronous release of neurotransmitter packets from the nerve terminals following presynaptic activation, and are thereby affected by TTX. These underlying differences translate to differences in the evoked postsynaptic potentials, with the sEJPs reflecting very rapid spatial and temporal decays in comparison to EJPs (Tomita, 1967; Appukuttan et al., 2015b). It is pertinent to highlight that the above does not hold true for sEJPs in the intestinal smooth muscle, which differ from other

autonomic neuromuscular junctions via their sensitivity to TTX, wider spatial spread and being produced from the synchronous activation of a population of enteric motor neurons (Spencer et al., 2001).

We have in the past proposed that the diversity in AP profiles arises predominantly from varying levels of superposition of a more or less stereotypical "native" AP with a second more variable component. The latter being contributed by junction potentials with a broad range of amplitudes and dynamics (Padmakumar et al., 2012), as illustrated in **Figure 1**. A similar observation was made earlier in skeletal muscles by Fatt and Katz (1951). They have shown that the shape of an AP changes when it propagates away from the site of initiation (see section 4), with the foot of the action potential notably changing from convex-upwards to concave-upwards. As smooth muscle cells form electrical syncytia, it is probable that an AP generated at one cell could assume different shapes as it propagates to other cells. In the present work, we test this hypothesis by comparing results obtained from experiments and simulations. Accordingly, the focus of this study has been restricted to the subset of APs with a neurogenic basis. It is pertinent to emphasize that the aim of the work presented here is to demonstrate that syncytial interactions can be an important factor for AP diversity, and that some potential insights could be availed by analyzing the individual AP profiles. We do not seek to dismiss other possible factors leading to AP diversity, such as variations in ionic channel compositions and/or other mechanisms. This study is particularly important in view of the diversity in AP profiles observed even from a single cell during a continuous recording, without external interventions.

2. METHODS

2.1. Electrophysiological Recordings

Mice of the C57BL/6 strain, of either gender, weighing 18–30 g, were sacrificed by head concussion followed by cervical dislocation. Efforts were undertaken to minimize the number of animals used and their suffering. After removing the urinary bladder, the connective tissue surrounding the bladder was withdrawn, while the urothelium was left intact. The ventral wall of the bladder was opened longitudinally from the neck (posterior) to the top of the dome (anterior). Tissue strips, containing a few bundles of smooth muscle, 3–4 mm long and 1–2 mm wide, were cut. Strips were pinned out on a Sylgard-lined plate at the bottom of a shallow chamber (volume, approximately 1 ml), which was mounted on the stage of an upright microscope. Preparations were superfused with warmed (35°C) physiological saline solution (PSS) (composition, mM: NaCl, 120; KCl, 5.9; $MgCl_2$, 1.2; $CaCl_2$ 2.5; $NaHCO_3$, 15.5; NaH_2PO_4, 1.2 and glucose, 11.5; gassed with 95% O_2 and 5% CO_2) at a constant flow rate (100 ml/h), maintaining a pH of 7.2–7.3 (Hashitani and Brading, 2003)

Preparations, once pinned, were allowed to equilibrate for a minimum of 30 min before initiating electrophysiological recordings. Individual DSM cells in muscle bundles were impaled with glass capillary microelectrodes, filled with 0.5 M KCl (tip resistance, 100–300 MΩ). Changes in membrane potential were recorded using a high input impedance amplifier (Axoclamp-2B, Axon Instruments, Inc., Sunnyvale, CA, USA), digitized using PowerLab/4SP (ADInstruments, Chalgrove, UK) at either 1 or 4 kHz, and stored on computer for later analysis.

2.2. Model Development

A previously established three-dimensional passive model of smooth muscle syncytium (Appukuttan et al., 2015b) was adopted and extended for this study. Modeling was undertaken employing the compartmental modeling technique on the NEURON simulation environment (Carnevale and Hines, 2006). Development of the syncytial model primarily involved the following steps: (i) development of a template model for individual DSM cells, (ii) designing a gap junctional coupling mechanism to electrically connect two cells, and

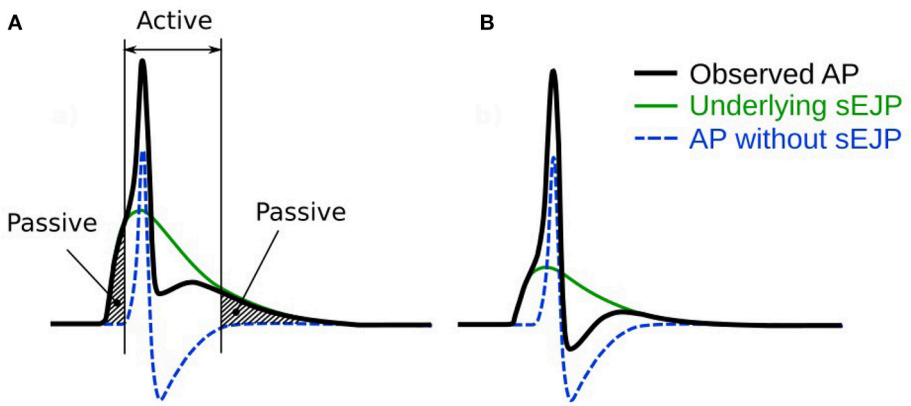

FIGURE 1 | An illustration of our hypothesis for the generation of APs. It is hypothesized that the convex-upward foot and the after-depolarization (ADP) are caused by the presence of an underlying spontaneous excitatory junction potential (sEJP, green curve) which initiates the AP (black curve). The dashed line represents the shape of the AP that would have been generated solely by the ion channel mechanisms if the underlying sEJP was absent. It can be observed that a larger underlying sEJP **(A)** would result in lowered foot convexity with a larger ADP and reduced AHP, compared to that of the APs with smaller underlying sEJP **(B)**. The passive and active regions of the AP are indicated in **(A)**.

(iii) building the syncytial topology by creating multiple cells using the template, positioning these in three-dimensional space, and coupling adjacent cells by means of the gap junction mechanism. **Table S1** summarizes the important model parameters. Individual detrusor smooth muscle cells are fusiform in shape, but were approximated to be cylindrical with a long and narrow profile: 200 μm in length and 6 μm in diameter (Fry et al., 1999; Appukuttan et al., 2015b). The number of compartments (segments) per cell was kept high (nseg = 51) to benefit from high spatial resolution within each cell, leading to each segment being <4 μm. Such a resolution permitted localized stimulation of individual cells.

The original syncytial model was purely passive, with the cells possessing no active ion channel mechanisms, and was used to investigate passive electrical properties of the DSM syncytium (Appukuttan et al., 2015b). As the present study aims to explore the diversity in AP profiles in syncytium, we augmented the syncytial model by endowing every DSM cell with the HH set of channels so as to enable the generation of action potentials. Adjacent cells were coupled by means of resistive pathways representing gap junctions which allowed bidirectional flow of current between the coupled cells. The magnitude and direction of gap junctional current was determined by the potential gradient between the coupled cells, and the extent of coupling. This is illustrated in **Figure S1A**. The gap junctional resistance, in the standard model, was kept as 30.6 MΩ (32.68 nS); but this has been varied in certain simulation settings and described accordingly. The cells were connected to form a cubic lattice arrangement of cells, thereby forming a three-dimensional syncytium (see **Figure S1B**). Under such a topology, each cell in the interior of the syncytium (i.e., non-peripheral) is electrically coupled to six other adjacent cells, two along each axis. Experimental findings have revealed functional syncytia to contain up to 100 cells (Neuhaus et al., 2002). To approximate this, the size of the syncytial model was set as 5-cube across all simulation scenarios, unless otherwise specified. Cells were stimulated by means of synaptic inputs, with the location of the stimulus being varied across the simulations. Synaptic activity was simulated by means of an AlphaSynapse in NEURON, which produces a localized conductance change in the membrane using an alpha function (Carnevale and Hines, 2006; Appukuttan et al., 2015b). The reversal potential of the synapse was kept at the default value of 0 mV. This injects inward current to the stimulated cell, except when the membrane potential overshoots 0 mV during an AP. The time constant of synaptic input was set to 10 ms, which is within the experimentally reported range of 5–89 ms (Young et al., 2008). We chose a value closer to the lower bounds in accordance with the shorter width of HH APs, thereby ensuring that an sEJP would not overly dominate the AP profile. Peak synaptic conductance, in the standard model, was adjusted to the minimal supra-threshold stimulus corresponding to the centroidal cell in the syncytium; the centroidal cell being the least excitable owing to its location. In certain simulation settings, the synaptic peak conductance was varied, and these changes have been highlighted wherever applicable.

2.3. Measurement of Correlation

Pearson's correlation coefficient (r) was evaluated to test the correlation between any two parameters of interest. In case of experimental recordings, the r-value was calculated for individual cells, and the confidence of the correlation trends are measured using Student's one sample t-test.

2.4. AP Features and Their Measurements

APs of a wide variety of shapes and sizes are discussed in the present study. It is imperative to quantifiably describe these AP profiles in order to distinguish and differentiate between them. To accomplish this, we follow the methodology adopted previously (Appukuttan et al., 2015a) of evaluating the following five features for each AP shape, as illustrated in **Figure 2**:

(i) *Height*: Maximum membrane depolarization (in mV) measured from the resting membrane potential (RMP) to the peak of the AP
(ii) *Width (Full Width at Half Maximum)*: Time (in ms) measured between the crossing of half the AP height across the rising and falling phases of the AP
(iii) *Convexity*: Provides a quantitative measure of the AP foot convexity; the foot of the AP being defined as the phase from the initiation of membrane depolarization to the AP threshold. The foot contributes in moving V_m from its resting level toward the threshold
(iv) *After-Hyperpolarization (AHP)*: Difference (in mV) measured between the RMP and the first local minimum following the AP peak
(v) *After-Depolarization (ADP)*: Difference (in mV) measured between the first local maximum following the AHP and the RMP

In a previous study, we have demonstrated that an appropriate technique to measure the AP foot convexity involves evaluation of the area enclosed between a pre-defined line and the AP foot (Appukuttan et al., 2017b). This technique is illustrated in **Figure 3**. The measure thus obtained is denoted as $C_{X,Y}$ indicating the measure of AP foot Convexity evaluated for a depolarization of Y mV over a time frame of X ms, where X and Y define the line. The values of X and Y for this study were selected in accordance with the requirements of this method (Appukuttan et al., 2017b). This approach has been shown to be more applicable over other methods such as evaluation of the radius of curvature along the AP curve.

3. RESULTS

Electrophysiological recordings from DSM cells demonstrated that important differences can be observed in the temporal profile of the individual APs. As illustrated in **Figure 4**, these variations include differences in their height, width, the shape of the AP foot and extent of hyperpolarization, and after-depolarization. The most common active signals observed in the DSM can very broadly be classified into two categories, as reported earlier (Meng et al., 2008; Hayase et al., 2009).

The first type has a fast rising phase ("spike-type") whereas the second type has a much slower ramp-like depolarization phase ("pacemaker-type"). For our study here, the action potentials of the pace-maker type were ignored as these are believed to originate from non-smooth muscle pace-making cells, perhaps the Interstitial Cells (ICs) (McCloskey and Gurney, 2002; Hashitani et al., 2004; Kubota et al., 2006; Shen et al., 2008). Our focus here lies in spontaneous action potentials of the spike-type—which is of neurogenic origin. Padmakumar et al. (2018) identified neurogenic and myogenic sAPs based on features evaluated from sAP profiles. For pooled data, they estimated that around 83% of the sAPs were of neurogenic origin. But the relative contributions from neurogenic and myogenic origins could vary significantly for individual cells.

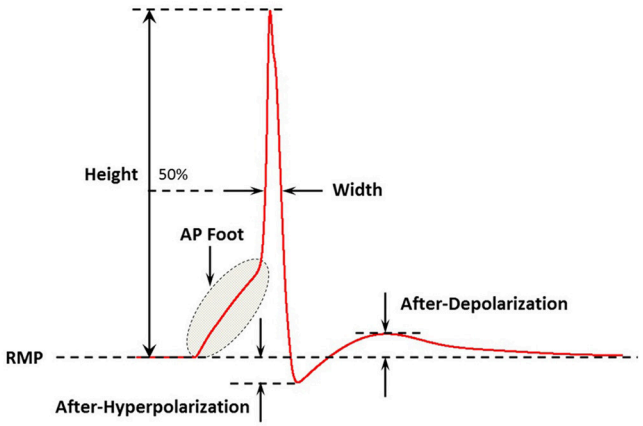

FIGURE 2 | A schematic figure showing the key features of the action potential profile which were used in the study. Adapted from Appukuttan et al. (2015a).

3.1. Analysis of Electrophysiological Recordings

After having removed APs of the pacemaker type from the analysis, recordings containing a minimum of 30 APs were shortlisted. APs contaminated by the interference of other independent APs or sEJPs were also removed from the study. This resulted in a collection of 11 cells from 6 animals with a total of 712 APs recorded in them. The overlapped plots of the APs in two of the cells are shown in **Figure 5**. Note the striking correlation of the foot and tail features of the two highlighted APs. The AP with a wider, more convex foot has a larger AHP and smaller ADP, and vice versa.

According to our hypothesis for diversity in AP shapes, every AP with a convex foot will have an underlying sEJP that elicited it (**Figure 1**). This underlying sEJP, via superposition, accounts for the observed profiles of the passive and active regions of the corresponding AP. As seen in **Figure 1**, the effect of sEJP would be present in the foot as well as in the tail. This implies that there should be a correlation between the features of the foot and tail of the AP.

The features, previously described in section 2.4, were determined for each of the APs. Once the features were obtained, the Pearson correlation coefficients between the features were calculated. Correlations were deemed statistically significant if the 99% confidence interval excluded zero. Strong correlations were found to exist between: (i) Height and Width (-0.63 ± 0.29; $P < 0.01$), (ii) Convexity and AHP (0.74 ± 0.08; $P < 0.01$), (iii) Convexity and ADP (-0.63 ± 0.16; $P < 0.01$), and (iv) AHP and ADP (-0.77 ± 0.14; $P < 0.01$). These correlations for all the 11 cells are shown in **Table 1**.

The Inter-Event Interval (IEI) histogram was computed for the collection of APs from each of the cells. One such example is shown in **Figure 6**. For all 11 cells tested, the trend was not significantly different from a single exponential function (Kolmogorov–Smirnov test with $P > 0.05$ for each

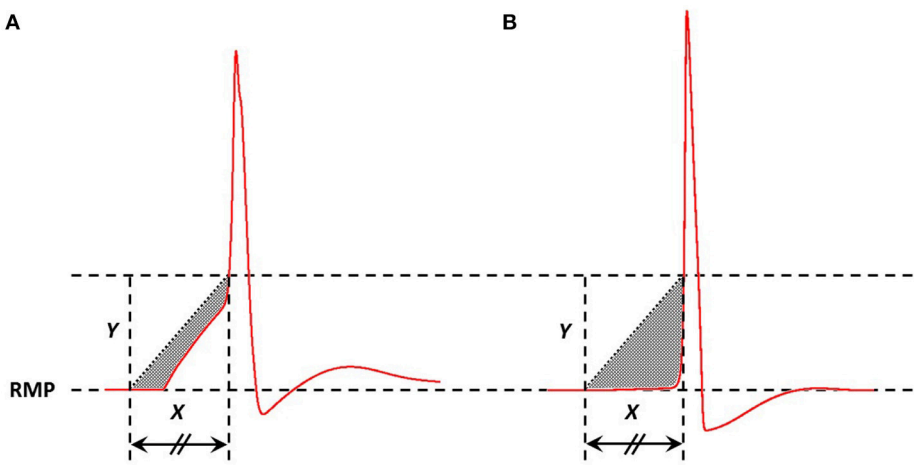

FIGURE 3 | Method adopted to quantify convexity of AP foot. The shaded area indicates the area between the AP curve and the straight line joining the two pre-defined points. Area below the straight line is considered as negative area and that above, if present, as positive (absent in above cases). Here, the signal in **(A)** has a greater value of convexity than that in **(B)**.

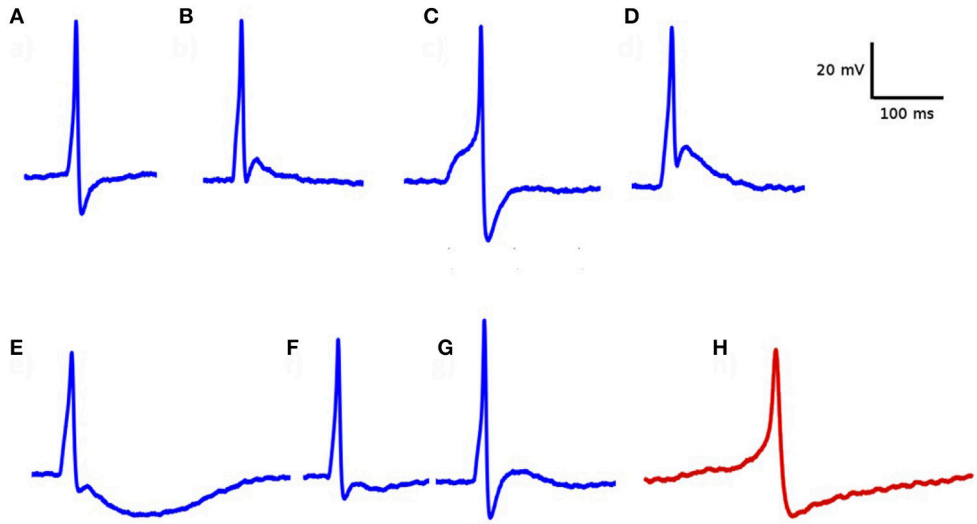

FIGURE 4 | Diversity in action potential shapes observed in detrusor smooth muscle. **(A–G)** action potentials recorded from a single detrusor smooth muscle cell. All of these have convex-upward feet, indicating that they are of neurogenic origin. **(H)** An example of "pace-maker" type action potential, given for comparison. Note the ramp-type foot and the lack of after-depolarization. These types of APs are believed to have a myogenic origin.

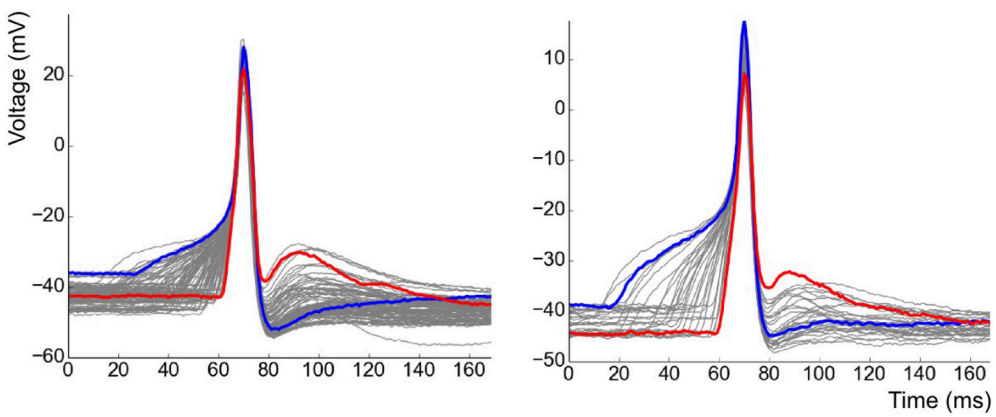

FIGURE 5 | Collection of all APs observed in two of the cells superimposed over one another. Examples of strongly contrasting shapes have been highlighted in each case.

cell), signifying that the APs are independent, stochastic events. The occurrence of any AP does not influence the occurrence or non-occurrence of others APs.

3.2. Analysis of AP Diversity in Simulation Studies

To analyze action potential shapes computationally using our model, we (i) stimulated the centroid cell in our syncytium and recorded the APs generated at each cell in the syncytium for different sizes of syncytium, and (ii) stimulated each cell in a 5-cube syncytium, one after another, and recorded the APs recorded at specific locations within the syncytium. This was an extension of the simulations undertaken previously (Appukuttan et al., 2015a), with a requirement for more detailed analysis. It was observed that APs of a variety of shapes and sizes were produced in the model, with an evident gradation from one type to another. **Figure 7** illustrates a few of these AP profiles recorded at different locations in the syncytium. The AP profiles were analyzed by quantifying the five features discussed in section 2.4. All five features were found to exhibit a notable spread across the ensemble of AP profiles. The AP height varied by over 35 mV (range: 68.2 to 105.4 mV) with APs recorded at the vertex cells being the largest, and reduction in the height when moving closer to the interior of the syncytium. The stimulated cells produced the APs with smallest heights, but with largest widths, as seen for cell A in **Figure 7** (pink trace). Also, only these cells, and to an extent their immediately neighboring cells, produced APs with convex AP feet. The majority of the cells in the syncytium exhibited a more "concave-upwards" rise to the AP peak, as has been reported previously (Appukuttan et al., 2017b). This

TABLE 1 | Correlations observed between the features measured from experimentally recorded data for 11 cells.

Cell No.	Height vs. Width	$C_{25,30}$ vs. AHP	$C_{25,30}$ vs. ADP	AHP vs. ADP
1	−0.54	0.81	−0.88	−0.95
2	−0.04	0.74	−0.75	−0.91
3	−0.62	0.70	−0.76	−0.89
4	−0.90	0.78	−0.64	−0.64
5	−0.78	0.83	−0.69	−0.75
6	−0.79	0.74	−0.46	−0.73
7	−0.86	0.86	−0.59	−0.62
8	−0.72	0.66	−0.75	−0.82
9	−0.80	0.63	−0.39	−0.51
10	−0.73	0.81	−0.57	−0.80
11	−0.13	0.63	−0.44	−0.83
Mean	−0.63	0.74	−0.63	−0.77
SD	0.29	0.08	0.16	0.14

The mean and standard deviation of the correlations are also shown.

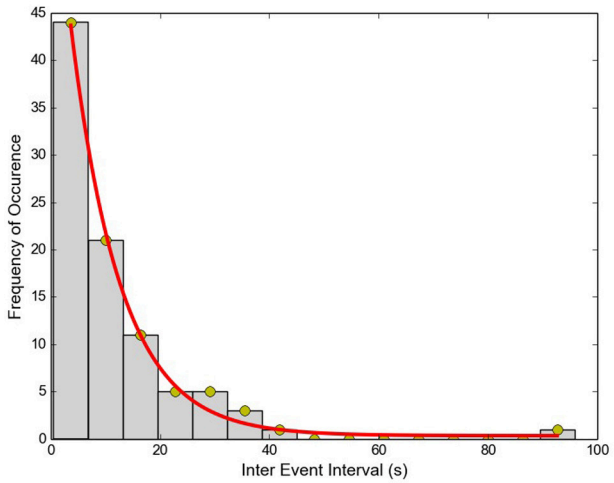

FIGURE 6 | Inter-Event interval histogram for APs recorded from a single cell. Red line shows the exponential fit to data ($R^2 = 0.99$).

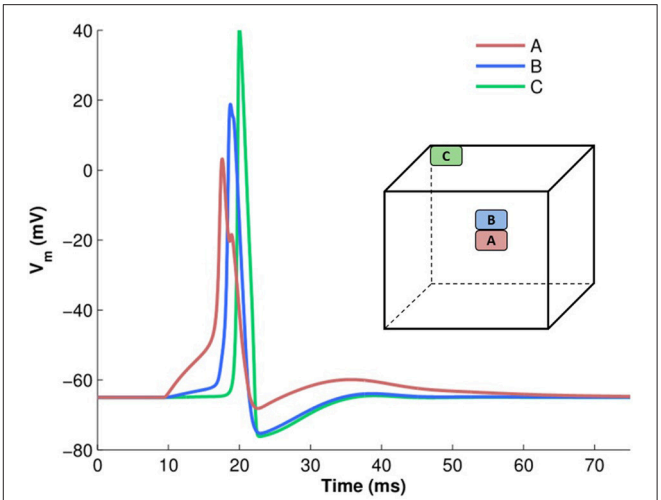

FIGURE 7 | Examples of variety in AP shapes observed in a 5-cube syncytium when stimulated at the centroid cell. The cube illustrates the location from where each recording is obtained. The APs have been aligned at the instant of AP initiation.

TABLE 2 | Correlation between AP features from simulations for syncytia of varying sizes, when stimulus is applied at the centroid cell and APs are recorded at every cell.

Correlation	Stimulated at centroid, Syncytium size:			
	3-Cube	5-Cube	7-Cube	15-Cube
Height vs. Width	−0.94	−0.92	−0.93	−0.93
$C_{25,10}$ vs. AHP	−0.93	−0.88	−0.89	−0.76
$C_{25,10}$ vs. ADP	0.96	0.91	0.90	0.85
AHP vs. ADP	−0.99	−1.00	−1.00	−0.95

TABLE 3 | Correlation between AP features from simulations for a syncytium of size 5-cube, when stimulus is applied successively at each cell and APs are recorded at specific locations.

Correlation	Stimulated at all cells, Recorded at:			
	Centroid	Surface	Edge	Vertex
Height vs. Width	−0.88	−0.94	−0.86	−0.83
$C_{25,10}$ vs. AHP	−0.88	−0.74	−0.69	−0.66
$C_{25,10}$ vs. ADP	0.92	0.79	0.74	0.7
AHP vs. ADP	−1.00	−1.00	−1.00	−1.00

is seen for cell C in **Figure 7** (green trace). The extent of after-hyperpolarization (AHP) and after-depolarization (ADP) also varied across the syncytium, depending on the syncytial location of the cell in which the AP was recorded. The stimulated cells, and its neighbors, produced APs with a lower level of AHP and a higher ADP, while the trend was opposite for the more distant cells.

From the above observations, it is discernible that the five AP features evaluated here share strong correlations. **Tables 2**, **3** summarize the correlation coefficients between the AP features under different settings. As expected from above, the AP height shares a strong negative correlation (−0.83 to −0.94) with the AP width. Similarly, a strong negative correlation (−0.95 to −1.00) exists between the extent of AHP and ADP. However, AP convexity shares a strong negative correlation (−0.66 to −0.93) with the extent of AHP, and a strong positive correlation (0.70 to 0.96) with the level of ADP.

It can be observed that the correlations obtained for Convexity vs. AHP and Convexity vs. ADP, are contrary to those evaluated from the experimental studies. Such a contradiction could stem from the lack of propagated APs in the bundled detrusor and the abundance of the same in the simulated undifferentiated syncytium. This was tested using another simulation setting, in which all the cells in the syncytium were stimulated successively

TABLE 4 | Correlation between AP features from simulations for syncytia of varying sizes, when stimulus is applied successively at each cell and APs are recorded only from the stimulated cells.

Correlation	Stimulated at all cells, Syncytium Size:			
	3-Cube	5-Cube	7-Cube	15-Cube
Height vs. Width	−1.00	−0.98	−0.99	−0.99
$C_{25,10}$ vs. AHP	0.81	0.73	0.67	0.65
$C_{25,10}$ vs. ADP	−0.95	−0.93	−0.94	−0.97
AHP vs. ADP	−0.90	−0.83	−0.75	−0.71

and only the APs elicited at the stimulated cells were recorded. This ensured that the propagated APs were eliminated from the analysis. The correlation values obtained from these simulations are tabulated in **Table 4**. It can be noted that the contradicting feature correlations, i.e., Convexity vs. AHP and Convexity vs. ADP, are now flipped, and match the correlation trends obtained from the experimental APs.

The above simulations indicated that when an underlying sEJP was present, the correlation of convexity and ADP was negative, while that of convexity and AHP was positive. These trends were flipped around in the case of propagated APs, which had no underlying sEJPs. The variation in the three features—convexity, AHP, and ADP—for different amplitudes of underlying sEJP are shown in **Figure 8**. The red traces show data for APs elicited at the centroid cell by a range of synaptic conductances. The green traces show data for APs elicited at a vertex cell, and subsequently propagated to the centroid cell in the presence of an underlying sEJP of varying synaptic conductance levels. As the correlation trends are opposite in these two cases, these can serve as indicators for determining the nature of the APs origin.

The observation of the discrepancies between the features of experimentally obtained and simulated APs indicate that the model does not accurately reflect the true biophysical environment. One aspect where the real detrusor syncytium and the computational model employed here could differ is the intensity of the gap junctional coupling between the cells. In order to investigate the effect of variations in gap-junction coupling on the correlation values between the AP features, another set of simulations were conducted.

In one such study, the strength of gap junctional conductance, G_{gap}, was varied in the range of 5–250 nS while maintaining the homogeneity of the syncytium. This range is a subset of the experimentally reported range of G_{gap} values. For each conductance level, all the cells in the syncytium were sequentially stimulated via synaptic input of sufficiently large intensity so as to elicit an AP at every cell in the syncytium, for all values of G_{gap} in the range. Thus, the stimulus intensity was maintained constant throughout this set of simulations. For each value of G_{gap}, the features of the APs observed at specific locations of the syncytium were evaluated and their correlation coefficients were determined. The plots of the correlation coefficients obtained for each of the G_{gap} values are given in **Figure 9**. It can be observed from the figure that the panels AHP vs. ADP and Height vs. Width shows strong correlations throughout the range of G_{gap} values whereas the panels involving convexity ($C_{X,Y}$ vs. AHP; $C_{X,Y}$ vs. ADP) show significant variations in correlation values, even displaying a reversal of the sign of correlation coefficient for very low values of G_{gap}.

Another study involving a heterogeneous variation in the gap junction coupling is described in the **section S2** of the supplementary document. A summary of all simulation experiments conducted in this work is tabulated in **Table 5**.

4. DISCUSSION

In the current study we have restricted our focus to spontaneous action potentials. The origin of these signals is still open to debate. Previous studies have indicated that most of the APs observed under resting conditions are driven by sEJPs (Young et al., 2008). However, there are other studies which suggest a myogenic origin for these signals (Hashitani and Brading, 2003). Our understanding is that regular/periodic action potential firing is likely to be myogenic in origin, perhaps generated by pacemaking cells electrically coupled to the smooth muscle cells, whereas asynchronous/stochastic action potential firing may be driven by spatio-temporally random ATP release from autonomic nerve terminals. Studies excluding the possibility of a neural basis for these signals tested the effects of drugs such as tetrodotoxin and atropine, and found that the signals were not inhibited (Hashitani et al., 2001). Tetrodotoxin inhibits nerve AP-based, but not spontaneous, neurotransmitter release and atropine blocks the ACh receptors on the post-synaptic side. As the varicosities in the detrusor co-transmit both ATP and ACh, it is possible that the spontaneous release of neurotransmitters, evidenced by the presence of sEJPs, is responsible for eliciting the spontaneous action potentials.

Action potentials are commonly referred to as all-or-none signals as they are found to propagate without any change in amplitude or shape, setting them apart from graded potentials such as junction potentials and electrotonic potentials. But this does not always hold true, and fails under certain conditions. It is reported that in long continuous axons or muscle fibers, differences are observed in the AP profiles when recorded at varying distances from the site of initiation (Fatt and Katz, 1951). They also demonstrated that with increase in the distance from the site of stimulus (i.e., the end-plate), the height of the AP increased and the AP foot progressively transformed from being convex-upwards to concave-upwards. Also, at recordings taken closer to the end-plate, a "hump" is seen following the peak indicating the underlying end plate potential (EPP; skeletal muscle equivalent of sEJP) due to the continued action of the neurotransmitter.

The AP, though considered an active signal generated by the membrane, has passive components as well. The part of the AP starting from the instant at which the membrane voltage reaches threshold, to the end of the repolarization phase is mostly governed by the properties of the active ion channels present in the cell membrane. However, the rest of the AP, namely the foot and the end of the tail—shown by the shaded regions in **Figure 1A**—are predominantly influenced by the passive

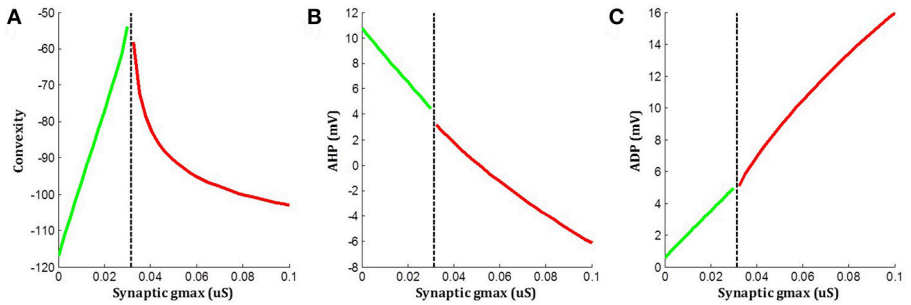

FIGURE 8 | Variations in **(A)** convexity, **(B)** AHP, and **(C)** ADP with change in underlying sEJP. Red traces show data for APs elicited at the centroid cell by a range of synaptic conductances. Green traces show data for APs propagated to the centroid cell in the presence of an underlying sEJP of varying synaptic conductances. The maximum and minimum value of synaptic conductance for the green and red traces, respectively, corresponds to the minimum conductance required for eliciting an AP at the centroid cell.

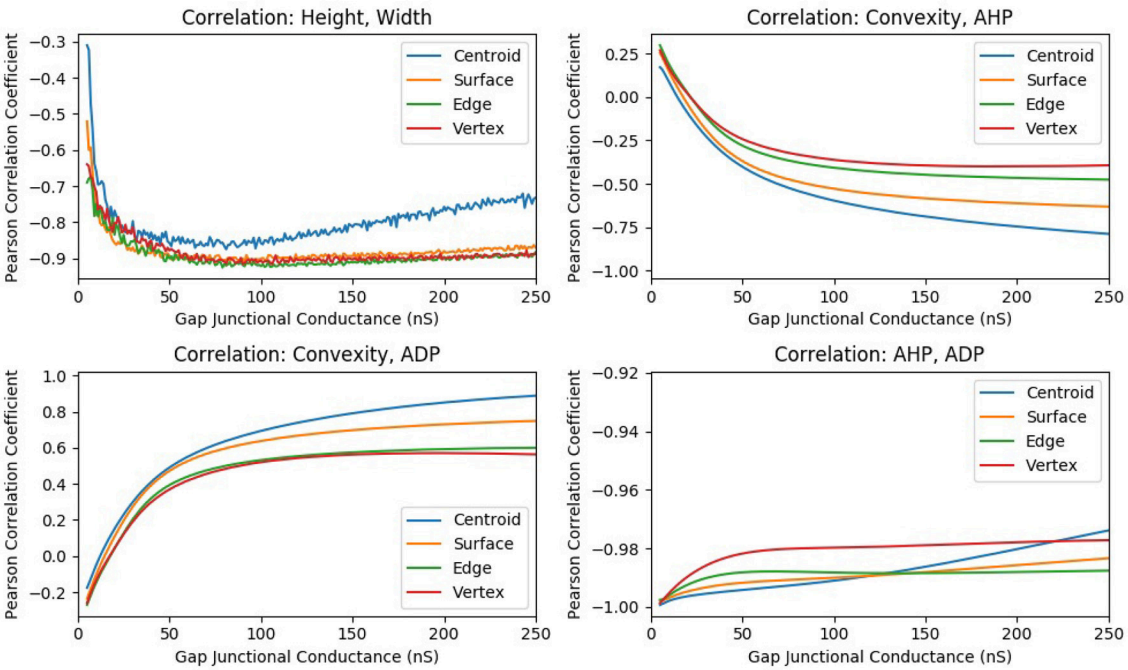

FIGURE 9 | The change in correlation coefficient between various parameters with respect to the gap junction coupling between the smooth muscle cells in the syncytium. The intensity of suprathreshold stimulus was maintained constant across all simulations.

properties of the cell membrane. Our hypothesis predicts strong correlations between the Convexity, AHP, and ADP of the APs. From **Figure 1**, it can be observed that the taller the underlying sEJP, the smaller the convexity. A tall sEJP would result in a more depolarized AP tail as it has a more lasting influence. This results in a positive correlation between convexity and AHP. The ADP, according to the hypothesis, is created by the underlying sEJP and would not be seen in the propagated APs. The ADP is measured in the direction opposite to AHP. Hence when the AP tail rises, the ADP increases and vice versa. So a negative correlation is expected between the convexity and the ADP and also between the AHP and ADP. The strong correlations obtained between convexity, AHP, and ADP from experimental recordings are in accordance with expectations. This strongly supports the hypothesis that there is an sEJP underlying these APs.

But in simulations using our computational model of the smooth muscle syncytium, a strong negative correlation was found between the convexity and AHP, and a strong positive correlation between convexity and ADP. This is caused by the fact that in the simulations, all the APs measured, except for the one at the site of stimulus, were propagated APs. As these have no underlying sEJP, the convexity would be low, with a concave upwards AP foot, while the AHP would be maximum—resulting in a negative correlation. In addition, these propagated signals would not exhibit an ADP. Such propagated APs were

not frequently observed in our experimental recordings. As explained below and backed by experimental findings, this could be attributed to the pattern of innervation and the size of the syncytium containing the recorded cell. Thus, the nature of correlations between the convexity and ADP/AHP is able to provide an indication of the nature of the APs—whether propagated, or originated at the recorded cell (or in close proximity to it).

Our interpretation is that all the APs observed in the experimental recordings are either locally generated within the cell, by neurotransmitter release from a nearby varicosity, or propagated to it from such a cell in very close vicinity. This release of neurotransmitter would not be nerve-evoked, but arise from the asynchronous release of neurotransmitter packets from the nerve terminals. This random nature of occurrence of APs is confirmed by the exponential trend of the Inter-Event Interval (IEI) histogram. If such is the case, then to explain the wide variety of shapes observed from the intracellular recordings, and their high frequency of occurrence, it is expected that the cells are densely innervated. Studies have shown that the detrusor tissue is densely innervated (Gabella, 1995; Drake et al., 2000, 2003), with around 3 to 4 varicosities per cell (Daniel et al., 1983), consistent with this idea. To verify the experimental correlation trends computationally, we modified the simulation analysis to only include APs recorded at the site of stimulus. Every cell in the syncytium was successively stimulated and the APs elicited at these cells were recorded. It was found that the correlation trends for convexity with AHP and ADP now flipped to match those observed experimentally, with the other correlation trends remaining similar. For example, in a syncytium of size 5-cube, convexity and AHP had a positive correlation of 0.73, while convexity and ADP had a negative correlation of −0.93 (**Table 4**).

Also, passive signals decay quickly with distance, and thus they cannot be recorded in distant cells. The sEJPs can be detected only at cells in the immediate vicinity, as reported in our earlier work (Appukuttan et al., 2015b). Therefore, in smaller sized syncytia it is likely that the AP recorded at each cell would be influenced by the passively propagated sEJP to varying extents, whereas in larger syncytia the majority of the cells would be unaffected by the sEJP and exhibit a purely propagated AP. This is exemplified in **Table 2** where we can see that the correlation of convexity with AHP and ADP deteriorate with increasing size of the simulated syncytium. In the case of the detrusor, experimental studies suggest that the bundles are quite small in size (Hashitani et al., 2001; Neuhaus et al., 2002). Hence it is expected that there is a lack of propagated APs, characterized by their low convexity and high AHP, in the experimental recordings. Correspondingly, in pathology characterized by stronger coupling (Mills et al., 2000) and thus greater electrical reach, there is a likelihood to observe a greater proportion of APs with concave-upwards foot, analogous to propagated APs.

A strong negative correlation exists between the AP height and width. This is also observed in the simulation studies, with the APs having smaller height recorded closer to the site of stimulation. Several factors may contribute to this trend. The site of initiation has to depolarize a larger volume, as every other cell connected to it is at rest, and hence undergoes rapid charge dissipation, resulting in a slower rate of depolarization and a much reduced AP height. This may be further accentuated by the fact that an increased latency in attaining its threshold will result in the inactivation and activation of a higher fraction of Na^+/Ca^{2+} and K^+ channels, respectively. In addition, the synaptic conductance at the stimulated cell acts as a shunting pathway, resulting in a lowered input resistance and thereby reduced membrane potential (Fatt and Katz, 1951).

With the help of above inferences, it is now potentially feasible to characterize the cell environment by evaluating the sAP profile. For example, large amplitudes suggest that the cell is located near the periphery of the DSM bundle, whereas smaller amplitudes are indicators of being located near the center and being well connected with the neighboring cells. Presence of ADP along with foot convexity would indicate that the cell receives neurotransmitter input from a nearby varicosity. On the contrary, if the sAP does not exhibit foot convexity and ADP, it implies that the cell exhibits a propagating sAP, which in turn reveals that the cell is part of a larger bundle and being well-coupled to the neighboring cells. From the width of the stimulus evoked sAP, the gap junction connectivity can be estimated. Cells well-coupled to neighboring cells would exhibit sAPs having a larger width, and vice versa. The above are

TABLE 5 | Summary of the various simulation scenarios employed.

Table 2	*Varied parameter:*	Size of the syncytium
	Stimulated at:	Centroidal cell
	Recorded from:	All cells
	Data analysis:	Collated by syncytial size
	Number of sims:	4; one per syncytial size
Table 3	*Varied parameter:*	Recording site
	Stimulated at:	Each cell; one at a time
	Recorded from:	Specific locations
	Data analysis:	Collated by location
	Number of sims:	125; one per stimulated cell
Table 4	*Varied parameter:*	Recording site, Size of the syncytium
	Stimulated at:	Each cell; one at a time
	Recorded from:	Stimulated cell
	Data analysis:	Collated by syncytial size
	Number of sims:	3870; one per stimulated cell per syncytial size
Figure 9	*Varied parameter:*	Strength of gap junctional coupling
	Stimulated at:	Each cell; one at a time
	Recorded from:	Specific locations
	Data analysis:	Collated by location per coupling strength
	Number of sims:	30750: one per stimulated cell per coupling strength
Table S1	*Varied parameter:*	Number of coupled cells
	Stimulated at:	Each cell; one at a time
	Recorded from:	Stimulated cell
	Data analysis:	Collated by configuration of coupled cells
	Number of sims:	750; one per simulated cell per coupling configuration

preliminary interpretations, and would need to be further refined following enhancements to the model as proposed ahead.

The simulation studies involving modification of gap junctional conductance of the computational model helped reinforce our reasoning for the observed discrepancy between the correlation trends observed in the experimental and simulation studies. This is elaborated further in **section S3** of the supplementary document. One of the objectives of exploring a wide range of values is to explore the effect of variations in such parameters over a wide range of biologically plausible settings in order to study the effects on bladder functioning both in physiology and disease. The range of gap junctional coupling values explored here cover a broad range of experimentally reported values. Christ et al. (2003) have reported a range between 5 and 20 nS for the rat bladder. Other studies have reported intercellular coupling strengths in biological tissues to be as high as 250 ns (Maurer and Weingart, 1987; Lin and Veenstra, 2004), and even higher (Kameyama, 1983). It may be inferred from the simulations that the non-monotonic variation of the convexity parameter with respect to the amplitude of the underlying sEJP causes a reversal of correlation values. This indicates that the "convexity" parameter, on its own, may not be an accurate indicator for the underlying sEJP amplitude.

4.1. Limitations of the Study

While the results presented here reinforce our hypothesis for the AP generation mechanism, and is capable of explaining several of the observed AP shapes (**Figure 4**), however, we believe that other factors and mechanisms could also be involved in influencing AP shapes, such as the pacemaker type AP (**Figure 4H**) and APs with a prolonged after-hyperpolarization phase (**Figure 4E**). It is therefore relevant to reiterate here that we do not seek to dismiss other possible factors as contributing to AP diversity, such as variations in ionic channel compositions and/or other mechanisms.

As stated earlier, we have opted for a simpler and well-understood AP model in the current study. The HH model employed here basically considers two ionic species (Na^+ and K^+) and defines a voltage-gated channel mechanism for each. It should be borne in mind that the detrusor smooth muscle system involves several ionic species with a wide ensemble of ionic channels. These include both voltage-gated (e.g., L-type Ca^{2+}, T-type Ca^{2+}) as well as ligand-gated (e.g., Ca^{2+} activated BK, IK, SK) channels. Moreover, the intracellular Ca^{2+} dynamics holds potential to exert a consequential influence over the functioning of these channels. Thus, there potentially exists an even larger scope for diversity in the AP profiles observed in the detrusor.

4.2. Extensions to the Model

With our current level of understanding, we believe it is inconceivable to predict the relative contributions of the various factors toward the observed AP profile. We believe it is necessary to reduce these down into simpler intelligible units and identify their individual contributions, before attempting to explore the interplay between the various mechanisms. The present study sheds light on one such mechanism, namely the syncytial nature of the detrusor smooth muscle.

The ensemble of ion channels and associated calcium dynamics appropriate to reproduce the detrusor AP is another such mechanism. Such a model has not yet been satisfactorily developed. In the past, a model for uterine smooth muscle AP has been reported (Tong et al., 2011) by demonstrating its electrical response in a single cell environment. Some of us are currently involved in developing a similar detrusor specific AP model, which when embedded in the current syncytial model would render it biologically more accurate.

The current model could be further elaborated by endowing it with spatial heterogeneity. Such heterogeneity is known to exist physiologically, as evidenced by the presence of smooth muscle bundles (Brading, 1997), and varying degrees of electrical connectivity between cells (Bramich and Brading, 1996). Certain outcomes of heterogeneous coupling within the syncytium have been presented in the supplementary document (**section S2**). The existence of cell bundles that differ in size constitutes another source of heterogeneity. Variations of such nature can be relatively easily accommodated in the syncytial model employed here, with the capacity to closely evaluate the outcomes, but this requires awaiting the availability of relevant experimental data indicating such heterogeneity.

4.3. Conclusion

Our study has demonstrated that a homogeneous syncytium consisting of smooth muscle cells with identical membrane properties can produce APs of varying shapes. The variations in AP features obtained through simulations were similar in nature to those observed in the experimental APs. Closer examination of the differences between the experimental and simulated AP features and their correlations provided insight into the biophysical environment of the detrusor syncytium, such as the size of the bundles, the density of innervation, and the strength of gap junction coupling between cells. It could also be inferred that the fraction of the propagated action potentials is very low in the detrusor.

The work presented here provides a different approach to exploring the properties of a smooth muscle syncytium. In view of the diversity in AP profiles observed even from a single cell, the findings reported here hold much significance. Since it has now been demonstrated that the variations in AP shapes observed in the syncytium are influenced by syncytial properties, one can analyze the intracellular recordings from individual cells and potentially infer the syncytial environment in which that cell is located. By classifying the cells based on the variations displayed in their electrical activities, an understanding of different aspects of the syncytium could be obtained. Further, this mapping between the AP shape and the syncytial properties could also be used to delineate the syncytial changes during disease and provide a better understanding of pathological conditions.

ETHICS STATEMENT

The Institutional Animal Care and Use Committee (IACUC) covering the Department of Pharmacology, University of Oxford,

approved and had oversight of all animal experiments. All experiments were carried out during or before 2009, and were hence approved under Animals (Scientific Procedures) Act 1986, but are also consistent with both UK Animals (Scientific Procedures) Act (2013) and European Communities Council Directive 2010/63/EU.

AUTHOR CONTRIBUTIONS

SA designed the computational studies, performed the simulations, and wrote the first draft of the manuscript. MP designed the analysis of experimental data, carried out the statistical analysis, and contributed in writing the manuscript. JY and KB performed the electrophysiological recordings and helped revise the manuscript. RM contributed toward the interpretation of the results and in revising the manuscript.

FUNDING

The work was supported by grants from the Department of Biotechnology (DBT), India (BT/PR12973/MED/122/47/2016), and the UKIERI (UKUTP20110055).

SUPPLEMENTARY MATERIAL

The Supplementary Material for this article can be found online at: https://www.frontiersin.org/articles/10.3389/fphys.2018.01300/full#supplementary-material

REFERENCES

Andersson, K.-E. (2010). Detrusor myocyte activity and afferent signaling. *Neurourol. Urodyn.* 29, 97–106. doi: 10.1002/nau.20784

Andersson, K.-E. (2011). Antimuscarinic mechanisms and the overactive detrusor: an update. *Eur. Urol.* 59, 377–386. doi: 10.1016/j.eururo.2010.11.040

Appukuttan, S., Brain, K., and Manchanda, R. (2015a). Syncytial basis for diversity in spike shapes and their propagation in detrusor smooth muscle. *Procedia Comput. Sci.* 51, 785–794. doi: 10.1016/j.procs.2015.05.199

Appukuttan, S., Brain, K. L., and Manchanda, R. (2015b). A computational model of urinary bladder smooth muscle syncytium. *J. Comput. Neurosci.* 38, 167–187. doi: 10.1007/s10827-014-0532-6

Appukuttan, S., Padmakumar, M., Brain, K., and Manchanda, R. (2017b). A method for the analysis of ap foot convexity: insights into smooth muscle biophysics. *Front. Bioeng. Biotechnol.* 5:64. doi: 10.3389/fbioe.2017.00064

Appukuttan, S., Brain, K., and Manchanda, R. (2017a). Investigation of action potential propagation in a syncytium. *Biomed. Res. J.* 4, 102–115.

Brading, A. (2006). Spontaneous activity of lower urinary tract smooth muscles: correlation between ion channels and tissue function. *J. Physiol.* 570, 13–22. doi: 10.1113/jphysiol.2005.097311

Brading, A. F. (1997). A myogenic basis for the overactive bladder. *Urology* 50, 57–67.

Brading, A. F. and Brain, K. L. (2011). "Ion channel modulators," in *Handbook of Experimental Pharmacology: Urinary Tract,* eds K.E. Andersson and M. C. Michel (Berlin; Heidelberg: Springer), 375–393. doi: 10.1007/978-3-642-16499-6_18

Bramich, N. J., and Brading, A. F. (1996). Electrical properties of smooth muscle in the guinea-pig urinary bladder. *J. Physiol.* 492(Pt 1), 185–198.

Carnevale, N. T., and Hines, M. L. (2006). *The NEURON Book*. Cambridge: Cambridge University Press.

Chapple, C. R., Artibani, W., Cardozo, L. D., Castro-Diaz, D., Craggs, M., Haab, F., et al. (2005). The role of urinary urgency and its measurement in the overactive bladder symptom syndrome: current concepts and future prospects. *BJU Int.* 95, 335–340. doi: 10.1111/j.1464-410X.2005.05294.x

Christ, G. J., Day, N. S., Day, M., Zhao, W., Persson, K., Pandita, R. K., et al. (2003). Increased connexin43-mediated intercellular communication in a rat model of bladder overactivity *in vivo*. *Am. J. Physiol.Regul. Integr. Comp. Physiol.* 284, R1241–R1248. doi: 10.1152/ajpregu.00030.2002

Daniel, E., Cowan, W., and Daniel, V. (1983). Structural bases for neural and myogenic control of human detrusor muscle. *Can. J. Physiol. Pharmacol.* 61, 1247–1273.

Drake, M. J., Hedlund, P., Harvey, I. J., Pandita, R. K., Andersson, K.-E., and Gillespie, J. I. (2003). Partial outlet obstruction enhances modular autonomous activity in the isolated rat bladder. *J. Urol.* 170, 276–279. doi: 10.1097/01.ju.0000069722.35137.e0

Drake, M. J., Hedlund, P., Mills, I. W., McCoy, R., McMurray, G., Gardner, B. P., et al. (2000). Structural and functional denervation of human detrusor after spinal cord injury. *Lab. Invest.* 80, 1491–1499. doi: 10.1038/labinvest.3780158

Fatt, P., and Katz, B. (1951). An analysis of the end-plate potential recorded with an intra-cellular electrode. *J. Physiol.* 115, 320–370.

Fry, C., Cooklin, M., Birns, J., and Mundy, A. (1999). Measurement of intercellular electrical coupling in guinea-pig detrusor smooth muscle. *J. Urol.* 161, 660–664.

Fry, C. H., Skennerton, D., Wood, D., and Wu, C. (2002). The cellular basis of contraction in human detrusor smooth muscle from patients with stable and unstable bladders. *Urology* 59, 3–12. doi: 10.1016/S0090-4295(01)01632-6

Fry, C. H., Sui, G.-P., Severs, N. J., and Wu, C. (2004). Spontaneous activity and electrical coupling in human detrusor smooth muscle: implications for detrusor overactivity? *Urology* 63, 3–10. doi: 10.1016/j.urology.2003.11.005

Gabella, G. (1995). The structural relations between nerve fibres and muscle cells in the urinary bladder of the rat. *J. Neurocytol.* 24, 159–187.

Hashitani, H. and Brading, A. F. (2003). Ionic basis for the regulation of spontaneous excitation in detrusor smooth muscle cells of the guinea-pig urinary bladder. *Br. J. Pharmacol.* 140, 159–169. doi: 10.1038/sj.bjp.0705320

Hashitani, H., Fukuta, H., Takano, H., Klemm, M. F., and Suzuki, H. (2001). Origin and propagation of spontaneous excitation in smooth muscle of the guinea-pig urinary bladder. *J. Physiol.* 530, 273–286. doi: 10.1111/j.1469-7793.2001.0273l.x

Hashitani, H., Yanai, Y., and Suzuki, H. (2004). Role of interstitial cells and gap junctions in the transmission of spontaneous Ca^{2+} signals in detrusor smooth muscles of the guinea-pig urinary bladder. *J. Physiol.* 559, 567–581. doi: 10.1113/jphysiol.2004.065136

Hayase, M., Hashitani, H., Kohri, K., and Suzuki, H. (2009). Role of K^+ channels in regulating spontaneous activity in detrusor smooth muscle *in situ* in the mouse bladder. *J. Urol.* 181, 2355–2365. doi: 10.1016/j.juro.2009.01.013

Kameyama, M. (1983). Electrical coupling between ventricular paired cells isolated from guinea-pig heart. *J. Physiol.* 336, 345–357.

Kubota, Y., Biers, S. M., Kohri, K., and Brading, A. F. (2006). Effects of imatinib mesylate (Glivec®) as a C-kit tyrosine kinase inhibitor in the guinea-pig urinary bladder. *Neurourol. Urodyn.* 25, 205–210. doi: 10.1002/nau.20085

Lin, X., and Veenstra, R. D. (2004). Action potential modulation of connexin40 gap junctional conductance. *Am. J. Physiol. Heart Circ. Physiol.* 286, H1726–H1735. doi: 10.1152/ajpheart.00943.2003

Maurer, P., and Weingart, R. (1987). Cell pairs isolated from adult guinea pig and rat hearts: effects of $[ca^{2+}]_i$ on nexal membrane resistance. *Pflügers Archiv.* 409, 394–402.

McCloskey, K. D., and Gurney, A. M. (2002). Kit positive cells in the guinea pig bladder. *J. Urol.* 168, 832–836. doi: 10.1016/S0022-5347(05)64752-0

Meng, E., Young, J. S., and Brading, A. F. (2008). Spontaneous activity of mouse detrusor smooth muscle and the effects of the urothelium. *Neurourol. Urodyn.* 27, 79–87. doi: 10.1002/nau.20456

Mills, I. W., Greenland, J. E., McMurray, G., McCoy, R., Ho, K. M., Noble, J. G., et al. (2000). Studies of the pathophysiology of idiopathic detrusor instability: the physiological properties of the detrusor smooth muscle and its pattern of innervation. *J. Urol.* 163, 646–651. doi: 10.1016/S0022-5347(05)67951-7

Milsom, I., Abrams, P., Cardozo, L., Roberts, R., Thüroff, J., and Wein, A. (2001). How widespread are the symptoms of an overactive bladder and how are

they managed? a population-based prevalence study. *BJU Int.* 87, 760–766. doi: 10.1046/j.1464-410x.2001.02228.x

Neuhaus, J., Wolburg, H., Hermsdorf, T., Stolzenburg, J.-U., and Dorschner, W. (2002). Detrusor smooth muscle cells of the guinea-pig are functionally coupled via gap junctions *in situ* and in cell culture. *Cell Tissue Res.* 309, 301–311. doi: 10.1007/s00441-002-0559-2

Padmakumar, M., Bhuvaneshwari, K., and Manchanda, R. (2012). "Classification and analysis of electrical signals in urinary bladder smooth muscle using a modified vector quantization technique," in *Signal Processing and Communications (SPCOM), 2012 International Conference on* (Bangalore: IEEE), 1–5.

Padmakumar, M., Brain, K. L., Young, J. S., and Manchanda, R. (2018). A four-component model of the action potential in mouse detrusor smooth muscle cell. *PLoS ONE* 13:e0190016. doi: 10.1371/journal.pone.0190016

Petkov, G. V. (2011). Role of potassium ion channels in detrusor smooth muscle function and dysfunction. *Nat. Rev. Urol.* 9, 30–40. doi: 10.1038/nrurol.2011.194

Shen, W.-H., Xiong, E.-Q., Song, B., Li, W.-B., Lu, G.-S., Li, L.-K., et al. (2008). Identification of pacemaker-like current in interstitial cells of Cajal in bladder of adult guinea pigs. *Acta Acad. Med. Militaris Tertiae* 7:008.

Spencer, N. J., Hennig, G. W., and Smith, T. K. (2001). Spatial and temporal coordination of junction potentials in circular muscle of guinea-pig distal colon. *J. Physiol.* 535, 565–578. doi: 10.1111/j.1469-7793.2001.00565.x

Spencer, N. J., Hennig, G. W., and Smith, T. K. (2002). Electrical rhythmicity and spread of action potentials in longitudinal muscle of guinea pig distal colon. *Am. J. Physiol. Gastrointest. Liver Physiol.* 282, G904–G917. doi: 10.1152/ajpgi.00345.2001

Steers, W. D., and Tuttle, J. B. (2009). Role of ion channels in bladder function and voiding disorders. *Curr. Bladder Dysfunct. Rep.* 4, 125–131. doi: 10.1007/s11884-009-0018-y

Tomita, T. (1967). Current spread in the smooth muscle of the guinea-pig vas deferens. *J. Physiol.* 189, 163–176.

Tong, W.-C., Choi, C. Y., Kharche, S., Holden, A. V., Zhang, H., and Taggart, M. J. (2011). A computational model of the ionic currents, Ca^{2+} dynamics and action potentials underlying contraction of isolated uterine smooth muscle. *PLoS ONE* 6:e18685. doi: 10.1371/journal.pone.0018685

Young, J. S., Meng, E., Cunnane, T. C., and Brain, K. L. (2008). Spontaneous purinergic neurotransmission in the mouse urinary bladder. *J. Physiol.* 586, 5743–5755. doi: 10.1113/jphysiol.2008.162040

Conflict of Interest Statement: The authors declare that the research was conducted in the absence of any commercial or financial relationships that could be construed as a potential conflict of interest.

frontiers in Physiology

ORIGINAL RESEARCH
published: 28 August 2018
doi: 10.3389/fphys.2018.01114

Slow Recovery of Excitability Increases Ventricular Fibrillation Risk as Identified by Emulation

Brodie A. Lawson[1], Kevin Burrage[1,2], Pamela Burrage[1], Christopher C. Drovandi[1] and Alfonso Bueno-Orovio[2]*

[1] ARC Centre of Excellence for Mathematical and Statistical Frontiers, School of Mathematical Sciences, Queensland University of Technology, Brisbane, QLD, Australia, [2] Department of Computer Science, University of Oxford, Oxford, United Kingdom

Purpose: Rotor stability and meandering are key mechanisms determining and sustaining cardiac fibrillation, with important implications for anti-arrhythmic drug development. However, little is yet known on how rotor dynamics are modulated by variability in cellular electrophysiology, particularly on kinetic properties of ion channel recovery.

Methods: We propose a novel emulation approach, based on Gaussian process regression augmented with machine learning, for data enrichment, automatic detection, classification, and analysis of re-entrant biomarkers in cardiac tissue. More than 5,000 monodomain simulations of long-lasting arrhythmic episodes with Fenton-Karma ionic dynamics, further enriched by emulation to 80 million electrophysiological scenarios, were conducted to investigate the role of variability in ion channel densities and kinetics in modulating rotor-driven arrhythmic behavior.

Results: Our methods predicted the class of excitation behavior with classification accuracy up to 96%, and emulation effectively predicted frequency, stability, and spatial biomarkers of functional re-entry. We demonstrate that the excitation wavelength interpretation of re-entrant behavior hides critical information about rotor persistence and devolution into fibrillation. In particular, whereas action potential duration directly modulates rotor frequency and meandering, critical windows of excitability are identified as the main determinants of breakup. Further novel electrophysiological insights of particular relevance for ventricular arrhythmias arise from our multivariate analysis, including the role of incomplete activation of slow inward currents in mediating tissue rate-dependence and dispersion of repolarization, and the emergence of slow recovery of excitability as a significant promoter of this mechanism of dispersion and increased arrhythmic risk.

Conclusions: Our results mechanistically explain pro-arrhythmic effects of class Ic anti-arrhythmics in the ventricles despite their established role in the pharmacological management of atrial fibrillation. This is mediated by their slow recovery of excitability mode of action, promoting incomplete activation of slow inward currents and therefore

OPEN ACCESS

Edited by:
Bas J. Boukens, University of Amsterdam, Netherlands

Reviewed by:
Richard David Walton, Université de Bordeaux, France
Ruben Coronel, University of Amsterdam, Netherlands

****Correspondence:***
Brodie A. Lawson
b.lawson@qut.edu.au

Specialty section:
This article was submitted to Cardiac Electrophysiology, a section of the journal Frontiers in Physiology

Received: *14 January 2018*
Accepted: *25 July 2018*
Published: *28 August 2018*

Citation:
Lawson BA, Burrage K, Burrage P, Drovandi CC and Bueno-Orovio A (2018) Slow Recovery of Excitability Increases Ventricular Fibrillation Risk as Identified by Emulation. Front. Physiol. 9:1114. doi: 10.3389/fphys.2018.01114

increased dispersion of repolarization, given the larger influence of these currents in modulating the action potential in the ventricles compared to the atria. These results exemplify the potential of emulation techniques in elucidating novel mechanisms of arrhythmia and further application to cardiac electrophysiology.

Keywords: rotors, arrhythmias (cardiac), fibrillation, excitability, refractoriness, emulation, machine learning, Gaussian process regression

1. INTRODUCTION

Self-sustaining patterns of aberrant excitation in the heart, re-entries, are the cause of dangerously accelerated heartrates (tachycardia) and complete losses of synchronized action (fibrillation) (Wit and Cranefield, 1978). Re-entrant circuits often form around unexcitable anatomical features such as veins, with the properties of these obstacles then primarily defining the resulting excitation behavior (Gough et al., 1985; Cherry et al., 2007). However, so-called "functional" re-entries can also develop and sustain themselves in unimpeded tissue (Moe and Abildskov, 1959; Allessie et al., 1977), manifesting as spiral waves that are clinically known as rotors (Pandit and Jalife, 2013). The behavior of functional re-entries depends on the electrophysiological properties of the cells composing cardiac tissue, which vary considerably among population members (Sims et al., 2008) and in different regions of the heart (Feng et al., 1998). Understanding the impact of this variability on the generation and persistence of arrhythmic events, and the corresponding implications for success or failure of anti-arrhythmic treatments, is a critical challenge in cardiac electrophysiology (Sobie, 2009; Sarkar et al., 2012; Muszkiewicz et al., 2016; Passini et al., 2017).

Arrhythmic risk is commonly analyzed in terms of "excitation wavelength" (Smeets et al., 1986; Rensma et al., 1988; Tse and Yan, 2017), the product of conduction velocity (CV) and the effective refractory period (ERP) or action potential duration (APD). This determines the minimum length for which re-entrant circuits will sustain electrical activity, and thus increasing wavelength discourages re-entry formation and maintenance (Wiener and Rosenblueth, 1946), and explains the mechanism of action for many anti-arrhythmic drug therapies (Wang et al., 1992). However, anti-arrhythmic drugs that increase wavelength by prolonging APD/ERP may also be pro-arrhythmic (Wolbrette, 2003; Elming et al., 2004), and class I anti-arrhythmic agents that decrease CV (and hence wavelength) are successfully used for rhythm control of atrial fibrillation (Nattel et al., 2003; Kneller et al., 2005). This points to a subtle and still poorly understood interplay between refractoriness and excitability in modulating re-entry. Of particular interest is post-repolarization refractoriness, given confounding evidence that suggests it as both an anti-arrhythmic and pro-arrhythmic mechanism (Kanki et al., 1998; Kirchhof et al., 1998; Muñoz et al., 2007; Coronel et al., 2012; Franz et al., 2014; Cabo, 2015).

Given the expense of experimentation in the heart, and the lack of direct and independent control over properties of interest (such as cell-level electrophysiological properties), *in silico* modeling serves as a critical tool for the understanding of arrhythmia (Zhou et al., 2018). Parameters encoding experimentally elusive properties can be systematically varied by the modeler, and large-scale interrogation of cardiac model output for different values of their parameters has enabled studies of variability (Sobie, 2009; Sarkar et al., 2012; Pathmanathan et al., 2015), parameter inference (Wallman et al., 2014; Johnstone et al., 2016), and the construction of *in silico* populations (Britton et al., 2013; Muszkiewicz et al., 2016; Passini et al., 2017; Lawson et al., 2018). With regard to the complex spatiotemporal dynamics of cardiac rotors, however, previous research has mostly focused on the variation of only one or two parameters at once (Efimov et al., 1995; Fenton and Karma, 1998; Qu et al., 2000; Pandit et al., 2005; Bartocci et al., 2011; Sánchez et al., 2012). Only a small number of studies have considered simultaneous variation in larger numbers of model parameters (Lee et al., 2016; Liberos et al., 2016), but mainly vary ionic current densities and not the kinetic properties of channel recovery. Quantitative understanding of how cell-level electrophysiological properties modulate the complex interactions between refractoriness and excitability when mediated by tissue coupling therefore remains severely lacking.

Emulation is a powerful technique for greatly reducing the computational cost associated with exploration of parameter variability in complex models that are time-intensive to simulate, with a history in climate modeling (Holden and Edwards, 2010) and engineering design (Simpson et al., 2001). In cardiac electrophysiology, while emulators have proved successful in the prediction of electrophysiological properties for single cells (Chang et al., 2015; Johnstone et al., 2016), and for the forward ECG problem (Geneser et al., 2008; Swenson et al., 2011; Johnston et al., 2017), their capabilities remain largely unexplored for the spatiotemporal dynamics of excitation. Only an initial study by the authors did emulate excitation waves in tissue, but in the context of predicting the shapes of steady state wavefronts (Lawson et al., 2017), with no consideration of the far more complex excitation patterns that define arrhythmia.

Here we present an emulation technique, specifically designed for models of cardiac electrophysiology, that significantly reduces the computational cost of exploring variability across many parameters and streamlines the analysis process. We demonstrate and validate our technique by emulating a suite of spatial biomarkers directly related to arrhythmic risk, and apply it to investigate the generation and persistence of rotor-derived tachycardic and fibrillatory excitation behaviors when all important factors modulating tissue excitability and refractoriness are allowed to simultaneously vary. New

electrophysiological insights associated with the cardiac excitation wavelength and of particular relevance for ventricular arrhythmias emerge, including the identification of increased risk of wave breakup in response to slower recovery of fast inward channels, and differential effects of decreasing slow inward current or increasing slow outward current despite both changes increasing ERP. Our method extends naturally to biophysically detailed models and realistic heart anatomies.

2. METHODS

2.1. Simulated Arrhythmias

Our study focuses on the impacts of variability in cell-level properties on the induction and persistence of re-entry in cardiac tissue. To avoid the impacts of other conflating factors we work in one of the simplest settings for simulating tachycardia and fibrillation. This is a two-dimensional layer of isotropic tissue, allowing for use of the monodomain formulation (Sundnes et al., 2006),

$$\frac{\partial u}{\partial t} = D\nabla^2 u + I_{\text{ion}} + I_{\text{stim}}. \quad (1)$$

Here the membrane potential (expressed in terms of dimensionless variable u) spreads by tissue coupling with associated constant D, kinetics of cellular excitation and repolarization are encoded in the I_{ion} term, and the external supply of stimulus is represented by I_{stim}. For the description of excitation and repolarization kinetics we selected the reduced Fenton–Karma model (Fenton and Karma, 1998) (hereafter FK model), given its relative speed of simulation and the rich set of re-entrant behaviors that it is capable of replicating (Fenton and Karma, 1998; Fenton et al., 2002). Importantly, the model has been shown to capture the essential tissue-scale properties governing re-entry, being capable of reproducing the re-entrant patterns of more physiologically detailed models for human cardiocytes in the atria (Lombardo et al., 2016), and with slight modifications to also fit action potential (AP) morphology, in the ventricles (Bueno-Orovio et al., 2008). As a reference, we select the parameters for the FK model (**Table 1**) that correspond to modified Beeler–Reuter dynamics (Beeler and Reuter, 1977; Courtemanche and Winfree, 1991), given the body of work examining the dynamics of waves of excitation in this model (Efimov et al., 1995; Courtemanche, 1996). Full model equations are provided in the **Supplementary Material**.

Simulation software was written in MATLAB, using a high-order numerical stencil as described in Bueno-Orovio et al. (2006). Briefly, a second-order Strang splitting (Strang, 1968) is used in time to separate the reaction and diffusion terms of the monodomain equation. The diffusive component is then integrated exactly in Fourier space using a cosine expansion to impose the required non-flux boundary conditions, whereas the reaction term is solved by the modified Euler method (with gating variables integrated by the Rush–Larsen scheme Rush and Larsen, 1978), therefore preserving global second-order time accuracy. All simulations were conducted on two-dimensional tissue layers of 15×15 cm in size to allow sufficient space for rotor accommodation, with a diffusion coefficient of $D = 1$ cm^2/s, constant time step of 0.1 ms, and a space discretization of 512 points in each space direction ($\sim$0.03 cm), allowed by the high-order convergence of Fourier spectral methods. The accuracy of the numerical simulations was verified in one-dimensional cables by halving the time and space integration steps. This resulted in $<$1% change in conduction velocity, even in the low excitability limit.

Re-entries are generated in our simulations via an S1–S2 stimulation protocol, with the S2 stimulus timed to produce directional block that quickly develops into a phase singularity (rotor tip). The first stimulus acts at one edge of the domain, generating a planar wave. Then, when the waveback of this wave has reached the middle of the domain (as judged by crossing $u =$

TABLE 1 | The variable parameters, which control the important properties of cell depolarization and repolarization in response to electrical stimulus.

Parameter	Base value	Variability	Description
g_{fi}	3 mS/cm^2	±30%	Maximum conductance of fast inward (activation) current
g_{so}	0.02 mS/cm^2	±20%	Maximum conductance of slow outward (repolarization) current for activated cell
$g_{so(\text{rest})}$	0.12 mS/cm^2	±30%	Maximum conductance of slow outward (repolarization) current for inactivated cell
g_{si}	0.0223 mS/cm^2	±20%	Maximum conductance of slow inward (plateau) current
τ_v^+	3.33 ms	±50%	Time constant for inactivation of fast inward current
τ_{v1}^-	1,000 ms	±50%	Initial time constant for reactivation of fast inward current (cell below activation threshold)
τ_{v2}^-	19.6 ms	±50%	Secondary time constant for reactivation of fast inward current (cell below activation threshold)
τ_w^+	667 ms	±50%	Time constant for inactivation of slow inward current
τ_w^-	11 ms	±50%	Time constant for reactivation of slow inward current
u_c	0.13	–	Membrane potential (dimensionless) above which the cell is considered activated
u_{si}	0.85	–	Membrane potential (dimensionless) at which the slow inward current activates
u_v	0.055	–	Membrane potential (dimensionless) at which the rate of fast inward channel recovery switches
k	10	–	Steepness of the smoothed step function used in the expression for the slow inward current

Base values for all parameters are those specified by Fenton and Karma for recreating modified Beeler-Reuter dynamics with their model (Fenton and Karma, 1998), except $g_{fi} = 3$ mS/cm^2, chosen in order to better explore the variety of rotor trajectories. Grayed out parameters were not varied in the final exploration of the full model, with variation in τ_w^- removed after preliminary analysis suggested it was of low importance.

u_{crit} at this location), a second stimulus is provided to one whole quadrant on the wave's back side. With appropriate selection of u_{crit} (here $u_{crit} = 0.05$), excitation can propagate in one cardinal direction and not the other, resulting in the generation of a rotor tip in the center of the domain, at the corner of the second stimulated region (**Figure 1A**). We use the algorithm described by Fenton and Karma (1998) to track the position of rotor tips. Each simulation was run for 8,000 ms after the initial induction of a rotor, but terminated prematurely if all rotor activity died out.

2.2. Data Generation and Biomarker Choice

Training and test data used to construct and validate emulators were generated by running the model for different combinations of parameter values across the space of interest, with the design of these computational experiments selected via Latin hypercube sampling (Mckay et al., 1979) by MATLAB's *lhsdesign* function. This provides data that is better distributed across the parameter space, improving classifier and emulator performance.

We created two sets of *in silico* data in order to explore the impacts of variability in electrophysiological parameters. Firstly, we introduced variability into two model parameters, g_{fi} and g_{so}, which are the two current conductances most directly controlling CV and APD, respectively. Such data allowed us to explicitly visualize and thus better demonstrate the effectiveness of our classification and emulation techniques. The second set of *in silico* data allows eight model parameters to vary, including the main current conductances and time constants regulating excitability and repolarization in the model (see **Table 1**). The reduced dataset was composed of 2,000 simulated

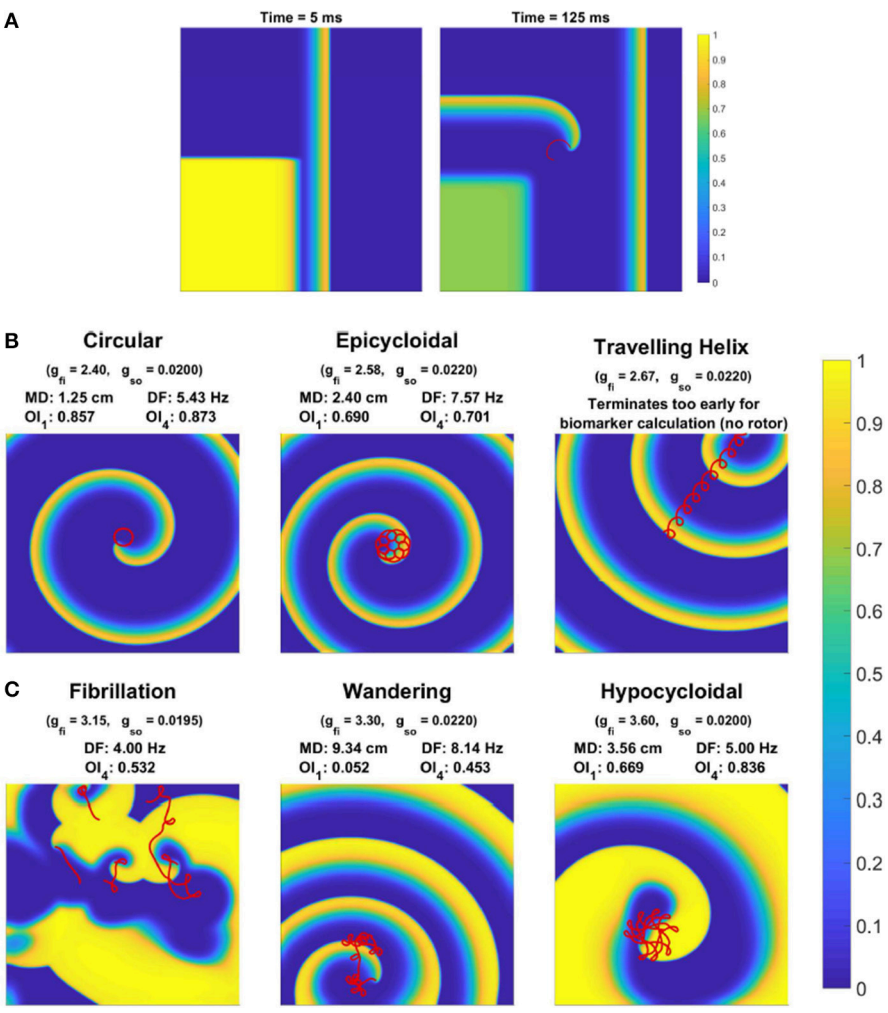

FIGURE 1 | Behavior of rotor-driven re-entries varies significantly in response to electrophysiological variability. **(A)** Induction of a rotor via cross field S1–S2 stimulus, as demonstrated by the membrane potential field 5 and 125 ms after the S2 stimulus. The S1 stimulus creates a planar wave traveling to the right, and the square region stimulated by the S2 stimulus overlaps with the waveback of the initial wave, creating directional block. While excitation propagates upwards, tissue to the right eventually recovers and allows for excitation to curl into this region, forming the beginning of a rotor-driven re-entry. **(B)** Example rotor trajectories and the corresponding excitation field for different choices of some model parameters. All snapshots are taken at 3,000 ms (except for the helix, which terminates early). The last 1,200 ms of rotor tip movement in each case is visualized in red. Values for the spatial biomarkers maximum distance (MD), dominant frequency (DF), and organization indices (OI) are also presented.

electrophysiological scenarios, and the full dataset involved 3,500 due to the higher-dimensional parameter space requiring additional data to be resolved to sufficient accuracy. Variability was accounted as uniform distributions on model parameters (Britton et al., 2013), with ranges of variability as detailed in **Table 1**. These are consistent with the larger ranges of variability considered in previous studies (Britton et al., 2013; Liberos et al., 2016; Muszkiewicz et al., 2016; Zhou et al., 2016), given the normalized magnitude of the transmembrane potential in the FK model.

Depending on the specific choice of values for these electrophysiological properties, simulations exhibited a range of behaviors. When tissue excitability is too weak, excitation does not propagate and no rotor can form. A rotor also fails to form if cell refractoriness is too long, as the tissue stimulated by the S2 stimulus remains unexcitable and blocks the rotation of the rotor tip, forcing it to collide with the domain boundary and be eliminated. Rotors that are successfully induced can either persist, wander the domain until they are eliminated by a boundary, or devolve into wave breakup corresponding to fibrillation. **Figure 1B** shows the main rotor behaviors that could be observed. We represented the output of each simulation as a classification of the overall behavior observed, and a set of "spatial biomarkers" that serve as quantitative measures of rotor dynamics and the associated arrhythmic risk. As detailed by **Table 2**, model output was classified into the four categories suggested above, namely a lack of rotor formation, formation of a stable rotor, formation of a transient rotor, or fibrillatory dynamics. This classification becomes important for constructing predictive emulators, as we explain below.

For biomarkers, we measured steady-state CV and APD prior to the establishment of re-entry, given that they are key properties in determining the cardiac wavelength. These were measured using the S1 stimulus, and so refer to the CV and APD of planar waves in the tissue. We term these the "tissue-level" biomarkers, given that they can be experimentally measured at this scale. For stable rotors, we recorded the greatest distance between any two points on the rotor's trajectory (after it had been given a chance to stabilize), and the organization index derived from the main peak in power spectrum (OI_1), as measures of the critical size of tissue substrate required to support such a rotor, and the complexity of its trajectory, respectively. Additionally, we created several virtual probes throughout the domain at regular intervals, that measured the time course of the membrane potential at their location. The power spectrum of each of these signals was averaged, and then used to calculate the standard organization index using the main four peaks in power spectrum (OI_4), as well as the dominant frequency (DF). These provide a measure of the level of chaos present in the rotor dynamics, and the effective rate of induced tachycardia, respectively. Each of these biomarkers, along with more detail regarding their calculation, is provided in **Table 3**. The values of these biomarkers for different types of rotor behavior are also included in **Figure 1B**.

2.3. Gaussian Process Emulation

For emulation, we make use of Gaussian process (GP) regression, as introduced for the emulation of computer models by Sacks et al. (1989). GP regression creates an approximation to the model's response surface for each of the spatial biomarkers, by making use of the generated training data. A good reference for this approach is Rasmussen and Williams (2006). Separate GPs are used for each of the biomarkers, with these GPs characterized by a function $\mu(\boldsymbol{\theta})$ that defines the mean of the process (in the absence of data) at any point in the parameter space, $\boldsymbol{\theta}$, and a covariance function, $k(\boldsymbol{\theta}, \boldsymbol{\theta}')$ that defines the covariance between any two points in the parameter space, $\boldsymbol{\theta}$ and $\boldsymbol{\theta}'$. For the basic forms of these functions, we select for the mean function a linear trend, and for the covariance function the Matern-5/2 covariance,

$$k(\boldsymbol{\theta}, \boldsymbol{\theta}') = \sigma^2 \left(1 + \sqrt{5}r + \frac{5r^2}{3}\right) \exp\left(-\sqrt{5}r\right) + \sigma_n^2 \delta_{\boldsymbol{\theta},\boldsymbol{\theta}'},$$
$$r = \sqrt{\sum_{i=1}^{D} \frac{(\theta_i - \theta_i')^2}{l_i^2}}. \quad (2)$$

This function simply dictates that GP predictions at two sets of parameter values $\boldsymbol{\theta}$ and $\boldsymbol{\theta}'$ become more correlated as the two points in parameter space become closer, but with this measure of "closeness" defined such that each dimension in the parameter space can contribute differently (encoded by the choice of l_i's). The values of these l_i's are determined during the training process, and thus the method automatically determines the relative importance of each variable in $\boldsymbol{\theta}$ toward the output being emulated (known as automatic relevance determination). Here σ controls the overall amount of variance (and covariance) of the process, and σ_n the noise in the data (with the Kronecker delta used to ensure it contributes to variance at any point, but not covariance). In the case of emulation, the data is output from a deterministic computer simulation and so technically $\sigma_n = 0$, but its inclusion can regularize the process and we here do not assume $\sigma_n = 0$.

Given a set of values for the hyperparameters $\mathbf{l} = (l_1, l_2, ..., l_D)$, σ and σ_n, the likelihood of generating the training data with the corresponding GP may be analytically calculated (Rasmussen and Williams, 2006). Thus, we may choose these hyperparameters, along with those specifying the mean function, by maximizing this likelihood using MATLAB's built-in function *fitrgp*. Importantly, maximization of this likelihood naturally corresponds to optimizing a balance between data fit and model complexity, discouraging over-fitting (Rasmussen and Williams, 2006).

Once the GP's hyperparameters have been determined, predictions can then be made using simple matrix-matrix and matrix-vector products, if the inverse of the covariance matrix (covariances between all training points) is stored during the training process. Emulator predictions are thus extremely rapid, and the optimization problem involved with training the emulator can be greatly accelerated by the use of derivative information, which can be calculated at very little additional computational cost (Rasmussen and Williams, 2006). The primary cost remains running the simulator in order to generate the initial training data, but this is easily performed in parallel.

TABLE 2 | The four classifications used to separate different model behaviors, and the conditions used to automatically classify simulation output into each.

Name	Classification conditions	Interpretation
No rotor	No rotor forms, or fails to complete at least one rotation, as judged by detecting APs at probes close to each corner of the domain	Tissue excitability is too weak to propagate signals, or APD is too long for a rotor to rotate after S2 stimulus
Stable rotor	Rotor activity persists for full simulation time and conditions for *Fibrillation* are not met	Persistent rotor-driven tachycardia
Transient rotor	Rotor activity ceases before simulation end, and conditions for *Fibrillation* are not met	Transient rotor-driven tachycardia that self-terminates
Fibrillation	At least five individual rotor tips (phase singularities) that each exist for at least 50 ms form during simulation	Wave breakup that produces a transient or persistent episode of fibrillation

Five phase singularities are required to confidently identify wave breakup, as interactions with the initial condition can occasionally produce multiple rotors even when electrophysiological dynamics do not support wave breakup. The last two classifications are combined in much of the work into a single classification, labeled "Chaotic."

TABLE 3 | The biomarkers used to characterize simulation behavior, and their interpretations with regard to arrhythmias.

Biomarker name	Measurement	Interpretation
Conduction velocity	Time taken for S1 pulse to cross two markers	Affects inherent rotation rate, wavelength
Action potential duration	Time taken for tissue stimulated by the S1 pulse to return to u_{crit} after depolarisation	Affects availability of excitable tissue, wavelength
Maximum distance	Maximum distance between any two points on the rotor tip's trajectory	Critical size required for rotor persistence
Dominant frequency	Location of largest peak in the power spectrum of the signal recorded by virtual probes	Severity of resultant tachycardia
Organization index 1	Proportional contribution of the largest peak in the power spectrum of a single rotor's trajectory to the total power contained in that spectrum	Complexity of a stable rotor's trajectory
Organization index 4	Proportional contribution of the four largest peaks in the power spectrum recorded by virtual probes, to the total power contained in that spectrum	Regularity of rotor circulation

2.4. Emulator Partitioning

GP regression assumes a smooth response of each output to changes in the parameters. Predictions thus suffer when there are critical values of the parameters that cause a sudden change in any of the outputs. Our simulations of rotor dynamics certainly exhibit this property, due to sharp transitions, for example, from simulations that generate a single rotor to simulations that fail to propagate, and from single persistent rotors to wave breakup. It thus becomes necessary to divide the parameter space into separate regions that can then each be emulated by their own Gaussian process. Some previous approaches to this problem in the literature have allowed the boundaries between regions to also be determined during the training process, by defining their locations either using regression trees (Gramacy and Lee, 2008) or Voronoi tesselations (Kim et al., 2005) and then exploring this augmented space via Bayesian sampling techniques. The power of these approaches in detecting where boundaries should be located, without any specification from the user about model behavior (unsupervised learning), comes at the cost of a much longer training process and the risk of determining incorrect boundary locations. In our case, we classify model outputs according to a compact number of general rotor behaviors (**Table 2**), and hence can take a supervised learning approach. Supervised learning has been used previously in the context of spiral waves in cardiac tissue, but for the separate problem of detecting rotors from image data (Grosu et al., 2009).

With the training data classified into the different behaviors in **Table 2**, multi-class classification techniques can then be used to predict which category of behavior any given set of parameter values is expected to produce. As long as the regions that correspond to the different behaviors can be well-separated, this leads to distinct regions that can each be assigned their own GP emulator. For a classification model, we use a set of support vector machines (SVM) (Cortes and Vapnik, 1995) that each individually make binary classification predictions, but together form an ensemble that performs multi-class classification. Gaussian kernels (radial basis functions) are used, with hyperparameters selected to optimize performance under five-fold cross validation by MATLAB's *fitcecoc*. The "coding design" used to perform multi-class classification is also selected as part of this optimization process, between either one-against-one or one-against-all (see Hsu and Lin, 2002 for a comparison of these and other designs).

2.5. Calculation of Mean Effects

In using our emulator to explore the dynamics of the full model, we calculate the mean effect of each of its parameters upon our spatial biomarkers, a type of global sensitivity analysis (Oakley and O'Hagan, 2004; Chang et al., 2015). These are calculated by averaging over the effects of variability in all other parameters, providing a sense of how a single given parameter affects the output in question among a variable population. Denoting our partitioned emulator $\mathcal{Y}$ and using Monte Carlo integration to perform this averaging, the mean effect of a variable θ_i on a given

model output y is given by

$$\bar{y}(\theta_i) \approx \frac{1}{N}\sum_{j=1}^{N} \mathcal{Y}(\boldsymbol{\lambda}_j, \theta_i). \quad (3)$$

Here each $\boldsymbol{\lambda}_j$ is a random realization of all other parameters in $\boldsymbol{\theta}$, selected according to their distributions. For the model outputs that can take on null values, we choose to calculate the average over only those sampled points where the emulator predicts non-null values.

We again use LHS to improve the overall coverage over the parameter space in calculating these expectations, and choose a large $N = 100,000$ to ensure good accuracy in integrating over the effects of variability in the other parameters. With eight variables and 100 points used to represent the functions defined in Equation (3), in total we perform 80 million emulated runs of the two-dimensional FK model. The necessity of emulation in performing such analyses for cardiac electrophysiological models is clear.

3. RESULTS

3.1. Important Features of Rotor-Driven Re-entry Are Not Explained by CV and APD

Our generated *in silico* data allows us to rigorously explore how well the effects of electrophysiological variability on rotor inducibility and maintenance are captured by the tissue-level biomarkers that can be more readily measured, the steady-state values of CV and APD. The large extent of variability in model parameters resulted in a corresponding amount of variation in CV and APD, with a good spread across the space of these biomarkers, as illustrated in **Figure 2**. Points in this figure are color-coded according to the type of re-entrant behavior observed in each simulation, revealing a few distinct regions of the biomarker space where behavior is consistent.

Especially predictable are the cases where no re-entry could be induced, suggesting that APD and CV are generally sufficient in themselves for describing the inducibility of re-entry. This includes both the case where CV is very low and excitation fails to properly propagate, and the case where APD is too high and thus the critical length is too long for the spiral wave's tip to successfully rotate before colliding with the simulation boundary. A faster CV decreases the critical APD value beyond which rotors fail to form, because the wavetip travels further while waiting for tissue to recover its excitability. This agrees well with the known importance of wavelength in defining the critical length of re-entrant paths (Wiener and Rosenblueth, 1946; Rensma et al., 1988).

On the other hand, there are large regions of the biomarker space where similar values for the biomarkers result in wholly different re-entrant behaviors, highlighting the importance of finer-scale ionic effects in governing which rotors are likely to persist, annihilate themselves, or exhibit breakup into fibrillation. Transient rotors arise most frequently when conduction and repolarization are both fast, and when APD values are moderate, slow conduction promotes fibrillation while fast conduction promotes stable rotors.

On the whole, these tissue-level biomarkers inform well the critical length required for re-entry establishment, but only poorly the type of re-entrant behavior will result in the case of a spiral wave. Variability in the cell properties themselves, ion

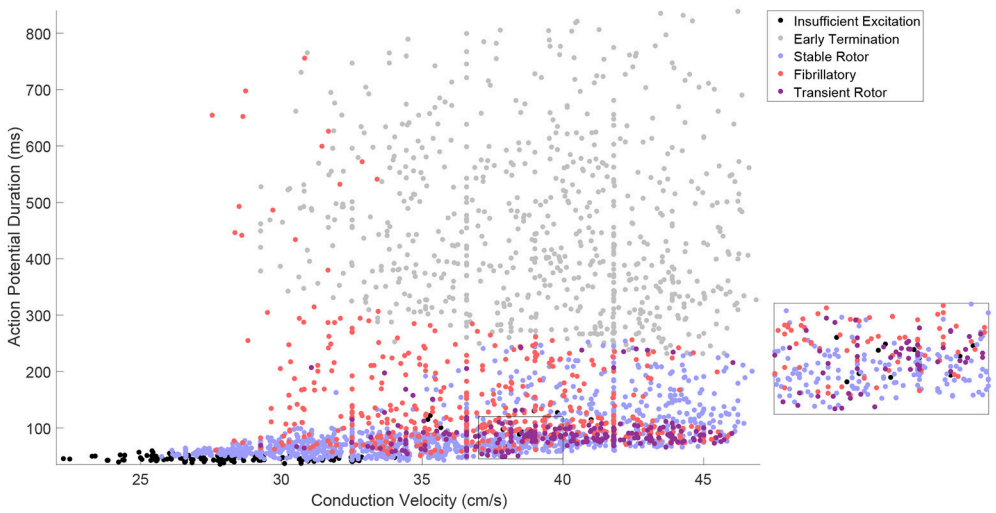

FIGURE 2 | The tissue-level biomarkers CV and APD fail to predict rotor-driven re-entry behavior. The classes of model behavior observed for different values of the tissue-level biomarkers, CV, and APD, with variability in all major model parameters. Classes are assigned according to **Table 2**, but with the "No Rotor" classification further separated into failure to propagate excitation and early termination (almost always due to APD being too long to successfully induce a rotor with the S1–S2 stimulus) in order to make the visualization more informative. There are regions of the biomarker space where behavior is largely predictable, but on the whole, the class of behavior cannot be predicted from these biomarkers alone and clearly depends on further electrophysiological factors. This is best demonstrated by regions like the one shown in the inset.

channel conductances and time constants, must be considered directly in order to properly understand how this variability manifests in different re-entrant behaviors and the severity of the arrhythmias that result. Furthermore, these findings highlight the importance of looking beyond excitation wavelength when evaluating the anti- or pro-arrhythmic properties of drug treatments.

3.2. Partitioned Emulation of Spatial Biomarkers Captures the Complex Dependence of Re-entrant Behavior on Ionic Properties

3.2.1. Classifier and Emulator Predictions

In the case where only two parameters are varied, forward simulation provides enough information about the effects of variability to validate our classification and emulation techniques. This additionally allows for emulator predictions to be visualized, and thus to confirm that our selected spatial biomarkers appropriately capture the important features of rotor-driven re-entry.

Figure 3A shows how the automatically-detected class of rotor behavior changes in response to differences in the excitability of tissue (via g_{fi}), and the rate of repolarization (via g_{so}). Well-defined regions of the parameter space that correspond to the different behaviors can be clearly observed, but no boundaries can be drawn to separate the different classes in the top right of the parameter space. This issue is largely addressed by combining the "fibrillatory" and "transient rotor" classes together into a single "chaotic" rotor class, after which SVM classification successfully identifies the different regions and attains an accuracy of 96% on the data not used for training. The

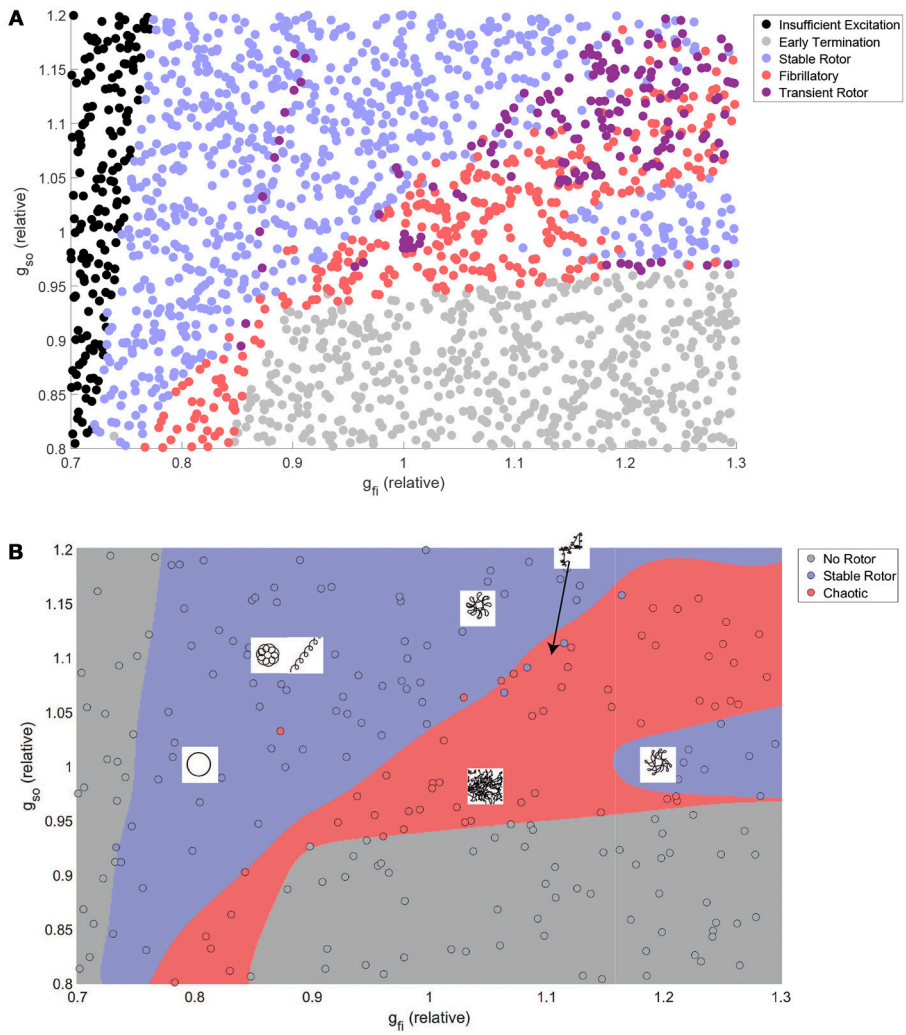

FIGURE 3 | The class of re-entrant behavior exhibits complex dependence on ionic properties, but is well predicted by SVM classification. **(A)** Training and test data after classification using the rules in **Table 2**. Distinct parameter regimes that correspond to the different behaviors can be observed, but with small numbers of data points, predominantly in the fibrillatory region, that disrupt clean separations of the parameter space. **(B)** Combination of rotors that annihilate themselves with those that exhibit wave breakup into a single "chaotic" classification allows high-accuracy prediction of rotor behavior by an SVM classifier model. Also displayed are schematic diagrams indicating the different types of rotor path that can be generated in various regions throughout the parameter space.

classifier model is thus appropriate for use in defining boundaries for partitioned emulation.

Despite very complex dependencies of the spatial biomarkers upon the values of these two channel densities, our partitioned emulation approach is able to very successfully capture the response surfaces implied by the data (**Figure 4**), allowing prediction of these important re-entrant properties at any point in the parameter space. The accuracy of these predictions is confirmed by comparing the data points not used in training against the emulated surface at those points, with the greatest majority of points falling very close to the line of equality (Figure S1). Importantly, the use of our partitioned emulation technique proves to significantly improve accuracy as compared to a traditional GP emulation approach using only a single emulator.

Training of the set of partitioned emulators required less than seven minutes, but the cost of generating the 2,000 simulations for use as training and test data required more than 2,000 h of computational time (albeit spread across multiple cores on our high performance computing platform). The time required for the emulator to generate predicted biomarker values at a set of 2,000 additional points randomly sampled across the parameter space was 0.23 s, indicating a speedup of eight orders of magnitude when considering serial implementation. Even making good use of supercomputer architecture, the speedup was about six orders of magnitude, indicating the power of emulation for studies of variability in cardiac electrophysiology models. These immense savings offered by the emulator allow further simulations to be generated almost immediately, enabling analyses such as the one that follows for a larger number of variable parameters.

Given the cost of generating the initial data used to construct our partitioned emulators, a natural question is how classifier and emulator performance depend upon the amount of training data used. In terms of accurately predicting the classes of the data reserved for testing, the strong performance of the SVM classifier remained even when using much less data for training (Figure S2). However the more data that is used, the better the precise locations of the boundaries between classes can be determined. Emulator performance depended strongly on the performance of the classifier, and 600 pieces of training data produced emulators almost as accurate as those trained with 1,800 pieces of data. It should be noted, however, that when a larger number of parameters is varied, a greater amount of training data will likely be required to successfully resolve classification boundaries and response surfaces.

3.2.2. Capture of Electrophysiological Dynamics

The emulated surfaces for the biomarkers defining excitation wavelength, CV, and APD, demonstrate intuitive responses, to an extent, to variability in the two considered current densities (**Figure 4**). CV depends especially on the velocity of the AP upstroke, and so is especially sensitive to the conductance of the fast inward current (g_{fi}) and only very slightly impacted by the conductance of the slow outward current (g_{so}). APD depends strongly on the strength of the slow outward current, but importantly only above some critical level of fast inward current density. This effect arises because only sufficiently strong excitations are able to drive the AP upstroke beyond the activation threshold of the model's equivalent of the Ca^{2+} current. "Incomplete" excitations that fail to significantly activate this current result in very short APs, the duration of which are not strongly affected by either g_{fi} or g_{so}.

As the conductance of the fast inward current is increased, a shift of rotor trajectories from circular to epicycloidal, then hypocycloidal paths is well established (Efimov et al., 1995; Fenton and Karma, 1998). We observe this same behavior (see example trajectories in **Figures 1B**, **3B**), with such information encoded in the maximum distance and OI_1 biomarkers. Specifically, the tightening of circular trajectories results in a decrease in core size until trajectories become epicycloidal, at which point sizes start increasing again, peaking for the case of traveling helices that collide with the boundary before paths become hypocycloidal. OI_1 has a maximal value for the circular paths, decreased for epicycloidal and hypocycloidal trajectories, with severely reduced values for traveling helices and the high-excitability cases where trajectories meander much more.

The frequency of re-entry, controlled by the angular velocity of a spiral wave's core, depends on both the availability of excitable tissue and the speed at which re-entry can propagate into this tissue. Thus tachycardic severity increases in response to an increase in either of g_{fi} and g_{so}. However, the nature of this increase depends on the type of rotor-driven re-entry, with circular rotor cores very sensitive to tissue excitability while rotors with hypocycloidal or meandering trajectories are barely affected. The final biomarker, OI_4, successfully identifies what we term rotor "stability," consistently taking on higher values when a rotor remains fixed in a single general location, as opposed to meandering or devolving into fibrillation. This biomarker thus serves as an indicator for the risk of wave breakup.

Several interesting observations can be made from the initial data presented up to this point. **Figure 3** shows that rotor annihilation by antagonizing the outward current invariably involves first crossing through the chaotic regime. This suggests that if such treatments fail to sufficiently increase the critical length, and hence destroy a re-entry completely, they may instead trigger fibrillation, an effect we explore further in the analyses that follow. The sharp increase in maximum distance and decrease in OI_1 at the boundary between the stable and chaotic regions also suggests that rotor meander in general is an indicator for increased susceptibility to wave breakup. Lastly, we observe that for all biomarkers (less marked perhaps for CV) the dependence on either of the two parameters depends strongly upon the value chosen for the other. Thus we must consider variability in all properties of interest at once, in order to ensure that the conclusions drawn are not significantly biased by the specific set of base parameter values chosen. This is one of the advantages we achieve in the following section via emulation.

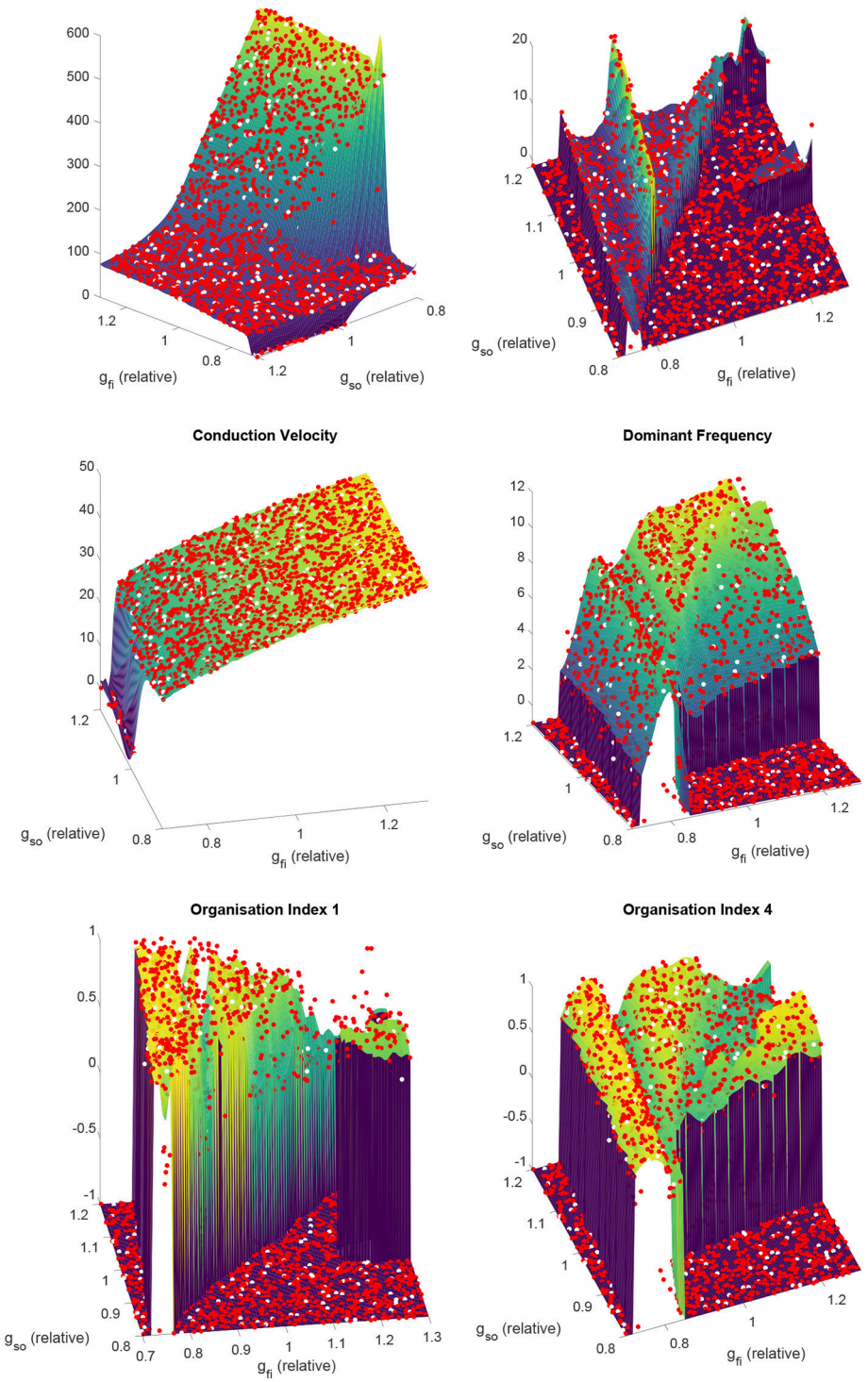

FIGURE 4 | Partitioned emulation successfully captures the complex dependencies of important descriptors of re-entry on the electrophysiological substrate. The response surfaces predicted by the partitioned emulator for each biomarker are shown, along with the training data (red) used in their construction. Null values for biomarkers are denoted by a value of −1. Performance can be judged by considering the unseen test data (white), which demonstrate great agreement with the surfaces that indicate the emulator's predictions. This is achieved despite the complex and non-monotonic nature of the dependence of these biomarkers on the two varied parameters.

3.3. Classification and Emulation Identify Key Ionic Effects Underlying Functional Re-entry

3.3.1. Partitioned Emulation Is an Important Tool for Understanding Variability in Cardiac Electrophysiology Models

The previous section demonstrated the importance of allowing different electrophysiological properties to vary simultaneously, in order to properly understand how the effects of variation in these different properties (including the effects of drug treatments) together determine re-entrant behavior. However, when our full set of electrophysiological properties are all allowed to vary, we lose the ability to use forward simulation to properly explore the parameter space due to its high dimensionality. Here the SVM classifier model and associated emulators become invaluable tools, to enrich the data and to make the calculation of the main effects of each parameter possible, thus allowing us to quantify how each individual ionic property contributes to the type of arrhythmia that develops, as well as its relative severity. We select the majority of the *in silico* data (3,200 out of 3,500 points) to be used for training the classifier model and emulator, in order to attain the best performance possible when the emulator is then used outside of the dataset to calculate the main effects of the parameters.

Although the predictions of the emulators and classifier model they depend upon cannot be simply visualized when these many parameters are varied, the test data not involved in the training process can be used to evaluate their performance. The increased dimensionality makes both the classification and emulation problems significantly more difficult, but the SVM classifier still achieves an accuracy of 81%. Emulation performance is also diminished as compared to the lower-dimensional problem, but remains good enough that the emulator is suitable for the efficient and automatic extraction of hidden data trends (Figure S3). Use of our partitioning technique resulted in more than a fivefold decrease in root mean square error, as compared to traditional GP emulation. Importantly, the differences incurred by emulation are not strongly biased, with no consistent under-estimation or over-estimation. The strong performance of the classifier and emulator on the two-parameter problem suggests that the reduction in performance for the eight parameter problem is simply due to the increased amount of training data required to fully resolve such complex dynamics across a high-dimensional space, and thus may be improved simply by further additional runs of the simulator.

3.3.2. Slower Recovery of Fast Inward Channels Can Increase Arrhythmic Risk

Using our emulators to rapidly evaluate Equation (3), we quantify using mean effects how the different parameters controlling excitability and its recovery impact upon the important features of our simulated re-entries. We re-iterate that these insights are not the same as would be obtained by simply varying each individual parameter in turn, but instead represent the overall effects of the parameters upon variability in the others. This improves the generalizability of the conclusions we draw in the face of both physiological variability and uncertainty in the most appropriate base values of the parameters in a model.

Figure 5 shows how the spatial biomarkers we use to quantify re-entry properties depend on the parameters controlling tissue excitability. Targeting the current density of the fast inward channels (g_{fi}) largely impacts CV by modulating upstroke velocity and AP amplitude, as well as regulating APD owing to the effect discussed previously where only sufficiently strong excitations are able to fully activate the slow inward current (Fenton and Karma, 1998). An increased fast inward channel density therefore increases the excitation wavelength by simultaneously augmenting APD and CV. However, the dependence of the maximum distance traveled by a rotor on this property is quite complex, where the multiple peaks in this biomarker correspond to shifts through different types of rotor trajectories (circles into epicycloids into helices into hypocycloids, as also observed in the two-parameter case), here further complicated by the variability in other cell properties. Increased channel density also tends to increase the complexity of the rotor trajectory (lower OI_1), as the faster propagation causes the rotor to attempt to rotate more quickly (increased DF), promoting tip-wake interactions. The risk of breakup (lower OI_4) is however reduced, as in these situations the rotor tip makes longer linear runs along lines of conduction block. Note, however, that both the complexity of re-entry and the risk of breakup are reduced (higher OI_1 and OI_4, respectively) for decreasing values of g_{fi}, in spite of this implying a reduction of the excitation wavelength. This corresponds newly to situations of weak excitability, where the slow inward current can never activate and the APD rate-dependence is significantly lost, preventing repolarization heterogeneities that can lead to wave breakup.

The discussion above additionally applies to fast inward current inactivation (τ_v^+), given its concomitant role in modulating upstroke velocity and AP amplitude. However, a slower inactivation of the fast inward current (larger τ_v^+) results in a more marked decrease of the maximum distance traveled by a rotor, in spite of yielding an equivalent increase of the excitation wavelength and DF. This increases the chances of wavefront-waveback interactions, further increasing the complexity of the rotor trajectories (lower OI_1), and risk of breakup (lower OI_4).

Increasing the ERP by slowing the recovery of the fast inward channels (larger τ_{v2}^-) makes it harder for rotors to rotate, with re-entrant paths occupying more space and triggering the tissue at a slower rate in this case. This is captured by the mean effects of τ_{v2}^- for maximum distance and dominant frequency, and is achieved in the absence of any changes on either steady-state CV or APD. However, the organization indices show less expected responses to variability in this parameter. The complexity of rotor trajectories (OI_1) show no significant dependence on recovery of excitability. More remarkably, the risk of breakup (lower OI_4) actually *increases* in this case, as the slower recovery of excitability lengthens the timing window in which the fast inward channels are only partially recovered and weak excitations can be triggered. These weak excitations fail to completely activate the slow inward current, creating large APD discrepancies across the tissue and thus an increased repolarization heterogeneity and hence fibrillation. Importantly, this result challenges the hypothesis that

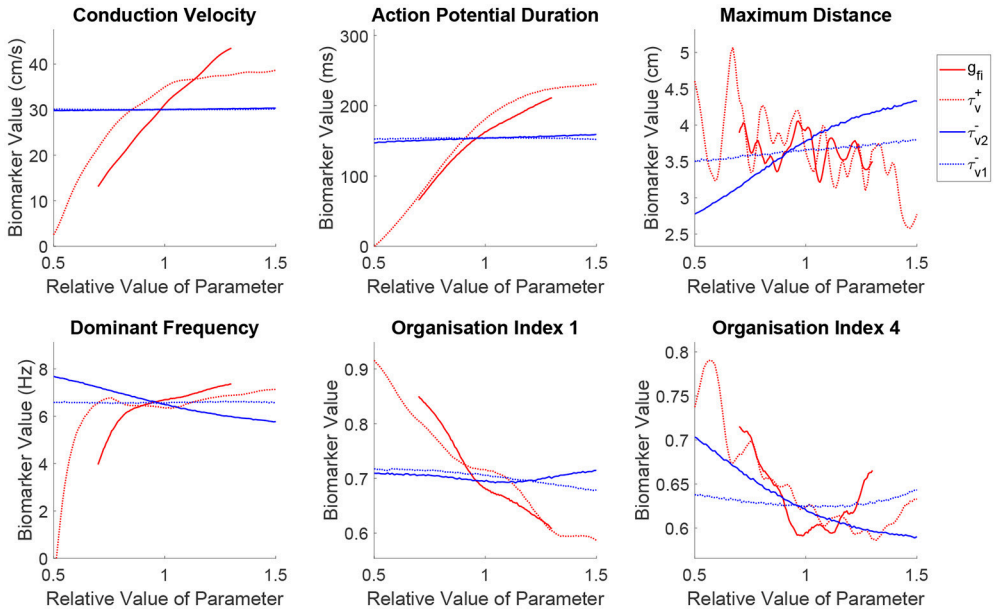

FIGURE 5 | Sustained re-entries respond more consistently to the recovery of tissue excitability than to fast inward current amplitude, but slowed recovery incurs an increased risk of wave breakup. Main effects of the parameters controlling tissue excitability and its recovery. Excitability strongly controls the shape of wavetip trajectories (OI_1) and rotor stability (OI_4), but has less consistent effect on the critical amount of tissue for sustained re-entry (maximum distance) and re-entrant frequency. On the other hand, by modulating ERP, recovery of fast inward channels does predictably control core size and frequency in sustained re-entries, but notably, slower recovery (increased ERP) is linked to an *increased* risk of wave breakup.

increased ERP may be protective in all cases against fibrillation by increasing the excitation wavelength (Smeets et al., 1986; Lee et al., 2013).

3.3.3. APD Modulation of Cardiac Wavelength Directly Controls Key Re-entry Properties, but Not Risk of Breakup

Just as in the previous section, we use the mean effects to quantitatively explore the impacts of variability in the parameters controlling repolarization on our set of spatial biomarkers, with the results visualized in **Figure 6**. Variability in any of the cell properties governing repolarization has essentially no effect on CV, whilst APD is strongly affected by the conductances of the two primary currents active during repolarization (g_{so} and g_{si}). Notably, the inactivation of the slow inward current (τ_w^+) has a not insignificant effect on APD (slower inactivation of the slow inward current prolongs the AP), but this parameter proves less important in controlling any of the considered re-entry biomarkers.

Variability in the primary repolarization current modulates APD and by extension ERP, determining the availability of excitable tissue for a spiral wave's tip as it rotates. A weaker repolarization (smaller g_{so}) increases APD, resulting in longer critical lengths and slower re-entrant DF. Variability in repolarization exerts stronger control and with more monotonic trends over these biomarkers as compared with excitability. ERP then modulates the overall size and angular velocity of these trajectories, which for reduced repolarization (smaller g_{so}) translates into a smaller complexity of rotor trajectories (increased OI_1) and reduced risk of fibrillatory and other chaotic behaviors (increased OI_4), nicely fulfilling the excitation wavelength hypothesis.

The effects described above are largely mirrored by the slow inward current, corresponding to its role in opposing repolarization. An increased current density (larger g_{si}) prolongs the AP plateau and therefore APD/ERP, increasing the critical size and decreasing the DF of re-entry and exerting a more dominant effect on the shape of rotor trajectories (increased OI_1) compared to the repolarization currents. However, when the conductance of the slow outward current is increased, a sharp decrease in rotor stability is observed (reduced OI_4), followed by an approximately level trend, which contradicts the excitation wavelength hypothesis given the increased ERP. The de-stabilizing effect of increased conductance of the slow inward current can be explained by the increased rate-dependence of the tissue, exacerbating spatial dispersion of repolarization that may arise and thus promoting wave breakup. In the context of rotor stability, this control over rate dependence is seen here to be more important than the current's control over APD, explaining some of the failure in using APD and CV to predict the class of re-entrant behavior that has been previously discussed.

3.3.4. Critical Windows of Excitability Determine Risk of Breakup

Our main effect analysis implicates the AP upstroke and the strength of the slow inward current as key factors controlling the likelihood that a rotor-driven re-entry devolves into fibrillation, along with an increased risk associated with slow recovery

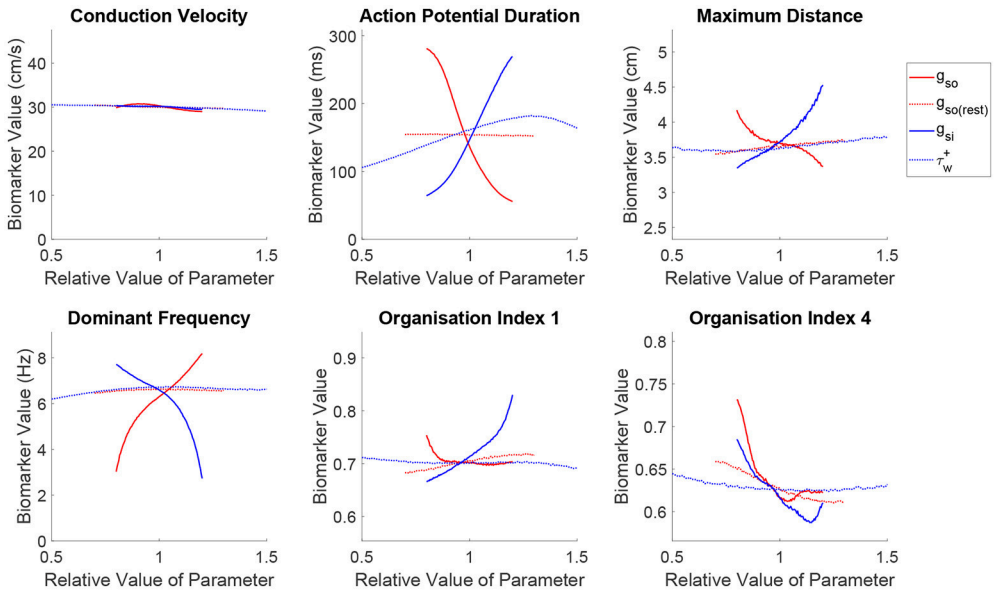

FIGURE 6 | Slow inward current exhibits important effects on re-entrant behavior beyond its control of APD. Main effects of the parameters controlling tissue repolarization. The conductances of the two currents that control APD are seen to strongly affect the critical size and frequency of rotor-driven re-entry, according to their modulation of ERP. However, the strengths of both of these currents exhibit a similar effect on rotor stability despite their opposing influences on APD/ERP, highlighting the importance of subtler restitution effects controlling the risk of breakup. The slow inward current also emerges as an important controller of the complexity of wavetip trajectory in the case of stable spiral waves.

of excitability. Using the classifier model, we now explore precisely how these cell properties together determine when such chaotic dynamics arise. Visualizations are presented in the form of two-dimensional maps (non-specified parameters held to base values), although our classifier automatically takes the simultaneous variability in all parameters into account.

Figure 7 shows how changes in excitability, as modulated by the conductance of the fast inward current, affects the balance of slow inward and outward currents in determining rotor stability. As implied by our former analysis of the main effects of g_{fi}, when excitation is too weak, all formed rotors remain stable as the slow inward current is not fully activated, diminishing the rate-dependence of the tissue. As the density of the fast inward current increases, the region of chaotic re-entrant behaviors determined by the balance between the slow inward and outward currents (which together primarily determine APD except when excitability is too weak) shifts significantly. This confirms that APD/ERP does not serve as a suitable predictor for the risk of fibrillation, and given the complex dependency on excitability we see here and in the main effects (**Figure 5**), neither does the cardiac wavelength as the product of CV and ERP. On the other hand, regardless of the strength of fast inward current, increased slow inward current is seen here to always carry a greater risk of wave breakup (provided APD is not so long that a rotor fails to be induced). This points to the importance of Ca^{2+} antagonism as a potential anti-arrhythmic mechanism (Merillat et al., 1990).

We next further explore our observation that slower recovery of excitability corresponds to decreased re-entrant stability, despite increasing ERP. **Figure 8** visualizes the effects of different time constants of fast inward channel recovery (τ_{v2}^-) on how the stability of re-entry is modulated by the two factors previously identified as critical determinants of fibrillatory behavior (conductances of the fast inward and slow inward currents). These parameter maps further support the results of the previous section, namely that increased slow inward current increases risk of fibrillation and that there exists a critical window of fast inward current density for initiation of wave breakup. The effect of delaying the recovery of excitability is clearly seen in shifting the high end of this critical window to higher values of g_{fi}. The stable re-entries that are affected by this are rotors with cores making long runs followed by rapid rotations (**Figure 3**), characteristic of human ventricular rotor dynamics (Bueno-Orovio et al., 2008). Finally, we note that when fast inward current inactivation (τ_v^+) is varied instead of g_{fi} (as the additional main determinant of tissue excitability), the resulting classification maps display all of the same key behaviors (Figure S4). This strongly suggests that the existence of critical windows of excitability is not only limited to the density of the fast inward current (as corroborated by the mean effect analysis of CV and OI_4 presented in **Figure 5**), with delayed fast inward inactivation as an additional pro-arrhythmic mechanism of risk of wave breakup.

4. DISCUSSION

In this work, we provide new mechanistic insights on the important interplay between cardiac refractoriness and arrhythmic risk, by identifying that both a slower recovery of fast inward channels or an increase of slow outward currents can promote chaotic rotor dynamics and wave breakup. This

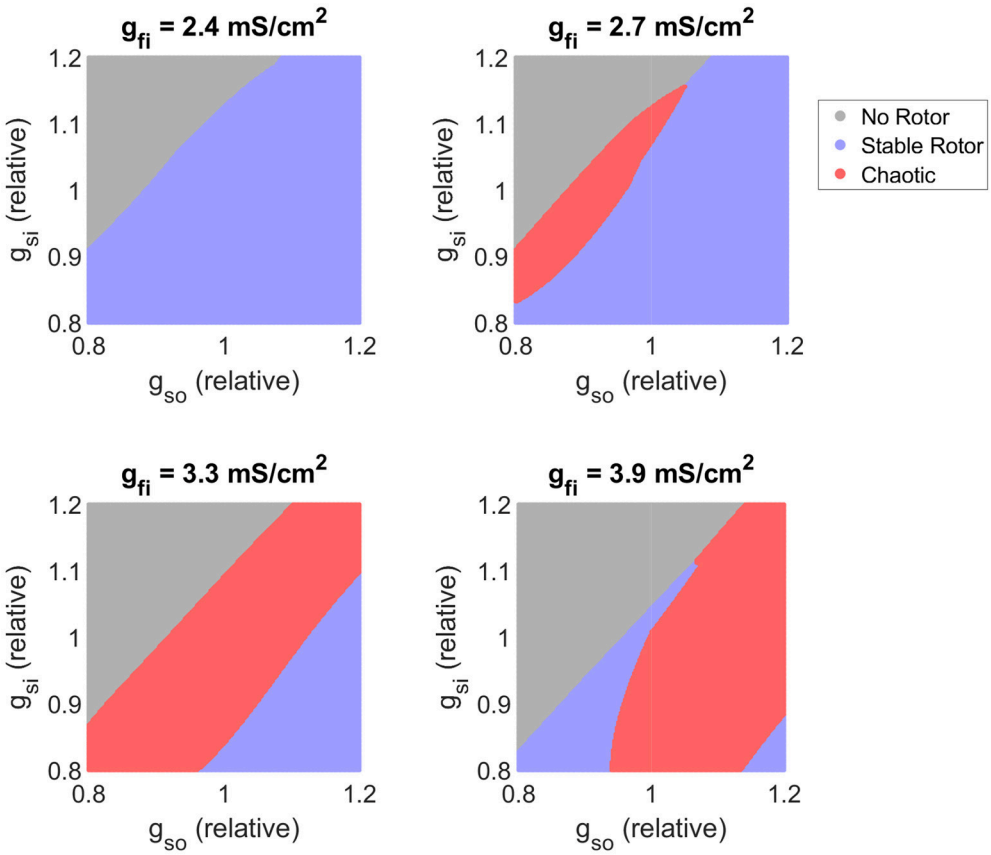

FIGURE 7 | Variability in excitability critically determines the balance of slow current conductances that produces chaotic re-entrant behaviors. Parameter maps as predicted by the classifier model. As tissue excitability (as controlled by the conductance of the fast inward current) increases, the balance of inward and outward currents that triggers chaotic re-entry behaviors shifts, highlighting its importance in interpreting APD in terms of fibrillation risk. Increased slow inward current is here consistently associated with an increased risk of wave breakup.

is in spite of increased ERP in each case, with arrhythmic risk mediated by an enlarged dispersion of repolarization associated with rate dependence. Our insights were only made possible by the development of a novel approach to constructing partitioned emulators synergistically coupled to cardiac electrophysiological simulations. This allowed not only data enrichment, but the automatic detection, classification, and analysis of different re-entrant behaviors, and quantitative determination of how the different electrophysiological properties modulating tissue excitability and refractoriness control the behavior of rotor-driven arrhythmias.

Steady-state properties of the tissue, APD, and CV, emerged as good predictors only for the critical amount of tissue required to sustain a rotor upon induction, but unable to identify chaotic regimes or susceptibility to wave breakup. The slope of the APD restitution curve, which quantifies the adaptation of APD to the pacing rate, has been well studied as a potential means of predicting rotor break-up (Nolasco and Dahlen, 1968; Karma, 1994; Qu et al., 2000; Nash et al., 2006), appealing because it can also be readily measured experimentally. However, flattening of this slope has been proposed as both an anti-arrhythmic target (Qu et al., 1999; Garfinkel et al., 2000) and a potentially pro-arrhythmic property (Franz, 2003), and a steep slope provides no guarantee of fibrillatory activity (Cherry and Fenton, 2004). Furthermore, recent studies have also demonstrated that APD restitution slope is primarily determined by steady-state APD (Bányász et al., 2009; Bárándi et al., 2010), and that normalizing the restitution curve as percentual changes of steady-state APD abolishes the differences in restitution slope in a variety of interventions (Shattock et al., 2017). This reinforces the role of steady state APD (and therefore excitation wavelength) for mechanistic investigation of re-entry, but also highlights the importance of considering the impacts of variation in cell-level properties directly as we do here, instead of just in terms of their modulation of tissue-level properties.

Variability in fast inward channel conductance and inactivation had an inconsistent effect on the critical size of rotors and for the most part little effect on the dominant frequency, despite directly controlling CV. These properties proved the primary determinant of wavetip trajectory for stable rotors, and their inconsistent effect on core size is thus explained by the shifting through the several different types of trajectory.

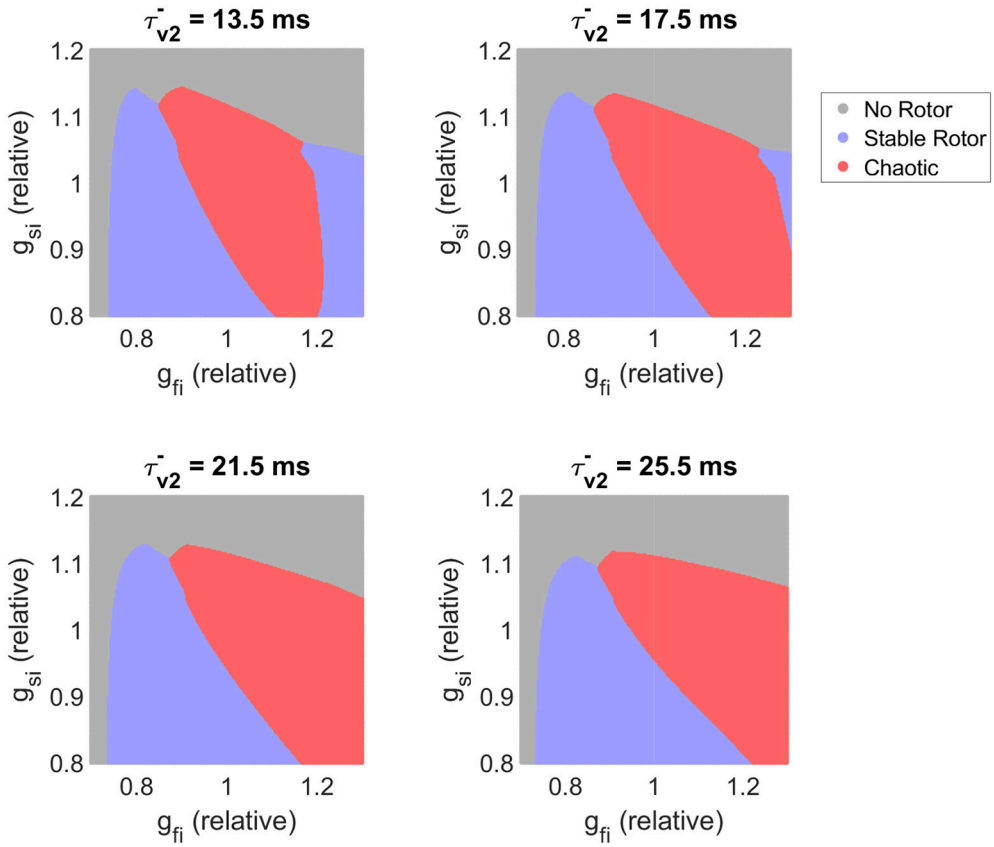

FIGURE 8 | Slower recovery of excitability widens the critical window of fast inward current density that can trigger breakup, and shifts this window to higher amounts of current density. Parameter maps as predicted by the classifier model. For the lower values of τ^-_{v2} plotted, the existence of a critical window of fast inward current strength associated with highest risk of wave breakup is clearly seen. As slow inward current increases in strength, this window widens and shifts to lower g_{fi} values. Slower recovery of fast inward channel availability (larger τ^-_{v2}) corresponds on the whole to destabilization of functional re-entry, but the specific effect depends also on the conductance of this current.

Only in the specific case of re-entries driven by circular rotor cores could rate control be achieved by slowed conduction. On the other hand, core size and frequency of re-entry depended much more consistently on the availability of excitable tissue (ERP), a function of both the recovery of excitability and the rate of repolarization. These results agree with the relative success of anti-arrhythmics that prolong ERP in treating ventricular tachycardias (Haverkamp et al., 1997; deSouza et al., 2015), the sustainability and severity of which depend critically on these two biomarkers. However, this effect must be considered in tandem with the potential pro-arrhythmic effects of such treatments that we discuss subsequently.

Depending on the electrophysiological properties of the simulated tissue, we observed wave breakup into fibrillation (potentially transitory or sustained for the full duration of simulation). Increased slow inward current was consistently associated with wave breakup, but increased slow outward current failed to show the opposite effect. This strongly suggests that it is not physiological variability in APD/ERP that controls breakup, and instead implicates the importance of slow inward currents in defining the extent of rate-dependence in the tissue and hence promoting dispersion of repolarization. In fact, we do note that some treatments that decrease ERP by antagonizing slow inward currents can trigger a reversion from ventricular fibrillation by reducing spatial dispersion of repolarization (Kimura et al., 2005; Bossu et al., 2018), consistent with these conclusions. Additionally, we observed a critical window of tissue excitability as a function of fast inward channel density that presents the highest risk of wave breakup. When excitability is too low, complete activation of the slow inward current does not occur regardless of activation timing, preventing spatial dispersion of recovery and hence breakup. When excitability is too high, the rotor tip exhibits longer linear runs between its rotations, and thus has reduced opportunity to interact with its own wake, as well as a much-increased probability of colliding with tissue boundaries and hence annihilating itself before an episode of fibrillation can occur.

Reduced sodium channel availability by slow recovery of the fast inward channels emerged as a significant promoter of chaotic behavior like wave breakup, by increasing the aforementioned dispersion of repolarization associated to differential activation of slow inward currents. Such a mechanism is indeed expected to

be of greater importance in the ventricles, where Ca^{2+} currents play a greater role in modulating rate dependence as compared to the more triangular APs in the atria (Sánchez et al., 2012). These results thus mechanistically explain the good performance of class Ic anti-arrhythmics in terminating atrial fibrillation, but at the cost of increased susceptibility to ventricular arrhythmias. This is for example the case of pilsicainide, a class Ic agent with slow recovery kinetics, successful in the clinical management of atrial fibrillation (Kanki et al., 1998; Fukuda et al., 2011) in spite of reports of its involvement in precipitating ventricular Torsade de Pointes (TdP) arrhythmias and sudden cardiac death (Nakatani et al., 2014), as further corroborated by its "possible risk" TdP category in the CredibleMeds database (Woosley and Romer, 1999). These results also hold for the controversial role of flecainide, another class Ic agent especially successful in the treatment of atrial fibrillation (Wang et al., 1992; Aliot et al., 2011), but with "known risk" TdP category (Woosley and Romer, 1999; Nasser et al., 2015), although its potent inhibition of potassium repolarizing currents can also mediate its pro-arrhythmic profile (Paul et al., 2002; Melgari et al., 2015; Passini et al., 2017).

Our findings with regard to the stability of functional re-entries were further supported and refined by the predictions of our SVM classifier model. After identifying the important ionic properties underlying risk of wave breakup, visualization of the classifier's predictions confirmed the importance of slow inward current density, the existence of critical windows of excitability, and the inability to rely upon APD or excitation wavelength as biomarkers for the risk of wave breakup. Furthermore, the pro-arrhythmic potential of slowed recovery of excitability was suggested to be of stronger importance for rotor cores that move via a pattern of a long run followed by a tight rotation, potentially differentiating the cases discussed above where class Ic anti-arrhythmics may or may not induce fibrillation in the ventricles.

Importantly, each of these observations on properties of re-entry and susceptibility to breakup have been obtained while considering variability across a large number of electrophysiological properties. The emergence of these behaviors across significant variation in the parameters suggests that they are in fact core electrophysiological behaviors, and not simply limited to the regime implied by the base parameter values considered in the FK model. Promisingly, a recent study using a biophysically-detailed model to explore variability in ionic current conductances with regard to the meander of rotor-driven re-entries in the atria also identified the Ca^{2+} and Na^{+} current densities as the most important parameters (Liberos et al., 2016), agreeing with their observed importance here, and reinforcing the potential of reduced ionic models to capture tissue-level dynamics of cardiac electrophysiology.

Methodologically, our work is probably the most comprehensive computational investigation to date of the complex interplay between cardiac excitability and refractoriness in modulating rotor-driven arrhythmic behavior and susceptibility to breakup, comprising more than 5,000 forward simulations of long-lasting arrhythmic episodes, further enriched to 80 million electrophysiological scenarios by the innovative application of emulation to this field. Despite the existence of clear bifurcations and chaotic regimes, our classification and emulation approaches proved capable of predicting with good accuracy the nature of rotor behavior and important spatial biomarkers characterizing rotor-driven re-entry, even with a relatively large number of electrophysiological properties allowed to vary. The highly complex and non-monotonic response surfaces for spatial biomarkers of re-entry presented in this study further illustrate that the dynamics of arrhythmia and fibrillation in cardiac tissue cannot be predicted by simple fits to the data such as linear regression. On the other hand, these are accurately and automatically captured by the use of emulation, also serving to eliminate representation bias in data analysis and interpretation. Altogether, our work exemplifies a synergistic combination of supercomputing, machine learning, and advanced statistical methods, pushing the frontiers of big data applications for investigations on cardiac electrophysiology.

Due to our specific focus on rotor dynamics, we have used here the reduced FK model (Fenton and Karma, 1998), which accurately captures the restitution properties of cardiac tissue but does not contain biophysical representations of each of the many currents that govern the APs of cardiac cells. Now that our approach to emulating cardiac electrophysiology models has been validated, further exploration of the impacts of variability in tissue excitability and refractoriness could be obtained by applying these techniques to biophysically detailed models with full characterization of ion channel kinetics, which may offer additional insights into how different anti-arrhythmic agents could be expected to perform in a variable population. However, and in spite of its reduced complexity, it is important to note that predictions on mechanisms of wave instability using the FK model have been confirmed with more sophisticated models (Rappel, 2001; ten Tusscher and Panfilov, 2006). Another natural extension is the emulation of spatial biomarkers for simulations on anatomically accurate geometries, thus incorporating structural effects and making the cases where a rotor fails to develop due to collision with the domain boundaries much more physiologically relevant. Such extensions to the cardiac model would not require any adjustment to our method for emulation, beyond perhaps the creation of additional classifications to categorize any new patterns of model behavior that might arise.

In conclusion, we have demonstrated how emulation can be adapted to models that govern the complex spatiotemporal dynamics of re-entry in cardiac electrophysiology. We have used the great reduction in computational cost offered by emulation in order to further explore how variability in tissue excitability, repolarization, and post-repolarization refractoriness all affect whether rotor-driven re-entries are electrophysiologically supported, the likelihood that they exhibit wave breakup and the severity of the arrhythmias that they induce. This variability analysis did not require the fixing of key model parameters to specific values, making the results much more generalizable. This type of approach is of especial relevance in cardiac electrophysiology, where parameter variability is known to be important, and has a significant effect on the interpretation of both experimental and modeling studies.

AUTHOR CONTRIBUTIONS

All authors contributed to the development of the presented methodology. BL, CD, and AB-O implemented the methodology and performed simulations. BL, KB, PB, and AB-O performed analysis of the results. All authors contributed to the drafting and refinement of the manuscript.

FUNDING

BL, PB, and KB are supported by the Australian Research Council under grant number CE140100049. CD is supported by the Australian Research Council's Discovery Early Career Researcher Award scheme under grant number DE160100741. AB-O is supported by a British Heart Foundation (BHF) Intermediate Basic Science Research Fellowship (FS/17/22/32644), an Impact for Infrastructure Award of the National Centre for the Replacement, Refinement & Reduction of Animals in Research (NC/P001076/1), and the Oxford BHF Centre of Research Excellence (RE/13/1/30181).

ACKNOWLEDGMENTS

Computational resources and services used in this work were provided by the HPC and Research Support Group, Queensland University of Technology, Brisbane, Australia. BL would like to thank the members of the Computational Cardiovascular Science group in the Department of Computer Science at the University of Oxford for hosting his visit and discussions regarding this work in September and October 2017.

SUPPLEMENTARY MATERIAL

The Supplementary Material for this article can be found online at: https://www.frontiersin.org/articles/10.3389/fphys.2018.01114/full#supplementary-material

REFERENCES

Aliot, E., Alessandro, C., Crijns, H. J., Goette, A., and Tamargo, J. (2011). Twenty-five years in the making: flecainide is safe and effective for the management of atrial fibrillation. *Europace* 13, 161–173. doi: 10.1093/europace/euq382

Allessie, M. A., Bonke, F. I. M., and Schopman, F. J. G. (1977). Circus movement in rabbit atrial muscle as a mechanism of tachycardia III. The "leading circle" concept: a new model of circus movement in cardiac tissue without the involvement of an anatomical obstacle. *Circ. Res.* 41, 9–18. doi: 10.1161/01.RES.41.1.9

Bányász, T., Horváth, B., Virág, L., Bárándi, L., Szentandrássy, N., Harmati, G., et al. (2009). Reverse rate dependency is an intrinsic property of canine cardiac preparations. *Cardiovasc. Res.* 84, 237–244. doi: 10.1093/cvr/cvp213

Bárándi, L., Virág, L., Jost, N., Horváth, Z., Koncz, I., Papp, R., et al. (2010). Reverse rate-dependent changes are determined by baseline action potential duration in mammalian and human ventricular preparations. *Basic Res. Cardiol.* 105, 315–323. doi: 10.1007/s00395-009-0082-7

Bartocci, E., Singh, R., von Stein, F. B., Amedome, A., Caceres, A. J. J., Castillo, J., et al. (2011). Teaching cardiac electrophysiology modeling to undergraduate students: laboratory exercises and GPU programming for the study of arrhythmias and spiral wave dynamics. *Adv. Physiol. Educ.* 35, 427–437. doi: 10.1152/advan.00034.2011

Beeler, G. W., and Reuter, H. (1977). Reconstruction of the action potential of ventricular myocardial fibres. *J. Physiol.* 268, 177–210. doi: 10.1113/jphysiol.1977.sp011853

Bossu, A., Joutman, M. J. C., Meijborg, V. M. F., Varkevisser, R., Beekman, Henriette, D. M., et al. (2018). Selective late sodium current inhibitor GS-458967. *Br. J. Pharmacol.* 175, 2470–2482. doi: 10.1111/bph.14217

Britton, O. J., Bueno-Orovio, A., Van Ammel, K., Lu, H. R., Towart, R., Gallacher, D. J., et al. (2013). Experimentally calibrated population of models predicts and explains intersubject variability in cardiac cellular electrophysiology. *Proc. Natl. Acad. Sci. U.S.A.* 110, E2098–E2105. doi: 10.1073/pnas.1304382110

Bueno-Orovio, A., Cherry, E. M., and Fenton, F. H. (2008). Minimal model for human ventricular action potentials in tissue. *J. Theor. Biol.* 253, 544–560. doi: 10.1016/j.jtbi.2008.03.029

Bueno-Orovio, A., Pérez-García, V. M., and Fenton, F. H. (2006). Spectral methods for partial differential equations in irregular domains: the spectral smoothed boundary method. *SIAM J. Sci. Comput.* 28, 886–900. doi: 10.1137/040607575

Cabo, C. (2015). Post-repolarization refractoriness increases vulnerability to block and initiation of reentrant impulses in heterogeneous infarcted myocardium. *Comput. Biol. Med.* 65, 209–219. doi: 10.1016/j.compbiomed.2015.04.037

Chang, E. T. Y., Strong, M., and Clayton, R. H. (2015). Bayesian sensitivity analysis of a cardiac cell model using a Gaussian process emulator. *PLoS ONE* 10:e0130252. doi: 10.1371/journal.pone.0130252

Cherry, E. M., Ehrlich, J. R., Nattel, S., and Fenton, F. H. (2007). Pulmonary vein reentry - properties and size matter: insights from a computational analysis. *Heart Rhythm* 4, 1553–1562. doi: 10.1016/j.hrthm.2007.08.017

Cherry, E. M., and Fenton, F. H. (2004). Suppression of alternans and conduction blocks despite steep APD restitution: electrotonic, memory, and conduction velocity restitution effects. *Am. J. Physiol. Heart Circ. Physiol.* 286, H2332–H2341. doi: 10.1152/ajpheart.00747.2003

Coronel, R., Janse, M. J., Opthof, T., Wilde, A. A., and Taggart, P. (2012). Postrepolarization refractoriness in acute ischemia and after antiarrhythmic drug administration: action potential duration is not always an index of the refractory period. *Heart Rhythm* 9, 977-982. doi: 10.1016/j.hrthm.2012.01.021

Cortes, C., and Vapnik, V. (1995). Support-vector networks. *Mach. Learn.* 20, 273–297.

Courtemanche, M. (1996). Complex spiral wave dynamics in a spatially distributed ionic model of cardiac electrical activity. *Chaos* 6, 579–600.

Courtemanche, M., and Winfree, A. T. (1991). Re-entrant rotating waves in a Beeler-Reuter based model of two-dimensional cardiac electrical activity. *Int. J. Bifurcation Chaos* 1, 431–444.

deSouza, I. S., Martindale, J. L., and Sinert, R. (2015). Antidysrhythmic drug therapy for the termination of stable, monomorphic ventricular tachycardia: a systematic review. *Emerg. Med. J.* 32, 161–167. doi: 10.1136/emermed-2013-202973

Efimov, I. R., Krinsky, V. I., and Jalife, J. (1995). Dynamics of rotating vortices in the beeler-reuter model of cardiac tissue. *Chaos Solitons Fractals* 5, 513–526. doi: 10.1016/0960-0779(95)95761-F

Elming, H., Brendorp, B., Pehrson, S., Pedersen, O. D., Køber, L., and Torp-Petersen, C. (2004). A benefit-risk assessment of class III antiarrhythmic agents. *Expert. Opin. Drug Saf.* 3, 559–577. doi: 10.1517/14740338.3.6.559

Feng, J., Yue, L., Wang, Z., and Nattel, S. (1998). Ionic mechanisms of regional action potential heterogeneity in the canine right atrium. *Circ. Res.* 7, 541–551. doi: 10.1161/01.RES.83.5.541

Fenton, F. H., Cherry, E. M., Hastings, H. M., and Evans, S. J. (2002). Multiple mechanisms of spiral wave breakup in a model of cardiac electrical activity. *Chaos* 12, 852–892. doi: 10.1063/1.1504242

Fenton, F. H., and Karma, A. (1998). Vortex dynamics in three-dimensional continuous myocardium with fiber rotation: filament instability and fibrillation. *Chaos* 8, 20–47. doi: 10.1063/1.166311

Franz, M. R. (2003). The electrical restitution curve revisited: steep or flat slope—which is better? *J. Cardiovasc. Electrophysiol.* 14, S140–S147. doi: 10.1046/j.1540.8167.90303.x

Franz, M. R., Gray, R. A., Karasik, P., Moore, H. J., and Singh, S. N. (2014). Drug-induced post-repolarization refractoriness as an antiarrhythmic principle and its underlying mechanism. *Europace* 16, iv39–iv45. doi: 10.1093/europace/euu274

Fukuda, K., Watanabe, J., Yagi, T., Wakayama, Y., Nakano, M., Kondo, M., et al. (2011). A sodium channel blocker, pilsicainide, produces atrial post-repolarization refractoriness through the reduction of sodium channel availability. *Tohoku J. Exp. Med.* 225, 35–42. doi: 10.1620/tjem.225.35

Garfinkel, A., Kim, Y. H., Voroshilovsky, O., Qu, Z., Kil, J. R., Lee, M. H., et al. (2000). Preventing ventricular fibrillation by flattening cardiac restitution. *Proc. Natl. Acad. Sci. U.S.A.* 97, 6061–6066. doi: 10.1073/pnas.090492697

Geneser, S. E., Kirby, R. M., and MacLeod, R. S. (2008). Application of stochastic finite element methods to study the sensitivityof ECG forward modeling to organ conductivity. *IEEE Trans. Biomed. Eng.* 55, 31–40. doi: 10.1109/TBME.2007.900563

Gough, W. B., Mehra, R., Restivo, M., Zeiler, R. H., and El-Sherif, N. (1985). Reentrant ventricular arrhythmias in the late myocardial infarction period in the dog: 13. correlation of activation and refractory maps. *Circ. Res.* 57, 432–442. doi: 10.1161/01.RES.57.3.432

Gramacy, R. B., and Lee, Herbert, K. H. (2008). Bayesian treed Gaussian process models with an application to computer modeling. *J. Am. Stat. Assoc.* 103, 1119–1130. doi: 10.1198/016214508000000689

Grosu, R., Smolka, S. A., Corradini, F., Wasilewska, A., Entcheva, E., and Bartocci, E. (2009). Learning and detecting emergent behaviour in networks of cardiac myocytes. *Commun. ACM* 52, 97–105. doi: 10.1145/1467247.1467271

Haverkamp, W., Martinez-Rubio, A., Hief, C., Lammers, A., M uhlenkamp, S., Wichter, T., et al. (1997). Efficacy and safety of *d,l*-sotalol in patients with ventricular tachycardia and in survivors of cardiac arrest. *J. Am. Coll. Cardiol.* 30, 487–495. doi: 10.1016/S0735-1097(97)00190-3

Holden, P. B., and Edwards, N. R. (2010). Dimensionally reduced emulation of an AOGCM for application to integrated assessment modelling. *Geophys. Res. Lett.* 37:L21707. doi: 10.1029/2010GL045137

Hsu, C.-W., and Lin, C.-J. (2002). A comparison of methods for multiclass support vector machines. *IEEE Trans. Neural Netw.* 13, 415–425. doi: 10.1109/72.991427

Johnston, B. M., Coveney, S., Chang, E. T. Y., Johnston, P. R., and Clayton, R. H. (2017). Quantifying the effect of uncertainty in input parameters in a simplified bidomain model of partial thickness ischaemia. *Med. Biol. Eng. Comput.* 56, 761–780. doi: 10.1007/s11517-017-1714-y

Johnstone, R. H., Chang, E. T. Y., Bardenet, R., de Boer, T. P., Gavaghan, D. J., Pathmanathan, P., et al. (2016). Uncertainty and variability in models of the cardiac action potential: can we build trustworthy models? *J. Mol. Cell. Cardiol.* 96, 49–62. doi: 10.1016/j.yjmcc.2015.11.018

Kanki, H., Mitamura, H., Takatsuki, S., Sueyoshi, K., Shinagawa, K., Sato, T., et al. (1998). Postrepolarization refractoriness as a potential anti-atrial fibrillation mechanism of pilsicainide, a pure sodium channel blocker with slow recovery kinetics. *Cardiovasc. Drugs Ther.* 12, 475–482. doi: 10.1023/A:1007758217189

Karma, A. (1994). Electrical alternans and spiral wave breakup in cardiac tissue. *J. Appl. Physiol.* 4, 461–472. doi: 10.1063/1.166024

Kim, H.-M., Mallick, B. K., and Holmes, C. C. (2005). Analyzing nonstationary spatial data using piecewise Gaussian processes. *J. Am. Stat. Assoc.* 100, 653–668. doi: 10.1198/016214504000002014

Kimura, H., Kawahara, K., Yamauchi, Y., and Miyaki, J. (2005). On the mechanisms for the conversion of ventricular fibrillation to tachycardia by perfusion with ruthenium red. *J. Electrocardiol.* 38, 364–370. doi: 10.1016/j.jelectrocard.2005.05.007

Kirchhof, P. F., Fabritz, C. L., and Franz, M. R. (1998). Postrepolarization refractoriness versus conduction slowing caused by class I antiarrhythmic drugs: antiarrhythmic and proarrhythmic effects. *Circulation* 97, 2567–2574. doi: 10.1161/01.CIR.97.25.2567

Kneller, J., Kalifa, J., Zou, R., Zaitsev, A. V., Warren, M., Berenfeld, O., et al. (2005). Mechanisms of atrial fibrillation termination by pure sodium channel blockade in an ionically-realistic mathematical model. *Circ. Res.* 96, e35–e47. doi: 10.1161/01.RES.0000160709.49633.2b

Lawson, B. A. J., Drovandi, C. C., Burrage, P., Rodriguez, B., and Burrage, K. (2017). "Dimension reduction for the emulation of cardiac electrophysiology models for single cells and tissue," in *Computing in Cardiology (Conference Proceedings)* (Long Beach, CA).

Lawson, B. A. J., Drovandi, C. C., Cusimano, N., Burrage, P., Rodriguez, B., and Burrage, K. (2018). Unlocking data sets by calibrating populations of models to data density: a study in atrial electrophysiology. *Sci. Adv.* 4:e1701676. doi: 10.1126/sciadv.1701676

Lee, A. M., Aziz, A., Didesch, J., Clark, K. L., Schuessler, R. B., and Damiano, R. J. (2013). Importance of atrial surface area and refractory period in sustaining atrial fibrillation: testing the critical mass hypothesis. *J. Thorac. Cardiovasc. Surg.* 146, 593–598. doi: 10.1016/j.jtcvs.2012.04.021

Lee, Y.-S., Hwang, M., Song, J.-S., Li, C., Joung, B., Sobie, E. A., et al. (2016). The contribution of ionic currents to rate-dependent action potential duration and pattern of reentry in a mathematical model of human atrial fibrillation. *PLoS ONE* 11:0150779. doi: 10.1371/journal.pone.0150779

Liberos, A., Bueno-Orovio, A., Rodrigo, M., Ravens, U., Hernandez-Romero, I., Fernandez-Aviles, F., et al. (2016). Balance between sodium and calcium currents underlying chronic atrial fibrillation termination: an *in silico* intersubject variability study. *Heart Rhythm* 13, 2358–2365. doi: 10.1016/j.hrthm.2016.08.028

Lombardo, D. M., Fenton, F. H., Narayan, S. M., and Rappel, W.-J. (2016). Comparison of detailed and simplified models of human atrial myocytes to recapitulate patient specific properties. *PLoS Comp. Biol.* 12:e1005060. doi: 10.1371/journal.pcbi.1005060

Mckay, M. D., Beckman, R. J., and Conover, W. J. (1979). A comparison of three methods for selecting values of input variables in the analysis of output from a computer code. *Technometrics* 21, 239–245.

Melgari, D., Zhang, Y., El Harchi, A., Dempsey, C. E., and Hancox, J. C. (2015). Molecular basis of hERG potassium channel blockade by the class Ic antiarrhythmic flecainide. *J. Mol. Cell. Cardiol.* 86, 42–53. doi: 10.1016/j.yjmcc.2015.06.021

Merillat, J. C., Lakatta, E. G., Hano, O., and Guarnieri, T. (1990). Role of calcium and the calcium channel in the initiation and maintenance of ventricular fibrillation. *Circ. Res.* 67, 1115–1123.

Moe, G. K., and Abildskov, J. A. (1959). Atrial fibrillation as a self-sustaining arrhythmia independent of focal discharge. *Am. Heart J.* 58, 59–70.

Muñoz, V., Grzeda, K. R., Desplantez, T., Pandit, S. V., Mironov, S., Taffet, S. M., et al. (2007). Adenoviral expression of I_{Ks} contributes to wavebreak and fibrillatory conduction in neonatal rat ventricular cardiomyocyte monolayers. *Circ. Res.* 101, 475–483. doi: 10.1161/CIRCRESAHA.107.149617

Muszkiewicz, A., Britton, O. J., Gemmell, P., Passini, E., Sanchez, C., Zhou, X., et al. (2016). Variability in cardiac electrophysiology: using experimentally-calibrated populations of models to move beyond the single virtual physiological human paradigm. *Prog. Biophys. Mol. Biol.* 120, 115–127. doi: 10.1016/j.pbiomolbio.2015.12.002

Nakatani, S., Taniike, M., Makino, N., Egami, Y., Shutta, R., Tanouchi, J., et al. (2014). A case of sudden cardiac death due to pilsicainide-induced Torsades de Pointes. *Korean Circ. J.* 44, 122–124. doi: 10.4070/kcj.2014.44.2.122

Nash, M. P., Bradley, C. P., Sutton, P. M., Clayton, R. H., Kallis, P., Hayward, M. P., et al. (2006). Whole heart action potential duration restitution properties in cardiac patients: a combined clinical and modelling study. *Exp. Physiol.* 91, 339–354. doi: 10.1113/expphysiol.2005.031070

Nasser, M., Idris, S., Marinelli, K., and Machado, C. (2015). Flecainide-induced Torsades de pointes: case report and review of literature. *Rev. Cardiovasc. Med.* 16, 214–220. doi: 10.3909/ricm0761

Nattel, S., Kneller, J., Zou, R., and Leon, L. J. (2003). Mechanisms of termination of atrial fibrillation by Class I antiarrhythmic drugs: evidence from clinical, experimental, and mathematical modeling studies. *J. Cardiovasc. Electrophysiol.* 14, S133–S139. doi: 10.1046/j.1540.8167.90302.x

Nolasco, J. B., and Dahlen, R. W. (1968). A graphic method for the study of alternation in cardiac action potentials. *J. Appl. Physiol.* 25, 191–196.

Oakley, J. E., and O'Hagan, A. (2004). Probabilistic sensitivity analysis of complex models: a Bayesian approach. *J. R. Statist. Soc. B* 66, 751–769. doi: 10.1111/j.1467-9868.2004.05304.x

Pandit, S. V., Berenfeld, O., Anumonwo, J. M. B., Zaritski, R. M., Kneller, J., Nattel, S., et al. (2005). Ionic determinants of functional reentry in a 2-D model of human atrial cells during simulated chronic atrial fibrillation. *Biophys. J.* 88, 3806–3821. doi: 10.1529/biophysj.105.060459

Pandit, S. V., and Jalife, J. (2013). Rotors and the dynamics of cardiac fibrillation. *Circ. Res.* 112, 849–862. doi: 10.1161/CIRCRESAHA.111.300158

Passini, E., Britton, O. J., Lu, H. R., Rohrbacher, J., Hermans, A. N., Gallacher, D. J., et al. (2017). Human *in silico* drug trials demonstrate higher accuracy than animal models in predicting clinical pro-arrhythmic cardiotoxicity. *Front. Physiol.* 8:668. doi: 10.3389/fphys.2017.00668

Pathmanathan, P., Shotwell, M. S., Gavaghan, D. J., Cordeiro, J. M., and Gray, R. A. (2015). Uncertainty quantification of fast sodium current steady-state inactivation for multi-scale models of cardiac electrophysiology. *Prog. Biophys. Mol. Biol.* 117, 4–18. doi: 10.1016/j.pbiomolbio.2015.01.008

Paul, A., Witchel, H., and Hancox, J. C. (2002). Inhibition of the current of heterologously expressed HERG potassium channels by flecainide and comparison with quinidine, propafenone and lignocaine. *Br. J. Pharmacol.* 136, 717–729. doi: 10.1038/sj.bjp.0704784

Qu, Z., Kil, J., Fagen, X., Garfinkel, A., and Weiss, J. N. (2000). Scroll wave dynamics in a three-dimensional cardiac tissue model: roles of restitution, thickness and fiber rotation. *Biophys. J.* 78, 2761–2775. doi: 10.1016/S0006-3495(00)76821-4

Qu, Z., Weiss, J. N., and Garfinkel, A. (1999). Cardiac electrical restitution properties and stability of reentrant spiral waves: a simulation study. *Am. J. Physiol. Heart Circ. Physiol.* 276, H269–H283.

Rappel, W. J. (2001). Filament instability and rotational tissue anisotropy: a numerical study using detailed cardiac models. *Chaos* 11, 71–80. doi: 10.1063/1.1338128

Rasmussen, C. E., and Williams, C. K. I. (2006). *Gaussian Processes for Machine Learning*. Bognor Regis: MIT Press.

Rensma, P. L., Allessie, M. A., Lammers, W. J., Bonke, F. I., and Schalij, M. J. (1988). Length of excitation wave and susceptibility to reentrant atrial arrhythmias in normal conscious dogs. *Circ. Res.* 62, 395–410.

Rush, S., and Larsen, H. (1978). A practical algorithm for solving dynamic membrane equations. *IEEE Trans. Biomed. Eng.* 25, 389–392.

Sacks, J., Welch, W. J., Mitchell, T. J., and Wynn, H. P. (1989). Design and analysis of computer experiments. *Stat. Sci.* 4, 409–423.

Sánchez, C., Corrias, A., Bueno-Orovio, A., Davies, M., Swinton, J., Jacobson, I., et al. (2012). The Na^+/K^+ pump is an important modulator of refractoriness and rotor dynamics in human atrial tissue. *Am. J. Physiol. Heart Circ. Physiol.* 302, H1146–H1159. doi: 10.1152/ajpheart.00668.2011

Sarkar, A. X., Christini, D. J., and Sobie, E. A. (2012). Exploiting mathematical models to illuminate electrophysiological variability between individuals. *J. Physiol.* 590, 2555–2567. doi: 10.1113/jphysiol.2011.223313

Shattock, M. J., Park, K. C., Yang, H. Y., Lee, A. W. C., Niederer, S., MacLeod, K. T., et al. (2017). Restitution slope is principally determined by steady-state action potential duration. *Cardiovasc. Res.* 113, 817–828. doi: 10.1093/cvr/cvx063

Simpson, T. W., Peplinski, J. D., Koch, P. N., and Allen, J. K. (2001). Metamodels for computer-based engineering design: survey and recommendations. *Eng. Comput.* 17, 129–150. doi: 10.1007/PL00007198

Sims, C., Reisenweber, S., Viswanathan, P. C., Choi, B.-R., Walker, W. H., and Salama, G. (2008). Sex, age, and regional differences in L-type calcium current are important determinants of arrhythmia phenotype in rabbit hearts with drug-induced long QT type 2. *Circ. Res.* 102, e86–e100. doi: 10.1161/CIRCRESAHA.108.173740

Smeets, J. L. R. M., Allessie, M. A., Lammers, W. J. E. P., Bonke, Felix, I. M., and Hollen, J. (1986). The wavelength of the cardiac impulse and reentrant arrhythmias in isolated rabbit atrium: the role of heart rate, autonomic transmitters, temperature and potassium. *Circ. Res.* 58, 96–108.

Sobie, E. A. (2009). Parameter sensitivity analysis in electrophysiological models using multivariable regression. *Biophys. J.* 96, 1264–1274. doi: 10.1016/j.bpj.2008.10.056

Strang, G. (1968). On the construction and comparison of difference schemes. *SIAM J. Numer. Anal.* 5, 506–517.

Sundnes, J., Lines, G. T., Cai, X., Nielsen, B. F., Mardal, K., and Tveito, A. (2006). *Computing the Electrical Activity in the Heart*. Berlin; Heidelberg: Springer-Verlag.

Swenson, D. J., Geneser, S. E., Stinstra, J. G., Kirby, R. M., and MacLeod, R. S. (2011). Cardiac position sensitivity study in the electrocardiographic forward problem using stochastic collocation and boundary element methods. *Ann. Biomed. Eng.* 39, 2900–2910. doi: 10.1007/s10439-011-0391-5

ten Tusscher, K. H. W. J., and Panfilov, A. V. (2006). Alternans and spiral breakup in a human ventricular tissue model. *Am. J. Physiol. Heart Circ. Physiol.* 291, H1088–H1100. doi: 10.1152/ajpheart.00109.2006

Tse, G., and Yan, B. P. (2017). Traditional and novel electrocardiographic conduction and repolarization markers of sudden cardiac death. *Europace* 19, 712–721. doi: 10.1093/europace/euw280

Wallman, M., Smith, N. P., and Rodriguez, B. (2014). Computational methods to reduce uncertainty in the estimation of cardiac conduction properties from electroanatomical recordings. *Med. Image Anal.* 18, 228–240. doi: 10.1016/j.media.2013.10.006

Wang, Z., Pagé, P., and Nattel, S. (1992). Mechanism of flecainide's antiarrhythmic action in experimental atrial fibrillation. *Circ. Res.* 71, 271–287.

Wiener, N., and Rosenblueth, A. (1946). The mathematical formulation of the problem of conduction of impulses in a network of connected excitable elements, specifically in cardiac muscle. *Arch. Inst. Cardiol. Mex.* 16, 205–265.

Wit, A. L., and Cranefield, P. F. (1978). Reentrant excitation as a cause of cardiac arrhythmias. *Am. J. Physiol.* 235, H1–H7.

Wolbrette, D. L. (2003). Risk of proarrhythmia with class III antiarrhythmic agents: sex-based differences and other issues. *Am. J. Cardiol.* 91, 39D–44D. doi: 10.1016/S0002-9149(02)03378-7

Woosley, R., and Romer, K. (1999). *QTdrugs List*. AZCERT, Inc. Available online at: www.crediblemeds.org. [Online] (Accessed April 1, 2018).

Zhou, X., Bueno-Orovio, A., Orini, M., Hanson, B., Hayward, M., Taggart, P., et al. (2016). *In vivo* and *in silico* investigation into mechanisms of frequency dependence of repolarization alternans in human ventricular cardiomyocytes. *Circ. Res.* 118, 266–278. doi: 10.1161/CIRCRESAHA.115.307836

Zhou, X., Bueno-Orovio, A., and Rodriguez, B. (2018). *In silico* evaluation of arrhythmia. *Curr. Opin. Physiol.* 1, 95–103. doi: 10.1016/j.cophys.2017.11.003

Conflict of Interest Statement: The authors declare that the research was conducted in the absence of any commercial or financial relationships that could be construed as a potential conflict of interest.

The reviewer RC and handling editor declared their shared affiliation at the time of the review.

frontiers in Physiology

ORIGINAL RESEARCH
published: 22 June 2018
doi: 10.3389/fphys.2018.00764

Killing Many Birds With Two Stones: Hypoxia and Fibrosis Can Generate Ectopic Beats in a Human Ventricular Model

Rafael Sachetto[1,2], *Sergio Alonso*[2,3] *and Rodrigo Weber dos Santos*[2]*

[1] Department of Computer Science, Universidade Federal de São João del-Rei, São João del-Rei, Brazil, [2] Graduate Program in Computational Modeling, Universidade Federal de Juiz de Fora, Juiz de Fora, Brazil, [3] Department of Physics, Universitat Politècnica de Catalunya, Barcelona, Spain

During cardiac diseases many types of anatomical and functional remodeling of cardiac tissue can occur. In this work, we focus on two conditions: hypoxia and fibrosis, which are part of complex pathological modifications that take place in many cardiac diseases (hypertrophic cardiomyopathy, hypertensive heart disease, and recurrent myocardial infarction) and respiratory diseases (obstructive pulmonary disease, obstructive sleep apnea, and cystic fibrosis). Using computational models of cardiac electrophysiology, we evaluate if the interplay between hypoxia and fibrosis is sufficient to trigger cardiac arrhythmia. We study the mechanisms behind the generation of ectopic beats, an arrhythmic trigger also known as premature ventricular contractions (PVCs), in regions with high hypoxia and fibrosis. First, we modify an electrophysiological model of myocytes of the human left ventricle to include the effects of hypoxia. Second, diffuse fibrosis is modeled by randomly replacing cardiac myocytes by non-excitable and non-conducting cells. The Monte Carlo method is used to evaluate the probability of a region to generate ectopic beats with respect to different levels of hypoxia and fibrosis. In addition, we evaluate the minimum size of three-dimensional slabs needed to sustain reentries for different stimulation protocols. The observed mechanism behind the initiation of ectopic beats is unidirectional block, giving rise to sustained micro-reentries inside the region with diffuse fibrosis and hypoxia. In summary, our results suggest that hypoxia and fibrosis are sufficient for the creation of a focal region in the heart that generates PVCs.

Keywords: ectopic beats, fibrosis, hypoxia, cardiac electrophysiology, heart simulations, percolation threshold, micro-reentries

OPEN ACCESS

Edited by:
Flavio H. Fenton,
Cornell University, United States

Reviewed by:
Olivier Bernus,
Université de Bordeaux, France
Richard H. Clayton,
University of Sheffield,
United Kingdom

***Correspondence:**
Rodrigo Weber dos Santos
rodrigo.weber@ufjf.edu.br

Specialty section:
This article was submitted to Computational Physiology and Medicine, a section of the journal Frontiers in Physiology

Received: *15 January 2018*
Accepted: *31 May 2018*
Published: *22 June 2018*

Citation:
Sachetto R, Alonso S and dos Santos RW (2018) Killing Many Birds With Two Stones: Hypoxia and Fibrosis Can Generate Ectopic Beats in a Human Ventricular Model. Front. Physiol. 9:764. doi: 10.3389/fphys.2018.00764

1. INTRODUCTION

Cardiovascular diseases frequently promote life-threatening arrhythmias. For some diseases, studies suggest the existence of anatomical triggers for dangerous arrhythmias (de Bakker et al., 1988; Haïssaguerre et al., 1998; Ng, 2006; Jalife, 2011). These pathological regions would repeatedly re-excite the neighboring cardiac tissue, acting as sources, drivers, or foci of ectopic beats. Any area of the heart other than the sinoatrial node, which originates a heart beat is an ectopic pacemaker. In particular, when the region is in the left ventricle, it is the source of premature ventricular contractions (PVCs) (Boineau and Cox, 1973; Ruberman et al., 1977).

In this work, we use a computational model of the human left ventricle to investigate the generation of ectopic beats in a heterogeneous cardiac region under hypoxia and with diffuse fibrosis. Hypoxia accounts for the lack of blood supply for the cardiac tissue, whereas fibrosis is related to the increase of collagen and fibroblast as a reparative or reactive process. Hypoxia can significantly change cardiac electrophysiology and fibrotic regions are non-conducting and non-exciting areas that increase the conduction heterogeneity of cardiac tissue.

The number, diversity and types of processes in cardiac diseases that result on functional or anatomical modifications can be overwhelming, as well as the complexity of their multifaceted interactions. Nevertheless, these two processes, hypoxia and fibrosis, are common in many different cardiac diseases and have been suggested to be related to cardiac arrhythmia. For instance, there is a variety of diseases that can compromise the micro-structure of cardiac tissue in the ventricles via the process of fibrosis. This is the case in hypertrophic cardiomyopathy (HCM) (Maron, 2002), hypertensive heart disease (HHD) (Diamond and Phillips, 2005), and myocardial infarction (MI) (Schmidt et al., 2007). In turn, these diseases, all with the substrate of fibrosis, can also, due to different reasons, induce hypoxia or acute ischemia, and trigger fatal arrhythmias.

Hypertrophic cardiomyopathy is the most common cause of sudden death in young athletes. It is characterized by cardiac and myocyte hypertrophy, myocyte disarray, and fibrosis. Sudden cardiac death may be the first manifestation of the disease. Approximately 70% of all patients with HCM die suddenly (Maron et al., 1995; Ho et al., 2010; Namboodiri and Francis, 2010; Alkon et al., 2012). The high arrhythmic propensity in HCM is due to the combination of the abnormal substrate, like fibrosis, and ischemia or hypoxia (Alkon et al., 2012), in general associated with intense physical exercise. Extreme physical exercise may induce, in HCM patients, diastolic pressure and volume overload of the ventricles, and hypoxemia, i.e., low oxygen saturation in the blood. These can result in a transitory ischemia, usually near the endocardial region. Ventricular arrhythmias related with exercise are strongly correlated to cardiac fibrosis in patients with hypertrophic cardiomyopathy (van Rijsingen et al., 2011). The arrhythmias originate from areas with a high extent of fibrosis or from regions directly adjacent to these areas.

Hypertensive heart disease comprises of structural, functional, and endothelial processes that alter coronary hemodynamics and ventricular function. As in HCM, ventricular enlargement or hypertrophy is also combined with fibrosis. In addition, changes in coronary arterial flow involve ventricular wall compression, luminal obstruction, the increased wall thickening of the hypertensive arteriole and reduced ventricular wall vascularity (Frohlich, 2001). These pathophysiological changes are frequently associated with ischemic heart disease and the combination with the fibrotic substrate increases the risk of sudden cardiac death (Frohlich, 2000).

Most of myocardial infarction (MI) involves the occlusion of a coronary artery of the ventricle or other types of coronary artery diseases. In the acute phase, ischemia and necrosis (Chiong et al., 2011) appear. Early revascularization and the use of new medicaments greatly contribute to improve survival to acute MI. During the healing phase of MI, fibrosis substitutes necrotic cells (Shi et al., 2017). However, post-MI patients remain at substantial risk for ventricular arrhythmias (Pouleur et al., 2010). In fact, most of the deaths in post-MI patients are due to arrhythmia and recurrent MI, i.e., a second episode of acute MI at the same region of the first one (Ørn et al., 2005). Therefore, once again, we recognize the existence of a heterogeneous substrate that involves fibrosis from the first MI episode, hypoxia and ischemia during the recurrent MI, and the relation to fatal arrhythmias.

The aforementioned cardiac diseases suggest a sequence of events: structural changes that involve fibrosis are followed by hypoxia or ischemia, that in turn results in cardiac arrhythmia. However, the relation between fibrosis and hypoxia is not trivial. For instance, some respiratory diseases that involve chronic, transitory, or intermittent hypoxia induce the process of fibrosis in cardiac tissue, and increase the occurrence of cardiac arrhythmias. Studies in patients with chronic obstructive pulmonary disease (COPD), obstructive sleep apnea (OSA), and with cystic fibrosis (CF) have shown that low oxygen saturation during exercise may predispose them to cardiac ventricular arrhythmias (Cheong et al., 1990; Ruf and Hebestreit, 2009; Cintra et al., 2010). Cardiac arrhythmia has been also reported in patients with sleep apnea syndrome (SAS) (Guilleminault et al., 1983). In turn, chronic hypoxia induces cardiomyocyte hypertrophy and interstitial fibrosis in the LV myocardium (Miwa and Sasaguri, 2007; Yamashita et al., 2007). In fact, cardiac fibrosis can develop from different stimuli, including ischemia, inflammation, pressure overload and volume overload. A common feature of all these stimuli is tissue hypoxia, either directly or indirectly, due to increase of oxygen consumption by infiltrating inflammatory cells and activated resident cells (Gao et al., 2014). This process is referred as hypoxia-induced fibrosis and has been a recent important topic of research (Darby and Hewitson, 2016). During chronic hypoxia and pathological repair, the hypoxia pathway might be responsible for driving the process of fibrosis (Watson et al., 2013; Shi et al., 2017).

In summary, hypoxia and fibrosis in the heart appear in many cardiovascular diseases, HCM, HHD, Recurrent MI, and respiratory diseases, COPD, OSA, CF, SAS. In addition, all these diseases are related to cardiac arrhythmias. In this paper, we use a computational model to investigate if the combination of these two pathological processes, hypoxia and fibrosis, is sufficient for the genesis of ectopic beats, a known trigger for life-threatening arrhythmias.

We modified an electrophysiological model of myocytes of the left ventricle (Ten Tusscher and Panfilov, 2006) to include the effects of hypoxia as previously presented in Shaw and Rudy (1997). Diffuse fibrosis is modeled by randomly replacing cardiac myocytes by non-excitable and non-conducting cells. This approach has been employed in a large number of scientific studies to model fibrosis in ventricular (Ten Tusscher and Panfilov, 2007; McDowell et al., 2011; Kazbanov et al., 2016) and atrial (Cherry et al., 2007; McDowell et al., 2015; Alonso et al., 2016) tissues. This approach is justified due to: the lack of a

non-invasive technique that can capture the 3D micro-structure of a region with fibrosis; and the complex, distinct and almost unpredictable patterns of fibrosis as identified by histological images (Boineau and Cox, 1973; Campos et al., 2012). As we include this random feature in our simulations, the Monte Carlo method is used to calculate the probability of an injured region to behave as an ectopic pacemaker, assuming that two values characterize the injured tissue: the percentage of fibrosis and the degree of hypoxia.

The results of our simulations suggest that injured regions with both hypoxia and fibrosis generate ectopic beats. Simulations considering only one of these two processes, i.e., only hypoxia or only fibrosis, do not show ectopic beats. The mechanism behind the generation of ectopic beats is unidirectional block, which triggers sustained micro-reentries inside the region with diffuse fibrosis and hypoxia. The analysis of the probability distributions reveals that the simulations that generate ectopic beats have a percentage of fibrosis between 37 and 65%. In addition, the highest probability of ectopic beat formation is obtained for percentages of fibrosis near the percolation threshold, a pure topological metric. This is in agreement with previous results (Alonso and Bär, 2013; Gouvêa de Barros et al., 2015; Alonso et al., 2016). We also observe that the probability increases with the level of hypoxia, i.e., the scenario with most severe hypoxia is the one with highest probability of generation of ectopic beats. Finally, we study how reentries and ectopic beats depend on: (1) the shape of the simulated tissue, cubic vs. rectangular; (2) the total size of the tissue; and (3) the protocol to introduce the action potential wave into the injured tissue.

2. MATERIALS AND METHODS

2.1. Modeling Normal and Cardiac Myocytes During Hypoxia

In order to model the cellular dynamics in our computational experiments, we consider the ten Tusscher model (TT3) of human ventricle myocyte electrophysiology (Ten Tusscher and Panfilov, 2006). For the dynamics of the cellular transmembrane potential (V) the following ion currents are considered:

$$C_m \frac{\partial V}{\partial t} = I_{ion} = I_{Na} + I_{K1} + I_{to} + I_{Kr} + I_{Ks} + I_{CaL} + I_{NaCa} + I_{NaK} + I_{pCa} + I_{pK} + I_{bCa} + I_{bNa} + I_{KATP}; \quad (1)$$

where C_m is the membrane capacitance. Note that I_{ion} includes currents from ion channels, exchangers and pumps. Almost all currents depend on the transmembrane potential and on gating variables, $\boldsymbol{\eta}$, of the Hodgkin-Huxley type.

We modified the ten Tusscher et al. model (Ten Tusscher and Panfilov, 2006) to simulate hypoxia by introducing a K^+ current activated by Adenosine triphosphate (ATP) called $I_{K(ATP)}$ and modifying the $P_{Ca(L)}$ conductivity to be also dependent on ATP. This formulation for modeling hypoxia was introduced before in Shaw and Rudy (1997), although similar alternative formulations are also possible (Kazbanov et al., 2014).

Different degrees of Hypoxia can be simulated by changing the values of $[ATP_i]$ from normal (6 mM) to acute (2 mM). According to Shaw and Rudy (1997), this ranges are likely to occur also during acute ischemia. **Table 1** shows the impact of the reduction of $[ATP_i]$, due to hypoxia on the properties of Action Potential Duration (APD), velocity of action potential propagation, and wave length. Whereas APD depends on the level of hypoxia, velocity is basically constant, as can be seen in **Table 1**.

2.2. Action Potential Propagation on Cardiac Tissue

The coupling of cells in three-dimensional tissues is modeled with the monodomain formulation, which is given in terms of the transmembrane potential V and the vector of state variables, $\boldsymbol{\eta}$:

$$\beta C_m \frac{\partial V}{\partial t} + \beta I_{ion}(V, \boldsymbol{\eta}) = \nabla \cdot (\boldsymbol{\sigma} \nabla V) + I_{stim}, \quad (2)$$

$$\frac{\partial \boldsymbol{\eta}}{\partial t} = \boldsymbol{f}(V, \boldsymbol{\eta}), \quad (3)$$

where β is the surface-volume ratio, C_m is the membrane capacitance, I_{ion} the total ion current, I_{stim} is the current due to an external stimulus, and $\boldsymbol{\sigma}$ is the monodomain conductivity tensor. The model is further equipped with appropriate initial conditions and no–flux boundary conditions ($\mathbf{n} \cdot \sigma \nabla V = 0$), i.e., the boundary of the tissue is considered to be isolated.

In order to solve the monodomain equations and simulate the action potential propagation in the heterogeneous tissue we used an efficient parallel cardiac solver described in Sachetto Oliveira et al. (2017). This solver uses the Rush-Larsen method to solve the ODEs associated with the TT3 model and the finite volumes method do solve the partial differential equation (PDE) (Equation 2), and can be configured to disconnect a random percentage ϕ of $(100\,\mu\text{m})^3$ volumes, allowing us to model diffuse fibrosis, as described next. The time step (Δt) was set to 0.02 ms for the numerical solution of both ODEs and PDE.

2.3. Model of Fibrosis

Different types of fibrosis can be observed depending on its spatial distribution (Nguyen et al., 2014): compact, interstitial, patchy, and diffuse. In this work, we consider diffuse fibrosis, which corresponds to the distribution of fibrotic tissue among myocytes in such a way fibrotic and normal tissues are interleaved, forming a complex maze.

TABLE 1 | Impact of the reduction of $[ATP_i]$, due to hypoxia, on the properties of APD, velocity of AP propagation, and wave length.

ATPi (mM)	APD (ms)	Velocity (cm s^{-1})	Wave length (cm)
2	21	31.4	0.66
3	48	33.3	1.6
4	140	34.0	4.7
5	260	34.2	8.9
6	330	34.2	11.3

We model diffuse fibrosis by randomly removing active tissue volumes of the size of $(100\,\mu m)^3$ creating completely disconnected inert regions. The $(100\,\mu m)^3$ is roughly the length of individual cells in the longitudinal direction of the tissue. Such approach has been extensively employed before (Ten Tusscher and Panfilov, 2007; Alonso and Bär, 2013; Kazbanov et al., 2016; Vigmond et al., 2016) to study the formations of ectopic beats and reentries in the tissue. The maze of conducting tissue mixed with fibrosis produces fractionated AP propagation.

Fibrosis is modeled via the parameter σ in Equation (2). If the fraction of fibrosis in a particular region is ϕ, we assign $\sigma = 0$ to a given cell with a probability of ϕ. A cell with $\sigma = 0$ is considered inactive and disconnected from the surrounding cells.

When the fraction ϕ of fibrosis is high, action potential does not propagate through the tissue. On the other hand, action potential wave propagates when the fraction is small. There are intermediate values of ϕ where these two regimes clash and waves are able to propagate in a certain direction but not in the opposite direction due to source-sink mismatches, giving rise to unidirectional blocks responsible for the breakup of the propagating waves. Such effect depends also on the level of ionic remodeling due to hypoxia in the tissue. As explained before, in order to model the degree of hypoxia we change the value of $[ATP_i]$.

2.4. Calculation of Percolation Threshold

Waves break in a window of values of the fibrosis fraction in the tissue (ϕ). The window of values is close to the percolation threshold of the grid. Such value corresponds to the maximum fraction of fibrosis at which there is still a path composed of healthy cells connecting one side to the other of the system. Typical theoretical calculations of percolation threshold are done for large systems involving a huge number of cells and therefore, finite sizes effects are discarded. However, a fibrotic region has a finite size and its format or geometry may influence the results. For this reason, we statistically calculate the percolation threshold for the next two types of geometries:

- A rectangular slab of tissue of horizontal lengths $4 \times 4\,cm^2$ and different thickness: from a single layer (formally a two dimensional grid of cells) to around 25 layers of cells, see **Figure 1A**.
- A cubic domain formed by a N^3 cells, where we vary the length N from 2 cells to around 30, see **Figure 1B**.

For each pair (N, ϕ) we randomly generate 100 different heterogeneous grids and evaluate numerically if the generated models permit the wave propagation from one side to the other. With the results, percolation threshold, ϕ_{th}, is calculated via linear interpolation. The resulting dependence of ϕ_{th} on N is presented in **Figure 1**. As previously noted, for a single layer we approach the two-dimensional limit, see **Figure 1A**. For slabs with thickness higher than 20 layers the resulting value of ϕ_{th} is already close to the theoretical three-dimensional limit value, see **Figure 1A**. For cubic domains the three-dimensional limit is the same that in the previous case for large systems, see **Figure 1B**. However, for small system the behavior differs from the two-dimensional limit, see **Figure 1B**.

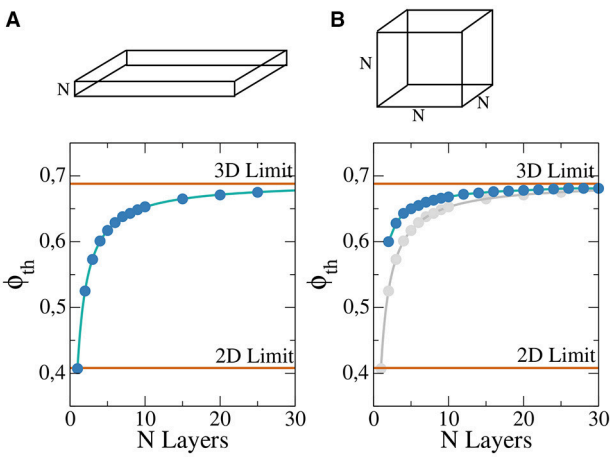

FIGURE 1 | Percolation threshold of a rectangular slab of tissue composed by regular cubic grid of cells for different thickness N in a system $400 \times 400 \times N$ **(A)** and cubic system for different lengths of the cube $N \times N \times N$ **(B)**. For comparison the analytic limits corresponding to infinite two and three dimensional systems are shown (red lines). Numerical fit (solid blue line) has been calculate to guide the eye and permit to extrapolate to possible higher values of N. For comparison, **(B)** also presents the results of **(A)** in gray.

3. RESULTS

3.1. Rectangular Slab With a Central Injured Region

First we consider a rectangular slab of healthy tissue with a circular injured region with fibrosis and hypoxia, as shown in **Figures 2A–H**. If this injured region is small enough, the action potential wave rapidly propagates around, enters from the whole border and excites the whole injured region almost simultaneously. However, if the injured region is large, the wave enters first from the left (from the stimulus side). Since the rest of the border is excited later, propagation in this case is mainly from left to right. If the fraction ϕ of fibrosis is close to the percolation limit of the grid (Alonso and Bär, 2013; Alonso et al., 2016) the waves propagate slower inside the injured region in comparison with the speed on the healthy tissue, see **Figures 2C,D**. This propagation inside the injured region is highly irregular and continuous break-ups and fusions of waves can occur, see **Figures 2C–E**. For a certain random combination of cells, the tissue forms source-sink mismatches and unidirectional blocks, i.e., the wave can not propagate from left to right, but can propagate later in the opposite direction (right to left), see **Figures 2F,G**. The resulting wave in the injured region arrives to the left border and can re-excite the healthy tissue giving rise to an ectopic beat, see **Figure 2H**. If the leaving wave interacts with a previous wave it can break and generate a rotor. A video of this simulation can be found in the Supplementary Material.

The generation of reentries depends on different factors, such as the degree of fibrosis and hypoxia. In simulations considering only one of these two processes, i.e., only hypoxia or only fibrosis, ectopic beats are not observed. The fraction of fibrosis of the tissue has to be close to the percolation value of the discrete grid

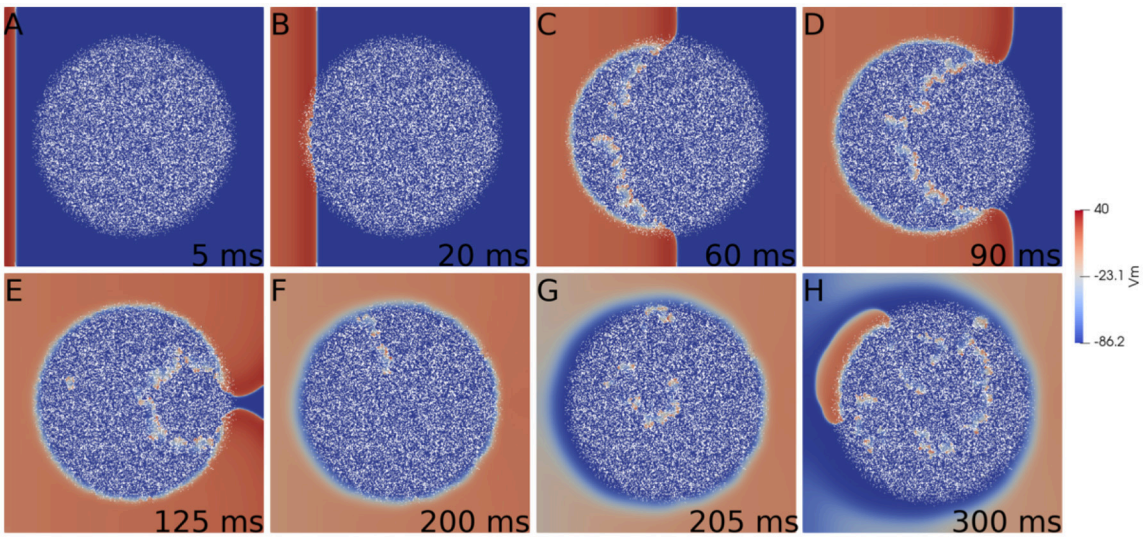

FIGURE 2 | Reentry due to a circular region with fibrosis and hypoxia in the middle of a rectangular slab of cardiac tissue. Different panels show the evolution of the action potential.

of cells, see **Figure 1**. **Figure 3** shows the probability distribution of reentries as function of the fraction ϕ for different thickness of the slab.

We have analyzed three degrees of hypoxia for different thickness of the slab, see **Figure 3**. With low degree of hypoxia ($[ATP_i] = 4$ mM) reentries are very unlikely to occur and appear for values of ϕ close to the percolation threshold. For severe hypoxia ($[ATP_i] = 2$ mM) there is a higher probability of reentries which occur in a wider window of values of the fraction of fibrosis.

3.2. Rectangular Slab With Fibrosis and Hypoxia

The size of the injured region is relevant in the formation of sustained reentries. We perform several simulations using different tissue sizes to demonstrate this relation. First we increase the injured region to cover the whole tissue and a wave is induced at the border of the system for different degrees of fibrosis and hypoxia. The results are shown in **Figure 4** and are comparable with the results obtained with a restricted circular injured region shown in **Figure 3**.

Although the probability of reentries are systematically higher when the whole slab is injured, the range of fibrosis with reentries is basically the same. The probability of reentries increases with the thickness of the slab and, for 10 layers of cells, the probability of reentry for high degree of hypoxia arrives at 100% for several values of ϕ, as we can see in **Figure 4C**.

3.3. Minimum Size of a 2D Injured Rectangular Slab That Sustains Reentries

The difference between the probabilities of reentry obtained in **Figure 3**, **4** is due to the difference of size of the injured region. Whereas, for example, in **Figure 3A** the total injured area is 6.16 cm^2, in **Figure 3A** the injured area is the whole slab, corresponding to 16 cm^2.

Next we study the minimum area needed to generate reentries. We use a single layer rectangular slab (2D) and reduce its size systematically. We evaluate the probability of reentries for different values of ϕ keeping $[ATP_i] = 2$ mM. The same approach is used in the next sections.

We obtain one reentry over one hundred tries for $\phi = 0.38$ and $\phi = 0.40$ in a system formed by $7 \times 7\,mm^2$ square (see **Figure 5A**). However, we did not find any reentry in smaller systems. Note that as our tissue mesh is formed by finite volumes of $(100\,\mu m)^3$, the total number of volumes in such minimum system is 4900.

A comparison between a reentry in the smallest tissue and a typical reentry in a much bigger system is shown in **Figure 5**. Whereas, for the first case, the excitation can propagate inside the injured region without a clear structure, i.e., in a very fractionated fashion, the reentry shown in the big injured region appears with a well defined shape.

3.4. Minimum Size of a 3D Injured Rectangular Slab That Sustains Reentries

One could consider that the total number of finite volumes (FVs) is the most relevant feature that defines the minimum size of the injured region, i.e., a tissue with a high number of injured FVs would have a high probability to generate reentries. To check this hypothesis we perform numerical simulations in a three-dimensional rectangular slab of tissue keeping the thickness constant, 10 layers of cells, and we evaluate the minimum volume under these conditions.

We obtain a single reentry over 25 tries for $\phi = 0.62$ in a system formed by a slab with a volume of $7 \times 7 \times 1\,mm^3$. The two-dimensional version of this slab is actually the same case

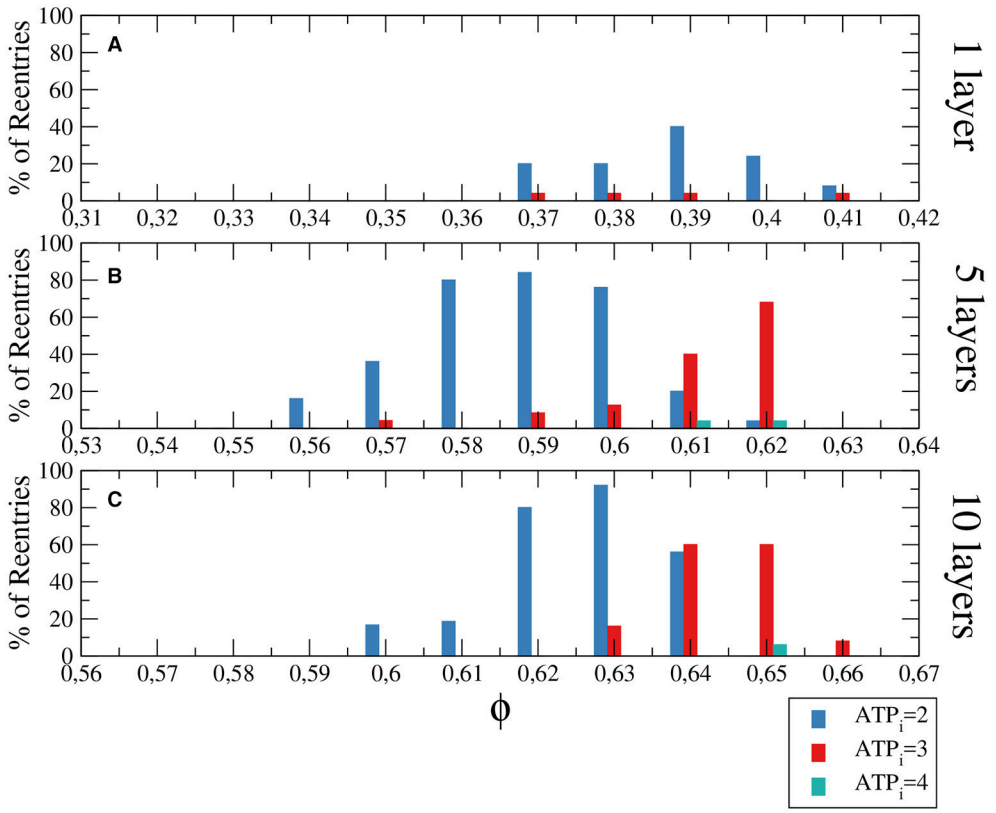

FIGURE 3 | Histograms with the percentage of reentries in a rectangular slab of tissue with an injured circular region with different levels of hypoxia (ATP_i) and fibrosis (ϕ). For a two dimensional system corresponding to a tissue with a single layer of cells reentries occurs at low fraction of fibrosis **(A)**, while for 5 layers **(B)** and 10 layers **(C)** the probabilities of reentries increase and reentries occur at higher fractions of fibrosis. The probability to find a reentry decreases for higher values of ATP_i. The size of the slab is 4 × 4 cm; The injured region occupies a circular region with radius equal to 1.4 cm.

discussed in the previous section. The total number of FVs in such minimum 3D system is 49000, which is 10 times bigger than the number of FVs in 2D. Therefore, these results indicate that the total number of FVs (or myocytes) inside the injured region is not the only relevant parameter for the generation of reentries.

3.5. Minimum Size of a 3D Injured Cubic Slab That Sustains Reentries

Next we change the geometry of the domain. We define a cubic injured tissue formed by $L \times L \times L\,\text{cm}^3$, where L is the length of the cube. We vary the volume by modifying L.

Following the same type of initial condition employed along the previous studies, we systematically reduce the size of the cube to estimate the minimum size which sustains reentries. We find reentries in a cube with $L = 0.4$ cm. In this case the total number of FVs in such minimum system is 64000, which is actually larger than the number of FVs in the previous rectangular three-dimensional slabs (which was 49000).

3.6. Dependence on the Initial Perturbation

The minimum size of a cube to obtain reentries also depends on the initial perturbation. The simulations done previously in the whole tissue slabs are initiated with a perturbation in one of the faces of the volume. However, in the case of the circular injured region in the middle of the slab, see **Figure 2** the perturbation from the exterior of the slab continuously trigger the entrance of the wave from different positions. Therefore, the propagation of the waves toward the injured region is different than the oversimplified version shown for example in **Figure 5**. In order to study how reentries depend on the way AP propagates toward the injured region we implemented and analyzed different initial perturbations, or stimulations, in a cubic domain with fibrosis and hypoxia. See three examples of reentries in **Figure 6** with different initial protocols (videos are available in the Supplementary Material).

We apply several protocols to evaluate the effect of the initial perturbation. We initially perturb a different number of faces of the cubic domain. The most effective way to initiate a reentry inside the cubic domain is the introduction of a perturbation in one face of the cube. Such case is discussed in the previous section, and a particular realization with the minimum size where reentries are observed is shown in **Figure 6A**. The increase of the size of the injured cube increases the number of reentries (with the same number of statistically independent realizations), as shown in **Figure 7**. Similar minimum size was obtained when two

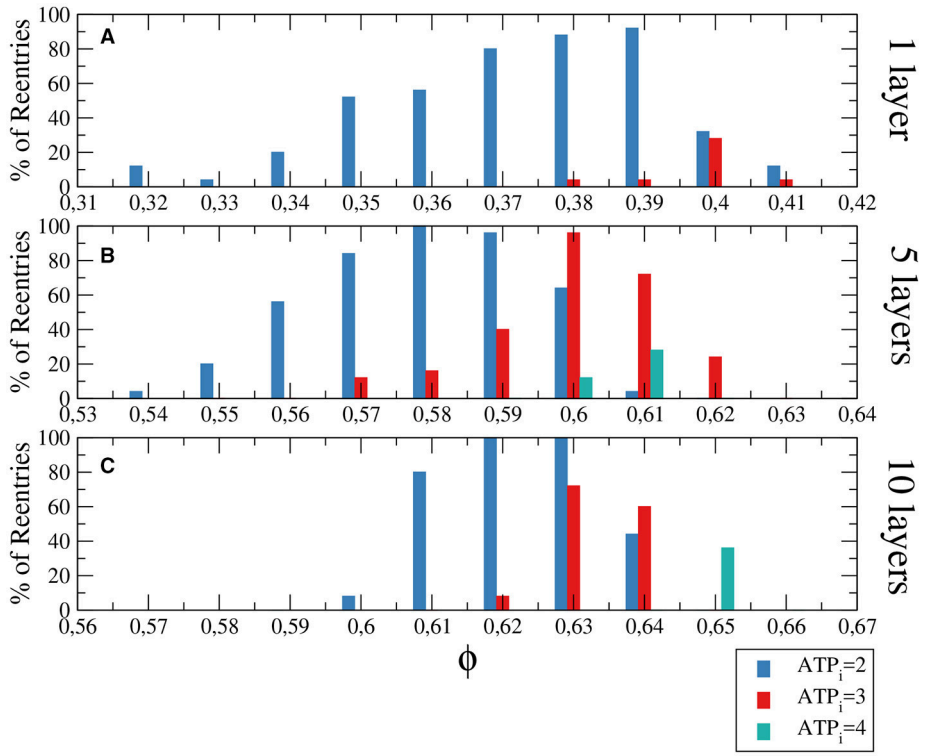

FIGURE 4 | Histograms with the percentage of reentries in a rectangular slab with different levels of hypoxia (ATP_i) and fibrosis (ϕ). For a two dimensional system corresponding to a tissue with a single layer of cells reentries occurs at low fraction of fibrosis **(A)**, while for 5 layers **(B)** and 10 layers **(C)** the percentages of reentries are higher and occur at higher fractions of fibrosis. The probability to find a reentry decreases for higher values of ATP_i. The size of the slab is $4 \times 4 \times N$ cm.

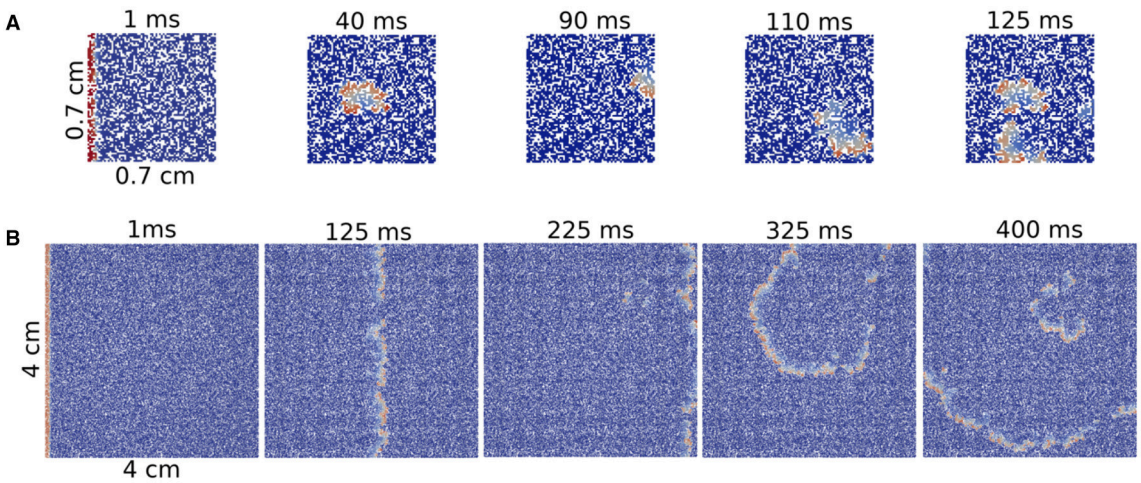

FIGURE 5 | Reentries in different sizes of 2D rectangular slabs of cardiac tissue at different time steps. Reentry obtained in a small system with size $7 \times 7 \times 0.1$ mm **(A)** and reentry obtained in a two-dimensional system with size $40 \times 40 \times 0.1$ mm **(B)**.

adjacent faces of the injured cube were perturbed simultaneously. However, the probability to induce a reentry is systematically smaller than the previous case, see **Figure 7**.

The application of the initial perturbation in four of the faces of the cube synchronizes the excitation inside the injured cube and increases drastically the minimum size needed to obtain reentries. With this stimulus protocol, the minimum size that present reentries increases to $L = 6$ mm, corresponding to a total of 216000 finite volumes. See an example of a reentry in such case in **Figure 6B**.

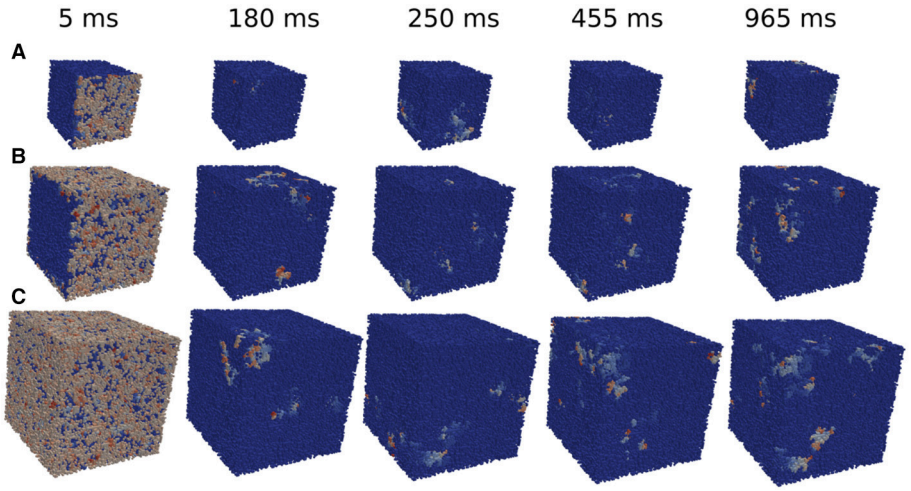

FIGURE 6 | Reentries obtained in cubic grids for different initial protocols and time steps. Activation of a single face of a cubic domain of 0.4 × 0.4 × 0.4 cm **(A)**. Activation of four faces of a cubic domain of 0.6 × 0.6 × 0.6 cm **(B)**. Simultaneous activation of the six faces of a cubic domain of 0.8 × 0.8 × 0.8 cm **(C)**.

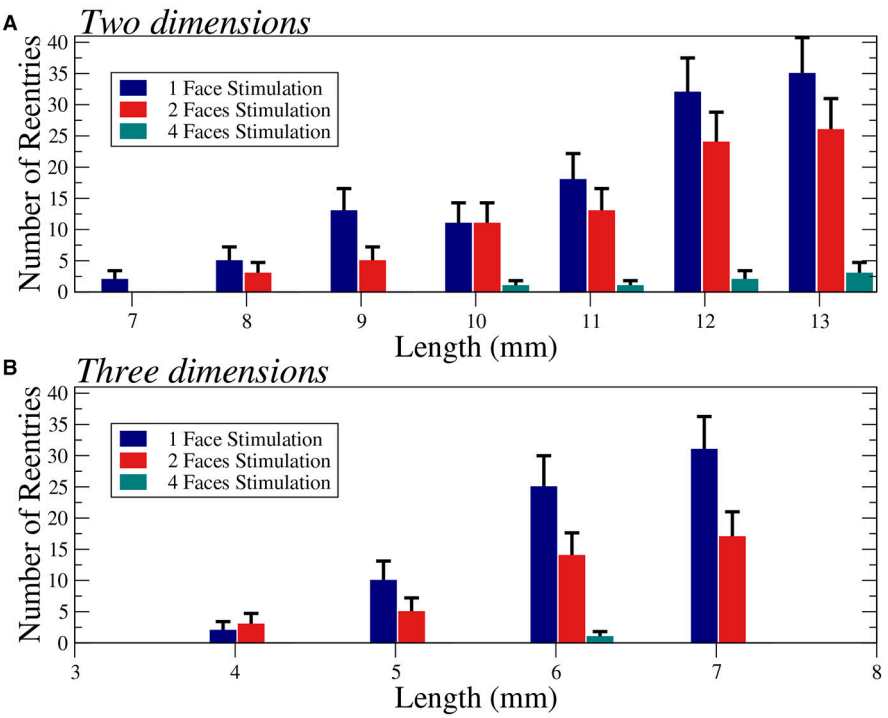

FIGURE 7 | Number of reentries obtained for different sizes of two-dimensional squares **(A)** and three-dimensional cubes **(B)** under different initial perturbation protocols. A total of 600 **(A)** and 300 **(B)** simulations per bar were performed with six different values of the fraction of fibrosis $\phi = 0.35$, 0.36. 0.37, 0.38, 0.39, and 0.40 **(A)** and three different values of the fraction of fibrosis $\phi = 0.62$, 0.63, 0.64 **(B)**, both with $[ATP_i]$ at 2 mM. Error bars are calculated assuming a binomial distribution for the generation of reentries.

Finally, we consider the effect of the simultaneous excitation of all the six faces of the cube and reentries are only obtained with a cube of size $L = 8$ mm, corresponding to a total number of 512000 FVs. See an example of reentry induced by the complete excitation of the six faces of a cube with $L = 8$ mm in **Figure 6C**.

For the sake of completeness, we have evaluated the changes on the number of reentries for different sizes in two dimensional tissues, see **Figure 7A**. In two dimensions we observe a similar behavior and for highly synchronized perturbations (four faces) the minimum size is much

larger than for less synchronized stimulations (one or two faces).

4. DISCUSSION

The computer simulations presented in this work suggest that the combination of fibrosis and hypoxia in a localized region of the myocardium can provide a sufficient condition for the genesis of ectopic beats. The mechanism behind the generation of ectopic beats is unidirectional block inside a region with diffuse fibrosis and hypoxia, where micro-reentries are formed. We note that, although specific regions have been correlated with the generation of ectopic beats, such as the pulmonary veins (Haïssaguerre et al., 1998) during atrial fibrillation or border zone of infarct regions after coronary occlusion (Boineau and Cox, 1973), the mechanism behind this remains unclear. Along decades experiments and numerical simulations have suggested several candidates: abnormal automaticity, triggered activity, such as early or delayed after depolarization, micro-reentries, or even the combination of some of these three (Jalife, 2011). Multiple data available in the literature supports all these mechanisms. Probably, each one might be more specific to a particular disease. However, the results in this work may somehow defy this common sense. Micro-reentries could arise from the combination of hypoxia and fibrosis, two cardiac conditions that appear together in many heart diseases, as hypertrophic cardiomyopathy, hypertensive heart disease, recurrent myocardial infarction, and even in respiratory diseases, such as obstructive pulmonary disease, obstructive sleep apnea and cystic fibrosis. Therefore, our results suggests that a single mechanism could be behind many different pathologies.

It is interesting to note also that among these three mechanism, only micro-reentry, as first proposed to explain PVCs in Boineau and Cox (1973), already suggested that both the electrophysiology as well as the micro-structure of cardiac tissue should be taken into account. Both abnormal automaticity and triggered activity mechanisms focus only on electrophysiology aspects of single myocytes. Nevertheless, recent studies have shown that the presence of fibrosis or other non-conductive or non-excitable cells is of extreme importance in the generation of ectopic beats, even when the altered electrophysiology of myocytes reflects abnormal automaticity or triggered activities (Pumir et al., 2005; Zimik et al., 2015). Therefore, it seems that recent studies are converging toward mechanisms that combine both electrophysiological and micro-structural changes in order to explain the genesis of dangerous ectopic beats.

In this work, we used simple computational models to reproduce hypoxia and diffuse fibrosis. Nevertheless, the result of this combination is far from trivial. First, in the simulations that considered only one of these two processes, i.e., only hypoxia or only fibrosis, ectopic beats were not created. However, even when both conditions were considered, ectopic beats were not always present. This combination does not result in an all-or-none mechanism. The generation of ectopic beats depended on many aspects that were evaluated in this work: percentage of fibrosis, fibrosis pattern, level of hypoxia, size of the injured tissue, its shape, and how AP waves enter the injured region. The way fibrosis is distributed within cardiac tissue was modeled stochastically. Therefore, we used the Monte Carlo method to calculate the probability of an injured tissue to generate ectopic beats.

By varying the percentage of fibrosis and level of hypoxia we observed that the probability of micro-reentries increases with the level of hypoxia, i.e., the scenario with most severe hypoxia was the one with the highest number of reentries. In addition, the simulations that generated ectopic beats had percentages of fibrosis between 37 and 65%, and the highest number of reentries was obtained using percentages of fibrosis near the percolation threshold, a pure topological metric. This is in agreement with our previous results (Alonso and Bär, 2013; Gouvêa de Barros et al., 2015; Alonso et al., 2016).

In these previous studies, we have considered simple and phenomenological models of cardiac myocytes to study the effects of atrial fibrillation (Alonso et al., 2016) or we have considered realistic models of mouse ventricular tissue (Gouvêa de Barros et al., 2015). Here, we consider a human ventricular model (Ten Tusscher and Panfilov, 2006) where hypoxia could be studied at different degrees. The common features of all these studies are the basis of the investigated mechanism of micro-reentry: (1) Diffuse fibrosis generates complex and long reentrant paths within the damaged region; (2) Both action potential and wavelength are short for the cases of mouse AP, remodeled AP due to atrial fibrillation, or, in this paper, remodeled AP due to hypoxia in myocytes of the human ventricle. The combination of long pathways and short wavelengths allows micro-reentry circuits to be formed.

The probability of a compromised region to become an ectopic pacemaker is higher for large damaged regions. We have confirmed this hypothesis with our simulations using both two and three-dimensional systems, see **Figure 7**. These simulations also show the minimum sizes of the domains where reentries were obtained. The dependence on the size supports the idea that if the system is large, source-sink mismatches are more likely to appear together with long reentrant pathways. Nevertheless, our results suggest that the relation between size and probability of reentry is not trivial and the shape of the injured region and the way AP waves enter it play important roles.

For instance, in **Table 2** we summarize our results in terms of minimum required sizes to generate reentries for different tissue geometries and different stimulation protocols. By comparing the simulations that used the same stimulation protocol (stimulus from a single face) we observe that the minimum volume in cm^3 may vary substantially: $70 \times 70 \times 1$ ($0.005\,cm^3$), $70 \times 70 \times 10$ ($0.05\,cm^3$), and $40 \times 40 \times 40$ ($0.064\,cm^3$). In fact, our results suggest that it is easier to generate an ectopic beat on flat geometries or on thin slabs than on cubics geometries. Coincidentally, the most common infarct is known to be the sub-endocardial one, with a geometry of the damage tissue that can be described as a thin slab near the endocardial surface of the heart. Nevertheless, if we keep the geometry fixed **Figure 7** clearly shows that by increasing the volume or size of the injured region sustained reentries are more likely to occur.

TABLE 2 | Minimum sizes needed to support reentries using different geometries and different stimulation protocols. FV, Finite Volume.

Grid	Perturbation	Geometry (FVs)	# FVs	Total volume (cm^3)
$L \times L \times 1$	1 Face	$70 \times 70 \times 1$	4900	0.005
$L \times L \times 1$	2 Faces	$80 \times 80 \times 1$	6400	0.006
$L \times L \times 1$	4 Faces	$100 \times 100 \times 1$	10000	0.01
$L \times L \times 10$	1 Face	$70 \times 70 \times 10$	49000	0.05
$L \times L \times L$	1 Face	$40 \times 40 \times 40$	64000	0.064
$L \times L \times L$	4 Faces	$60 \times 60 \times 60$	216000	0.216
$L \times L \times L$	6 Faces	$80 \times 80 \times 80$	512000	0.512

Table 2 also shows how micro-reentries depend on the different possible entrances of the wave into the injured region. We have found that when the borders are well synchronized the minimum injured volume that is needed to generate reentries is much bigger than when the borders are loosely synchronized. For instance, the last three lines of **Table 2** show the minimum volumes for different initial conditions when the geometry of the injured region is a cube, see also **Figures 6** , **7**.

Our results on the minimum size of fibrotic regions can be compared with measurements taken from human ventricles with late-enhancement magnetic resonance imaging (LE-MRI). The studies reported in Wu et al. (1998); Ørn et al. (2007), and de Haan et al. (2011) reported scars of a minimum size around 0.1 cm^3 for patients with a history of ventricular tachycardia. In our simulations we have found that it is possible to generate an ectopic pacemaker on injured regions with much smaller sizes (one order of magnitude smaller). This discrepancy could be related to the lack of spatial resolution of nowadays LE-MRI exams. Nevertheless, the presented minimum size regions have very low probability to behave as an ectopic pacemaker, see **Figures 6** , **7**. Therefore, although the occurrence of reentries in such small regions is theoretically possible, it is very unlike to occur.

There are many limitations in this study. First, we have used simple models for both fibrosis and hypoxia. For instance, different types of fibrosis can be observed (Nguyen et al., 2014): compact, interstitial, patchy and diffuse. In this work we have only used a simple model for diffuse fibrosis. In addition, the results and conclusions presented in this work should be taken cautiously. As we have previously mentioned, although hypoxia and fibrosis are found together in many heart and respiratory diseases, they are usually accompanied by many other pathological conditions. Although the complex interactions of pathological conditions other than hypoxia and fibrosis are out of the scope of this work, we list here a few interactions that deserve further investigations in future works. In respiratory diseases hypoxia has been co-observed with oxidative stress (Yin et al., 2012; Ramond et al., 2013; Debevec et al., 2017). It has been shown that the combination of hypoxia and oxidative stress can be quite complex, involve multiple scales of cellular metabolism and lead to further reduction of APD (Zhou et al., 2009). In the case of acute ischemia, whereas hypoxia is present and has been shown to be the condition that most affects AP waveform (Shaw and Rudy, 1997), hyperkalemia and acidosis are also important conditions that can considerably reduce AP wave velocity and, as consequence, further reduce wavelength. Whether the aforementioned conditions could, in theory, corroborate with the described micro-reentry mechanism, and increase the probability of the genesis of ectopic beats, other conditions could counteract it. For instance, during fibrosis a possible connection between myocytes and fibroblasts could increase the APDs of myocytes (Kohl and Gourdie, 2014). However, it is still an open question if fibroblasts are electrically coupled to the myocytes (Kohl and Gourdie, 2014). Therefore, we employ here a simple approach assuming that fibroblasts do not interact electrically with myocytes and they basically act as barriers to the action potential propagation. This approach has been employed in a large number of scientific studies on the modeling of fibrosis in ventricular (Ten Tusscher and Panfilov, 2007; McDowell et al., 2011; Kazbanov et al., 2016) and atrial (Cherry et al., 2007; Alonso et al., 2016; McDowell et al., 2015) tissues. Such approach has been also employed in highly detailed microscopic models of cardiac tissues where cells are disconnected by barriers or by dead cells (Jacquemet and Henriquez, 2009; Hubbard and Henriquez, 2014; Gouvêa de Barros et al., 2015). Other studies consider different approaches to model the electrical interaction between fibroblasts and the myocytes (Xie et al., 2009; Nayak et al., 2017). Finally, we highlight that this is a pure theoretical study, and therefore, further experimental validations are pending.

In summary, the combination of fibrosis with hypoxia in a localized region of the myocardium can provide the sufficient condition for the genesis of ectopic beats and reentries in a human ventricular model. The size, shape and geometry of the injured region, as well as the electrophysiology remodeling due to hypoxia are important features that determine the probability of an affected region to behave as an ectopic pacemaker, a trigger for life-threatening arrhythmias.

AUTHOR CONTRIBUTIONS

RS, SA, and RdS conceived the numerical experiments. RS conducted the numerical experiments.RS, SA, and RdS analyzed the results. All authors reviewed the manuscript.

FUNDING

We acknowledge support from CAPES by the grant 88881.065002/2014-01 of the Brazilian program Science without borders, and from MINECO of Spain under the Ramon y Cajal program with the grant number RYC-2012-11265.

ACKNOWLEDGMENTS

We would like to thank UFSJ, UFJF, CAPES, FAPEMIG, CNPq, and FINEP.

SUPPLEMENTARY MATERIAL

The Supplementary Material for this article can be found online at: https://www.frontiersin.org/articles/10.3389/fphys.2018.00764/full#supplementary-material

REFERENCES

Alkon, J., Friedberg, M. K., Manlhiot, C., Manickaraj, A. K., Kinnear, C., McCrindle, B. W., et al. (2012). Genetic variations in hypoxia response genes influence hypertrophic cardiomyopathy phenotype. *Pediatr. Res.* 72, 583–592. doi: 10.1038/pr.2012.126

Alonso, S., and Bär, M. (2013). Reentry near the percolation threshold in a heterogeneous discrete model for cardiac tissue. *Phys. Rev. Lett.* 110:158101. doi: 10.1103/PhysRevLett.110.158101

Alonso, S., Dos Santos, R. W., and Bär, M. (2016). Reentry and ectopic pacemakers emerge in a three-dimensional model for a slab of cardiac tissue with diffuse microfibrosis near the percolation threshold. *PLoS ONE* 11:e0166972. doi: 10.1371/journal.pone.0166972

Boineau, J. P., and Cox, J. L. (1973). Slow ventricular activation in acute myocardial infarction: a source of re-entrant premature ventricular contractions. *Circulation* 48, 702–713.

Campos, F. O., Prassl, A. J., Seemann, G., Weber dos Santos, R., Plank, G., and Hofer, E. (2012). Influence of ischemic core muscle fibers on surface depolarization potentials in superfused cardiac tissue preparations: a simulation study. *Med. Biol. Eng. Comput.* 50, 461–472. doi: 10.1007/s11517-012-0880-1

Cheong, T. H., Magder, S., Shapiro, S., Martin, J. G., and Levy, R. D. (1990). Cardiac arrhythmias during exercise in severe chronic obstructive pulmonary disease. *Chest* 97, 793–797.

Cherry, E. M., Ehrlich, J. R., Nattel, S., and Fenton, F. H. (2007). Pulmonary vein reentry—properties and size matter: insights from a computational analysis. *Heart Rhythm* 4, 1553–1562. doi: 10.1016/j.hrthm.2007.08.017

Chiong, M., Wang, Z. V., Pedrozo, Z., Cao, D. J., Troncoso, R., Ibacache, M., et al. (2011). Cardiomyocyte death: mechanisms and translational implications. *Cell Death Dis.* 2, e244. doi: 10.1038/cddis.2011.130

Cintra, F. D., Makdisse, M. R., Oliveira, W. A., Rizzi, C. F., Luiz, F. O., Tufik, S., et al. (2010). Exercise-induced ventricular arrhythmias: analysis of predictive factors in a population with sleep disorders. *Einstein (São Paulo)* 8, 62–67. doi: 10.1590/s1679-45082010ao1469

Darby, I. A. and Hewitson, T. D. (2016). Hypoxia in tissue repair and fibrosis. *Cell Tissue Res.* 365, 553–562. doi: 10.1007/s00441-016-2461-3

de Bakker, J. M., van Capelle, F. J., Janse, M. J., Wilde, A. A., Coronel, R., Becker, A. E., et al. (1988). Reentry as a cause of ventricular tachycardia in patients with chronic ischemic heart disease: electrophysiologic and anatomic correlation. *Circulation* 77, 589–606.

de Haan, S., Meijers, T. A., Knaapen, P., Beek, A. M., van Rossum, A. C., and Allaart, C. P. (2011). Scar size and characteristics assessed by cmr predict ventricular arrhythmias in ischaemic cardiomyopathy: comparison of previously validated models. *Heart* 97, 1951–1956. doi: 10.1136/heartjnl-2011-300060

Debevec, T., Millet, G. P., and Pialoux, V. (2017). Hypoxia-induced oxidative stress modulation with physical activity. *Front. Physiol.* 8:84. doi: 10.3389/fphys.2017.00084

Diamond, J. A. and Phillips, R. A. (2005). Hypertensive heart disease. *Hypertens. Res.* 28, 191. doi: 10.1291/hypres.28.191

Frohlich, E. (2000). Ischemia and fibrosis: the risk mechanisms of hypertensive heart disease. *Braz. J. Med. Biol. Res.* 33, 693–700. doi: 10.1590/S0100-879X2000000600010

Frohlich, E. D. (2001). Fibrosis and ischemia: the real risks in hypertensive heart disease. *Am. J. Hypertens.* 14, 194S–199S. doi: 10.1016/S0895-7061(01)02088-X

Gao, Y., Chu, M., Hong, J., Shang, J., and Xu, D. (2014). Hypoxia induces cardiac fibroblast proliferation and phenotypic switch: a role for caveolae and caveolin-1/pten mediated pathway. *J. Thorac. Dis.* 6, 1458–1568. doi: 10.3978/j.issn.2072-1439.2014.08.31

Gouvêa de Barros, B., Weber dos Santos, R., Lobosco, M., and Alonso, S. (2015). Simulation of ectopic pacemakers in the heart: multiple ectopic beats generated by reentry inside fibrotic regions. *Biomed. Res. Int* 2015:713058. doi: 10.1155/2015/713058

Guilleminault, C., Connolly, S. J., and Winkle, R. A. (1983). Cardiac arrhythmia and conduction disturbances during sleep in 400 patients with sleep apnea syndrome. *Am. J. Cardiol.* 52, 490–494.

Haïssaguerre, M., Jaïs, P., Shah, D. C., Takahashi, A., Hocini, M., Quiniou, G., et al. (1998). Spontaneous initiation of atrial fibrillation by ectopic beats originating in the pulmonary veins. *N. Engl. J. Med.* 339, 659–666.

Ho, C. Y., López, B., Coelho-Filho, O. R., Lakdawala, N. K., Cirino, A. L., Jarolim, P., et al. (2010). Myocardial fibrosis as an early manifestation of hypertrophic cardiomyopathy. *N. Engl. J. Med.* 363, 552–563. doi: 10.1056/NEJMoa1002659

Hubbard, M. L. and Henriquez, C. S. (2014). A microstructural model of reentry arising from focal breakthrough at sites of source-load mismatch in a central region of slow conduction. *Am. J. Physiol. Heart Circ. Physiol.* 306, H1341–H1352. doi: 10.1152/ajpheart.00385.2013

Jacquemet, V. and Henriquez, C. S. (2009). Genesis of complex fractionated atrial electrograms in zones of slow conduction: a computer model of microfibrosis. *Heart Rhythm* 6, 803–810. doi: 10.1016/j.hrthm.2009.02.026

Jalife, J. (2011). Déjà vu in the theories of atrial fibrillation dynamics. *Cardiovasc. Res.* 89, 766–775. doi: 10.1093/cvr/cvq364

Kazbanov, I. V., Clayton, R. H., Nash, M. P., Bradley, C. P., Paterson, D. J., Hayward, M. P., et al. (2014). Effect of global cardiac ischemia on human ventricular fibrillation: insights from a multi-scale mechanistic model of the human heart. *PLoS Comput. Biol.* 10:e1003891. doi: 10.1371/journal.pcbi.1003891

Kazbanov, I. V., Ten Tusscher, K. H., and Panfilov, A. V. (2016). Effects of heterogeneous diffuse fibrosis on arrhythmia dynamics and mechanism. *Sci. Rep.* 6:20835. doi: 10.1038/srep20835

Kohl, P. and Gourdie, R. G. (2014). Fibroblast–myocyte electrotonic coupling: does it occur in native cardiac tissue? *J. Mol. Cell. Cardiol.* 70:37–46. doi: 10.1016/j.yjmcc.2013.12.024

Maron, B. J. (2002). Hypertrophic cardiomyopathy: a systematic review. *JAMA* 287, 1308–1320. doi: 10.1001/jama.287.10.1308

Maron, B. J., Pelliccia, A., and Spirito, P. (1995). Cardiac disease in young trained athletes: insights into methods for distinguishing athlete's heart from structural heart disease, with particular emphasis on hypertrophic cardiomyopathy. *Circulation* 91, 1596–1601.

McDowell, K. S., Arevalo, H. J., Maleckar, M. M., and Trayanova, N. A. (2011). Susceptibility to arrhythmia in the infarcted heart depends on myofibroblast density. *Biophys. J.* 101, 1307–1315. doi: 10.1016/j.bpj.2011.08.009

McDowell, K. S., Zahid, S., Vadakkumpadan, F., Blauer, J., MacLeod, R. S., and Trayanova, N. A. (2015). Virtual electrophysiological study of atrial fibrillation in fibrotic remodeling. *PLoS ONE* 10:e0117110. doi: 10.1371/journal.pone.0117110

Miwa, Y. and Sasaguri, T. (2007). Hypoxia-induced cardiac remodeling in sleep apnea syndrome: involvement of the renin-angiotensin-aldosterone system. *Hypertens. Res.* 30, 1147–1149. doi: 10.1291/hypres.30.1147

Namboodiri, N. and Francis, J. (2010). Ventricular arrhythmias in hypertrophic cardiomyopathy-can we ever predict them? *Indian Pacing Electrophysiol. J.* 10, 112.

Nayak, A. R., Panfilov, A., and Pandit, R. (2017). Spiral-wave dynamics in a mathematical model of human ventricular tissue with myocytes and purkinje fibers. *Phys. Rev. E* 95:022405. doi: 10.1103/PhysRevE.95.022405

Ng, G. A. (2006). Treating patients with ventricular ectopic beats. *Heart* 92, 1707–1712. doi: 10.1136/hrt.2005.067843

Nguyen, T. P., Qu, Z., and Weiss, J. N. (2014). Cardiac fibrosis and arrhythmogenesis: the road to repair is paved with perils. *J. Mol. Cell. Cardiol.* 70, 83–91. doi: 10.1016/j.yjmcc.2013.10.018

Ørn, S., Cleland, J. G., Romo, M., Kjekshus, J., and Dickstein, K. (2005). Recurrent infarction causes the most deaths following myocardial infarction with left ventricular dysfunction. *Am. J. Med.* 118, 752–758. doi: 10.1016/j.amjmed.2005.02.010

Ørn, S., Manhenke, C., Anand, I. S., Squire, I., Nagel, E., Edvardsen, T., et al. (2007). Effect of left ventricular scar size, location, and transmurality on left ventricular remodeling with healed myocardial infarction. *Am. J. Cardiol.* 99, 1109–1114. doi: 10.1016/j.amjcard.2006.11.059

Pouleur, A.-C., Barkoudah, E., Uno, H., Skali, H., Finn, P. V., Zelenkofske, S. L., et al. (2010). Pathogenesis of sudden unexpected death in a clinical trial of patients with myocardial infarction and left ventricular dysfunction, heart failure, or both. *Circulation* 122, 597–602. doi: 10.1161/CIRCULATIONAHA.110.940619

Pumir, A., Arutunyan, A., Krinsky, V., and Sarvazyan, N. (2005). Genesis of ectopic waves: role of coupling, automaticity, and heterogeneity. *Biophys. J.* 89, 2332–2349. doi: 10.1529/biophysj.105.061820

Ramond, A., Godin-Ribuot, D., Ribuot, C., Totoson, P., Koritchneva, I., Cachot, S., et al. (2013). Oxidative stress mediates cardiac infarction aggravation

induced by intermittent hypoxia. *Fundam. Clin. Pharmacol.* 27, 252–261. doi: 10.1111/j.1472-8206.2011.01015.x

Ruberman, W., Weinblatt, E., Goldberg, J. D., Frank, C. W., and Shapiro, S. (1977). Ventricular premature beats and mortality after myocardial infarction. *N. Engl. J. Med.* 297, 750–757.

Ruf, K. and Hebestreit, H. (2009). Exercise-induced hypoxemia and cardiac arrhythmia in cystic fibrosis. *J. Cyst. Fibros.* 8, 83–90. doi: 10.1016/j.jcf.2008.09.008

Sachetto Oliveira, R., Martins Rocha, B., Burgarelli, D., Meira, W., Constantinides, C., and Weber dos Santos, R. (2017). Performance evaluation of gpu parallelization, space-time adaptive algorithms, and their combination for simulating cardiac electrophysiology. *Int. J. Numer. Methods Biomed. Eng.* e2913. doi: 10.1002/cnm.2913

Schmidt, A., Azevedo, C. F., Cheng, A., Gupta, S. N., Bluemke, D. A., Foo, T. K., et al. (2007). Infarct tissue heterogeneity by magnetic resonance imaging identifies enhanced cardiac arrhythmia susceptibility in patients with left ventricular dysfunction. *Circulation* 115, 2006–2014. doi: 10.1161/CIRCULATIONAHA.106.653568

Shaw, R. M. and Rudy, Y. (1997). Electrophysiologic effects of acute myocardial ischemia: a theoretical study of altered cell excitability and action potential duration. *Cardiovasc. Res.* 35, 256–272.

Shi, H., Zhang, X., He, Z., Wu, Z., Li, Y., and Rao, L. (2017). Metabolites of hypoxic cardiomyocytes induce the migration of cardiac fibroblasts. *Cell. Physiol. Biochem.* 41, 413–421. doi: 10.1159/000456531

Ten Tusscher, K. and Panfilov, A. (2006). Cell model for efficient simulation of wave propagation in human ventricular tissue under normal and pathological conditions. *Phys. Med. Biol.* 51, 6141. doi: 10.1088/0031-9155/51/23/014

Ten Tusscher, K. H. and Panfilov, A. V. (2007). Influence of diffuse fibrosis on wave propagation in human ventricular tissue. *Europace* 9(Suppl. 6), vi38–vi45. doi: 10.1093/europace/eum206

van Rijsingen, I., Bekkers, S., Schalla, S., Hermans-van Ast, J., Snoep, G., Alzand, B. S., et al. (2011). Exercise related ventricular arrhythmias are related to cardiac fibrosis in hypertrophic cardiomyopathy mutation carriers. *Netherlands Heart J.* 19, 168–174. doi: 10.1007/s12471-011-0090-8

Vigmond, E., Pashaei, A., Amraoui, S., Cochet, H., and Hassaguerre, M. (2016). Percolation as a mechanism to explain atrial fractionated electrograms and reentry in a fibrosis model based on imaging data. *Heart Rhythm* 13, 1536–1543. doi: 10.1016/j.hrthm.2016.03.019

Watson, C. J., Collier, P., Tea, I., Neary, R., Watson, J. A., Robinson, C., et al. (2013). Hypoxia-induced epigenetic modifications are associated with cardiac tissue fibrosis and the development of a myofibroblast-like phenotype. *Hum. Mol. Genet.* 23, 2176–2188. doi: 10.1093/hmg/ddt614

Wu, K. C., Zerhouni, E. A., Judd, R. M., Lugo-Olivieri, C. H., Barouch, L. A., Schulman, S. P., et al. (1998). Prognostic significance of microvascular obstruction by magnetic resonance imaging in patients with acute myocardial infarction. *Circulation* 97, 765–772.

Xie, Y., Garfinkel, A., Camelliti, P., Kohl, P., Weiss, J. N., and Qu, Z. (2009). Effects of fibroblast-myocyte coupling on cardiac conduction and vulnerability to reentry: a computational study. *Heart Rhythm* 6, 1641–1649. doi: 10.1016/j.hrthm.2009.08.003

Yamashita, C., Hayashi, T., Mori, T., Tazawa, N., Kwak, C.-J., Nakano, D., et al. (2007). Angiotensin ii receptor blocker reduces oxidative stress and attenuates hypoxia-induced left ventricular remodeling in apolipoprotein e–knockout mice. *Hypertens. Res.* 30, 1219. doi: 10.1291/hypres.30.1219

Yin, Z., Li, T., Chen, Y., Zhao, L., and Yang, Y. (2012). Chronic intermittent hypoxia induces high blood pressure and oxidative stress in rats. *Heart* 98(Suppl. 2):E121. doi: 10.1136/heartjnl-2012-302920b.28

Zhou, L., Cortassa, S., Wei, A.-C., Aon, M. A., Winslow, R. L., and O'Rourke, B. (2009). Modeling cardiac action potential shortening driven by oxidative stress-induced mitochondrial oscillations in guinea pig cardiomyocytes. *Biophys. J.* 97, 1843–1852. doi: 10.1016/j.bpj.2009.07.029

Zimik, S., Nayak, A. R., and Pandit, R. (2015). A computational study of the factors influencing the pvc-triggering ability of a cluster of early afterdepolarization-capable myocytes. *PLoS ONE* 10:e0144979. doi: 10.1371/journal.pone.0144979

Conflict of Interest Statement: The authors declare that the research was conducted in the absence of any commercial or financial relationships that could be construed as a potential conflict of interest.

frontiers in Physics

ORIGINAL RESEARCH
published: 22 June 2018
doi: 10.3389/fphy.2018.00063

Synchronization of Pacemaking in the Sinoatrial Node: A Mathematical Modeling Study

Daniel Gratz[1,2], *Birce Onal*[1,2], *Alyssa Dalic*[1,2] *and Thomas J. Hund*[1,2,3]*

[1] The Dorothy M. Davis Heart and Lung Research Institute, The Ohio State University Wexner Medical Center, Columbus, OH, United States, [2] Department of Biomedical Engineering, College of Engineering, The Ohio State University, Columbus, OH, United States, [3] Department of Internal Medicine, The Ohio State University Wexner Medical Center, Columbus, OH, United States

Computational studies using mathematical models of the sinoatrial node (SAN) cardiac action potential (AP) have provided important insight into the fundamental nature of cell excitability, cardiac arrhythmias, and potential therapies. While the impact of ion channel dynamics on SAN pacemaking has been studied, the governing dynamics responsible for regulating spatial and temporal control of SAN synchrony remain elusive. Here, we attempt to develop methods to explore cohesion in a network of coupled spontaneously active SAN cells. We present the updated version of a previously published graphical user interface *LongQt*: a cross-platform, threaded application for advanced cardiac electrophysiology studies that does not require advanced programming skills. We incorporated additional features to the existing *LongQt* platform that allows users to (1) specify heterogeneous gap junction conductivity across a multicellular grid, and (2) set heterogeneous ion channel conductance across a multicellular grid. We developed two methods of characterizing the synchrony of SAN tissue based on alignment of activation in time and similarity of voltage peaks among clusters of functionally related cells. In pairs and two-dimensional grids of coupled cells, we observed a range of conductivities (0.00014–0.00033 1/Ω-cm) in which the tissue was more susceptible to developing asynchronous spontaneous pro-arrhythmic behavior (e.g., spiral wave formation). We performed parameter sensitivity analysis to determine the relative impact of ion channel conductances on cycle length (CL), diastolic and peak voltage, and synchrony measurements in isolated and coupled cell pairs. We also defined measurements of evaluating synchrony based on peak AP voltage and the rate of wave propagation. Cell-to-cell coupling had a non-linear effect on the relationship between ion channel conductances, AP properties, and synchrony measurements. Our simulations demonstrate that conductivity plays an important role in regulating synchronous firing of heterogeneous SAN tissue, and demonstrate how to evaluate the role of coupling and ion channel conductance in pairs and grids of SAN cells. We anticipate that the approach outlined here will facilitate identification of key cell- and tissue-level factors responsible for cardiac disease.

Keywords: sinoatrial node, synchrony, computational modeling, coupling, ion channel

OPEN ACCESS

Edited by:
Flavio H. Fenton,
Cornell University, United States

Reviewed by:
Fei Geng,
McMaster University, Canada
Yanyan Ji,
Georgia Institute of Technology, United States

***Correspondence:**
Thomas J. Hund
thomas.hund@osumc.edu

Specialty section:
This article was submitted to Biomedical Physics, a section of the journal Frontiers in Physics

Received: *15 December 2017*
Accepted: *04 June 2018*
Published: *22 June 2018*

Citation:
Gratz D, Onal B, Dalic A and Hund TJ (2018) Synchronization of Pacemaking in the Sinoatrial Node: A Mathematical Modeling Study. Front. Phys. 6:63. doi: 10.3389/fphy.2018.00063

INTRODUCTION

The sinoatrial node (SAN) generates the electrical impulse that coordinates mechanical contraction of the heart [1, 2]. Proper SAN function is an essential component for normal pacemaking at baseline and heart rate variation in response to external regulators such as exercise or stress [3, 4]. SAN dysfunction is common in a wide variety of cardiac diseases, and is characterized by sinus bradycardia, sinus pause, and/or inappropriate heart rate responses to exercise and stress [5]. Regulation of SAN activity has great therapeutic potential for a rapidly aging population where SAN disease affects 1 in 600 heart patients over the age of 65 [6]. The only effective treatment for patients with chronic symptomatic sinus node dysfunction is pacemaker implantation [7].

SAN cells demonstrate spontaneous action potential (AP) activity and exhibit a wide variety of dynamic phenomena similar to other coupled oscillators, including collective synchronization [8]. One challenge for studying synchronization of cardiac pacemaking activity is the multiscalar and heterogeneous nature of the sinus node. Pacemaking is governed by a delicate source-sink relationship between the SAN and surrounding atria defined by the need for a relatively small structure (SAN) to excite a much larger tissue mass (surrounding atria) [9, 10]. This source-sink relationship is altered in disease due to increased fibrosis and/or cell loss leading to a shift of the primary pacemaker site, emergent behavior of ectopic foci, or otherwise reduced capacity for SAN pacemaking [11–13]. There is a critical need to expand knowledge regarding regulation of membrane ion channels in the SAN, as well as to further develop quantitative tools to assess the sensitivity of the SAN to changes in coupling and ion channel regulation [14].

Mathematical modeling has been used to investigate and advance our understanding of cardiac electrophysiology, arrhythmia mechanisms, and potential therapies [15]. Models have been particularly helpful in elucidating the ionic basis of SAN activity and cardiac pacemaking [16, 17]. For example, SAN cell models have furthered our understanding of the relative importance of coupling between Ca^{2+} cycling and membrane ion channels in automaticity [18] and the genetic basis of human SAN disease [19]. At the same time, multicellular models of coupled SAN cells have demonstrated dynamic changes in the location of the primary pacemaker site in response to β-adrenergic stimulation [20]. Other studies have coupled heterogeneous cell types in multicellular preparations to examine the influence of inexcitable cells (e.g., fibroblasts) on pacemaking [21, 22].

Although mathematical modeling has undoubtedly advanced our understanding of SAN function, there remain significant barriers to more widespread use of mathematical modeling and simulation in the field. To reduce these barriers a cross-platform user interface called *LongQt* has been developed for advanced cardiac electrophysiology and arrhythmia simulations [23]. Here, we present an extended user interface for *LongQt*, which adds support for performing advanced multicellular simulations. With this added utility, the influence of perturbations in SAN cell electrophysiology (ion channel conductance and gap junction conductivity) on synchronization of coupled heterogeneous SAN cells was investigated. Two complimentary measures were defined to quantify the level of synchronization between coupled cells: synchrony factor and peak transmembrane potential ($V_{m,peak}$) similarity. Parameter sensitivity analysis was performed in single cells and in coupled cell pairs to determine the impact of ion channel and gap junction properties on cycle length (CL), peak and diastolic V_m, and measures of synchrony. Finally, we performed two-dimensional simulations in a network of 7 × 7 heterogeneous SAN cells to examine the influence of cell properties and gap junction conductivity on pacemaking. These studies generate a number of interesting findings, including: (1) conductivity caused small but potentially important differences in the relative impact of ion channel conductances on AP properties in coupled cells; (2) a specific coupling range promoted emergent asynchronous behavior; and (3) quantitative measurements were defined to evaluate synchrony based on peak AP voltage and the rate of propagation within a group of coupled firing cells. While our findings highlight the difficulty of relating events at the single cell level to an emergent behavior like pacemaking, they also point to more robust methods for understanding the ionic basis of cardiac pacemaking.

MATERIALS AND METHODS

Ion channel kinetics were simulated using an existing well-validated model of the rabbit SAN cell implemented in *LongQt* simulation software [23, 24] (**Figure 1A**). Briefly, the *LongQt* simulation software has three main user interfaces: the grid editor, the main user interface, and the grapher. The simulations performed for this study were set up using the grid editor, which allows the user to select tissue geometry and gap junction conductivity for a set of simulations. The files generated by the grid editor can be selected to run in the main user interface, which also allows the user to select the cell model and measure properties of the simulation. Simulation results generated at the end of the simulation can be visualized by the grapher interface.

Multicellular Simulations

Multicellular simulations were performed in either a cell pair or 7 × 7 grid. The two-dimensional cable equation was solved using the Peaceman-Rachford alternating direction implicit method. The level of conductivity between cells was perturbed about a default value of 0.33 1/Ω-cm. A heterogeneous population of SAN APs were created by varying eight ion channel conductances ($I_{Ca,L}$, I_{Catt}, I_h, I_{Kr}, I_{Ks}, I_{NCX}, I_{NaK}, I_{to}) lognormally, with a mean of 1 and a standard deviation of 0.2. Spontaneous APs were simulated for 50–100 s until steady state was reached. AP properties such as CL, $V_{m,peak}$, and maximum diastolic potential (MDP) were measured using *LongQt*. All other analysis was performed with scripts written in Python version 3, which are available on Github.

Synchrony Measurements

In order to develop measurements of synchrony in multicellular simulations, we organized APs from individual cells in the grid into "activation clusters," which represent a group of neighboring cells whose activation could be considered related both in time

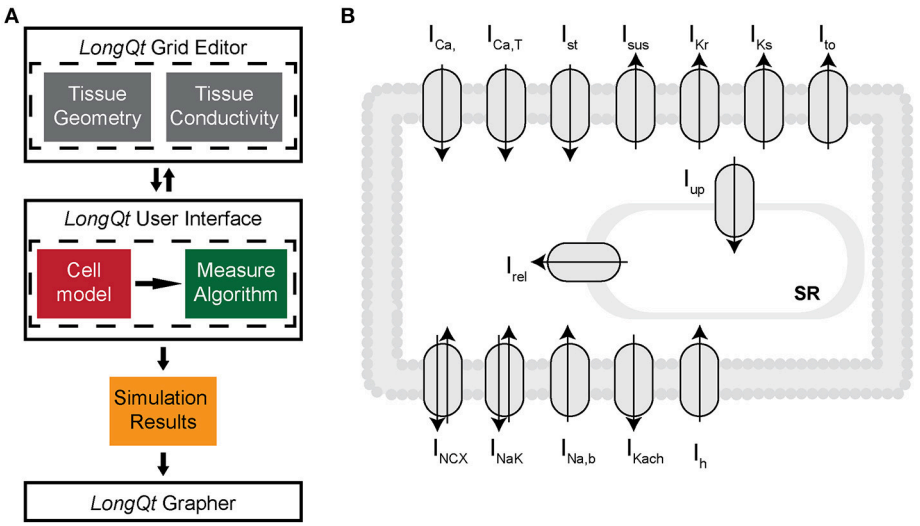

FIGURE 1 | (A) *LongQT* simulation software uses an object-oriented design where a "Cell" class describes the workings of an individual cell, i.e., Rabbit SAN cell vs. Human Ventricular cell. Cell classes then are used by "Protocol" classes to define what type of simulation is being run on the cell. This could be a simulation with constant stimulus or periodic stimulus. Simulations of fiber and grid tissue require additional objects that go between Protocols and Cells to define properties of the tissue like its geometry and conductivity. Finally there is a "Measure" class which tracks values such as Peak Voltage or Ca^{2+} minimum. **(B)** Schematic diagram of the rabbit SAN cell model, which includes mathematical representations of ion currents important for generating the sinoatrial node cell action potential: L-type and T-type Ca^{2+} currents (I_{CaL} and I_{CaT}), Rapid and slow components of the delayed rectifier K^+ currents (I_{Kr} and I_{Ks}), 4AP-sensitive transient outward and sustained K^+ currents (I_{to} and I_{Sus}), acetylcholine-sensitive K^+ current (I_{Kach}), Hyperpolarization-activated funny current (I_h), Na^+/Ca^{2+} exchanger (I_{NCX}), Na^+/K^+ pump (I_{NaK}), and Ca^{2+} signaling uptake (j_{up}) into the network sarcoplasmic reticulum (NSR), transfer (j_{tr}) into the junctional SR (JSR), and release (j_{rel}) into the subspace.

and space. To organize cells into clusters, we ordered them sequentially according to their respective activation times. The sequence was then processed in order and a cell was added to a cluster if its position was within three cells of any cell already in the cluster. For higher gap junction conductivities, we increased the spatial window to five cells to account for increased communication between cells. If an activated cell was not spatially close enough to any existing group of firing cells, then it was marked as the focus of a separate and distinct cluster. Any cluster would be considered complete when one of its constituent cells fired again. This allowed for characterization of multiple clusters simultaneously within the same grid (common in lower conductivity grids).

For example, given an ordered sequence of cell activation times $(Cell_{1,1}, Cell_{1,2}, Cell_{5,5}, Cell_{1,1}, Cell_{1,3})$, where $\text{Cell}_{i,j}$ is located in the i^{th} row and j^{th} column of a two-dimensional grid, the clustering algorithm would select $Cell_{1,1}$ as the beginning of a new cluster, C_1, as there are no other existing clusters. The second cell in the sequence, $Cell_{1,2}$, would then be added to C_1 as it is within three cells of $Cell_{1,1}$. $Cell_{5,5}$, however, is too far away from C_1 and so would be marked as the beginning of a new cluster, C_2. Since $Cell_{1,1}$ is already assigned to C_1, its appearance a second time in the sequence causes the algorithm to initialize a new cluster C_3. Finally, the last element in the sequence, $Cell_{1,3}$, would be added to C_3.

$V_{\text{m,peak}}$ similarity is calculated as the inverse of the standard deviation of $V_{\text{m,peak}}$ in each cluster. The synchrony factor is calculated as the inverse of the slowest propagation time between the closest cells in a cluster. These two measurements are then weighted by the size of the cluster in order to account for the number of oscillators in the network.

Software and Hardware

LongQt simulation software utilizes the *Qt* application framework (version 5.6 or later found at https://www.qt.io) and may be compiled to run on Mac (OS X 10.10 or later), Windows (version 7 or later) or Linux systems. Python bindings for *LongQt* are available for more extensive simulation use. Compiled versions of *LongQt* are available as downloadable executable files under the "Research" section of the Hund lab website[1], and are accessible through Github[2]. *LongQt* incorporates C++ code for the Kurata SAN cell model (**Figure 1B**). Differential equations for the simulated model are solved in *LongQt* using the forward Euler approach, with a maximum timestep of 0.05 ms and a minimum timestep of 0.005 ms. A subset of simulations were run using Ohio Supercomputer Center resources [25]. Data supporting conclusions of this manuscript are available upon request to the corresponding author.

RESULTS

Effect of Coupling on Parameter Sensitivity in Coupled Pairs of Sinoatrial Node Cells

Parameter sensitivity analysis has been performed mostly on models of the single cell to elucidate mechanisms underlying

[1]https://hundlab.engineering.osu.edu
[2]https://github.com/hundlab

cardiac AP generation [26–30]. Using the extended *LongQt* platform, we sought to address the extent to which coupling influences the dynamics of synchronous firing in a network of SAN oscillators with heterogeneous ion channel activity. We first coupled a simulated wild-type (WT) to a variant SAN cell (scaling factors defined as follows: $I_{Ca,L} = 3.19472$, $I_{Catt} = 2.59237$, $I_h = 2.64054$, $I_{Kr} = 2.3018$, $I_{Ks} = 2.93799$, $I_{NCX} = 2.79239$, $I_{NKA} = 2.45686$, $I_{to} = 2.06311$) and observed spontaneous AP properties for coupled and uncoupled pairs (**Figures 2**, **3**). As expected, despite very different AP properties of the individual cells, a normal degree of coupling eliminated differences between the two cells. Interestingly, the steady-state CL, DDR, and MDP values of the coupled cells were closer to that of the single cell with the shortest CL (in this case, the variant cell). This phenomenon is consistent with observations of shifts of the SAN pacemaker site in cardiac disease from the original area of excitation to areas with the earliest depolarization [31].

To provide insight into the influence of coupling on spontaneous AP dynamics, we performed parameter sensitivity analysis on the single cell by generating 616 AP variants and performing linear regression on the dataset. We compared these results to a separate regression analysis on a dataset where the variant was coupled to a WT cell (**Figure 4**). For the most part, regression coefficients relating ion channel conductances to AP properties were similar for single and coupled cells. For example, perturbations in maximal conductances of the L-type Ca^{2+} current ($I_{Ca,L}$) and the transport rate of the Na^+/K^+ ATPase (I_{NaK}) have a large positive influence on $V_{m,peak}$ in both single and coupled simulations, while perturbations in conductances of the T-type Ca^{2+} current (I_{Catt}), rapid delayed rectifier K^+ current (I_{Kr}), and transient outward K^+ current (I_{to}) are inversely related, i.e., an increase in I_{Catt}, I_{Kr}, or I_{to} decrease peak V_m. Despite the overall agreement, there are small but interesting differences between sensitivity of the single vs. coupled cell. First, while $I_{Ca,L}$ has a positive effect on CL and $V_{m,peak}$ in both single and coupled cells, its influence is diminished in the coupled cell. Likewise, coupling reduces the influence of $I_{Ca,L}$ on DDR and MDP. In contrast, our simulations predict that coupling increases the effect of I_{Kr}, at least with respect to DDR and CL.

To provide additional insight into the influence of coupling strength on sensitivity analysis, we performed 6160 simulations (10 conductivities, 616 simulations of a WT cell coupled to a variant cell) over a range of conductivities (**Figure 5**). In many instances, the regression coefficients mapping ion channel conductances to AP properties were found to be independent of coupling strength, especially for $V_{m,peak}$ and MDP. However, interesting exceptions to this behavior were observed for CL and DDR, where regression coefficients for specific ion channels were highly dependent on coupling strength (e.g., $I_{Ca,L}$, $I_{Ca,tt}$, I_h for CL and I_h and I_{Kr} for DDR) This series of simulations suggests that the relative importance of specific ion channels for cardiac pacemaking changes in subtle but important ways across a range of coupling values.

We sought to explore coupling effects over a range of 25 different coupling strengths with a WT cell coupled to 20 different variants (totaling 500 different simulations of two coupled cells). We plotted the average steady-state values of the MDP, $V_{m,peak}$, and CL for both the coupled WT and variant cells at each coupling value. As expected, values for MDP, $V_{m,peak}$, and CL converge in the WT and variant cell as gap junction conductivity increases (**Figure 6**). Interestingly, CL appears to synchronize at lower conductivity values compared to other AP properties. Furthermore, a small window of interesting dynamics characterized by increased standard deviation values for AP properties was observed around $10^{-3.8}$ 1/Ω-cm.

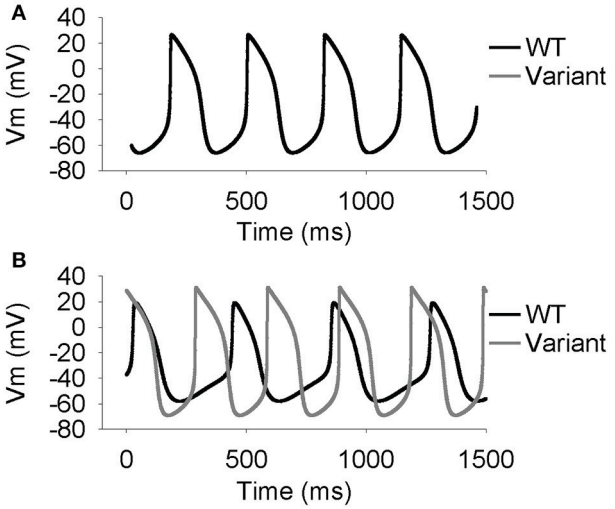

FIGURE 2 | Simulated spontaneous SAN action potentials in one WT cell and one cell with lognormally perturbed ion channel factors. Simulations were run to steady state (50 s). **(A)** At a conductivity of 0.33 (1/Ω-cm), which is the normal conductivity between two WT cells, the cells synchronize both the voltages and the times at which they fire. **(B)** At a conductivity of 0 (1/Ω-cm) the cells are uncoupled and act the same as if they were run independently.

Effect of Coupling in Two-Dimensional Simulations of Heterogeneous SAN Cells

We hypothesized that the range of conductivities identified in **Figure 6** with large standard deviations would promote asynchronous activity in two-dimensional simulations of heterogeneous SAN cells. We simulated 7 × 7 grids of variant SAN cells with homogeneous cell-to-cell coupling, for 25 different conductivities. At low coupling values most SAN cells oscillate without interacting with each other (**Supplementary Videos 1, 2**). The range of values indicated by arrows in **Figure 6** was also the range in which spiral wave activity was sustained in the two-dimensional grid simulation (**Supplementary Videos 3, 4**). For higher degrees of cell-to-cell coupling, cells across the grid were fully synchronized (**Supplementary Videos 5, 6**). This set of simulations suggests that coupling can promote an arrhythmogenic substrate, even in a small group of pacemaker cells.

Quantifying Synchrony in Two-Dimensional Simulations of Heterogeneous SAN Cells

We sought to quantify the level of synchrony in a two-dimensional grid in order to quantitatively distinguish between spiral wave formation (**Supplementary Videos 3, 4**), completely asynchronous activity (**Supplementary Videos 1, 2**) and

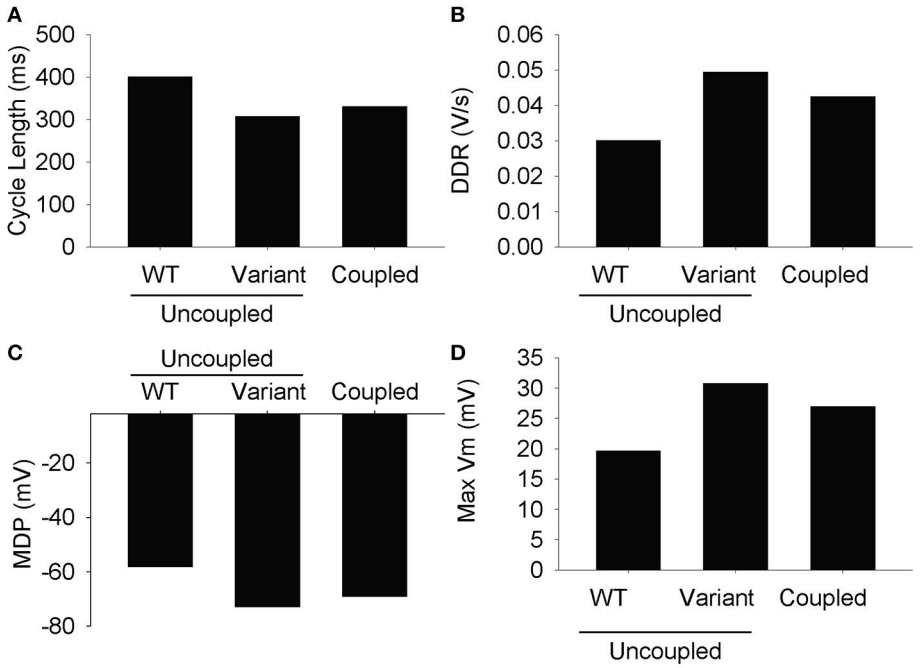

FIGURE 3 | Measured steady state values from the last action potential in the simulation. The differences between the two cells are resolved at full conductivity to a value somewhere between the two cells. **(A)** Cycle length, **(B)** diastolic depolarization rate, **(C)** max diastolic potential, (**D**) max voltage.

synchronous firing (**Supplementary Videos 5, 6**). Plotting beat-to-beat CL for all 49 cells in a 7 × 7 grid for three different gap junction conductivities demonstrates a wide range of steady-state CLs when the propagating wave is random (**Figure 7A**), large deviations when spiral waves are formed (**Figure 7B**, <20 s), and a uniform CL across the grid when the tissue is oscillating synchronously (**Figure 7B**, >20 s and **Figure 7C**). Plotting beat-to-beat CL at normal conductivities shows uniform CL across all cells in the simulation (**Figure 7C**).

The synchrony factor, which represents the inverse of the longest conduction time between two cells in the same cluster, approaches zero and demonstrates noise (0.5 amplitude trace) for chaotic asynchronous simulations where the cells are not interacting with each other (**Figure 7D**). When coupling is in a range that sustains spiral wave activation, the spiral waves can be visualized in the peaks and valleys of synchrony factor over time (**Figure 7E**, <20 s). As coupling increases to normal consistent propagation across the entire grid, the synchrony factor increases and maintains a steady value (**Figure 7E**, >20 s and **Figure 7F**). Synchrony factor values above 1 consistently represented fully synchronized grids, and below 0.5 consistently represented asynchronous random poorly coupled oscillations.

$V_{\mathrm{m,peak}}$ similarity, which represents the inverse of the standard deviation of peak voltages in one beat, approaches zero with high-amplitude fluctuations for chaotic asynchronous simulations (**Figure 7G**). As a simulation transitions from asynchronous (**Figure 7H**, <5 s) to an organized, complex activation (spiral wave, **Figure 7H**, >5 and <20 s) $V_{\mathrm{m,peak}}$ similarity rapidly reaches a single steady-state value after a brief period of low amplitude fluctuation. Synchronized activation produces a large steady-state value for $V_{\mathrm{m,peak}}$ similarity with a brief latency (**Figure 7I**). These results demonstrate the utility of quantifying synchrony measures to distinguish between random, spiral, and synchronous propagating waves sustained by coupling differences in heterogeneous SAN tissue. $V_{\mathrm{m,peak}}$ similarity values above 15 consistently represented fully synchronized grids, and below 10 consistently represented asynchronous random poorly coupled oscillations.

We performed parameter sensitivity analysis on coupled cells to determine the relative ion channel contributions to the synchrony factor and peak voltage similarity measurement (same 616 simulations as **Figures 4A–D**). At normal gap junction conductivity, synchrony factor is not dominated by any single ion channel conductance (relatively small regression coefficients for all conductances) with surprisingly little contribution from I_{h} (**Figure 8A**). However, $I_{\mathrm{Ca,L}}$ and I_{NaK} both had a large negative contribution and I_{to} a large positive contribution to $V_{\mathrm{m,peak}}$ similarity (**Figure 8B**). The relationships observed in **Figure 8B** also seemed to be an inverse of the contributions to peak voltage in previous simulations (**Figure 4A**). When we performed parameter sensitivity analysis over a range of conductivities, we observed that the relationship between each individual ion channel's contribution and synchrony factor was non-linear with respect to conductivity (**Figure 4C**). Interestingly, any shifts from a positive to negative contribution occurred in the range of 10^{-4} 1/Ω-cm which is the same range that we observed sustained spiral wave activity (**Supplementary Videos 3, 4**) and large standard deviations in CL (**Figure 6C**).

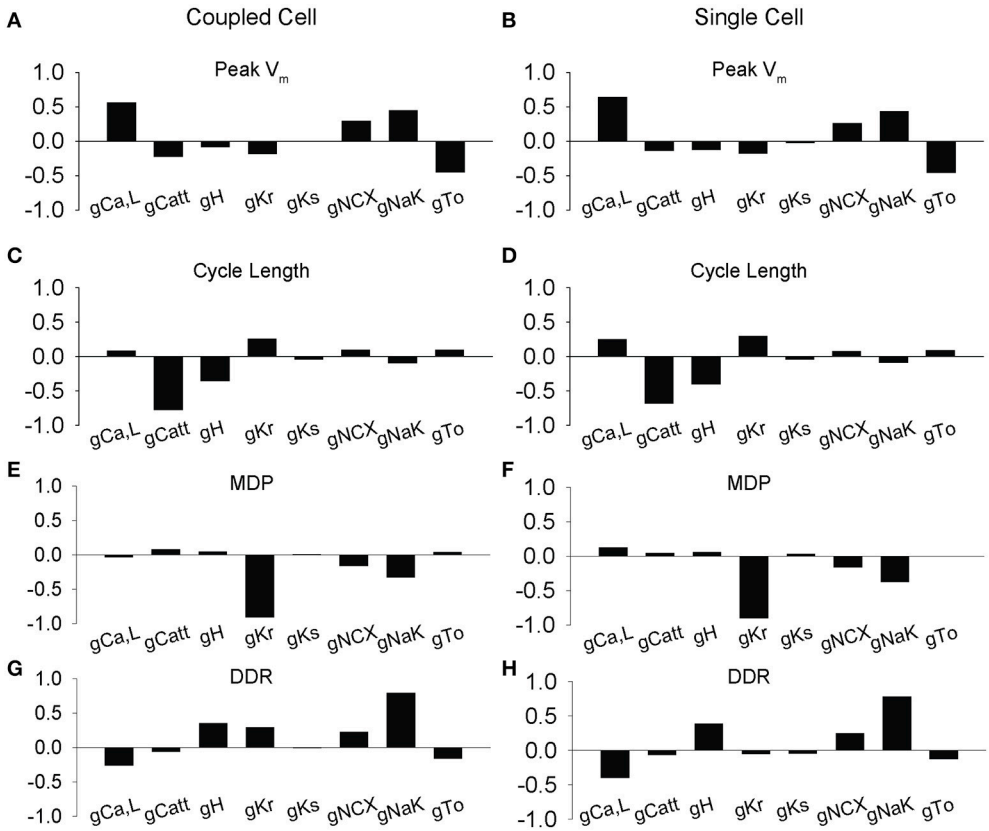

FIGURE 4 | Partial least-squares regression analysis of ionic gating variables in the rabbit sinus node model. Regression coefficients showing how changes in model parameters affect membrane dynamics in two coupled simulated SAN cells. 616 simulations were performed at a normal coupling strength (0.33) between one WT and one variant cell with random ion channel factors (L-type Ca^{2+} current $I_{Ca,L}$, T-Type Ca^{2+} current $I_{Ca,T}$, hyperpolarization-activated current I_H, rapidly activating delayed rectifying K^+ current I_{Kr}, slowly activating delayed rectifying K^+ current I_{Ks}, Na^+/Ca^{2+} exchanger I_{NCX}, Na^+/K^+ ATP-ase I_{NaK}, transient outward K^+ current I_{to}) perturbed over a lognormal distribution, with a mean of 1.0 and a standard deviation of 0.2. Parameter sensitivities of ion channel conductance parameters affect **(A–B)** peak membrane voltage, **(C–D)** cycle length, **(E–F)** max diastolic potential (MDP), and **(G–H)** diastolic depolarization rate (DDR). The impact of $I_{Ca,L}$, I_{Catt}, I_{to}, I_{Kr}, and I_{NaK} contributed highly to membrane voltage dynamics including peak ($I_{Ca,L}$, I_{NaK}, I_{to}), cycle length (I_{Catt}), diastolic membrane voltage (I_{Kr}, I_{NaK}), and diastolic depolarization rate (I_{NaK}).

DISCUSSION

In this study, we use mathematical modeling to explore the role of coupling on spontaneous AP dynamics and synchronization of pacemaking. Our simulations led to a number of important findings, including: (1) While parameter sensitivity analysis reveals a similar relationship between ion channel conductances and AP properties in single and coupled cells, our simulations predict small but potentially important differences, including complicated effects of coupling on the influence of $I_{Ca,L}$ and I_{Kr}; (2) a specific coupling range in simulations promoted complex emergent behavior (including spiral wave activation) and at values higher than this coupling range cells fired together synchronously; (3) We define an approach for first defining groups of related cells (activation clusters) and then characterizing their synchrony (synchrony factor and peak voltage similarity), which facilitates quantification and visualization of synchronous behavior in a two-dimensional heterogeneous grid of SAN cells. Our studies are distinct from previous studies investigating coupling between spontaneously activating oscillators in that we employ an AP model that describes detailed ion channel kinetics. Another novel aspect of this set of studies is the introduction of updated *LongQt* simulation software to explore the impact of heterogeneous ion channel expression and gap junction conductivity in multicellular simulations. *LongQt* is cross-platform and available for download at hundlab.org, and may be useful in future exploration of conductivity in two-dimensional simulated tissue.

Previous studies have explored coupling inhomogeneity between simulated SAN cells and observed trends of synchronous firing and heterogeneous tissue becoming homogeneous through a democratic entrainment process at sufficient coupling values [20, 32, 33]. Our studies also support the theory of a democratic entrainment process both at the level of two coupled cells (**Figure 6**) where both cells adjusted their transmembrane dynamics to adjust to a new value that was distinct from firing alone. All grid simulations with uniform wave propagation began activation from a cluster of cells firing together rather than a

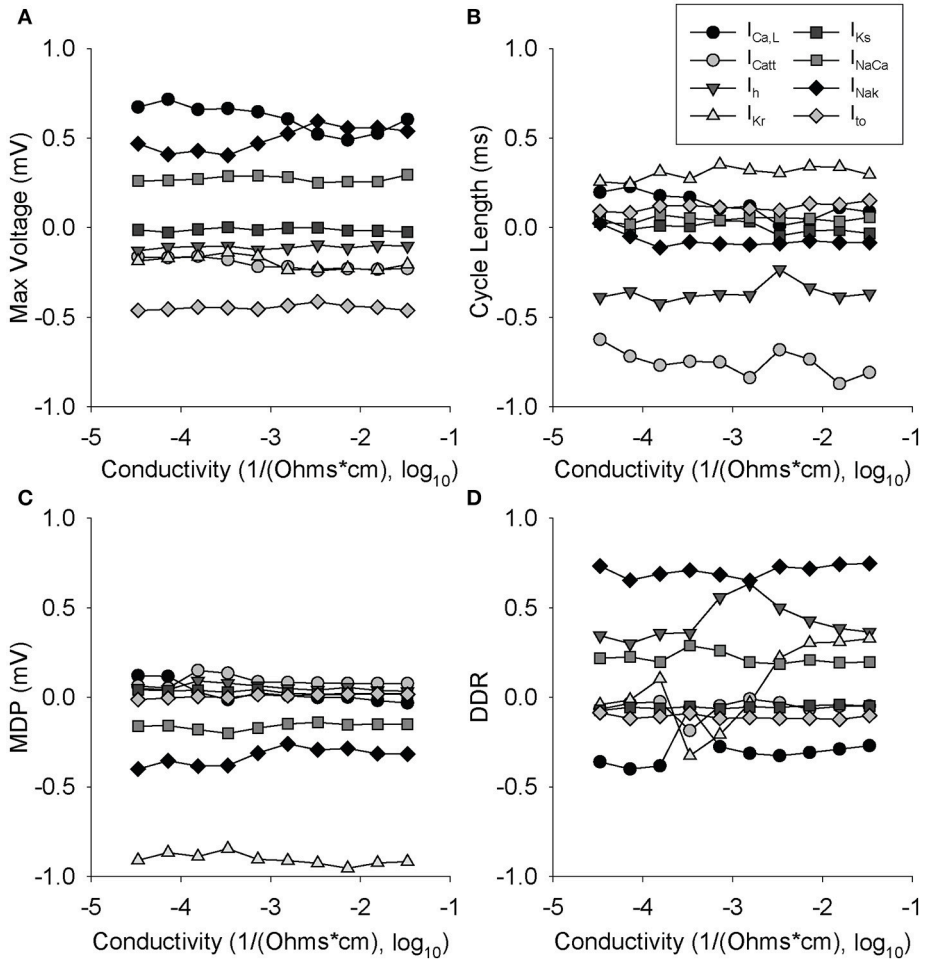

FIGURE 5 | Partial least-squares regression analysis of ionic gating variables vs. cell conductivity. Two cells were paired where one was lognormally perturbed with a mean of 1 and a standard deviation of 0.2, while the other cell was WT. 616 simulations were run at each conductivity for the least-squares regression at each of 10 different conductivities. Regression coefficients are shown over a range of gap junction conductivities for: **(A)** Max voltage, **(B)** cycle length, **(C)** max diastolic potential, **(D)** diastolic depolarization rate.

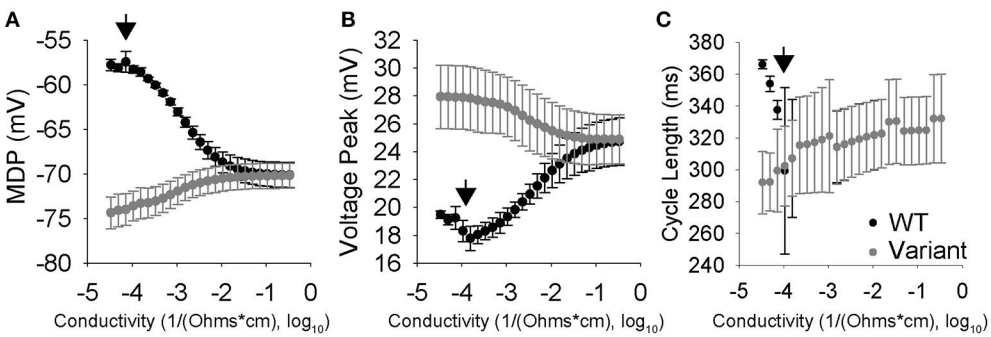

FIGURE 6 | Conductivity vs. cell properties for two coupled SAN cells where one cell was perturbed lognormally, while the other cell is a WT. Data points are the average of 20 simulations with the error bars corresponding to one standard deviation. **(A)** Max diastolic potential vs. Conductivity. Max diastolic potential synchronizes at higher conductivities and the means become equal around $10^{-1.6}$ 1/Ω-cm. Larger standard deviations are observed around 10^{-4} 1/Ω-cm. **(B)** Peak voltage vs. conductivity. Peak voltage equalizes at higher conductivities and the means become equal around 10^{-1} 1/Ω-cm. Larger standard deviations are observed in the 10^{-4} and 10^{-3} 1/Ω-cm range. **(C)** Cycle Length vs. Conductivity. Cycle length synchronization happens at much lower conductivities than the others, with the means equalizing between 10^{-4} and 10^{-3} 1/Ω-cm. It is in this range that the cells are highly interactive but not fully able to synchronize, which is indicated by large standard deviations.

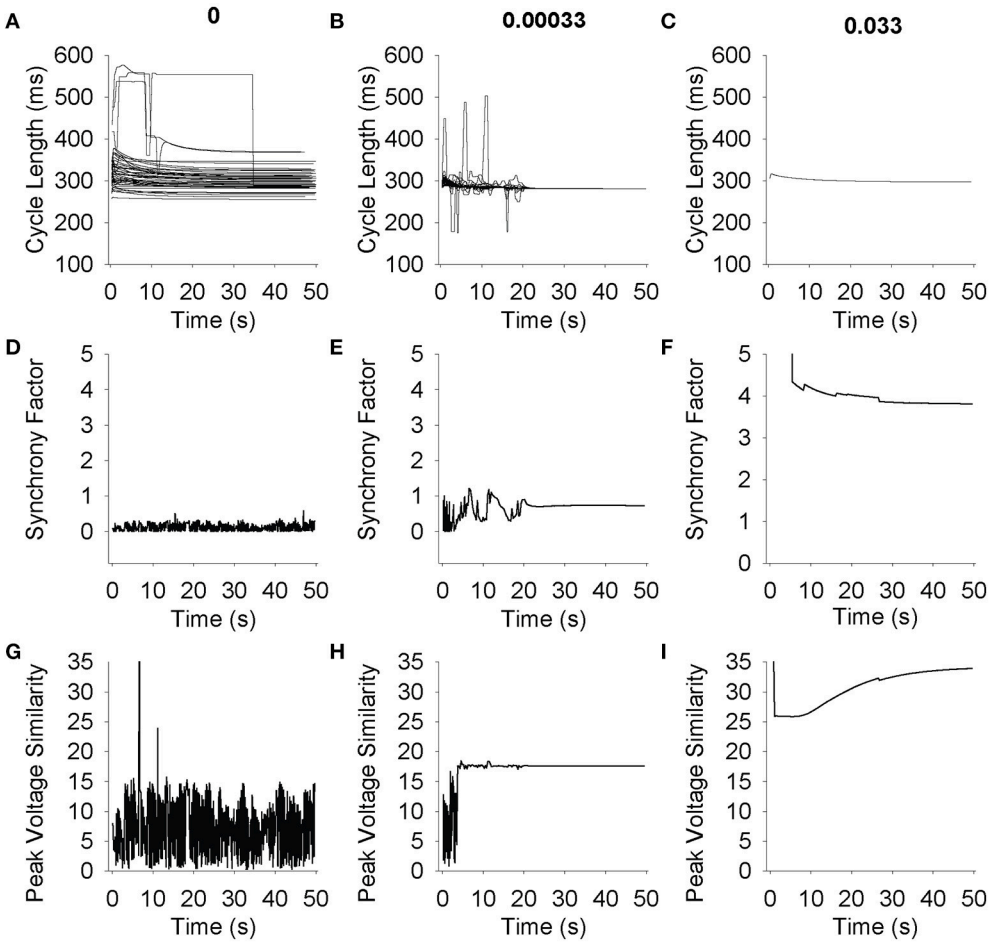

FIGURE 7 | Simulations were run on a 7 × 7 grid for 50 s. Each cell was randomly perturbed using a lognormal distribution with a mean of 1 and a standard deviation of 0.2. **(A–C)** Cycle length for 49 cells is shown over time. At low conductivities **(A)** cells do not synchronize, and as conductivity increases the cells begin to interact and find a common cycle length **(B)** and eventually fire at a common cycle length immediately **(C)**. **(D–F)** Synchrony factor vs. Time. The synchrony factor measurement is the longest amount of time it takes the peak of the action potential to propagate from any cell to its neighbor. Low values indicate random and low synchrony factor waves **(D)**. The larger peaks and valleys that appear in higher conductivities **(E)** correlate with spiral wave formation and multiple wave fronts in the grid. When cells interact and fire in cohesive synchronization **(F)**, synchrony factor becomes higher and stabilizes. **(G–I)** Peak voltage similarity vs. Time. The peak voltage similarity measurement is the inverse of the standard deviation of the voltage values across the grid. Low conductivities indicate random noisy peak voltage similarity waves **(G)**. As conductivity increases, peak voltage similarity increases and stabilizes initial noisy values **(H)**. At higher conductivities, peak voltage similarity display no errant behavior **(I)**.

single cellular driver (**Supplementary Videos 1–6**). This cluster size was different for different coupling values, indicating that the multicellular simulations demonstrated mutual entrainment of SAN cells.

The SAN is a small structure that is insulated from the rest of the right atrium, and employs a limited number of conduction pathways in order to activate the surrounding tissue [34, 35]. In the SAN, cells form groups with high degrees of coupling between cells in a group and much lower amounts of coupling at the border of groups [36, 37]. Conduction barriers due to fibrosis or structural remodeling may inhibit healthy SAN activation, and initiate SAN microreentrant waves [38]. Previous simulation studies have observed that microreentrant conduction was not sustained by AP changes, and required a large center of fibrotic tissue to produce microreentry [22]. We identified a specific range of low coupling that sustained emergent spiral wave behavior in a heterogeneous grid of SAN APs, indicating that increased coupling is a crucial component to synchronization of pacemaker cells and sufficient coupling may override differences in cell-to-cell transmembrane dynamics. Notably, our simulations did not require implementing a "track" of fibrotic tissue around which the AP wave could propagate, but still resulted in emergent behavior. The synchrony factor measurement, which best represents how closely together cells are firing within a beat, demonstrated a non-linear relationship with respect to coupling (**Figure 8A**). This further supports the idea that coupling non-linearly alters the ability of SAN cells to fire synchronously.

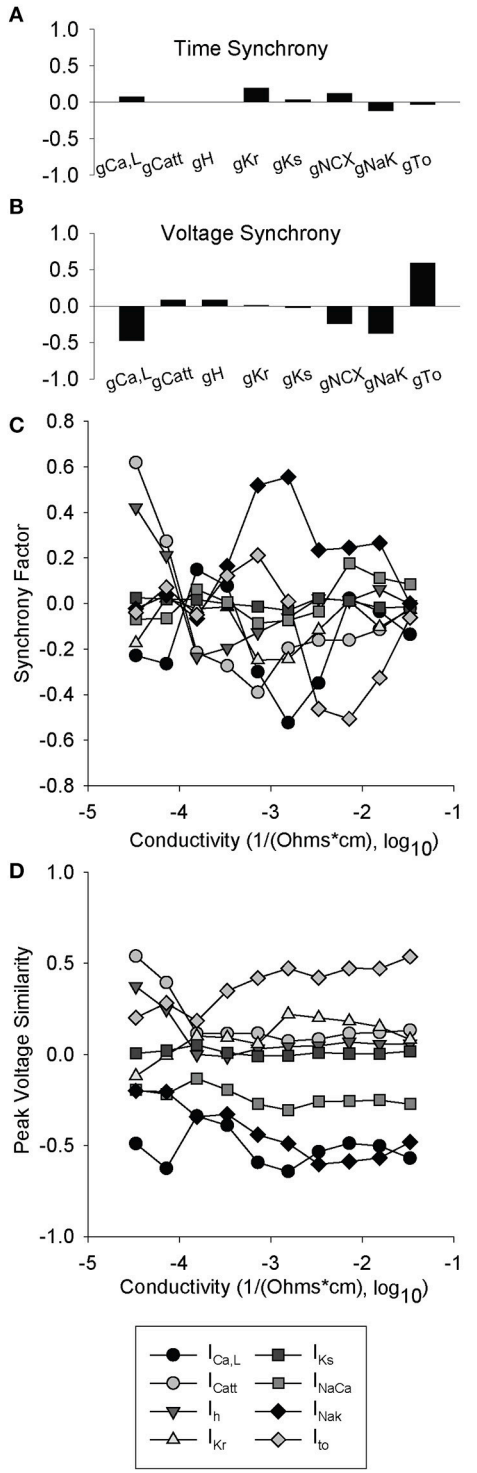

FIGURE 8 | Partial least-squares regression analysis of synchrony factor and peak voltage similarity metrics. 616 simulations were run with two paired cells where one was lognormally perturbed with a mean of 1 and a standard deviation of 0.2, while the other cell was a WT. Ion channel coefficients did not have a significant impact on **(A)** synchrony factor. In contrast, parameter sensitivity analysis indicates that the impact of $I_{Ca,L}$, I_{NaK}, and I_{to} greatly

(Continued)

FIGURE 8 | impact the **(B)** peak voltage similarity metric. **(C,D)** Partial least-squares regression analysis of ionic gating variables vs. cell conductivity. At each conductivity simulations were run as in **(A)** and **(B)** and a total of 10 different conductivities were examined. **(C)** Synchrony factor is very non-linear with a range between 10^{-4} and 10^{-3} 1/Ω-cm in which all the ion channel coefficients are very close to 0. **(D)** Peak voltage similarity is mostly linear with an exception between 10^{-4} and 10^{-3} 1/Ω-cm where most of the ion channel coefficients pinch toward 0.

In previous work, Michaels et al. examined the effects of cell-to-cell coupling strength on entrainment [20, 33]. They tested both paired cells as well as small grids. In paired cells they observed that the cells tended to synchronize to a CL closer to the faster cell. In a grid they found that the apparent wave front slowed as coupling strength decreased, however they did not see spiral waves or other conduction issues. They also tested a grid with a partial wall of inexcitable tissue and found that the cells on the other side were still trained, although slightly delayed.

Shifts in the location and size of the SAN pacemaker may occur as a compensatory mechanism in response to sinus node dysfunction, vagal nerve stimulation, or pharmacological block of the Na^+ current or L-type Ca^{2+} current [31]. Our simulations show that a heterogeneous SAN with low coupling will sustain pro-arrhythmic behavior, but increasing coupling may help synchronize the entire grid. A shift in size and location of the pacemaker may be beneficial due to coupling changes; this shift transforms the pacemaker into a larger group of highly coupled cells, which our simulations show can synchronize through a democratic entrainment process regardless of ion channel heterogeneity. These studies also suggest that altering gap junction coupling in the SAN may promote healthy pacemaking activity.

The studies presented here perform a variety of parameter sensitivity analyses in order to deconstruct the relationship between ion channel conductance, conductivity, SAN transmembrane properties (DDR, MDP, peak voltage, and CL), and the proposed measurements of synchrony (synchrony factor and peak voltage similarity). Both $I_{Ca,L}$ and I_{Kr} demonstrated a high contribution to transmembrane dynamics and non-linear behavior with respect to transmembrane properties and synchrony metrics. This is further supported by experimental evidence of sinus node impairment or dysfunction related to modulation of L-type Ca^{2+} current [39, 40] or hERG channel function [41, 42]. The parameter sensitivity analysis also demonstrates that the relationship between specific ion channel conductances may vary depending on cell-to-cell coupling values (**Figures 5**, **8**). This suggests that it is not necessarily sufficient to extrapolate effects of single cell perturbation to emergent behavior at the tissue level.

The emergent behavior of coupled oscillators has been widely explored in both computational and experimental studies of multiple areas of biology such as mitochondrial, circadian rhythms, synaptic firing, and broader ecological studies. Synchronization and its quantification has been widely discussed in networks of coupled oscillators [43–46]. Our hope

is that these set of studies contributes to an already diverse set of work and adds to understanding of the impact of ion channel behaviors as well as coupling in the SAN pacemaker. We also believe that the synchrony metrics presented here would be useful for quantifying dynamics in larger tissue experiments such as optical mapping experiments. Future studies quantifying synchronization of coupled SAN oscillators in tissue or determining the impact of ion channel changes on generation of microreentrant arrhythmias may help support the findings in the simulations shown here.

LIMITATIONS

While these mathematical modeling studies are based on a well-validated single cell model of the rabbit SAN AP, the two-dimensional simulations have important limitations based on experimental data. For the sake of simplicity, SAN cells were coupled in a uniform rectangular grid with homogeneous coupling strengths, but this does not match the detailed physiology of the three-dimensional atrium. Similarly, heterogeneity of the SAN is modeled as either a gradient with AP differences between the central and periphery of the node, or a mosaic with a variable mix of SAN and atrial cells from periphery to the center. The gradient model is supported by a wide range of experimental data and simulations showing a change in the transmembrane properties of the SAN between the periphery and the center, a change in the density of ion channels responsible for I_{Na} and I_f, and a lack of atrial cells in the center of the SAN [47, 48]. The studies presented here more closely represent the mosaic model, but are distinct in that only SAN cells are implemented (no randomly placed atrial cells are simulated in the grid simulations). It is also important to note that the grid used in our studies contains a relatively small number of cells compared to the actual SAN. However, based on previous work [36, 37], it is possible to consider each cell in the grid as representative of a group of cells so that the behavior observed in our grid should scale to larger dimensions. Finally, these simulations did not implement parasympathetic stimulation of tissue, or patch of atrial tissue surrounding the SAN to further explore activation of atrial tissue by the SAN complex. This is especially important to note in two-dimensional simulations using a rabbit SAN model, since the architecture of the rabbit sinus node and its subsequent conduction pathways is distinct from human [31]. Conductivities between cells in these simulations were fixed, so the tubular shape of cells was ignored. In addition, we observed emergent behavior at the edges of large grid simulations, which may be an artifact of the simulation setup. While outside the scope of the current study, going forward it would be interesting to design experiments to test model predictions in in *ex vivo* preparations.

AUTHOR CONTRIBUTIONS

DG, BO, AD, and TH participated in design of study; DG, AD, and BO performed simulations, analyzed data, and wrote the manuscript; DG, BO, and TH revised the manuscript.

FUNDING

This work was supported by NIH (grant numbers HL114893, HL134824, HL135096 to TH; HL129766 to BO); James S. McDonnell Foundation (to TH); Saving tiny Hearts Society (to TH); and a TriFit Challenge grant from Ross Heart Hospital and Davis Heart and Lung Research Institute.

SUPPLEMENTARY MATERIAL

The Supplementary Material for this article can be found online at: https://www.frontiersin.org/articles/10.3389/fphy.2018.00063/full#supplementary-material

Supplementary Videos 1–6 | Movies of cell voltages in 7 × 7 grids depicting asynchronous activity (**Video 1**), spiral waves (**Video 3**), and synchronous activity (**Video 5**) from **Figure 7**. As propagation across the grid happens very quickly, the movies are slowed by a factor of 2X. The end of the spiral wave from **Figure 7B** thus happens at $t = 40$ s in the video as opposed to $t = 20$ s in the simulation. Additional movies depicting clusters in the same 7 × 7 grids from **Figure 7** are labeled **Videos 2, 4, 6** for asynchronous, spiral waves, and synchronous activity, respectively. These movies show clusters of cell action potentials forming and then being removed. Colors for the clusters repeat regularly and are not for any purpose besides distinguishing the clusters. As the time for a cluster to propagate is very fast, these movies are slowed by a factor of 4X. All movies were created at a constant 40 fps using python plotting library (matplotlib).

REFERENCES

1. Dobrzynski H, Boyett MR, Anderson RH. New insights into pacemaker activity: promoting understanding of sick sinus syndrome. *Circulation* (2007) **115**:1921–32. doi: 10.1161/CIRCULATIONAHA.106.616011
2. Mangoni, ME, Nargeot J. Genesis and regulation of the heart automaticity. *Physiol Rev.* (2008) **88**:919–82. doi: 10.1152/physrev.00018.2007
3. Quinn TA, Kohl P. Mechano-sensitivity of cardiac pacemaker function: pathophysiological relevance, experimental implications, and conceptual integration with other mechanisms of rhythmicity. *Prog Biophys Mol Biol.* (2012) **110**:257–68. doi: 10.1016/j.pbiomolbio.2012.08.008
4. Dobrzynski H, Anderson RH, Atkinson A, Borbas Z, D'Souza A, Fraser JF, et al. Structure, function and clinical relevance of the cardiac conduction system, including the atrioventricular ring and outflow tract tissues. *Pharmacol Ther.* (2013) **139**:260–88. doi: 10.1016/j.pharmthera.2013.04.010
5. Semelka M, Gera J, Usman S. Sick sinus syndrome: a review. *Am Fam Physician* (2013) **87**:691–6.
6. Gosney M, Harper A, Conroy S. *Geriatric Medicine*. Oxford: Oxford University Press (2012).
7. Vardas PE, Simantirakis, EN, Kanoupakis EM. New developments in cardiac pacemakers. *Circulation* (2013) **127**:2343–50. doi: 10.1161/CIRCULATIONAHA.112.000086
8. Aschoff J. (ed.). (1981). "Annual rhythms in man," in *Biological Rhythms* (Boston, MA: Springer).
9. Unudurthi SD, Wolf, RM, Hund TJ. Role of sinoatrial node architecture in maintaining a balanced source-sink relationship and synchronous cardiac pacemaking. *Front Physiol.* (2014) **5**:446. doi: 10.3389/fphys.2014.00446
10. Wolf RM, Glynn P, Hashemi S, Zarei K, Mitchell CC, Anderson ME, et al. Atrial fibrillation and sinus node dysfunction in human ankyrin-B syndrome: a computational analysis. *Am J Physiol Heart Circ Physiol.* (2013) **304**:H1253–66. doi: 10.1152/ajpheart.00734.2012

11. Sanders P, Kistler PM, Morton JB, Spence, SJ, Kalman JM. Remodeling of sinus node function in patients with congestive heart failure: reduction in sinus node reserve. *Circulation* (2004) **110**:897–903. doi: 10.1161/01.CIR.0000139336.69955.AB
12. Lou Q, Hansen BJ, Fedorenko O, Csepe TA, Kalyanasundaram A, Li N, et al. Upregulation of adenosine A1 receptors facilitates sinoatrial node dysfunction in chronic canine heart failure by exacerbating nodal conduction abnormalities revealed by novel dual-sided intramural optical mapping. (2014) *Circulation* **130**:315–24. doi: 10.1161/CIRCULATIONAHA.113.007086
13. Fedorov VV, Glukhov AV, Chang R. Conduction barriers and pathways of the sinoatrial pacemaker complex: their role in normal rhythm and atrial arrhythmias. *Am J Physiol Heart Circ Physiol.* (2012) **302**:H1773–83. doi: 10.1152/ajpheart.00892.2011
14. Glynn P, Onal B, Hund TJ. Cycle length restitution in sinoatrial node cells: a theory for understanding spontaneous action potential dynamics. *PloS ONE* (2014) **9**:e89049. doi: 10.1371/journal.pone.0089049
15. Glynn P, Unudurthi SD, Hund TJ. Mathematical modeling of physiological systems: an essential tool for discovery. *Life Sci.* (2014) **111**:1–5. doi: 10.1016/j.lfs.2014.07.005
16. Wilders R. 25 Years of SA nodal cell modeling. In: *Annual International Conference of the IEEE Engineering in Medicine and Biology – Proceedings.* Lyon (2007), p. 152–5. doi: 10.1109/IEMBS.2007.4352245
17. Maltsev VA, Yaniv Y, Maltsev AV, Stern, MD, Lakatta EG. Modern perspectives on numerical modeling of cardiac pacemaker cell. *J Pharmacol Sci.* (2014) **125**:6–38. doi: 10.1254/jphs.13R04CR
18. Maltsev AV, Maltsev VA, Stern MD. Stabilization of diastolic calcium signal via calcium pump regulation of complex local calcium releases and transient decay in a computational model of cardiac pacemaker cell with individual release channels. *PLoS Comput Biol.* (2017) **13**:e1005675. doi: 10.1371/journal.pcbi.1005675
19. Fabbri A, Fantini M, Wilders, R, Severi S. Computational analysis of the human sinus node action potential: model development and effects of mutations. *J Physiol.* (2017), **595**:2365–96. doi: 10.1113/JP273259
20. Michaels DC, Matyas EP, Jalife J. Mechanisms of sinoartrial pacemaker synchronization: a new hypothesis. *Circ Res.* (1987) **61**:704–14. doi: 10.1161/01.RES.61.5.704
21. Greisas, A, Zlochiver S. Modulation of cardiac pacemaker inter beat intervals by sinoatrial fibroblasts - a numerical study. *Conf. Proc. IEEE Eng. Med. Biol. Soc.* (2016) **2016**:165–8. doi: 10.1109/EMBC.2016.7590666
22. Kharche SR, Vigmond E, Efimov, IR, Dobrzynski H. Computational assessment of the functional role of sinoatrial node exit pathways in the human heart. *PloS ONE* (2017) **12**:e0183727. doi: 10.1371/journal.pone.0183727
23. Onal B, Gratz, D, Hund T. LongQt: a cardiac electrophysiology simulation platform. *MethodsX* (2016) **3**:589–99. doi: 10.1016/j.mex.2016.11.002
24. Kurata Y, Hisatome I, Imanishi, S, Shibamoto T. Dynamical description of sinoatrial node pacemaking: improved mathematical model for primary pacemaker cell. *Am J Physiol Heart Circ Physiol.* (2002) **283**:H2074–101. doi: 10.1152/ajpheart.00900.2001
25. Ohio Supercomputer Center. *Ohio Supercomputer Center*. Columbus OH (1987).
26. Sobie EA. parameter sensitivity analysis in electrophysiological models using multivariable regression. *Biophys J.* (2009) **96**:1264–74. doi: 10.1016/j.bpj.2008.10.056
27. Onal B, Gratz, D, Hund TJ. Ca^{2+}/calmodulin kinase II-dependent regulation of atrial myocyte late Na^{+} current, Ca^{2+} cycling and excitability: a mathematical modeling study. *Am J Physiol Heart Circ Physiol.* (2017) **313**:H1227–39. doi: 10.1152/ajpheart.00185.2017
28. Unudurthi SD, Wu X, Qian L, Amari F, Onal B, Li N, et al. Two-pore K+ channel TREK-1 regulates sinoatrial node membrane excitability. *J Am Heart Assoc.* (2016) **5**:e002865. doi: 10.1161/JAHA.115.002865
29. Sobie, EA, Sarkar AX. Regression methods for parameter sensitivity analysis: applications to cardiac arrhythmia mechanisms. *2011 Annual International Conference of the IEEE Engineering in Medicine and Biology Society*, IEEE (2011), p. 4657–60. doi: 10.1109/IEMBS.2011.6091153
30. Sarkar AX, Christini, DJ, Sobie EA. Exploiting mathematical models to illuminate electrophysiological variability between individuals. *J Physiol.* (2012), **590**:2555–67. doi: 10.1113/jphysiol.2011.223313
31. Boyett MR, Honjo, H, Kodama I. The sinoatrial node, a heterogeneous pacemaker structure. *Cardiovasc Res.* (2000) **47**:658–87. doi: 10.1016/S0008-6363(00)00135-8
32. Abramovich-Sivan, S, Akselrod S. Phase response curve based model of the SA node: simulation by two-dimensional array of pacemaker cells with randomly distributed cycle lengths. *Med Biol Eng Comput.* (1999) **37**:482–91. doi: 10.1007/BF02513334
33. Michaels DC, Matyas, EP, Jalife J. Dynamic interactions and mutual synchronization of sinoatrial node pacemaker cells: a mathematical model. *Circ Res.* (1986) **58**:706–20. doi: 10.1161/01.RES.58.5.706
34. Fedorov VV, Glukhov AV, Chang R, Kostecki G, Aferol H, Hucker WJ, et al. Optical mapping of the isolated coronary-perfused human sinus node. *J Am Coll Cardiol.* (2010) **56**:1386–94. doi: 10.1016/j.jacc.2010.03.098
35. Monfredi O, Dobrzynski H, Mondal T, Boyett MR, Morris GM. The anatomy and physiology of the sinoatrial node-a contemporary review. *Pacing Clin Electrophysiol.* (2010) **33**:1392–406. doi: 10.1111/j.1540-8159.2010.02838.x
36. James TN. The sinus node. *Am J Cardiol.* (1977) **40**:965–86. doi: 10.1016/0002-9149(77)90048-0
37. Archiv P, Joumal E. Membrane currents in the rabbit sinoatrial node cell as studied by the double microelectrode method. *Pflfigers Arch.* (1976) **364**:45–52. doi: 10.1007/BF01062910
38. Glukhov AV, Fedorov VV, Anderson ME, Mohler PJ, Efimov IR. Functional anatomy of the murine sinus node: high-resolution optical mapping of ankyrin-B heterozygous mice. *Am J Physiol Heart Circ Physiol.* (2010) **299**:H482-91. doi: 10.1152/ajpheart.00756.2009
39. Yada H, Murata M, Shimoda K, Yuasa S, Kawaguchi H, Ieda M, et al. Dominant negative suppression of rad leads to QT prolongation and causes ventricular arrhythmias via modulation of L-type Ca^{2+} channels in the heart. *Circ Res.* (2007) **101**:69–77. doi: 10.1161/CIRCRESAHA.106.146399
40. Zhang H, Sun AY, Kim JJ, Graham V, Finch EA, Neplioue I, et al. STIM1–Ca^{2+} signaling modulates automaticity of the mouse sinoatrial node. *Proc Natl Acad Sci USA.* (2015) **112**:E5618–27. doi: 10.1073/pnas.1503847112
41. Swan H, Viitasalo M, Piippo K, Laitinen P, Kontula K, Toivonen L. Sinus node function and ventricular repolarization during exercise stress test in long QT syndrome patients with KvLQT1 and HERG potassium channel defects. *J Am Coll Cardiol.* (1999) **34**:823–9.
42. Nawathe PA, Kryukova Y, Oren RV, Milanesi R, Clancy CE, Lu JT, et al. An LQTS6 MiRP1 mutation suppresses pacemaker current and is associated with sinus bradycardia. *J Cardiovasc Electrophysiol.* (2013) **24**:1021–7. doi: 10.1111/jce.12163
43. Winfree AT. *The Geometry of Biological Time*. New York, NY: Springer New York (2001).
44. Osipov GV, Kurths J, Zhou C. *Synchronization in Oscillatory Networks*. Berlin, Heidelberg: Springer Berlin Heidelberg (2007).
45. Berridge MJ, Rapp PE. A comparative survey of the function, mechanism and control of cellular oscillators. *J Exp Biol.* (1979) **81**:217–79.
46. Kawamura Y. Phase synchronization between collective rhythms of fully locked oscillator groups. *Sci Rep.* (2015) **4**:4832. doi: 10.1038/srep04832
47. Zhang H, Holden AV, Boyett MR. Gradient model versus mosaic model of the sinoatrial node. *Circulation* (2001) **103**:584–8. doi: 10.1161/01.CIR.103.4.584
48. Cloherty SL, Dokos S, Lovell NH. Qualitative support for the gradient model of cardiac pacemaker heterogeneity. *2005 IEEE Engineering in Medicine and Biology 27th Annual Conference*, Shanghai: IEEE (2005) p. 133–6.

Conflict of Interest Statement: The authors declare that the research was conducted in the absence of any commercial or financial relationships that could be construed as a potential conflict of interest.

frontiers in Physics

ORIGINAL RESEARCH
published: 07 June 2018
doi: 10.3389/fphy.2018.00057

Microscopic Isthmuses and Fibrosis Within the Border Zone of Infarcted Hearts Promote Calcium-Mediated Ectopy and Conduction Block

Fernando O. Campos[1], Yohannes Shiferaw[2], Rodrigo Weber dos Santos[3], Gernot Plank[4] and Martin J. Bishop[1]*

[1] School of Biomedical Engineering and Imaging Sciences, King's College London, London, United Kingdom, [2] Department of Physics, California State University, Northridge, CA, United States, [3] Graduate Program in Computational Modelling, Federal University of Juiz de Fora, Juiz de Fora, Brazil, [4] Institute of Biophysics, Medical University of Graz, Graz, Austria

Ventricular tachycardia (VT) secondary to myocardial infarction (MI) remain a major cause of sudden death in adults. Premature ventricular complexes (PVCs), the first initiating beats of a portion of these arrhythmias, arise from triggered activity in the infarct border zone (BZ). At the cellular scale, spontaneous calcium release (SCR) events are a known cause of triggered activity and have been reported in cells that survive MI. At the tissue scale, fibrosis has been shown to play an important role in creating the substrate for VT. However, the interplay between SCR-mediated triggered activity and fibrosis upon VT formation in infarcted hearts has not been fully investigated. Here, we conduct *in-silico* experiments to assess how macroscopic and microscopic anatomical properties of the BZ can create a substrate for SCR-mediated VT formation. To study this question, we employ a stochastic subcellular-scale model of SCR events and action potential to simulate different cardiac preparations. Within 2D sheet models with idealized infarct scars and BZ we show that the probability of PVCs is higher, 55%, in preparations with thin conducting isthmuses (0.2 mm) transcending the scar. In an anatomically-detailed model of the rabbit ventricles with a realistic representation of intramural scars, we show that the heart's protective source-sink mismatch prevents ectopy. Furthermore, we demonstrate that fibrosis disrupts this antiarrhythmic mechanism making PVCs more likely. PVC probability is highest ($\geq$25%) when fibrosis accounts for 60 and 90% of the BZ in the 2D sheet and the 3D anatomical model, respectively. Above these thresholds, PVC occurrence decreases because of: (1) the reduced number of myocytes in the BZ; (2) conduction block. Block is caused either by disconnection of BZ cells from the myocardium or due to source-sink mismatches at regions of rapid tissue expansion. Moreover, while outward propagation to healthy tissue may fail, PVCs traveling inward through the scar might encounter more favorable loading conditions. These PVCs may exit to the myocardium and reenter back at the region of block. Overall, our findings indicate that thin isthmuses and strands of myocytes interspersed with fibrosis can be arrhythmogenic. Ablation of these microscopic structures may prevent VT formation.

Keywords: myocardial infarction, isthmus, fibrosis, arrhythmia, triggered activity, calcium, computer simulation

OPEN ACCESS

Edited by:
Ewald Moser,
Medizinische Universität Wien, Austria

Reviewed by:
Fei Geng,
McMaster University, Canada
Winfried Mayr,
Medizinische Universität Wien, Austria

****Correspondence:***
Gernot Plank
gernot.plank@medunigraz.at

Specialty section:
This article was submitted to Biomedical Physics, a section of the journal Frontiers in Physics

Received: *15 December 2017*
Accepted: *18 May 2018*
Published: *07 June 2018*

Citation:
Campos FO, Shiferaw Y, Weber dos Santos R, Plank G and Bishop MJ (2018) Microscopic Isthmuses and Fibrosis Within the Border Zone of Infarcted Hearts Promote Calcium-Mediated Ectopy and Conduction Block. Front. Phys. 6:57. doi: 10.3389/fphy.2018.00057

1. INTRODUCTION

Cardiovascular diseases, such as myocardial infarction (MI), continue to be the leading cause of morbidity and sudden death globally. MI is a common consequence of coronary artery disease, in which a narrowing or occlusion of an artery prevents the supply of oxygen-rich blood to the heart. A series of changes in the infarct region results in deterioration of electrical activity that has been shown to set the stage for ventricular tachycardias (VTs) [1, 2], the major cause of sudden cardiac arrest after MI [3]. Experimental evidence suggests that a variety of these arrhythmias are attributed to focal excitations in the infarct border zone (BZ) [4]. Electrophysiological and structural remodeling following MI render the region of injury more prone to reentry and triggered activity due to delayed afterdepolarizations (DADs) [1, 2].

At the cellular scale, DAD-triggered activity has been associated with "spontaneous" calcium (Ca^{2+}) release (SCR) events from the sarcoplasmic reticulum [5, 6]. Such abnormal Ca^{2+} releases have been reported in Ca^{2+} overloaded myocytes [7], inherited heart rhythm disturbances [8], heart failure [9] as well as in cells that survive in the infarcted heart [10, 11]. DADs can be divided into subthreshold or suprathreshold depending on whether their amplitude is below or above the threshold for action potential (AP) initiation, respectively. At the tissue level, a triggered propagating AP would only be possible if the net ionic current generated by cells undergoing DADs within a given volume of myocardial tissue is sufficient to excite downstream coupled myocytes [12, 13]. This transition from single-cell to tissue/organ events depends on the electrotonic load posed by the surrounding myocardium that acts as sink for the source of depolarizing current produced by the triggered AP [13]. In MI, this protective source-sink mechanism is altered by reduced cell-to-cell coupling caused either by remodeling of gap junctions [14] or deposition of fibrous tissue as a result of wound healing [15]. While the infarct scar is important to maintain the structure of the heart wall, fibrotic inlays in the BZ have the undesired effect of disrupting the intracellular matrix. Consequently, the number of downstream cells that are coupled to each myocyte is reduced.

The notion that DADs are more likely to summate to trigger organ-scale premature ventricular complexes (PVCs) in regions experiencing lower electrotonic load has been supported by recent findings from our group [16, 17] as well as others [13]. Using *in-silico* experiments we have demonstrated that electrotonic loading conditions in the structurally healthy heart favor the origin of SCR-mediated PVCs in the 1D His-Purkinje system (HPS) instead of the 3D ventricles [16]. Similar to the HPS, where cells are electrically isolated from the myocardium by collagen sheaths [18], interstitial and patchy fibrosis in the infarct BZ [19, 20] can separate myocyte bundles reducing source-sink mismatches that prevent PVC formation in well coupled tissue.

While the link between subcellular SCR events and PVC formation in the structurally healthy ventricles has been a topic of intense research [8, 16, 21], the mechanism by which stochastic SCR events in cells that survive in the infarcted heart can summate to trigger PVCs remains to be elucidated. The goal of this study is to investigate the conditions under which SCR-mediated triggered activity in the infarct BZ can initiate arrhythmogenic PVCs (see schematic diagram in **Figure 1**). Our hypotheses are that (1) triggered activity in thin conducting isthmus within the scar or in myocytes from the BZ interspersed with fibrosis can summate to form ectopic focal sources due to the reduced electrotonic load on these cells; (2) source-sink mismatches at regions of abrupt tissue expansion such as the mouth of an isthmus or at the border between fibrotic and healthy tissue can lead to unidirectional block of PVCs setting the stage for VTs. These hypotheses are tested with the aid of state-of-the-art computer simulations within idealized as well as anatomically realistic cardiac infarct models prone to PVC formation induced by stochastic SCR events.

2. METHODS

2.1. Model of SCR and Ventricular AP

A stochastic phenomenological mathematical model of SCR events [22] was coupled to the Mahajan-Shiferaw (MSH) model [23] and used to simulate cellular dynamics in the myocardium as well as in the BZ. In this phenomenological model, a SCR event is represented as a Ca^{2+} wave that is nucleated in the cell and then propagating in a fire-diffuse-fire way [22]. The phenomenological model accounts for experimentally observed features of SCR events and has a dependence on SR Ca^{2+} load ensuring that SCR events are more likely to occur as the SR becomes overloaded

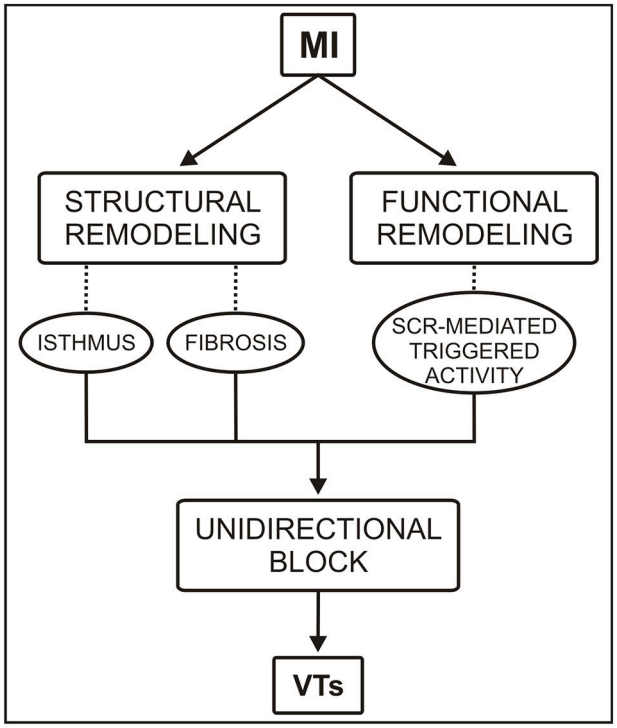

FIGURE 1 | Conceptual diagram of the roles of functional and structural remodeling involved in a portion of ventricular tachycardias (VTs) following myocardial infarction (MI). SCR = spontaneous Ca^{2+} release.

[7]. Following our previous computational studies [16, 17], key parameters of the MSH model were modified to increase its propensity for Ca^{2+}-mediated DADs. Specifically, Ca^{2+} overload was induced by increasing extracellular Ca^{2+} concentration from 1.8 to 4 mmol/L, the strength of the electrogenic sodium-calcium exchange current (I_{NCX}) was doubled and the maximum conductance of the inward rectifier potassium current (I_{K1}) was decreased to 30% of its control value. If not stated otherwise, these values were used throughout the study.

2.2. Geometrical Models

Different geometrical finite element (FE) models were used throughout to simulate electrical activity in cardiac tissue: 2D sheets with idealized representations of infarct scars and BZ and an anatomically-detailed rabbit biventricular (BiV) model with a realistic representation of an intramural scar. The major components of the FE models are outlined below.

2.2.1. 2D Sheets With Idealized Scar

2D sheet models consisting of a square 4×4 cm with nodal spacing of 200 μm (40,000 quadrilateral FEs) were constructed to investigate the role of conducting isthmuses transcending the scar on the probability, timing and location of SCR-mediated triggered activity. Each model included an idealized infarct region representing a scar with an isthmus with different widths [24]. A transition region consisting of BZ myocytes surrounding the isthmus and scar region was also included in the models. A schematic of the 2D computational models is shown in **Figure 2A**. The radii of the scar and BZ were set to 15 and 17 mm, respectively, giving an isthmus length of 30 mm and a transition distance of 2 mm between the scar and healthy myocardium. The width of the isthmus w_{isth} was varied between 0.2 and 8 mm to approximately represent microscopic tracts of surviving myocardium interspersed with fibrosis [19] as well as macroscopic channels within the scar [25, 26]. In addition, a 2D sheet with w_{isth} progressively widening from 0.2 to 4 mm was built to study the effects of geometrical asymmetries on formation and conduction of PVCs. The scar tissue was represented as being necrotic, i.e., by imposing no-flux boundary condition at its interface [27]. Isotropic tissue conductivity was assigned to the tissue with a value of 0.14 S/m [28] to dissect out the role of the isthmus' width on PVC formation.

2.2.2. Biventricular Scar Anatomy Model

The rabbit BiV model in this study is a tetrahedral FE model including realistic fiber architecture [29]. The model contains 547,680 myocardial nodes defining 3,073,529 tetrahedral elements with a mean discretization of 279 μm. Within this BiV model, an anatomically-detailed region of infarct scar and corresponding BZ was assigned according to a previous study from our group [30]. The scar anatomy in this study was defined representing approximate infarct regions created following occlusion of the left anterior descending (LAD) coronary artery (see **Figure 3**). The intracellular domain, comprising of both myocardium and BZ, was modeled with anisotropic conductivities values of 0.14 and 0.019 S/m along and transverse to the fiber direction, respectively [28]. This modeling choice allowed us to rule out any effects due to fiber disarray as well as to scrutinize the role of structural heterogeneities in the infarct BZ.

2.3. Modeling Fibrosis in the BZ

Fibrosis in all geometrical models was modeled by including synthetic patterns of non-conducting tissue in the BZ [31–33] (see **Figure 2B**). Fibrosis patterns were generated by randomly transforming some of the BZ myocytes in fibrosis, i.e., non-conducting material. The amount of fibrosis in relation to myocardium in the BZ (FIB_{BZ}) was varied from 0% (no fibrosis) to 100% in steps of 10%. Five fibrotic patterns were constructed for each FIB_{BZ}. Fibrosis is modeled here in the same way as the scar, i.e., by imposing no-flux boundary conditions along the interface.

2.4. Governing Equations

Electrical activity within the geometrical models was simulated using the monodomain equations expressed as:

$$\nabla \cdot (\boldsymbol{\sigma_m} \nabla V_m) = \beta I_m, \tag{1}$$

$$C_m \frac{\partial V_m}{\partial t} + I_{ion}(V_m, \boldsymbol{\eta}) - I_{stim} = I_m, \tag{2}$$

$$\frac{\partial \boldsymbol{\eta}}{\partial t} = f(V_m, \boldsymbol{\eta}) \tag{3}$$

where $\boldsymbol{\sigma_m} = diag(\sigma_{ml}, \sigma_{mt}, \sigma_{mt})$ is the harmonic mean conductivity tensor or the effective bulk conductivity [34]; V_m is the transmembrane voltage; β is the surface to volume ratio; I_m is the transmembrane current density; C_m is the membrane capacitance per unit area; I_{ion} is the density of the total ionic current flowing through the membrane channels, pumps and exchangers; and I_{stim} is the stimulus current density. I_{ion} depends on V_m as well as on a set of state variables $\boldsymbol{\eta}$ which describes channel gating and ionic concentrations according to the vector-valued function $f(V_m, \boldsymbol{\eta})$. Ionic dynamics I_{ion}, $\boldsymbol{\eta}$ and $f(V_m, \boldsymbol{\eta})$ were represented by the MSH rabbit ventricular cell model [23].

Solutions to the monodomain Equations (1–3) within the cardiac models were performed using the Cardiac Arrhythmia Research Package (CARP) [35].

2.5. Computational Protocols

2.5.1. Single-Cell Simulations

Similar to experimental protocols [7], extracellular Ca^{2+} in the DAD-prone MSH myocyte model was increased from 1.8 mmol/L to 4 mmol/L. The model was then paced at 2.0 Hz for 100 cycles to stabilize. At the end of the pacing protocol, the diastolic Ca^{2+} load in the SR increased from 1,200 μmol/L (control value) to 1,600 μmol/L (Ca^{2+} overload). Single-cell model states at the end of the pacing protocol were stored and used as initial conditions for the tissue models.

2.5.2. Tissue Simulations

Tissue models in this study were initialized with stabilized single-cell model states to avoid the computational burden associated with pacing tissue preparations. In the 2D sheet models, a stimulus current was applied in the lowermost portion of the tissue (**Figure 2**) while the BiV model was paced at the apex

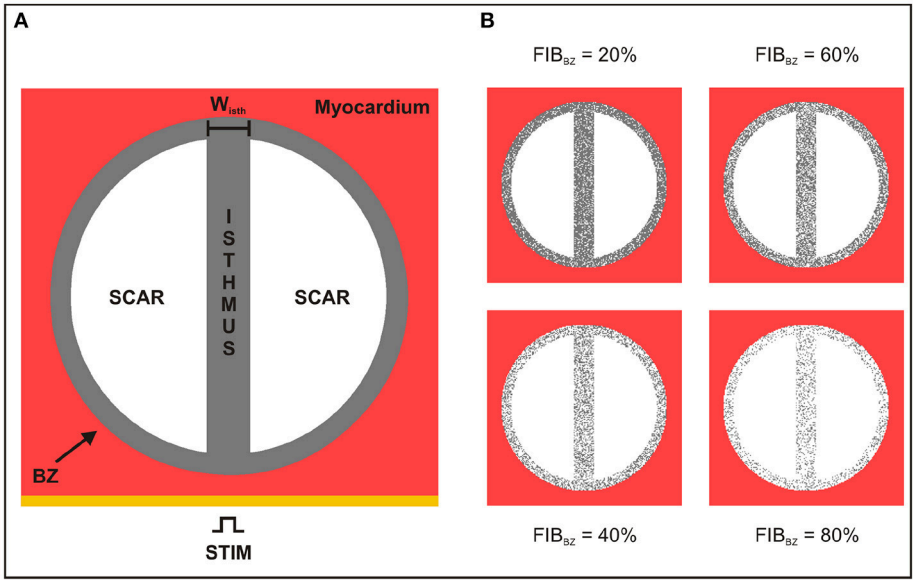

FIGURE 2 | Schematic of the 2D sheet computational model. **(A)** The idealized infarct consisting of a circular region representing the BZ (gray), which contains two circular segments representing the scar (white), is surrounded by healthy myocardium (red). The BZ region contains an isthmus of width w_{isth} separating the scars. **(B)** 2D sheet computational model with different degree of fibrosis in the BZ (FIB_{BZ}).

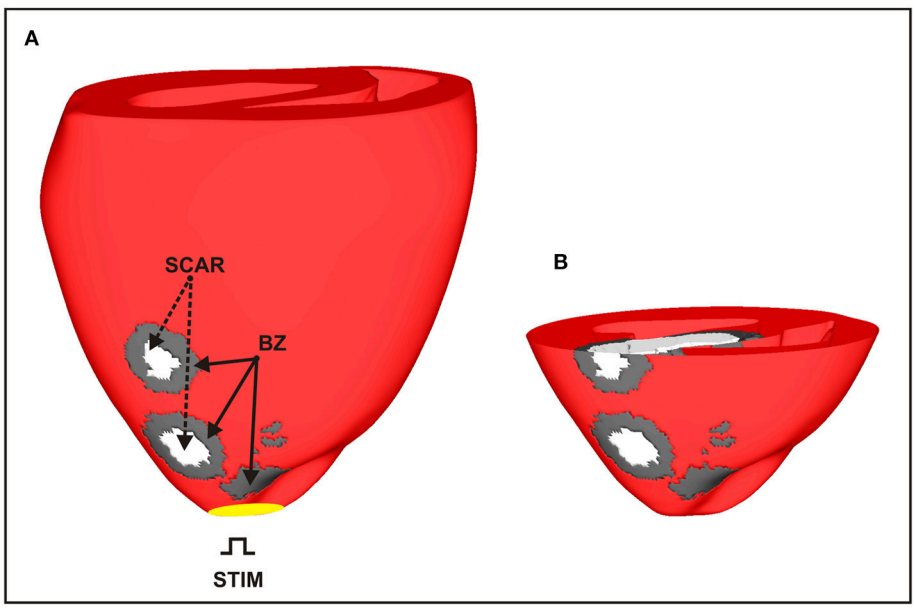

FIGURE 3 | Anatomically-based representation of infarct scar and BZ within the BiV model based on infarct formation following occlusion of the LAD. **(A)** Healthy ventricular tissue is shown in red with necrotic scar in white and BZ tissue in gray. **(B)** Short-axis clipping plane view highlighting intramural scar anatomy.

(see **Figure 3**). In both cases, the stimulus was followed by a 1,500-ms pause in order to see whether PVCs would emerge. Controlled stimuli followed by a halt in pacing is a widely used protocol as it allows for the correct characterization of triggered activity [7, 22]. SCR events were inhibited in the myocardium to investigate abnormal triggered activity only in cells in the infarct BZ. Moreover, due to the stochastic nature of the SCR events, $N = 100$ simulations for each set of experiments were performed. Further details on the *in-silico* simulation protocols used in this study have been provided in a recent publication [16].

2.6. Data Analysis

The number of simulations in which a PVC was observed, n, was recorded to compute the probability $p_{PVC} = n/N$ during

the pacing pause. PVCs that did not activate more than 50% of the ventricles were not computed in p_{PVC}. Furthermore, location as well as the waiting time until the onset of a PVC, t_{PVC}, was determined as the time instant of a triggered AP crossing -10 mV.

3. RESULTS

In accordance with the protocol described previously, 100 simulations were conducted for each experiment in order to compute statistics on probability, location and timing of SCR-mediated PVCs.

3.1. Ectopy in 2D Sheets With Idealized Scars

Figure 4 shows snapshots of the wave propagation pattern of a paced beat followed by a PVC in a 2D sheet with a 4-mm isthmus. The excitation wavefront resulting from the paced beat ($t = 5$ ms) can be seen to propagate quickly through both myocardium and isthmus ($t = 75$ ms). SCR events in myocytes from the BZ led to DADs that summated to trigger a PVC at time $t = 850$ ms within the isthmus. The PVC successfully propagated to both proximal and distal mouths (relative to the stimulus site) of the isthmus (870 ms $\leq$ t $\leq$ 880 ms) entering the myocardium where both wavefronts collide at about $t = 920$ ms.

3.1.1. 2D Sheets With Different Isthmus Widths

Probability, timing and location of PVCs within the 2D models as a function of isthmus' width are shown in **Figures 5**, **6**. p_{PVC} decreases as the width of the isthmus increases dropping from 55% in the 2D sheet with a microscopic isthmus ($w_{isth} = 0.2$ mm) to 0% in the sheet with a 8-mm macroscopic channel. In addition, PVCs arose earlier on average within cardiac tissues with thinner isthmuses. t_{PVC} was 805 $\pm$ 30 ms in the sheet with 0.2 mm isthmus compared to 843 $\pm$ 33 ms in the 2D sheet with an isthmus 10x larger ($w_{isth} = 2$ mm). **Figure 6** shows the location of ectopic focal sources in the sheets with $w_{isth} = 0.2$, 2, and 4 mm. Although all myocytes were undergoing SCR events in the BZ, PVCs only originated in the isthmus. Furthermore, foci were found throughout the isthmus and away from both mouths. The minimum focus-to-mouth distance was 2.61 and 14.14 mm for $w_{isth} = 0.2$ mm and $w_{isth} = 4$ mm, respectively. Only one PVC was detected in $N = 100$ experiments with the cardiac sheet with a 4-mm isthmus (focus as well as propagation pattern are shown in **Figure 4**).

3.1.2. Effect of Fibrosis in the BZ

To assess the effect of fibrosis density on PVC formation, synthetic fibrosis patterns were added to the BZ of the 2D cardiac sheet with a 4-mm isthmus (see **Figure 2B**). **Figure 7** shows the spatial distribution of V_m at different times in a 2D sheet with fibrotic density $FIB_{BZ} = 50\%$. Unlike in the control case, **Figure 4**, where the paced beat traveled with the same velocity throughout the myocardium and the isthmus, conduction was slower within the fibrotic model due to the more complex pathway the wavefront had to travel. The PVC in the fibrotic BZ model originated earlier, $t = 772$ ms, than in the control case ($t = 850$ ms), but took longer to exit at the proximal mouth of

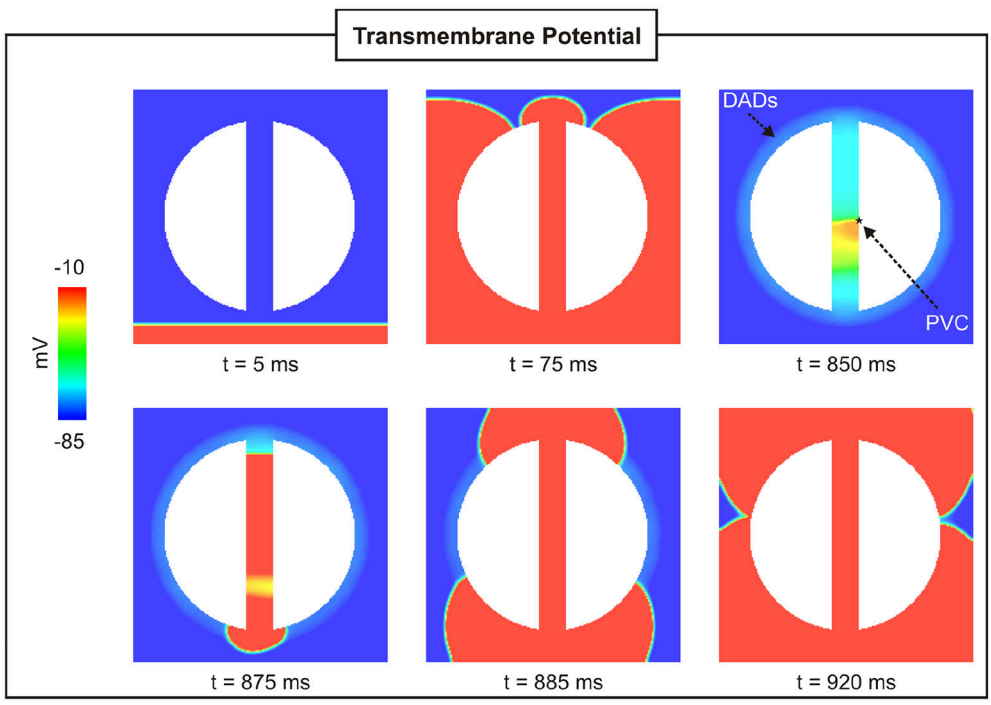

FIGURE 4 | PVC formation in a 2D sheet with the isthmus width of 4 mm. V_m maps at different times showing a paced beat ($t = 5$ ms) followed by a PVC ($t = 850$ ms) in the isthmus.

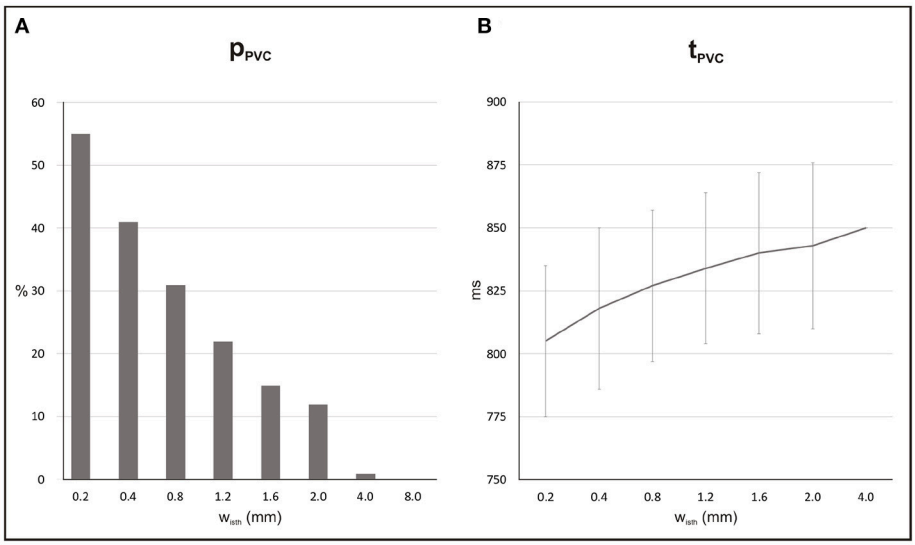

FIGURE 5 | Statistics of SCR-mediated PVCs in 2D sheets with different isthmus widths (w_{isth}). **(A)** Probability p_{PVC} of SCR-mediated PVCs. **(B)** Average waiting time t_{PVC}.

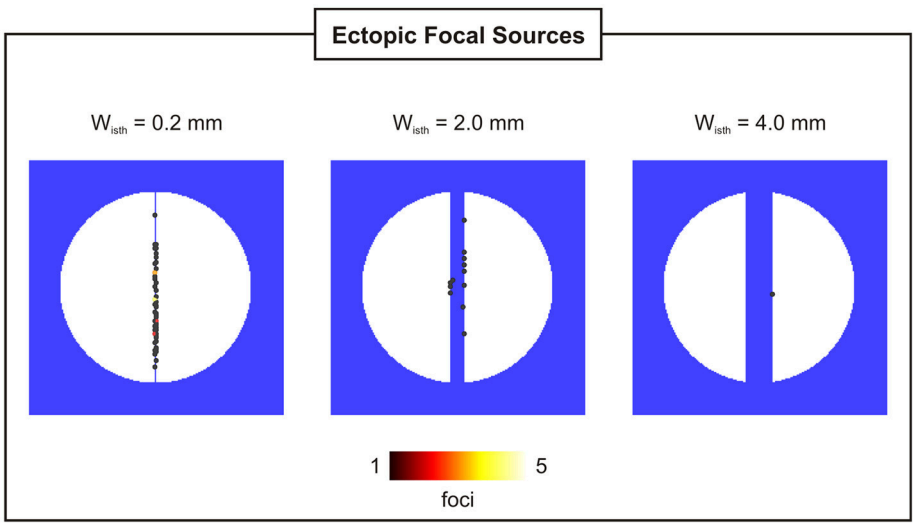

FIGURE 6 | Location and incidence of PVCs in 2D sheets with isthmus widths of 0.2, 2, and 4 mm.

the isthmus (43 ms compared to 25 ms with no fibrosis). It can be seen at time $t = 850$ ms that clusters of cells in isthmus as well as in the BZ (areas enclosed by circles) are not activated by the wavefronts since they are separated from the rest of the conducting tissue by fibrosis.

Statistics and location of PVCs in the 2D sheet with different fibrotic patterns inserted in the BZ are presented in **Figures 8**, **9**. For each FIB_{BZ}, five fibrotic patterns were constructed and added to the BZ of the 2D sheet model resulting in a total of $N = 5 \times 100$ simulations per FIB_{BZ}. Note that, in **Figure 8A**, PVCs become more likely as the amount of fibrosis in the BZ increases with maximum $p_{PVC} = 25\%$ for $FIB_{BZ} = 60\%$. Above this threshold, p_{PVC} decreased and dropped to zero in 2D sheets with densely fibrotic BZs ($FIB_{BZ} \geq 80\%$) due to the reduced number of cells available to trigger a PVC. p_{PVC} also varied for the same FIB_{BZ} because of differences in the randomness of the pattern (topology) of the fibrotic region. In the case of $FIB_{BZ} = 60\%$, for instance, p_{PVC} was 9% (N = 100) and $p_{PVC} = 39\%$ ($N = 100$) for the least and most arrhythmogenic fibrotic patterns, respectively.

Figure 8B shows that reduced cell coupling caused by fibrosis facilitated triggered activity at the cellular level to form PVCs earlier than in the control 2D sheet: $t_{PVC} = 792$ ms $\pm$ 34 ms for $FIB_{BZ} = 60\%$ compared to $t_{PVC} = 850$ ms for $FIB_{BZ} = 0\%$. As can be seen in **Figure 9**, most PVCs originated within the isthmus,

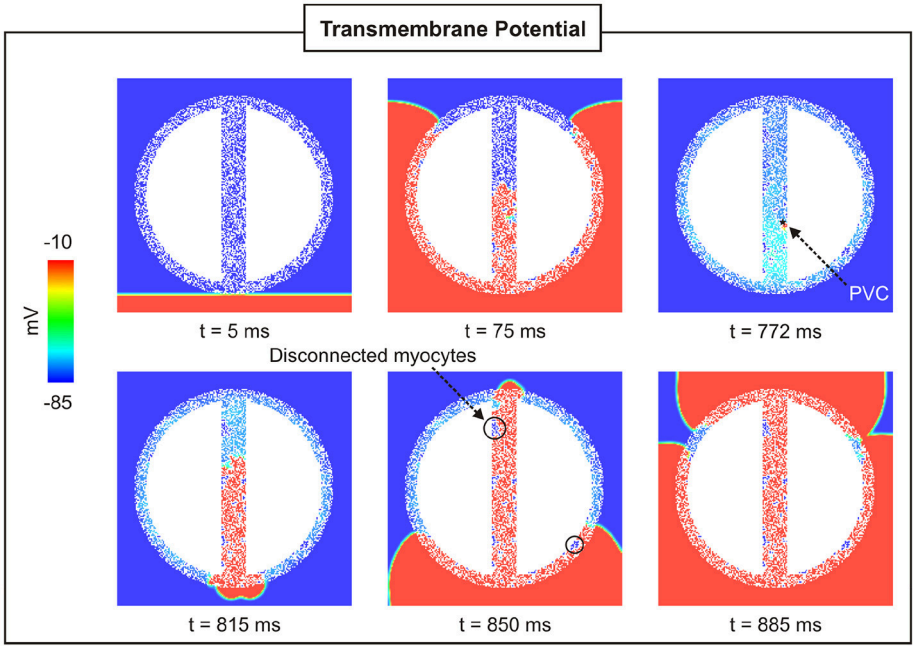

FIGURE 7 | PVC formation in a 2D sheet with $w_{isth} = 4$ mm and $FIB_{BZ} = 50\%$. V_m maps at different times showing a paced beat ($t = 5$ ms) followed by a PVC ($t = 772$ ms) in the isthmus.

but foci were also found in cells interspersed with fibrosis in the BZ ($FIB_{BZ} = 70\%$). Although triggered activity was observed in clusters of cells in 2D sheets with highly fibrotic BZs ($FIB_{BZ} \geq 70\%$), they did not propagate to the myocardium as they were located in isolated regions confined by patches of fibrosis.

3.1.3. Unidirectional Conduction Block and Reentry

Unidirectional block was only observed in experiments with a particular topology of the 2D sheet with $FIB_{BZ} = 60\%$ exhibiting regions of abrupt tissue expansion. However, no reentries were detected in any of the simulations performed above. In order to investigate whether reentry can occur resulting from the combination of unidirectional block of SCR-mediated PVCs and slow conduction, the experiment with the 2D sheet with $FIB_{BZ} = 60\%$ was repeated but with tissue conductivity reduced by 50%. In addition, a 2D sheet with a thin isthmus that progressively widens from 0.2 mm (proximal mouth) to 4 mm (distal) was employed to further study effects of thin-to-thick tissue expansion on block and reentry of PVCs. Reentries induced by PVCs were observed in 41 and 71% of all simulations ($N = 100$) on the 2D sheet with a widening of w_{isth} and the 2D sheet with $FIB_{BZ} = 60\%$, respectively. **Figure 10** illustrates how heterogeneities in both w_{isth} and FIB_{BZ} can lead to unidirectional conduction block due to source-sink mismatch. In both cases, a PVC is initiated by suprathreshold DADs near the proximal mouth of the isthmus (indicated by a star). Both PVCs failed to propagate from the proximal exit site to the myocardium due to unfavorable loading conditions. The PVCs propagated along the isthmus toward the distal mouth, where they entered the myocardium. The PVCs then proceeded to propagate around the scar arriving at the proximal mouth and entered the isthmus at the proximal mouth, setting up a reentrant circuit (see also Supplemental Movies 1, 2).

3.2. PVC Formation in the Biventricular Scar Anatomy Model

The BiV model was employed to investigate PVC formation in an anatomically-accurate infarct model of the rabbit ventricles (see **Figure 3**). Similar to the 2D sheet models, $N = 100$ simulations were performed to account for the stochastic properties of the phenomenological model of SCRs. SCR events were not capable of overcoming the ventricles source-sink mismatch to trigger a PVC in any of the simulations. In order to study whether fibrosis can disrupt this protective mechanism and promote PVCs, random synthetic fibrosis patterns were also added to the BZ of the BiV model. The activation sequence of a PVC computed in the BiV model with $FIB_{BZ} = 90\%$ is illustrated in **Figure 11**. The PVC originated at $t = 910$ ms in surviving strands of myocardium within the macroscopic isthmus between two scars in the intraventricular septum (star), entered the healthy myocardium at about $t = 945$ ms and propagated throughout the ventricles.

Probability and timing of SCR-mediated PVCs are shown in **Figure 12**. Results refer to $N = 5$ (topologies) $\times$ 100 simulations for each FIB_{BZ}. p_{PVC} increased from 1 to 52% while t_{PVC} shortened from 856 ± 35 ms to 827 ± 43 ms in simulations with $FIB_{BZ} = 70$ and 90%, respectively. Similar to the experiments with the idealized 2D infarct model, PVCs were most likely near a FIB_{BZ} threshold which was shifted from $FIB_{BZ} = 60\%$ in the 2D sheet to $FIB_{BZ} = 90\%$ in the 3D BiV model. Differences

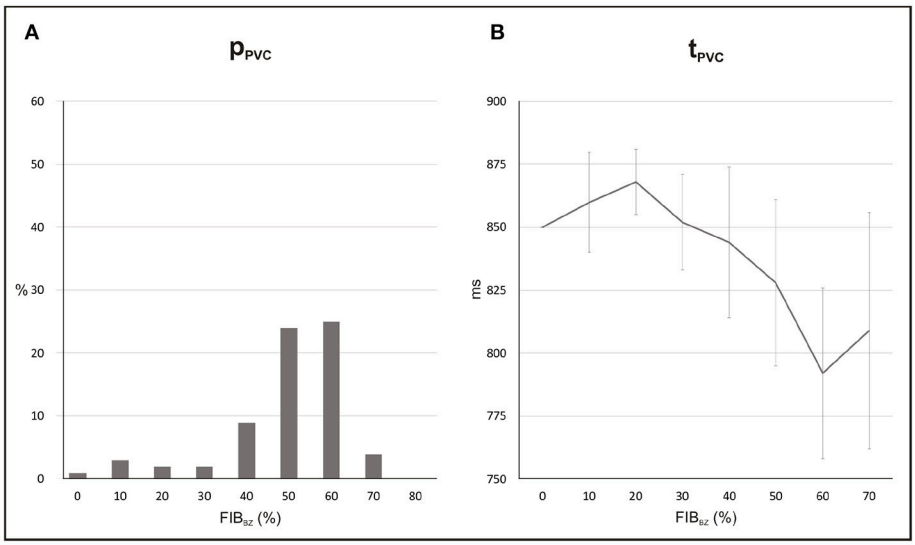

FIGURE 8 | Statistics of PVCs in 2D sheets with different FIB_{BZ}. **(A)** Probability p_{PVC} of SCR-mediated PVCs. **(B)** Average waiting time t_{PVC}.

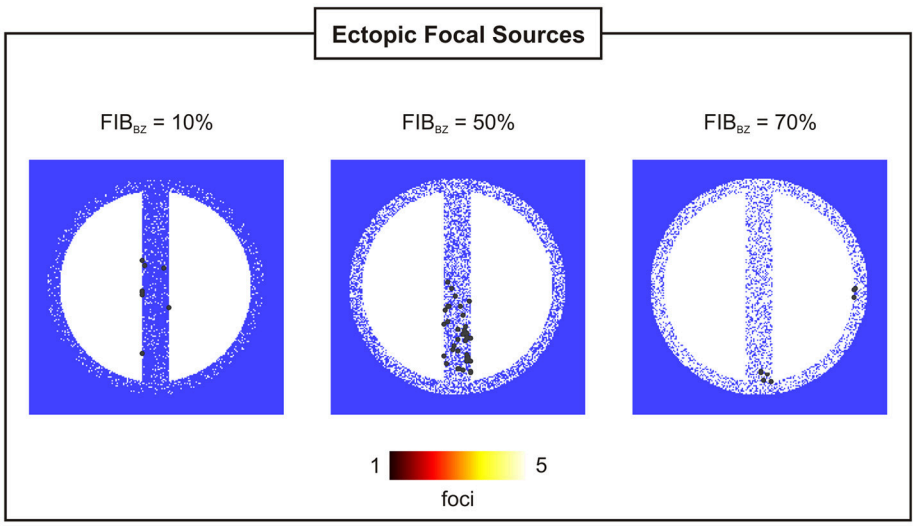

FIGURE 9 | Location and incidence of PVCs in 2D sheets with $w_{isth} = 4$ mm and $FIB_{BZ} = 10$, 50, and 70%.

in the synthetic patterns of fibrosis added to the BZ were also translated into increased or decreased propensity to PVC formation. In the BiV model with $FIB_{BZ} = 90\%$, 34 PVCs ($N = 100$ simulations) were observed in the least arrhythmogenic of the fibrotic topologies compared to $p_{PVC} = 70\%$ in the most arrhythmogenic one. However, no reentrant episodes were observed in any of the experiments performed with the BiV model.

4. DISCUSSION

In this study we made use of computer simulations to investigate the interplay between SCR-mediated triggered activity and structural remodeling in the infarct BZ upon arrhythmogenic PVC formation. An experimentally based model of SCR events at the subcellular scale was coupled to a model for the rabbit ventricular AP to simulate Ca^{2+}-mediated triggered activity within cells in idealized 2D infarct tissue as well as in a BiV scar anatomy model. Simulation results showed that different anatomical properties of the BZ altered loading conditions which (1) increased the probability of SCR-mediated PVCs; and (2) facilitated unidirectional conduction block of PVCs. Regions of lower electrotonic load such as narrow isthmuses within the necrotic scar favored PVC formation. In addition, at the microscopic scale, the presence of fibrosis in the infarct BZ decoupled cells reducing the number of downstream coupled

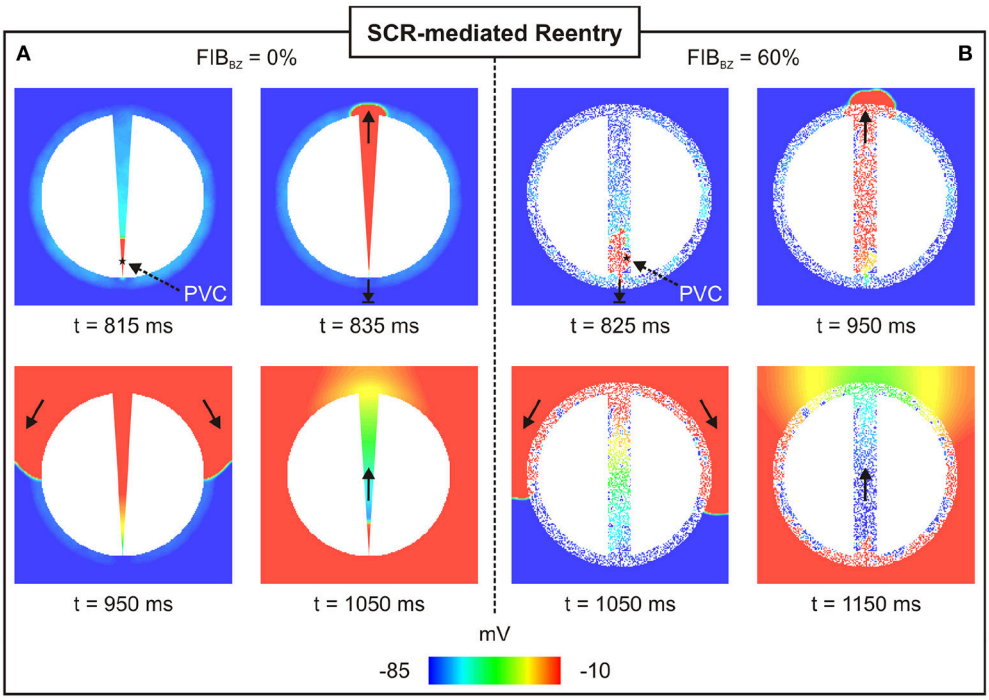

FIGURE 10 | Arrhythmia induced by a SCR-mediated PVC. Reentry induced by a PVC in a **(A)** 2D sheet with w_{isth} progressively widening from 0.2 mm (proximal to the stimulus) to 4 mm (distal mouth); and **(B)** 2D sheet with $w_{isth} = 4$ mm and $FIB_{BZ} = 60\%$. V_m maps at different times showing PVCs triggered near the proximal mouth. Bold arrows depict successful propagation as well as unidirectional conduction block.

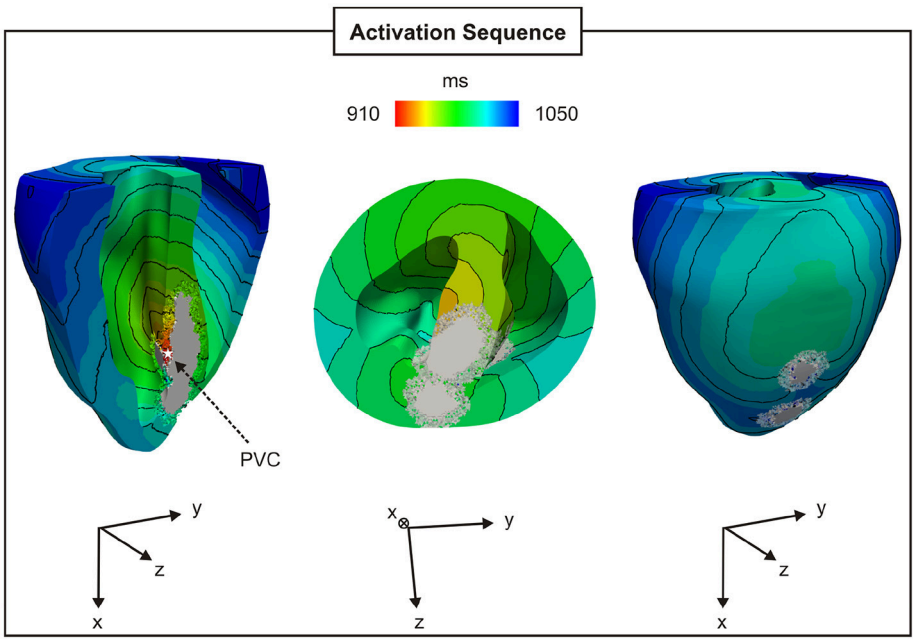

FIGURE 11 | PVC formation in the rabbit BiV model with $FIB_{BZ} = 90\%$. Activation sequence on the endocardial and epicardial surfaces of a PVC originating between two scars in the intraventricular septum (star).

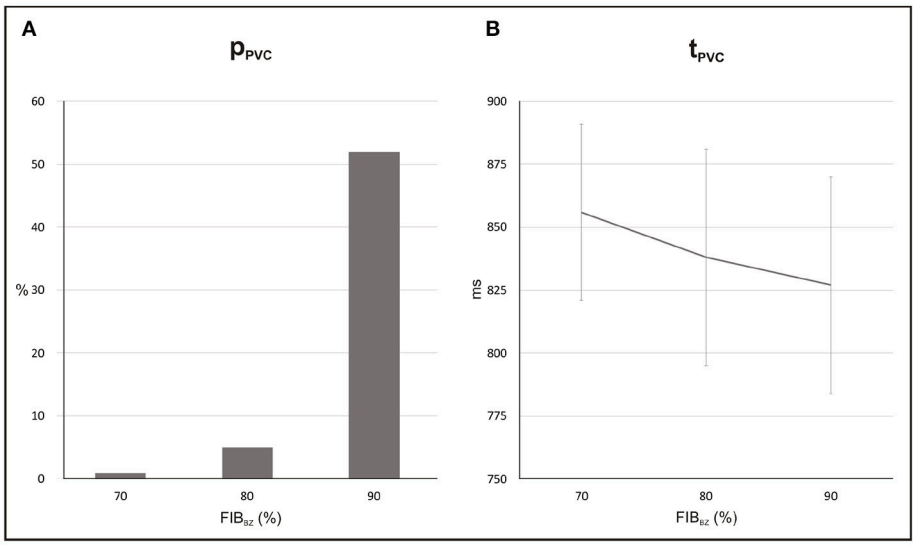

FIGURE 12 | Statistics of PVCs in the BiV model with different degree of fibrosis in the BZ (FIB_{BZ}). **(A)** Probability p_{PVC} of SCR-mediated PVCs. **(B)** Average waiting time t_{PVC}.

myocytes increasing p_{PVC}. Finally, fibrosis also gave rise to regions of rapid tissue expansion from the BZ to the myocardium that enhanced source-sink mismatch facilitating unidirectional conduction block.

4.1. The Role of Electrotonic Load

Electrotonic modulation is a crucial factor preventing DADs from triggering propagating PVCs in tissue. Ectopy is only possible if errant cells undergoing DADs are capable of generate sufficient source current to bring the surrounding quiescent tissue, that acts as sink, to the activation threshold [12, 13]. Using computer simulations, [13] demonstrated that the source-sink mismatch was most severe in higher-dimensional cardiac tissue than in a 1D cable of coupled myocytes. However, PVCs in their models were evoked by synchronized DADs in a fixed number of cells rather than by stochastic SCRs and Ca^{2+} waves. In the present study, we made use of a stochastic phenomenological model [22] accounting for experimentally observed features of SCR events to investigate the electrotonic modulation of triggered activity in postinfarct tissue. Our findings (see **Figure 5**) suggest that PVCs are most likely to arise in thin conducting channels resembling 1D strands of cells. Simulations within 2D models with idealized infarct geometries demonstrated that p_{PVC} was highest (55%) in the sheet model with the thinnest conducting isthmus ($w_{isth} = 0.2$ mm) and gradually decreased as the size of the isthmus increased. This is because myocytes within the isthmus, which is enclosed on either side by scar, experience a lower electrotonic loading than the rest of the tissue. Such electrotonic effect can be seen in **Figure 6**. PVCs originated everywhere throughout the isthmus, but were found to lie away from both proximal and distal mouths (minimum focus-to-mouth distance was 2.61 mm for $w_{isth} = 0.2$ mm) due to unfavored loading conditions in regions of abrupt tissue expansion [36, 37]. As the size of the isthmus increases, the electrotonic load on cells comes closer to that of a well-coupled 2D cardiac tissue. As a consequence, the number of cells that have to undergo sufficiently well synchronized DADs increases [13] making p_{PVC} less likely as well as delaying t_{PVC} [16].

In-silico experiments with the BiV scar anatomy model showed that the protective source-sink mismatch in the 3D ventricles prevented SCR-mediated DADs from triggering PVCs in the infarct BZ. This is in line with our previous findings in structurally normal ventricles, where we have shown that PVCs originate earlier and with overwhelming likelihood in the 1D HPS than in the 3D myocardium [16, 17]. Absence of PVCs in the BiV model is likely due to the geometry of the BZ used here. The 3D infarct morphology reflects tissue damage resulting from coronary artery occlusion, which can vary size and structure depending on individual variability in coronary anatomy and the extent of collaterals [38]. Different scar anatomy models with thinner isthmuses (<1 mm) could potentially result in PVCs.

Although triggered activity is more likely to form PVCs within thin isthmuses, successful propagation of these PVCs to the myocardium depends on local electrotonic conditions at the mouth of the isthmus. The cardiac safety factor for propagation has been shown to be minimum near regions of thin-to-thick tissue expansion [36], such as the mouth of the isthmus, where source current generated by the excited cells is insufficient to activate the downstream tissue [37]. Sink effects at the mouth of the isthmus can also be altered by elevations in V_m resulting from subthreshold DADs [17]. On one hand, depolarization of resting potential bring the cells closer to the threshold of the fast sodium current facilitating propagation [39]. On the other hand, long lasting DADs ultimately lead to inactivation of sodium channels promoting conduction block [17, 40]. Indeed, simulation results (see Supplementary Results, Figure S1 in

supplementary materials) demonstrate that propagation of an AP initiated within the thinnest isthmus, $w_{isth} = 0.2$ mm, to the myocardium depended on the amplitude of DADs at the exit site. Subthreshold DADs with lower amplitudes led to conduction block at isthmus' mouth, whereas DADs close to the activation threshold favored conduction of triggered APs to the myocardium. This finding is corroborated by our previous study [16], where SCR events happening in the whole ventricles, as a result of heart failure, gave rise to a global depolarization that gradually drove the tissue to the firing threshold.

4.2. Fibrosis and PVC Formation

Fibrosis plays an important role in the formation and persistence of a variety of cardiac arrhythmias [41]. As illustrated in **Figure 7**, fibrosis disrupts the intracellular matrix creating complex microscopic pathways through which the wavefront has to travel following zig-zag courses [42]. Such structural alterations lead to: (1) conduction slowing, a factor known to promote arrhythmias by shortening the wavelength [43]; and (2) electrogram fractionation [44] typically used in clinical practice to identify ablation targets [45]. Fibrosis has also been suggested to promote triggered activity by reducing the protective source-sink mismatch of tightly coupled tissue [15]. Xie et al. [13] have shown that the required number of contiguous myocytes exhibiting synchronized DADs decreases when tissue coupling is reduced by the presence of fibrosis. In their *in-silico* models, fibrosis was represented by fibroblasts randomly interposed either at the ends or sides of myocytes. The authors concluded that fibroblasts placed exclusively between the sides of myocytes had a major effect on PVC formation since they separate cells, turning a 2D tissue into a stack of longitudinal 1D fibers [13]. Fibrosis in all models employed in our study was modelled by randomly removing myocytes from the BZ [32]. Increased levels of fibrosis in the infarct BZ FIB_{BZ} gave rise to complex arrangements between cells resembling 1D strands or 2D clusters. Consequently, PVC formation is favored (**Figures 8–12**) as the downstream loading on errant myocytes interspersed with fibrosis is lower due to the reduced number of cells coupled to each other.

A critical FIB_{BZ} value above which p_{PVC} decreases and becomes zero was observed in both geometrical models used in this work. Moreover, this threshold increased from $FIB_{BZ} = 60\%$ in 2D sheet to $FIB_{BZ} = 90\%$ in the 3D BiV model. Interestingly, recent studies have suggested a strong correlation between arrhythmogenesis and the percolation threshold [31–33]. This topological metric is a mathematical concept related to percolation theory, which describes the process of a moving substance passing through a medium with random structure. Although, quantitatively the critical FIB_{BZ} values in this work differ from the percolation threshold [32], qualitatively our results showing that the FIB_{BZ} threshold increases with tissue dimensionality are in line with the findings of Alonso et al. [32]. However, wavefronts in their work were initiated by pacing the tissue rather than by stochastic firing of errant cells. Here we demonstrated SCR-mediated PVCs are most likely in infarct models with FIB_{BZ} close to a critical value. The decrease in p_{PVC} in **Figure 8A** and **Figure 12A** above this FIB_{BZ} threshold results from the combination of two factors. First, the replacement of myocytes by fibrosis reduced the amount of current sources contributing to the formation of an ectopic focus. Second, even though DADs could summate across cells to trigger an AP, propagation to the myocardium was not possible due to conduction block. Blocked PVCs in fibrotic BZs were either because the focal sources were disconnected from the rest of the tissue (see **Figure 7**) or due to unfavorable source-sink mismatch caused by thin-to-thick expansions from the BZ to the healthy myocardium (**Figure 10**).

Furthermore, not only the amount of fibrosis but also its texture may be a key arrhythmogenic factor [41]. Unlike in previous studies [13, 33], where percolation was used with different rules for myocyte removal to produce diffuse or interstitial fibrosis, the effects of different textures were investigated here simply by creating different random fibrotic BZs for a given FIB_{BZ}. Propensity for PVC formation varied substantially from one topology (randomness of the pattern) to another in both geometrical models. In the 2D cardiac sheet with $FIB_{BZ} = 60\%$, p_{PVC} varied between 9% and 39% whereas in the 3D BiV model ($FIB_{BZ} = 60\%$) p_{PVC} was within the $34\% \leq p_{PVC} \leq 70\%$ range.

4.3. Mechanism for SCR-Mediated Arrhythmogenesis

4.3.1. Unidirectional Conduction Block

Recently, Connolly et al. [24] have demonstrated that a premature stimulus capturing inside the isthmus may be blocked from propagating to the myocardium as the effective refractory period (ERP) was shown to be higher at the isthmus' proximal mouth. However, the induced PVC could still propagate further toward the distal end, where the tissue had recovered excitability, and reenter back around the scar [24]. In this work we have shown that conduction block can occur as a result of source-sink mismatch rather than heterogeneities in AP duration or in the ERP. This mechanism is illustrated in **Figure 10** as well as in Supplemental Movies 1, 2, where SCR-mediated DADs achieved sufficient synchrony to trigger a PVC in the thinner end of the isthmus (**Figure 10A**) or in myocytes interspersed with fibrosis (**Figure 10B**). On one hand, myocytes located on these regions experienced a lower electrotonic load which favored PVC formation. On the other hand, unfavorable source-sink conditions at the proximal mouth caused by rapid tissue expansion led to unidirectional conduction block. This novel mechanism demonstrated here was theorized by Nguyen et al. [15]. The authors proposed that a PVC triggered in 1D-like tracts of myocytes separated by fibrosis in the infarct BZ may propagate both ways. They suggested that, outward propagation to the well-coupled healthy tissue may fail since the current source from the triggered AP in these strands of myocardium is suddenly diluted into a greater number of neighboring quiescent cells. However, inward propagation through the scar might encounter more favorable loading conditions caused by a progressive widening of the surviving myocardial bundles until the interface with normal myocardium [15]. The findings from our study show systematically how fibrosis in the infarct heart can alter

local source-sink mismatch and directly facilitate unidirectional conduction block of PVCs induced by stochastic SCR events.

4.3.2. Wavelength and Reentrant Circuits

While a PVC can exit at the distal mouth and travel around the scar, it can only reenter back at the proximal site if the cells have regained excitability. Thus, electrophysiological changes promoting slow conduction or shortening of the ERP are key factors in the success of a reentrant circuit [43]. No reentrant episodes were observed in any of the experiments using tissue conductivities obtained from experiments with the healthy mammalian heart [28]. Additional simulations with geometrical models prone to unidirectional block were performed with tissue conductivities reduced by 50%, mimicking altered cell-to-cell known to happen in pathological settings such as heart failure [2], to investigate whether PVCs can form a reentrant wave. Examples of reentries induced by SCR-mediated PVCs on two different 2D infarct models are shown in **Figure 10**. The reduced tissue conductivity shortened the wavelength allowing the PVC to reenter at the proximal site as the tissue in that region had regained excitability. See Supplemental Movies 1, 2 for further details.

No reentries were detected in any of the experiments with the BiV model. As discussed previously, this is probably because of the geometry of the BZ. Other scar anatomies with different fibrotic patterns could give rise to arrhythmogenic 3D source-sink asymmetries at the boundaries with the healthy myocardium increasing the likelihood of unidirectional conduction block and reentry.

4.4. Clinical Implications

Reentrant VTs in the postinfarction heart have been associated with the presence of a critical conducting isthmus within the scar [25, 26]. The identification of such conducting channels is of great clinical significance as they provide an important target for catheter ablation therapy [26, 30]. Here we demonstrated that isthmuses also provide a substrate for PVC formation, the first initiating beats of a variety of VTs. Our results suggest that ablation of isthmuses therefore may not only interrupt a reentrant pathway, but also prevent the formation of ectopic focal sources. Moreover, advances have been made toward regeneration of cardiac tissue following MI [46], but knowledge of possible beneficial as well as adverse (proarrhythmic) outcomes is still limited. While the ultimate goal of regenerative therapy is to replace scar tissue by new contracting myocytes, an overactive tissue healing repair can lead to collagen accumulation in the BZ [46]. Our biophysically detailed simulations showed that increased levels of fibrosis in the BZ reduce local source-sink mismatch favoring PVC formation. Finally, reduced excitability due to blocking of sodium channels by antiarrhythmic drugs or sodium channelopathies associated with long Q-T and Brugada syndromes [47] have been shown to create a potent substrate for arrhythmia induction by PVCs [17, 40, 48]. In the infarcted heart, sodium current reduction can further enhance source-sink mismatches causing unidirectional block of PVCs at regions of abrupt tissue expansion.

4.5. Study Limitations

The SCR-mediated PVCs in this study were induced by increasing extracellular Ca^{2+} concentration. However, SCR events in cells that survive in the infarct BZ may occur as a result of sympathetic nerve remodeling [49] as well as increased levels of Ca^{2+}/calmodulin-dependent protein kinase II (CaMKII) autophosphorylation [50]. Nevertheless, abnormal SCRs and Ca^{2+} wave activity has been shown to be the underlying cause of DADs in cells that survive in the BZ [10, 11] and are accounted for in our phenomenological model. Furthermore, while other remodeling processes are known to take place in ischemia and infarction [1, 39, 51], only modifications that increase propensity of the MSH model to DAD-triggered activity were implemented here [16, 17]. This modeling choice allowed us to precisely assess how stochastic triggered activity in cells that survive MI can form organ-scale PVCs. Collagen deposition is also one of the hallmarks of structural remodeling in the BZ [19]. Fibrosis is included in our models by randomly removing myocytes from the BZ. Although fibrosis distribution can be obtained from imaging data [33], the simplistic synthetic patterns of fibrosis used in this work allowed us to investigate how degree as well as texture of fibrosis influence PVC formation. Finally, fibrosis was modeled by removing FEs representing myocardium from the geometrical models. While more sophisticated techniques exist [27], overall behavior would be qualitatively similar since wave propagation would still have to travel tortuous pathways.

5. CONCLUSIONS

In this work, state-of-the-art computational models were employed to investigate whether Ca^{2+}-mediated ectopy is facilitated by macroscopic as well as microscopic anatomical properties of the BZ of infarcted hearts. Our *in-silico* experiments have demonstrated that thin isthmuses transcending the non-conducting scar as well as strands of surviving myocytes interspersed with fibrosis are sources of PVCs initiated by abnormal SCR events. Triggered activity within thin strands of myocytes is more likely to summate and form PVCs due to the lesser electrotonic load on these cells. While the heart's antiarrhythmic source-sink mismatch prevented PVC formation in macroscopic isthmuses, fibrosis was shown to disrupt this protective mechanism favoring arrhythmogenic focal sources. Moreover, fibrosis contributed to unidirectional block of PVCs and when combined with slow conduction made the tissue vulnerable to reentry. Our simulation results suggest that catheter ablation of isthmuses as well as fibrotic BZ tissue can be highly effective against ectopy in postinfarct ventricles.

AUTHOR CONTRIBUTIONS

FC, YS, RW, GP, and MB conceived and designed the experiments. FC performed the experiments. FC and MB analyzed the data. YS and GP contributed reagents, materials, analysis tools. FC and MB wrote the paper.

FUNDING

This research was supported by the National Institute for Health Research (NIHR) Clinical Research Facility at Guy's and St. Thomas' National Health Service (NHS) Foundation Trust and NIHR Biomedical Research Centre based at Guy's and St. Thomas' NHS Foundation Trust and King's College London. The views expressed are those of the authors and not necessarily those of the NHS, the NIHR or the Department of Health. Open access for this article was funded by King's College London. FC and MB acknowledge the support of the British Heart Foundation through Project Grant PG/16/81/32441. YS was supported by the National Heart, Lung, and Blood Institute (RO1-119095). FC and RW were supported by CNPq (Conselho Nacional de Desenvolvimento Científico e Tecnológico) - Brazil. RW was also supported by the National Council for the Improvement of Higher Education (CAPES), Minas Gerais State Foundation for Research Development (FAPEMIG) and Federal University of Juiz de Fora. GP acknowledges the support of the National Institutes of Health (grant number 1RO1 HL 10119601) and the Austrian Science Fund (FWF) within the SFB Mathematical Optimization and Applications in Biomedical Sciences (grant number F3210-N18). MB acknowledges the support of the UK Medical Research Council through a New Investigator Research Grant number MR/N011007/1.

SUPPLEMENTARY MATERIAL

The Supplementary Material for this article can be found online at: https://www.frontiersin.org/articles/10.3389/fphy.2018.00057/full#supplementary-material

REFERENCES

1. Janse MJ, Wit AL. Electrophysiological mechanisms of ventricular arrhythmias resulting from myocardial ischemia and infarction. *Physiol Rev.* (1989) **69**:1049–169. doi: 10.1152/physrev.1989.69.4.1049
2. Nattel S, Maguy A, Bouter SL, Yeh YH. Arrhythmogenic ion-channel remodeling in the heart: heart failure, myocardial infarction, and atrial fibrillation. *Physiol Rev.* (2007) **87**:425–56. doi: 10.1152/physrev.00014.2006
3. John RM, Tedrow UB, Koplan BA, Albert CM, Epstein LM, Sweeney MO, et al. Ventricular arrhythmias and sudden cardiac death. *Lancet* (2012) **380**:1520–9. doi: 10.1016/S0140-6736(12)61413-5
4. Chou CC, Zhou S, Hayashi H, Nihei M, Liu YB, Wen MS, et al. Remodelling of action potential and intracellular calcium cycling dynamics during subacute myocardial infarction promotes ventricular arrhythmias in Langendorff-perfused rabbit hearts. *J Physiol.* (2007) **580**(Pt.3):895–906. doi: 10.1113/jphysiol.2006.120659
5. Boyden PA, Pu J, Pinto J, Keurs HE. Ca^{2+} transients and Ca^{2+} waves in purkinje cells: role in action potential initiation. *Circ Res.* (2000) **86**:448–55. doi: 10.1161/01.RES.86.4.448
6. Schlotthauer K, Bers DM. Sarcoplasmic reticulum Ca^{2+} release causes myocyte depolarization: underlying mechanism and threshold for triggered action potentials. *Circ Res.* (2000) **87**:774–80. doi: 10.1161/01.RES.87.9.774
7. Wasserstrom JA, Shiferaw Y, Chen W, Ramakrishna S, Patel H, Kelly JE, et al. Variability in timing of spontaneous calcium release in the intact rat heart is determined by the time course of sarcoplasmic reticulum calcium load. *Circ Res.* (2010) **107**:1117–26. doi: 10.1161/CIRCRESAHA.110.229294
8. Priori SG, Napolitano C, Tiso N, Memmi M, Vignati G, Bloise R, et al. Mutations in the cardiac ryanodine receptor gene (hRyR2) underlie catecholaminergic polymorphic ventricular tachycardia. *Circulation* (2001) **103**:196–200. doi: 10.1161/01.CIR.103.2.196
9. Hoeker GS, Katra RP, Wilson LD, Plummer BN, Laurita KR. Spontaneous calcium release in tissue from the failing canine heart. *Am J Physiol Heart Circ Physiol.* (2009) **297**:H1235–42. doi: 10.1152/ajpheart.01320.2008
10. Boyden PA, Barbhaiya C, Lee T, ter Keurs HEDJ. Nonuniform Ca^{2+} transients in arrhythmogenic Purkinje cells that survive in the infarcted canine heart. *Cardiovasc Res.* (2003) **57**:681–93. doi: 10.1016/S0008-6363(02)00725-3
11. Hirose M, Stuyvers BD, Dun W, ter Keurs HE, Boyden PA. Function of Ca^{2+} release channels in Purkinje cells that survive in the infarcted canine heart: a mechanism for triggered Purkinje ectopy. *Circ Arrhythm Electrophysiol.* (2008) **1**:387–95. doi: 10.1161/CIRCEP.107.758110
12. Fozzard HA, Schoenberg M. Strength-duration curves in cardiac Purkinje fibres: effects of liminal length and charge distribution. *J Physiol.* (1972) **226**:593–618. doi: 10.1113/jphysiol.1972.sp009999
13. Xie Y, Sato D, Garfinkel A, Qu Z, Weiss JN. So little source, so much sink: requirements for afterdepolarizations to propagate in tissue. *Biophys J.* (2010) **99**:1408–15. doi: 10.1016/j.bpj.2010.06.042
14. Cabo C, Yao J, Boyden PA, Chen S, Hussain W, Duffy HS, et al. Heterogeneous gap junction remodeling in reentrant circuits in the epicardial border zone of the healing canine infarct. *Cardiovasc Res.* (2006) **72**:241–9. doi: 10.1016/j.cardiores.2006.07.005
15. Nguyen TP, Qu Z, Weiss JN. Cardiac fibrosis and arrhythmogenesis: the road to repair is paved with perils. *J Mol Cell Cardiol.* (2014) **70**:83–91. doi: 10.1016/j.yjmcc.2013.10.018
16. Campos FO, Shiferaw Y, Prassl AJ, Boyle PM, Vigmond EJ, Plank G. Stochastic spontaneous calcium release events trigger premature ventricular complexes by overcoming electrotonic load. *Cardiovasc Res.* (2015) **107**:175–83. doi: 10.1093/cvr/cvv149
17. Campos FO, Shiferaw Y, Vigmond EJ, Plank G. Stochastic spontaneous calcium release events and sodium channelopathies promote ventricular arrhythmias. *Chaos* (2017) **27**:093910. doi: 10.1063/1.4999612
18. Vigmond EJ, Stuyvers BD. Modeling our understanding of the His-Purkinje system. *Prog Biophys Mol Biol.* (2016) **120**:179–88. doi: 10.1016/j.pbiomolbio.2015.12.013
19. Rutherford SL, Trew ML, Sands GB, LeGrice IJ, Smaill BH. High-resolution 3-dimensional reconstruction of the infarct border zone: impact of structural remodeling on electrical activation. *Circ Res.* (2012) **111**:301–11. doi: 10.1161/CIRCRESAHA.111.260943
20. Sosnovik DE, Wang R, Dai G, Wang T, Aikawa E, Novikov M, et al. Diffusion spectrum MRI tractography reveals the presence of a complex network of residual myofibers in infarcted myocardium. *Circ Cardiovasc Imaging* (2009) **2**:206–12. doi: 10.1161/CIRCIMAGING.108.815050
21. Myles RC, Wang L, Kang C, Bers DM, Ripplinger CM. Local beta-adrenergic stimulation overcomes source-sink mismatch to generate focal arrhythmia. *Circ Res.* (2012) **110**:1454–64. doi: 10.1161/CIRCRESAHA.111.262345
22. Chen W, Aistrup G, Wasserstrom JA, Shiferaw Y. A mathematical model of spontaneous calcium release in cardiac myocyte. *Am J Physiol Heart Circ Physiol.* (2011) **300**:H1794–805. doi: 10.1152/ajpheart.01121.2010
23. Mahajan A, Shiferaw Y, Sato D, Baher A, Olcese R, Xie LH, et al. A rabbit ventricular action potential model replicating cardiac dynamics at rapid heart rates. *Biophys J.* (2008) **94**:392–410. doi: 10.1529/biophysj.106.98160
24. Connolly AJ, Bishop MJ. Computational representations of myocardial infarct scars and implications for Arrhythmogenesis. *Clin Med Insights Cardiol.* (2016) **10**(Suppl. 1):27–40. doi: 10.4137/CMC.S39708
25. Mountantonakis SE, Park RE, Frankel DS, Hutchinson MD, Dixit S, Cooper J, et al. Relationship between voltage map "channels" and the location of critical isthmus sites in patients with post-infarction cardiomyopathy

and ventricular tachycardia. *J Am Coll Cardiol.* (2013) **61**:2088–95. doi: 10.1016/j.jacc.2013.02.031
26. de Chillou C, Groben L, Magnin-Poull I, Andronache M, MagdiAbbas M, Zhang N, et al. Localizing the critical isthmus of postinfarct ventricular tachycardia: the value of pace-mapping during sinus rhythm. *Heart Rhythm.* (2014) **11**:175–81. doi: 10.1016/j.hrthm.2013.10.042
27. Costa CM, Campos FO, Prassl AJ, dos Santos RW, Sánchez-Quintana D, Hofer HAE, et al. An efficient finite element approach for modeling fibrotic clefts in the heart. *IEEE Trans Biomed Eng.* (2014) **61**:900–10. doi: 10.1109/TBME.2013.2292320
28. Clerc L. Directional differences of impulse spread in trabecular muscle from mammalian heart. *J Physiol.* (1976) **255**:335–46. doi: 10.1113/jphysiol.1976.sp011283
29. Vetter FJ, McCulloch AD. Three-dimensional analysis of regional cardiac function: a model of rabbit ventricular anatomy. *Prog Biophys Mol Biol.* (1998) **69**:157–83. doi: 10.1016/S0079-6107(98)00006-6
30. Hill YR, Child N, Hanson B, Wallman M, Coronel R, Plank G, et al. Investigating a novel activation-repolarisation time metric to predict localised vulnerability to reentry using computational modelling. *PLoS ONE* (2016) **11**:e0149342. doi: 10.1371/journal.pone.0149342
31. de Barros BG, dos Santos RW, Lobosco M, Alonso S. Simulation of ectopic pacemakers in the heart: multiple ectopic beats generated by reentry inside Fibrotic Regions. *Biomed Res Int*. (2015) **2015**:713058. doi: 10.1155/2015/713058
32. Alonso S, dos Santos RW, Bär M. Reentry and ectopic pacemakers emerge in a three-dimensional model for a slab of cardiac tissue with diffuse microfibrosis near the percolation threshold. *PLoS ONE* (2016) **11**:e0166972. doi: 10.1371/journal.pone.0166972
33. Vigmond E, Pashaei A, Amraoui S, Cochet H, Hassaguerre M. Percolation as a mechanism to explain atrial fractionated electrograms and reentry in a fibrosis model based on imaging data. *Heart Rhythm.* (2016) **13**:1536–43. doi: 10.1016/j.hrthm.2016.03.019
34. Bishop MJ, Plank G. Representing cardiac bidomain bath-loading effects by an augmented monodomain approach: application to complex ventricular models. *IEEE Trans Biomed Eng.* (2011) **58**:1066–75. doi: 10.1109/TBME.2010.2096425
35. Vigmond E, Hughes M, Plank G, Leon L. Computational tools for modeling electrical activity in cardiac tissue. *J Electrocardiol.* (2003) **36**:69–74. doi: 10.1016/j.jelectrocard.2003.09.017
36. Boyle PM, Vigmond EJ. An intuitive safety factor for cardiac propagation. *Biophys J.* (2010) **98**:L57–9. doi: 10.1016/j.bpj.2010.03.018
37. Connolly A, Trew ML, Smaill BH, Plank G, Bishop MJ. Local gradients in electrotonic loading modulate the local effective refractory period: implications for Arrhythmogenesis in the infarct border Zone. *IEEE Trans Biomed Eng.* (2015) **62**:2251–9. doi: 10.1109/TBME.2015.2421296
38. Richardson WJ, Clarke SA, Quinn TA, Holmes JW. Physiological implications of myocardial scar structure. *Compr Physiol.* (2015) **5**:1877–909. doi: 10.1002/cphy.c140067
39. Campos FO, Prassl AJ, Seemann G, dos Santos RW, Plank G, Hofer E. Influence of ischemic core muscle fibers on surface depolarization potentials in superfused cardiac tissue preparations: a simulation study. *Med Biol Eng Comput*. (2012) **50**:461–72. doi: 10.1007/s11517-012-0880-1
40. Liu MB, de Lange E, Garfinkel A, Weiss JN, Qu Z. Delayed afterdepolarizations generate both triggers and a vulnerable substrate promoting reentry in cardiac tissue. *Heart Rhythm.* (2015) **12**:2115–24. doi: 10.1016/j.hrthm.2015.06.019
41. de Jong S, van Veen TA, van Rijen HV, de Bakker JM. Fibrosis and cardiac arrhythmias. *J Cardiovasc Pharmacol.* (2011) **57**:630–8. doi: 10.1097/FJC.0b013e318207a35f
42. de Bakker JM, van Capelle FJ, Janse MJ, Tasseron S, Vermeulen JT, de Jonge N, et al. Slow conduction in the infarcted human heart. "Zigzag" course of activation. *Circulation* (1993) **88**:915–26.
43. Smeets JL, Allessie MA, Lammers WJ, Bonke FI, Hollen J. The wavelength of the cardiac impulse and reentrant arrhythmias in isolated rabbit atrium. The role of heart rate, autonomic transmitters, temperature, and potassium. *Circ Res.* (1986) **58**:96–108.
44. Campos FO, Wiener T, Prassl AJ, dos Santos RW, Sánchez-Quintana D, Ahammer H, et al. Electroanatomical characterization of atrial microfibrosis in a histologically detailed computer model. *IEEE Trans Biomed Eng.* (2013) **60**:2339–49. doi: 10.1109/TBME.2013.2256359
45. Lau DH, Zeemering S, Maesen B, Kuklik P, Verheule S, Schotten U. Catheter ablation targeting complex fractionated atrial electrogram in atrial fibrillation. *J Atr Fibrill.* (2013) **6**:907. doi: 10.4022/jafib.907
46. Ongstad EL, Gourdie RG. Can heart function lost to disease be regenerated by therapeutic targeting of cardiac scar tissue? *Semin Cell Dev Biol.* (2016) **58**:41–54. doi: 10.1016/j.semcdb.2016.05.020
47. Bezzina C, Veldkamp MW, van Den Berg MP, Postma AV, Rook MB, Viersma JW, et al. A single Na(+) channel mutation causing both long-QT and Brugada syndromes. *Circ Res.* (1999) **85**:1206–13. doi: 10.1161/01.RES.85.12.1206
48. Boyle PM, Park CJ, Arevalo HJ, Vigmond EJ, Trayanova NA. Sodium current reduction unmasks a structure-dependent substrate for arrhythmogenesis in the normal ventricles. *PLoS ONE* (2014) **9**:e86947. doi: 10.1371/journal.pone.0086947
49. Chen PS, Chen LS, Cao JM, Sharifi B, Karagueuzian HS, Fishbein MC. Sympathetic nerve sprouting, electrical remodeling and the mechanisms of sudden cardiac death. *Cardiovasc Res.* (2001) **50**:409–16. doi: 10.1016/S0008-6363(00)00308-4
50. Hund TJ, Decker KF, Kanter E, Mohler PJ, Boyden PA, Schuessler RB, et al. Role of activated CaMKII in abnormal calcium homeostasis and INa remodeling after myocardial infarction: insights from mathematical modeling. *J Mol Cell Cardiol.* (2008) **45**:420–8. doi: 10.1016/j.yjmcc.2008.06.007
51. Arevalo HJ, Vadakkumpadan F, Guallar E, Jebb A, Malamas P, Wu KC, et al. Arrhythmia risk stratification of patients after myocardial infarction using personalized heart models. *Nat Commun.* (2016) **7**:11437. doi: 10.1038/ncomms11437

Conflict of Interest Statement: The authors declare that the research was conducted in the absence of any commercial or financial relationships that could be construed as a potential conflict of interest.

The reviewer WM and handling editor declared their shared affiliation.

frontiers in Physiology

ORIGINAL RESEARCH
published: 04 June 2018
doi: 10.3389/fphys.2018.00673

A Minimal Model Approach for Analyzing Continuous Glucose Monitoring in Type 2 Diabetes

Pranay Goel[1]*, *Durga Parkhi*[2], *Amlan Barua*[3], *Mita Shah*[4] and *Saroj Ghaskadbi*[5]

[1] Department of Biology, Indian Institute of Science Education and Research, Pune, India, [2] Indian Institute of Science Education and Research, Pune, India, [3] Department of Mathematics, Indian Institute of Technology, Dharwad, India, [4] Global Hospitals, Mumbai, India, [5] Department of Zoology, Savitribai Phule Pune University, Pune, India

Continuous glucose monitoring (CGM), a technique that records blood glucose at a regular intervals. While CGM is more commonly used in type 1 diabetes, it is increasingly becoming attractive for treating type 2 diabetic patients. The time series obtained from a CGM provides a rich picture of the glycemic state of the subjects and may help have tighter control on blood sugar by revealing patterns in their physiological responses to food. However, despite its importance, the biophysical understanding of CGM is far from complete. CGM data series is complex not only because it depends on the composition of the food but also varies with individual physiology. All of these make a full modeling of CGM data a difficult task. Here we propose a simple model to explain CGM data in type 2 diabetes. The model combines a relatively simple glucose-insulin dynamics with a two-compartment food model. Using CGM data of a healthy and a diabetic individual we show that this model can capture liquid meals well. The model also allows us to estimate the parameters in a relatively straightforward manner. This opens up the possibility of personalizing the CGM data. The model also predicts insulin time series from the model, and the rate of appearance of glucose due to food. Our methodology thus paves the way for novel analyses of CGM which have not been possible before.

Keywords: continuous glucose monitoring, minimal model, type 2 diabetes, insulin estimation, glucose rate of appearance

OPEN ACCESS

Edited by:
S Sridhar,
Robert Bosch Centre for Cyber-Physical Systems, Indian Institute of Science, India

Reviewed by:
Sergei Pereverzyev,
Johann Radon Institute for Computational and Applied Mathematics (RICAM), Austria
Arun Babu Puthuparambil,
Indian Institute of Science, India

***Correspondence:**
Pranay Goel
pgoel@iiserpune.ac.in

Specialty section:
This article was submitted to Computational Physiology and Medicine, a section of the journal Frontiers in Physiology

Received: *01 November 2017*
Accepted: *15 May 2018*
Published: *04 June 2018*

Citation:
Goel P, Parkhi D, Barua A, Shah M and Ghaskadbi S (2018) A Minimal Model Approach for Analyzing Continuous Glucose Monitoring in Type 2 Diabetes. Front. Physiol. 9:673. doi: 10.3389/fphys.2018.00673

1. INTRODUCTION

Diabetes is a disease in which glucose is the central measure not only of pathogenesis and diagnosis but also its treatment. Clinically, blood glucose is typically measured as fasting and postprandial plasma glucose, or as glycated hemoglobin. There has been considerable interest in technologies that ease glucose monitoring and improve the resolution of data collection. Continuous glucose monitoring (CGM) uses a sensor, typically fixed on the arm, reports blood glucose every 15 min for a 2 week period. This is a high quality, high time resolution methodology that is becoming increasingly available. The U.S. Food and Drug Administration, for example, has recently approved use of the FreeStyle Libre Flash CGM (FDA News Release – 2017, 2017) sensor. CGM has the potential to help millions of people the world over who struggle chronically with obesity and diabetes (Bode, 2000; Klonoff, 2005; Deiss et al., 2006; Murphy et al., 2008; Juvenile Diabetes Research Foundation Continuous Glucose Monitoring Study Group et al., 2009): It holds the promise of utilizing information contained in the time series to not only gain insight into food

habits, and discover (un)healthy dietary patterns but also to determine effective interventions. However, interpreting CGM traces is complex and often subjective, and there are no consensus algorithms to aid the design of appropriate interventions. Techniques aimed at improving the analyses of blood glucose monitoring are an active field of research (McDonnell et al., 2005; Clarke and Kovatchev, 2009; Signal et al., 2013; Kirchsteiger et al., 2016). This paper is a first attempt at describing models that can potentially help us understand CGM time series in type 2 diabetes.

At a more fundamental level, CGM reveals differences in the blood glucose *rhythms* of diabetic patients compared to healthy persons, which is considerably more information than just comparisons of the average glucose. Generally speaking, the glucose rhythm in the diabetic can be expected to be more irregular than of a healthy person. **Figure 1** shows the CGMs of a healthy subject and a diabetic patient. It is immediately apparent that the mean glucose is considerably higher in the diabetic case. A spectral analysis confirms that there is a sharp peak in the frequency distribution corresponding to a 24-h period (largely due to a periodicity of food intake). While these are straightforward metrics in the time and frequency domains there is considerable additional nuance in these traces, which will be the focus of our attention here. We shall attempt to model the details of the glucose *pulsatility*; this invariably means having to explain the glucose transients that follow meals, breakfast, lunch, dinner, and others. Naively, glucose pulses are driven by food intake, and the restoration of glucose to basal levels (homeostasis) involves the hormone insulin. However, this simplistic fiction hides enormous complexity, and it is fair to say that this process is not yet fully understood. In other words, our model will also encounter this difficulty in one form or another.

In a minimal view of the process, glucose *increase* is driven by hepatic release of blood glucose following food intake, and its *disposal* is driven by (i) insulin-dependent clearance into the peripheral tissue, and (ii) other insulin-independent tissues. The rate of appearance of glucose in the blood following a meal is complicated not only by food composition but also the individual's physiological response to different foods. While glycemic response to a food is correlated to its *glycemic index* (GI), a quantity that expresses how readily it is assimilated and glucose appears in the blood, GI is known to be centered on the ingested *food*, and ignores any person specific physiology. It has been shown that the glycemic response to (the same) food varies considerably between people; interestingly, it appears to depend, in particular, on gut microbiome composition amongst other factors (Zeevi et al., 2015; Korem et al., 2017). A complete, dynamic description of a CGM trace from first principles—that is, starting from a knowledge of foods eaten—appears to be challenging at this time.

On the other hand, there is a considerable body of work centered on modeling glucose and insulin dynamics in type 2 diabetes; for a recent review see (Goel, 2017). One strategy that is often used is to follow the response to a controlled bolus of food. A typical setting is an oral glucose tolerance test (OGTT), in which a very sweet drink (the dose is often 75 grams of glucose) is taken rapidly, and glucose samples are drawn from the blood every 30 min up to 2 h afterwards. Mathematical models involving coupled glucose and insulin dynamics have been used to describe this data in great detail. A significant review of the state-of-the art in this field, in particular of the work of Cobelli and coworkers spanning several decades, appears in Cobelli et al. (2009). We note that while modeling OGTT, and to a lesser extent "mixed-meal" data, are quite mature, to the best of our knowledge a model suitable for CGM has not yet been described. There are several considerations that seem to argue against simply extending one of the earlier models to CGM. The current models involve a number of compartments, not only for glucose and insulin but also liver, muscle and adipose, the gastro-intestinal tract, and so on. As such, it is difficult to envisage the numerous model parameters can all be identified from CGM data alone. In the models described in Cobelli et al. (2009), for example, parameters were discovered using glucose tolerance tests together with various other techniques, such as radio-labeled tracers. Not only are these difficult and expensive experiments in themselves but reproducing these outside the scope of specialized studies is impractical.

Our interest in this paper is to describe a minimal mathematical model useful for exploring CGM data. We restrict ourselves largely to CGM data collection; however, we note that it is plausible to add a few other commonplace measurements including (i) the use of fingerstick glucose measurement, and (ii) a professional (laboratory-based) fasting and postprandial glucose, glycated hemoglobin and insulin measurements carried out a few times while the CGM sensor is implanted. This additional data can help in determining the model, as we describe below. While it is difficult to expect to be able to describe the glucose transient following each meal, we show that liquid meals are relatively easy to describe; this insight will be used to fit model parameters. In other words, we propose a novel strategy for the model personalization of individual CGM data. Our methodology also helps us recover the *insulin* time series corresponding to the CGM, using the fitted model. Further, it is also possible to estimate the time series corresponding to the appearance of glucose due to food. Finally, we estimate clinically important parameters corresponding to the insulin secretion capacity of the pancreas and insulin resistance, and compare them between the normal and diabetic cases. Our methodology appears to be suitable for CGM users widely, with few additional measurements required.

2. MODELS AND METHODS

2.1. Data Collection

The digital CGM records of two individuals, a diabetic patient undergoing treatment and a healthy subject, were analyzed retrospectively. Note that the patient is not in a controlled environment, they carry out their daily activities independently with the sensor attached to them. The CGM sensor is about the size of a coin, and is typically affixed to the arm. The patient is fully ambulatory and only minimally aware of the sensor, that is, it does not interfere with most routine activities. The sensor collects data continuously for about 2 weeks.

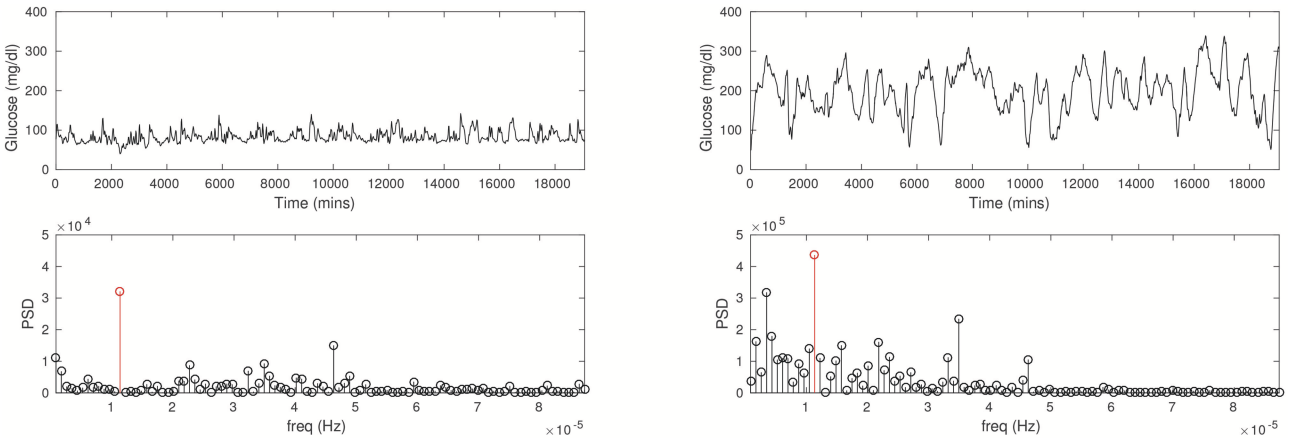

FIGURE 1 | The CGM time series recorded for a healthy, non-diabetic subject (Left column) and a diabetic patient (Right column). Notice the average glucose is substantially lower in the non-diabetic (about 100 mg/dl) than in the diabetic (about 200 mg/dl). The glucose pulses are of large amplitude in the diabetic, and appear to be wider as well. Power spectral density (PSD; second row) shows a prominent peak at a period of about 24 h in either case (red stems), although the frequency profiles are not similar.

All subjects gave written informed consent for use of their data. A separate approval from the Institutional Ethics Committee of Global Hospitals was not requested since data from only two individuals was analyzed here, and this does not represent a full scale human clinical study. In particular, diabetes treatment and CGM monitoring is at the discretion of the doctor and patient, and data was only analyzed after data collection.

2.2. A Minimal Model of Glucose and Insulin Dynamics

We adapt a glucose–insulin model due to (Topp et al., 2000), and add food dynamics to it as follows.

2.2.1. Food Dynamics

The digestion of food is modeled using two-compartment dynamics. Food enters the first compartment, the stomach, q_{sto}, and is passed along to a second compartment, collectively called the "gut", q_{gut}, from which glucose is assimilated into the bloodstream. Thus,

$$\frac{dq_{sto}}{dt} = -k_{sto}\ q_{sto}, \tag{1}$$

$$\frac{dq_{gut}}{dt} = k_{sto}\ q_{sto} - k_{gut}\ q_{gut}, \tag{2}$$

where $q_{sto} \leftarrow q_{sto} + food_i$ is the food intake at times t_i. We demonstrate below that this is a good model that captures the glucose response to liquid foods. Modeling mixed-meals is considerably more complex and is not carried out here, however, we show that an average description can sometimes be achieved by modeling such meals with the two-compartment model above, except with a different value of k_{gut}. That is, for liquid meals we take $k_{gut} \equiv k_{gut,l}$ while for a mixed-meal we set $k_{gut} \equiv k_{gut,mm}$.

2.2.2. The Topp Model of Glucose–Insulin Dynamics

The $G - I$ model for the dynamics of glucose and insulin is:

$$\frac{dG}{dt} = R_0 - (EG_0 + S_I I)G + k_{gut} q_{gut}, \tag{3}$$

$$\frac{dI}{dt} = I_{max}\frac{G^2}{\alpha + G^2} - k_I I, \tag{4}$$

where glucose absorption occurs from q_{gut}. R_0 stands for a basal production of glucose and EG_0 is insulin-independent glucose utilization, S_I is insulin sensitivity and determines the insulin-dependent glucose clearance from the blood. I_{max} is the maximal rate of insulin secretion from the pancreas and k_I the rate at which insulin is cleared (largely by the liver). G is measured in mg/dl, and I in μU/ml.

2.3. Model Fitting

We fit parameters of the model following a standard optimization approach. The cost function we optimize typically involves the CGM time series around the pulse that we wish to focus on fitting.

The simulation of the model ODEs is carried out as follows. At time $t = t_0$, there is no food in the system and we allow the model to evolve; for each food that enters the system, q_{sto} is adjusted to a value $q_{sto} + food_i$ where $food_i$ is the spike in the value of q_{sto} at time t_i. The $food_i$ are a part of the optimization problem. The optimization algorithm then identifies the model parameters and food sizes; the cost function minimized is a squared difference between experimental values of CGM and simulation.

Numerical experiments indicate that the parameters EG_0 and α are not identifiable; these values are kept fixed (see **Table 1** for the values) close to the nominal values used in Topp et al. (2000). The steady state of insulin can be obtained from Equation (4) as $\frac{I_{max}G_{ss}^2}{\alpha+G_{ss}^2}/k_I$; since we assume we know the fasting insulin from a laboratory measurement in our method, we allow k_I to be

TABLE 1 | Parameters corresponding to the non-diabetic and diabetic CGM time series.

Parameter	Non-diabetic	Diabetic	Units
R_0	2.1	2.5	$\text{mgdl}^{-1}\text{min}^{-1}$
E_{G0}	1×10^{-3}	2.5×10^{-3}	min^{-1}
S_I	3.06×10^{-3}	1.14×10^{-3}	$\text{ml}\ \mu\text{U}^{-1}\text{min}^{-1}$
α	1×10^{4}	1×10^{4}	$\text{mg}^2\text{dl}^{-2}$
I_{max}	0.28	0.93	$\mu\text{U ml}^{-1}\text{min}^{-1}$
k_I	0.01	0.06	min^{-1}
k_{sto}	0.036	0.026	min^{-1}
$k_{gut,l}$	0.098	0.026	min^{-1}
$k_{gut,mm}$	0.011	–	min^{-1}

determined by the above, namely, $k_I \equiv \frac{I_{max}G_{ss}^2}{\alpha+G_{ss}^2}/I_{ss}$. For the non-diabetic case we use $G_{ss} = 90$ and $I_{ss} = 12.4$, and for the diabetic case $G_{ss} = 195$ and $I_{ss} = 12.5$.

The model simulations and optimization are carried out in MATLAB. `ode45` is used for ODE integration, while fitting uses a combination of `patternsearch` and `fmincon` with suitable constraints. Optimzation iterations were terminated when the relative changes in all elements of the parameter vector were lower than a nominal tolerance of 10^{-6}.

3. RESULTS

3.1. CGM of a Non-diabetic Subject

We found that a few "landmark" pulses are sufficient to estimate the $G - I$ model. In **Figure 2** we fit three peaks that had a significant liquid component to it. The resulting model parameters are shown in **Table 1**.

The following quick checks indicate this is a reasonable fit: The relative sizes of food estimates, the three q_{sto} pulses, are commensurate with the corresponding glucose peaks, and with the diet diary. The insulin response is peaked similarly, as expected. In particular, the physiological range of insulin is typically between 2 and 25 μU/ml, consistent with the result here. Insulin peaks occur slightly later than the glucose peaks. Finally, note that the response to liquid meal at 450 min is fit well (this is by design: That pulse is weighted relatively heavily in the cost function) while the other two responses to mixed meals are more complex (especially the postprandial clearance), and these are fit in an "average" sense, in line with expectation.

Note the resting glucose and insulin obtained through the fitting process. The resting insulin is approximately 9 μU/ml, slightly lower than the laboratory fasting insulin measurement, 12.5. This appears to be consistent with the observation that resting glucose over this epoch is close to 70 mg/dl.

These fits suggest a straightforward procedure for obtaining a personalized model of CGM, that is, for fitting model parameters to describe a particular time series. An "isolated" liquid meal – that is, taken with a sufficient gap before and after it – is described well by the present model, and one readily recovers all parameters through optimization.

3.2. CGM of a Diabetic Patient

We optimize over a suitable peak in the CGM of a diabetic patient in a manner similar to that of the non-diabetic case. Most meals for this individual were of mixed-meal type, however, we noted a few that were liquid meals. One such peak we believe was due to a liquids taken around 1,200 min, see **Figure 3**. Once again, fitting this peak allows us to recover suitable model parameters; these are listed in **Table 1**. One feature to note is that the EG_0 appears to be larger for this individual (this can be estimated by fitting a later night portion of the CGM, when insulin is not likely to be dominant, with an exponential).

3.3. Insight Into Diabetogenesis

A comparison of the parameters between the non-diabetic and diabetic cases is instructive. We note, first, that our procedure seems to be robust in determining parameters. In particular, we obtain the clinically important parameters, S_I and I_{max} among other things. We generally expect that insulin sensitivity ought to be lowered in diabetes. Maximal secretion typically first rises as diabetes develops (to account for the increasing demand that hyperglycemia places on it), and as exhaustion sets in, secretion deteriorates. From **Table 1** it is seen that the estimated I_{max} is larger for the diabetic patient; this can either be because insulin is in the compensatory phase of diabetogenesis, or as is more likely, the result of secretagogue drugs prescribed to them. S_I, on the other hand, is lower for the diabetic person as expected.

3.4. Estimation of Insulin

An immediate application of personalizing the model fits is to estimate insulin. Insulin is not easy to measure clinically as it is expensive and requires drawing blood. Furthermore, no technology exists currently for continuous *insulin* monitoring. Using the model fit it is possible to estimate insulin with the same time resolution as CGM. We show this next.

We design an observer (Moreno, 2000; Robenack and Goel, 2007), $\hat{I}$, to estimate the insulin dynamics, $\frac{dI}{dt} = I_\infty(G) - k_I I$, Equation 4. We note that the equation

$$\frac{d\hat{I}}{dt} = I_\infty(G_{data}) - k_I\hat{I}, \tag{5}$$

driven by G_{data}, the CGM time series, converges exponentially to the true dynamics of the system, that is, $\hat{I} \to I$, since the error, $e \equiv I - \hat{I}$ satisfies $\dot{e} = -k_I e$. In other words, apart from an initial transient that corresponds to the time constant with which the error dissipates, $1/k_I$, $\hat{I}$ reports the times series I.

Figure 4 shows the insulin estimated for the non-diabetic case. Insulin is obtained continuously in time, and since it requires only the glucose data it can be computed even without a detailed knowledge of the food intake. Notice that the insulin in **Figure 2** is computed for the glucose corresponding to the three food peaks, whereas the insulin in **Figure 4** is computed using the observer above from the CGM data, and is a faithful representation of its co-variation with glucose; in particular, $\hat{I}$ can be seen to be considerably more nuanced.

Apart from being a very useful facility in general, this technique can be particularly valuable in a setting where one

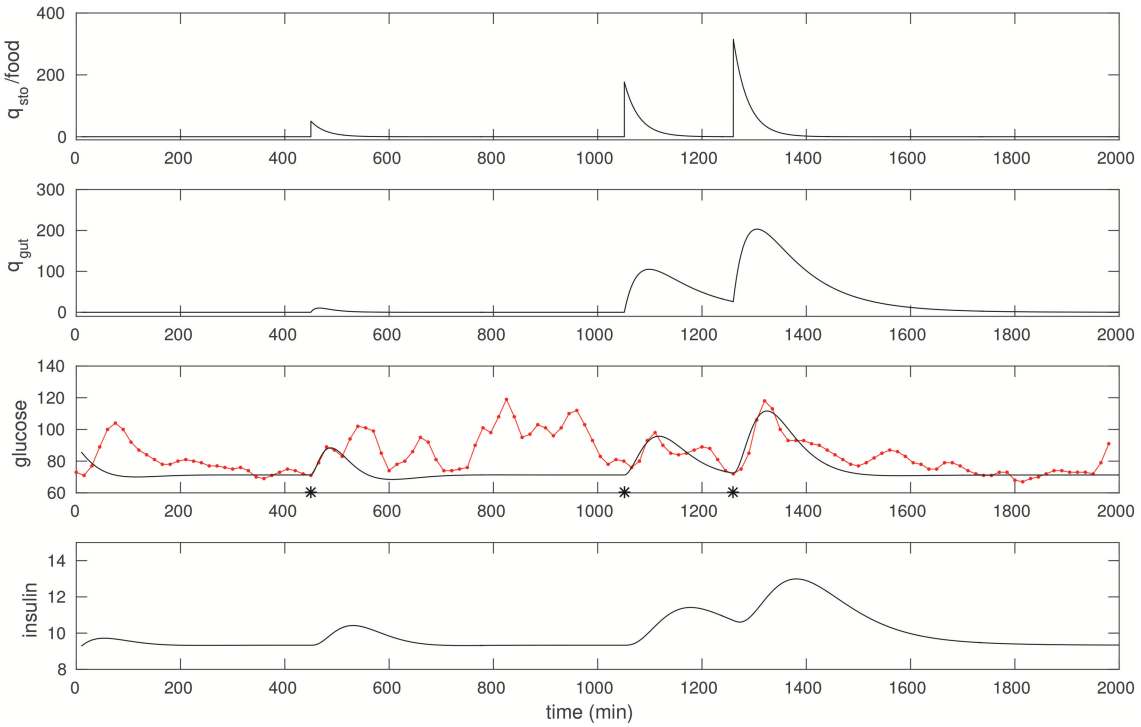

FIGURE 2 | The CGM of around 24 h of a non-diabetic subject, starting at midnight. The glucose data (red) is overlaid with the model simulation (black). Three foods were selected, and the times they were taken (450, 1,051, and 1,260 respectively) were recalled from the food diary; these are marked with asterisks. The first is a liquid meal at breakfast while the other two are mixed meals (the last one being dinner). These food pulses were fit; the fitted q_{sto} amplitudes are 50, 177, and 316 respectively.

wishes to know the insulin response to a certain food. There are theories of obesity [the "carbohydrate–insulin model"; (see, for example, Ludwig and Friedman, 2014; Goel, 2017)] as well as diabetes (Corkey, 2012; Goel, 2015) that rest on the insulin response to food. It would be interesting to evaluate the techniques here in the context of such studies.

3.5. Estimation of the Rate of Appearance of Glucose

It is interesting to know what is the rate of appearance of glucose, *Ra*, due to food. That is, in Equation 3, $\frac{dG}{dt} = g(G,I) + Ra$, where $g(G,I) = R_0 - (EG_0 + S_I I)G$ and Ra is modeled as $k_{gut}q_{gut}$. However, we would like to solve an inverse problem to directly determine what the *Ra* is more generally. In other words, given that we have estimated the model parameters, we would like to design an input observer for *Ra*. An estimate of *Ra* can be computed as

$$Ra = \frac{dG_{data}}{dt} - R_0 + (EG_0 + S_I\hat{I})G_{data}, \tag{6}$$

where $\frac{dG_{data}}{dt}$ is computed directly from differentiating the CGM time series, and insulin is estimated via $\hat{I}$, Equation 5. The observed *Ra* is shown in **Figure 4**, lower. A spline fit was used to determine the required derivative in order to reduce numerical inaccuracy. For comparison, we have overlaid the solution from **Figure 2**, that is, *Ra* computed from the input observer is compared to the case with three food pulses, modeled as $Ra \equiv k_{gut}q_{gut}$. The correspondence between the two is excellent for the fully liquid meal, and reasonable for the other two as well.

The input observer for *Ra* thus gives us an excellent facility not only to discover the effect of different foods on the appearance of glucose in the blood but also for carrying out modeling studies to try and explain mixed meals. This will be investigated in greater detail in future work.

4. DISCUSSION

In our view CGM is a very powerful data collection tool in diabetes. Despite its importance, models do not yet exist for describing it. Here we show that parts, if not all, of the data can be explained rather simply, and more importantly, one can recover all of the model parameters required to fit CGM time series individually. Our key observation is that liquids seem to pass through the gut in a fairly stereotyped manner, and we are able to model this successfully. We demonstrate that the glycemic response to a liquid meal, especially one that is well separated from other food intakes, can be used to fit a minimal mathematical model, and identify all the parameters needed to describe glucose and insulin dynamics well. Thus, our prescription for fitting a personalized model to a CGM time series is simply ask the patient to take a liquid meal by itself.

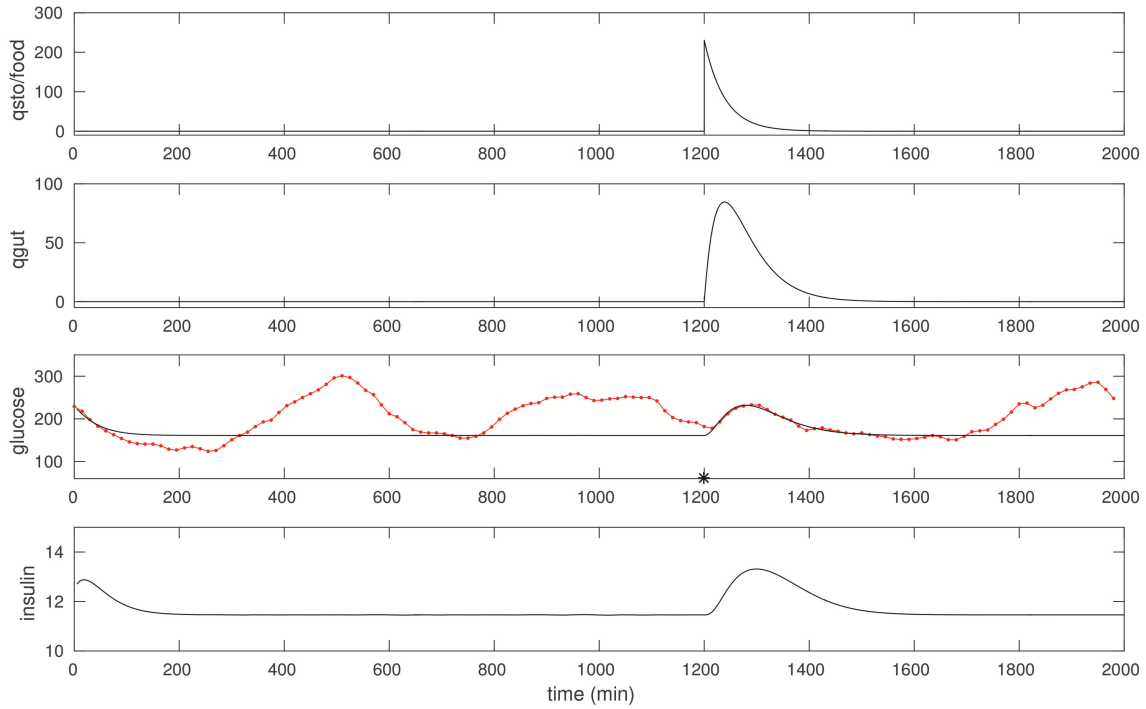

FIGURE 3 | The CGM of about 24 h of a diabetic subject, starting at around 0400 h. The glucose data (red) is overlaid with the model simulation (black). An isolated (liquid) food pulse at 1,200 min in this trace has been fit. EG_0 was set to 2.5×10^{-3}, the other parameters were estimated as in the non-diabetic case; see text for details. The fitted q_{sto} amplitude is 230.

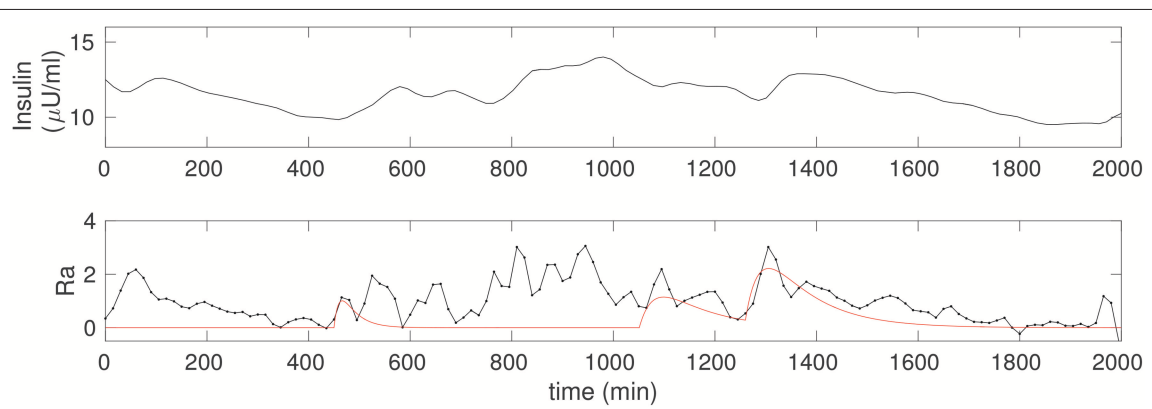

FIGURE 4 | (Upper) The insulin time series corresponding to the non-diabetic glucose from **Figure 2**, estimated from the fitted model. Notice that, apart from an initial transient, the insulin is estimated throughout, and this does not require any knowledge of the food input. **(Lower)** The estimate of the rate of appearance of glucose due to food, *Ra* (black). The simulation of $k_{gut}q_{gut}$ from **Figure 2** is overlaid (red) for comparison.

In some respects this is similar to an OGTT test, however, there are differences: For one, our method does not require the meal to be in glucose or sucrose form, and it is not necessary to know the quantity a priori; the algorithm determines it anyway. This makes our method flexible, and practical. Finally, we recover the clinically important indices of insulin resistance and secretory capacity that have been traditionally used to describe the progression, and state of the disease. We are also able to use the model to estimate a corresponding insulin time series, as well as the rate of appearance of glucose due to food.

Our model can be refined further if additional measurements can be taken. In particular, more insulin measurements taken during the CGM period can substantially improve the fits, especially of insulin.

It is straightforward to record food timings in a diary, and this very useful to the model fitting. We note that the time

at which the food intake is *started* was more important than when it was completed. Complex food models can presumably use more information. More generally, it is of great interest to explain the glycemic response to different foods, and while the observer we have constructed for R_a greatly helps facilitate this, we have not offered any particular direction in that regard in this paper. Our preliminary attempts at using Type I mixed-meal models (see Li et al., 2016 for details), to explain that data in **Figure 2** for example, indicate these models do not appear to be satisfactory. We hope to examine this further in future work.

One weakness of our study is that hypoglycemic events, in general, are not captured well by this model. This is because the model focuses on glucose and insulin dynamics, that is, on postprandial events when glucose is elevated. That our simple model is unable to capture hypoglycemia is not too surprising, considering the complexity associated with understanding this phenomena in general (American Diabetes Association Workgroup on Hypoglycemia, 2005; Unger, 2012; Elliott et al., 2016). A substantial body of literature exists trying to explain it in different contexts such as in juvenile diabetes (Juvenile Diabetes Research Foundation Continuous Glucose Monitoring Study Group et al., 2011), or for type I diabetes patients (Kim et al., 2011), and in assessing its impact on productivity (Brod et al., 2011). Notably, Sampath et al. (2016) have recently proposed a machine learning algorithm that combines different glycemic indices to successfully predict occurrences of nocturnal hypoglycemic incidents. In order to model hypoglycemic events more carefully the model should probably be extended to include glucagon dynamics as well; these questions will be explored further in future work.

There have been concerns raised previously that because CGM sensors measure interstitial glucose, that is, in a remote compartment just below the skin, this may be different from blood glucose that is measured in a fingerstick or laboratory testing. A number of studies have been carried out to model a relationship between the two (see for example Cobelli et al., 2009). In addition, there appears to be a small time lag (about 5 min) between the CGM and blood glucose. On the other hand, it is now widely accepted that CGM readings do not require confirmation (calibration) against a laboratory (or fingerstick) sampling (FDA News Release – 2017, 2017). For instance, the mean absolute relative difference (MARD) between the Freestyle Libre sensor reading and capillary blood glucose (BG) has previously been reported to be about 11.4% overall (Bailey et al., 2015). Our own tests comparing random samples (RBS) of blood glucose (laboratory testing) to the sensor indicate a strong correlation, $G_{CGM} = 0.96\ RGB - 14$ ($n = 35$, $R = 0.97$; data not shown). In this study we have ignored any calibration considerations between blood glucose and sensor readings, and any time lag; we have tacitly assumed laboratory and sensor readings and are directly compatible. It will be of interest to establish more carefully how to adapt the model to explain such differences, if any. More generally, uncertainty quantification for our model will be carried out elsewhere.

Despite the numerous limitations of understanding CGM data in all its complexity, we have shown that a minimal model is readily identifiable from the time series. We have thus provided a proof of concept that our methodology appears to be viable strategy toward a personalized analysis of CGM. This holds tremendous potential for various kinds of investigations, not only to recommend diet and lifestyle interventions but also test the exact effect of drugs. While such details are beyond the scope of the present paper, we hope the results presented here pave the way for further research in this direction.

AUTHOR CONTRIBUTIONS

PG, MS, and SG designed the study. PG designed the analysis. PG, DP, and AB carried out the simulations. PG and AB wrote the paper, together with MS and SG.

ACKNOWLEDGMENTS

We wish to thank the two subjects whose CGM we have analyzed in this paper for consenting to share their data.

REFERENCES

American Diabetes Association Workgroup on Hypoglycemia (2005). Defining and reporting hypoglycemia in diabetes: a report from the American Diabetes Association Workgroup on Hypoglycemia. *Diab. Care* 28, 1245–1249. doi: 10.2337/diacare.28.5.1245

Bailey, T., Bode, B. W., Christiansen, M. P., Klaff, L. J., and Alva, S. (2015). The performance and usability of a factory-calibrated flash glucose monitoring system. *Diab. Technol. Ther.* 17, 787–794. doi: 10.1089/dia.2014.0378

Bode, B. W. (2000). Clinical utility of the continuous glucose monitoring system. *Diab. Technol. Therapeut.* 2(Suppl. 1), 35–41. doi: 10.1089/15209150050214104

Brod, M., Christensen, T., Thomsen, T. L., and Bushnell, D. M. (2011). The impact of non-severe hypoglycemic events on work productivity and diabetes management. *Value Health* 14, 665–671. doi: 10.1016/j.jval.2011.02.001

Clarke, W., and Kovatchev, B. (2009). Statistical tools to analyze continuous glucose monitor data. *Diab. Technol. Therap.* 11, S-45–S-54. doi: 10.1089/dia.2008.0138

Cobelli, C., Man, C. D., Sparacino, G., Magni, L., De Nicolao, G., and Kovatchev, B. P. (2009). Diabetes: models, signals, and control. *IEEE Rev. Biomed. Eng.* 2, 54–96. doi: 10.1109/RBME.2009.2036073

Corkey, B. E. (2012). Diabetes: have we got it all wrong? Insulin hypersecretion and food additives: cause of obesity and diabetes? *Diab. Care* 35, 2432–2437. doi: 10.2337/dc12-0825

Deiss, D., Bolinder, J., Riveline, J. P., Battelino, T., Bosi, E., Tubiana-Rufi, N., et al. (2006). Improved glycemic control in poorly controlled patients with type 1 diabetes using real-time continuous glucose monitoring. *Diab. Care* 29, 2730–2732. doi: 10.2337/dc06-1134

Elliott, L., Fidler, C., Ditchfield, A., and Stissing, T. (2016). Hypoglycemia event rates: a comparison between real-world data and randomized controlled trial populations in insulin-treated diabetes. *Diab. Ther.* 7, 45–60. doi: 10.1007/s13300-016-0157-z

FDA News Release – 2017 (2017). *FDA Approves First Continuous Glucose Monitoring System for Adults Not Requiring Blood Sample Calibration*. Available online at: https://www.fda.gov/NewsEvents/Newsroom/PressAnnouncements/ucm577890.htm

Goel, P. (2015). Insulin resistance or hypersecretion? The βIG picture revisited. *J. Theor. Biol.* 384, 131–139. doi: 10.1016/j.jtbi.2015.07.033

Goel, P. (2017). "Chapter 13 - theoretical advances in type 2 diabetes," in *Disease Modelling and Public Health, Part A*, Vol. 36 of *Handbook of Statistics*, eds A. S. S. Rao, S. Pyne, and C. Rao (Amsterdam: Elsevier), 369–395.

Juvenile Diabetes Research Foundation Continuous Glucose Monitoring Study Group, Beck, R. W., Hirsch, I. B., Laffel, L., Tamborlane, W. V., Bode, B. W., et al. (2009). The effect of continuous glucose monitoring in well-controlled type 1 diabetes. *Diab. Care* 32, 1378–1383. doi: 10.2337/dc09-0108

Juvenile Diabetes Research Foundation Continuous Glucose Monitoring Study Group, Fiallo-Scharer, R., Cheng, J., Beck, R. W., Buckingham, B. A., Chase, H. P., et al. (2011). Factors predictive of severe hypoglycemia in type 1 diabetes. *Diab. Care* 34, 586–590. doi: 10.2337/dc10-1111

Kim, S. K., Suh, S., Kim, M. Y., Chung, H. S., Hur, K. Y., Kim, S. W., et al. (2011). Three-day continuous glucose monitoring for rapid assessment of hypoglycemic events and glycemic variability in type 1 diabetic patients. *Endocrine J.* 58, 535–541. doi: 10.1507/endocrj.K10E-378

Kirchsteiger, H., Jorgensen, J., Renard, E., and del Re, L., (eds.). (2016). *Prediction Methods for Blood Glucose Concentration. Design, Use and Evaluation. Lecture Notes in Bioengineering*, Vol. 7. New York, NY: Springer.

Klonoff, D. C. (2005). Continuous glucose monitoring. *Diab. Care* 28, 1231–1239. doi: 10.2337/diacare.28.5.1231

Korem, T., Zeevi, D., Zmora, N., Weissbrod, O., Bar, N., Lotan-Pompan, M., et al. (2017). Bread affects clinical parameters and induces gut microbiome-associated personal glycemic responses. *Cell Metab.* 25, 1243–1253. doi: 10.1016/j.cmet.2017.05.002

Li, Y., Chow, C. C., Courville, A. B., Sumner, A. E., and Periwal, V. (2016). Modeling glucose and free fatty acid kinetics in glucose and meal tolerance test. *Theor. Biol. Med. Model.* 13:8. doi: 10.1186/s12976-016-0036-3

Ludwig, D. S., and Friedman, M. I. (2014). Increasing adiposity: consequence or cause of overeating? *JAMA* 311, 2167–2168. doi: 10.1001/jama.2014.4133

McDonnell, C. M., Donath, S. M., Vidmar, S. I., Werther, G. A., and Cameron, F. J. (2005). A novel approach to continuous glucose analysis utilizing glycemic variation. *Diab. Technol. Therapeut.* 7, 253–263. doi: 10.1089/dia.2005.7.253

Moreno, J. (2000). "Unknown input observers for siso nonlinear systems," in *39th Conference on Decision and Control*, Vol. 1 (New York, NY), 790–801. doi: 10.1109/CDC.2000.912865

Murphy, H. R., Rayman, G., Lewis, K., Kelly, S., Johal, B., Duffield, K., et al. (2008). Effectiveness of continuous glucose monitoring in pregnant women with diabetes: randomised clinical trial. *BMJ* 337:a1680. doi: 10.1136/bmj.a1680

Robenack, K., and Goel, P. (2007). Observer based measurement of the input current of a neuron. *Medit. J. Meas. Control* 3, 22–29.

Sampath, S., Tkachenko, P., Renard, E., and Pereverzev, S. V. (2016). Glycemic control indices and their aggregation in the prediction of nocturnal hypoglycemia from intermittent blood glucose measurements. *J. Diab. Sci. Technol.* 10, 1245–1250. doi: 10.1177/1932296816670400

Signal, M., Thomas, F., Shaw, G. M., and Chase, J. G. (2013). Complexity of continuous glucose monitoring data in critically ill patients: continuous glucose monitoring devices, sensor locations, and detrended fluctuation analysis methods. *J. Diab. Sci. Technol.* 7, 1492–1506. doi: 10.1177/193229681300700609

Topp, B., Promislow, K., deVries, G., Miura, R. M., and Finegood, D. T. (2000). A model of beta-cell mass, insulin, and glucose kinetics: pathways to diabetes. *J. Theor. Biol.* 206, 605–619. doi: 10.1006/jtbi.2000.2150

Unger, J. (2012). Uncovering undetected hypoglycemic events. *Diab. Metab. Syndr. Obes. Targets Ther.* 5:57. doi: 10.2147/DMSO.S29367

Zeevi, D., Korem, T., Zmora, N., Israeli, D., Rothschild, D., Weinberger, A., et al. (2015). Personalized nutrition by prediction of glycemic responses. *Cell* 163, 1079–1094. doi: 10.1016/j.cell.2015.11.001

Conflict of Interest Statement: The authors declare that the research was conducted in the absence of any commercial or financial relationships that could be construed as a potential conflict of interest.

The reviewer ABP and handling Editor declared their shared affiliation.

frontiers in Physics

ORIGINAL RESEARCH
published: 25 May 2018
doi: 10.3389/fphy.2018.00039

Spatiotemporal Permutation Entropy as a Measure for Complexity of Cardiac Arrhythmia

Alexander Schlemmer[1,2]*, *Sebastian Berg*[1,2], *Thomas Lilienkamp*[1,2], *Stefan Luther*[1,2,3,4,5] *and Ulrich Parlitz*[1,2,3]

[1] Research Group Biomedical Physics, Max Planck Institute for Dynamics and Self-Organization, Göttingen, Germany, [2] Institute for Nonlinear Dynamics, Georg-August-Universität Göttingen, Göttingen, Germany, [3] German Center for Cardiovascular Research (DZHK), Partner-Site Göttingen, Göttingen, Germany, [4] Institute of Pharmacology and Toxicology, University Medical Center Göttingen, Göttingen, Germany, [5] Department of Physics and Bioengineering, Northeastern University, Boston, MA, United States

Permutation entropy (PE) is a robust quantity for measuring the complexity of time series. In the cardiac community it is predominantly used in the context of electrocardiogram (ECG) signal analysis for diagnoses and predictions with a major application found in heart rate variability parameters. In this article we are combining spatial and temporal PE to form a spatiotemporal PE that captures both, complexity of spatial structures and temporal complexity at the same time. We demonstrate that the spatiotemporal PE (STPE) quantifies complexity using two datasets from simulated cardiac arrhythmia and compare it to phase singularity analysis and spatial PE (SPE). These datasets simulate ventricular fibrillation (VF) on a two-dimensional and a three-dimensional medium using the Fenton-Karma model. We show that SPE and STPE are robust against noise and demonstrate its usefulness for extracting complexity features at different spatial scales.

Keywords: permutation entropy, cardiac arrhythmia, Fenton-Karma simulation, complexity, excitable media, phase singularities

OPEN ACCESS

Edited by:
Alain J. Pumir,
École Normale Supérieure de Lyon, France

Reviewed by:
Tommaso Gili,
Enrico Fermi Center, Italy
Jacobo Cal-Gonzalez,
Medizinische Universität Wien, Austria
Sergio Alonso,
Universitat Politecnica de Catalunya, Spain

***Correspondence:**
Alexander Schlemmer
alexander.schlemmer@ds.mpg.de

Specialty section:
This article was submitted to Biomedical Physics, a section of the journal Frontiers in Physics

Received: *15 January 2018*
Accepted: *13 April 2018*
Published: *25 May 2018*

Citation:
Schlemmer A, Berg S, Lilienkamp T, Luther S and Parlitz U (2018) Spatiotemporal Permutation Entropy as a Measure for Complexity of Cardiac Arrhythmia. Front. Phys. 6:39. doi: 10.3389/fphy.2018.00039

1. INTRODUCTION

A healthy heart is driven by periodic plane waves propagating over the cardiac tissue. These waves can turn into potentially life-threatening self-sustained arrhythmias which are governed by reentrant spiral-wave activity of different levels of complexity [1, 2].

A detailed understanding of the complexity of cardiac arrhythmias and the organization of spiral-wave activity is crucial for the development of improved methods for the treatment of cardiac arrhythmias [3–5].

In the healthy sinus rhythm a lot of information about the state of the heart is already contained in the frequency and timings of individual heartbeats. Furthermore, the ECG is one of the most important clinical tools for the identification of deviations from the normal rhythm and is prevalently used for medical diagnoses. In case of cardiac arrhythmias with a spatiotemporally more unordered state, measures that allow for a quantification of the spatiotemporal complexity of the system provide valuable information that can be used for investigating the mechanisms behind the onset of arrhythmia and their possible termination.

In the picture of an arrhythmia being composed of many interacting spiral waves or three-dimensional rotors, often the concept of phase singularities is used to assess the degree of organization. A high number of phase singularities (NPS) corresponds to a state with more rotors

and therefore indicates a situation with higher complexity. However, in experimental situations where usually surface electric activity of the heart is measured by optical mapping using fluorescent dyes, several practical problems arise:

- As only two-dimensional information of a three-dimensional medium is recorded, phenomena on the surface can not always be suitably approximated by the concept of phase singularities. For example, focal activity on the surface, which can be produced by spirals located far away from the surface, would not be covered by NPS.
- Noise can significantly impair the detection of phase singularities, so usually the application of spatial kernel-smoothing and temporal bandapass filters is required.
- Usually high-level algorithms for a reliable computation of NPS involve sophisticated tracking algorithms for phase singularities over time. These methods can be computationally intensive and prevent real-time applications.

To tackle these problems other suitable methods for characterizing and quantifying spatiotemporal complexity are desired. In this article we show how a spatial and a spatiotemporal version of PE can be used to accomplish this task.

Permutation entropy (PE, [6]) is a measure which is widely used to analyse the complexity of time series signals. In the cardiac community it is so far mainly used for analysis of ECG signals, especially for the analysis of heart rate variability [7]. The concept has already been extended to two-dimensional patterns [8] and applied to optical imaging of cardiac cell culture [9].

Furthermore, its robustness against noise and the possibility to study complexity on different scales will be subject to this study. As our main motivation for the investigation of these methods is their potential application in experiments, we frame this numeric comparison to a realistic experimental setting: As will be explained in section 2.6 a dataset from a three-dimensional Fenton-Karma simulation is used to generate "artificial camera data". This means that we use four two-dimensional projections of the three-dimensional simulations to approximate an experimental camera setup. Additionally, we use an algorithm for computing NPS which can also be employed for experimental data. This algorithm is presented in section 2.5 and makes use of some improved strategies to reliably detect and track spiral waves on experimental cardiac tissue.

2. METHODS

This section will explain the concept of spatial and spatiotemporal PE. It also intruduces a specialized algorithm for tracking phase singularities which is used for comparison with the permutation entropy based complexity measures. Section 2.6 describes the simulations that were used to create the two numerical datasets which are subject of this investigation.

2.1. Permutation Entropy (PE)

PE [6, 7, 10] is a method for quantifying the complexity of a time series using the distribution of order patterns. Order patterns are small segments of time series of length D which are characterized solely by the relative order of their constituents. The segments, also called words $\tilde{w}_i = w_{i,1}, \ldots, w_{i,D}$ of length D, are extracted from the original time series $x_1, x_2, \ldots, x_N$ by taking successive elements x_i which can be separated by a time delay or lag L_t: $\tilde{w}_i = x_i, x_{i+L_t}, x_{i+2L_t}, \ldots, x_{i+(D-1)L_t}$. Using these words the original time series can be transformed into a symbolic time series $\{s_i\}$ by computing the permutation index that quantifies the relative order of the $w_{i,j}$:

$$s_i = \sum_{j=1}^{D-1} (D-j)! \lambda_{i,j} \tag{1}$$

$$\lambda_{i,j} = \sum_{k=j+1}^{D} \begin{cases} 1 & \text{if } w_{i,j} < w_{i,k} \\ 0 & \text{else} \end{cases} \tag{2}$$

This procedure is illustrated in **Figure 1A** for $D = 3$ and $L_t = 1$. PE is then defined as the Shannon entropy of the relative frequencies p_j, $j \in \{1, \ldots, D!\}$ of the symbols s_i within the time series:

$$H = -\sum_{j=1}^{D!} p_j \log_2 p_j \tag{3}$$

2.2. Spatial Permutation Entropy (SPE)

The two-dimensional extension of PE which we call SPE is similar to Ribeiro et al. [8] and has been previously applied to optical mapping data of cardiac cell culture in Schlemmer et al. [9]. For SPE symbols are extracted from two-dimensional images as depicted in **Figure 1B** by sampling words $\tilde{w}_{i_1,i_2}$ of length $D \times D$ from the two dimensional data $M \in \mathbb{R}^{n_1 \times n_2}$

$$\begin{aligned} \tilde{w}_{i_1,i_2} = m_{i_1,i_2}, m_{i_1+L_x,i_2}, m_{i_1+2L_x,i_2}, \ldots\ m_{i_1+(D-1)L_x,i_2}, \\ m_{i_1,i_2+L_x}, \ldots, m_{i_1+(D-1)L_x,i_2+(D-1)L_x} \end{aligned} \tag{4}$$

with a spatial separation L_x which replaces the one dimensional lag. So each word contains data from a grid of $D \times D$ points which are separated in both directions by the spatial separation L_x. The number of possible symbols is $(D \cdot D)!$ which grows very rapidly with D. Therefore, we choose $D = 2$ which leads to the simplified form:

$$\tilde{w}_{i_1,i_2} = m_{i_1,i_2}, m_{i_1+L_x,i_2}, m_{i_1,i_2+L_x}, m_{i_1+L_x,i_2+L_x} \tag{5}$$

which is also shown in **Figure 1B**.

The grid is moved over all possible positions within the image leading to a distribution p_j of symbols s_{i_1,i_2} which are computed using (Equation 2). SPE is defined as the Shannon entropy (Equation 3) of this symbol distribution.

2.3. Spatiotemporal Permutation Entropy (STPE)

A natural extension of this approach to three-dimensional data can be constructed by sampling the words from volumes instead of images. This enables us to take into account spatial and temporal dimensions at the same time. It is obvious that a lot of different possibilities exist to actually sample three dimensional

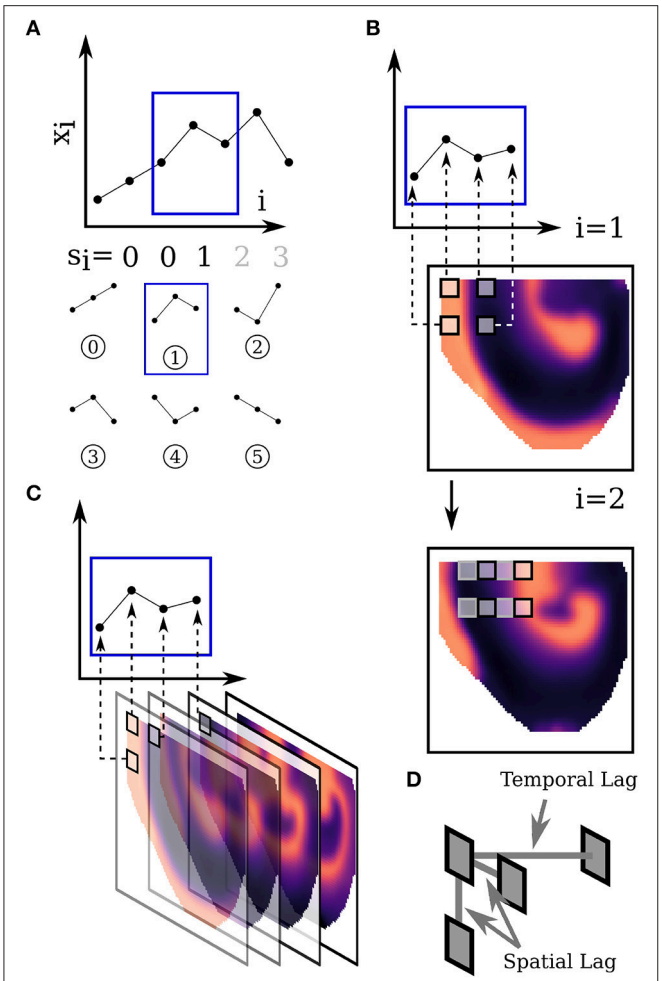

FIGURE 1 | Construction of temporal **(A)**, spatial **(B)** and spatiotemporal **(C)** PE. **(D)** Shows the tripod used for STPE. See text in sections 2.1, 2.2, 2.3 for details. **(A)** Shows the extraction of one-dimensional order patterns from a time series x_i and the assignment to symbols s_i. **(B)** Illustrates how two-dimensional order patterns are sampled from an individual image. The 2×2 sampling-grid is moved over all possible positions of the image. **(C)** Sketches how three-dimensional order patterns are extracted from subsequent images which form the video under investigation.

data points. Since the number of possible symbols grows very rapidly with the number of sampling points we restrict this approach to a "sampling tripod" which is shown in **Figure 1D**. The words are defined as:

$$\tilde{w}_{i_1,i_2,i_3} = v_{i_1,i_2,i_3}, v_{i_1+L_x,i_2,i_3}, v_{i_1,i_2+L_x,i_3}, v_{i_1,i_2,i_3+L_t} \tag{6}$$

where $V \in \mathbb{R}^{n_1,n_2,n_t}$ denotes a spatiotemporal volume with the third axis being the temporal axis. n_1 and n_2 correspond to the image size and n_t is the total number of timesteps in the video. There also exists a high flexibility in the choice of sampling parameters for the different types of separation. We chose a distinct spatial separation L_x and a different temporal separation L_t. Analogous to SPE we can again assign order patterns s_{i_1,i_2,i_3} to the words using (Equation 2).

The procedure for extracting three-dimensional order patterns is sketched in **Figure 1C**. For computing the value of STPE at one timestep t all symbols s_{i_1,i_2,i_3} from a subvolume $V_{s,t} \in \mathbb{R}^{n_1,n_2,n_s} \subset V$ of the original video are taken into account to generate the distribution p_j of symbols s for this timestep and $t \leq i_3 < t + n_s$. n_s can be called the window size, because it denotes the temporal size of the subvolume of the video from which the symbol distribution is taken.

In summary the STPE method in the version described here comprises three parameters:

- L_x: The spatial separation which selects the spatial scale for highlighting complexity.
- L_t: The temporal lag which specifies the temporal scale taken into account for each word.
- n_s: The window size which indicates the length of the interval analyzed by the method at a single point in time.

Scanning of all parameters has revealed that wide ranges for L_x and L_t are possible to visualize changes in complexity for all datasets analyzed here. The spatial separation L_x has been found to display some fine-grained information which will be discussed in sections 3.1, 3.4. $L_t = 9$ which is on the order of a short action potential has been used in all analyses here. The window size has an effect that is similar to a smoothing window size: Small n_s will take into account only very few timesteps and therefore create results similar to SPE. This usually produces strong fluctuations as the exact distribution of spatial patterns is influenced by periodic fluctuations due to finite size effects. Therefore it is usually desirable to tune n_s to a typical periodicity within the video, like a small multiple of the period of spiral rotation. If n_s is chosen too high, changes in complexity are smoothed out. We use $n_s = 250$ throughout this study.

It is interesting to notice, that the order in which the points are sampled from the images or volumes does not change SPE and STPE. It solely influences the assignment of the patterns to symbols, but the distribution of symbols remains the same apart from this change in labels. We used the forward construction for sampling STPE which means that one sampling point is placed at $t + L_t$.

2.4. Normalized Quantities

For comparing SPE and STPE obtained for different parameters, especially different L_x, it is useful to use temporally normalized versions of the quantities. The reason for this is that for larger spatial separations the spatial and spatiotemporal permutation entropies usually increase. These quantities are normalized here by subtracting the temporal mean (MEAN) and afterwards dividing by the temporal standard deviation (STD). For comparison, the normalized NPS is defined analogously. So for time series STPE, SPE and NPS we obtain the three corresponding normalized quantities as:

$$\text{nSTPE} = \frac{\text{STPE} - \text{MEAN(STPE)}}{\text{STD(STPE)}} \tag{7}$$

$$\text{nSPE} = \frac{\text{SPE} - \text{MEAN(SPE)}}{\text{STD(SPE)}} \tag{8}$$

$$\mathrm{nNPS} = \frac{\mathrm{NPS} - \mathrm{MEAN(NPS)}}{\mathrm{STD(NPS)}} \quad (9)$$

2.5. Phase Singularity Tracking

Phase singularities (PS) are a widespread measure for the description of complexity of excitable media. They are found at the centers of rotation of spiral waves. In cardiac dynamics spirals and their breakup are directly related to the onset and sustaining of arrhythmias allowing for a straight-forward interpretation of PS statistics in this field of research. In this formalism every cell is assumed to undergo a phase oscillation between zero and 2π with neighboring cells typically having only a slight shift in their respective phases. In such systems points or defects where the phase is non-continuous are important features that follow certain topological laws [11].

In practice, especially with a noisy signal, PS tracking is non-trivial. Without enough smoothing an abundance of short lived PS can skew the result. Also in practice very short lived PS are often not of general interest, such as for example at the front of colliding waves, while the definition of the phase itself is not always unambiguous for high dimensional oscillators such as cardiac cells.

Unless, or even if, strong spatiotemporal smoothing is used, it is thus necessary to remove or ignore short lived PS as well as to be able to track the path of PS which can, in principle, move arbitrarily fast. Only by employing tracking reliable life times can be defined.

2.5.1. Definition of Phase

Within cardiac dynamics two main approaches for PS detection exist. One based on the definition of phases obtained from delay reconstruction [2, 12] or Hilbert transform of the signal and the other on finding of pivoting points or wave breaks based on threshold crossings [13–15]. Further improvements have been suggested for example by Rogers using wavefront tracking to improve the identification of PS [16].

The difference in these approaches lies in a slightly different phase definition. They use either a phase defined by delay embedding or the Hilbert transform, or apply threshold crossings which implicitly define a specific phase at the waves up- and downstroke. In the context of a phase defined using embedding PS are usually detected by a line integral around the current position. When using thresholds PS are naturally found at the end of lines of same phase given by the points where up- and downstroke meet. Both concepts are equivalent when interpreting the wavefront and -back each as a phase step of π.

The methodology used here is an improved detection procedure based on the aforementioned concepts. Our method is based on the idea that the upstroke is the single well and clearly defined phase, though the exact classification as such will in practice always depend on choosing some threshold. Further, we will later assume that after each upstroke the cardiac cell has a refractory period, removing the necessity of also reliably finding the APD.

After possibly preprocessing with a spatial smoothing (not done in this simulation study, see section 3.3), instead of using thresholds to identify the upstroke we use the local maximum of a correlation with a smooth upstroke-like wavelet (**Figure 2B**). Additionally for each pixel a threshold is set, below which a maximum is ignored, since small local maxima may arise due to noise. During this step local maxima which are very close are discarded picking the most prominent upstrokes first. An example of this procedure is shown in **Figure 2**. After identification the times when each upstroke occurred are stored. This is used as input for the PS identification and tracking since the time of the upstrokes defines a zero phase at the wavefront.

2.5.2. Tracking of PS

To track PS including their exact trajectories we now make two additional assumptions. First, we assume that there exists a period of time τ during which a wavefront will have traveled at least one pixel, so a slowest reasonable conduction velocity.

For our data here, this threshold for the period of time is set to 8 frames. Second, we assume that no further upstroke will occur within a time of 2τ, so 16 frames, so that the wavefront may be uniquely identified as those edges where on one side activation had occurred within the last 8 frames and on the other side activation will occur no more than 8 frames later.

This behaves much like defining a specific zero phase at the upstroke time and increases this phase to π within the time τ

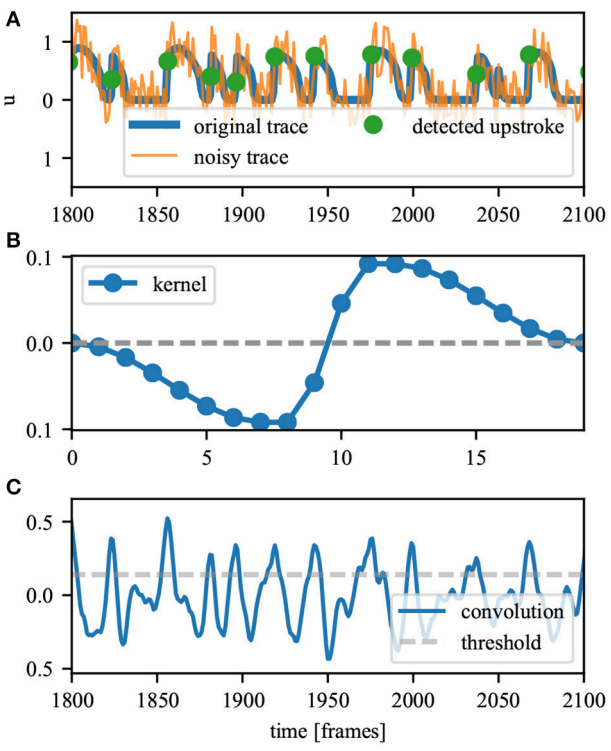

FIGURE 2 | Sketch of the method used for defining the upstrokes. **(A)** The original and noisy time trace. The dots show the final times of the upstroke based on the noisy time trace. **(B)** The kernel which is correlated with the noisy signal in **(A)** to find the upstroke position. **(C)** Result of the correlation of the noisy signal in **(A)** and the kernel in **(B)**. Local maxima identify the upstroke position (as indicated in **A**). A threshold is used to ignore unclear events.

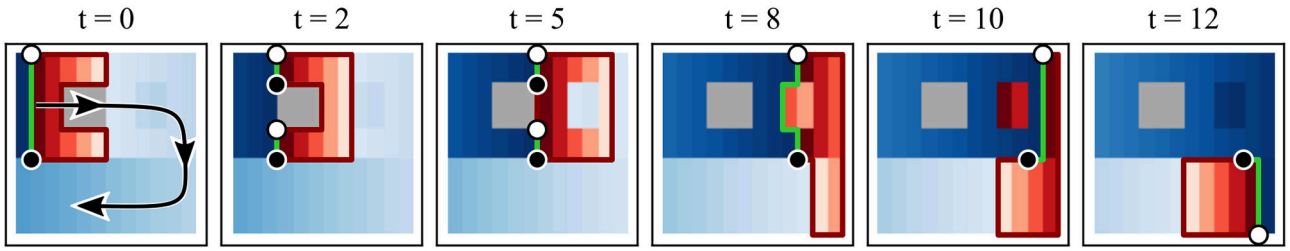

FIGURE 3 | Sketch of the PS tracking. The plot shows a clockwise rotating spiral with the green line identifying the wave front. The spiral movement is indicated by the arrow in the first panel. Red colors indicate those pixels that will be activated within the next five frames with the darkest red indicating activation within the next timestep. Blue colors show those areas that were recently activated with lighter colors indicating a longer time since the last activation. PS are identified by black or white dots. The wavefront connects a PS pair, while their possible future track is identified by a red line. In this plot $\tau = 5$. $t = 2$ and 5 show the behavior at an inactive (gray) area, $t = 8$ and 10 at an prematurely activated area and $t = 12$ at the turning point.

and to $-\pi$ for times activated within τ before the upstroke. All other times would be assumed to have phase π.

Figure 3 sketches this procedure and shows that tracking becomes unambiguous, no matter how fast a PS moves. A linear reentry is shown with an inactive region and an area for which activation is delayed. Since it is known which area will be activated within the next τ time units (red area), the red lines surrounding the area identify the possible path for the PS, including possible annihilation. At $t = 2$ the inactive region leads to the creation of a new pair, which then annihilates at $t = 6$. At $t = 8$ we see that a short delay in activation times will not affect the PS positions. The PS that could be considered existing in this area are filtered due to their comparatively short lifespan. The activity may also be viewed as focal or just noise. At $t = 10$ and 12 the black PS is considered stationary, since slow conduction can be assumed to be happening in vertical direction as well (activation occurs within τ).

Technically, this is implemented by looking τ time units into the future and then finding the edges between the area activated within τ using the marching squares algorithm [17]. These edges can then be defined as either wavefront or possible future path. In rare cases of a checkerboard like pattern, two PS within a PS pair may lie above each other at this time and the pair is removed immediately.

Using this method, we find all PS including their tracks between frames and which pairs are created/annihilated. Short lived PS ($\leq \tau$) are then removed in a greedy fashion starting with the one having the shortest lifetime. Note that removing one PS pair can increase the lifespan of another since its path may have been broken by a short lived pair. In a last processing step PS at an outside edge or only shortly disconnected due to noise are not considered valid PS. For example, this step would hide the white outer PS in **Figure 3**.

To summarize our method:

- After a possible spatial smoothing the upstroke time is defined as the local maximum of its correlation with an upstroke-like wavelet. While the action potential shape, especially close to the PS, is typically not clear in experimental data during ventricular fibrillation, the wavefront is still characterized by an increase in membrane potential which is quantified by this correlation.
- The phase is then effectively defined by the upstroke time and assumed to advance by π each before and after the upstroke within a constant time τ.
- τ defines a limit on the slowest wave propagation that is not considered a new wave initiation while 2τ is the assumed (minimal) refractory period, so that no second upstroke can occur within this period of time. These assumptions implicitly filter some PS with lifespan shorter then τ.
- The exact track for each PS can be defined by following the area of next activation.
- Tracking allows for short living PS pairs to be removed starting with the PS with shortest lifespan.

The constant τ and thus reliance on an assumed refractory period is a certain limitation. However, we believe that all approaches implicitly have similar limitations due to the methods of filtering or phase definition used. Different methods of PS tracking will behave differently especially in rare events or when it comes to the exact position of a non-stationary PS.

In general, however, we believe that the approach described here is comparably robust and allows for a straight forward tracking of PS movement over time with clear assumptions about how the phase behaves after an upstroke.

2.6. Numerical Simulations

Episodes of ventricular fibrillation have been simulated on a realistic rabbit heart geometry obtained from a previously recorded computer tomography scan (CT scan). A system of coupled reaction-diffusion equations was used to describe the evolution of the membrane potential V_m which determines the electrical excitation patterns in the heart, where the Fenton-Karma model [18] was used to model the local cell dynamics:

$$\frac{\partial V_m}{\partial t} = D\Delta V_m - I_{\text{ion}}(V_m, \mathbf{h})/C_m, \tag{10}$$

$$\frac{\partial v}{\partial t} = \Theta(V_c - V_m)(1 - v)\left(\frac{\Theta(V_m - V_v)}{\tau_{v1}^-} + \frac{\Theta(V_v - V_m)}{\tau_{v2}^-}\right) - \Theta(V_m - V_c)\frac{v}{\tau_v^+}, \tag{11}$$

$$\frac{\partial w}{\partial t} = \Theta(V_c - V_m)\frac{1-w}{\tau_w^-} - \Theta(V_m - V_c)\frac{w}{\tau_w^+}. \quad (12)$$

with the diffusion constant $D = 3.8 \times 10^{-2}\text{cm}^2/\text{s}$ and the electrical capacitance of the membrane per surface area of the cell membrane $C_m = 1\mu F/cm^2$. The ionic currents in Equation (10) are given by

$$I_{\text{ion}}(V_m, v, w) = -J_{fi}(V_m, v) - J_{so}(V_m) - J_{si}(V_m, w), \quad (13)$$

with

$$J_{fi}(V_m, v) = -\frac{v}{\tau_d}\Theta(V_m - V_c)(1 - V_m)(V_m - V_c), \quad (14)$$

$$J_{so}(V_m) = \frac{V_m}{\tau_0}\Theta(V_c - V_m) + \frac{1}{\tau_r}\Theta(V_m - V_c), \quad (15)$$

$$J_{si}(V_m, w) = -\frac{w}{2\tau_{si}}\left(1 + \tanh\left[k(V_m - V_c^{si})\right]\right). \quad (16)$$

The parameter set shown in **Table 1** (taken from [19]) depicts the chosen parameters, which promote spiral wave break-up. During the simulations, snapshots of the membrane potential V_m were taken each 10 time units ($\widehat{=}$ 1 frame).

2.6.1. 3D Simulation Dataset

For the first dataset which we will refer to as the 3D simulation, Equations (10)–(12) were solved on a regular grid with a grid size of $(N_x, N_y, N_z) = (151, 165, 130)$ (with a grid spacing of $h = 0.013\text{cm}$) using an explicit Euler scheme. A time constant of $dt = 0.1$ was used, where one time unit may be interpreted as 1 ms for this model and parameter set. The diffusion and grid spacing were chosen to allow a realistic number of filaments to develop. No-flux boundary conditions at the irregular boundary of the realistic heart geometry have been implemented using the phase field method [20, 21]. During the simulations, the sinus rhythm was modeled by local stimuli at the apex of the heart. Episodes of spatio-temporal chaos were then initiated by the application of a far field shock. With the proper timing of this shock, the induced excitation wave creates spiral waves by the interaction with the refractive back of the plane wave which originated from the sinus rhythm. The surface activity was determined by detecting the outer layer of the simulation geometry, and then extracting the excitation patterns from four directions. By this procedure, the surface activity of two opposing directions complement each

TABLE 1 | Parameters used for numerical simulations of the Fenton-Karma model.

Parameter	Value
τ_v^+	3.33
τ_{v1}^-	15.6
τ_{v2}^-	5
τ_0	9
τ_r	34
τ_{si}	26.5
τ_w^+	350
τ_w^-	80
τ_d	0.407
V_c^{si}	0.45
V_c	0.15
V_v	0.04

This is parameter set five taken from Fenton et al. [19] and promotes spiral wave break-up.

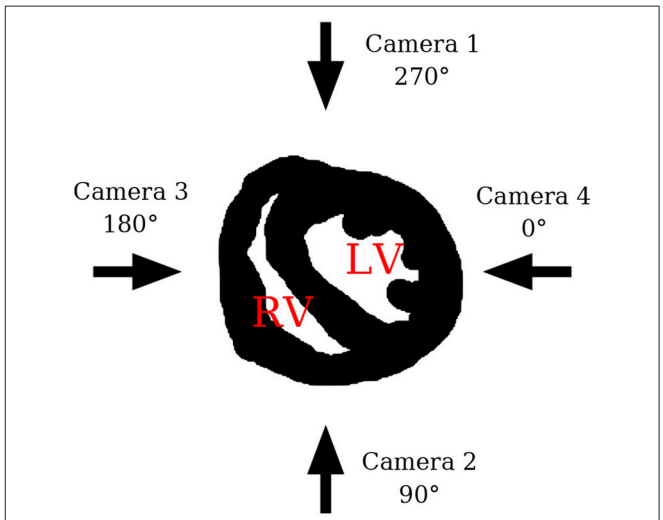

FIGURE 4 | Sketch showing the four different camera perspectives in relation to the heart. LV indicates the position of the left ventricle and RV the position of the right ventricle.

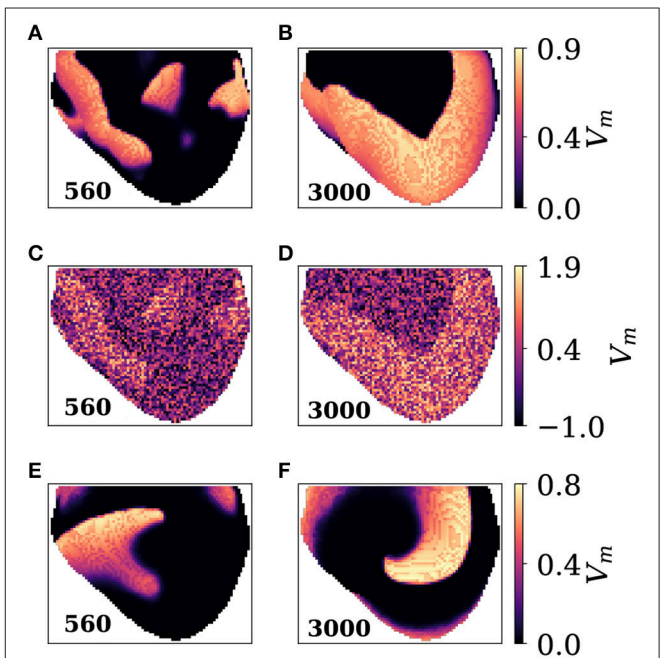

FIGURE 5 | Snapshots of the 3D simulation. **(A)** Camera 1 at frame 560 showing complex wave activity. **(B)** Camera 1 at frame 3000 showing plane waves. **(C,D)** Same as **A,B**, but with noise added at noise level two. **(E,F)** Frames 560 and 3000 seen by camera 2. Camera 2 is facing a spiral wave at frame 3000 which causes plane wave activity seen in **B**.

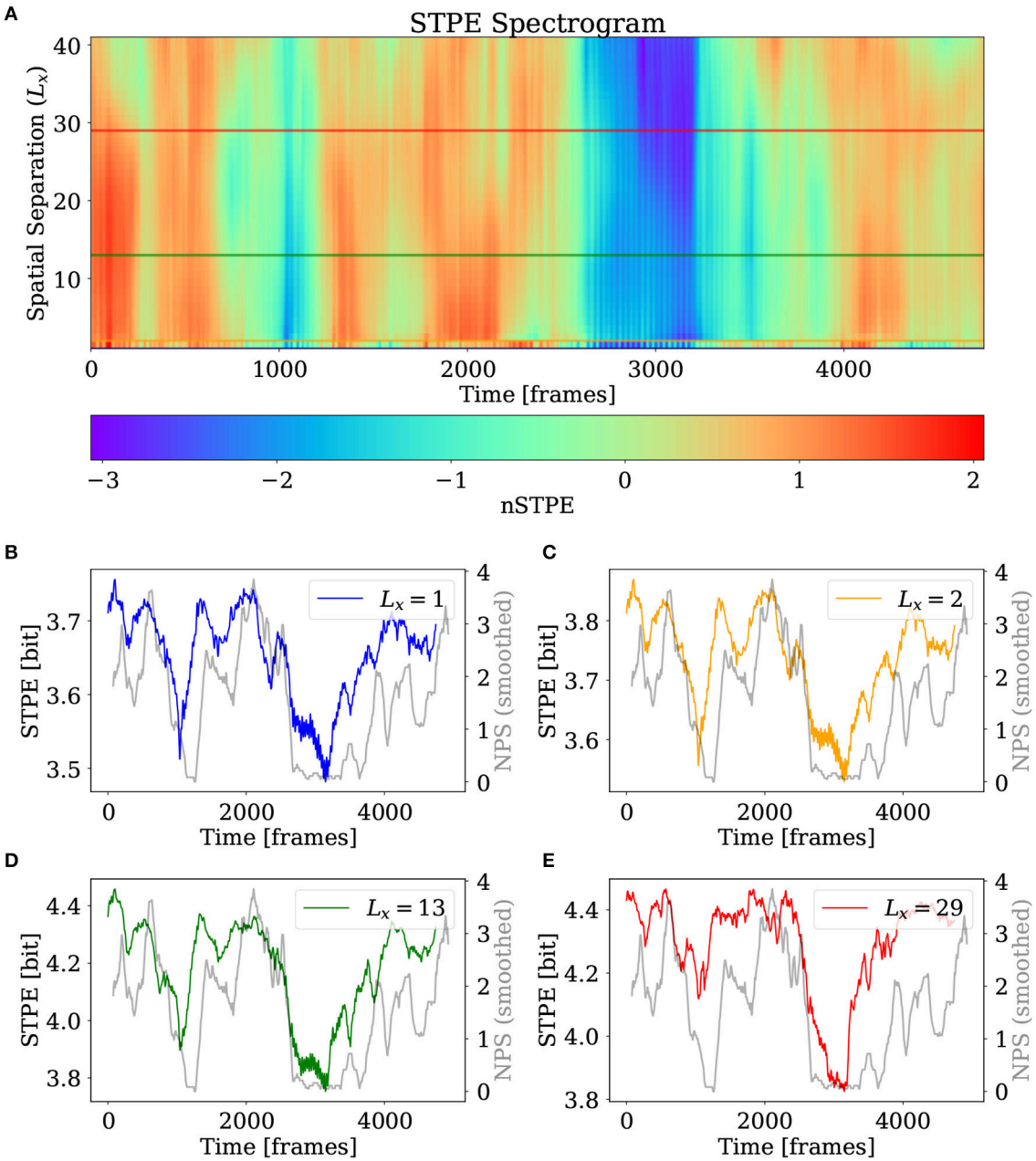

FIGURE 6 | (A) nSTPE displayed for different values of the spatial separation in a spectrogram-like view. **(B–E)** Show the time series for STPE at different values of the spatial separation together with NPS (gray). The values of L_x are given in the subfigure legends respectively. NPS has been smoothed using a moving average filter with a width of 155 frames.

other to the full surface activity. Thus, neighboring directions cover partially the same excitation activity. In analogy to the experimental setup the different directions are referred to as camera 1–4. A sketch of the setup is shown in **Figure 4**.

2.6.2. 2D Simulation Dataset

For the second dataset which we will refer to as the 2D simulation, parameters identical to the 3D version were used. The simulation grid was $(N_x, N_y) = (400, 400)$ with the same time step and grid spacing as before. Boundaries were implemented as no-flux boundary conditions and a circular inhomogeneity of radius 60 placed into the center and implemented using the phase field method [20, 21]. A single spiral wave was initiated and simulated for a transient of 5,000 time units before the actual simulation started.

2.6.3. Noise

For the investigation of the effect of noise on the quantities in section 3.3 uniformly distributed random numbers $r \in [-0.5, 0.5)$ have been added to V_m as:

$$V_{m,a} = V_m + r \cdot a \tag{17}$$

We will refer to the two noise amplitudes $a = 1$ and $a = 2$ as noise level one and two, respectively. Note that V_m is scaled between zero and one in the model.

The motivation for using this implementation of noise is that we want to investigate the effect of measurement noise which typically arise from optical instruments and camera chips. We explicitly do not want to investigate dynamical noise which would influence the evolution of the model differential equations, as this would lead to different and possibly more complex types of arrhythmia. Furthermore, we do not expect dynamical noise to have a strong influence on the comparison of the methods for quantifying complexity.

3. RESULTS

3.1. Parameter Scan of the Spatial Separation

In this section the effect of varying the spatial separation is investigated using the 3D simulation dataset which was introduced in section 2.6.1. **Figure 5** shows snapshots of the 3D simulation.

Figure 6 shows the result of STPE applied to the simulated VF using camera one. In order to show the effect of different values for the spatial separation L_x a spectrogram-like display has been created where the spatial separation is aligned on the y-axis and each row is one time series of nSTPE calculated using this value of L_x. **Figures 6B–E** show the time series for (non-normalized) STPE for different values of the spatial separation L_x.

For comparing the complexity as measured by STPE to a standard measure, NPS has been plotted in gray in **Figures 6B–E**. NPS can fluctuate heavily, therefore it has been smoothed here using a moving average filter with a width of 155 frames. It can be seen that starting from a spatial separation of $L_x = 2$ a drop in complexity around frame 2,700 is detected which corresponds to a drop in NPS to zero around the same time. A second very dominant drop in STPE is found around frame 1,000 which is in accordance with NPS which also drops to zero around the same time. In general the match between STPE and NPS seems to be quite good, although some differences are visible especially during the initial period of the simulation and at the end of the video.

The differences for different levels of L_x are not very pronounced for this dataset. However, the possibility to detect complexity at different scales can be a valuable feature of this method. Another example of a STPE spectrogram where differences between the different scales are visible is presented in section 3.4.

3.2. Comparison to SPE and NPS

To compare STPE, SPE, and NPS, the time series of these quantities have been plotted for each camera of the 3D simulation individually in **Figure 7**. NPS is smoothed with a running average filter with a width of 155 frames. NPS shows that the simulation contains varying complexity in all four camera videos. One special feature is the relatively long period of low complexity starting from approximately frame 2,700. It is visible that camera one (blue) and four (red) record an NPS of zero during this period. The value of NPS as seen from camera three (green) is between zero and one and the value of NPS for camera two (orange) remains approximately one at the same period indicating that one spiral is seen on camera two and partly on camera three while the other cameras register plane waves emerging from that spiral.

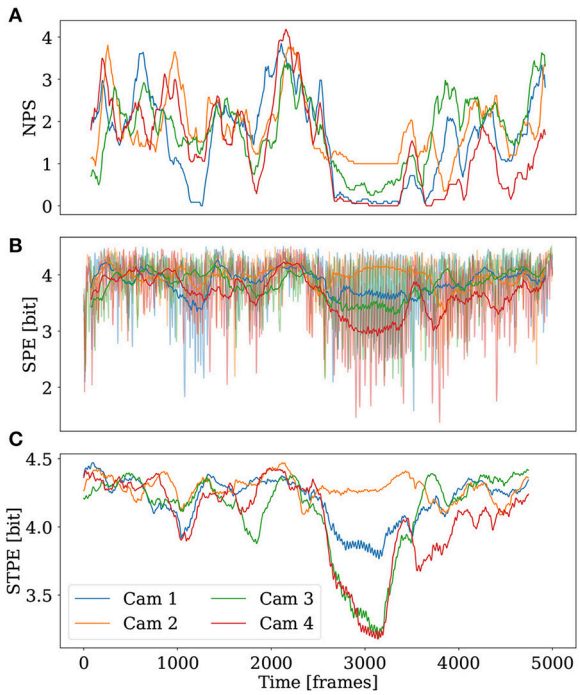

FIGURE 7 | NPS, SPE, and STPE for the four different cameras of the 3D simulation. The spatial separation was fixed to $L_x = 14$. **(A)** NPS, smoothed with a running average filter with a width of 155 frames. **(B)** The raw SPE time series are displayed transparently in **(B)** in the background. Smoothed time series of SPE are plotted in the foreground. A running average filter with a width of 155 frames has been used. **(C)** shows the STPE time series.

SPE shows a strongly fluctuating signal which is the reason why for easier interpretation the raw signal has been plotted transparent in the background with a smoothed version of SPE as a thick solid line. The smoothing has been applied using an running mean filter with window length of 155 frames. SPE also registers that during the long low complexity period camera four and partly also camera three and one reveal a low complexity period. At the same time SPE assigns a high complexity for camera two.

STPE shows a very pronounced drop in complexity for camera four and camera three at the long low complexity period, a much less pronounced drop in complexity for camera one and a high complexity in camera two. Similar to SPE also STPE assigns a higher value of complexity to camera one than to camera three

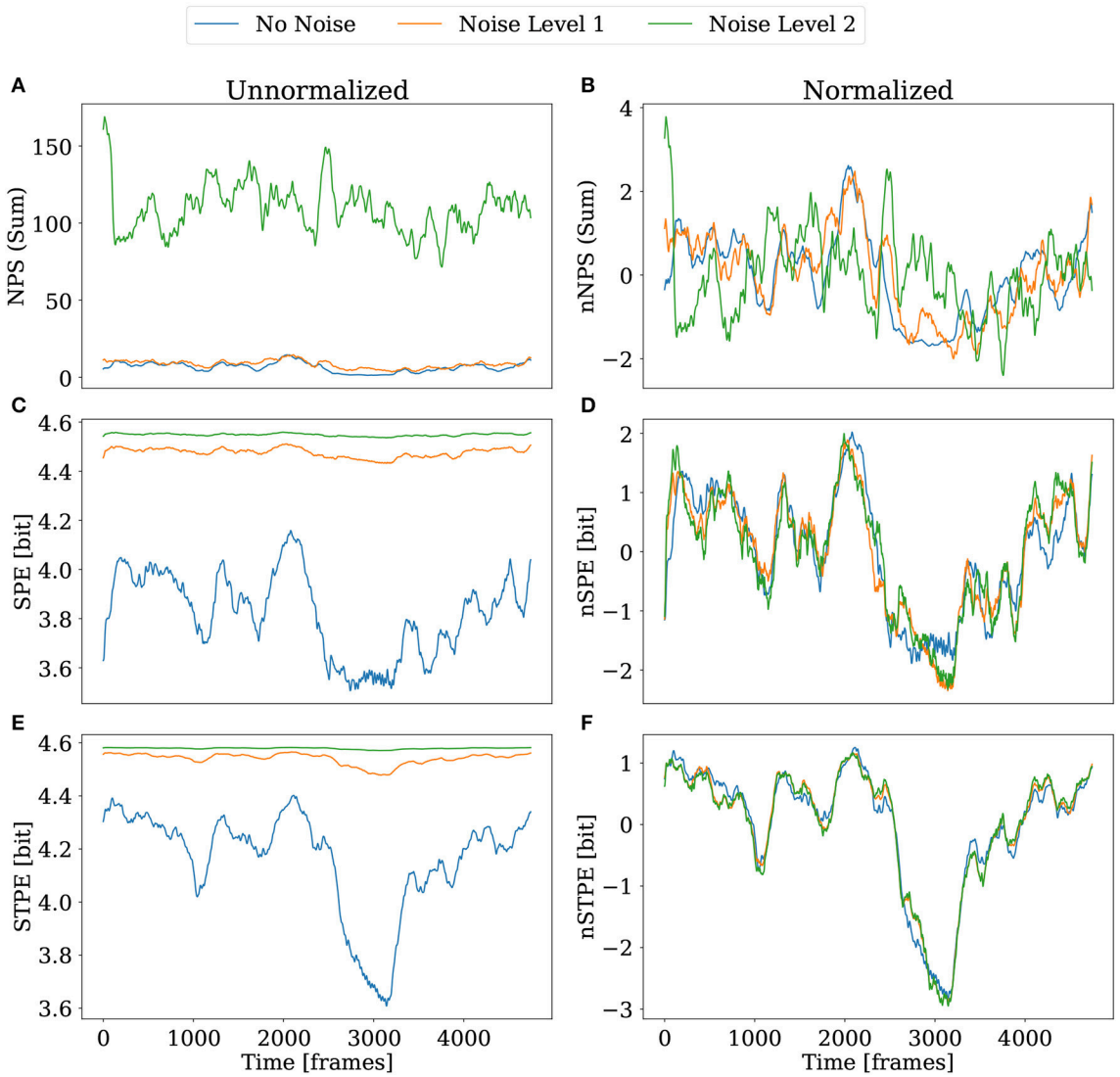

FIGURE 8 | Comparison of NPS, SPE, and STPE under the influence of noise for the case of the 3D simulation dataset. The left column shows the plain quantities without normalization. The right column shows the quantities again with normalization applied. **(A,B)** The sum of the NPS over all cameras. **(C,D)** Mean of SPE and nSPE over all cameras. **(E,F)** Mean of STPE and nSTPE over all cameras. STPE and SPE were computed with $L_x = 14$ for this comparison.

which is different to the information extracted from NPS during this period of time. This is a hint that in fact different information than mere information about spiral waves is extracted by the spatial- and spatiotemporal PE.

3.3. Robustness Against Noise

For testing the robustness against noise for SPE and STPE noisy versions of the 3D simulation datasets have been generated as described in section 2.6.3. **Figure 8** shows the result of applying NPS, SPE and STPE to the dataset with noise. As a simplification the results are not shown for each camera separately, but the sum of NPS over all cameras and the mean of the permutation entropy quantities are shown. In this case both are displayed, the plain quantities and the normalized quantities which had been introduced in section 2.4.

Our implementation of the NPS detection struggles to find PS in the presence of stronger noise (see also the comments in section 3.5.). While for noise level one (see section 2.6.3 for definitions) it is still possible to identify a period of time around frame 3,000 with less PS, this feature is completely gone for noise level two. As visible in **Figure 8A** the total number of PS increases strongly. In real applications this problem may be mitigated using smoothing.

SPE and STPE which are displayed in **Figures 8C,E** generally increase in absolute values. This can be explained by the fact that higher noise leads to a higher variety of order patterns resulting in a flatter distribution for p_j in Equation (3). However, it is still

possible to identify all features from the video without noise from the noisy data using the normalized versions of SPE and STPE. Especially in case of nSTPE in **Figure 8F** all three curves seem to overlap almost perfectly.

3.4. STPE Spectrogram for the 2D Simulation

In order to demonstrate that STPE can be tuned to detect complexities at different scales a parameter scan similar to the one in section 3.1 has been used to generate a STPE spectrogram. This time the method has been applied to the 2D simulation dataset described in section 2.6.2. To illustrate the activity visible in the simulation dataset snapshots are presented in **Figure 9**. This dataset features many interactions between spiral waves and different levels of complexity. Starting from approximately frame 3,740 only one spiral wave, which is pinned to the circular heterogeneity in the center, remains.

The STPE spectrogram is visible in **Figure 10**. This time in addition to the overview of different nSTPE at specific values of L_x in A, and four different excerpts of STPE at some scales, the four snapshots of the simulation which are displayed in **Figures 9A–D** are marked in **Figure 10A** as blue vertical lines with the corresponding letter.

It can be seen that the main transition in complexity, the takeover of one pinned spiral at the end of the simulation close to frame 3,700, is clearly visible on all scales. Furthermore it can be seen that the different scales are similar in many features. For example the two periods of high complexity around frames 600 and 2,200 are present in all scales analyzed here. Out of the four excerpts, the one for $L_x = 29$ seems to match the NPS time series best, but the complexity measured by NPS has a lot of similarity with all excerpts of STPE here.

Two very important differences among the different scales seen here are the drop in complexity at small scales approximately at frame 1,221 marked with the blue B and the big kink for STPE for $L_x > 80$ around frame 1,764 marked with the blue C. The former feature is not visible in STPE at larger scales while the latter low complexity phase is only reflected in larger scales.

3.5. Speed of Computations

For practical applications speed of computations of the specific methods are highly relevant. The algorithms involved in this article are written in Python using NumPy [22] and SciPy [23]. The implementations of SPE and STPE are written in Cython [24] which generates C code that is afterwards compiled to binary code. The algorithm requires only a single pass over the data and only few basic operations making the compiled code very efficient. The application of the PS analysis involves tracking of PS (see section 2.5.2) which becomes inefficient in the case of a large number of PS. Therefore, this method suffers a lot from noisy data which may in practice be smoothed, but kept here for demonstrational purposes. For comparison, our implementation needs approximately 6 min to identify and track the singularities for the 2D simulation dataset (without noise).

In contrast the speed of computation of SPE and STPE is independent of noise. For the 2D simulation dataset computation of SPE takes approximately 4.3 s and STPE needs less than 5 s. These values have been obtained using an Intel® Core™ i7-7500U processor at 2.7 GHz (Turbo Boost until 3.5GHz).

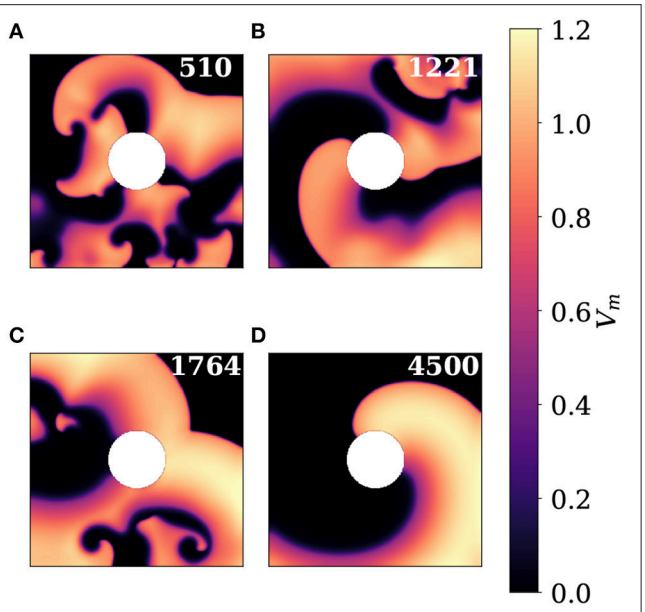

FIGURE 9 | Snapshots showing different regimes of complexity in the 2D simulation dataset. The white circle in the center is a non-conductive heterogeneity. **(A)** Frame 510 showing lots of interacting spiral waves. **(B)** Frame 1221 is taken from a regime with two spirals pinned to the heterogeneity and some remaining complex activity in the top right quadrant. **(C)** In frame 1764 several spiral waves contained mostly in the lower left triangle of the domain generate synchronized plane wave activity that travels to the upper right corner. **(D)** A single pinned spiral wave remains until the end of the video. This snapshot shows frame 4500.

4. DISCUSSION

In this article we have presented a detailed analysis of simulated excitable media using SPE and STPE as complexity measures. Because phase singularities can be thought of as the structuring elements of spiral-wave activity on the heart [1] we use it as the baseline for our comparisons.

We find that SPE and STPE can extract complexity information from simulated excitable media which partly corresponds to information extracted by PS analysis.

While the overlap between NPS and the spatial- and spatiotemporal PE is very high in many cases, some differences can be seen which stem from the fact that the PE quantifies the distribution of patterns on the medium and does not favor a specific type of phenomenon such as spiral waves.

We furthermore demonstrated that both, SPE and STPE are very robust under the influence of noise without any computational performance penalty. NPS, in contrast, breaks down for high levels of noise while becoming computationally even more demanding.

It was shown that STPE reveals different levels of complexity at different scales highlighting the possibility to tune it to specific patterns of interest.

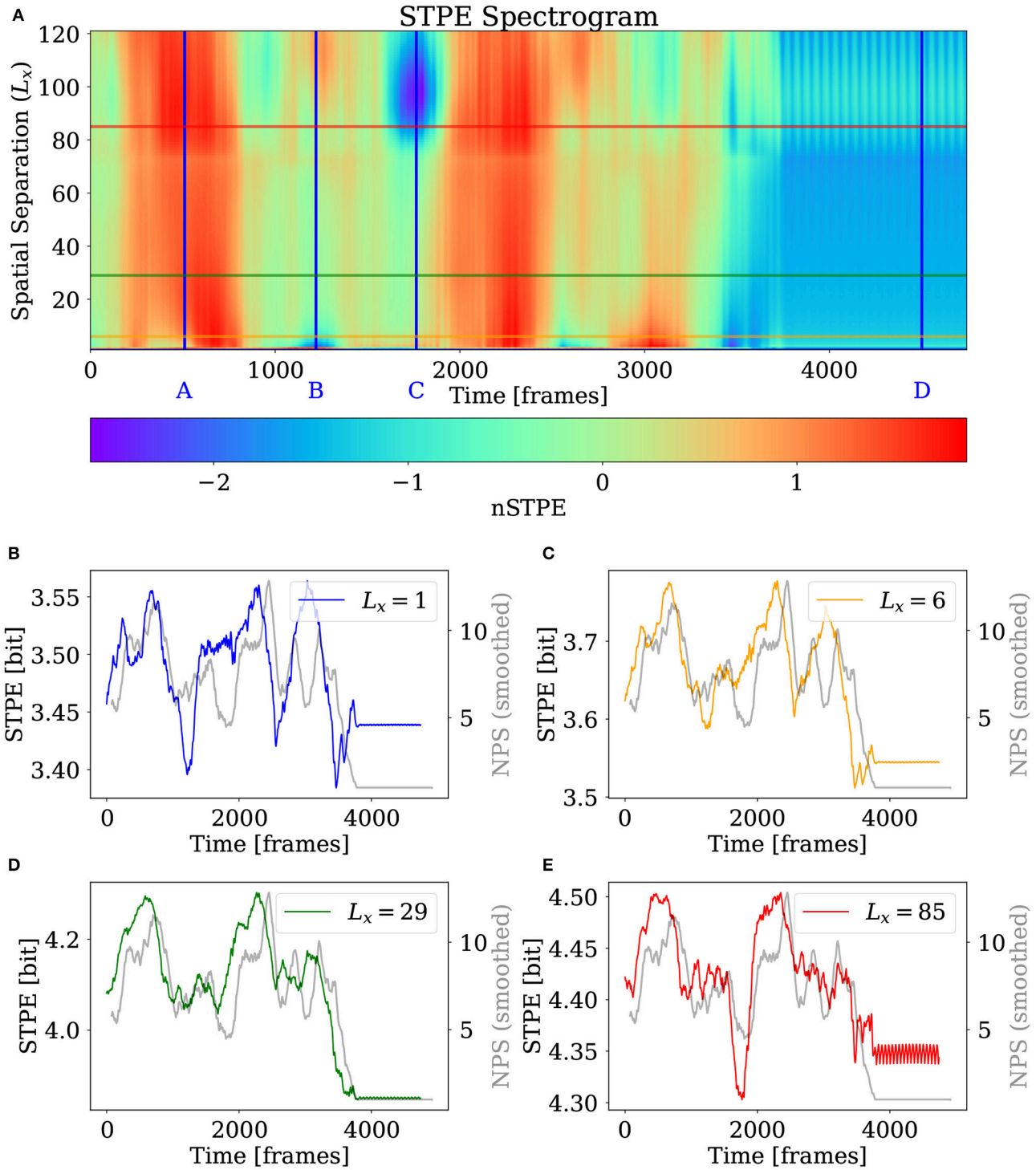

FIGURE 10 | STPE spectrogram and excerpts for the 2D simulation. **(A)** nSTPE displayed for different values of the spatial separation in a spectrogram-like view. The blue lines annotated with blue letters mark the frames which are shown in **Figures 9A–D**. **(B–E)** Show the time series for STPE at different values of the spatial separation together with NPS (gray). NPS has been smoothed using a moving average filter with a width of 155 frames.

In-depth interpretations of the exact levels of complexity at specific scales will require further analysis not covered by this article. However, we conclude that especially STPE provides a very good, fast, and robust alternative for distinguishing high complexity and low complexity periods. The larger speed may especially be relevant in an experiment where

time consuming PS analysis is not feasible. Even in a computational context permutation entropy provides a different approach for complexity estimation and comparison with other methods such as Lyapunov dimensions may be interesting, although they are not reliably available for experimental data.

Especially the low susceptibility to noise of SPE and STPE make them suitable for the analysis of massive data from *ex-vivo* experiments. We plan to apply these methods to recordings of *ex-vivo* hearts obtained in optical mapping experiments. For these data SPE and STPE can provide a complexity marker additional to phase singularity analysis which will be used for investigating the onset of arrhythmia, the mechanisms of termination and the analysis of complexity variations [25]. We plan to also adapt these methods to other types of signals from cardiac research. In particular the application to ECG signals involving multiple channels, where the low spatial resolution renders phase singularity analysis impossible, might be promising. In addition to the application to multichannel ECG, also investigations of the atrium with basket catheters may allow the transfer of SPE and STPE analysis to clinically relevant settings.

AUTHOR CONTRIBUTIONS

AS, UP, and SL designed research; AS and SB implemented the algorithms; TL and SB performed simulations; AS analyzed the data; AS, UP, SB, TL, and SL wrote the paper.

FUNDING

We acknowledge support from the German Federal Ministry of Education and Research (BMBF) (project FKZ 031A147, GO-Bio), the German Research Foundation (DFG) (Collaborative Research Centers SFB 1002 Project C3 and SFB 937 Project A18) and the German Center for Cardiovascular Research (DZHK e.V.). We thank the International Max Planck Research School (IMPRS) Physics of Biological and Complex Systems (PBCS) for financial support.

ACKNOWLEDGMENTS

We thank Daniel Hornung for providing the CT scan of the rabbit heart which was used for the three-dimensional simulation.

REFERENCES

1. Winfree AT. Electrical instability in cardiac muscle: phase singularities and rotors. *J Theor Biol.* (1989) **138**:353–405. doi: 10.1016/S0022-5193(89)80200-0
2. Gray RA, Pertsov AM, Jalife J. Spatial and temporal organization during cardiac fibrillation. *Nature* (1998) **392**:75–8. doi: 10.1038/32164
3. Fenton FH, Luther S, Cherry EM, Otani NF, Krinsky V, Pumir A, et al. Termination of atrial fibrillation using pulsed low-energy far-field stimulation. *Circulation* (2009) **120**:467–76. doi: 10.1161/CIRCULATIONAHA.108.825091
4. Pumir A, Sinha S, Sridhar S, Argentina M, Hrning M, Filippi S, et al. Wave-train-induced termination of weakly anchored vortices in excitable media. *Phys Rev E* (2010) **81**:010901. doi: 10.1103/PhysRevE.81.010901
5. Luther S, Fenton FH, Kornreich BG, Squires A, Bittihn P, Hornung D, et al. Low-energy control of electrical turbulence in the heart. *Nature* (2011) **475**:235–9. doi: 10.1038/nature10216
6. Bandt C, Pompe B. Permutation entropy: a natural complexity measure for time series. *Phys Rev Lett.* (2002) **88**:174102. doi: 10.1103/PhysRevLett.88.174102
7. Parlitz U, Berg S, Luther S, Schirdewan A, Kurths J, Wessel N. Classifying cardiac biosignals using ordinal pattern statistics and symbolic dynamics. *Comp Bio Med.* (2012) **42**:319–27. doi: 10.1016/j.compbiomed.2011.03.017
8. Ribeiro HV, Zunino L, Lenzi EK, Santoro PA, Mendes RS. Complexity-entropy causality plane as a complexity measure for two-dimensional patterns. *PLoS ONE* (2012) **7**:e40689. doi: 10.1371/journal.pone.0040689
9. Schlemmer A, Berg S, Shajahan TK, Luther S, Parlitz U. Quantifying spatiotemporal complexity of cardiac dynamics using ordinal patterns. In: *2015 37th Annual International Conference of the IEEE Engineering in Medicine and Biology Society (EMBC).* Milan (2015). p. 4049–4052.
10. Amigó J. *Permutation Complexity in Dynamical Systems.* Berlin, Heidelberg: Springer Berlin Heidelberg (2010).
11. Winfree AT. *The Geometry of Biological Time. vol. 12 of Interdisciplinary Applied Mathematics.* New York, NY: Springer (2001). doi: 10.1007/978-1-4757-3484-3
12. Iyer AN, Gray RA. An experimentalist's approach to accurate localization of phase singularities during reentry. *Ann Biomed Eng.* (2001) **29**:47–59. doi: 10.1114/1.1335538
13. Mandapati R, Asano Y, Baxter WT, Gray R, Davidenko J, Jalife J. Quantification of effects of global ischemia on dynamics of ventricular fibrillation in isolated rabbit heart. *Circulation* (1998) **98**:1688–96. doi: 10.1161/01.CIR.98.16.1688
14. Lee MH, Qu Z, Fishbein GA, Lamp ST, Chang EH, Ohara T, et al. Patterns of wave break during ventricular fibrillation in isolated swine right ventricle. *Am J Physiol Heart Circ Physiol.* (2001) **281**:H253–65. doi: 10.1152/ajpheart.2001.281.1.H253
15. Liu YB, Peter A, Lamp ST, Weiss JN, Chen PS, Lin SF. Spatiotemporal correlation between phase singularities and wavebreaks during ventricular fibrillation. *J Cardiovas Electrophysiol.* (2003) **14**:1103–09. doi: 10.1046/j.1540-8167.2003.03218.x
16. Rogers JM. Combined phase singularity and wavefront analysis for optical maps of ventricular fibrillation. *IEEE Trans Biomed Eng.* (2004) **51**:56–65. doi: 10.1109/TBME.2003.820341
17. Lorensen WE, Cline HE. Marching cubes: A high resolution 3D surface construction algorithm. In: *SIGGRAPH Computer Graphics.* Vol. 21, New York, NY: ACM (1987). p. 163–9. doi: 10.1145/37402.37422
18. Fenton F, Karma A. Vortex dynamics in three-dimensional continuous myocardium with fiber rotation: Filament instability and fibrillation. *Chaos Interdiscipl J Nonlin Sci.* (1998) **8**:20. doi: 10.1063/1.166311
19. Fenton FH, Cherry EM, Hastings HM, Evans SJ. Multiple mechanisms of spiral wave breakup in a model of cardiac electrical activity. *Chaos Interdiscipl J Nonlin Sci.* (2002) **12**:852–92. doi: 10.1063/1.1504242
20. Li X, Lowengrub J, Rätz A, Voigt A. Solving PDEs in complex geometries: a diffuse approach. *Commun Math Sci.* (2009) **7**:81–107. doi: 10.4310/CMS.2009.v7.n1.a4
21. Fenton FH, Cherry EM, Karma A, Rappel WJ. Modeling wave propagation in realistic heart geometries using the phase-field method. *Chaos Interdiscipl J Nonlin Sci.* (2005) **15**:013502. doi: 10.1063/1.1840311

22. van der Walt S, Colbert SC, Varoquaux G. The NumPy array: a structure for efficient numerical computation. *Comput Sci. Eng.* (2011) **13**:22–30. doi: 10.1109/MCSE.2011.37
23. Jones E, Oliphant T, Peterson P, et al. SciPy: Open source scientific tools for Python. (2001). Online; accessed 2018-01-15. Available online at: http://www.scipy.org/
24. Behnel S, Bradshaw R, Citro C, Dalcin L, Seljebotn DS, Smith K. Cython: the best of both worlds. *Comput Sci. Eng.* (2011) **13**:31–9. doi: 10.1109/MCSE.2010.118
25. Schlemmer A, Baig T, Luther S, Parlitz U. Detection and characterization of intermittent complexity variations in cardiac arrhythmia. *Physiol Measure.* (2017) **38**:1561. doi: 10.1088/1361-6579/aa7be0

Conflict of Interest Statement: The authors declare that the research was conducted in the absence of any commercial or financial relationships that could be construed as a potential conflict of interest.

frontiers in Physics

ORIGINAL RESEARCH
published: 10 April 2018
doi: 10.3389/fphy.2018.00030

Causal Scale of Rotors in a Cardiac System

Hiroshi Ashikaga[1,2*], *Francisco Prieto-Castrillo*[3,4,5], *Mari Kawakatsu*[6] and *Nima Dehghani*[7,8]

[1] IHU Liryc L'institut de Rythmologie et Modélisation Cardiaque, Hôpital Xavier Arnozan, Pessac, France, [2] Cardiac Arrhythmia Service, Johns Hopkins University School of Medicine, Baltimore, MD, United States, [3] Media Laboratory, Massachusetts Institute of Technology, Cambridge, MA, United States, [4] Harvard T. H. Chan School of Public Health, Harvard University, Boston, MA, United States, [5] BISITE Research Group, University of Salamanca, Salamanca, Spain, [6] Program in Applied and Computational Mathematics, Princeton University, Princeton, NJ, United States, [7] Department of Physics, Massachusetts Institute of Technology, Cambridge, MA, United States, [8] Center for Brains, Minds and Machines, Massachusetts Institute of Technology, Cambridge, MA, United States

Rotors of spiral waves are thought to be one of the potential mechanisms that maintain atrial fibrillation (AF). However, disappointing clinical outcomes of rotor mapping and ablation to eliminate AF raise a serious doubt on rotors as a macro-scale mechanism that causes the micro-scale behavior of individual cardiomyocytes to maintain spiral waves. In this study, we aimed to elucidate the causal relationship between rotors and spiral waves in a numerical model of cardiac excitation. To accomplish the aim, we described the system in a series of spatiotemporal scales by generating a renormalization group, and evaluated the causal architecture of the system by quantifying causal emergence. Causal emergence is an information-theoretic metric that quantifies emergence or reduction between micro- and macro-scale behaviors of a system by evaluating effective information at each scale. We found that the cardiac system with rotors has a spatiotemporal scale at which effective information peaks. A positive correlation between the number of rotors and causal emergence was observed only up to the scale of peak causation. We conclude that rotors are not the universal mechanism to maintain spiral waves at all spatiotemporal scales. This finding may account for the conflicting benefit of rotor ablation in clinical studies.

Keywords: complex systems, information theory, cardiac dynamics, rotors, atrial fibrillation

OPEN ACCESS

Edited by:
Flavio H. Fenton,
Cornell University, United States

Reviewed by:
Martin Bishop,
King's College London,
United Kingdom
Joakim Sundnes,
Simula Research Laboratory, Norway

***Correspondence:**
Hiroshi Ashikaga
hiroshi.ashikaga@ihu-liryc.fr

Specialty section:
This article was submitted to Computational Physics, a section of the journal Frontiers in Physics

Received: *04 December 2017*
Accepted: *23 March 2018*
Published: *10 April 2018*

Citation:
Ashikaga H, Prieto-Castrillo F, Kawakatsu M and Dehghani N (2018) Causal Scale of Rotors in a Cardiac System. Front. Phys. 6:30. doi: 10.3389/fphy.2018.00030

1. INTRODUCTION

The heart is a complex system consisting of five billion autonomous cardiomyocytes that interact with each other. This interaction leads to system behaviors at multiple scales. The dynamics of the rotating center ("*rotor*") of spiral waves [1, 2] is a macro-scale, emergent behavior of the cardiac system that is reducible to but cannot easily be explained by the dynamics of the individual cardiomyocytes at the microscopic scale [3–6]. For example, the determinants of rotor dynamics include ionic currents [7], action potential duration (APD) restitution properties, conduction velocity (CV) restitution properties [8], wavefront curvature of spiral waves [9], heterogeneity and anisotropy of the media, and coexisting rotors [10, 11].

Currently, rotors are thought to be one of the potential mechanisms that maintains atrial fibrillation (AF) in human [12], and early clinical attempts to target rotors with interventional catheter ablation therapy to eliminate AF showed promising results [13–15]. However, recent clinical trials have been disappointing [16–20]. Apart from the technical limitations associated with

rotor identification using clinically available systems [21], those negative findings raise a serious doubt on rotors as a macro-scale mechanism that *causes* the micro-scale behavior of individual cardiomyocytes to maintain spiral waves.

The micro- and macro-scale behaviors of a multi-scale system can be mathematically quantified by the information content of behaviors at each scale. For example, information-theoretic metrics such as the complexity profile [22] and the marginal utility of information [23] can quantitatively characterize the amount of information that is present in the system behavior at different scales. The downward causation [24–28] from macro- to micro-scale behaviors of the system is quantifiable as inter-scale downward information flow. We recently showed that the relationship between the number of rotors and downward information flow is nonlinear in a cardiac system [29]. At microscopic scales, higher numbers of rotors are associated with higher downward information flow. As the system description becomes more macroscopic, higher numbers of rotors are associated with lower downward information flow. This subtle but important finding suggests that rotors may not be a universal mechanism to maintain spiral waves at all scales. As the system is coarse-grained, rotors may lose their causal power to maintain spiral waves.

The aim of the study was to elucidate the causal relationship between rotors and spiral waves, and to identify the causal scale of rotors as a mechanism to maintain spiral waves. To accomplish the aim, we described rotors in a numerical model of cardiac excitation in a series of spatiotemporal scales by generating a renormalization group, and evaluate the causal architecture of the system by quantifying *causal emergence*. Causal emergence is an information-theoretic metric that quantifies emergence or reduction between micro- and macro-scale behaviors of a system by evaluating *effective information* at each spatiotemporal scale [30]. Effective information is a quantity that captures causal interactions of a system between its unconstrained repertoire of possible cause and a specific state of possible effect [31]. We hypothesized that a positive correlation between the number of rotors and causal emergence is not universally found in all the spatiotemporal scales of the cardiac system.

2. MATERIALS AND METHODS

We perform the simulation and the data analysis using Matlab R2016b (Mathworks, Inc.).

2.1. Model of Spiral Waves

We used a modified Fitzhugh–Nagumo model to represent cardiac action potential [32, 33]. This model accurately reproduces important properties of cardiac systems, including slowed conduction velocity, unidirectional block due to wavefront curvature, and spiral waves [34].

$$\frac{\partial v}{\partial t} = 0.26v\,(v - 0.13)(1 - v) - 0.1vr + I_{ex} + \nabla \cdot (D\nabla v) \quad (1)$$

$$\frac{\partial r}{\partial t} = 0.013\,(v - r) \quad (2)$$

where v is the transmembrane potential, r is the recovery variable, and I_{ex} is the external current [35]. D is the diffusion tensor, which is a diagonal matrix whose diagonal and off-diagonal elements are 1 and 0 mm^2/ms, respectively, to represent a 2-D isotropic system [34]. We used an isotropic, homogeneous model to avoid confounding the causal archtecture by tissue anisotropy and inhomogeneity. We solved the model equations using a finite difference method for spatial derivatives and explicit Euler integration for time derivatives assuming Neumann boundary conditions. We generated 1,000 sets of a 2-D 120×120 isotropic lattice of components ($= 11.9 \times 11.9$ cm) by inducing spiral waves with 40 random sequential point stimulations in 40 random components of the lattice (**Supplementary Movie 1**, section 3.2) [36]. In each component, we computed the time series for 10 s excluding the stimulation period with a time step of 0.063 ms, which was subsequently downsampled at a sampling frequency of 400 Hz.

We then defined the instantaneous phase $\phi(t)$ and the instantaneous amplitude $A(t)$ of $v(t)$ in each component via construction of the analytic signal $\xi(t)$, which is a complex function of time [37].

$$\xi(t) = v(t) + iv_H(t) = A(t)e^{i\phi(t)} \quad (3)$$

Here, $v_H(t)$ is the Hilbert transform of $v(t)$

$$v_H(t) = \frac{1}{\pi}\text{p.v.}\int_{-\infty}^{\infty}\frac{v(\tau)}{t-\tau}d\tau \quad (4)$$

where p.v. indicates that the integral is taken in the sense of the Cauchy principal value. We defined the rotor of the spiral wave as a phase singularity [38], where the phase is undefined because all phase values converge. The phase singularity can be localized through calculation of the topological charge n_t [39, 40].

$$n_t = \frac{1}{2\pi}\oint_c \nabla\phi \cdot d\vec{l} \quad (5)$$

where $\phi(\vec{r})$ is the local phase, and the line integral is taken over the path $\vec{l}$ on a closed curve c surrounding the singularity [41].

$$n_t = \begin{cases} +1 & \text{counterclockwise rotor} \\ -1 & \text{clockwise rotor} \\ 0 & \text{elsewhere} \end{cases} \quad (6)$$

In this study, $|n_t|$ was used to quantify the average number of rotors over the entire time series [42].

2.2. Renormalization Group

We generated a renormalization group of the system by a series of spatial and temporal transformation including coarse-graining and rescaling of the original microscopic description of the system. For each component, the time series of cardiac excitation was descretized to 1 when excited (during the APD at 90% repolarization, or APD_{90}) or 0 when resting (**Figure 1A**) [43]. Then we coarse-grained the system spatially and temporally with decimation by a factor of 2 (**Figure 1B**). Spatial decimation

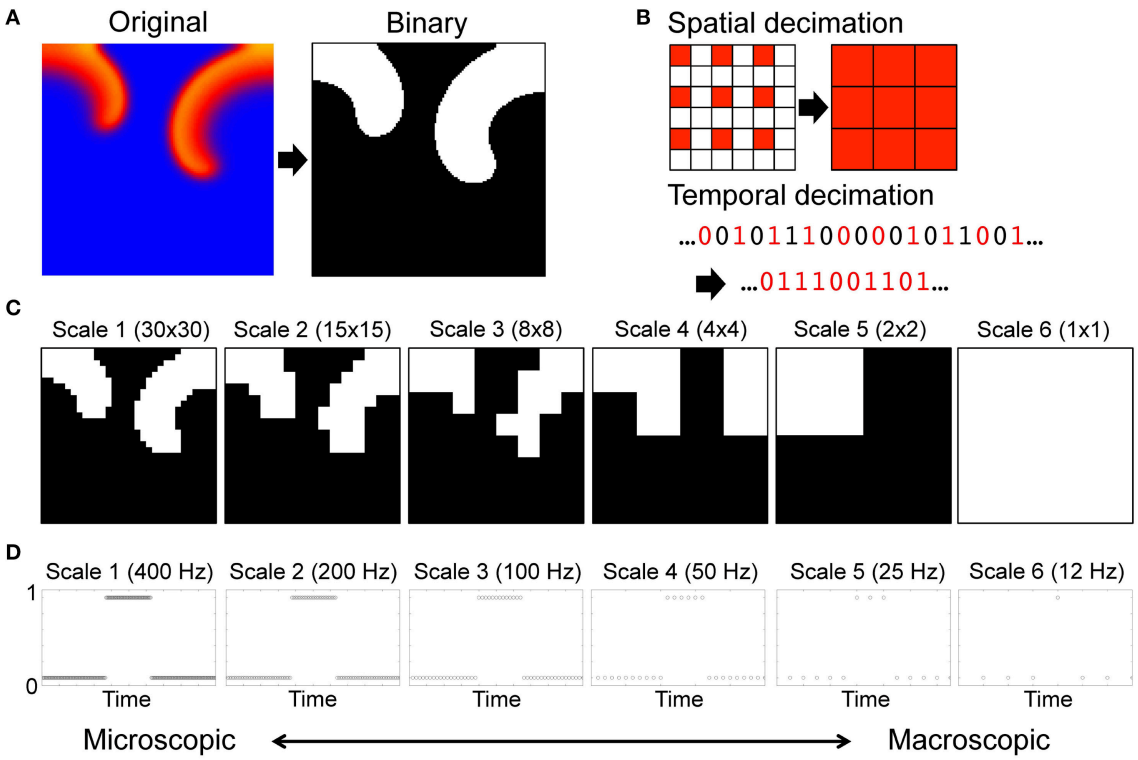

FIGURE 1 | Renormalization of a cardiac system with spiral waves. **(A)** Original description of the system. For each component, the time series of cardiac excitation is descretized to 1 (black) when excited (during the APD at 90% repolarization, or APD_{90}) or 0 (white) when resting. **(B)** Spatial and temporal decimation. Spatial decimation takes the value of cardiac excitation (0 or 1) at each time point in the component at the top left corner of a block of 2 × 2 immediately adjacent components of the system, and assigns the value to the corresponding site in the system at the next scale. Temporal decimation downsamples the time series of cardiac excitation by a factor of 2. **(C)** Spatial scales. Spatial scales include scale 1 (30 × 30 lattice), scale 2 (15 × 15 lattice), scale 3 (8 × 8 lattice), scale 4 (4 × 4 lattice), scale 5 (2 × 2 lattice), and scale 6 (1 × 1 lattice). **(D)** Temporal scales. Each circle represents a data sampling point. Temporal scales include scale 1 (400 Hz), scale 2 (200 Hz), scale 3 (100 Hz), scale 4 (50 Hz), scale 5 (25 Hz), and scale 6 (12 Hz).

transforms a $n \times n$ lattice into a $\frac{n}{2} \times \frac{n}{2}$ lattice by extracting the top left component of each 2 × 2 block (**Supplementary Movie 2**). Temporal decimation downsampled the binary time series of each component by a factor of 2. Using a combination of iterative coarse-graining in spatial and temporal axes we created a renormalization group of a total of 36 spatiotemporal scales of the system. The renormalization group included spatial scales 1 (30 × 30 lattice), 2 (15 × 15 lattice), 3 (8 × 8 lattice), 4 (4 × 4 lattice), 5 (2 × 2 lattice), and 6 (1 × 1 lattice) (**Figure 1C**), and temporal scales 1 (400 Hz), 2 (200 Hz), 3 (100 Hz), 4 (50 Hz), 5 (25 Hz), and 6 (12 Hz) (**Figure 1D**).

2.3. Effective Information

We treated each component on the lattice as a time-series process X. *Entropy* H of each time-series process X is

$$H(X) = -\sum_{x} p(x) \log_2 p(x) \tag{7}$$

where $p(x)$ denotes the probability density function of the time series generated by X. *Effective information* quantifies the information generated when the system enters a specific state of possible effect Y out of its unconstrained probability distribution of possible cause X [31].

$$EI(X \to Y) = I(X; Y) \tag{8}$$

$$= H(X) + H(Y) - H(X, Y) \tag{9}$$

$$= \sum_{x,y} p(x, y) \log_2 \frac{p(x, y)}{p(x)p(y)} \tag{10}$$

where X has a uniform probability distribution so that it provides the maximum entropy $H(X)_{max}$ [44]. $I(X; Y)$ is mutual information, $p(x, y)$ and $H(X, Y)$ denote the joint probability density function and the joint entropy of X and Y, respectively. Mutual information is originally a measure of statistical dependence to quantify how much information is shared between a source and a destination [45]. In this context, however, mutual information is applied between two time series of a system that is first perturbed into all possible states with equal probability and then observed as a sepcific state. Because of the system perturbations, mutual information here is a causal

measure, and thus effective information of the system is a state-independent information-theoretic measure of a system's causal architecture [30].

One can describe a $n \times n$ lattice at time t as a binary string of length $n \times n$. Therefore, the unconstrained repertoire of all possible causes X at time t_0 consists of 2^{n^2} possible states with equal probability $1/2^{n^2}$ at each time point. We defined the bin number b ($b < 2^{n^2}$) to calculate the probability distribution of X and Y, and we used $b = 2^{10} = 1,024$ in this study. Analytically, because X has a uniform probability distribution, the probability that X falls in one of the b bins at each time point is $1/b$. Therefore, entropy of X is equal to the maximum entropy (**Figure 2A**).

$$H(X) = -\sum_x p(x) \log_2 p(x) \tag{11}$$

$$= b \times (-\frac{1}{b} \log_2 \frac{1}{b}) \tag{12}$$

$$= \log_2 b \tag{13}$$

Numerically, X can be defined as a vector of uniformly distributed random numbers between 1 and $2^{n^2}-1$ for a time series of finite duration. Due to the discretization effect, the probability is non-uniform. Entropy is close to but not identical to the maximum entropy (**Figure 2A**). We generated 1,000 sets of X at each scale to vaidate the robustness of our effective information measure in the cardiac system with rotors (section 3.1). Similarly, Y can be defined as a vector of decimal numbers between 1 and $2^{n^2}-1$, each of which represents a specific state of the system with rotors (**Figure 2B**). *Causal emergence* is a difference in effective information between scales.

$$CE = EI(X_m \rightarrow Y_m) - EI(X_n \rightarrow Y_n) \tag{14}$$

where m and n are different scales of the system description from the renormalization group. When scale m is more macroscopic than scale $n (m > n)$, a positive CE indicates that the macroscopic behavior is emergence (downward causation), whereas a negative CE indicates that the macroscopic behavior is reduction (upward causation) [30]. In this study we quantified causal emergence with respect to the most microscopic system description with spatial scale = temporal scale = 1.

3. RESULTS

3.1. Evaluation of Variance of Effective Information to Quantify Rotor Dynamics

First, we evaluated the variance of effective information to describe rotor dynamics at each spatiotemporal scale. This allowed us to vaidate the robustness of our effective information measure in the cardiac system with rotors. We repeated 1,000 numerical computations of X and Y in a representative spiral wave data set to calculate entropy $H(X)$, $H(Y)$, $H(X, Y)$, then calculated $EI(X \rightarrow Y)$. Numerically, $H(X)$ is not uniquely determined due to the discretization effect, but the variance was small (**Figure 3**). Spatial coarse-graining had minimal impact on

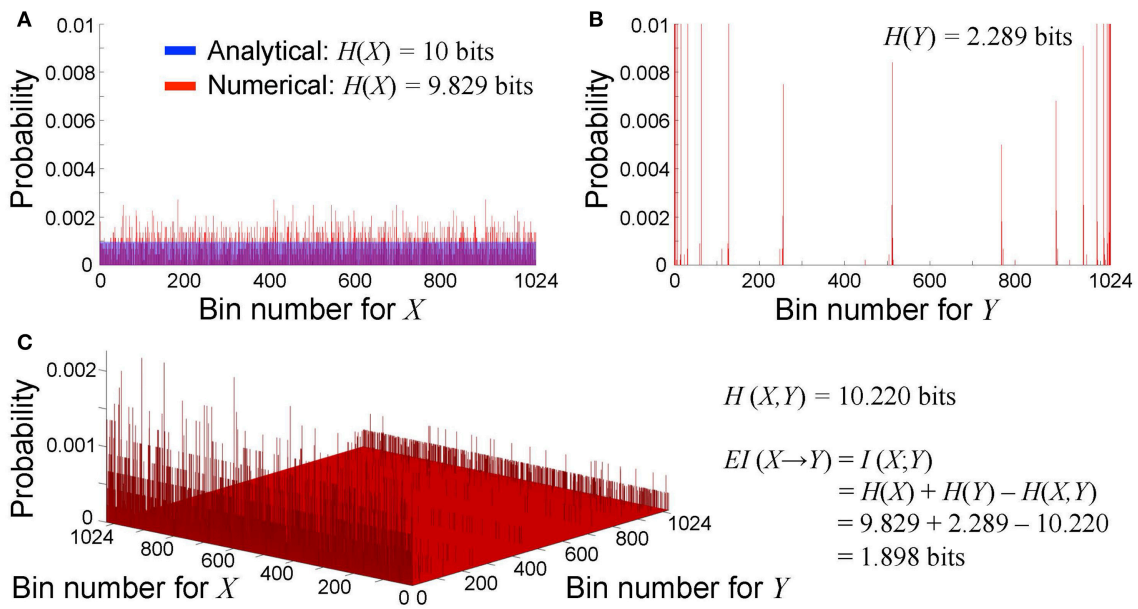

FIGURE 2 | Probability distribution of cause X and effect Y. We define the bin number $b = 2^{10}$ in this study. **(A)** Unconstrained probability distribution of possible cause X. Analytically, the probability of all bins is uniformly $1/b$ (shown in blue), and thus entropy is equal to the maximum entropy at $\log_2 b$=10 bits. In contrast, numerically, the probability is non-uniform due to the discretization effect (shown in red). Entropy is 9.829 bits, which close to but not identical to the maximum entropy. **(B)** Probability distribution of a specific state of possible effect Y. The probability is non-uniform. Entropy is 2.289 bits in this case. **(C)** Bivariate probability distribution of cause X and effect Y. Joint entropy is 10.220 bits in this case. Effective information from case X to effect Y is equal to mutual information between X and Y, thus is calculated as 1.898 bits.

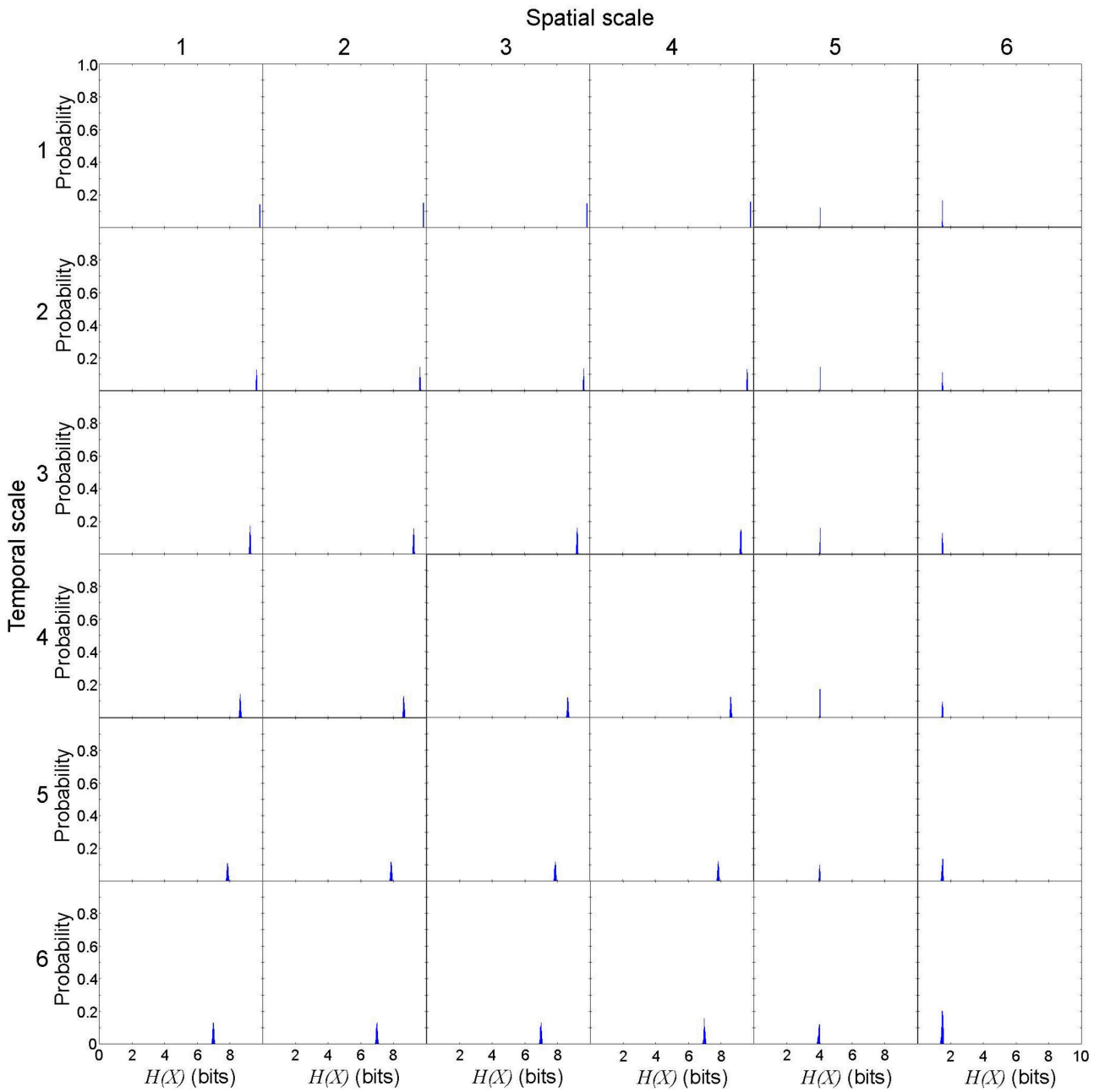

FIGURE 3 | Entropy of unconstrained probability distribution of possible cause X in a representative spiral wave data set. $H(X)$ is not uniquely determined due to the discretization effect, but the variance is small. Each subplot represents he probability distribution of $H(X)$. The columns represent the spatial scales (1 through 6) and the rows represent the temporal scales (1 through 6).

the probability ditribution of $H(X)$ from scales 1 through 4, but $H(X)$ steeply fell in scales 5 and 6. In contrast, temporal coarse-graining gradually shifted the distribution of $H(X)$ to the left. $H(Y)$ was uniquely determined because it represents a specific state of the system regardless of the spatiotemporal scale (**Figure 4**). In this case, spatial coarse-graining clearly increased the distribution of $H(Y)$ to the right, which peaked at scale 4 and decreased at scales 5 and 6. Similarly, temporal coarse-graining increased the distribution of $H(Y)$ to the right, which peaked at scale 4 and decreased at scales 5 and 6. The relationship between the spatiotemporal coarse-graining and the probability distribution of joint entropy $H(X, Y)$ was similar to that of $H(X)$ (**Figure 5**), and the variance remained small. Effective infromation $EI(X \rightarrow Y)$ peaked at spatial scale of 4 and temporal scale 5, and the variance of $EI(X \rightarrow Y)$ remained small (**Figure 6**). This findings indicates that, despite the discretization

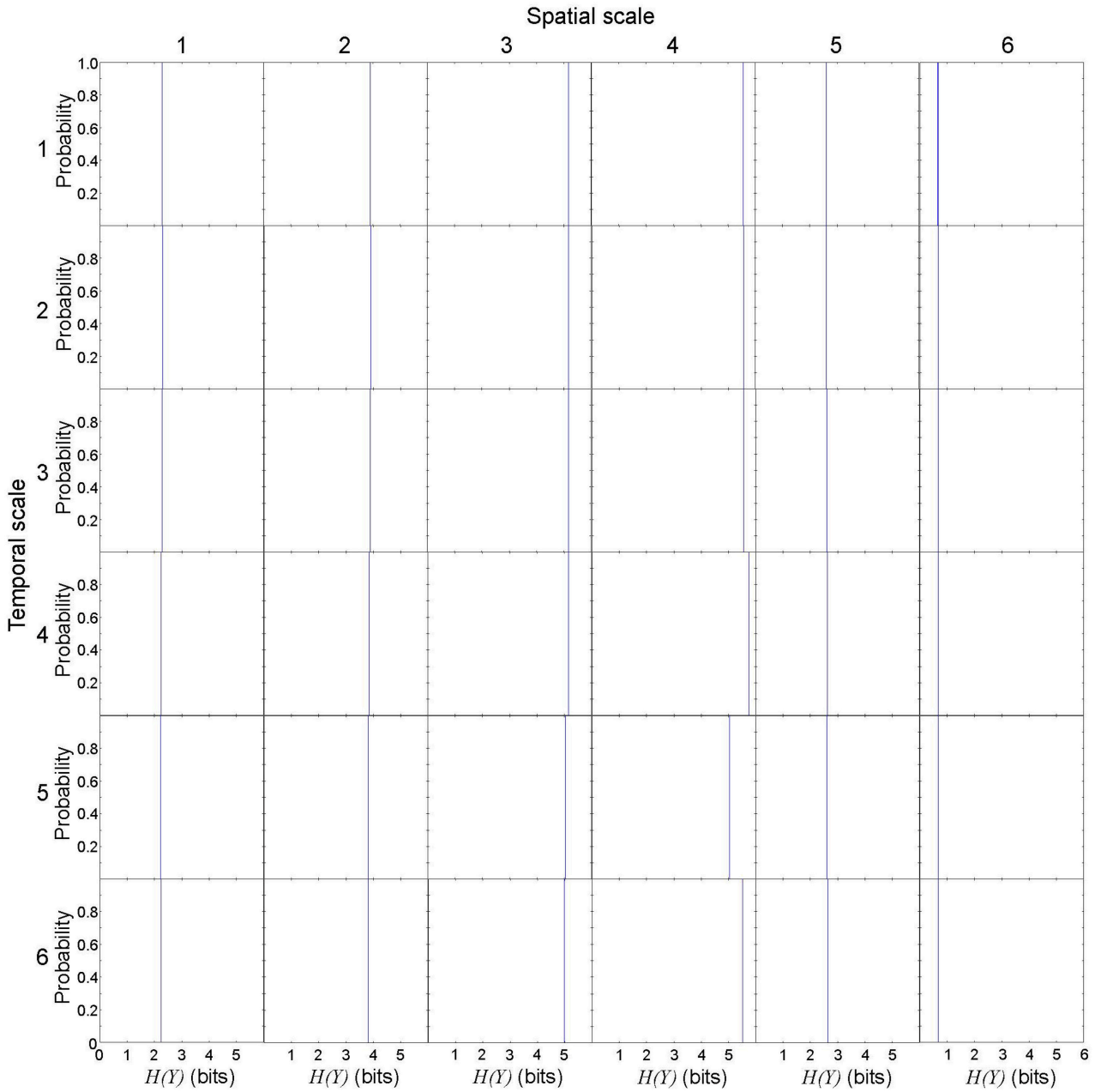

FIGURE 4 | Entropy of specific state of possible effect *Y* in a representative spiral wave data set. *H*(*Y*) is uniquely determined because it represents a specific state of the system regardless of the spatiotemporal scale. Each subplot represents the probability distribution of *H*(*Y*). The columns represent the spatial scales (1 through 6) and the rows represent the temporal scales (1 through 6).

effect, numerical computation of $EI(X \rightarrow Y)$ is robust with high reproducibility, and thus $EI(X \rightarrow Y)$ can be used to quantify the information of rotor dynamics at each spatiotemporal scale.

3.2. Evaluation of Effective Information in Aggregate Data Sets

Next, we quantified effective information to describe rotor dynamics at each spatiotemporal scale in 1,000 different sets of spiral waves with random initial conditions (**Figure 7**). This allowed us to analyze the causal architecture of the cardiac system with rotors in aggregate data sets, rather than focusing on one data set with a specific manifestation of rotor dynamics. Overall, effective information increased as the scale increased from microscopic to macroscopic descriptions of the system. However, effective information reached the global maximum at spatial scale = temporal scale = 4, beyond which effective information decreased (**Figure 7**). This finding indicates that the cardiac system with rotors has the most causal power at at spatial

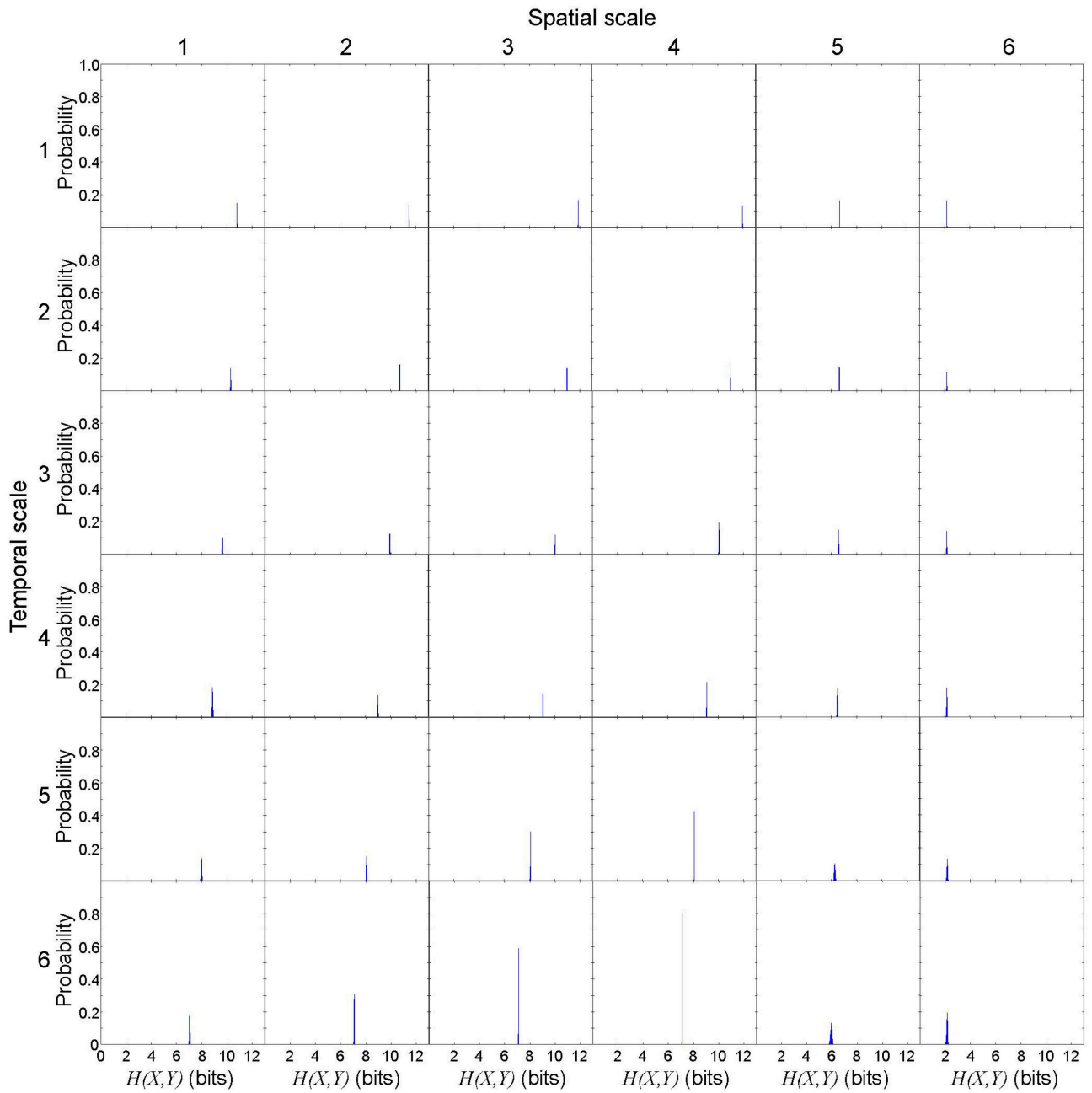

FIGURE 5 | Joint entropy of cause X and effect Y in a representative spiral wave data set. $H(X, Y)$ is not uniquely determined due to the discretization effect, but the variance is small. Each subplot represents the probability distribution of $H(X, Y)$. The columns represent the spatial scales (1 through 6) and the rows represent the temporal scales (1 through 6).

scale = temporal scale = 4. The behavior at this scale causes the behavior at more microscopic (downward causation) and macroscopic scales (upward causation). It is important to note that the scale of peak causation is not the most macroscopic scale (i.e., spatial scale = temporal scale = 6). We also found that the difference in effective information between scales was larger in spatial coarse-graining (**Figure 7B**) than that of temporal coarse-graining (**Figure 7C**), indicating that the impact of spatial coarse-graining on effective information was higher than that of temporal coarse-graining.

3.3. Relationship Between the Number of Rotors and Causal Emergence

Lastly, we evaluated the relationship between the number of rotors and causal emergence in the same 1,000 data sets used in section 3.1. This allowed us to relate the causal architecture

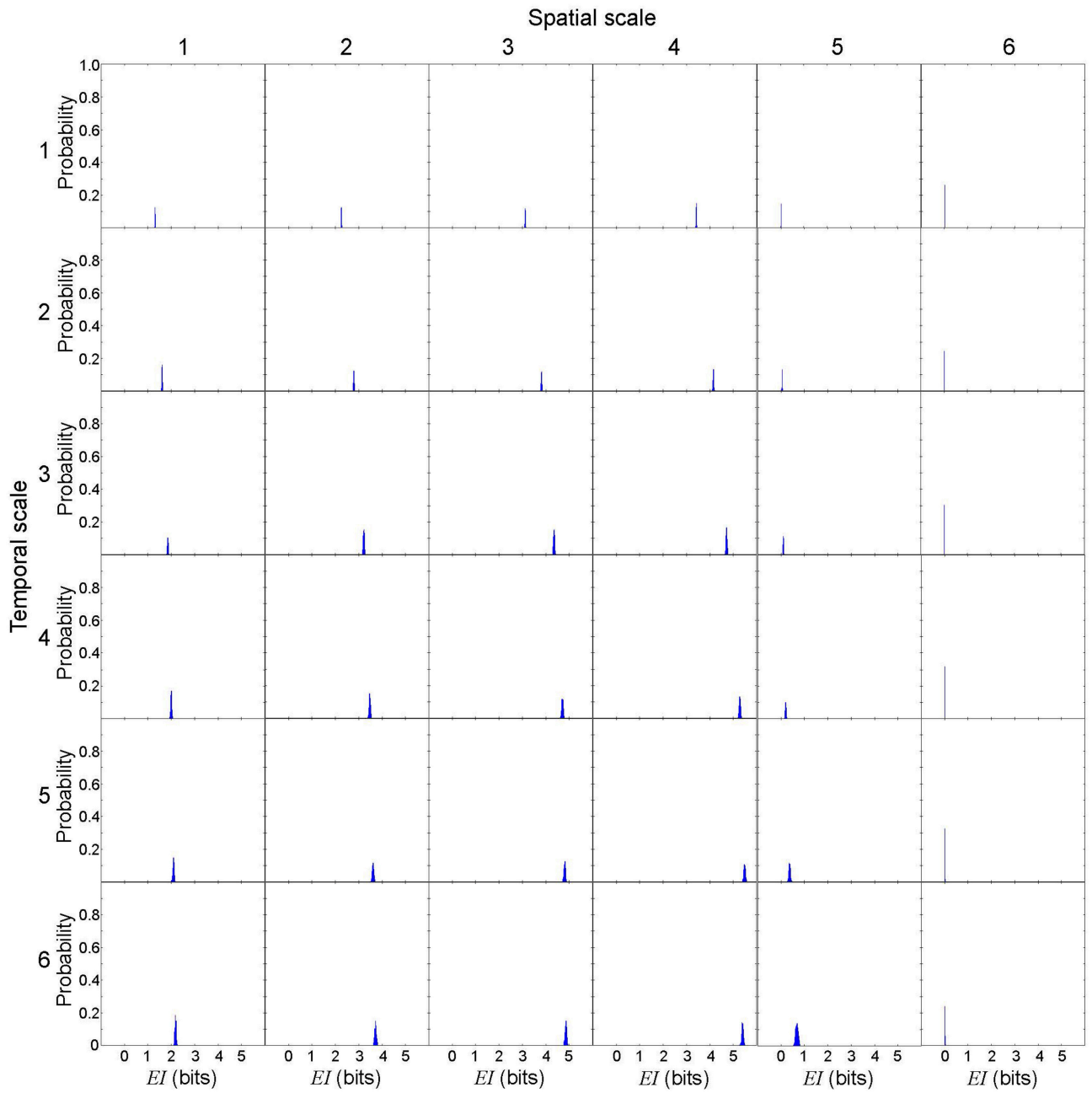

FIGURE 6 | Effective information from cause X to effect Y in a representative spiral wave data set. $EI(X \rightarrow Y)[= I(X; Y) = H(X) + H(Y) - H(X, Y)]$ is not uniquely determined due to the discretization effect, but the variance is small. Each subplot represents the probability distribution of $EI(X \rightarrow Y)$. The columns represent the spatial scales (1 through 6) and the rows represent the temporal scales (1 through 6).

of the cardiac system to rotor dynamics. The number of rotors ranged from 0 to 7, with a median of 3 (**Figure 8**). For system descriptions at spatial scale ≤ 4 and temporal scale ≤ 4, causal emergence was positive for all the data sets except a few where a rotor prematurely disappeared on its own (number of rotors ≤ 1, red dots in **Figure 9**). There was a significant positive correlation between the number of rotors and causal emergence. This finding indicates that rotor dynamics at those scales is an emergent behavior that causes the micro-scale behavior of the system. For system descriptions at spatial scale ≥ 5, causal emergence was negative for all the data sets, and there was a significant negative correlation between the number of rotors and causal emergence. This findings indicates that rotor dynamics at those scales is reducible to the micro-scale behavior of the system. For system descriptions at spatial scale $= 1$ and temporal scale ≥ 5, causal emergence scatters in positive and negative values. This

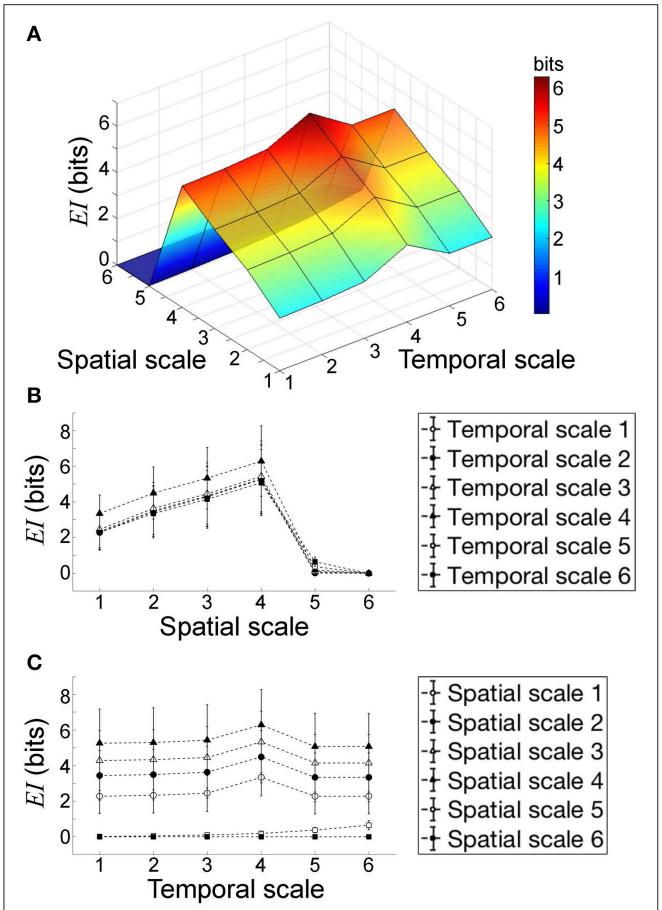

FIGURE 7 | Effective information of the system in aggregate data sets. **(A)** Overview. Each point indicates the mean effective information $EI(X \rightarrow Y)$ of 1,000 data sets at each spatiotemporal scale. $EI(X \rightarrow Y)$ reaches the global maximum at spatial scale = temporal scale = 4. **(B)** Effective information vs. spatial scale. **(C)** Effective information *vs.* temporal. Each point indicates the mean of *EI* of 1,000 data sets at each spatiotemporal scale.

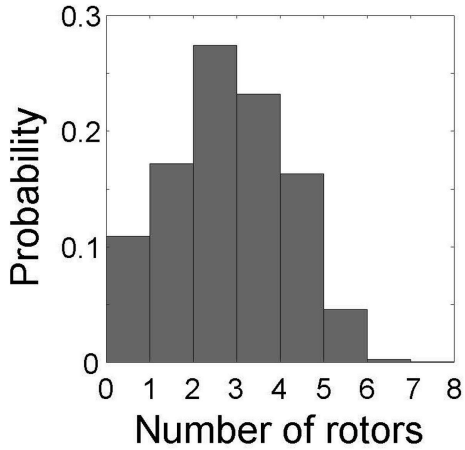

FIGURE 8 | Probability distribution of the number of rotors. The number of rotors ranges from 0 to 7 in 1,000 data sets.

finding indicates that the causal relationship at those scales is inconsistent. There was a significant negative correlation between the number of rotors and causal emergence at those scales, but the correlation coefficients were small ($r = -0.089$). For system descriptions at spatial scale = 2, 3, and 4 and temporal scale $\geq$ 5, causal emergence was almost always positive and there was a significant positive correlation between the number of rotors and causal emergence. This finding indicates that temporal coarse-graining has a smaller impact than spatial coarse-graining on the relationship between the number of rotors and causal emergence. This result is consistent with that of section 3.2.

4. DISCUSSION

4.1. Main Findings

First, the numerical computation of effective information in the cardiac system with rotors is robust with high reproducibility (**Figure 6**), despite the discretization effect associated with random generation of the unconstrained probability distribution of possible cause X. Therefore, our effective information measure is a reasonable information-theoretic metric to quantify the information generated for specific dynamics in the cardiac system with rotors at each spatiotemporal scale.

Next, there is a spatiotemporal scale at which effective information peaks in the cardiac system with rotors (**Figure 7**). This finding indicates that the most causal power of the system does not lie in the most microscopic (i.e., spatial scale = temporal scale = 1) nor the most macroscopic scale (i.e., spatial scale = temporal scale = 6). In other words, both downward and upward causation coexist in the cardiac system with rotors.

Lastly, a positive correlation between the number of rotors and causal emergence is not universally found in all the spatiotemporal scales of the cardiac system (**Figure 9**). For example, the number of rotors and causal emergence were positively correlated only up to the scale of peak causation, beyond which the correlation is not universally positive. This finding indicates that rotors are not the universal causal mechanism to maintain spiral wave dynamics at all spatiotemporal scales.

4.2. Quantifying Causal Architecture of Cardiac Systems

Our study highlights several innovative aspects. First, we utilized a multi-scale approach by generating a renormalization group where we applied iterated coarse-graining and rescaling [46] to the microscopic description of the cardiac system to construct a series of robust and minimal macroscopic descriptions (**Figure 1**). In our previous work, we have successfully applied the renormalization group to a cardiac system to quantify inter-scale information flow [29]. In this study, we coarse-grained the system descriptions in both spatial and temporal scales to quantify macro-scale behaviors while reducing the number of degrees of freedom. This approach is different from a conventional and common belief that a detailed, high-resolution modeling with

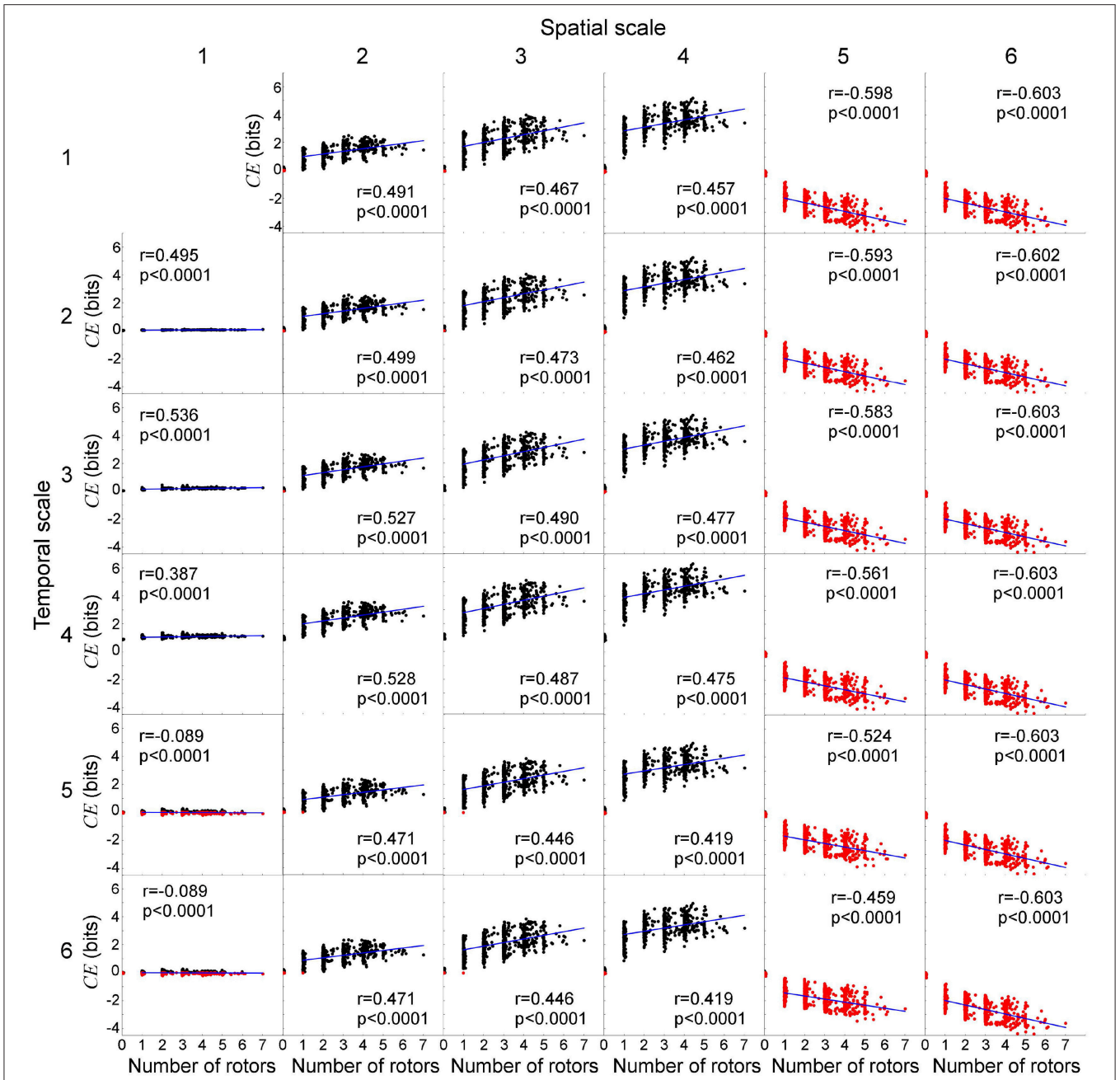

FIGURE 9 | Number of rotors and causal emergence. We quantify causal emergence (*CE*) with respect to the most microscopic system description at spatial scale = temporal scale = 1. Each subplot represents an association between the number of rotors and *CE* at each spatiotemporal scale. Black dots indicate $CE > 0$ (emergence), whereas red dots indicate $CE < 0$ (reduction). Blue lines indicate linear fit for the number of rotors ≥1. The columns represent the spatial scales (1 through 6) and the rows represent the temporal scales (1 through 6).

near-complete description of microscopic behaviors with infinite degrees of freedom is required to understand the macroscopic behavior of the cardiac system. Our results suggest that our approach is valid for achieving our aim to understand the macro-micro causal relationship between rotors and spiral waves in the cardiac system.

Second, we validated the robustness of effective information in a cardiac system (**Figure 6**). Effective information is equal to mutual information $I(X; Y)$ between the source X and the destination Y [30]. Mutual information is a measure of statistical dependence between X and Y [45], and is not a causal measure. However, by choosing X as a uniform probability distribution such that it provides the maximum entropy $H(X)_{max}$ [44], and Y as a specific state of dynamics, $I(X; Y)$ becomes a causal measure to quantify the information generated from X to Y (**Figure 2**) [47]. Our results suggest that our effective information measure

is robust with high reproducibility. Our results demonstrate that, because effective information sensitively captures the dynamics of the system, it is applicable to any multi-scale systems to quantify the causal architecture.

Lastly, we quantified causal emergence to evaluate the causal relationship between rotors and spiral waves to address whether rotors are the causal mechanism to maintain spiral waves, which is clinically important. Our result was unexpected; yes, rotors are the mechanism to maintain spiral waves, but not at all spatiotemporal scales. This result is consistent with our previous work evaluating inter-scale information flow [29]. Our result makes us reconsider a binary definition of a causal mechanism, where *A* either is or is not a cause of *B*. The binary definition of the causal mechanism may be both insensitive and simplistic, failing to capture important features of causal architecture. The finding that rotors are not the universal mechanism to maintain spiral waves at all scales may account for the conflicting benefit of rotor ablation in clinical studies, because the concept of scales has never been introduced as an independent variable in interventional catheter ablation therapy.

4.3. Clinical Implications

Successful treatment of arrhythmia requires targeted elimination of the mechanism that maintains arrhythmia, not the mechanism that triggers it. For example, in Wolff-Parkinson-White (WPW) syndrome, the ablation target is not the premature atrial complexes (PAC) that trigger atrioventricular reciprocating tachycardia (AVRT), one of the simplest forms of anatomical reentry. Instead, successful treatment of AVRT requires elimination of an accessory pathway (AP) connecting the atrium and the ventricle that maintains AVRT [48]. Because the mechanism that maintains AF remains unclear [12], catheter ablation of AF targets focal triggers mainly originating from the pulmonary veins (pulmonary vein isolation, PVI) [49, 50]. This approach remains far from curative, with recurrence rates up to 40% [51].

Our results suggest that the causal architecture analysis may guide the additional strategies of therapeutic intervention of AF, including the posterior wall isolation [52, 53], the stepwise approach [54–56], and the extensive ablation [57]. Those strategies, which are performed in addition to PVI, focus on segmenting the atria by linear lesions to reduce the mass of contiguous atrial tissue below an *effective size* needed to sustain fibrillation [58]. Up to now, those additional strategies have not produced significantly superior outcomes compared with the standard approach [51]. Because atrial segmentation disrupts the electrical conduction and changes the communication network topology within the atria [59], it is expected to alter the causal architecture of the system as well. Quantitative analysis of the causal architecture of the system using multi-electrode catheters may provide patient-specific diagnostic parameters that could potentially serve as a valid endpoint for therapeutic interventions. Further studies are required to link the causal architecture and clinical outcomes.

4.4. Limitations

We used a modified Fitzhugh-Nagumo model, which is a relatively simple model of excitable media. Because our aim was to study the causal relationship between rotors and spiral waves, we used an isotropic, homogeneous model to avoid confounding the causal architecture by tissue anisotropy and inhomogeneity. Further studies are required to assess the impact of tissue anisotropy and inhomogeneity on the causal relationship between rotors and spiral waves in a more realistic geometry of the heart.

4.5. Conclusions

Rotors are not the universal mechanism to maintain spiral waves at all scales in a cardiac system. This finding may account for the conflicting benefit of rotor ablation in clinical studies.

AUTHOR CONTRIBUTIONS

HA, FP-C, MK, and ND: jointly conceived research; HA: designed and performed research, analyzed data, and wrote the manuscript; FP-C, MK, and ND: reviewed the manuscript and provided critical intellectual input.

FUNDING

This work was supported by the Fondation Leducq Transatlantic Network of Excellence (to HA).

SUPPLEMENTARY MATERIAL

The Supplementary Material for this article can be found online at: https://www.frontiersin.org/articles/10.3389/fphy.2018.00030/full#supplementary-material

Supplementary Movie 1 | Random sequential point stimulations. We induce spiral waves by introducing 40 random sequential point stimulations in 40 random components of the lattice. In this example, random sequential point stimulations induce five spiral waves.

Supplementary Movie 2 | Renormalzation group. The movie shows a renormalization group of the cardiac system with two spiral waves by a series of transformation including coarse-graining and length rescaling (scale 1 through 6). For each component, the time series of cardiac excitation is descretized to 1 (black) when excited (during the APD at 90% repolarization, or APD_{90}) or 0 (white) when resting.

REFERENCES

1. Winfree A. Vortex action potentials in normal ventricular muscle. *Ann NY Acad Sci.* (1990) **591**:190–207.
2. Jalife J, Berenfeld O. Molecular mechanisms and global dynamics of fibrillation: an integrative approach to the underlying basis of vortex-like reentry. *J Theor Biol.* (2004) **230**:475–87. doi: 10.1016/j.jtbi.2004.02.024
3. Bedau MA. Weak emergence. *Noûs* (1997) **31**:375–99.
4. Seth AK. Measuring autonomy and emergence via Granger causality. *Artif Life* (2010) **16**:179–96. doi: 10.1162/artl.2010.16.2.16204

5. Bar-Yam Y. *Dynamics of Complex Systems*. Reading, MA: Addison-Wesley (1997).
6. Sayama H. *Introduction to the Modeling and Analysis of Complex Systems*. Geneseo, NY: State University of New York at Geneseo; Open SUNY Textbooks, Milne Library (2015).
7. Qu Z, Xie F, Garfinkel A, Weiss JN. Origins of spiral wave meander and breakup in a two-dimensional cardiac tissue model. *Ann Biomed Eng*. (2000) **28**:755–71. doi: 10.1114/1.1289474
8. Fenton FH, Cherry EM, Hastings HM, Evans SJ. Multiple mechanisms of spiral wave breakup in a model of cardiac electrical activity. *Chaos* (2002) **12**:852–92. doi: 10.1063/1.1504242
9. Cabo C, Pertsov AM, Baxter WT, Davidenko JM, Gray RA, Jalife J. Wave-front curvature as a cause of slow conduction and block in isolated cardiac muscle. *Circ Res*. (1994) **75**:1014–28.
10. Gray R. Theory of rotors and arrhythmias. In: *Cardiac Electrophysiology: From Cell to Bedside*. New York, NY: WB Saunders Co, Ltd. (2014). p. 341–50.
11. Biktashev VN. Drift of spiral waves. *Scholarpedia* (2007) **2**:1836. doi: 10.4249/scholarpedia.1836
12. Lip GYH, Fauchier L, Freedman SB, Van Gelder I, Natale A, Gianni C, et al. Atrial fibrillation. *Nat Rev Dis Primers* (2016) **2**:16016. doi: 10.1038/nrdp.2016.16
13. Narayan SM, Krummen DE, Shivkumar K, Clopton P, Rappel WJ, Miller JM. Treatment of atrial fibrillation by the ablation of localized sources: CONFIRM (Conventional Ablation for Atrial Fibrillation With or Without Focal Impulse and Rotor Modulation) trial. *J Am Coll Cardiol*. (2012) **60**:628–36. doi: 10.1016/j.jacc.2012.05.022
14. Miller JM, Kowal RC, Swarup V, Daubert JP, Daoud EG, Day JD, et al. Initial independent outcomes from focal impulse and rotor modulation ablation for atrial fibrillation: multicenter FIRM registry. *J Cardiovasc Electrophysiol*. (2014) **25**:921–9. doi: 10.1111/jce.12474
15. Narayan SM, Baykaner T, Clopton P, Schricker A, Lalani GG, Krummen DE, et al. Ablation of rotor and focal sources reduces late recurrence of atrial fibrillation compared with trigger ablation alone: extended follow-up of the CONFIRM trial (Conventional Ablation for Atrial Fibrillation With or Without Focal Impulse and Rotor Modulation). *J Am Coll Cardiol*. (2014) **63**:1761–8. doi: 10.1016/j.jacc.2014.02.543
16. Haissaguerre M, Hocini M, Denis A, Shah AJ, Komatsu Y, Yamashita S, et al. Driver domains in persistent atrial fibrillation. *Circulation* (2014) **130**:530–8. doi: 10.1161/CIRCULATIONAHA.113.005421
17. Benharash P, Buch E, Frank P, Share M, Tung R, Shivkumar K, et al. Quantitative analysis of localized sources identified by focal impulse and roter modulation mapping in atrial fibrillation. *Circ Arrhythm Electrophysiol*. (2015) **8**:554–61. doi: 10.1161/CIRCEP.115.002721
18. Gianni C, Mohanty S, Di Biase L, Metz T, Trivedi C, Gökoğlan Y, et al. Acute and early outcomes of focal impulse and rotor modulation (FIRM)-guided rotors-only ablation in patients with nonparoxysmal atrial fibrillation. *Heart Rhythm* (2016) **13**:830–5. doi: 10.1016/j.hrthm.2015.12.028
19. Berntsen RF, Håland TF, Skårdal R, Holm T. Focal impulse and rotor modulation as a stand-alone procedure for the treatment of paroxysmal atrial fibrillation: a within-patient controlled study with implanted cardiac monitoring. *Heart Rhythm* (2016) **13**:1768–74. doi: 10.1016/j.hrthm.2016.04.016
20. Buch E, Share M, Tung R, Benharash P, Sharma P, Koneru J, et al. Long-term clinical outcomes of focal impulse and rotor modulation for treatment of atrial fibrillation: a multicenter experience. *Heart Rhythm* (2016) **13**:636–41. doi: 10.1016/j.hrthm.2015.10.031
21. Aronis KN, Berger RD, Ashikaga H. Rotors: how do we know when they are real? *Circ Arrhythm Electrophysiol*. (2017) **10**:e005634. doi: 10.1161/CIRCEP.117.005634
22. Bar-Yam Y. Multiscale complexity/entropy. *Advs Complex Syst*. (2004) **7**:47–63. doi: 10.1142/S0219525904000068
23. Allen B, Stacey BC, Bar-Yam Y. Multiscale information theory and the marginal utility of information. *Entropy* (2017) **19**:273. doi: 10.3390/e19060273
24. Campbell DT. 'Downward causation' in hierarchically organised biological systems. In: Ayala FJ, Dobzhansky T, editors. *Studies in the Philosophy of Biology: Reduction and Related Problems*. London: Palgrave (1974). p. 179–86.
25. Auletta G, Ellis GF, Jaeger L. Top-down causation by information control: from a philosophical problem to a scientific research programme. *J R Soc Interface* (2008) **5**:1159–72. doi: 10.1098/rsif.2008.0018
26. Davies PCW. The physics of downward causation. In: Clayton P, Davies PCW, editors. *The Re-emergence of Emergence*. Oxford: Oxford University Press (2006). p. 35–52.
27. Davies PCW. The epigenome and top-down causation. *Interface Focus* (2011) **2**:42–8. doi: 10.1098/rsfs.2011.0070
28. Ellis GF. Top-down causation and emergence: some comments on mechanisms. *Interface Focus* (2011) **2**:126–40. doi: 10.1098/rsfs.2011.0062
29. Ashikaga H, James RG. Inter-scale information flow as a surrogate for downward causation that maintains spiral waves. *arXiv preprint arXiv:171110126*. (2017).
30. Hoel EP, Albantakis L, Tononi G. Quantifying causal emergence shows that macro can beat micro. *Proc Natl Acad Sci USA*. (2013) **110**:19790–5. doi: 10.1073/pnas.1314922110
31. Tononi G, Sporns O. Measuring information integration. *BMC Neurosci*. (2003) **4**:31. doi: 10.1186/1471-2202-4-31
32. Nagumo J, Arimoto S, Yoshizawa S. An active pulse transmission line simulating nerve axon. *Proc IRE* (1962) **50**:2061–70.
33. FitzHugh R. Impulses and physiological states in theoretical models of nerve membrane. *Biophys J*. (1961) **1**:445.
34. Rogers JM, McCulloch AD. A collocation-Galerkin finite element model of cardiac action potential propagation. *IEEE Trans Biomed Eng*. (1994) **41**:743–57.
35. Pertsov AM, Davidenko JM, Salomonsz R, Baxter WT, Jalife J. Spiral waves of excitation underlie reentrant activity in isolated cardiac muscle. *Circ Res*. (1993) **72**:631–50.
36. Ashikaga H, James RG. Hidden structures of information transport underlying spiral wave dynamics. *Chaos* (2017) **27**:013106. doi: 10.1063/1.4973542
37. Umapathy K, Nair K, Masse S, Krishnan S, Rogers J, Nash MP, et al. Phase mapping of cardiac fibrillation. *Circ Arrhythm Electrophysiol*. (2010) **3**:105–14. doi: 10.1161/CIRCEP.110.853804
38. Winfree AT. *When Time Breaks Down: The Three-Dimensional Dynamics of Electrochemical Waves and Cardiac Arrhythmias*. Princeton, NJ: Princeton University Press (1987).
39. Goryachev A, Kapral R. Spiral waves in chaotic systems. *Phys Rev Lett*. (1996) **76**:1619.
40. Mermin ND. The topological theory of defects in ordered media. *Rev Moder Phys*. (1979) **51**:591.
41. Bray MA, Wikswo JP. Use of topological charge to determine filament location and dynamics in a numerical model of scroll wave activity. *IEEE Trans Biomed Eng*. (2002) **49**:1086–93. doi: 10.1109/TBME.2002.803516
42. Aronis KN, Ashikaga H. Impact of number of co-existing rotors and inter-electrode distance on accuracy of rotor localization. *J Electrocardiol*. (2018) **51**:82–91. doi: 10.1016/j.jelectrocard.2017.08.032
43. Ashikaga H, Aguilar-Rodríguez J, Gorsky S, Lusczek E, Marquitti FMD, Thompson B, et al. Modelling the heart as a communication system. *J R Soc Interface* (2015) **12**:20141201. doi: 10.1098/rsif.2014.1201
44. Jaynes ET. Information theory and statistical mechanics. *Phys Rev*. (1957) **106**:620.
45. Shannon CE. A mathematical theory of communication. *Bell Syst Tech J*. (1948) **27**:623–56.
46. Kadanoff LP. Scaling laws for Ising models near Tc. *Physics* (1966) **2**: 263–72.
47. Hoel EP. When the map is better than the territory. *Entropy* (2017) **19**:188. doi: 10.3390/e19050188
48. Page RL, Joglar JA, Caldwell MA, Calkins H, Conti JB, Deal BJ, et al. 2015 ACC/AHA/HRS Guideline for the Management of Adult Patients with Supraventricular Tachycardia: a Report of the American College of Cardiology/American Heart Association Task Force on Clinical Practice Guidelines and the Heart Rhythm Society. *Heart Rhythm* (2016) **13**:e136–221. doi: 10.1161/CIR.0000000000000310
49. Haissaguerre M, Jaïs P, Shah DC, Takahashi A, Hocini M, Quiniou G, et al. Spontaneous initiation of atrial fibrillation by ectopic beats originating in the pulmonary veins. *N Engl J Med*. (1998) **339**:659–66.
50. Calkins H, Hindricks G, Cappato R, Kim YH, Saad EB, Aguinaga L, et al. 2017 HRS/EHRA/ECAS/APHRS/SOLAECE expert consensus statement on

catheter and surgical ablation of atrial fibrillation. *Heart Rhythm* (2017) **14**:e275–444. doi: 10.1016/j.hrthm.2017.05.012
51. Verma A, Jiang Cy, Betts TR, Chen J, Deisenhofer I, Mantovan R, et al. Approaches to catheter ablation for persistent atrial fibrillation. *N Engl J Med*. (2015) **372**:1812–22. doi: 10.1056/NEJMoa1408288
52. Sanders P, Hocini M, Jaïs P, Sacher F, Hsu LF, Takahashi Y, et al. Complete isolation of the pulmonary veins and posterior left atrium in chronic atrial fibrillation. Long-term clinical outcome. *Eur Heart J*. (2007) **28**:1862–71. doi: 10.1093/eurheartj/ehl548
53. Chen J, Off MK, Solheim E, Schuster P, Hoff PI, Ohm OJ. Treatment of atrial fibrillation by silencing electrical activity in the posterior inter-pulmonary-vein atrium. *Europace* (2008) **10**:265–72. doi: 10.1093/europace/eun029
54. Jaïs P, Hocini M, Hsu LF, Sanders P, Scavee C, Weerasooriya R, et al. Technique and results of linear ablation at the mitral isthmus. *Circulation* (2004) **110**:2996–3002. doi: 10.1161/01.CIR.0000146917.75041.58
55. Fassini G, Riva S, Chiodelli R, Trevisi N, Berti M, Carbucicchio C, et al. Left mitral isthmus ablation associated with PV isolation: long-term results of a prospective randomized study. *J Cardiovasc Electrophysiol*. (2005) **16**:1150–6. doi: 10.1111/j.1540-8167.2005.50192.x
56. Scherr D, Khairy P, Miyazaki S, Aurillac-Lavignolle V, Pascale P, Wilton SB, et al. Five-year outcome of catheter ablation of persistent atrial fibrillation using termination of atrial fibrillation as a procedural endpoint. *Circ Arrhythm Electrophysiol*. (2015) **8**:18–24. doi: 10.1161/CIRCEP.114.001943
57. Di Biase L, Burkhardt JD, Mohanty P, Mohanty S, Sanchez JE, Trivedi C, et al. Left atrial appendage isolation in patients with longstanding persistent AF undergoing catheter ablation: BELIEF trial. *J Am Coll Cardiol*. (2016) **68**:1929–40. doi: 10.1016/j.jacc.2016.07.770
58. Panfilov AV. Is heart size a factor in ventricular fibrillation? Or how close are rabbit and human hearts? *Heart Rhythm* (2006) **3**:862–4. doi: 10.1016/j.hrthm.2005.12.022
59. Tao S, Way SF, Garland J, Chrispin J, Ciuffo LA, Balouch MA, et al. Ablation as targeted perturbation to rewire communication network of persistent atrial fibrillation. *PLoS ONE* (2017) **12**:e0179459. doi: 10.1371/journal.pone.0179459

Conflict of Interest Statement: The authors declare that the research was conducted in the absence of any commercial or financial relationships that could be construed as a potential conflict of interest.

frontiers in Physiology

REVIEW
published: 09 April 2018
doi: 10.3389/fphys.2018.00356

Modeling the Electrophysiological Properties of the Infarct Border Zone

Caroline Mendonca Costa[1]*, *Gernot Plank*[2], *Christopher A. Rinaldi*[3], *Steven A. Niederer*[1] *and Martin J. Bishop*[1]

[1] School of Biomedical Engineering and Imaging Sciences, King's College London, London, United Kingdom, [2] Department of Biophysics, Medical University of Graz, Graz, Austria, [3] Cardiac Department, St. Thomas' Hospital, London, United Kingdom

Ventricular arrhythmias (VA) in patients with myocardial infarction (MI) are thought to be associated with structural and electrophysiological remodeling within the infarct border zone (BZ). Personalized computational models have been used to investigate the potential role of the infarct BZ in arrhythmogenesis, which still remains incompletely understood. Most recent models have relied on experimental data to assign BZ properties. However, experimental measurements vary significantly resulting in different computational representations of this region. Here, we review experimental data available in the literature to determine the most prominent properties of the infarct BZ. Computational models are then used to investigate the effect of different representations of the BZ on activation and repolarization properties, which may be associated with VA. Experimental data obtained from several animal species and patients with infarct show that BZ properties vary significantly depending on disease's stage, with the early disease stage dominated by ionic remodeling and the chronic stage by structural remodeling. In addition, our simulations show that ionic remodeling in the BZ leads to large repolarization gradients in the vicinity of the scar, which may have a significant impact on arrhythmia simulations, while structural remodeling plays a secondary role. We conclude that it is imperative to faithfully represent the properties of regions of infarction within computational models specific to the disease stage under investigation in order to conduct *in silico* mechanistic investigations.

Keywords: cardiac electrophysiology, myocardial infarct, infarct border zone, gray zone, computational modeling

OPEN ACCESS

Edited by:
Flavio H. Fenton,
Cornell University, United States

Reviewed by:
T. Alexander Quinn,
Dalhousie University, Canada
Candido Cabo,
The City University of New York, United States

***Correspondence:**
Caroline Mendonca Costa
caroline.mendonca_costa@kcl.ac.uk

Specialty section:
This article was submitted to Cardiac Electrophysiology, a section of the journal Frontiers in Physiology

Received: *06 December 2017*
Accepted: *22 March 2018*
Published: *09 April 2018*

Citation:
Mendonca Costa C, Plank G, Rinaldi CA, Niederer SA and Bishop MJ (2018) Modeling the Electrophysiological Properties of the Infarct Border Zone. Front. Physiol. 9:356. doi: 10.3389/fphys.2018.00356

1. INTRODUCTION

Cardiovascular disease represents 31% of all worldwide mortality with Coronary Heart Disease (CHD) responsible for an estimated 41% of these deaths (WHO, 2015). CHD results from the obstruction of a coronary artery causing ischemia, i.e., the interruption of blood supply to the myocardium, which can cause severe ventricular arrhythmias (VA) and sudden cardiac death (SCD) (Janse and Wit, 1989; Rodríguez et al., 2006; Ferrero et al., 2014) as well as irreversible tissue damage, known as myocardial infarction (MI).

Arrhythmias associated with CHD are generally thought to be due to re-entry, however, the cause and specific type of re-entry varies over time after ischemia onset. Specifically, CHD can be divided into three phases according to the type of VA most commonly observed, namely, the acute, sub-acute and healing/healed phases. The acute phase comprises the first hour after ischemia onset. VA in this phase is due to functional re-entry (Liang et al., 2013) or spontaneous activity (Pollard et al., 2002). The sub-acute phase comprises the next 72 h after ischemia onset and

VA in this phase is thought to be due to abnormal automaticity of Purkinje cells that survive in the subendocardium (Fenoglio et al., 1976; Liang et al., 2013). In patients who survive acute and sub-acute ischemia, the myocardium begins to heal. During the healing phase, dead cardiomyocytes are slowly replaced by collagen leading to the formation of a scar with a dense collagenous core surrounded by a thin layer of surviving myocardium, known as the infarct border zone (BZ). Several studies have reported altered electro-anatomical properties at the BZ of healing and healed (chronic) infarcts (Gardner et al., 1985; Ursell et al., 1985), which may be associated with the development of re-entry (Kléber and Rudy, 2004). However, the underlying mechanisms are not fully understood and may differ depending on the specific electro-anatomical changes that occur within the BZ.

The risk of VA is high among patients with chronic infarct and about 12.5% suffer from SCD 2 years post-MI (Raviele et al., 1998). Thus, risk stratification is crucial to identify patients at high risk of developing VA to plan appropriate therapy. Currently, identification of high risk patients largely relies on global measures of left ventricular (LV) function, which poorly reflect electro-anatomical changes underlying the formation of arrhythmias in MI patients. Scar tissue heterogeneity, measured from late gadolinium enhancement (LGE) magnetic resonance imaging (MRI) as the volume of BZ relative to LV volume, has recently been shown to predict VA risk in patients with chronic MI (Schmidt et al., 2007; Kwon et al., 2015) and may improve risk stratification. More recently, computer models built upon patient specific anatomy have been used to predict VA risk in patients with chronic MI with very promising results. Specifically, the Virtual-heart Arrhythmia Risk Predictor (VARP) was shown to be a better predictor of VA than scar heterogeneity and other conventional indices in a cohort of 41 patients Arevalo et al. (2016). Similar approaches have also been employed by other groups to study the effect of scar morphology on VA inducibility (Ringenberg et al., 2012) and to predict VA inducibility and circuit morphology (Chen et al., 2015).

Computer models are a promising strategy to study arrhythmia mechanisms as well as predict arrhythmia risk, as described above. However, building personalized ventricular computer models of patients with MI remains a challenging task. It requires identifying (segmenting) the anatomy of the heart, the infarct scar and the BZ from imaging data and combining it with a mathematical description of the patient's EP based ideally on non-invasive, clinical data, such as the electrocardiogram (ECG). However, the ECG does not allow identifying specific regional differences in EP properties, such as action potential duration (APD) and conduction velocity (CV). Particularly, in the case of computer models of MI, identifying the specific EP properties of the BZ from the ECG is virtually impossible, as the BZ can be as thin as a few hundred micrometers Bakker et al. (1988). Consequently, most computer models rely on experimental data to assign BZ properties. However, experimental results are afflicted with significant uncertainty and may vary depending on the animal species and experimental conditions. As a result, recent image-based computer models of MI have chosen different computational representations of the EP properties of the BZ (McDowell et al., 2011; Ringenberg et al., 2012; Sermesant et al., 2012; Arevalo et al., 2013). These may largely affect generation and sustenance of VA (Cabo and Boyden, 2003; Decker and Rudy, 2010), thus, having important consequences in the interpretation of VA simulations.

The aim of this article is two-fold. First, we review experimental data available in the literature to identify which EP properties of the BZ are most consistently reported and, thus, would be most appropriate to include in computer models of MI. Finally, we use idealized 2D models of scar and BZ to quantify the consequences of different computational representations of the BZ in repolarization characteristics, which may play a role in VA simulations.

2. REVIEW OF EXPERIMENTAL DATA OF THE ELECTROPHYSIOLOGICAL REMODELING WITHIN THE INFARCT BORDER ZONE

In this section, we investigate the EP properties of the infarct BZ based on experimental data on action potentials and ionic currents characteristics as well as morphological properties available in the literature. We focus on data obtained during and after scar formation, which occurs over the first few days or the first weeks after infarction depending on the species (Richardson et al., 2015). Reviews on simulation and experimental studies during acute ischemia can be found elsewhere (Rodríguez et al., 2006; Ferrero et al., 2014).

A schematic representation of the distinct types of BZ are shown in **Figure 1**, where myocardium is represented in pink, the scar core in black and the BZ in gray. The epicardial BZ refers to the layer of myocardium that survives below the epicardial surface, the endocardial BZ refers to the layer that survives below the endocardial surface, and the intramural BZ refers to the BZ in the mid-myocardium surrounding the scar core. As shown in **Figure 1**, the endocardial BZ is divided into the endocardial-central BZ and the endocardial-lateral BZ. Although the epicardial BZ may also contain a lateral BZ, this region was not identified in our literature review. However, we illustrate an epicardial-lateral BZ here for the sake of completeness. Similarly, an intramural BZ is also illustrated in **Figure 1**, although no measurements in this region were found in the literature. When the BZ region was not specified in a study, we use the broad term BZ. While some of the studies included in our review may have confounded BZ with scar isthmus measurements, this was not clear from their methods and so measurements were assumed to be representative of a homogeneous BZ region. As such, we illustrate the scar and BZ as homogeneous structures, without any islands of surviving tissue or isthmuses.

Qualitative findings from the experimental studies found in the literature are summarized in **Table 1**. The species, the BZ region from where samples were obtained, the time period when recordings were made, the EP properties, and the structural properties found in each study are shown. Results range from data obtained *in vivo* and *ex vivo* from canine, feline, swine, murine, and rabbit models of infarct, as well as *ex vivo* data

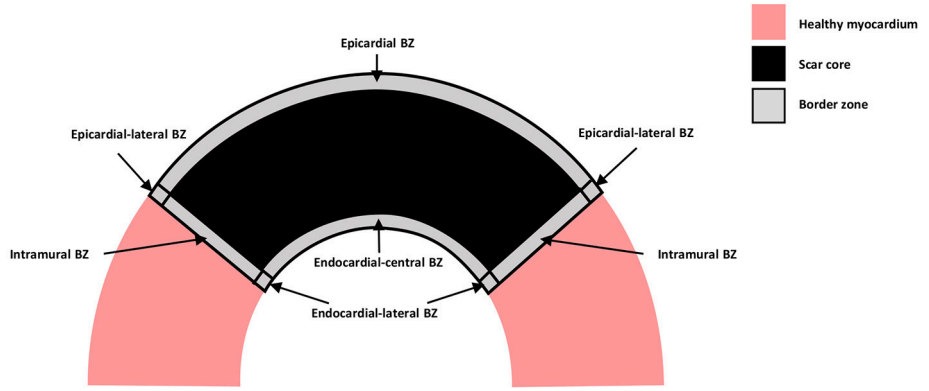

FIGURE 1 | Schematic representation of the distinct types of BZ. Healthy myocardium is represented in pink, scar core in black and BZ in gray.

from patients with prior MI. In the animal models, infarct was induced either via permanent ligation or temporary occlusion of one or more coronary arteries. EP recordings were obtained via several methods, such as micro electrodes, balloon electrodes, suction pipettes, and optical mapping. Morphology of the scars was analyzed via histological slices or confocal microscopy.

In the next two sections we analyse the experimental data presented in **Table 1**. We divided our findings into infarct healing (less than 5 weeks after MI) and healed infarct (at least 5 weeks after MI), based on histological evidence from patients post-MI (Fishbein et al., 1978).

2.1. The Infarct Border Zone During Infarct Healing

2.1.1. Electrophysiological Remodeling

The fast sodium current (I_{Na}) is the main inward current during membrane depolarization and the main determinant of maximum upstroke velocity (MUV) and action potential amplitude (APA) in a single cell. Thus, a reduction in I_{Na} (Pu and Boyden, 1997; Baba et al., 2005) during infarct healing is directly associated with a slower MUV (Spear et al., 1983; Ursell et al., 1985) and reduced APA (Spear et al., 1983; Gardner et al., 1985; Lue and Boyden, 1992) at this stage of MI. A reduction in this current has also been associated with post-repolarization refractoriness (Lue and Boyden, 1992; Pu and Boyden, 1997; Baba et al., 2005).

Following the AP upstroke, I_{Na} starts to deactivate. In most mammals, with exception of the guinea pig (Varro et al., 1993), I_{Na} deactivation is accompanied by activation of the transient outward potassium current (I_{to}). The latter is a repolarizing current and is responsible for the early repolarization phase (notch), which follows depolarization. Accordingly, a reduction in I_{to} (Lue and Boyden, 1992; Dun et al., 2004) is thought to be responsible for the absence of a notch in the AP of cells from the canine epicardial BZ (Lue and Boyden, 1992).

Depolarizing calcium currents are activated following early repolarization. These currents, particularly the L-type calcium current (I_{CaL}), oppose repolarization and it is the balance between these and the repolarizing (potassium) currents that keeps the AP at a plateau in most species, except rat and mice (Varro et al., 1993). Thus, reduced density of the I_{CaL} will generally accelerate repolarization, shortening the APD. Accordingly, reduced density of I_{CaL} was observed in canine BZ (Dun et al., 2004; Baba et al., 2005) and was associated with APD shortening in this species (Baba et al., 2005). This current also plays a major role in calcium dynamics and its impairment is associated with dysfunctional myocyte contraction in rabbits (Litwin and Bridge, 1971).

When I_{CaL} deactivates, membrane repolarization begins. The rapid (I_{Kr}) and slow (I_{Ks}) components of delayed rectifier currents are the main repolarization currents, thus, reduced density of these currents (Jiang et al., 2000) slows repolarization causing APD prolongation. However, APD prolongation was reported only by one study during the healing phase (Lue and Boyden, 1992), while most studies report APD shortening (Spear et al., 1983; Gardner et al., 1985; Ursell et al., 1985; Baba et al., 2005; Chou et al., 2007; Pop et al., 2012) or even normal APD (Mills et al., 2005).

In general, changes in individual ionic currents should be analyzed with caution when studying changes in AP characteristics, such as APA, MUV, and APD, since it is the interaction between several currents which will determine AP characteristics. It is also important to realize that the data listed in **Table 1** was obtained from a variety of species in which ionic currents are expressed to different extents leading to variations in overall AP characteristics (Varro et al., 1993). Thus, changes in a particular ionic current may have different relative effects between cells from different species. Nonetheless, the experimental data in **Table 1** suggests that APD is generally shorter in the BZ during infarct healing despite individual changes in ionic currents and species differences.

2.1.2. Structural Remodeling

CV is influenced by several factors, such as I_{Na} density, GJ conductance and extracellular conductivity. Reduced I_{Na} density (Pu and Boyden, 1997; Baba et al., 2005) and decreased transverse GJ conductance (Yao et al., 2003) are associated with reduced CV in tissue when considered individually (Rohr et al.,

TABLE 1 | Experimental data on EP and structural properties of the BZ.

Study	Species	Stage	Region	EP prop.	Structural prop.
Lue and Boyden, 1992	Dog	5 d	Epi BZ	$\downarrow I_{to}$ $\uparrow APD_{100}$ $\downarrow$APA	–
Pu and Boyden, 1997	Dog	5 d	Epi BZ	$\downarrow I_{Na}$	–
Jiang et al., 2000	Dog	5 d	Epi BZ	$\downarrow I_{Kr}$ $\downarrow I_{Ks}$	–
Dun et al., 2004	Dog	5–14 d 8 w	Epi BZ	$\downarrow I_{to}$ $\downarrow I_{CaL}$ $\downarrow I_{CaL}$	–
Baba et al., 2005	Dog	5 d	Epi BZ	$\downarrow I_{CaL}$ $\downarrow I_{Na}$ $\downarrow APD_{90}$	–
Cabo et al., 2006	Dog	4–5 d	Epi BZ	–	$\downarrow G_{Trans}$ GJ lat $\downarrow$CV
Ursell et al., 1985	Dog	5 d 2 w 8 w	Epi BZ	$\downarrow$MUV $\downarrow APD_{90}$ $\downarrow$ APA nEG $\downarrow APD_{90}$ nAPD nMUV nAPA	nCV Fibrosis $\downarrow$CV iso Disarray Fibrosis
Gardner et al., 1985	Dog	5 d 2 w 8 w	Epi BZ	$\downarrow$MUV $\downarrow APD_{90}$ $\downarrow$APA nEG $\downarrow APD_{90}$ fEG nAPD nMUV nAPA fEG	nCV Fibrosis $\downarrow$CV iso Disarray Fibrosis
Spear et al., 1983	Dog	3–5 d 8–15 d	Epi BZ	$\downarrow$MUV $\downarrow APD_{30}$ $\downarrow$APA $nAPD_{100}$ $\downarrow APD_{30}$ $nAPD_{100}$	–
Luke and Saffitz, 1991	Dog	3–10 w	Epi BZ	–	$\downarrow$GJ density Fibrosis
Peters et al., 1997	Dog	4 d	Epi BZ	–	GJ lat
Yao et al., 2003	Dog	5 d	Epi BZ	–	$\downarrow G_{Trans}$
Pinto et al., 1997	Cat	2–4 m	EndoL BZ	$\downarrow I_{CaL}$	–
Kimura et al., 1986	Cat	2–6 m	EndoL BZ EndoC BZ	$\downarrow APD_{90}$ $\downarrow$APA $\uparrow APD_{90}$	– –
Wong et al., 1982	Cat	2–7 m	EndoL BZ EndoC BZ	$\downarrow APD_{90}$ $\uparrow APD_{90}$	– –
Myerburg et al., 1982	Cat	2–4 m	EndoC BZ	$\uparrow APD_{90}$	Fibrosis
Kimura et al., 1988	Cat	2–4 m	EndoC BZ	$nAPD_{50}$ $nAPD_{90}$	–
Pop et al., 2012	Pig	4 w	Epi BZ	$\downarrow$APD $\downarrow$MUV $\downarrow$APA	$\downarrow$CV Disarray
Denisko et al., 2017	Pig	5 w	BZ	nAPD	–
Mills et al., 2005	Mouse	7 d	Epi BZ	$nAPD_{90}$	$\downarrow CV_{Trans}$ Fibrosis
Rutherford, 2013	Mouse	14 d	BZ	–	$\downarrow CV_{Trans}$ Fibrosis Disarray
Weigand et al., 2016	Mouse	6 w	Epi BZ	$nAPD_{90}$	–
Chou et al., 2007	Rabbit	7 d	BZ	$\downarrow APD_{80}$	–
Lee et al., 2013	Rabbit	5 w	BZ	$\uparrow I_{KAS}$ $\downarrow APD_{80}$	–
Litwin and Bridge, 1971	Rabbit	8 w	BZ	$\downarrow I_{CaL}$ $\uparrow APD_{90}$	–
Walker et al., 2007	Rabbit	8 w	BZ	Abnormal AP	$\downarrow$CV
Spear et al., 1979	Human	1 m+	EndoC BZ	$\uparrow APD_{90}$	Fibrosis

(Continued)

TABLE 1 | Continued

Study	Species	Stage	Region	EP prop.	Structural prop.
Dangman et al., 1982	Human	12 m+	EndoL BZ	$nAPD_{90}$	–
			EndoC BZ	$\uparrow APD_{90}$	–
Smith et al., 1991	Human	–	EndoC BZ	–	GJ lat Fibrosis
					Disarray
Kostin et al., 2003	Human	–	BZ	–	GJ lat Fibrosis
					Disarray
Bakker et al., 1988	Human	16 d+	EndoC BZ	fEG	$\downarrow CV_{Trans}$
					Disarray
					Fibrosis
Pogwizd et al., 1992	Human	4 m+	BZ	fEG	$\downarrow CV_{Trans}$
					Disarray
					Fibrosis

Disease stage is presented in days (d), weeks (w), or months (m). In most studies, a distinction between epicardium (Epi) BZ, endocardial-central (EndoC) BZ, and endocardial-lateral (EndoL) BZ was made. EP properties (prop.) include action potential duration (APD), maximum upstroke velocity (MUV), action potential amplitude (APA), fast sodium current (I_{Na}), L-type calcium current (I_{CaL}), rapid and slow rectifying potassium currents (I_{Kr} and I_{Ks}, respectively), the transient potassium current (I_{to}), the Apamin-sensitive potassium current (I_{KAS}) and electrograms (EG), normal (nEG) or fractionated (fEG). Structural properties include, gap junction (GJ) transverse conductance (G_{trans}) and lateralization (lat), conduction velocity (CV), and the presence of fibrosis or (fiber) disarray. Arrows indicate increased (↑) or decreased (↓) quantities relative to normal myocardium, whereas "n" indicates normal or unchanged characteristics.

1998; Dhillon et al., 2013). Conduction slowing and decreased GJ conductance were observed in canine epicardial BZ tissue 4–5 days after MI (Cabo et al., 2006). However, the relationship between the two was not clear, as GJ remodeling varied between different BZ regions and confounding factors such as ion channel remodeling may have affected measurements of CV. Conversely, no conduction slowing was observed in two other studies on canine epicardial BZ 5 days after MI (Gardner et al., 1985; Ursell et al., 1985). This may be explained by the fact that cells at the canine epicardial BZ were often separated by interstitial edema (Ursell et al., 1985), which will potentially increase extracellular conductivity and compensate for the conduction slowing caused by reduced I_{Na} density and GJ conductance (Cabo and Boyden, 2009). On the other hand, conduction slowing in the direction transverse to fibers was observed in murine at 7 (Mills et al., 2005) and 14 (Rutherford, 2013) days after MI, respectively. However, conduction slowing in these cases was associated with the presence of interstitial fibrosis, which interrupts propagation transverse to fibers causing local propagation delays. Interstitial fibrosis appears after 2 weeks in canine (Gardner et al., 1985; Ursell et al., 1985) and it was occasionally associated with electrogram fractionation, but no apparent conduction slowing at this stage (Gardner et al., 1985).

Spatial distribution of GJ also plays a role in CV. In normal tissue, GJ are mainly located at the ends of cells, called intercalated disks. This characteristic distribution is largely responsible for CV anisotropy, which is slower transverse to fibers and normal to the sheet orientation. Thus, it is intuitive that an increased concentration of GJ at the lateral boundaries of cells, known as GJ lateralization, would lead to decreased anisotropy of CV. GJ lateralization has been observed at the canine epicardial BZ 4 and 5 days after MI (Peters et al., 1997; Cabo et al., 2006) and was associated with improved conduction transverse to fibers (Cabo et al., 2006). However, it is also possible that some of the GJ located at the lateral of remodeled cells are not functional (Matsushita et al., 1999). Thus, fully understanding the role that GJ lateralization at the BZ may play on CV requires further studies.

2.2. The Infarct Border Zone in Healed Infarcts

2.2.1. Electrophysiological Remodeling

2.2.1.1. Epicardial and endocardial-lateral border zones

Calcium sensitive potassium currents are activated by calcium overload and blocked by Apamin (Adelman et al., 2012). Although these currents are not typically present in normal ventricles, the Apamin-sensitive potassium current (I_{KAS}) has recently been found to be upregulated at the BZ of rabbits with healed infarcts (Lee et al., 2013). In addition, reduced I_{CaL} density has been reported in canine (Dun et al., 2004), feline (Pinto et al., 1997), and rabbits (Litwin and Bridge, 1971) with healed infarcts. Both upregulation of I_{KAS} and downregulation of I_{CaL} accelerate repolarization causing APD shortening. In fact, APD shortening was reported both in feline (Pinto et al., 1997) and rabbit (Lee et al., 2013) in association with these currents. APD shortening was also found in feline (Wong et al., 1982; Kimura et al., 1986), although measurements of neither I_{CaL} nor I_{KAS} were reported in those studies. On the other hand, the canine (Gardner et al., 1985; Ursell et al., 1985), porcine (Denisko et al., 2017), murine (Weigand et al., 2016), and human (Dangman et al., 1982) BZ of healed infarcts exhibit normal APD, while APD prolongation has also been found in rabbits with healed infarcts (Litwin and Bridge, 1971).

While altered I_{KAS} and I_{CaL} were associated with APD shortening in feline (Pinto et al., 1997) and rabbit (Lee et al., 2013), changes in individual currents only tell part of the story, as experimental conditions and the stage of MI may also influence APD. The latter is well exemplified in two studies (Gardner et al., 1985; Ursell et al., 1985), where canine epicardial BZ tissue was

studied from 1 day to 8 weeks after MI. These studies report shorter APD at 1 day, 5 days and 2 weeks after MI, where APD is progressively shortened after MI and is shortest at 2 weeks. However, after 2 weeks, the APD begins to increase and returns to normal values after 8 weeks. Similarly, normal APD values were also found in murine epicardial BZ tissue 6 weeks after MI (Weigand et al., 2016), suggesting that the healing process is complete earlier in this species.

Rabbits are a particular case among the studies shown in **Table 1**, as they exhibit a shorter APD_{80} 5 weeks after MI (Lee et al., 2013), but a longer APD_{90} by 8 weeks (Litwin and Bridge, 1971). This discrepancy in APD values reported may be explained by differences in pacing protocols and restitution characteristics. Although both studies observed APD shortening when increasing pacing frequency (Litwin and Bridge, 1971; Lee et al., 2013), the pacing frequency for baseline APD measurements was higher in Lee et al. (2013) (3 Hz) than in Litwin and Bridge (1971) (0.5 Hz). This might explain the shorter baseline APD reported by the former compared to the latter. Walker et al. (2007) also applied higher pacing rates (3–6 Hz) than Litwin and Bridge (1971). However, although abnormal APs were reported in the BZ, the specific characteristics of these APs were not described.

The fact that APD shortening was found in feline 2 months after MI, but not in canine murine, and humans might be explained by differences in the specific coronary occlusion techniques implemented. For instance, the ligation technique employed in the feline experiments (Myerburg et al., 1982; Wong et al., 1982; Kimura et al., 1986, 1988; Pinto et al., 1997) was specifically developed to induce long term EP changes after MI (Myerburg et al., 1977), whereas the ligation technique employed in the murine experiments (Mills et al., 2005; Rutherford, 2013; Weigand et al., 2016) was designed to reduce infarct size and mortality rate after acute ischemia (Maclean et al., 1978), thus, likely attenuating EP remodeling in healed infarcts. Moreover, coronary occlusion followed by reperfusion was performed in canine (Spear et al., 1983) and the total repolarization time (APD_{100}) was normal 5 and 14 days after MI, suggesting that this technique might also attenuate EP remodeling in healed infarcts. Is it worth noting that, reperfusion following coronary occlusion is typical in patients which are treated in hospital for MI. Although this technique may cause what is known as reperfusion injury, the canine results with reperfusion (Spear et al., 1983) point to a faster healing process resulting in less or even no EP remodeling in the clinical setting. This hypotheses is supported by the APD measured at the endocardial-lateral BZ in one patient with healed infarct, which was not significantly different than the APD of remote tissue (Dangman et al., 1982) and by the mean activation recovery interval values, as an APD surrogate, measured at the BZ of swine 5 weeks after MI, which show that values are not significantly different than in normal tissue, neither in the epicardium, nor in the endocardium (Denisko et al., 2017).

2.2.1.2. Endocardial-central border zone

A thin rim (less than 800 μm Bakker et al., 1988) of myocardium is known to survive just below the endocardial surface overlying the core of the infarct scar in humans (Spear et al., 1979; Dangman et al., 1982; Bolick et al., 1986; Bakker et al., 1988; Smith et al., 1991), feline (Myerburg et al., 1982; Wong et al., 1982; Kimura et al., 1986, 1988) and rabbit (Walker et al., 2007), which we refer to as the endocardial-central BZ. Most APD measurements in this region show a longer APD compared with remote (normal) tissue (Spear et al., 1979; Dangman et al., 1982; Myerburg et al., 1982; Wong et al., 1982; Kimura et al., 1986). However, a later study by Kimura et al. (1988) show that APDs in the endocardial-central BZ are not significantly longer than the APD in remote tissue. The authors argue that this discrepancy is likely due to differences in experimental conditions. Specifically, their LV preparation was perfused through the coronary arteries (Kimura et al., 1988), whereas the preparations in the earlier studies were superfused (Myerburg et al., 1982; Wong et al., 1982; Kimura et al., 1986). When LV preparations are superfused, the cells in the mid-myocardium may be hypoxic, resulting in APD shortening. This effect was demonstrated in a recent study using computational models (Campos et al., 2012). Since the endocardial-central BZ is isolated from the mid-myocardium, as it overlies the core of dense fibrosis, this region is less affected by a hypoxic mid-myocardium. Consequently, the APD in the remote tissue is likely to be shorter than in the endocardial-central BZ, as reported in feline (Myerburg et al., 1982; Wong et al., 1982; Kimura et al., 1986) and human (Spear et al., 1979; Dangman et al., 1982) superfused preparations. Thus, considering the likelihood of such a significant experimental artifact highlighted by Kimura et al. (1988) and the fact that no ionic remodeling was found in the feline endocardial-central BZ (Kimura et al., 1986), we conclude that the APD in the endocardial-central BZ of healed infarcts is likely not significantly different from the normal myocardium.

Such experimental artifacts may also have affected the APD measurements reported in the feline endocardial-lateral BZ, which was shorter than both remote and endocardial-central BZ tissue (Myerburg et al., 1982; Wong et al., 1982; Kimura et al., 1986). However, APD values of the endocardial-lateral BZ were not reported in the coronary perfused feline preparations (Kimura et al., 1988). On the other hand, APD values in this region were normal in human superfused preparations (Dangman et al., 1982). Therefore, further experimental studies would be required to determine the effect of superfusion on the APD of the endocardial-lateral BZ.

2.2.2. Structural Remodeling

The presence of fibrosis is frequently reported in the BZ of healed infarcts (Myerburg et al., 1977; Spear et al., 1979; Gardner et al., 1985; Ursell et al., 1985; Bakker et al., 1988; Luke and Saffitz, 1991; Smith et al., 1991; Pogwizd et al., 1992; Kostin et al., 2003). While interstitial fibrosis would impair conduction transverse to fibers (Bakker et al., 1988; Pogwizd et al., 1992), thus, increasing anisotropy, the presence of patchy fibrosis locally blocks propagation both longitudinally and transverse to fibers, leading to non-uniform anisotropy throughout the tissue. Both types of fibrosis are associated with fractionated electrograms (Gardner et al., 1985; Ursell et al., 1985; Bakker et al., 1988; Pogwizd et al., 1992). In addition, fibers in the BZ of

healed infarcts are often reported to be in disarray (Gardner et al., 1985; Ursell et al., 1985; Pogwizd et al., 1992; McGuire et al., 1996; Kostin et al., 2003; Pop et al., 2012). When increased and/or non-uniform anisotropy are combined with fiber disarray, conduction may appear isotropic and slow at the macroscopic scale, whereas local conduction slowing in the transverse direction may occur at the microscopic scale. In fact, slow and isotropic propagation was observed at the BZ of healed canine infarcts (Gardner et al., 1985; Ursell et al., 1985). On the other hand, although GJ lateralization was observed in patients with healed infarcts (Smith et al., 1991; Kostin et al., 2003), its role in propagation at the BZ remains to be fully determined, as previously discussed.

2.2.3. Summary

The experimental findings listed in **Table 1** clearly demonstrate that (1) the EP and structural properties of the BZ vary significantly from 3 days to 12 months after infarct, allowing a clear separation between the healing (3 days to 5 weeks) and healed phases (more than 5 weeks), (2) APD at the BZ is shorter than normal or remote tissue during the healing phase, (3) APD at the BZ in healed infarcts is not significantly different than normal or remote tissue (4) conduction slowing is mostly associated with the presence of fibrosis, which starts to appear at the BZ 7 days after infarct, (5) the BZ of healed infarcts is mostly marked by the presence of fibrosis and fiber disarray leading to slow conduction and loss of anisotropy, respectively.

3. COMPUTATIONAL REPRESENTATIONS OF THE INFARCT BORDER ZONE

Increased dispersion of repolarization has been associated with life-threatening arrhythmias (Kléber and Rudy, 2004; Clayton and Holden, 2005; Coronel et al., 2009). Repolarization dispersion is mainly determined by the spatial distribution of repolarization times in cardiac tissue, which are in turn determined by local APD and CV. Thus, changes in the spatial distribution of APD and CV may introduce repolarization heterogeneity, increasing dispersion of repolarization, in turn affecting predicted arrhythmia vulnerability. Experimental data presented in **Table 1** shows that APD may be shorter or longer at the BZ depending on the stage of infarct healing, species and the specific BZ region, while slow conduction and fiber disarray were a common find at the BZ of healed infarcts. However, the consequences of changes in APD, CV and fiber orientation at the BZ on the spatial distribution and resulting dispersion of repolarization in the vicinity of the scar are unclear. Thus, we created idealized 2D computational models of scar and BZ, where APD, tissue conductivities and fiber orientation are modified at the BZ. We simulated steady-state activation and repolarization sequences and computed local activation and repolarization times and gradients of repolarization times. The cellular action potential and 2D tissue models are described in the next section followed by simulation results.

3.1. Idealized Computational Models

We created modified AP models based on the Ten Tusscher model of human ventricular cells (ten Tusscher et al., 2006), where one model has a longer APD and the other has a shorter APD. A longer APD was obtained by decreasing the conductance of the I_{Ks} current, g_{Ks}, to 50% of the control value, whereas a shorter APD was obtained by increasing g_{Ks} to 200% of the control value. We chose g_{Ks}, as it yields the most significant effect on the APD of the Ten Tusscher model (Mirams et al., 2014). The APD of the shorter and longer APD models were approximately 40 ms shorter and longer than the control value, respectively, based on APD values found in the literature (Litwin and Bridge, 1971; Ursell et al., 1985). The APs generated by the two modified models as well as the control model with unmodified parameters are shown in **Figure 2A**.

A rectangular tissue setup with a circular scar was created to investigate changes in the spatial distribution of repolarization gradients for different computational representations of the BZ. Specifically, a 30×30 mm^2 finite element (FE) grid of triangular elements with mean edge length of 50 μm was created. A schematic representation of our tissue setup is shown in **Figure 2B**. The scar core was modeled as an insulator by removing the elements defined as scar core from the FE grid. This simple representation was chosen over a more realistic anatomical representation of the myocardium and scar to avoid confounding factors, such as ventricular wall and scar shape, scar location and transmurality, as well as apico-basal and transmural fiber rotation.

The cardiac monodomain model was used to simulate electrical propagation in the tissue. Normal anisotropic bulk conductivities were set to 0.1890 and 0.0690 S/m in the longitudinal and transverse directions, respectively. Using an automatic parameterization approach (Costa et al., 2013), these conductivities yield velocities of 0.6 and 0.4 m/s, consistent with velocities in normal ventricular myocardium (Caldwell et al., 2009). The computational representations of the EP properties of the BZ were based on the findings listed in **Table 1**. These include: shorter, normal, or longer APD, normal conductivities, decreased transverse conductivity representing slow transverse propagation due to the presence of interstitial fibrosis, or decreased isotropic conductivities representing slow isotropic propagation, and horizontally or randomly oriented fibers representing normal fiber alignment and fiber disarray, respectively. The decreased transverse conductivity value was set to 10% of the normal value, as done in recent simulations studies (Arevalo et al., 2013, 2016), yielding a velocity of 0.12 m/s. The isotropic conductivities were computed based on the CV measured at the BZ with decreased transverse conductivities and randomly aligned fibers (0.4 m/s) using an automatic approach (Costa et al., 2013). The conductivity values used are shown in **Table 2**. A cell capacitance of $1\mu F/cm^2$ and a surface-to-volume ratio of 0.14 μm^{-1} were used in all simulations.

The monodomain equation coupled with the Ten Tusscher ionic model was solved using the Cardiac Arrhythmia Research Package (CARP) (Vigmond et al., 2003, 2008). The cell model was stimulated 100 times prior to tissue simulations to achieve steady-state. The final state of gating variables was saved and given as input to the tissue simulations. The tissue was then stimulated 5 times at a constant cycle length of 500 ms to achieve steady-state. Activation time was computed as the time tissue

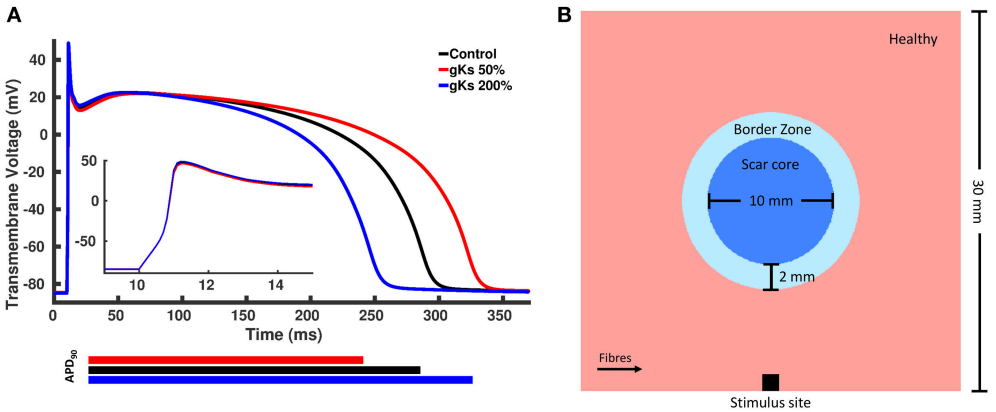

FIGURE 2 | (A) Action potentials of the control and two modified models. The blue line represents the model with shorter action potential duration (APD) obtained by increasing the conductance of the slow rectifying potassium current, g_{Ks}, to 200% of the control value, whereas the red line represents the model with longer APD obtained by decreasing g_{Ks} to 50% of the control value and the black line represented the control model with unchanged parameters. **(B)** Rectangular tissue model with a circumferential scar. The whole tissue measures 30 mm × 30 mm, where the scar core measures 10 mm in diameter and is surrounded by a 2 mm thick BZ. Healthy myocardium is represented in pink, scar core in dark blue and BZ in light blue. Fibers in healthy myocardium are always aligned with the x axis, whereas at the BZ, fibers are either aligned with the x axis or randomly oriented. Stimuli are delivered at the center of the bottom tissue edge.

TABLE 2 | Conductivity types and values used in the 2D simulations.

Type	Longitudinal (S/m)	Transverse (S/m)
Normal anisotropic	0.1890	0.0690
Decreased transverse	0.1890	0.0069
Decreased isotropic	0.0689	0.0689

reached a threshold of −20 mV and repolarization time was computed as the time tissue reached a threshold of −70 mV after depolarization. The repolarization gradient was computed as the magnitude of the spatial gradient of the repolarization time at each grid point.

3.2. Activation Times

The activation times for four computational representations of the BZ with normal APD, the conductivities shown in **Table 2**, and horizontal and random fibers are shown in **Figure 3**. The activation sequences for the BZ with normal conductivities, with decreased transverse conductivities and random fibers, and with reduced isotropic conductivities are very similar to each other. Particularly, the activation sequences of the latter two are nearly identical. On the other hand, an abrupt transition from normal to very slow conduction (30% slower) when the BZ is represented with decreased transverse conductivities and horizontal fibers causes a significant activation delay. This effect is seen as crowding of isolines at the bottom of the BZ on the second left panel of **Figure 3**.

3.3. Repolarization Times and Gradients

Repolarization times and gradients computed for each model are shown in **Figure 4**. The repolarization time maps shown in the left column describe the repolarization sequence for each AP model. Note that the presence of a longer or shorter APD at the BZ distorts the isolines, which accumulate at the bottom and top edges of the BZ for the longer and shorter APD models, respectively. Where the isolines accumulate, large repolarization gradients are seen in the second to fifth columns, left to right. Particularly, gradients above 5 ms/mm extend up to 50 mm around the BZ when APD is shortened at the BZ and up to 30 mm when APD is prolonged for all conductivities. Similar to the activation times, the different conductivities also have a less prominent effect on the spatial distribution of repolarization gradients. However, when the transverse conductivity is severely reduced thus reducing electrotonic load in the transverse direction, gradients become sharper and the spatial pattern is distorted. Particularly, decreased transverse conductivity introduces large sharp gradients at the top and bottom edges of the BZ when combined with horizontally aligned fibers, whereas, small patches of large gradients appear when decreased transverse conductivity is combined with randomly oriented fibers. Macroscopically, the spatial distribution of gradients of the model with decreased transverse conductivity and randomly oriented fibers is similar to the models with normal conductivity and decreased isotropic conductivities and horizontally aligned fibers. It is worth mentioning that the scale of gradients (0–5 ms/mm) was chosen for visualization purposes only. The minimum repolarization gradient required for unidirectional block was determined experimentally as 3.2 ms/mm (Laurita and Rosenbaum, 2000). The repolarization gradients in our simulations were often much larger than 3.2 ms/mm, being as large as 25 ms/mm at the edge of the BZ in the models with altered APD, decreased transverse conductivity and horizontal fibers.

4. DISCUSSION

In this study, we presented a literature review on experimental data of the EP and structural properties of the infarct BZ. Experimental data show that BZ properties change over time

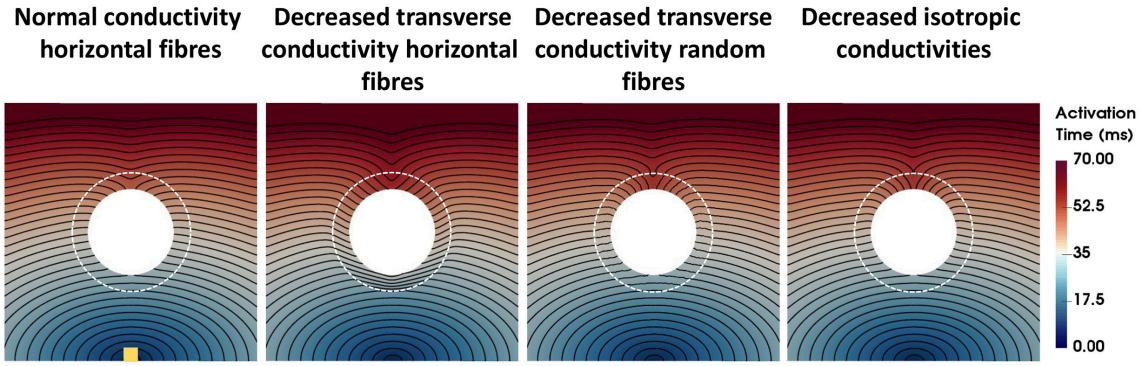

FIGURE 3 | Activation times for four computational representations of the BZ with normal APD. The Scar core is shown as a white filled circle, whereas the interface of BZ with normal tissue is marked as a dashed white circle. The stimulus site is represented by the yellow square at the bottom left panel. The stimulus site was the same for all simulations. Activation times ranging from 0 ms (blue) to 70 ms (red) are shown for the four models. The columns show, from left to right, the models with normal conductivity, decreased transverse conductivity with horizontal fibers, decreased transverse conductivity with random fibers, and decreased isotropic conductivities in the BZ.

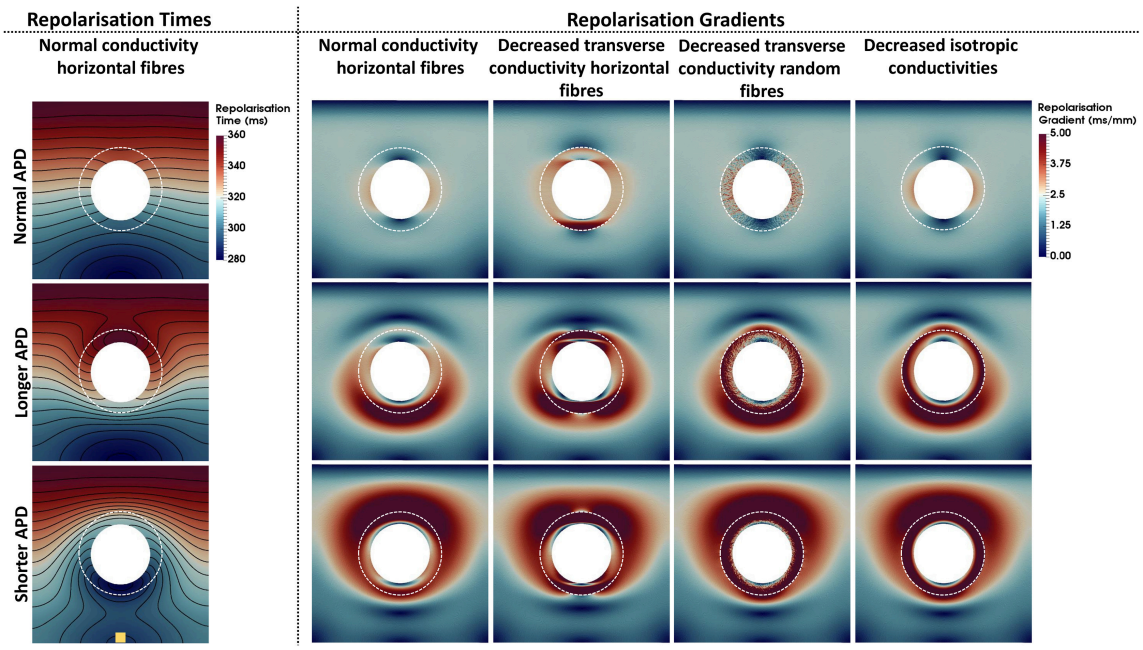

FIGURE 4 | Repolarization times and gradients computed for the 12 computational representations of the BZ. The Scar core is shown as a white filled circle, whereas the interface of BZ with normal tissue is marked as a dashed white circle. The stimulus site is represented by the yellow square at the bottom left panel. The stimulus site was the same for all simulations. The left column shows the repolarization time maps. Repolarization times ranging from 280 ms (blue) to 360 ms (red) are shown for the models with normal conductivities and horizontal fibers. The second to fifth columns from left to right show the repolarization gradients. Gradients range from 0 ms/mm (dark blue) to 5 ms/mm (dark red). The upper, central, and bottom rows show the models where the APD was set to normal, longer, or shorter than normal tissue, respectively. The second to fifth columns show, from left to right, the models with normal conductivity, decreased transverse conductivity with horizontal fibers, decreased transverse conductivity with random fibers, and decreased isotropic conductivities in the BZ.

after coronary occlusion. During infarct healing (<5 weeks), the majority of studies find that the BZ exhibits a shorter APD, slower MUV and decreased APA than normal and or remote tissue. Two weeks following occlusion fibrosis starts to appear and this coincides with conduction slowing. As the infarct heals (>5 weeks), APD, MUV and APA return to normal values in the majority of studies independent of species. We used idealized computational models to study the impact of these different electrophysiological and structural changes reported to occur within the BZ on repolarization gradients within the vicinity of regions of infarct scar. Our simulation results show that repolarization gradients, as a proxy for arrhythmogenic risk, are highly dependent on the specific conductivity and APD values as well as fiber orientation used to represent the

BZ. Unsurprisingly, those models with specific APD alterations assigned to BZ showed the largest repolarization gradients. These findings thus highlight the need to accurately model the BZ in computer models that are based on experimental data.

4.1. Impact of Different Computational Representations of the Infarct Border Zone on Activation and Repolarization

The experimental findings listed in **Table 1** demonstrate that APD is shorter than normal during infarct healing, whereas APD in healed infarcts is likely normal. When implementing local differences in APD in our computer models, repolarization gradients as large as 25 ms/mm appear in and around the BZ. In general, the intrinsic APD of a cell, i.e., the APD defined by ionic properties, is smoothed out when cells are coupled due to electrotonic interaction between neighboring cells. This so-called electrotonic effect is modulated by tissue conductivity, with larger conductivities leading to more smoothing. In fact, despite the large difference in APD between cells of healthy and BZ tissue (∼40 ms), repolarization gradients due to longer or shorter APD are smoothed out between the two regions for all BZ conductivites, but to different degrees (**Figure 4**). Particularly, reduced transverse conductivity leads to decreased electrotonic load in the transverse direction, introducing sharp gradients at the BZ and increasing spatial heterogeneity. This effect is observed both with horizontally and randomly aligned fibers, however, large gradients are restricted to small localized regions within the BZ when fibers are randomly aligned. On the other hand, APD differences are smoothed out to a larger extent with normal and reduced isotropic conductivities.

It is worth mentioning that, the sharp gradients observed in the case of decreased transverse conductivity are a result of an extreme reduction in conductivity. To investigate whether a gradual transition between healthy and BZ tissue would affect results, we performed one additional simulation, where we implement a smooth transition between healthy and BZ tissue for the case of decreased transverse conductivity (see Figure S1 in Supplementary Material). This approach resulted in a slightly smoother repolarization gradient, but did not qualitatively alter our results and conclusions. Moreover, since the exact nature of such a gradual reduction in conductivity is not currently known, employing such approach would require a detailed modeling investigation which is out of the scope of this study.

Several experimental studies listed in **Table 1** report decreased CV at the BZ ranging from 50% (Mills et al., 2005) to 10% (Gardner et al., 1985; Ursell et al., 1985) slower. However, decreased conductivities yielding slower conduction in the BZ only significantly affected activation times (**Figure 3**) and repolarization gradients (**Figure 4**) in our simulations when the transverse velocity was reduced to 30% of the normal value (0.12 m/s instead of 0.4 m/s).

In general, slow conduction in the BZ is associated with the presence of interstitial and patchy fibrosis as well as fiber disarray during late infarct healing and in healed infarcts. Our simulations show that the combination of interstitial fibrosis (represented by decreased transverse conductivity) and fiber disarray (represented by randomly aligned fibers) lead to spatial distributions of repolarization gradients that are macroscopically very similar to those obtained with decreased isotropic conductivities. These findings thus indicate that conduction in the BZ of infarcts older than 2 weeks is likely slow and isotropic, as reported in the canine epicardial BZ of healed infarcts (Ursell et al., 1985).

Based on experimental findings and our simulation results, we conclude that the macroscopic EP properties of BZ are best represented by (1) reduced MUV, APA and APD without conductivity changes during early (<7 days) infarct healing, (2) shorter APD and decreased isotropic conductivities during late infarct healing (7 days to 5 weeks), and (3) normal APD and decreased isotropic conductivities in healed (more than 5 weeks) infarcts, regardless of the specific sub-region (endo-central, endo-lateral, epi).

4.2. The Role of Myofibroblasts

Myofibroblasts are largely responsible for tissue repair following cardiac injury, particularly infarction (Baum et al., 2011). Recently, myofibroblasts have been found to form hetero-cellular connections at the BZ of healed cryoinjury scars (Quinn et al., 2016), however, their contribution to the electrical properties of the infarct BZ remains unclear. Due to their more positive resting potential relative to cardiomyocytes, myofibroblasts coupled to cardiomyocytes may act as an electrical sink affecting excitability, CV and APD (Rohr, 2012). These changes might be associated with increased likelihood of arrhythmia (Rohr, 2012) depending on myofibroblast density (McDowell et al., 2011).

Although the data presented in **Table 1** did not explicitly include myofibroblasts, any effect they might have had in the electrical properties of the BZ would be implicitly accounted for in measurements of AP characteristics and CV. Thus, we do not expect the presence of myofibroblasts to significantly alter our conclusions based on the experimental data and simulation results presented in this study.

4.3. Comparison With Recent Simulation Studies

Recent simulation studies using image-based models of infarct have relied on experimental data to model the EP properties of the BZ. Specifically, the BZ was modeled with reduced MUV and APA (Arevalo et al., 2013, 2008, 2016; McDowell et al., 2011; Rantner et al., 2012; Ringenberg et al., 2012; Ashikaga et al., 2013; Deng et al., 2015, 2016) and longer APD (Arevalo et al., 2013, 2008, 2016; McDowell et al., 2011; Ng et al., 2012; Rantner et al., 2012; Ringenberg et al., 2012; Ashikaga et al., 2013; Deng et al., 2015, 2016). Altered AP characteristics in the BZ were obtained by modifying individual ionic currents (Arevalo et al., 2013, 2008, 2016; McDowell et al., 2011; Rantner et al., 2012; Ringenberg et al., 2012; Ashikaga et al., 2013; Deng et al., 2015, 2016) based on experimental measurements of canine 5 days after MI (Pu and Boyden, 1997; Jiang et al., 2000; Yao et al., 2003; Dun et al., 2004), which lead to a longer APD (Decker and Rudy, 2010), or based on data obtained from feline 2 months after MI (Myerburg et al., 1982). However, while decreased MUV and APA are reported

in canine (Spear et al., 1979; Ursell et al., 1985) during infarct healing, most experimental data listed in **Table 1** show a shorter APD in the same phase, particularly 5 days after infarct (Spear et al., 1983; Gardner et al., 1985; Ursell et al., 1985; Baba et al., 2005).

The transverse conductivity was reduced to 10% of the normal value (Arevalo et al., 2008, 2013, 2016; McDowell et al., 2011; Rantner et al., 2012; Ashikaga et al., 2013; Deng et al., 2015, 2016) to represent decreased gap junctional conductance in the canine epicardial BZ 5 days after infarct (Yao et al., 2003). Although the relationship between conduction slowing transverse to fibers and GJ remodeling is not entirely clear (Cabo et al., 2006), slow transverse conduction was reported in murine 7 days after MI (Mills et al., 2005), where the authors report the presence of fibrosis, but do not report fiber disarray. This suggests that representing the BZ with reduced transverse conductivity may be appropriate in the presence of fibrosis without fiber disarray. The BZ was also represented with conductivity 3 times slower than healthy myocardium (Ng et al., 2012), consistent with the values estimated in porcine ventricles (Pop et al., 2012). However, the authors used an isotropic setup, where changes in fiber orientation cannot be represented.

4.4. Consequences for Arrhythmia Simulations

Re-entrant arrhythmias in patients with MI typically originate at the scar, particularly at the BZ (Bakker et al., 1988; Pogwizd et al., 1992). The core of the scar alone creates an area of anatomical, or fixed, conduction block, providing a substrate for anatomical re-entry. In the case of anatomical re-entry, the minimal length of the re-entrant pathway has to exceed the wavelength of excitation (Rohr et al., 1998), which can be defined as the product of CV and effective refractory period, which is largely determined by APD. The experimental data presented in this study shows that the BZ is characterized by short APD during infarct healing and slow conduction both during healing and in healed infarcts. Thus, the specific EP properties of the BZ may shorten the wavelength and increase the likelihood of arrhythmia.

While slow conduction is in general associated with increased arrhythmogenesis (Rohr et al., 1998; Kléber and Rudy, 2004), reduction of the transverse conductivity leading to slow conduction in the direction transverse to fibers, will shorten the wavelength in one direction increasing the chance of unidirectional block and re-entry (Saffitz and Kléber, 2012). This scenario may cause a type of re-entry know as anisotropic re-entry, which is characterized by conduction block in the transverse direction, owing to reduced transverse conductivity, but successful conduction in the longitudinal direction (Spach and Josephson, 1994). Decreased transverse conductivities also lead to large repolarization gradients in the BZ, which may also be associated with functional re-entry (Kléber and Rudy, 2004), although to a lesser extent. On the other hand, altered APD at the BZ leads to much larger repolarization gradients. Particularly, a shorter APD will also shorten the wavelength, making the formation of a sustained re-entrant circuit more likely. On the other hand, a longer APD at the BZ may be arrhythmogenic in the presence of an isthmus (Connolly and Bishop, 2016), where propagation is initially blocked, due to increased refractoriness, but might enter the isthmus creating a re-entrant circuit.

Increased refractoriness may also be caused by reduced I_{Na}. Specifically, reduced I_{Na} in canine 5 days after MI (Lue and Boyden, 1992; Pu and Boyden, 1997; Baba et al., 2005) decreases excitability leading to post-repolarization refractoriness and thus an elongated effective refractory period (ERP) (Pu and Boyden, 1997). Thus, while the APD of a BZ cell may be shorter at this stage of MI the ERP may be longer (Gough et al., 1985; Pu and Boyden, 1997) potentially affecting arrhythmia mechanisms. While we have not included changes in I_{Na} in our computational models, the role of post-repolarization refractoriness in propagation block has been investigated in recent simulation studies (Cabo and Boyden, 2003; Decker and Rudy, 2010). In fact, post-repolarization refractoriness due to reduced I_{Na} was shown to be a major determinant of the vulnerable window for conduction block under fast pacing rates (Decker and Rudy, 2010).

In the case of chronic infarcts, our simulations show that the presence of interstitial fibrosis and fiber disarray may lead to large but localized repolarization gradients, as these gradients are mostly smoothed out by electrotonic interaction with the healthy tissue. In certain scenarios, these localized gradients may be sufficient to cause uni-directional conduction block of a nearby ectopic focus, which are known to be more likely to occur in the BZ tissue (Bakker et al., 1988; Pogwizd et al., 1992). Alternatively, they may cause heterogeneous conduction slowing of a preceding wavefront or potentially initiate wavebreak. Overall slow conduction in the BZ leading to wavelength shortening may contribute to anatomical re-entry, as an ectopic focus originating near the scar (Bakker et al., 1988; Pogwizd et al., 1992) may encounter a pathway larger than the wavelength and, thus, generate a re-entrant circuit. Thus, in this scenario, the anatomical properties of the scar and its BZ may play a more prominent role in re-entry than AP characteristics.

In summary, the remodeled infarct BZ may be associated with increased risk of re-entrant arrhythmias and the specific mechanism of re-entry will depend on the EP and structural properties of the BZ. These, in turn, depend on the specific stage of infarct healing. Thus, accurately modeling the EP properties of the BZ according to the stage of MI being modeled is crucial for arrhythmia simulations which aim at understanding arrhythmia mechanism and, particularly, predicting arrhythmia risk in patients with infarct.

AUTHOR CONTRIBUTIONS

Jointly developed the structure and arguments for the paper: CMC, MB, SN. Performed the literature review and experiments: CMC. Analyzed the data: CMC, MB, SN. Wrote the first draft of the manuscript: CMC. Contributed to the writing of the manuscript: MB, SN, GP, CR. Agree with manuscript results and conclusions: CMC, MB, SN, GP, CR. Made critical revisions

and approved final version: CMC, MB, SN, GP, CR. All authors reviewed and approved of the final manuscript.

FUNDING

The research was funded/supported by the National Institute for Health Research (NIHR) Biomedical Research Centre and CRF based at Guy's and St Thomas' NHS Foundation Trust and King's College London. The views expressed are those of the author(s) and not necessarily those of the NHS, the NIHR or the Department of Health. This work was also supported by the Wellcome EPSRC Centre for Medical Engineering at King's College London (WT 203148/Z/16/Z), by the Medical Research Council (MR/N011007/1), and by the British Heart Foundation (RE/08/003, PG/15/91/31812, and PG/16/81/32441).

ACKNOWLEDGMENTS

The authors kindly thank Dr. Godfrey Smith and Dr. Bruce Smaill for helpful discussion.

SUPPLEMENTARY MATERIAL

The Supplementary Material for this article can be found online at: https://www.frontiersin.org/articles/10.3389/fphys.2018.00356/full#supplementary-material

REFERENCES

Adelman, J. P., Maylie, J., and Sah, P. (2012). Channels: form and function. *Annu. Rev. Physiol.* 74, 245–69. doi: 10.1146/annurev-physiol-020911-153336

Arevalo, H., Plank, G., Helm, P., Halperin, H., and Trayanova, N. (2013). Tachycardia in Post-Infarction Hearts: insights from 3D Image-Based Ventricular Models. *PLoS ONE* 8:e68872. doi: 10.1371/journal.pone.0068872

Arevalo, H. J., Helm, P. A., and Trayanova, N. A. (2008). Development of a model of the infarcted canine heart that predicts arrhythmia generation from specific cardiac geometry and scar distribution. *Comput. Cardiol.* 35, 497–500. doi: 10.1109/CIC.2008.4749087

Arevalo, H. J., Vadakkumpadan, F., Guallar, E., Jebb, A., Malamas, P., Wu, K. C., et al. (2016). Arrhythmia risk stratification of patients after myocardial infarction using personalized heart models. *Nat. Commun.* 7:11437. doi: 10.1038/ncomms11437

Ashikaga, H., Arevalo, H., Vadakkumpadan, F., Blake, R. C., Bayer, J. D., Nazarian, S., et al. (2013). Feasibility of image-based simulation to estimate ablation target in human ventricular arrhythmia. *Heart Rhythm* 10, 1109–1116. doi: 10.1016/j.hrthm.2013.04.015

Baba, S., Dun, W., Cabo, C., and Boyden, P. A. (2005). Remodeling in cells from different regions of the reentrant circuit during ventricular tachycardia. *Circulation* 112, 2386–2396. doi: 10.1161/CIRCULATIONAHA.105.534784

Baum, J., Duffy, H. S., and Israel, B. (2011). Fibroblasts and Myofibroblasts: what are we talking about? *J. Cardiovasc. Pharmacol.* 57, 376–379. doi: 10.1097/FJC.0b013e3182116e39

Bolick, D., Hackel, D., Reimer, K., Ideker, R. E. (1986). Quantitative analysis of myocardial infarct structure in patients with ventricular tachycardia. *Circulation* 74, 1266–1279. doi: 10.1161/01.CIR.74.6.1266

Cabo, C., and Boyden, P. A. (2003). Electrical remodeling of the epicardial border zone in the canine infarcted heart: a computational analysis. *Am. J. Physiol. Heart Circ. Physiol.* 284, H372–H384. doi: 10.1152/ajpheart.00512.2002

Cabo, C., and Boyden, P. A. (2009). Extracellular space attenuates the effect of gap junctional remodeling on wave propagation: a computational study. *Biophys. J.* 96, 3092–3101. doi: 10.1016/j.bpj.2009.01.014

Cabo, C., Yao, J., Boyden, P. A., Chen, S., Hussain, W., Duffy, H. S., et al. (2006). Heterogeneous gap junction remodeling in reentrant circuits in the epicardial border zone of the healing canine infarct. *Cardiovas. Res.* 72, 241–249. doi: 10.1016/j.cardiores.2006.07.005

Caldwell, B. J., Trew, M. L., Sands, G. B., Hooks, D. A., LeGrice, I. J., and Smaill, B. H. (2009). Three distinct directions of intramural activation reveal nonuniform side-to-side electrical coupling of ventricular myocytes. *Circ. Arrhyth. Electrophysiol.* 2, 433–440. doi: 10.1161/CIRCEP.108.830133

Campos, F. O., Prassl, A. J., Seemann, G., Dos Santos, R. W., Plank, G., and Hofer, E. (2012). Influence of ischemic core muscle fibers on surface depolarization potentials in superfused cardiac tissue preparations: a simulation study. *Med. Biol. Eng. Comput.* 50, 461–472. doi: 10.1007/s11517-012-0880-1

Chen, Z., Sohal, M., Voigt, T., Sammut, E., Tobon-Gomez, C., Child, N., et al. (2015). Myocardial tissue characterization by cardiac magnetic resonance imaging using T1 mapping predicts ventricular arrhythmia in ischemic and non-ischemic cardiomyopathy patients with implantable cardioverter-defibrillators. *Heart Rhythm.* 12, 792–801. doi: 10.1016/j.hrthm.2014.12.020

Chou, C.-C., Zhou, S., Hayashi, H., Nihei, M., Liu, Y.-B., Wen, M.-S., et al. (2007). Remodelling of action potential and intracellular calcium cycling dynamics during subacute myocardial infarction promotes ventricular arrhythmias in Langendorff-perfused rabbit hearts. *J. Physiol.* 580, 895–906. doi: 10.1113/jphysiol.2006.120659

Clayton, R. H., and Holden, A. V. (2005). Dispersion of cardiac action potential duration and the initiation of re-entry: a computational study. *Biomed. Eng. Online* 4:11. doi: 10.1186/1475-925X-4-11

Connolly, A. J., and Bishop, M. J. (2016). Computational representations of myocardial infarct scars and implications for arrhythmogenesis. *Clin. Med. Insights Cardiol.* 10, 27–40. doi: 10.4137/CMC.S39708

Coronel, R., Wilms-Schopman, F. J., Opthof, T., and Janse, M. J. (2009). Dispersion of repolarization and arrhythmogenesis. *Heart Rhythm.* 6, 537–543. doi: 10.1016/j.hrthm.2009.01.013

Costa, C. M., Hoetzl, E., Rocha, B. M., Prassl, A. J., and Plank, G. (2013). Automatic parameterization strategy for cardiac flectrophysiology simulations. *Comput. Cardiol.* 40, 373–376.

Dangman, K. H., Danilo, P., Hordof, A. J., Mary-Rabine, L., Reder, R. F., and Rosen, M. R. (1982). Electrophysiologic characteristics of human ventricular and purkinje fibers. *Circulation* 65, 362–369. doi: 10.1161/01.CIR.65.2.362

de Bakker, J. M., van Capelle, F. J., Janse, M. J., Wilde, A. A., Coronel, R., Becker, A. E., et al. (1988). Reentry as a cause of ventricular tachycardia in patients with chronic ischemic heart disease: electrophysiologic and anatomic correlation. *Circulation* 77, 589–606. doi: 10.1161/01.CIR.77.3.589

Decker, K. F., and Rudy, Y. (2010). Ionic mechanisms of electrophysiological heterogeneity and conduction block in the infarct border zone. *Am. J. Physiol. Heart. Circ. Physiol.* 299, H1588–H1597. doi: 10.1152/ajpheart.00362.2010

Deng, D., Arevalo, H., Pashakhanloo, F., Prakosa, A., Ashikaga, H., McVeigh, E., et al. (2015). Accuracy of prediction of infarct-related arrhythmic circuits from image-based models reconstructed from low and high resolution MRI. *Front. Physiol.* 6:282. doi: 10.3389/fphys.2015.00282

Deng, D., Arevalo, H. J., Prakosa, A., Callans, D. J., and Trayanova, N. A. (2016). A feasibility study of arrhythmia risk prediction in patients with myocardial infarction and preserved ejection fraction. *Europace* 18, iv60–iv66. doi: 10.1093/europace/euw351

Denisko, D., Oduneye, S., Krahn, P., Ghate, S., Lashevsky, I., Wright, G., et al. (2017). "Analysis of activation-recovery intervals from intra-cardiac electrograms in a pre-clinical chronic model of myocardial infarction," in *Functional Imaging and Modelling of the Heart. FIMH 2017. Lecture Notes in Computer Science*, Vol. 10263, eds M. Pop and G. Wright (Cham: Springer), 280–288. doi: 10.1007/978-3-319-59448-4_27

Dhillon, P. S., Gray, R., Kojodjojo, P., Jabr, R., Chowdhury, R., Fry, C. H., et al. (2013). Relationship between gap-junctional conductance and conduction velocity in mammalian myocardium. *Circ. Arrhyth. Electrophysiol.* 6, 1208–1214. doi: 10.1161/CIRCEP.113.000848

Dun, W., Baba, S., Yagi, T., and Boyden, P. A. (2004). Dynamic remodeling of K+ and Ca2+ currents in cells that survived in the epicardial border zone of canine healed infarcted heart. *Am. J. Physiol. Heart. Circ. Physiol.* 287, H1046–H1054. doi: 10.1152/ajpheart.00082.2004

Fenoglio, J. J., Albala, A., Silva, F. G., Friedman, P. L., and Wit, A. L. (1976). Structural basis of ventricular arrhythmias in human myocardial infarction: a hypothesis. *Hum. Pathol.* 7, 547–563.

Ferrero, J. M., Trenor, B., and Romero, L. (2014). Multiscale computational analysis of the bioelectric consequences of myocardial ischaemia and infarction. *Europace* 16, 405–415. doi: 10.1093/europace/eut405

Fishbein, M. C., Maclean, M., and Maroko, P. R. (1978). The histopathologic evolution of myocardial infarction. *Chest* 73, 843–849.

Gardner, P. I., Ursell, P. C., Fenoglio, J. J., and Wit, A. L. (1985). Electrophysiologic and anatomic basis for fractionated electrograms recorded from healed myocardial infarcts. *Circulation* 72, 596–611.

Gough, W. B., Mehra, R., Restivo, M., Zeiler, R. H., and El-Sherif, N. (1985). Reentrant ventricular arrhythmias in the late myocardial infarction period. 13. Correlation of Activation and Refractory Maps. *Circulation* 67, 11–24.

Janse, M. J., and Wit, A. L. (1989). Electrophysiological mechanisms of ventricular arrhythmias resulting from myocardial ischemia and infarction. *Physiol. Rev.* 69, 1049–1169.

Jiang, M., Cabo, C., Yao, J.-A., Boyden, P. A., and Tseng, G.-N. (2000). Delayed rectifier K currents have reduced amplitudes and altered kinetics in myocytes from infarcted canine ventricle. *Cardiovasc. Res.* 48, 34–43. doi: 10.1016/S0008-6363(00)00159-0

Kimura, S., Bassett, A. L., Cameron, J. S., Huikuri, H., Kozlovskis, P. L., and Myerburg, R. J. (1988). Cellular electrophysiological changes during ischemia in isolated, coronary-perfused cat ventricle with healed myocardial infarction. *Circulation* 78, 401–406. doi: 10.1161/01.CIR.78.2.401

Kimura, S., Bassett, A. L., Gaide, M. S., Kozlovskis, P. L., and Myerburg, R. J. (1986). Regional changes in intracellular potassium and sodium activity after healing of experimental myocardial infarction in cats. *Circ. Res.* 58, 202–208. doi:10.1161/01.RES.58.2.202

Kléber, A., and Rudy, Y. (2004). Basic mechanisms of cardiac impulse propagation and associated arrhythmias. *Physiol. Rev.* 84, 431–488. doi: 10.1152/physrev.00025.2003

Kostin, S., Rieger, M., Dammer, S., Hein, S., Richter, M., Klövekorn, W. P., et al. (2003). Gap junction remodeling and altered connexin43 expression in the failing human heart. *Mol. Cell. Biochem.* 242, 135–144. doi: 10.1023/A:1021154115673

Kwon, D. H., Asamoto, L., Popovic, Z. B., Kusunose, K., Robinson, M., Desai, M., et al. (2015). Infarct characterization by delayed enhancement cardiac magnetic resonance imaging is a powerful independent and incremental predictor of mortality in patients with advanced ischemic cardiomyopathy. *Circ. Cardiovasc. Imaging* 7, 796–804. doi: 10.1161/CIRCIMAGING.114.002077

Laurita, K. R., and Rosenbaum, D. S. (2000). Interdependence of modulated dispersion and tissue structure in the mechanism of unidirectional block. *Circ. Res.* 87, 922–928. doi: 10.1161/01.RES.87.10.922

Lee, Y. S., Chang, P.-C., Hsueh, C.-H., Maruyama, M., Park, H. W., Rhee, K.-S., et al. (2013). Apamin-sensitive calcium-activated potassium currents in rabbit ventricles with chronic myocardial infarction. *J. Cardiovasc. Electrophysiol.* 24, 1144–1153. doi: 10.1111/jce.12176

Liang, J. J., Prasad, A., and Cha, Y.-M. (2013). Temporal evolution and implications of ventricular arrhythmias associated with acute myocardial infarction. *Cardiol. Rev.* 21, 289–294. doi: 10.1097/CRD.0b013e3182a46fc6

Litwin, S. E., and Bridge, J. H. (1971). Enhanced Na+/Ca2+ exchange in the infarcted heart implications for excitation-contraction coupling. *Circ. Res.* XIII, 437–445. doi:10.1161/01.RES.29.5.437

Lue, W. M., and Boyden, P. A. (1992). Abnormal electrical properties of myocytes from chronically infarcted canine heart. Alterations in Vmax and the transient outward current. *Circulation* 85, 1175–1188. doi: 10.1161/01.CIR.85.3.1175

Luke, R. A., and Saffitz, J. E. (1991). Remodeling of ventricular conduction pathways in healed canine infarct border zones. *J. Clin. Invest.* 87, 1594–1602. doi: 10.1172/JCI115173

Maclean, D., Fishbein, M. C., Braunwald, E., and Maroko, P. R. (1978). Long-term preservation of ischemic myocardium after experimental coronary artery occlusion. *J. Clin. Invest.* 61, 541–551. doi: 10.1172/JCI108965

Matsushita, T., Oyamada, M., Fujimoto, K., Yasuda, Y., Masuda, S., Wada, Y., et al. (1999). Remodeling of cell-cell and cell extracellular matrix interactions at the border zone of rat myocardial infarcts. *Circulation* 85, 1046–1055. doi: 10.1161/01.RES.85.11.1046

McDowell, K. S., Arevalo, H. J., Maleckar, M. M., and Trayanova, N. A. (2011). Susceptibility to arrhythmia in the infarcted heart depends on myofibroblast density. *Biophys. J.* 101, 1307–1315. doi: 10.1016/j.bpj.2011.08.009

McGuire, M. A., de Bakker, J. M., Vermeulen, J. T., Moorman, A. F. M., Loh, P., Thibault, B., et al. (1996). Atrioventricular junctional tissue: discrepancy between histological and electrophysiological characteristics. *Circulation* 94, 571–577. doi: 10.1161/01.CIR.94.3.571

Mills, W. R., Mal, N., Forudi, F., Popovic, Z. B., Penn, M. S., et al. (2005). Optical mapping of late myocardial infarction in rats. *Am. J. Physiol. Heart. Circ. Physiol.* 290, H1298–H1306. doi: 10.1152/ajpheart.00437.2005

Mirams, G. R., Davies, M. R., Brough, S. J., Bridgland-Taylor, M. H., Cui, Y., Gavaghan, D. J., et al. (2014). Prediction of thorough QT study results using action potential simulations based on ion channel screens. *J. Pharmacol. Toxicol. Methods* 70, 246–254. doi: 10.1016/j.vascn.2014.07.002

Myerburg, R. J., Epstein, K., Gaide, M. S., Wong, S. S., Castellanos, A., Gelband, H., et al. (1982). Cellular electrophysiology in acute and healed experimental myocardial infarction. *Ann. N.Y. Acad. Sci.* 382, 90–115. doi: 10.1111/j.1749-6632.1982.tb55210.x

Myerburg, R. J., Gelband, H., Nilsson, K., Sung, R. J., Thurer, R. J., Morales, A. R., et al. (1977). Long-term electrophysiological abnormalities resulting from experimental myocardial infarction in cats. *Circ. Res.* 41, 73–84. doi: 10.1161/01.RES.41.1.73

Ng, J., Jacobson, J. T., Ng, J. K., Gordon, D., Lee, D. C., Carr, J. C., et al. (2012). Virtual electrophysiological study in a 3-dimensional cardiac magnetic resonance imaging model of porcine myocardial infarction. *JAC* 60, 423–430. doi: 10.1016/j.jacc.2012.03.029

Peters, N. S., Coromilas, J., Severs, N. J., and Wit, A. L. (1997). Disturbed Connexin43 gap junction distribution correlates with the location of reentrant circuits in the epicardial border zone of healing canine infarcts that cause ventricular tachycardia. *Circulation* 95, 988–996. doi: 10.1161/01.CIR.95.4.988

Pinto, J. M., Yuan, F., Wasserlauf, B. J., Bassett, A. L., and Myerburg, R. J. (1997). Regional gradation of L-type calcium currents in the feline heart with a healed myocardial infarct. *J. Cardiovasc. Electrophysiol.* 8, 548–560. doi: 10.1111/j.1540-8167.1997.tb00823.x

Pogwizd, S. M., Hoyt, R. H., Saffitz, J. E., Corr, P. B., Cox, J. L., and Cain, M. E. (1992). Reentrant and focal mechanisms underlying ventricular tachycardia in the human heart. *Circulation* 86, 1872–1887. doi: 10.1161/01.CIR.86.6.1872

Pollard, A. E., Cascio, W. E., Fast, V. G., and Knisley, S. B. (2002). Modulation of triggered activity by uncoupling in the ischemic border: a model study with phase 1b-like conditions. *Cardiovasc. Res.* 56, 381–392. doi: 10.1016/S0008-6363(02)00598-9

Pop, M., Sermesant, M., Liu, G., Relan, J., Mansi, T., Soong, A., et al. (2012). Construction of 3D MR image-based computer models of pathologic hearts, augmented with histology and optical fluorescence imaging to characterize action potential propagation. *Med. Image Anal.* 16, 505–523. doi: 10.1016/j.media.2011.11.007

Pu, J., and Boyden, P. A. (1997). Alterations of Na currents in myocytes from epicardial border zone of the infarcted heart. *Circ. Res.* 81, 110–119. doi: 10.1161/01.RES.81.1.110

Quinn, T. A., Camelliti, P., Rog-Zielinska, E. A., Siedlecka, U., Poggioli, T., O'toole, E. T., et al. (2016). Electrotonic coupling of excitable and nonexcitable cells in the heart revealed by optogenetics. *Proc. Natl. Acad. Sci. U.S.A.* 113, 14852–14857. doi: 10.1073/pnas.1611184114

Rantner, L. J., Arevalo, H. J., Constantino, J. L., Efimov, I. R., Plank, G., and Trayanova, N. A. (2012). Three-dimensional mechanisms of increased vulnerability to electric shocks in myocardial infarction: altered virtual electrode polarizations and conduction delay in the peri-infarct zone. *J. Physiol.* 590, 4537–4551. doi: 10.1113/jphysiol.2012.229088

Raviele, A., Bonso, A., Gasparini, G., and Themistoclakis, S. (1998). "Prophylactic implantation of implantable cardioverter/defibrillators in post-myocardial infarction patients," in *Cardiac Arrhythmias, Pacing & Electrophysiology. Developments in Cardiovascular Medicine*, Vol. 201 (Dordrecht: Springer), 305–310. doi: 10.1007/978-94-011-5254-9_43

Richardson, W. J., Clarke, S. A., Alexander Quinn, T., and Holmes, J. W. (2015). Physiological implications of myocardial scar structure. *Compr. Physiol.* 5, 1877–1909. doi: 10.1002/cphy.c140067

Ringenberg, J., Deo, M., Devabhaktuni, V., Filgueiras-Rama, D., Pizarro, G., Ibanez, B., et al. (2012). Automated segmentation and reconstruction of patient-specific cardiac anatomy and pathology from *in vivo* MRI. *Meas. Sci. Technol.* 23, 125405–125418. doi: 10.1088/0957-0233/23/12/125405

Rodríguez, B., Trayanova, N., and Noble, D. (2006). Modeling cardiac ischemia. *Ann. N.Y. Acad. Sci.* 1080, 395–414. doi: 10.1196/annals.1380.029

Rohr, S. (2012). Arrhythmogenic implications of fibroblast-myocyte interactions. *Circ. Arrhythm. Electrophysiol.* 5, 442–452. doi: 10.1161/CIRCEP.110.957647

Rohr, S., Kucera, J. P., and Kleber, A. G. (1998). Slow conduction in cardiac tissue, I : effects of a reduction of excitability versus a reduction of electrical coupling on microconduction. *Circ. Res.* 83, 781–794. doi: 10.1161/01.RES.83.8.781

Rutherford, S. L. (2013). *Myocardial Infarct Border Zone Structure and its Effects on Electrical Function of the Heart*. PhD thesis, The University of Auckland.

Saffitz, J. E., and Kléber, A. G. (2012). Gap junctions, slow conduction, and ventricular tachycardia after myocardial infarction. *J. Am. College Cardiol.* 60, 1111–1113. doi: 10.1016/j.jacc.2012.05.020

Schmidt, A., Azevedo, C. F., Cheng, A., Gupta, S. N., Bluemke, D. A., Foo, T. K., et al. (2007). Infarct tissue heterogeneity by magnetic resonance imaging identifies enhanced cardiac arrhythmia susceptibility in patients with left ventricular dysfunction. *Circulation* 115, 2006–2014. doi: 10.1161/CIRCULATIONAHA.106.653568

Sermesant, M., Chabiniok, R., Chinchapatnam, P., Mansi, T., Billet, F., Moireau, P., et al. (2012). Patient-specific electromechanical models of the heart for the prediction of pacing acute effects in CRT: a preliminary clinical validation. *Med. Image Anal.* 16, 201–215. doi: 10.1016/j.media.2011.07.003

Smith, J. H., Green, C. R., Peters, N. S., Rothery, S., Severst, N. J., and Severs, N. J. (1991). Altered patterns of gap junction distribution in ischemic heart disease an immunohistochemical study of human myocardium using laser scanning confocal microscopy. *Am. J. Pathol.* 139, 801–21.

Spach, M. S., and Josephson, M. E. (1994). Initiating reentry: the role of nonuniform anisotropy in small circuits. *J. Cardiovasc. Electrophysiol.* 5, 182–209. doi: 10.1111/j.1540-8167.1994.tb01157.x

Spear, J. F., Horowitz, L. N., Hodess, A. B., MacVaugh, H., and Moore, E. N. (1979). Cellular electrophysiology of human myocardial infarction. 1. Abnormalities of cellular activation. *Circulation* 59, 247–256. doi: 10.1161/01.CIR.59.2.247

Spear, J. F., Michelson, E. L., and Moore, E. N. (1983). Cellular electrophysiologic characteristics of chronically infarcted myocardium in dogs susceptible to sustained ventricular tachyarrhythmias. *J. Am. College Cardiol.* 1, 1099–1110. doi: 10.1016/S0735-1097(83)80112-0

ten Tusscher, K. H., Panfilov, A. V., and Tusscher, T. (2006). Alternans and spiral breakup in a human ventricular tissue model. *Am. J. Physiol. Heart. Circ. Physiol.* 291, 1088–1100. doi: 10.1152/ajpheart.00109.2006

Ursell, P. C., Gardner, P. I., Albala, A., Fenoglio, J. J., and Wit, A. L. (1985). Structural and electrophysiological changes in the epicardial border zone of canine myocardial infarcts during infarct healing. *Circ. Res.* 56, 436–451. doi: 10.1161/01.RES.56.3.436

Varro, A., Lathrop, D. A., Hester, S. B., Nfingtsi, P. P., and Papp, J. G. Y. (1993). Cardiology Ionic currents and action potentials in rabbit, rat, and guinea pig ventricular myocytes. *Basic Res.* 188, 93–102.

Vigmond, E. J., Hughes, M., Plank, G., and Leon, L. J. (2003). Computational tools for modeling electrical activity in cardiac tissue. *J. Electrocardiol.* 36, 69–74. doi: 10.1016/j.jelectrocard.2003.09.017

Vigmond, E. J., Weber dos Santos, R., Prassl, A. J., Deo, M., and Plank, G. (2008). Solvers for the cardiac bidomain equations. *Prog. Biophys. Mol. Biol.* 96, 3–18. doi: 10.1016/j.pbiomolbio.2007.07.012

Walker, N. L., Burton, F. L., Kettlewell, S., Smith, G. L., and Cobbe, S. M. (2007). Mapping of epicardial activation in a rabbit model of chronic myocardial infarction: response to atrial, endocardial and epicardial pacing. *J. Cardiovasc. Electrophysiol.* 18, 862–868. doi: 10.1111/j.1540-8167.2007.00858.x

Weigand, K., Witte, R., Moukabary, T., Chinyere, I., Lancaster, J., Pierce, M. K., et al. (2016). *In vivo* electrophysiological study of induced ventricular tachycardia in intact rat model of chronic ischemic heart failure. *IEEE Trans. Biomed. Eng.* 64, 1393–1399. doi: 10.1109/TBME.2016.2605578

WHO (2015). *Cardiovascular Diseases*. Technical Report.

Wong, S. S., Bassett, A. L., Cameron, J. S., Epstein, K., Kozlovskis, P., and Myerburg, R. J. (1982). Dissimilarities in the electrophysiological abnormalities of lateral border and central infarct zone cells after healing of myocardial infarction in cats. *Circ. Res.* 51, 486–493. doi: 10.1161/01.RES.51.4.486

Yao, J. A., Hussain, W., Patel, P., Peters, N. S., Boyden, P. A., and Wit, A. L. (2003). Remodeling of gap junctional channel function in epicardial border zone of healing canine infarcts. *Cir. Res.* 92, 437–443. doi: 10.1161/01.RES.0000059301.81035.06

Conflict of Interest Statement: The authors declare that the research was conducted in the absence of any commercial or financial relationships that could be construed as a potential conflict of interest.

frontiers in Physiology

ORIGINAL RESEARCH
published: 04 April 2018
doi: 10.3389/fphys.2018.00239

Confocal Microscopy-Based Estimation of Parameters for Computational Modeling of Electrical Conduction in the Normal and Infarcted Heart

Joachim Greiner[1,2†], *Aparna C. Sankarankutty*[1,3†], *Gunnar Seemann*[4,5], *Thomas Seidel*[6*] *and Frank B. Sachse*[1,3*]

[1] *Nora Eccles Harrison Cardiovascular Research and Training Institute, University of Utah, Salt Lake City, UT, United States,* [2] *Institute of Biomedical Engineering, Karlsruhe Institute of Technology, Karlsruhe, Germany,* [3] *Bioengineering Department, University of Utah, Salt Lake City, UT, United States,* [4] *Institute for Experimental Cardiovascular Medicine, University Heart Center, Medical Center University of Freiburg, Freiburg, Germany,* [5] *Faculty of Medicine, Albert Ludwigs University of Freiburg, Freiburg, Germany,* [6] *Institute for Cellular and Molecular Physiology, University of Erlangen-Nuremberg, Erlangen, Germany*

OPEN ACCESS

Edited by:
Hans Dierckx,
Ghent University, Belgium

Reviewed by:
Candido Cabo,
The City University of New York, United States
David Sedmera,
Charles University, Czechia

****Correspondence:***
Thomas Seidel
thomas.seidel@fau.de
Frank B. Sachse
frank.sachse@utah.edu

† These authors have contributed equally to this work.

Specialty section:
This article was submitted to Cardiac Electrophysiology, a section of the journal Frontiers in Physiology

Received: *15 January 2018*
Accepted: *06 March 2018*
Published: *04 April 2018*

Citation:
Greiner J, Sankarankutty AC, Seemann G, Seidel T and Sachse FB (2018) Confocal Microscopy-Based Estimation of Parameters for Computational Modeling of Electrical Conduction in the Normal and Infarcted Heart. Front. Physiol. 9:239. doi: 10.3389/fphys.2018.00239

Computational modeling is an important tool to advance our knowledge on cardiac diseases and their underlying mechanisms. Computational models of conduction in cardiac tissues require identification of parameters. Our knowledge on these parameters is limited, especially for diseased tissues. Here, we assessed and quantified parameters for computational modeling of conduction in cardiac tissues. We used a rabbit model of myocardial infarction (MI) and an imaging-based approach to derive the parameters. Left ventricular tissue samples were obtained from fixed control hearts (animals: 5) and infarcted hearts (animals: 6) within 200 μm (region 1), 250–750 μm (region 2) and 1,000–1,250 μm (region 3) of the MI border. We assessed extracellular space, fibroblasts, smooth muscle cells, nuclei and gap junctions by a multi-label staining protocol. With confocal microscopy we acquired three-dimensional (3D) image stacks with a voxel size of 200 × 200 × 200 nm. Image segmentation yielded 3D reconstructions of tissue microstructure, which were used to numerically derive extracellular conductivity tensors. Volume fractions of myocyte, extracellular, interlaminar cleft, vessel and fibroblast domains in control were (in %) 65.03 ± 3.60, 24.68 ± 3.05, 3.95 ± 4.84, 7.71 ± 2.15, and 2.48 ± 1.11, respectively. Volume fractions in regions 1 and 2 were different for myocyte, myofibroblast, vessel, and extracellular domains. Fibrosis, defined as increase in fibrotic tissue constituents, was (in %) 21.21 ± 1.73, 16.90 ± 9.86, and 3.58 ± 8.64 in MI regions 1, 2, and 3, respectively. For control tissues, image-based computation of longitudinal, transverse and normal extracellular conductivity yielded (in S/m) 0.36 ± 0.11, 0.17 ± 0.07, and 0.1 ± 0.06, respectively. *Conductivities were markedly increased in regions 1 (+75, +171, and +100%), 2 (+53, +165, and +80%), and 3 (+42, +141, and +60%).* Volume fractions of the extracellular space including interlaminar clefts strongly correlated with conductivities in control and MI hearts. Our study provides novel quantitative data for computational modeling of conduction in normal and MI hearts. Notably, our study

introduces comprehensive statistical information on tissue composition and extracellular conductivities on a microscopic scale in the MI border zone. We suggest that the presented data fill a significant gap in modeling parameters and extend our foundation for computational modeling of cardiac conduction.

Keywords: cardiac modeling, cardiac tissue, myocardial infarction, tissue conductivity, electrical conduction

INTRODUCTION

Cardiac diseases, such as myocardial infarction (MI), are often associated with an increased risk of arrhythmia, which results from remodeling of cellular electrophysiology and tissue electrical properties. Computational modeling is a major research approach to study underlying mechanisms and effects of cardiac diseases, as well as cardiac physiology (Sachse, 2004; Moreno and Clancy, 2009; Clayton et al., 2011).

Established models of cardiac electrical conduction include the monodomain and bidomain models. More recently, multidomain models of cardiac conduction were introduced (Sachse et al., 2009). Computational simulations with these models commonly require discretization of spatial domains with finite element or finite difference methods. Models of cellular electrophysiology are assigned to elements or nodes of the computational mesh of conduction models. These models of cellular electrophysiology describe voltages across the cell membrane V_m and associated membrane currents. Commonly, only models of myocyte electrophysiology are considered, because myocytes occupy most of the volume in cardiac tissues and with some exceptions, the contribution of other cells to conduction is thought to be marginal throughout the normal heart. Models of myocyte electrophysiology have been developed for various species and anatomical regions (Lloyd et al., 2008; Fink et al., 2011). However, various experimental findings suggest that non-myocytes, in particular, fibroblasts, myofibroblasts and macrophages, contribute to cardiac conduction and arrhythmia (Gaudesius et al., 2003; Miragoli et al., 2006; Zlochiver et al., 2008; Quinn et al., 2016; Hulsmans et al., 2017). Electrophysiological models of these cells have been developed and their effects on conduction can be simulated using multi-domain models.

Beyond cell models, intracellular electrical conductivities σ_i and, for the bidomain and multidomain models, extracellular electrical conductivities σ_e are assigned to elements or nodes in a mesh for modeling of cardiac conduction. These conductivities describe electrical properties resulting from tissue microstructure including the distribution and shape of cells, their intercellular coupling and the distribution of extracellular space. Commonly the conductivities are described by tensors of 2nd order to account for anisotropy, i.e., a strong directional dependence of conductivity characteristic for cardiac tissues. Interestingly, only a small number of studies have reported on anisotropic intra- and extracellular conductivities of cardiac tissues. Noteworthy are in particular studies analyzing electrical measurements on right ventricular (RV) trabecular bundles of calf (Clerc, 1976) and left ventricular (LV) subepicardial myocardium of canine (Roberts et al., 1979; Roberts and Scher, 1982). These studies yielded bidomain conductivities distinguishing between longitudinal and transverse conductivities of the extracellular and intracellular space, which relate to longitudinal and transverse orientation of the local myocytes. Recent work aims at establishing bidomain conductivities accounting for longitudinal and transverse orientation of myocytes as well as the orientation of myocyte sheets (Legrice et al., 1995; Hooks et al., 2002, 2007; Johnston, 2016). These sheets have been identified using optical and electron microscopy in LV and RV tissues of canine. The myocyte sheets are separated by interlaminar clefts. Our recent study revealed the presence of sheets in LV myocardium of rabbit and in a rabbit model of myocardial infarction (MI) (Seidel et al., 2016).

Difficulties in implementing simulations with computational models are related to identifying conductivities and other crucial parameter values for a specific tissue type and species. Selection of conductivities and many other modeling parameters for diseased cardiac tissues is even more difficult, because we do not have a similar solid foundation of measurement studies as for control tissues. Bidomain conductivities for modeling of conduction in MI have not been measured, but are estimated based on simple assumptions or indirect measurements. Currently, we have only a vague understanding of how disease-associated remodeling of tissue microstructure influences conductivities. However, new research tools, in particular, advanced microscopy methods, allow us now to comprehensively quantify remodeling in diseased cardiac tissues. In case of MI, tissue remodeling goes beyond the actual infarct scar and affects microstructure of the adjacent myocardium. Major microstructural remodeling of the infarct border zone is related to fibrosis, i.e., the increase of extracellular matrix proteins as well as volume fractions of extracellular space, fibroblasts, and myofibroblasts (Krenning et al., 2010). Fibrosis in the border zone is accompanied by reduction of volume fraction of myocytes, their coupling by gap junctions, and myocyte hypertrophy (Luke and Saffitz, 1991; Yao et al., 2003).

Here, we investigated how tissue microstructure and its variability in the normal and MI heart are reflected in parameters for conduction models. We applied an animal model of MI and a microscopic imaging-based approach to derive modeling parameters. A particular focus was on computational estimation and statistical prediction of electrical conductivities of the extracellular domain. We assessed the effect of extracellular space and interlaminar clefts on electrical conductivities.

METHODS

Animal Models

All animal experiments were approved by the Institutional Animal Care and Use Committee (IACUC) of the University of

Utah. Studies were performed on New Zealand White rabbits with a weight of 2.5–3 kg. Five animals served as control. We induced LV MI in six animals by ligation of a coronary artery as previously described (Hu et al., 2010). Hearts were harvested after 3 weeks. We visually confirmed success of the MI model. Infarct scars were present in the apical region of the free left-ventricular wall in all MI animals.

Preparation and Labeling of Samples for Imaging

Hearts were rapidly excised and retrogradely perfused with 2.5% paraformaldehyde solution for 10 min. Transmural biopsies of 5 mm diameter oriented normal to the epicardial surface were obtained from the lateral LV free wall of control hearts. Similar biopsies from MI hearts were taken by placing the center of the biopsy punch on the epicardial or endocardial MI border zone. Biopsies were incubated in 30% sucrose solution for 2–3 h, frozen in optimal cutting temperature compound (Sakura Finetek Europe B.V., Alphen aan den Rijn, Netherlands) and then cryosectioned into slices with a thickness of 100 μm. Subepicardial and midwall slices were washed three times in phosphate-buffered saline (PBS). Primary antibodies ab11369 (Abcam, Cambridge, UK), A5228 and V6630 (Sigma-Aldrich, St. Louis, MO, USA) were applied at a concentration of 1:200 in blocking solution to bind to the proteins connexin 43 (Cx43), alpha smooth muscle actin (α-SMA) and vimentin, respectively. Slices were incubated for at least 8 h on a rocker at room temperature. After washing with PBS, corresponding goat anti-mouse secondary antibodies A21044 (conjugated to AF 594, Thermo Fisher Scientific, Waltham, MA, USA), A21137 (conjugated to AF 555, Thermo Fisher Scientific), and A21240 (conjugated to AF 647, Thermo Fisher Scientific) were applied at 1:200 in blocking solution together with DAPI (D3571, Thermo Fisher Scientific) at 3 μg/ml to label the nuclei. After incubation of the slices for at least 6 h on rocker at room temperature, they were washed with PBS and incubated with wheat germ agglutinin (WGA) conjugated to CF488A (Biotium Inc., Fremont, CA, USA) at a concentration of 40 μg/mL in PBS for at least 4 h to label the glycocalyx and extracellular matrix proteins. Slices were then washed in PBS. All used antibodies and fluorescent markers are listed in Table S1. We used a compression-free mounting method (Seidel et al., 2016). In short, slices were mounted on a coverslip using Fluoromount-G (#17984-25, Electron Microscopy Science, Hatfield, PA, USA) and stored in a humidity-controlled box. After drying for 24 h, samples were protected from desiccation by coating with varnish.

Imaging Using Scanning Confocal Microscopy

Prepared coverslips were imaged using a laser scanning confocal microscope Leica TCS SP8 with a 40x oil immersion objective at a resolution of 1,024 × 1,024 pixels and an image size of 204 × 204 μm.

In tissue samples from MI hearts, the infarct scar was identified as fibrotic tissue without any myocytes. We took images within 200 μm (region 1), within 250–750 μm (region 2) and within 1,000–1,250 μm (region 3) of the scar border. Only image stacks without labeling or imaging artifacts as well as without presence of larger vessels were selected for further processing. A rotation of the field of view was applied before acquisition to yield a uniform myocyte orientation parallel to y axis. Three-dimensional image stacks were acquired in 3 sequences comprising 2, 2, and 1 channel(s) each, to collect signals from DAPI, Cx43, WGA, α-SMA, and vimentin, which were excited by lasers of wavelengths 405, 594, 488, 561, and 633 nm, respectively. Image stacks of 200–300 images covered the depth of each sample with a spacing of 200 nm between the images. Beyond individual image stacks, we also acquired 3D tile scan images covering larger regions of interest.

To compensate for decreasing signal intensity at increased depths within the tissue, excitation compensation was applied by linearly increasing the laser power with depth. Imaging software used was LAS X (version 1.1.0 and higher, Leica).

Image Preprocessing and Segmentation

We described our methods and software tools for preprocessing and segmentation of three-dimensional images of cardiac tissues previously (Seidel et al., 2016). In short, Gaussian and mean filters were used to reduce noise in the acquired image stacks. We performed an attenuation correction to account for depth-dependent signal attenuation and the linear increase of laser power in our imaging protocol. A deconvolution method based on the Richardson-Lucy algorithm with previously measured point spread function was used to reduce blurring.

We produced signal intensity profiles of the five channels of a representative 3D tile scan spanning from the infarct scar to region 3. Signal intensity was averaged along the depth and width of the image stack. Normalized values of mean intensities over every 100 μm was plotted against the distance from the scar border.

For 3D reconstruction, a semi-automatic segmentation approach based on multiple watersheds was used to segment myocyte, interlaminar cleft, and vessel domains (Seidel et al., 2013). Occasionally, when the WGA signal was insufficient for accurate watershed segmentation, manual separation of segments was performed using the volume segmentation and processing tool Seg3D (SCI, 2015). After segmentation of myocytes, capillaries were identified and dilated to include vessel walls, containing endothelial, smooth muscle cells, and pericytes. Assuming that beyond myocytes and vessel-associated cells, only fibroblasts and myofibroblasts exhibit a significant cell population in the studied samples, we segmented the fibroblast and myofibroblast domain using histogram-based thresholding on DAPI, vimentin and α-SMA images as previously described (Seidel et al., 2016). Briefly, nuclei not associated with myocytes or proximal to vessels were attributed to the fibroblast or myofibroblast domain, dependent on proximity to vimentin and α-SMA-positive regions, respectively. Fibroblasts were defined as exclusively vimentin-positive cells not proximal to vessels. Myofibroblasts were defined as vimentin- and α-SMA-positive cells not proximal to vessels.

Extracellular space was defined by the residual space after the exclusion of segmented myocytes, vessels, fibroblasts,

and myofibroblasts. We also measured the volume ratio of interlaminar clefts V_{cleft}, which are a component of the extracellular domain (Legrice et al., 1995). Interlaminar clefts were identified as continuous regions in the extracellular space with low WGA signal due to reduced collagen density. Segmented image stacks were sequentially combined to generate comprehensive 3D reconstructions of tissue microstructure.

We calculated volume fractions of the myocyte V_{myo}, fibroblast V_{fibro}, myofibroblast $V_{myofibro}$, extracellular V_e (including V_{cleft}), and vessel domain V_{vessel} for control tissue and for regions 1–3 from the 3D reconstructions.

We defined fibrosis as the excess of fibroblasts and myofibroblasts as well as extracellular space excluding interlaminar clefts vs. control tissue. Accordingly, we calculated the degree of fibrosis in region x, where x is 1–3, from volume fractions of relevant tissue constituents as:

$$\begin{aligned} Fibrosis_{region\ x} = &\left(V_{region\ x,e} - V_{region\ x,cleft} + V_{region\ x,fibro}\right. \\ &\left. + V_{region\ x,myofibro}\right) - \left(V_{control,e} - V_{control,cleft}\right. \\ &\left. + V_{control,fibro} + V_{control,myofibro}\right) \end{aligned} \quad (1)$$

Image-Based Computation of Extracellular Conductivities

Similar as in our prior work (Schwab et al., 2013), the 3D reconstructions of tissue microstructure were used to construct conductivity models, assuming that only the extracellular space contributes to extracellular current flow. The segmented extracellular space was further refined by the addition of a thresholded WGA image (mode + 1SD) inside the myocyte domain to conservatively preserve the interface of the extracellular space to the myocytes. We checked for alignment of tissue microstructure with the coordinate system of the conductivity model using principal component analysis of the 10 largest myocytes and the largest cleft of each stack. Stacks with fiber orientation or cleft orientation deviating from this definition were appropriately rotated. After rotation, the stacks were cropped to avoid undefined regions.

In order to derive the homogenized conductivities, an electrical field was applied to the extracellular conductivity model. The electrical field was incorporated in the model with Dirichlet boundary conditions. The field was applied in three axes of the coordinate system: longitudinal, i.e., along the myocyte fiber orientation, transverse, i.e., normal to the fiber orientation and in cleft plane, and normal, i.e., normal to both the fiber orientation and cleft plane. We denoted these directions with the subscripts l, t, and n respectively. We assumed a conductivity value of 2 S/m for the extracellular space (Foster and Schwan, 1989). The extracellular potential distribution ϕ_e was obtained by solving the resulting homogenous Laplace equation for a given extracellular conductivity distribution σ_e:

$$\nabla \cdot (\sigma_e \nabla \phi_e) = 0$$

Surfaces of the extracellular conductivity model were assigned no-flux Neumann boundary conditions. From the potential distribution of the extracellular domain, the mean directional current densities $J_{e,l}$, $J_{e,t}$, and $J_{e,n}$ were calculated. The current densities were used to derive the homogenized extracellular conductivities in the defined directions:

$$\sigma_{e,x} = \frac{J_{e,x}}{E_{e,x}}$$

A central finite difference scheme was used to numerically discretize the simulation domain. The resulting linear systems of equations were solved using the scientific computing library PETSc (Balay et al., 1997). The external library, Hypre, provided the parallel algebraic multigrid preconditioner BoomerAMG (Falgout and Yang, 2002), which was used in combination with PETSc's implementation of the iterative flexible generalized minimal residual (FGMRES) method. Algorithm configuration for the algebraic multigrid was optimized using the software package SMAC (Hutter et al., 2011) on a small test case. This yielded a V-cycle multigrid with a threshold for strong coupling of 0.12, HMIS-coarsening with one level of aggressive coarsening, extended+i interpolation, Schwartz-type smoothers and a CF-relaxation scheme. The iterative solver was stopped when the residual norm of the original linear system was $<10^{-10}$. For post-processing and visualization, we used MATLAB (version 2016b and higher, MathWorks, Inc., Natick, MA, USA) and Paraview (version 5.4 and higher, Kitware, Clifton Park, New York, USA) respectively.

Numerical Verification

To verify our numerical method of estimating a homogenized conductivity, we performed a series of tests. We chose non-intersecting rectangular blocks as the testing geometry, as the derivation of the analytical solution is straightforward. The blocks were assigned to the extracellular conductivity model, whereas the remainder of the simulation domain was set non-conductive. For these geometries, a conductivity estimation was performed in each direction as described in section Image-Based Computation of Extracellular Conductivities. For varying geometries and simulation domains in the order of $40 \times 40 \times 40\,\mu m$ and a spatial discretization of 200 nm, the error of the estimated conductivity was of the order 10^{-8}.

Statistical Analyses

Statistical data are presented as mean ± standard deviation (SD). For each parameter tested, regions 1–3 and control were compared using the Holm-Bonferroni method for correction of multiple comparison. P-values were calculated using unpaired, two-tailed t-tests. A significance level (alpha) of 0.05 was used. Statistical relationships between tissue constituents and conductivities were analyzed using simple and multiple linear regression. The goodness of fit was measured by the coefficient of determination (R^2). All statistical analyses were performed in MATLAB.

RESULTS

Remodeling of Myocardium in MI Animals

We studied tissue remodeling in the MI heart using the methods for fluorescent labeling and 3D tile scanning confocal microscopy

as described above. Overview images with a field of view of 1495.8 × 204.8 × 60.6 µm and zooms into specific regions are shown in **Figure 1**. Furthermore, we calculated profiles of fluorescence intensities to describe the spatial relationship of tissue constituents vs. infarct distance in **Figure 2**.

The tile scanning covered part of the infarct scar and adjacent ventricular myocardium exhibiting different types and degrees of remodeling. Imaging of WGA-labeled tissue provided insights into the remodeling of extracellular matrix, which was extensively increased in the infarct scar and border zone (**Figure 2**). In comparison, myocardium at more distant sites exhibited reduced WGA signal, indicating normal amounts of extracellular space. Myocytes in close proximity to the MI (**Figure 1B**) were hypertrophic and, as a result of interstitial fibrosis, less densely packed vs. more distant myocytes (**Figures 1C,D**).

Images of DAPI yielded information on the distribution of cell nuclei (**Figures 1E–H**). A high nucleus density was revealed within the infarct scar (**Figure 2**), reflecting increased amounts of small cells, e.g. fibroblasts, myofibroblasts and macrophages. The intensity of Cx43 increased with infarct distance (**Figures 1J–L**). Accordingly, minima and maxima of Cx43 intensity were visible for scar and distant myocardium, respectively (**Figure 2**).

The distribution of α-SMA was heterogeneous with a significant increase near the infarct border zone (**Figures 1M–P**). Also, small regions of increased α-SMA intensity were found throughout myocardium distant from the scar. While α-SMA is a marker not only of myofibroblasts, but also of smooth muscle cells, for instance in the wall of blood vessels, the spatial distribution of α-SMA signal in the infarct border zone (**Figure 1M**) suggests abundance of myofibroblasts.

The spatial distribution of vimentin signal was qualitatively similar to the distribution of DAPI and α-SMA signal (**Figures 1Q–T**). However, the maximum of vimentin signal was found slightly more distant from the infarct border (250 µm) than the maximum of α-SMA signal (150 µm). In cardiac tissues, vimentin is a marker of fibroblasts, myofibroblasts, smooth muscle and endothelial cells.

For the subsequently described 3D reconstructions of tissue microstructure, we applied segmentations of capillaries to avoid that vessel associated vimentin-positive cells are misclassified as fibroblasts. We identified fibroblasts as non-vessel associated, vimentin-positive and α-SMA-negative. Based on these criteria, sparse vimentin signal in **Figure 1T** and Figure S1 points at the presence of fibroblasts.

Three-Dimensional Reconstruction and Analyses of Myocardium in Control and MI Animals

We acquired 3D image stacks from myocardium of the LV free wall in the normal heart (animals: 5, images: 8) and of region 1 (proximal, animals 4, images: 5), region 2 (adjacent, animals 6, images: 6), and region 3 (distal, animals: 4, images: 5) of the MI hearts. Raw sections from example image stacks are presented in the Figures S1–S4, respectively. Corresponding preprocessed images are shown in Figures S5–S8. An exemplary reconstruction from a control heart is shown in **Figure 3**. As in our prior work (Schwab et al., 2013; Seidel et al., 2013, 2016), the reconstruction recapitulates major features of ventricular myocardium, in particular, the dense arrangement and high volume fraction of myocytes (70.30%). While size and shape of myocytes was diverse, their long axes were approximately parallel. Myocytes were in close proximity to small blood vessels with a diameter and wall composition characteristic for capillaries. Capillaries were in general aligned with myocyte long axes. The reconstruction describes also the distribution of vimentin-positive cells, supposedly fibroblasts, which exhibit only a small volume fraction (1.03%). The tissue presented only marginal regions with α-SMA signal (0.02%), suggesting absence of myofibroblasts.

An exemplary reconstruction from the MI border zone (region 1) is shown in **Figure 4**. The reconstruction highlights various types of MI-associated tissue remodeling including reduced density and hypertrophy of myocytes, decreased capillary density, increased volume fractions of extracellular space and fibroblasts as well as the abundance of myofibroblasts.

We also present a reconstruction of distal tissue (region 3, ∼1 mm infarct distance) in the MI heart (**Figure 5**). In many aspects, the tissue microstructure appeared similar as for control tissue. V_{myo} and V_e were only marginally different. In contrast to control tissue, the region exhibited α-SMA positive cells, suggesting the presence of myofibroblasts.

The 3D reconstructions allowed us to calculate V_{myo}, V_{fibro}, $V_{myofibro}$, V_{vessel}, and V_e. From 3D reconstructions of interlaminar clefts (see examples in Figure S9), we estimated V_{cleft}. The volume fractions are summarized in **Figure 6** and **Table 1**. The analyses revealed an increase of V_e, accompanied by decreased V_{myo} in regions 1 and 2 vs. control tissue. We also noted an increase of $V_{myofibro}$ in regions 1–3 vs. control. V_{vessel} in regions 1 and 2 was decreased vs. control. In our experimental groups, V_{fibro} exhibited a high standard deviation vs. mean.

We calculated the volume fractions of fibrotic tissue for control and MI regions 1–3 (**Figure 7A**). Regions 1 and 2 of MI hearts exhibited increased fraction of fibrotic tissue when compared with control. Additionally, the fibrotic tissue in region 3 was significantly lower than that in Region 1. The regional degree of fibrosis calculated from Equation 1 is presented in **Figure 7B**. The degree of fibrosis was significantly higher in region 1 and 2, but not in region 3, with respect to control. The degree ranged from 21.21 ± 1.73% in region 1 to 3.58 ± 8.64% in region 3. While fibrotic tissue was abundant close to the infarct, we observed high variabilities in more distant regions 2 and 3, as seen from high SD in those regions (**Figure 7B**).

Image-Based Calculation of Extracellular Conductivity of Control and MI Myocardium

We applied 3D reconstructions of tissue microstructure for computational measurements of extracellular conductivities. In these reconstructions, the orientation of myocytes was approximately parallel to the y-axis.

Exemplary conductivity models of control tissue with assigned electrodes for creating potential gradients in x-, y-, and z-direction are shown in **Figures 8A–C**, respectively. The

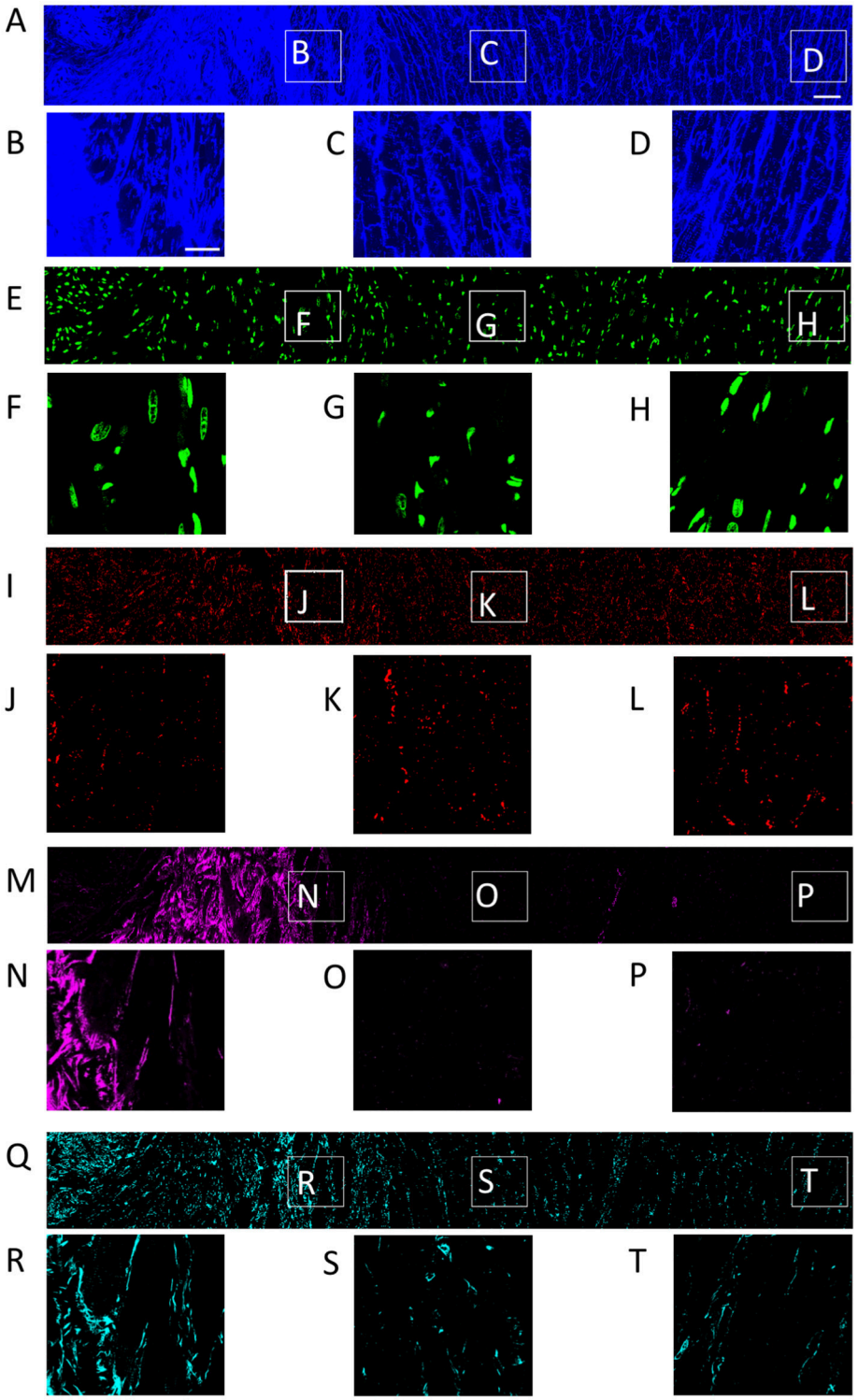

FIGURE 1 | Distribution of **(A)** WGA, **(E)** DAPI, **(I)** Cx43, **(M)** α-SMA, and **(Q)** vimentin in a single slice of an image stack from MI heart. Scar to region farthest from scar is shown from left to right. Zoom-in of regions identified in panel **(A)** are shown for each channel. Scale bar in **(A)** 50 μm. Applies to **(E,I,M,Q)**. Scale bar in **(B)** 20 μm. Applies to **(C,D, F–H, J–L, N–P, R–T)**.

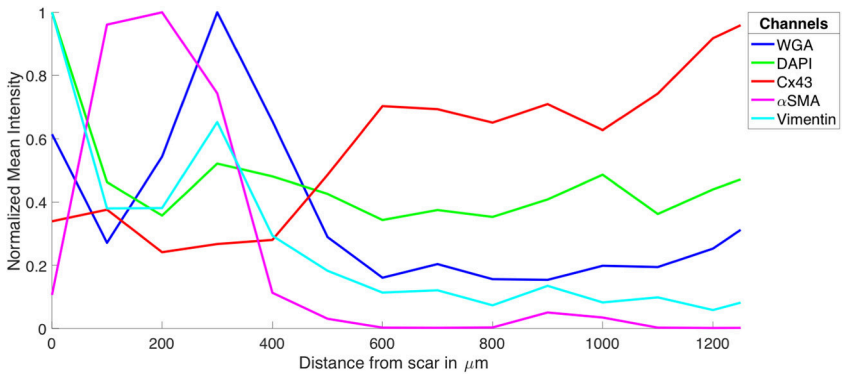

FIGURE 2 | Intensity profiles of DAPI, Cx43, WGA, α-SMA, and vimentin through MI to MI border zone to distal tissue. The profiles were generated from the image stacks represented in **Figure 1**.

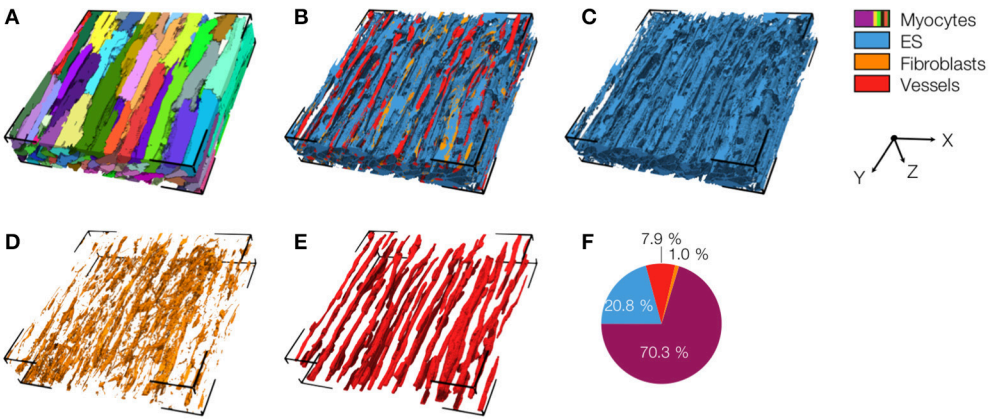

FIGURE 3 | 3D reconstruction of control myocardium with **(A)** cardiomyocytes, **(B)** complementary tissue constituents, **(C)** extracellular space, **(D)** fibroblasts, and **(E)** vessels. Volume fractions of tissue constituents are shown in **(F)**. The reconstruction has a size of 204.8 $\times$ 204.8 $\times$ 41.2 μm.

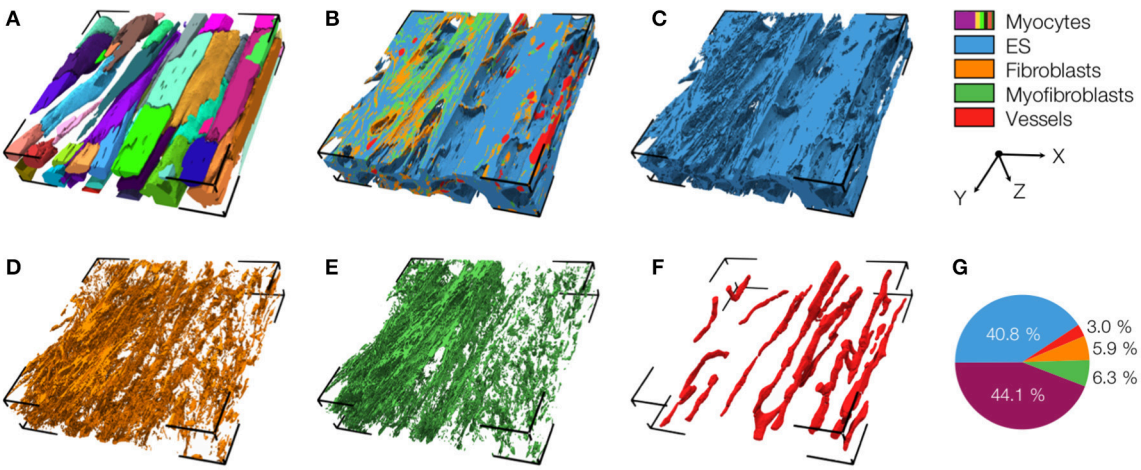

FIGURE 4 | 3D reconstruction of tissue in region 1 with **(A)** cardiomyocytes, **(B)** complementary tissue constituents, **(C)** extracellular space, **(D)** fibroblasts, **(E)** myofibroblasts, and **(F)** vessels. Volume fractions of tissue constituents are shown in **(G)**. The reconstruction has a size of 204.8 $\times$ 204.8 $\times$ 41.2 μm.

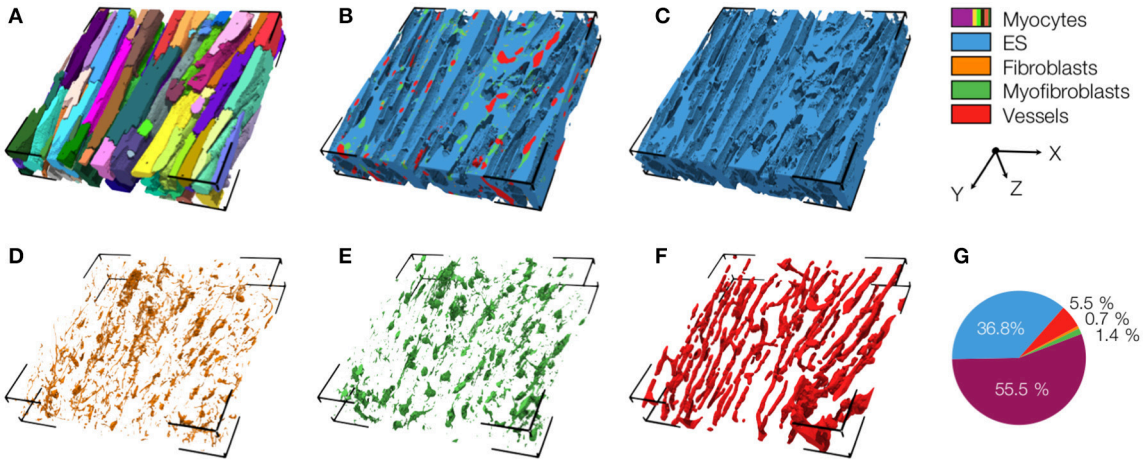

FIGURE 5 | 3D reconstruction of tissue in region 3 with **(A)** cardiomyocytes, **(B)** complementary tissue constituents, **(C)** extracellular space, **(D)** fibroblasts, **(E)** myofibroblasts, and **(F)** vessels. Volume fractions of tissue constituents are shown in **(G)**. The reconstruction has a size of 204.8 × 204.8 × 41.2 µm.

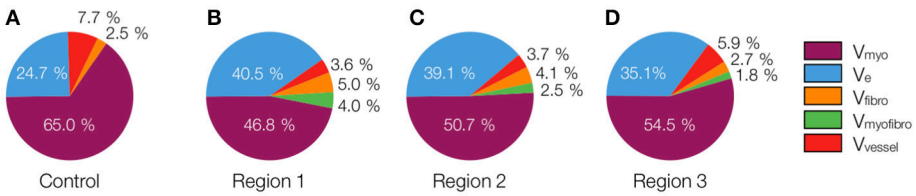

FIGURE 6 | Pie charts of volume fractions in **(A)** control, **(B)** region 1, **(C)** region 2, and **(D)** region 3. For statistical information and significance of differences see **Table 1**.

electrodes were applied to assign Dirichlet boundary conditions. **Figures 8D–F** present the calculated electrical potential distributions resulting from setting the Dirichlet boundary conditions to $\pm 1\,V$. The calculation of the electrical field is limited to the extracellular space. **Figures 8G–I** depict current densities calculated from the electrical potential distributions for the exemplary control. Calculated conductivities were $\sigma_{e,l} = 0.34$ S/m, $\sigma_{e,t} = 0.10$ S/m, and $\sigma_{e,n} = 0.10$ S/m for this tissue reconstruction.

We present similar illustrations for tissue reconstructions from region 1 and 3 in **Figures 9**, and **10**, respectively. Calculated conductivities for the tissue reconstruction for region 1 ($\sigma_{e,l} = 0.69$ S/m, $\sigma_{e,t} = 0.51$ S/m, and $\sigma_{e,n} = 0.20$ S/m) were larger than for control. Similarly, conductivities for the tissue reconstruction for region 3 were larger ($\sigma_{e,l} = 0.53$ S/m, $\sigma_{e,t} = 0.41$ S/m, and $\sigma_{e,n} = 0.15$ S/m) vs. control. The tissue reconstructions include pronounced interlaminar clefts associated with high current densities for application of voltage gradients in z-direction (**Figures 9I** and **10I**).

Statistical analysis of the computational measurements revealed an approximately linear relationship between V_e and the extracellular conductivities (**Figure 11**). The goodness of the fit to a linear model (assessed by R^2) as well as slopes of the regression line of V_e–$\sigma_{e,l}$ and V_e–$\sigma_{e,t}$ were higher than for V_e–$\sigma_{e,n}$. Regression analysis of V_{cleft} as well as V_e–V_{cleft} and extracellular conductivities revealed a weak fit ($R^2 < 0.5$) to a linear model. Slopes of the regression line of V_{cleft}–$\sigma_{e,l}$ and V_{cleft}–$\sigma_{e,t}$ were higher than for V_e–$\sigma_{e,l}$ and V_e–$\sigma_{e,t}$. However, the slope for V_e–$\sigma_{e,n}$ was similar as for V_{cleft}–$\sigma_{e,n}$.

The goodness of fit for linear regression between V_{cleft} and V_e–V_{cleft} was only 0.018. Multiple linear regression analysis with the two predicting variables V_e–V_{cleft} and V_{cleft} resulted in almost identical R^2 (Table S2) as presented in **Figures 11A–C**.

We present statistical data on measured extracellular conductivities for control and MI tissues in **Table 2**. Conductivities in fiber, transverse and sheet direction in region 1 were larger than corresponding conductivities in the control heart. Noteworthy is the pronounced increase of $\sigma_{e,t}$ in all MI regions vs. control (~2.4- to 2.7-fold). Conductivity in transverse direction of all the three MI regions and in fiber direction of region 1 were significantly increased vs. corresponding conductivities in control. The changes of conductivities were reflected in the decreased ratios $\sigma_{e,l}/\sigma_{e,t}$ and increased ratios $\sigma_{e,t}/\sigma_{e,n}$ in MI vs. control tissue.

DISCUSSION

Parameters of mathematical models crucially determine outcomes of computational simulations. It is thus surprising that for simulations of cardiac conduction our knowledge on modeling parameters and their variability is very limited, in particular for diseased tissues. Here, we addressed this problem

TABLE 1 | Calculated volume fractions of tissue constituents of control and MI hearts.

	V_{myo} [%]	V_e [%]	V_{cleft} [%]	$V_{vessels}$ [%]	V_{fibro} [%]	$V_{myofibro}$ [%]
Control ($n = 8$)	65.03 ± 3.6	24.68 ± 3.05	3.95 ± 4.84	7.71 ± 2.15	2.48 ± 1.11	0.09 ± 0.08
Region 1 ($n = 5$)	46.80 ± 4.49*	40.53 ± 6.33*	5.14 ± 3.78	3.64 ± 1.95*	5.00 ± 3.25	4.03 ± 3.46*
Region 2 ($n = 6$)	50.68 ± 10.87*	39.06 ± 10.44*	5.56 ± 5.40	3.65 ± 1.39*	4.12 ± 3.75	2.48 ± 1.95*
Region 3 ($n = 5$)	54.51 ± 10.95	35.12 ± 10.16	12.84 ± 8.29	5.87 ± 1.34	2.69 ± 2.36	1.81 ± 0.67*

*Values are presented as mean ± SD. Number of image stacks: n. Statistical significance vs. control are marked with *.*

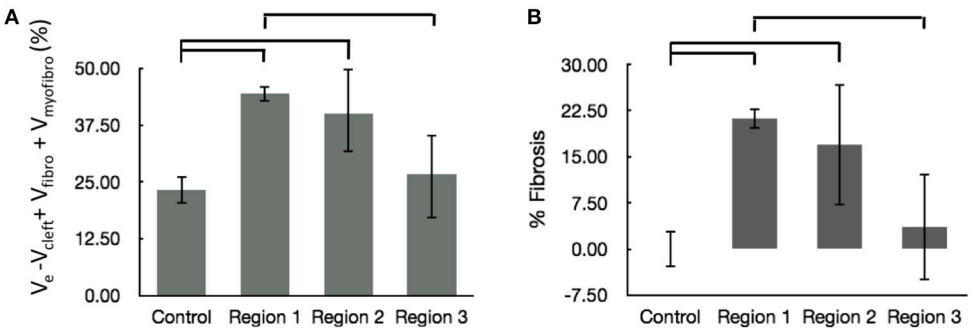

FIGURE 7 | Evaluation of fibrosis. **(A)** Sum of fractional volumes of domains contributing to fibrosis. **(B)** Degree of fibrosis in proximal, adjacent and distal regions to the MI calculated based on Equation (1). Brackets mark significant differences between groups.

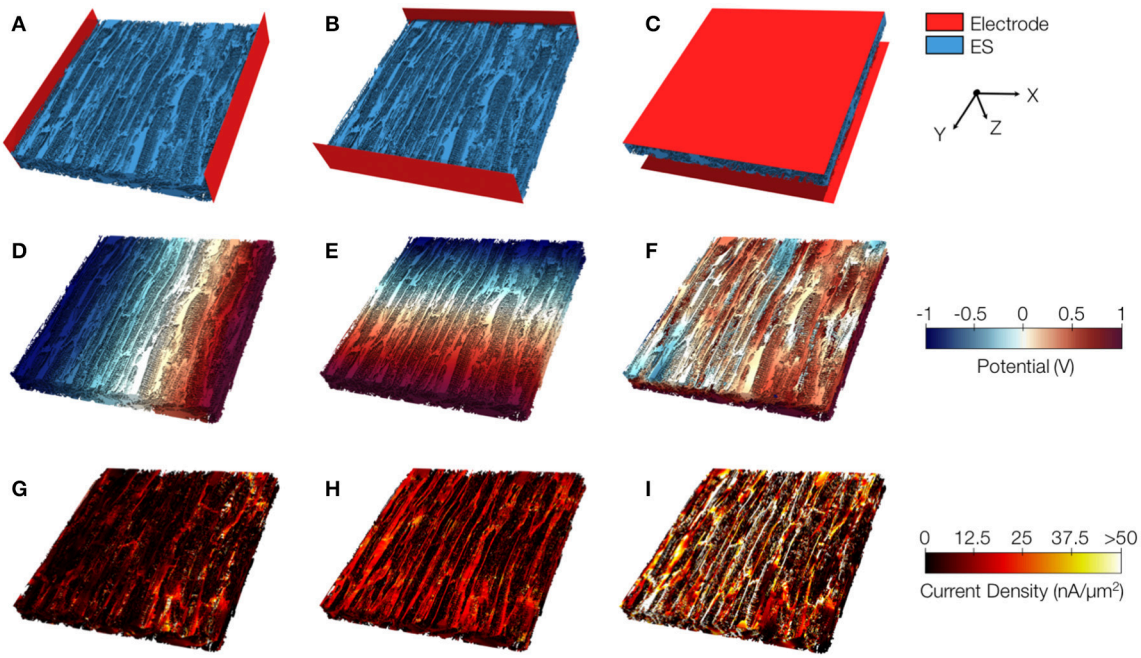

FIGURE 8 | Image-based computation of extracellular conductivity tensor for control tissue. 3D-reconstructions of the extracellular space with modeled electrodes for applying voltages in **(A)** x, **(B)** y, and **(C)** z-direction. Only half of the image stacks is shown. **(D–F)** Calculated potential distribution corresponding to **(A–C)**. **(G–I)** Calculated current density corresponding to **(D–F)**.

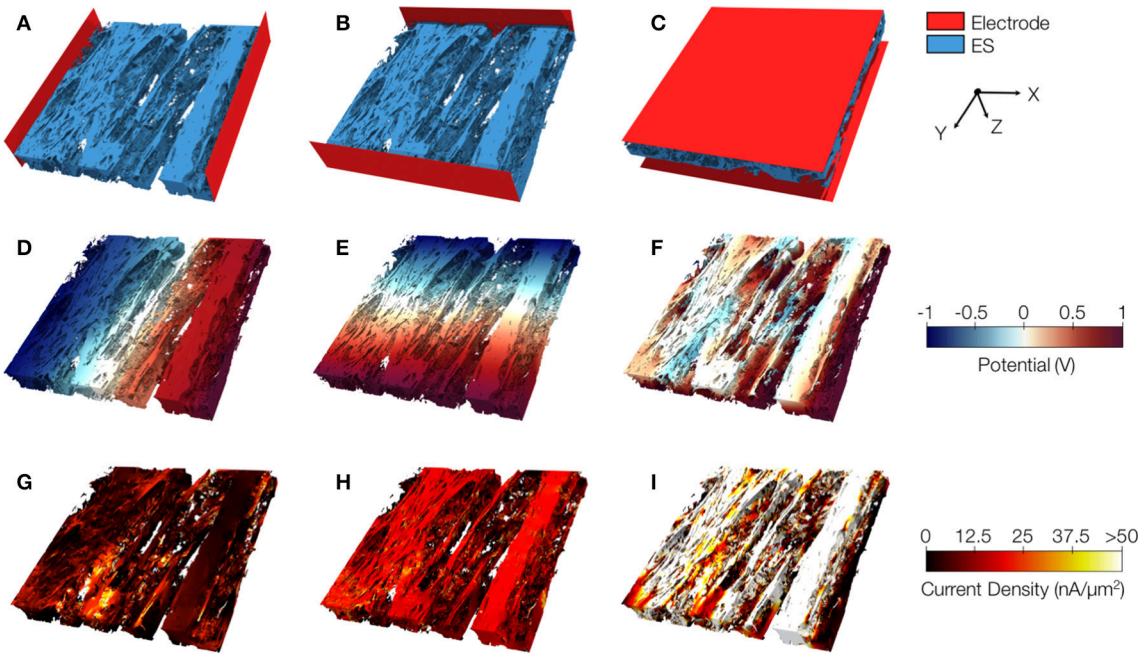

FIGURE 9 | Image-based computation of extracellular conductivity tensor for tissue in region 1. 3D-reconstructions of the extracellular space with modeled electrodes for applying voltages in **(A)** x, **(B)** y, and **(C)** z-direction. Only half of the image stacks is shown. **(D–F)** Calculated potential distribution corresponding to **(A–C)**. **(G–I)** Calculated current density corresponding to **(D–F)**.

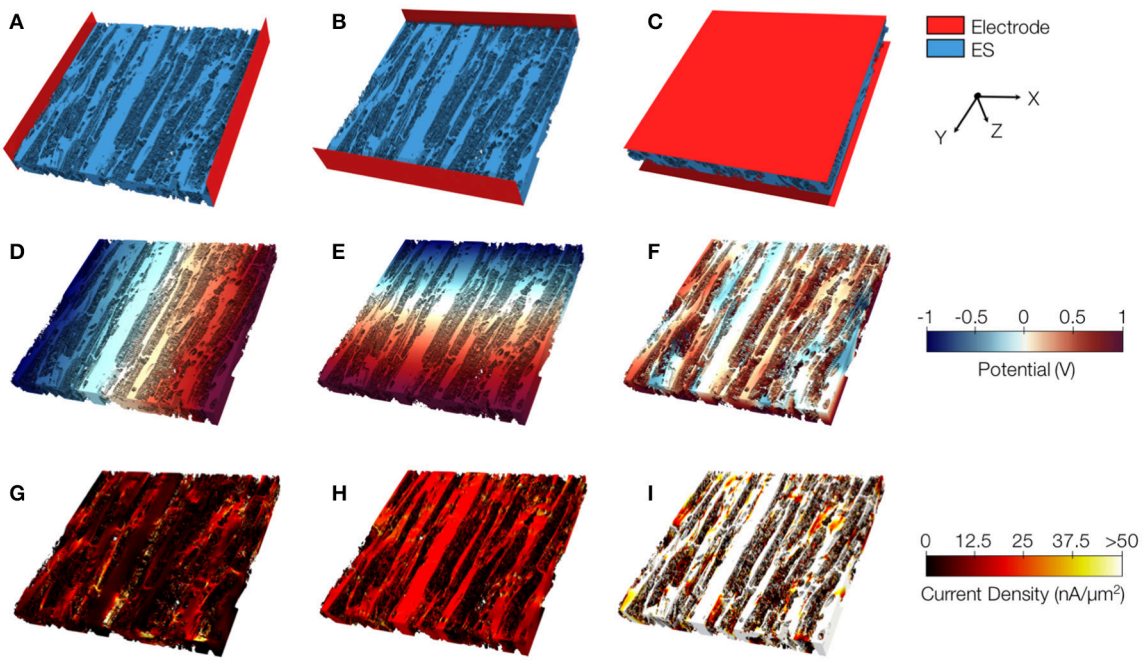

FIGURE 10 | Image-based computation of extracellular conductivity tensor for tissue in region 3. 3D-reconstructions of the extracellular space with modeled electrodes for applying voltages in **(A)** x, **(B)** y, and **(C)** z-direction. Only half of the image stacks is shown. **(D–F)** Calculated potential distribution corresponding to **(A–C)**. **(G–I)** Calculated current density corresponding to **(D–F)**.

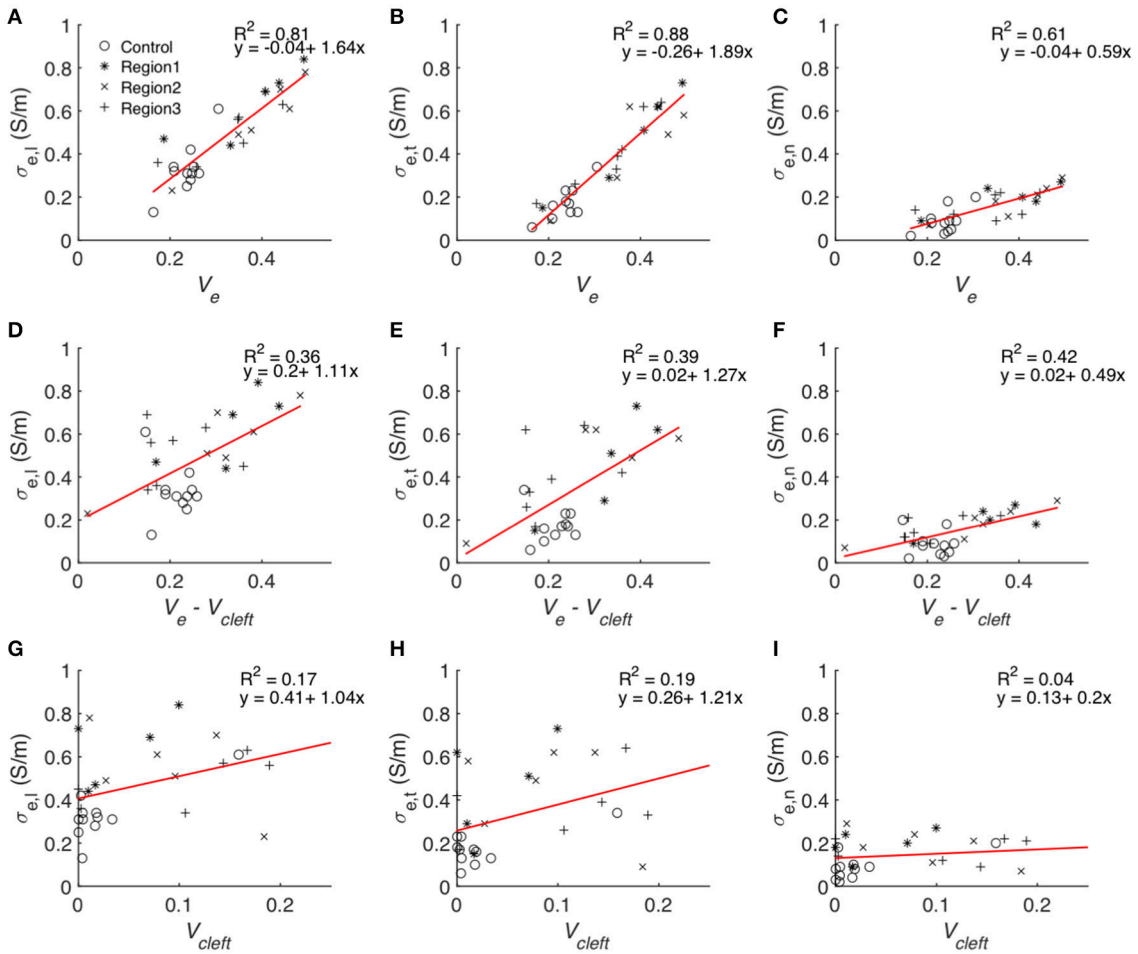

FIGURE 11 | Statistical analyses of the relationship between volume fractions of tissue constituents and calculated conductivities. Each symbol represents an image-based computation of conductivity. Linear regression modeled the relationship between V_e and **(A)** $\sigma_{e,l}$, **(B)** $\sigma_{e,t}$ and **(C)** $\sigma_{e,n}$, V_e–V_{cleft} and **(D)** $\sigma_{e,l}$, **(E)** $\sigma_{e,t}$ and **(F)** $\sigma_{e,n}$ as well as between V_{cleft} and **(G)** $\sigma_{e,l}$, **(H)** $\sigma_{e,t}$, and **(I)** $\sigma_{e,n}$.

TABLE 2 | Calculated extracellular conductivities and their ratios for control and MI tissues.

	$\sigma_{e,l}$ [S/m]	$\sigma_{e,t}$ [S/m]	$\sigma_{e,n}$ [S/m]	$\sigma_{e,l}/\sigma_{e,t}$	$\sigma_{e,t}/\sigma_{e,n}$
Control ($n = 8$)	0.36 ± 0.11	0.17 ± 0.07	0.10 ± 0.06	2.07	1.68
Region 1 ($n = 5$)	0.63 ± 0.17*	0.46 ± 0.23*	0.20 ± 0.07	1.38	2.35
Region 2 ($n = 6$)	0.55 ± 0.19	0.45 ± 0.22*	0.18 ± 0.08	1.23	2.45
Region 3 ($n = 5$)	0.51 ± 0.11	0.41 ± 0.17*	0.16 ± 0.06	1.25	2.48

*Conductivities are presented as mean value ± SD. Number of 3D reconstructions: n. Statistical significance vs. control are marked with *.*

and presented steps toward imaging-based measurement of parameters for models of electrical conduction in the normal and diseased heart.

Large overview images covering the scar and regions of interest illustrated pronounced changes in the distribution and volume fractions of different tissue constituents in the MI heart. We focused on quantifying volume fractions of tissue constituents and calculating extracellular conductivities. Fluorescent labeling and confocal microscopy allowed us to generate 3D reconstructions of tissue microstructure in control and diseased hearts. We analyzed these reconstructions to provide quantitative information on remodeling of volume fractions of tissue constituents in MI. Our approach quantified decreased V_{myo} accompanied by increased V_e proximal and adjacent to the scar (regions 1 and 2) vs. control tissue. We propose that the measured volume fractions provide a solid foundation for parameterization of models of cardiac conduction. For instance, the measurements can be used to adjust

volume fractions of the intracellular and extracellular domains in multidomain modeling (Sachse et al., 2009). Similarly, the provided information on V_{fibro} and $V_{myofibro}$ in control and MI tissue can be used to inform the design of computational studies of cardiac conduction. For example, the study design can reflect the presence of myofibroblasts found in MI regions, which may alter myocyte electrophysiology and impulse propagation as a result of myocyte-myofibroblast interactions. Moreover, this information can help to constrain the ranges of parameter sensitivity studies on effects of fibroblasts and myofibroblasts.

We applied the tissue reconstructions to calculate extracellular conductivity tensors in control and MI myocardium at the submillimeter scale (**Table 2**). Measurements of cardiac tissue conductivities using conventional electrode-based systems have not been performed at this scale. While single-cell membrane electrophysiology is accessible by patch clamp experiments, and has therefore been studied extensively, it remains difficult to measure conductivity parameters of myocardial tissue, especially on a small scale. Thus, mathematical models have been used to estimate these parameters. A comparison of our computational results with published measurements and model-based estimations of extracellular conductivities is presented in **Table 3**. Noteworthy, most prior measurements were obtained from normal tissues. Only a small number of studies presented all three components of the extracellular conductivity tensor. The spread of published values is large, which arguably reflects differences in experimental approach, species and tissue regions. Our result of $\sigma_{e,l} = 0.36 \pm 0.11$ S/m in LV tissue of control rabbit is close to a prior measurement of 0.40 S/m from RV papillary muscle in the same species (Kleber and Riegger, 1987).

An interesting finding was that the spread of calculated conductivities (see SD values in **Table 2**) is large, suggesting pronounced spatial heterogeneity of conductivity at the submillimeter scale for all our experimental groups. In general, computational models of cardiac conduction do not account for these spatial heterogeneities and apply homogeneous conductivity values. The new data presented in **Table 2** establish a basis for computational studies accounting for heterogeneous distribution of conductivities.

The contribution of heterogeneities in extracellular conductivities and tissue composition in various cardiac diseases may be assessed computationally using the approach described in this study. While our study focused on applications related to simulations of cardiac conduction, further potential applications include parameter estimation for simulations of cardiac biomechanics. It is well established that tissue remodeling such as fibrosis affects active and passive mechanical tissue properties. We suggest that the 3D reconstructions provide a basis for simulation of cardiac biomechanics at the submillimeter scale.

An important finding of our study is that V_e showed high variability at submillimeter scale. This variability in part results from the distribution of interlaminar clefts: They appear between lamina consisting of 3–5 myocyte layers. Assuming a myocyte height of 14 μm (Lasher et al., 2009) and an interstitial thickness of 3 μm, one would expect one cleft every 48–82 μm. Stack width in our images was ∼200 μm. Thus, depending on the imaged region and lamina width, two to four clefts were present in one stack, increasing variability in cleft volume fraction.

TABLE 3 | Extracellular conductivities for control and MI tissue.

References	Tissue type/location	Origin	$\sigma_{e,l}$ [S/m]	$\sigma_{e,t}$ [S/m]	$\sigma_{e,n}$ [S/m]
This study	Rabbit LV	Imaging	0.36	0.17	0.10
Clerc, 1976	Calf RV trabecula	Measurement	0.63	0.24	
Hand et al., 2009		Model	0.30	0.16	
Hooks et al., 2002	Rat LV	Model	0.26	0.11	0.11
Kleber and Riegger, 1987	Rabbit RV papillary	Measurement	0.40		
Roberts et al., 1979	Canine LV	Measurement	0.22	0.13	
Roberts and Scher, 1982	Canine LV	Measurement	0.12	0.08	
Schwab et al., 2013+	Rabbit LV	Imaging	0.26	0.22	0.13
Stinstra et al., 2005		Model	0.21	0.06	
MI					
	Rabbit LV				
This Study	0–0.2 mm	Imaging	0.63	0.46	0.20
	0.25–0.75 mm		0.55	0.45	0.18
	1–1.25 mm		0.51	0.41	0.16
	Rabbit LV				
Schwab et al., 2013+	0.5–5.5 mm	Imaging	0.26	0.20	0.17
	7.5–12.5 mm		0.40	0.29	0.31
	12.5–17.5 mm		0.28	0.27	0.17
	17.5–22.5 mm		0.28	0.19	0.17

+*Myocyte sheets and interlaminar clefts were not identified. Thus, conductivities are ordered by magnitude.*

Differences of volume fractions found between region 3 and control were not significant except for myofibroblasts, suggesting that at distances larger than 1 mm from the infarct, tissue composition tends to be largely unaffected by the infarct. Previous studies using rabbit MI models, but different methods of analysis (Driesen et al., 2007; Seidel et al., 2017), have shown a similar intactness of tissue distal from the scar. Interestingly, at 2 weeks after MI in rat, the transition from the infarcted to normal tissue occurred within only 200–300 μm (Rutherford et al., 2012), whereas at 2, 5, and 8 weeks of MI in sheep, fibrotic alterations were found also in myocardium remote from the infarct (Jackson et al., 2002). Thus, the width of the peri-infarct zone and remodeling seems species-dependent. We suggest that our methodology will be useful to characterize species-specific remodeling.

We note that many approaches have been developed to quantify fibrosis in histological sections. A common measure is quantification of collagen after Masson's trichrome staining in thin tissue sections. Also, WGA, which stains the extracellular matrix and the pericellular matrix, i.e., the glycocalyx, has been proposed for identification of collagen (Soderstrom, 1987; Emde et al., 2014). However, fibrosis is defined as the formation of excess connective tissue, which includes not only collagen and other proteins of the extracellular matrix, but also cells of fibrous connective tissue, such as fibroblasts

and myofibroblasts. To account for this definition and to quantify fibrosis more comprehensively, the presented study introduces a quantitative measure of cardiac fibrosis (Equation 1). We calculated the degree of fibrosis as the increased volume fraction of fibrotic tissue constituents in a region of interest vs. control. This included the increase of volume fractions of extracellular space without clefts, fibroblasts and myofibroblasts. As an alternative for comparing the degree of fibrosis between different tissue types, Equation (1) can be normalized by the volume fraction of non-fibrotic tissue constituents in control. The major contributor to fibrosis was increased V_e. In our calculation, we excluded volumes of interlaminar clefts, because those exhibited low WGA values indicating only marginal presence of collagen. We did not find increases of WGA intensity in clefts in MI. Our measure suggests that fibrosis is a decreasing function of distance from the infarct scar.

The presented conductivity analyses are based on approaches that we introduced earlier (Schwab et al., 2013). We note several important differences: The investigated tissue samples were more proximal to the MI than in our previous study (**Table 3**), which allowed us to describe more pronounced remodeling. Compared to the previously used threshold-based approach to segment image stacks into 4 domains (**Table 3**), we created more refined and accurate reconstructions of the tissue composition. This allowed us to augment our conductivity model with information about six domains. In particular the information on interlaminar clefts allowed us novel analyses. These clefts were not visible in many previous studies, because conventional mounting methods cause compression of tissue preparations. In the presented computational simulations, we increased the spatial resolution from 800 nm to 200 nm. Furthermore, an increased number of studied animals allowed us to perform statistical tests, which was not possible in previous work.

Several assumptions underlie the presented conductivity measurements. The exclusion of fibroblast and myofibroblast domains is motivated by the cell membrane of those cells, which poses a barrier for currents in the extracellular space. We excluded the vessel domain from the conductivity model with the reasoning that endothelial cells in the capillary wall represent a high resistivity for extracellular currents (Olesen and Crone, 1983; Stinstra et al., 2005). The myocyte segmentation was masked with a thresholded WGA image to conservatively reproduce the surface region between the extracellular space and myocytes. This step also added the transverse tubular system of the myocytes to the conductivity model. However, due to the simple structure of the transverse tubular system in rabbit (Savio-Galimberti et al., 2008), it is reasonable to assume that they do not contribute to extracellular conductivity in tissue.

Significant differences for several components of conductivity tensors were found in the border zone regions vs. control tissue. Longitudinal ($\sigma_{e,l}$) and transverse ($\sigma_{e,t}$) conductivities increased, whereas normal conductivities ($\sigma_{e,n}$) did not change significantly. Because the increase in transverse conductivity was more pronounced, anisotropy ($\sigma_{e,l}/\sigma_{e,t}$) was reduced by nearly 50% in the border zone vs. control. These findings are important for simulations of MI-associated arrhythmia. It has been shown in several studies that reduced anisotropy can lead to conduction block and trigger arrhythmia, especially at the transition from high to low intracellular conductivity (Rohr et al., 1997; Seidel et al., 2010). We suggest that reduced extracellular anisotropy in the border zone contributes to these effects. Our study provides parameter ranges to test this hypothesis in computational models.

A major finding of this study was the approximately linear relationship between all components of the conductivity tensor and V_e, which comprises V_{cleft}. Indeed, linear regression analysis showed that V_e is an excellent predictor of the measured conductivities (**Figure 11**). In comparison, V_{cleft} alone and V_e without V_{cleft} were weak predictors. We explain these findings by an additive effect of V_{cleft} to the prediction of extracellular conductivity using V_e without V_{cleft} only. We also found that V_{cleft} and V_e–V_{cleft} do not depend on each other. Excluding V_{cleft} from the predicting variable (**Figures 11G–I**) therefore leads to poor prediction of extracellular conductivity, despite the small volume contribution of the interlaminar clefts (Figure S9). These findings underpin the importance of structure-preserving mounting methods for image-based estimation of modeling parameters. We note that in addition to V_e knowledge on the orientation of myocyte fibers and lamina is necessary for predicting extracellular conductivities. Nevertheless, we suggest that the presented approach will enable efficient and accurate estimation of extracellular conductivity tensors from microscopic images.

LIMITATIONS

We acknowledge limitations regarding tissue processing and imaging. Most of these limitations were discussed in our prior work (Lackey et al., 2011; Schwab et al., 2013; Seidel et al., 2013, 2016, 2017). Tissue remodeling after MI is a dynamic process, which is not completed after 3 weeks as well as species and size dependent (Pfeffer and Braunwald, 1990). Thus, volume fractions presented for regions 1 to 3 will differ at later or earlier stages of the remodeling and for other species. We note that vimentin and α-SMA are not specific for fibroblasts and myofibroblasts. Hence, the fibroblast and myofibroblast domains presented here include other non-myocytes. Fixation and processing of tissue biopsies may cause artifacts, for example tissue shrinking or tearing. It is unclear if these changes affect all tissue components to the same degree. Since tissue stability is especially low in interlaminar clefts, due to reduced collagen content, clefts may be deformed. However, in our earlier work we showed that in intact, living tissue, clefts appear very similar to those observed in fixed, WGA-labeled tissue slices and that compression-free mounting preserves tissue structure vs. conventional methods (Seidel et al., 2016). Similarly, the volume fraction of blood vessels may depend on perfusion pressure during fixation. This would constitute a systematic error because all hearts were

perfused with the same system and pressure. The point spread function of a confocal microscope is anisotropic, thus blurring of, for example, the extracellular signal is more pronounced in laser light direction than transverse directions. With our imaging protocol, this might lead to higher conductivities in longitudinal and transverse vs. normal direction. Also, V_e might be overestimated near very thin intercellular spaces below the resolution limit. We reduced these issues by image deconvolution.

AUTHOR CONTRIBUTIONS

FS and TS: designed the study; JG, AS, and FS: drafted the manuscript; TS: performed surgeries; AS and TS: acquired image data; JG and AS: analyzed the data. All authors developed software for this project, interpreted the data, critically revised the manuscript, and approved the version to be published.

FUNDING

This work was supported by the Nora Eccles Treadwell Foundation and the American Heart Association (14POST19820010).

ACKNOWLEDGMENTS

We thank Mrs. Jayne Davis, Mrs. Nancy Allen, and Mr. Chris Hunter for technical support. We also thank Marcus Blackburn for contributing to segmentation of myocytes.

SUPPLEMENTARY MATERIAL

The Supplementary Material for this article can be found online at: https://www.frontiersin.org/articles/10.3389/fphys.2018.00239/full#supplementary-material

REFERENCES

Balay, S., Gropp, W. D., McInnes, L. C., and Smith, B. F. (1997). "Efficient management of parallelism in Object Oriented Numerical Software Libraries," in *Modern Software Tools in Scientific Computing,* eds E. Arge, A. M. Bruaset, and H. P. Langtangen (Birkhäuser Press), 163–120.

Clayton, R. H., Bernus, O., Cherry, E. M., Dierckx, H., Fenton, F. H., Mirabella, L., et al. (2011). Models of cardiac tissue electrophysiology: progress, challenges and open questions. *Prog. Biophys. Mol. Biol.* 104, 22–48. doi: 10.1016/j.pbiomolbio.2010.05.008

Clerc, L. (1976). Directional differences of impulse spread in trabecular muscle from mammalian heart. *J. Physiol.* 255, 335–346. doi: 10.1113/jphysiol.1976.sp011283

Driesen, R. B., Verheyen, F. K., Dijkstra, P., Thoné, F., Cleutjens, J. P., Lenders, M. H., et al. (2007). Structural remodelling of cardiomyocytes in the border zone of infarcted rabbit heart. *Mol. Cell. Biochem.* 302, 225–232. doi: 10.1007/s11010-007-9445-2

Emde, B., Heinen, A., Godecke, A., and Bottermann, K. (2014). Wheat germ agglutinin staining as a suitable method for detection and quantification of fibrosis in cardiac tissue after myocardial infarction. *Eur. J. Histochem.* 58:2448. doi: 10.4081/ejh.2014.2448

Falgout, R. D., and Yang, U. M. (2002). "hypre: a library of high performance preconditioners," in *ICCS '02 Proceedings of the International Conference on Computational Science-Part, III* (Amsterdam: Springer), 632–641.

Fink, M., Niederer, S. A., Cherry, E. M., Fenton, F. H., Koivumaki, J. T., Seemann, G., et al. (2011). Cardiac cell modelling: observations from the heart of the cardiac physiome project. *Prog. Biophys. Mol. Biol.* 104, 2–21. doi: 10.1016/j.pbiomolbio.2010.03.002

Foster, K. R., and Schwan, H. P. (1989). Dielectric properties of tissues and biological materials: a critical review. *Crit. Rev. Biomed. Eng.* 17, 25–104.

Gaudesius, G., Miragoli, M., Thomas, S. P., and Rohr, S. (2003). Coupling of cardiac electrical activity over extended distances by fibroblasts of cardiac origin. *Circ. Res.* 93, 421–428. doi: 10.1161/01.RES.0000089258.40661.0C

Hand, P. E., Griffith, B. E., and Peskin, C. S. (2009). Deriving macroscopic myocardial conductivities by homogenization of microscopic models. *Bull. Math. Biol.* 71, 1707–1726. doi: 10.1007/s11538-009-9421-y

Hooks, D. A., Tomlinson, K. A., Marsden, S. G., Legrice, I. J., Smaill, B. H., Pullan, A. J., et al. (2002). Cardiac microstructure implications for electrical propagation and defibrillation in the heart. *Circ. Res.* 91, 331–338. doi: 10.1161/01.RES.0000031957.70034.89

Hooks, D. A., Trew, M. L., Caldwell, B. J., Sands, G. B., Legrice, I. J., and Smaill, B. H. (2007). Laminar arrangement of ventricular myocytes influences electrical behavior of the heart. *Circ. Res.* 101, e103–e112. doi: 10.1161/CIRCRESAHA.107.161075

Hu, N., Straub, C. M., Garzarelli, A. A., Sabey, K. H., Yockman, J. W., and Bull, D. A. (2010). Ligation of the left circumflex coronary artery with subsequent MRI and histopathology in rabbits. *J. Am. Assoc. Lab. Anim. Sci.* 49, 838–844.

Hulsmans, M., Clauss, S., Xiao, L., Aguirre, A. D., King, K. R., Hanley, A., et al. (2017). Macrophages facilitate electrical conduction in the heart. *Cell* 169, 510.e20–522.e20. doi: 10.1016/j.cell.2017.03.050

Hutter, F., Hoos, H. H., and Leyton-Brown, K. (2011). Sequential model-based optimization for general algorithm configuration. *LION* 5, 507–523. doi: 10.1007/978-3-642-25566-3_40

Jackson, B. M., Gorman, J. H., Moainie, S. L., Guy, T. S., Narula, N., Narula, J., et al. (2002). Extension of borderzone myocardium in postinfarction dilated cardiomyopathy. *J. Am. Coll. Cardiol. 40*, 1160–1167; discussion: 1168–1171. doi: 10.1016/S0735-1097(02)02121-6

Johnston, B. M. (2016). Six conductivity values to use in the bidomain model of cardiac tissue. *IEEE Trans. Biomed. Eng.* 63, 1525–1531. doi: 10.1109/TBME.2015.2498144

Kléber, A. G., and Riegger, C. B. (1987). Electrical constants of arterially perfused rabbit papillary muscle. *J. Physiol.* 385, 307–324. doi: 10.1113/jphysiol.1987.sp016495

Krenning, G., Zeisberg, E. M., and Kalluri, R. (2010). The origin of fibroblasts and mechanism of cardiac fibrosis. *J. Cell. Physiol.* 225, 631–637. doi: 10.1002/jcp.22322

Lackey, D. P., Carruth, E. D., Lasher, R. A., Boenisch, J., Sachse, F. B., and Hitchcock, R. W. (2011). Three-dimensional modeling and quantitative analysis of gap junction distributions in cardiac tissue. *Ann. Biomed. Eng.* 39, 2683–2694. doi: 10.1007/s10439-011-0369-3

Lasher, R. A., Hitchcock, R. W., and Sachse, F. B. (2009). Towards modeling of cardiac micro-structure with catheter-based confocal microscopy: a novel approach for dye delivery and tissue characterization. *IEEE Trans. Med. Imaging* 28, 1156–1164. doi: 10.1109/TMI.2009.2017376

Legrice, I. J., Smaill, B. H., Chai, L. Z., Edgar, S. G., Gavin, J. B., and Hunter, P. J. (1995). Laminar structure of the heart: ventricular myocyte arrangement and connective tissue architecture in the dog. *Am. J. Physiol.* 269, H571–582. doi: 10.1152/ajpheart.1995.269.2.H571

Lloyd, C. M., Lawson, J. R., Hunter, P. J., and Nielsen, P. F. (2008). The CellML Model Repository. *Bioinformatics* 24, 2122–2123. doi: 10.1093/bioinformatics/btn390

Luke, R. A., and Saffitz, J. E. (1991). Remodeling of ventricular conduction pathways in healed canine infarct border zones. *J. Clin. Invest.* 87, 1594–1602. doi: 10.1172/JCI115173

Miragoli, M., Gaudesius, G., and Rohr, S. (2006). Electrotonic modulation of cardiac impulse conduction by myofibroblasts. *Circ. Res.* 98, 801–810. doi: 10.1161/01.RES.0000214537.44195.a3

Moreno, J. D., and Clancy, C. E. (2009). Using computational modeling to predict arrhythmogenesis and antiarrhythmic therapy. *Drug Discov. Today* 6, 71–84. doi: 10.1016/j.ddmod.2010.03.001

Olesen, S. P., and Crone, C. (1983). Electrical resistance of muscle capillary endothelium. *Biophys. J.* 42, 31–41. doi: 10.1016/S0006-3495(83)84366-5

Pfeffer, M. A., and Braunwald, E. (1990). Ventricular remodeling after myocardial infarction. Experimental observations and clinical implications. *Circulation* 81, 1161–1172. doi: 10.1161/01.CIR.81.4.1161

Quinn, T. A., Camelliti, P., Rog-Zielinska, E. A., Siedlecka, U., Poggioli, T., O'toole, E. T., et al. (2016). Electrotonic coupling of excitable and nonexcitable cells in the heart revealed by optogenetics. *Proc. Natl. Acad. Sci. U.S.A.* 113, 14852–14857. doi: 10.1073/pnas.1611184114

Roberts, D. E., and Scher, A. M. (1982). Effect of tissue anisotropy on extracellular potential fields in canine myocardium *in situ*. *Circ. Res.* 50, 342–351. doi: 10.1161/01.RES.50.3.342

Roberts, D. E., Hersh, L. T., and Scher, A. M. (1979). Influence of cardiac fiber orientation on wavefront voltage, conduction velocity, and tissue resistivity in the dog. *Circ. Res.* 44, 701–712. doi: 10.1161/01.RES.44.5.701

Rohr, S., Kucera, J. P., Fast, V. G., and Kleber, A. G. (1997). Paradoxical improvement of impulse conduction in cardiac tissue by partial cellular uncoupling. *Science* 275, 841–844. doi: 10.1126/science.275.5301.841

Rutherford, S. L., Trew, M. L., Sands, G. B., Legrice, I. J., and Smaill, B. H. (2012). High-resolution 3-dimensional reconstruction of the infarct border zone: impact of structural remodeling on electrical activation. *Circ. Res.* 111, 301–311. doi: 10.1161/CIRCRESAHA.111.260943

Sachse, F. B. (2004). *Computational Cardiology: Modeling of Anatomy, Electrophysiology, and Mechanics*. Heidelberg: Springer.

Sachse, F. B., Moreno, A. P., Seemann, G., and Abildskov, J. A. (2009). A model of electrical conduction in cardiac tissue including fibroblasts. *Ann. Biomed. Eng.* 37, 874–889. doi: 10.1007/s10439-009-9667-4

Savio-Galimberti, E., Frank, J., Inoue, M., Goldhaber, J. I., Cannell, M. B., Bridge, J. H., et al. (2008). Novel features of the rabbit transverse tubular system revealed by quantitative analysis of three-dimensional reconstructions from confocal images. *Biophys. J.* 95, 2053–2062. doi: 10.1529/biophysj.108.130617

Schwab, B. C., Seemann, G., Lasher, R. A., Torres, N. S., Wulfers, E. M., Arp, M., et al. (2013). Quantitative analysis of cardiac tissue including fibroblasts using three-dimensional confocal microscopy and image reconstruction: towards a basis for electrophysiological modeling. *IEEE Trans. Med. Imaging* 32, 862–872. doi: 10.1109/TMI.2013.2240693

SCI (2015). *"Seg3D" Volumetric Image Segmentation and Visualization.* Available online at: http://www.seg3d.org/ (Accessed 20 September 2017).

Seidel, T., Dräbing, T., Seemann, G., and Sachse, F. B. (2013). "A semi-automatic approach for segmentation of three-dimensional microscopic image stacks of cardiac tissue," in *Imaging and Modeling of the Heart. FIMH 2013*, Lecture Notes in Computer Science, Vol. 7945, eds S. Ourselin, D. Rueckert, and N. Smith (Berlin, Heidelberg: Springer), 300–307.

Seidel, T., Edelmann, J. C., and Sachse, F. B. (2016). Analyzing remodeling of cardiac tissue: a comprehensive approach based on confocal microscopy and 3D reconstructions. *Ann. Biomed. Eng.* 44, 1436–1448. doi: 10.1007/s10439-015-1465-6

Seidel, T., Salameh, A., and Dhein, S. (2010). A simulation study of cellular hypertrophy and connexin lateralization in cardiac tissue. *Biophys. J.* 99, 2821–2830. doi: 10.1016/j.bpj.2010.09.010

Seidel, T., Sankarankutty, A. C., and Sachse, F. B. (2017). Remodeling of the transverse tubular system after myocardial infarction in rabbit correlates with local fibrosis: a potential role of biomechanics. *Prog. Biophys. Mol. Biol.* 130, 302–314. doi: 10.1016/j.pbiomolbio.2017.07.006

Söderström, K. O. (1987). Lectin binding to collagen strands in histologic tissue sections. *Histochemistry* 87, 557–560. doi: 10.1007/BF00492470

Stinstra, J. G., Hopenfeld, B., and Macleod, R. S. (2005). On the passive cardiac conductivity. *Ann. Biomed. Eng.* 33, 1743–1751. doi: 10.1007/s10439-005-7257-7

Yao, J. A., Hussain, W., Patel, P., Peters, N. S., Boyden, P. A., and Wit, A. L. (2003). Remodeling of gap junctional channel function in epicardial border zone of healing canine infarcts. *Circ. Res.* 92, 437–443. doi: 10.1161/01.RES.0000059301.81035.06

Zlochiver, S., Muñoz, V., Vikstrom, K. L., Taffet, S. M., Berenfeld, O., and Jalife, J. (2008). Electrotonic myofibroblast-to-myocyte coupling increases propensity to reentrant arrhythmias in two-dimensional cardiac monolayers. *Biophys. J.* 95, 4469–4480. doi: 10.1529/biophysj.108.136473

Conflict of Interest Statement: The authors declare that the research was conducted in the absence of any commercial or financial relationships that could be construed as a potential conflict of interest.

frontiers in Physics

ORIGINAL RESEARCH
published: 27 February 2018
doi: 10.3389/fphy.2018.00015

Cardiac Re-entry Dynamics and Self-termination in DT-MRI Based Model of Human Fetal Heart

Irina V. Biktasheva[1,2*], *Richard A. Anderson*[3], *Arun V. Holden*[4], *Eleftheria Pervolaraki*[4] *and Fen Cai Wen*[1]

[1] Department of Computer Science, University of Liverpool, Liverpool, United Kingdom, [2] CEMPS, University of Exeter, Exeter, United Kingdom, [3] MRC Centre for Reproductive Health, University of Edinburgh, Edinburgh, United Kingdom, [4] School of Biomedical Sciences, University of Leeds, Leeds, United Kingdom

The effect of human fetal heart geometry and anisotropy on anatomy induced drift and self-termination of cardiac re-entry is studied here in MRI based 2D slice and 3D whole heart computer simulations. Isotropic and anisotropic models of 20 weeks of gestational age human fetal heart obtained from 100 μm voxel diffusion tensor MRI data sets were used in the computer simulations. The fiber orientation angles of the heart were obtained from the orientation of the DT-MRI primary eigenvectors. In a spatially homogeneous electrophysiological monodomain model with the DT-MRI based heart geometries, cardiac re-entry was initiated at a prescribed location in a 2D slice, and in the 3D whole heart anatomy models. Excitation was described by simplified FitzHugh-Nagumo kinetics. In a slice of the heart, with propagation velocity twice as fast along the fibers than across the fibers, DT-MRI based fiber anisotropy changes the re-entry dynamics from pinned to an anatomical re-entry. In the 3D whole heart models, the fiber anisotropy changes cardiac re-entry dynamics from a persistent re-entry to the re-entry self-termination. The self-termination time depends on the re-entry's initial position. In all the simulations with the DT-MRI based cardiac geometry, the anisotropy of the myocardial tissue shortens the time to re-entry self-termination several folds. The numerical simulations depend on the validity of the DT-MRI data set used. The ventricular wall showed the characteristic transmural rotation of the helix angle of the developed mammalian heart, while the fiber orientation in the atria was irregular.

Keywords: cardiac arrhythmias, anatomically realistic modeling, anisotropy, anatomy induced drift, FitzHugh-Nagumo model

OPEN ACCESS

Edited by:
S. Sridhar,
Robert Bosch Centre for Cyber-Physical Systems, Indian Institute of Science, India

Reviewed by:
Rupamanjari Majumder,
Leiden University Medical Center, Netherlands
Silvia Capuani,
Consiglio Nazionale Delle Ricerche (CNR), Italy

***Correspondence:**
Irina V. Biktasheva
ivb@liverpool.ac.uk

Specialty section:
This article was submitted to Biomedical Physics, a section of the journal Frontiers in Physics

Received: *03 November 2017*
Accepted: *08 February 2018*
Published: *27 February 2018*

Citation:
Biktasheva IV, Anderson RA, Holden AV, Pervolaraki E and Wen FC (2018) Cardiac Re-entry Dynamics and Self-termination in DT-MRI Based Model of Human Fetal Heart. Front. Phys. 6:15. doi: 10.3389/fphy.2018.00015

1. INTRODUCTION

Since the over a century ago hypothesis that cardiac re-entry underlies cardiac arrhythmias [1, 2], and the much later confirmation of the hypothesis in cardiac tissue experiment [3, 4], the re-entry (*aka* spiral wave in 2D, cardiac excitation vortex in 3D), its origin and its role in sustained arrhythmias and fibrillation, as well as a possibility of its effective control and defibrillation, have been an object of extensive theoretical study and modeling [5–20]. From experiment, it is an established point of view that cardiac arrhythmias are due to a complex combination of electrophysiological [21–23], structural [24–27], and anatomical [28, 29] factors which sustain cardiac re-entry [30–33].

The specific effect of the heart anisotropy and anatomy on cardiac re-entry dynamics is well appreciated [34–37], and has been studied in simplified mathematical and computer models [14–16, 38, 39]. The anisotropic discontinuities in the heart muscle have been commonly seen as a substrate for rise of cardiac re-entry due to the abrupt change in conduction velocity and wavefront curvature [14, 40, 41]. On the other hand, extensive mapping of cardiac myocyte orientation in mammalian hearts has shown that the transmural fiber arrangement, including the range of transmural change in fiber angle in ventricular wall, was consistent within a species, and varied between species [42, p. 173]. So that the anisotropic discontinuities observed in healthy hearts, and shown to be consistent within a species, might have been suspected to facilitate initiation of arrhythmias.

With the recent advance in DT-MRI technology and in High Performance Computing (HPC), the DT-MRI data sets, including anatomy and myofiber structure, can now be directly incorporated into anatomically realistic computer simulations [34, 43, 44], so that the anisotropy of the tissue in the *in silico* model can be switched on and off for the comparison between the isotropic and anisotropic conduction, in order to see the specific anatomy effects, as well as the interplay between the anatomy and anisotropy of an individual heart.

In this paper, we present DT-MRI based anatomically and myofiber structure realistic computer simulation study of cardiac re-entry dynamics in the *in silico* model of human fetal heart. The raw DT-MRI data [45] was segmented into the tissue/non-tissue pixels based on the MRI luminosity threshold, followed by the calculation of the fiber angles at each voxel from the diffusion-weighted DT-MRI images. The DT-MRI yields 3 eigenvalues, the primary (largest) eigenvalue was used to define local fiber orientations in the simulation study.

The main objectives are to clarify: (i) whether the anatomical settings of the fetal heart might support a positive filament tension re-entry, and (ii) what would it be the role of the heart anisotropy in that case. Here we demonstrate that anisotropy of the fetal heart rather facilitates self-termination of cardiac re-entry. In a 2D slice of the heart, the fiber anisotropy might change dynamics of the re-entry from pinned to anatomical re-entry. In the full 3D DT-MRI based model, depending on the location of re-entry initiation, the isotropic geometry of the heart might sustain perpetual re-entry even with a positive filament tension kinetics. While the same positive filament tension re-entry initiated at the same location of the fetal heart with the fiber anisotropy self-terminates within a fraction of the rotation period. Time of re-entry self-termination depends on the re-entry initial position. Anisotropy of the real heart speeds up re-entry self-termination. The geometry and anisotropy of the heart together ensure the fastest self-termination of cardiac re-entry.

The novel significance of our findings is that we demonstrate that the heart anisotropy might have rather anti-arrhythmic function as it facilitates fast self-termination of cardiac re-entry. A general role of fiber anisotropy in the genesis and sustenance of arrhythmias could be addressed by numerics even on idealized and simplified geometries with different spatial distributions of anisotropy. The biomedical question addressed in the manuscript is whether self-terminating ventricular arrhythmias can occur in a developing fetal heart, as has inferred from fECG data in Benson et al. [46].

2. MATERIALS AND METHODS

2.1. DT-MRI Data Sets

Tissue acquisition followed medical termination of pregnancy with written and informed consent, and Ethical approval from Lothian Research Ethics Committee (reference 08/S1101/1). Temporary storage of the tissue for imaging was in premises licensed under the UK 2004 Human Tissues Act.

The DT-MRI data set used in this study was of a 143 days gestational age (DGA) human fetal heart described in Pervolaraki et al. [45]. It was selected as by 143 days the smooth, transmural 120° transmural rotation in helix fiber angle is well established [45, 47, 48]. The heart was immersed in formalin shortly after dissection, and imaged in fomblin after two weeks in formalin.

MRI acquisition was performed in a Bruker Biospin (Ettlingen, Germany) 9.4 Tesla vertical NMR/S System with a 22 mm imaging coil for Hydrogen (1 H). A three-dimensional diffusion weighted spin echo sequence was carried out at 20°C with 0.1 mm^2 resolution, echo time = 15 ms, repetition time = 500 ms, with 6 averages and a b-value of 1,000 s/mm^2. In each scan, diffusion weighted images were obtained in 12 directions. The average scan time was 24 h.

2.2. DT-MRI Based Anatomy Model

Figure 1 shows a cross section of the 143 days of gestational age (DGA) fetal heart, with the already formed intramural myolaminar structure, and yet a bit irregular surface epicardial, endocardial, and septal fibers, see also Figure 4 in Pervolaraki et al. [45, p. 5] for the color-encoded fractional anisotropy (FA) and all the three components of the fiber angles in the human fetal heart. While in an adult heart, pinning of cardiac re-entry to endocardium structures such as pectinate muscles junction with crystae terminalis had been previously reported [31, 33, 49]. The DT-MRI based fetal heart model offered a unique opportunity to see whether the 20 weeks of gestation age intramural heart structure was capable to support cardiac re-entry, because at that fetal development stage it would not be possible yet for the re-entry to pin to the endocardium fine features, for these anatomical structures were yet to be developed later.

The DT-MRI data sets of the 128 × 128 × 128 voxels size, with voxel resolution of ∼100 μm, of 143 days of gestational age (DGA) human fetal heart [45], were converted into the BeatBox [44] regular Cartesian mesh `.bbg` geometry format, containing the DT-MRI Cartesian coordinates of the heart tissue points together with the corresponding components of the diffusion tensor primary eigenvectors [44]. The `.bbg` file is an ASCII text file, each line in which describes a point in a regular mesh in the following format:

```
x,y,z,status,fiber_x,fiber_y,fiber_z
```

Here `x, y, z` are integer Cartesian coordinates of a DT-MRI voxel, `status` is a flag with a nonzero-value for a tissue

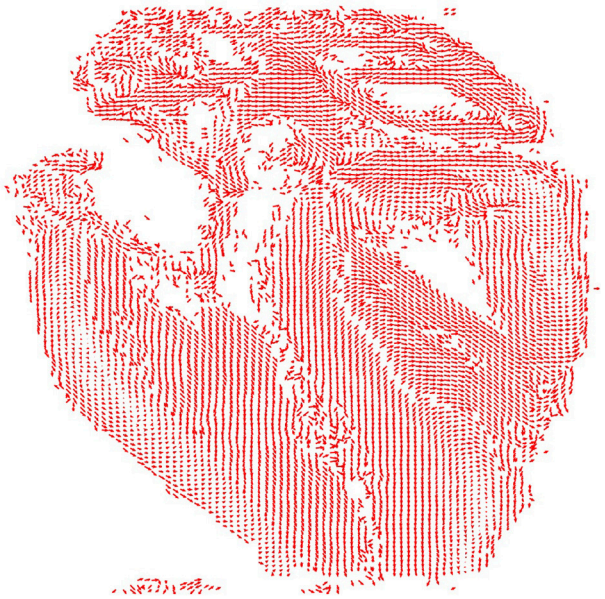

FIGURE 1 | The 143 DGA human fetal heart [45]. BeatBox [44] geometry `.bbg` format visualization with projections of the unit vectors of the local fiber orientation onto the cross-section plane: a smooth intramural fiber distribution has developed, with some surface irregular fibers from earlier developmental stages, as seen in Figure 4 [45, p. 5].

point, and `fiber_x`, `fiber_y`, `fiber_z` are x-, y- and z-components of the fiber orientation vector at that point. To reduce the size of the `.bbg` files, only the tissue points, that is points with non-zero `status` need to be specified, because the BeatBox solver will ignore the void points with zero status in any case. Although the original DT-MRI images data sets had $128 \times 128 \times 128$ voxels size, the actual dimensions of the fetal heart minimum bounding box were $67 \times 91 \times 128$, with 181070 tissue points.

The raw DT-MRI anatomy data [45] were segmented into the "tissue"/"not tissue" pixels discretion based on the MRI luminosity threshold, with the Cartesian fiber angles at each voxel obtained from the diffusion-weighted DT-MRI images. Only this basic segmentaion of the raw DT-MRI anatomy data [45] was taken into account in the computer simulation of cardiac re-entry dynamics, so we shall refer to it as the raw DT-MRI based anatomy model.

Any raw MRI and micro-CT image data show tiny bits of the preparation tissue, which usually get into the image together with the heart at the preparation stage. In the case of the raw DT-MRI image of the fetal heart [45], there happened to be a tiny bit of tissue at the bottom of the MRI image, adjacent to the apex of the fetal heart, see **Figure 1**, and the original Figure 2(a), last panel, in Pervolaraki et al. [45, p. 3]. In order to see whether this tiny "leftover" piece of the heart tissue is capable to affect the outcome of a re-entry simulation, we edited the MRI images in order to remove the "leftover" piece, and then considered a comparison of the re-entry simulation in the two 3D DT-MRI based heart models: (i) raw DT-MRI based anatomy model, and (ii) "edited" DT-MRI based anatomy model without the tiny "leftover" piece of the heart tissue.

In case of the 2D model of a slice of the heart, in order to construct the 2D diffusivity tensor, the fibers vectors were projected into the plane of the slice of the heart.

2.3. Cardiac Tissue Model

To investigate the effects of anatomy on cardiac re-entry dynamics we used *monodomain* tissue model with non-flux boundary conditions

$$\frac{\partial \mathbf{u}}{\partial t} = \mathbf{f}(\mathbf{u}) + \nabla \cdot \hat{\mathbf{D}} \nabla \mathbf{u}, \qquad \vec{n} \cdot \hat{\mathbf{D}} \nabla \mathbf{u}\Big|_G = 0, \tag{1}$$

where $\mathbf{u}(\vec{r}, t) = (u, v)^T$, $\vec{r}$ is the position vector, $\mathbf{f}(\vec{r}, t) = (f, g)^T$ is the FitzHugh-Nagumo [50] kinetics column-vector

$$f(u, v) = \alpha^{-1}(u - u^3/3 - v), \quad g(u, v) = \alpha\,(u + \beta - \gamma v), \tag{2}$$

with the parameter values $\alpha = 0.3$, $\beta = 0.71$, $\gamma = 0.5$, which in an infinite excitable medium support a rigidly rotating vortex with positive filament tension [51]. The simplified FHN model was intentionally chosen for this study in order to fully eliminate the possible effects of a realistic cell excitation kinetics, such as e.g., meander [50], alternans [52], negative filament tension [51], etc., and in order to enhance and highlight the pure effects of the heart anatomy and anisotropy on the cardiac re-entry outcome. $\hat{\mathbf{D}} = \mathbf{Q}\hat{P}$, where $\mathbf{Q} = \mathrm{diag}(1, 0) = \begin{bmatrix} 1 & 0 \\ 0 & 0 \end{bmatrix}$ is the matrix of the relative diffusion coefficients for u and v components, and $\hat{P} = [P_{jk}] \in \mathbb{R}^{3\times3}$ is the u component diffusion tensor, which has only two different eigenvalues: the bigger, simple eigenvalue $P_\parallel$ corresponding to the direction along the tissue fibers, and the smaller, double eigenvalue $P_\perp$, corresponding to the directions across the fibers, so that

$$P_{jk} = P_\perp \delta_{jk} + \left(P_\parallel - P_\perp\right) f_j f_k, \tag{3}$$

where $\vec{f} = (f_k)$ is the unit vector of the fiber direction; $\vec{n}$ is the vector normal to the tissue boundary G. In the isotropic simulation, $P_\parallel$ and $P_\perp$ values were fixed at $P_\parallel = P_\perp = 1$ [corresponding 1D conduction velocity 1.89, in the dimensionless units of Equations (1, 2)]. In the anisotropic simulations, $P_\parallel$ and $P_\perp$ values were fixed at $P_\parallel = 2$, $P_\perp = 0.5$ (corresponding conduction velocities 2.68 and 1.34 respectively). All the conduction velocities have been computed for the period waves with the frequency of the free spiral wave in the model, i.e., 11.36. With the isotropic diffusivity ($P_\parallel = P_\perp = 1$) equal to the geometric mean between the faster and the slower anisotropic diffusivities ($P_\parallel = 2, P_\perp = 1/2$), the isotropic conduction velocity 1.89 was almost exactly the same as the geometric mean $\approx$1.895 of the faster and slower (2.68 and 1.34 respectively) anisotropic conduction velocities, chosen in order

to minimize the maximal relative difference between the isotropic and anisotropic propagation speeds.

All the computer simulations presented here were done using the BeatBox [44] software package with the explicit time-step Euler scheme, on the Cartesian regular grid with space step discretization $\Delta x = 0.1$, time step discretization $\Delta t = 0.001$; 5-point stencil for isotropic, and 9-point stencil for anisotropic Laplacian approximation in 2D simulations; 7-point stencil for isotropic, and 27-point stencil for anisotropic Laplacian approximation in 3D simulations. The re-entry was initiated by the phase distribution method [53]: in the 2D simulations, at a prescribed location of the cross section of the DT-MRI based anatomical model shown in **Figure 1**; in the 3D simulations, at a prescribed location of the full DT-MRI based whole heart anatomical model.

The FHN model Equations (1, 2) is not biophysically detailed and is formulated in dimensionless units. So, for illustrative purposes only, if we took the FHN time unit to be 1 t.u. = 40 ms this would give the APD90 of 125.6 ms which is within the range reported e.g., by Zhu et al. [54]. The spiral wave period is then 454 ms: at our chosen kinetics parameters, the spirals in FHN model have a big core. With the space step discretization $\Delta x = 0.1$ in FHN simulations, whereas the real grid resolution is 100 μm = 0.1 mm, hence we would have the FHN space unit 1 s.u. = 1 mm. The (geometric mean) diffusivity of 1 s.u.^{2}/t.u. therefore works out as 0.025 mm^2/ms, and the corresponding conduction velocity of 1.89 s.u./t.u. is 0.04725 mm/ms. That gives a spiral wavelength of $\approx$21.45 mm. The conduction velocity thus obtained is within the range reported in Pervolaraki et al. [45], whereas the diffusivity is about four times smaller than the one used in Pervolaraki et al. [55]. We must stress here that, since the FHN kinetics is not biophysically detailed, one should not expect anything more than an order-of-magnitude correspondence with reality.

3. RESULTS

3.1. 2D MRI-Based "Slice" Simulations

In the 2D simulations, **Figure 2**, a counter-clockwise re-entry was initiated by the phase distribution method [53], with the initial center of rotation placed at the prescribed location $x_0 = 40, y_0 = 60$ in the 2D cross section of the DT-MRI based anatomical model shown in **Figure 1**.

In the **Figures 2A,B**, it can be seen that in both isotropic and anisotropic 2D simulations, at $t = 0$, there was identical location of the initial re-entry rotation center: roughly in the middle of the slice, in the vicinity of the septum cuneiform opening.

Figure 2A shows *isotropic* dynamics of the re-entry, that is with the fiber orientation data "turned OFF," so that only the geometry of the isotropic homogeneous slice affects the re-entry. While in an infinite medium the chosen FHN parameter values $\alpha = 0.3, \beta = 0.71, \gamma = 0.5$ produce rigidly rotating spiral [50], the boundaries of the fetal heart slice model cause the drift of the re-entry. The re-entry does not terminate because of the reflection from the inexcitable boundaries [12], but after the transient first rotation around the septum cuneiform opening, the tip of the re-entry firmly pins (at $t = 35$) to the sharp lower end of the cuneiform opening, see **Figure 2A**.

Figure 2B shows *anisotropic* dynamics of the re-entry, that is with the fiber orientation data "turned ON," so that both the geometry and the anisotropy of the otherwise homogeneous slice of the heart affect the dynamics of the re-entry, causing its drift. In the anisotropic slice, the re-entry also does not terminate at the inexcitable boundaries, but after a faster than in the previous isotropic case transient, compare the time units labels in the **Figures 2A,B**, the anisotropy of the medium turns the initial spiral wave into the fast anatomical re-entry around the septum cuneiform opening, see **Figure 2B**.

3.2. 3D Whole Heart MRI-Based Simulations

3.2.1. Raw DT-MRI Anatomy Model

In the 3D whole heart *raw* DT-MRI based simulations shown in the **Figures 3**, **4**, a counter-clockwise excitation vortex was initiated by the phase distribution method [53], with the initial position of the transmural vortex filament (yellow line) at the prescribed location *along the x axis* at $y_0 = 40, z_0 = 60$. It can be seen in **Figure 3** isotropic, and **Figure 4** anisotropic 3D simulations that, at $t = 0$, there was identical initial location of the filament of the excitation vortex: that is transmurally, roughly in the middle through the ventricles of the heart.

Figure 3 shows the *isotropic dynamics* of the excitation vortex, that is with the fiber orientation data "turned OFF," so that only the geometry of the otherwise isotropic homogeneous fetal heart affects dynamics of the vortex. At the chosen parameter values $\alpha = 0.3, \beta = 0.71, \gamma = 0.5$, the FHN vortex has positive filament tension [51], and, depending on topology of an isotropic homogeneous medium, either collapses or straightens up between parallel boundaries. In the isotropic simulations of the fetal heart, boundaries of the heart cause the vortex to drift and collapse. However, there exist initial locations of the excitation vortex, which although result in the drift of the vortex, still do not lead to the expected collapse of the vortex with positive filament tension. One of such outcomes is shown in the **Figure 3**. Here, following the geometry of the heart, after a very short transient, the initial vortex filament breaks into the two major pieces, each of which finds its own synchronous pathway in the "isotropic" fetal heart, resulting in the seemingly perpetual cardiac re-entry, which failed to self-terminate within the extended simulation time $t = 30$. **Figure 11** gives the summary of the simulation detail, where the maximum instant number of the filaments in the simulation was 9 at $t = 1.0$, the maximum instant total length of the filaments was 127.1 at $t = 1.6$; while the time average number of the filaments in the simulation was 3.4, and the time average total length of the filaments was 29.3. The time course of the instant number of filaments (blue dashed line) is shown in **Figure 12A**, and the time course of the instant total length of the filaments (blue dashed line) is shown in **Figure 12B**. It can be seen that, after a very fast transient increase in both the number of filaments and the total length of the filaments, these fail to disappear, and keep oscillating around above zero constants.

FIGURE 2 | Anisotropy effect in the 2D slice simulations, time shown under each panel in time units of Equations (1, 2). **(A)** *Isotropic conduction*: after the transient first rotation around the septum cuneiform opening, the slow excitation re-entry pins to the sharp low end of the opening in the fetal heart (See **Supplementary Video 1**). **(B)** *Anisotropic conduction*: after the fast transient first rotation around the septum cuneiform opening, the anisotropy of the fetal heart turns the initial spiral wave into the fast anatomical re-entry around the septum cuneiform opening (See **Supplementary Video 2**).

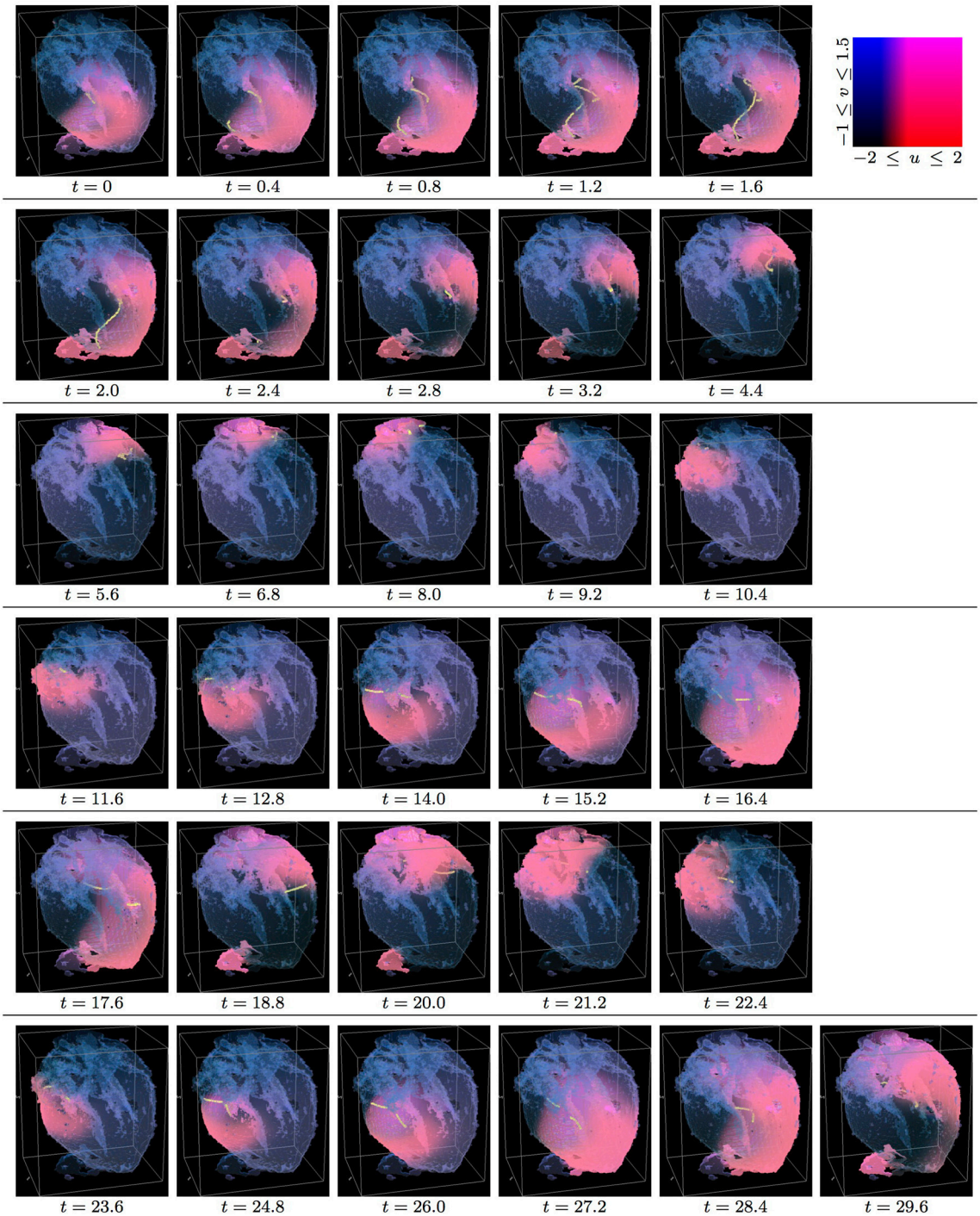

FIGURE 3 | Isotropic whole heart simulation. The translucent fetal heart is shown in blue, excitation front shown in red (see the color box in this figure), the yellow lines are the instant organizing filaments of the excitation vortices; time shown under each panel in time units of Equations (1, 2). After a short transient the organizing filament of the initial vortex breaks into the two short pieces each of which finds its own synchronous perpetual pathway, resulting in the perpetual cardiac re-entry in the fetal heart (See **Supplementary Video 3**).

Figure 4 shows *anisotropic dynamics* of the excitation vortex, that is with the fiber orientation data "turned ON," so that both the geometry and the anisotropy of the otherwise homogeneous model of the fetal heart affect dynamics of the vortex. Here, the anisotropy of the heart causes fast transient distortion of the filament, and drift toward the inexcitable boundary of the

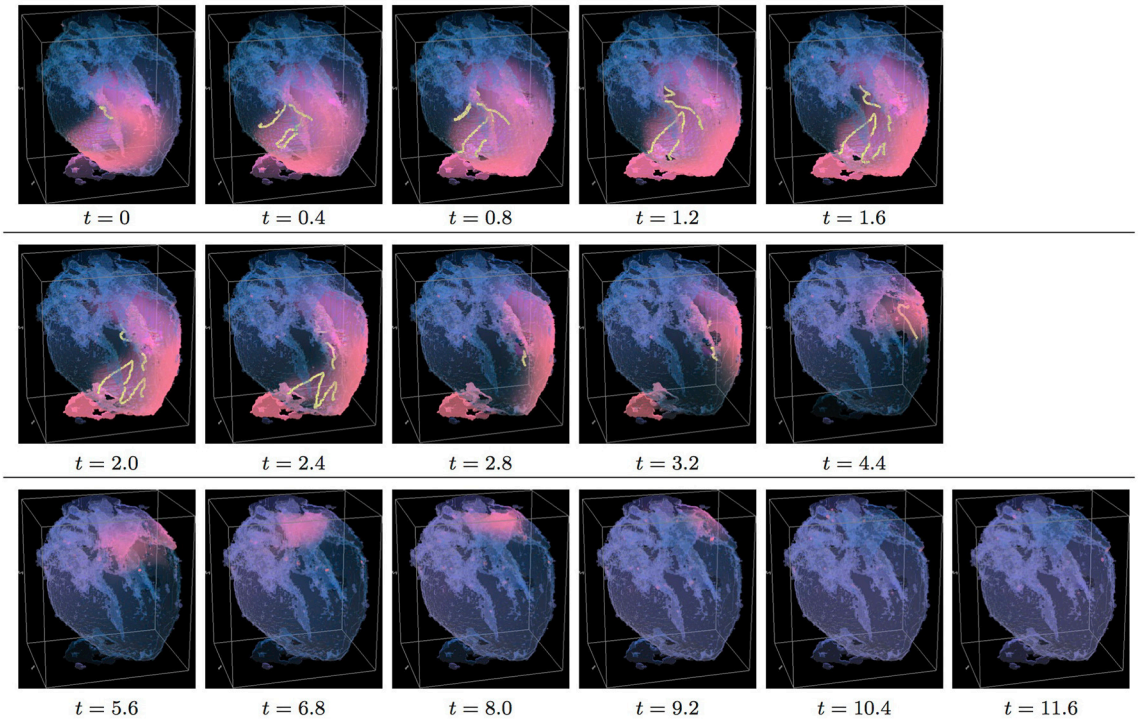

FIGURE 4 | Anisotropic whole heart simulation. The translucent fetal heart is shown in blue, excitation front shown in red (see the color box in **Figure 3**), the yellow lines are the instant organizing filaments of the excitation vortices; time shown under each panel in time units of Equations (1, 2). The anisotropy of the heart causes the fast transient distortion of the organizing filament of the initial excitation vortex and drift toward the inexcitable boundary of the heart, ultimately resulting in the very fast self termination of the excitation vortex (See **Supplementary Video 4**).

heart, followed by the very fast self-termination of the vortex by $t = 5.3$. The time course of the instant number of filaments (pink dotted line) is shown in **Figure 12A**, and the time course of the instant total length of the filaments (pink dotted line) is shown in **Figure 12B**. It can be seen that, after a very fast transient increase in both the number of the filaments and the total length of the filaments, all the filaments rapidly disappear. The maximum instant number of the filaments was 13 at $t = 0.8$, that is higher and achieved faster than in the isotropic conduction. The maximum instant total length of the filaments was 179.7 at $t = 1.8$, again much higher than in the isotropic conduction. The time average number of the filaments in the simulation was 6.5, twice higher than in the isotropic conduction, and the time average total length of the filaments was 91.2, three times higher than in the isotropic conduction, see the summary of the simulation detail in **Figure 11**.

In the 3D whole heart *raw* DT-MRI based simulations shown in the **Figures 3**, **4** a counter-clockwise excitation vortex was initiated by the phase distribution method [53], with the initial position of the transmural vortex filament (yellow line) at the prescribed location *along the y axis* at $x_0 = 40, z_0 = 60$, that is *perpendicular* to the initial orientation of the vortex filament shown in **Figures 3**, **4**. It can be seen in **Figure 5** isotropic, and in **Figure 6** anisotropic 3D simulations, that at $t = 0$, there was identical initial location of the filament of the excitation vortex: that is transmurally, roughly in the middle through the ventricles of the fetal heart, and *perpendicular* to the initial orientation of the vortex filament shown in **Figures 3**, **4**.

Figure 5 shows the *isotropic dynamics* of the excitation vortex, that is with the fiber orientation data "turned OFF," so that only the geometry of the otherwise isotropic homogeneous fetal heart affects dynamics of the vortex. Here, contrary to the expectation for the positive filament tension vortex to always contract, the organizing filament first transiently extends intramurally along the tissue walls, before the final break up into the two ring-like pieces, each of which then quickly contracts and terminates at the opposite base and apex regions of the heart by $t = 4$. The time course of the instant number of filaments (blue dashed line) is shown in **Figure 12C**, and the time course of the instant total length of the filaments (blue dashed line) is shown in **Figure 12D**. It can be seen that, after a very fast transient increase in both the number of the filaments and the total length of the filaments, all the filaments rapidly disappear. The maximum instant number of the filaments was 12 at $t = 1.4$, with the maximum instant total length of the filaments 188.0 achieved at $t = 1.5$. The time average number of the filaments in the simulation was 4.7, and the time average total length of the filaments was 80.5, see the summary of the simulation detail in **Figure 11**. It can be seen that in this isotropic conduction simulation, with just a different location/orientation of the initial vortex filament, the time average total length of the vortex filaments was two and a half times higher than in the

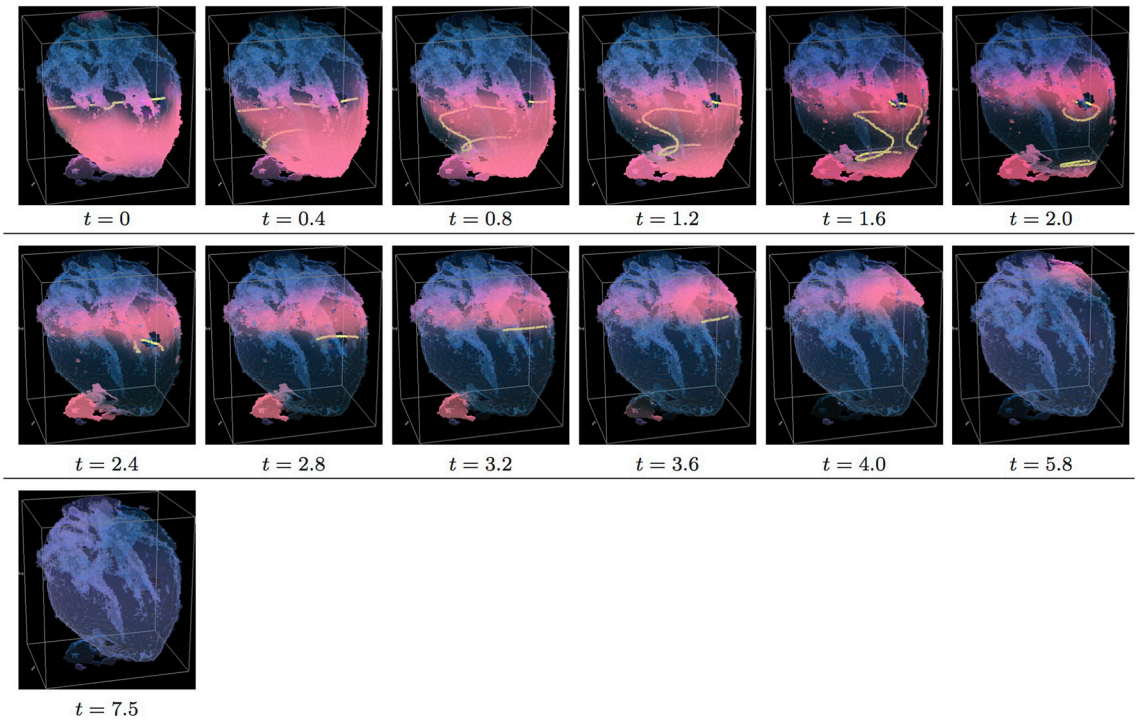

FIGURE 5 | Isotropic whole heart simulation. The translucent fetal heart is shown in blue, excitation front shown in red (see the color box in **Figure 3**), the yellow lines are the instant organizing filaments of the excitation vortices; time shown under each panel in time units of Equations (1, 2). After a short transient the organizing filament of the initial vortex breaks into the two pieces each of which fast terminates: one at the base and another at the apex of the heart (See **Supplementary Video 5**).

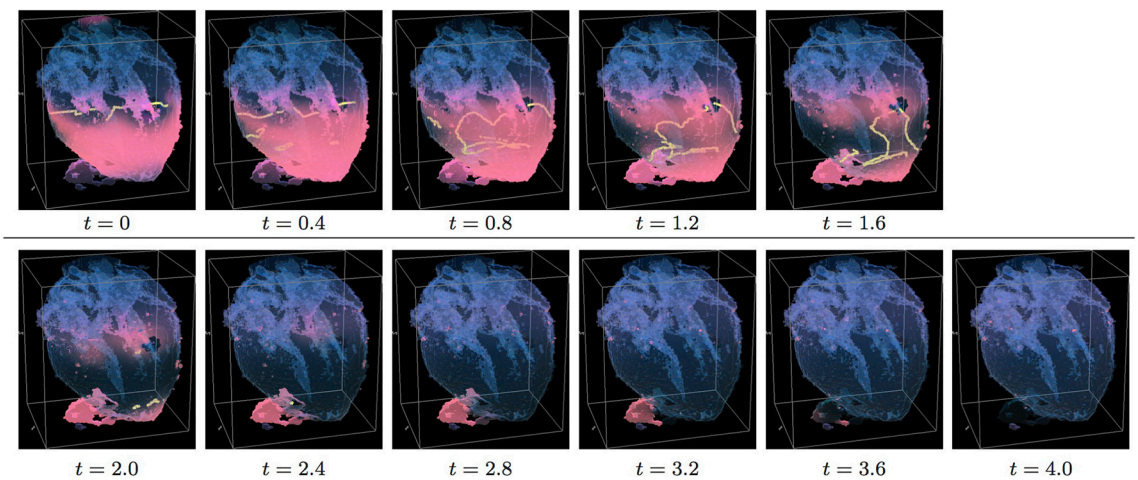

FIGURE 6 | Anisotropic whole heart simulation. The translucent fetal heart is shown in blue, excitation front shown in red (see the color box in **Figure 3**), the yellow lines are the instant organizing filaments of the excitation vortices; time shown under each panel in time units of Equations (1, 2). The anisotropy of the heart causes the fast transient distortion of the organizing filament of the initial excitation vortex, followed by the fast drift and self-termination at the apex of the heart (See **Supplementary Video 6**).

failed to self-terminate isotropic conduction simulation shown in **Figure 3**.

Figure 6 shows *anisotropic dynamics* of the excitation vortex, that is with the fiber orientation data "turned ON," so that both the geometry and the anisotropy of the otherwise homogeneous model of the heart affect dynamics of the vortex leading to its really fast termination at the apex of the heart by $t = 2.6$. The time course of the instant number of filaments (pink dotted line) is shown in **Figure 12C**, and the time course of the instant total length of the filaments (pink dotted line) is shown

in **Figure 12D**. It can be seen that, after a very fast transient increase in both the number of the filaments and the total length of the filaments, all the filaments rapidly disappear. The maximum instant number of the filaments was 17 at $t = 0.5$, that is higher and achieved faster than in the corresponding isotropic conduction shown in **Figure 5**. The maximum instant total length of the filaments was 278.6 at $t = 0.9$, again much higher than in the corresponding isotropic conduction. The time average number of the filaments in the simulation was 9.5, twice higher than in the isotropic conduction, and the time average total length of the filaments was 152.6, also twice higher than in the isotropic conduction, see the summary of the simulation detail in **Figure 11**.

It can be seen in the *raw* DT-MRI model simulations shown in **Figures 3**–**6**, that although the organizing filament of the vortex could not get through into the accidental "leftover" piece of tissue adjacent to the apical region, the piece still got activated, and could have served as an artificial "capacitor" affecting dynamics of the re-entry. In order to check whether this might be the case, we edited the original raw DT-MRI model by removing in the MRI the foreign "leftover" piece, and repeated the whole heart isotropic and anisotropic simulations from the same two orthogonal initial locations of the re-entry, similar to the shown in **Figures 3**–**6**.

3.2.2. "Edited" DT-MRI Anatomy Model

In the 3D whole heart *"edited"* MRI model simulations shown in the **Figures 7**, **8**, a counter-clockwise excitation vortex was initiated by the phase distribution method [53], with the initial position of the transmural vortex filament (yellow line) at the prescribed location *along the x axis* at $y_0 = 40, z_0 = 60$. It can be seen in **Figure 7** isotropic, and in **Figure 8** anisotropic 3D simulations, that, at $t = 0$, there was identical initial location of the filament of the excitation vortex: that is transmurally, roughly in the middle through the ventricles of the fetal heart, similar to the initial location of the vortex filament in the raw DT-MRI simulations shown in **Figures 3**, **4**.

Figure 7 shows *isotropic dynamics* of the vortex, that is with the fiber orientation data "turned OFF," so that only the geometry of the otherwise isotropic homogeneous fetal heart affects dynamics of the vortex. Here, following the geometry of the heart, the initial filament also breaks into the two major pieces, each of which also finds its own synchronous pathway similar to the beginning of the raw DT-MRI simulation shown in **Figure 3**. However, this time, after just a few rotations, the two re-entries find their end in their almost synchronous termination in the base region of the heart by $t = 16.9$. The time course of the instant number of filaments (green dashed line) is shown in **Figure 12A**, and the time course of the instant total length of the filaments (green dashed line) is shown in **Figure 12B**. It can be seen that, after a very fast transient increase in both the number of the filaments and the total length of the filaments, all the filaments rapidly disappear. The maximum instant number of the filaments was 9 at $t = 0.2$. The maximum instant total length of the filaments was 122.3 at $t = 0.7$. The time average number of the filaments in the simulation was 3.2, and the time average total length of the filaments was 28.7, see the summary of the simulation detail in **Figure 11**. It can be seen that, in the "edited" MRI isotropic simulation in **Figure 7**, the maximum instant and the time average number of the filaments, as well as the maximum instant and the time average total length of the filaments, were practically the same as in the corresponding raw MRI isotropic simulation with the failed to self-terminate re-entry shown in **Figure 3**. The only quantitative difference between the two isotropic simulations, i.e., the perpetual re-entry in **Figure 3** vs. the self-termination in **Figure 7**, was that, in the "edited" MRI isotropic simulation, without the "leftover" piece of tissue adjacent to the apex of the heart, the maximum instant number of the filaments, and the maximum instant total length of the filaments were achieved much faster: by $t = 0.2$ and $t = 0.7$ correspondingly.

Figure 8 shows *anisotropic dynamics* of the vortex, that is with the fiber orientation data "turned ON," so that both the geometry and the anisotropy of the otherwise homogeneous model of the heart affect dynamics of the vortex. Here, the anisotropy of the heart also causes significant transient distortion of the initial filament, followed by the fast drift toward the apex, with the ultimate termination at the AV border before a completion of a single rotation, very similar to the corresponding raw DT-MRI anisotropic simulation shown in **Figure 4**. However, in the "edited" MRI model without the "leftover" piece adjacent to the apex, repolarization of the heart is faster than it was in the presence of the "incidental capacitor" effect in the corresponding raw DT-MRI simulation shown in **Figure 4**. The time course of the instant number of filaments (red solid line) is shown in **Figure 12A**, and the time course of the instant total length of the filaments (red solid line) is shown in **Figure 12B**. It can be seen that, after a very fast transient increase in both the number of the filaments and the total length of the filaments, all the filaments rapidly disappear by $t = 4.8$. The maximum instant number of the filaments was 17 at $t = 0.4$, that is higher than in the corresponding raw anisotropic conduction shown in **Figure 4**, and twice higher than in the corresponding "edited" isotropic conduction shown in **Figure 7**. The maximum instant total length of the filaments was 180.3 at $t = 0.7$, similar to the corresponding raw anisotropic conduction shown in **Figure 4**, and much higher than in the corresponding "edited" isotropic conduction shown in **Figure 7**. The time average number of the filaments in the simulation was 6.3, similar to the corresponding raw anisotropic conduction shown in **Figure 4**, and twice higher than in the corresponding "edited" isotropic conduction shown in **Figure 7**. The time average total length of the filaments was 95.4, similar to the corresponding raw anisotropic conduction shown in **Figure 4**, and three times higher than in the corresponding raw isotropic conduction shown in **Figure 4**. Time to the maximum number of the filaments ($t = 0.4$), and time to the maximum total length of the filaments ($t = 0.7$), were similar to the corresponding "edited" isotropic conduction shown in **Figure 7**, and twice faster than in the corresponding raw anisotropic conduction shown in **Figure 4**, see the summary of the simulation detail in **Figure 11**. So, that the anisotropy of the heart increased the number and the total length of the filaments, and shortened the time to

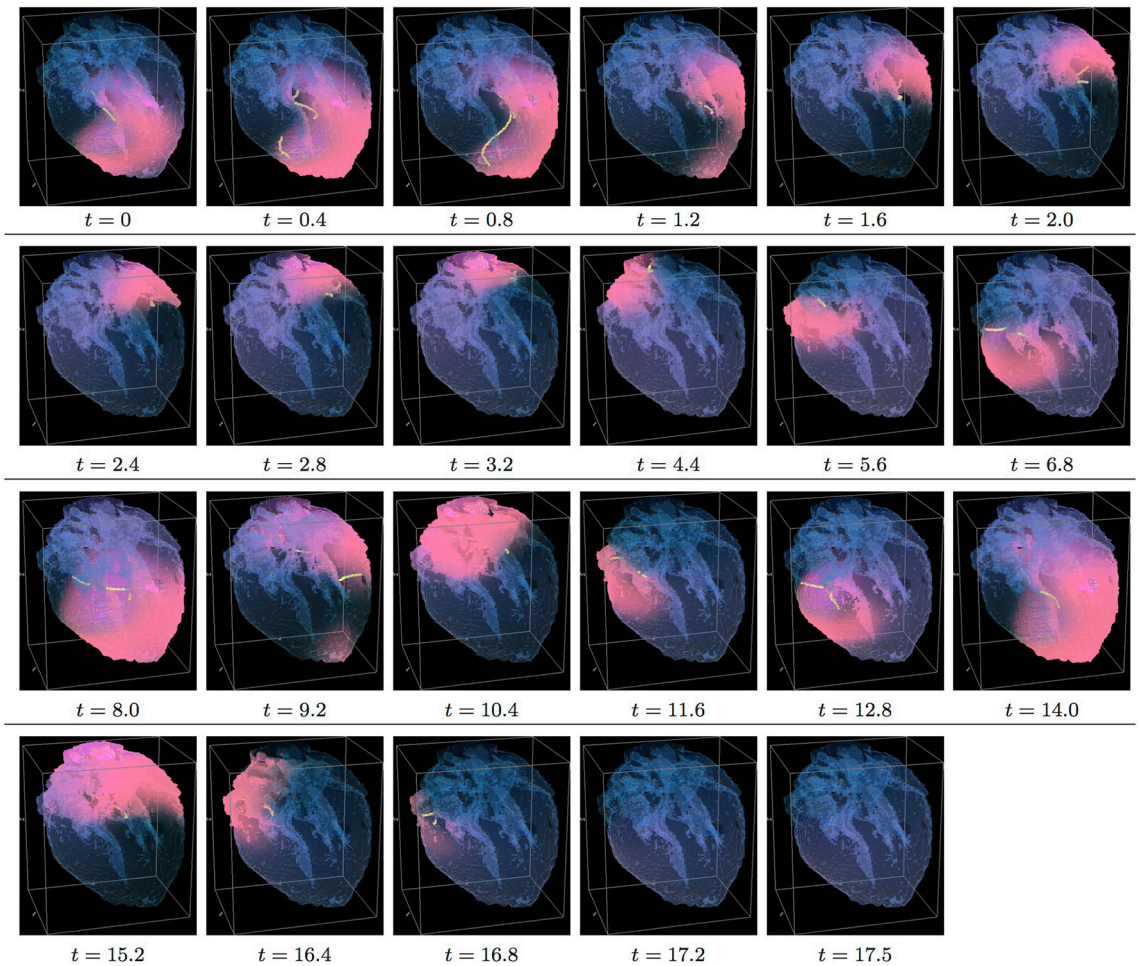

FIGURE 7 | Isotropic "edited" whole heart simulation. The translucent fetal heart is shown in blue, excitation front shown in red (see the color box in **Figure 3**), the yellow lines are the instant organizing filaments of the excitation vortices; time shown under each panel in time units of Equations (1, 2). After a short transient the organizing filament of the initial vortex breaks into the two short pieces each of which finds its own synchronous pathway, resulting after a few rotations in the synchronous termination of the filaments in the base of the fetal heart (See **Supplementary Video 7**).

self-termination by folds, while the "incidental capacitor" effect of the "leftover" piece adjacent to the apex slowed down the process.

In the 3D whole heart *"edited"* MRI simulations shown in **Figures 9**, **10**, a counter-clockwise excitation vortex was initiated by the phase distribution method [53], with the initial position of the transmural filament (yellow line) at the prescribed location *along the y axis* at $x_0 = 40, z_0 = 60$. It can be seen in **Figure 9** isotropic, and in **Figure 10** anisotropic 3D simulations, that at $t = 0$, there was the identical initial location of the filament: that is transmurally, roughly in the middle through the ventricles of the heart, perpendicular to the filament initial location in the "edited" MRI simulations shown in **Figures 7**, **8**, and similar to the initial location of the filament in the raw DT-MRI simulations shown in **Figures 5**, **6** .

Figure 9 shows "edited" MRI *isotropic dynamics* of the vortex, that is with the fiber orientation data "turned OFF," so that only the geometry of the otherwise isotropic homogeneous fetal heart affects the vortex. Here, again contrary to the expectation for a positive filament tension vortex to always contract, the organizing filament first transiently extends intramurally before breaking up into the two ring-like pieces, each of which quickly contracts and terminates at the opposite base and apex regions of the heart, identical to what was seen in the raw DT-MRI simulation shown in **Figure 5**. The time course of the instant number of filaments (green dashed line) is shown in **Figure 12C**, and the time course of the instant total length of the filaments (green dashed line) is shown in **Figure 12D**. It can be seen that, after a very fast transient increase both in the number of the filaments and in the total length of the filaments, all the filaments rapidly disappear by $t = 4.0$. The maximum instant number of the filaments was 12 at $t = 0.5$. The maximum instant total length of the filaments was 190.7 at $t = 1.5$. The time average number of the filaments in the simulation was 4.7, and the time average total length of the filaments was 82.9, see the summary of the simulation detail in **Figure 11**. So, from the comparison with the corresponding raw

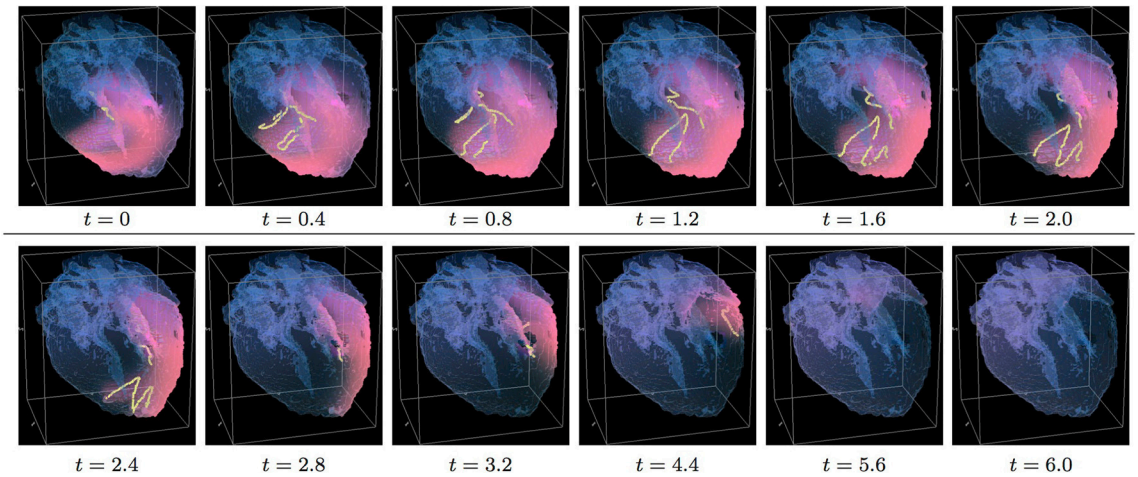

FIGURE 8 | Anisotropic "edited" whole heart simulation. The translucent fetal heart is shown in blue, excitation front shown in red (see the color box in **Figure 3**), the yellow lines are the instant organizing filaments of the excitation vortices; time shown under each panel in time units of Equations (1, 2). The anisotropy of the heart causes the significant transient distortion of the organizing filament of the initial vortex, followed by its fast drift toward the apex and the ultimate termination before completing a single rotation (See **Supplementary Video 8**).

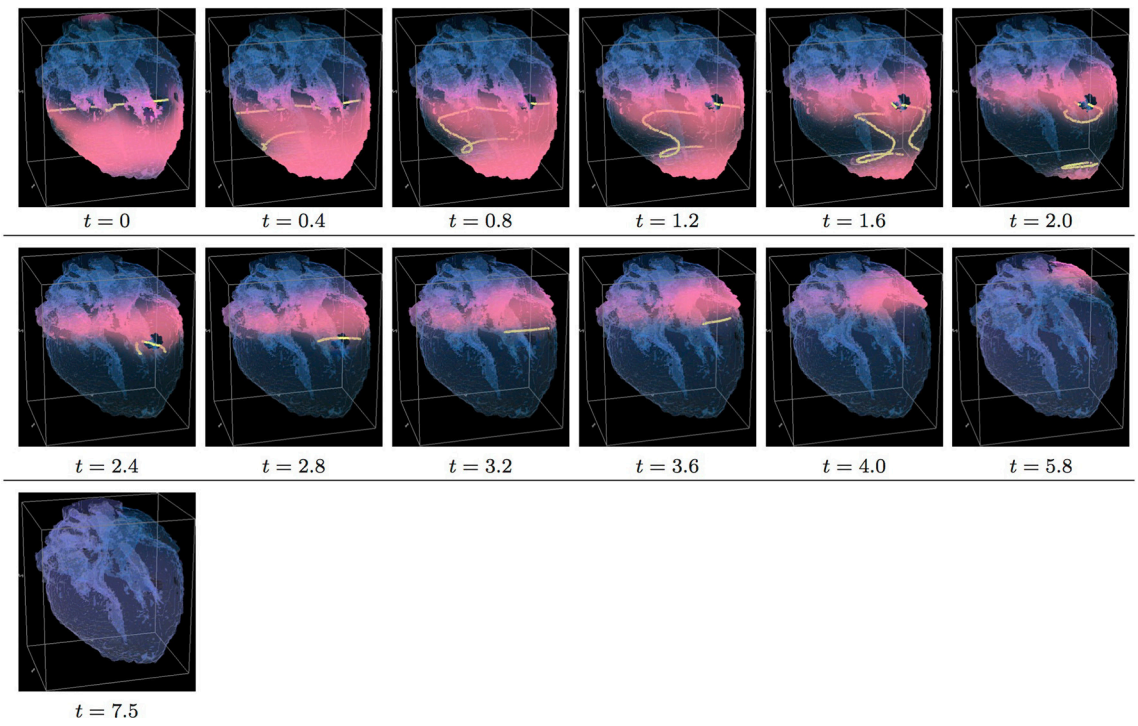

FIGURE 9 | Isotropic "edited" whole heart simulation. The translucent fetal heart is shown in blue, excitation front shown in red (see the color box in **Figure 3**), the yellow lines are the instant organizing filaments of the excitation vortices; time shown under each panel in time units of Equations (1, 2). After a short transient the organizing filament of the initial vortex breaks into the two pieces each of which fast terminates: one at the base and another at the apex of the heart (See **Supplementary Video 9**).

MRI isotropic simulation shown in **Figure 5**, it seems that, for that particular initial location of the filament, the "leftover" tissue did not play any role in the re-entry self-termination time.

Figure 10 shows *anisotropic dynamics* of the vortex, that is with the fiber orientation data "turned ON," so that both the geometry and the anisotropy of the otherwise homogeneous model of the heart affect the vortex, which, in the absence of the "incidental capacitor" effect of the "leftover" piece, results in the fastest possible termination of the re-entry at the apex of the heart by $t = 2.3$, before the vortex first rotation ever started. The

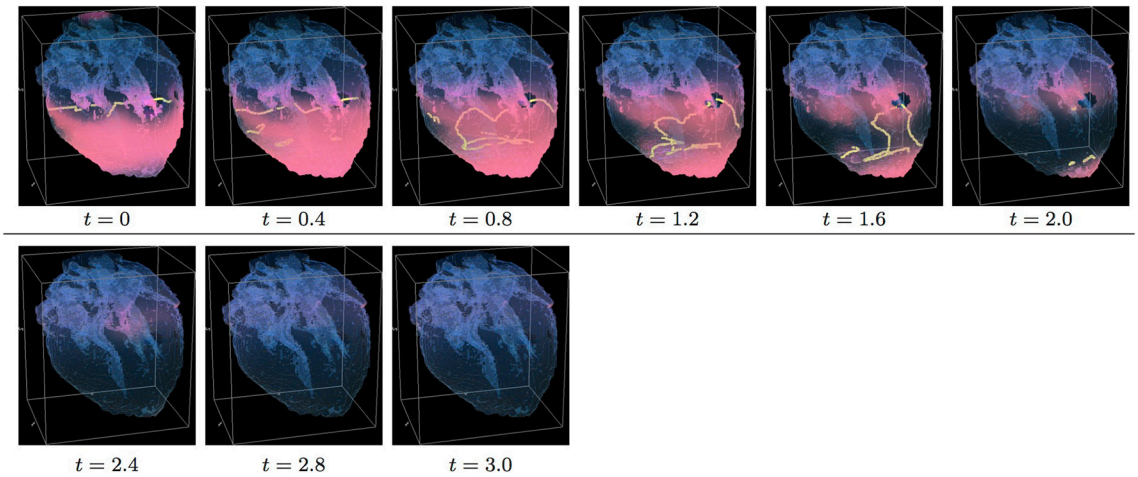

FIGURE 10 | Anisotropic "edited" whole heart simulation. The translucent fetal heart is shown in blue, excitation front shown in red (see the color box in **Figure 3**), the yellow lines are the instant organizing filaments of the excitation vortices; time shown under each panel in time units of Equations (1, 2). The anisotropy of the heart causes the fast significant transient distortion of the organizing filament of the initial excitation vortex, followed by the fast drift toward the apex and ultimate termination before the first rotation has ever started (See **Supplementary Video 10**).

re-entry termination time here is more than twice shorter than in both the raw MRI isotropic simulation shown in **Figure 5**, and in the "edited" isotropic simulations shown in **Figure 9**; shorter than in the corresponding simulation with the "incidental capacitor" effect shown in the **Figure 6**, and times shorter than in any of the simulations of the re-entry with the perpendicular initial location of the filament shown in the **Figures 3**, **4**, **7**, **8**. So, that the main reasons for the re-entry fastest self-termination seem to be the initial location of the filament and the anisotropy of the heart.

In **Figure 11**, we have summarized the results of the *raw* MRI simulations shown in **Figures 3–6**, and the *"edited"* MRI simulations shown in **Figures 7–10**. The re-entry termination time, in the time units of Equations (1, 2), is shown under each respected whole heart model initiation cite panel. It can be seen that the anisotropy of the heart causes at least twice faster termination of re-entry. It also can be seen that indeed the "leftover" piece of tissue connected to the apical region of the heart in the raw DT-MRI model served as an artificial "capacitor" affecting the re-entry dynamics, and significantly prolongated the life time of re-entry initiated at the particular location/orientation respective to the "capacitor".

Finally, the 3D anatomically realistic simulations of the fetal heart show that the anisotropy of the heart causes the fast transient increase in the number and the total length of the filaments, see **Figure 12**, with the typical fast drift toward the apex area of the heart, and re-entry self-termination, see also the movies in the Supplementary Material section.

4. DISCUSSION

Although the role of heart anatomy and anisotropy in the origin and sustainability of cardiac arrhythmias has been appreciated for a long time, there is limited experimental evidence to clarify detail of the heart anatomy effect on persistent cardiac arrhythmias and fibrillation. In particular, the theoretically plausible hypothesis that the anisotropic discontinuities in the heart might be a source of rise for cardiac re-entry due to the abrupt change in conduction velocity and wavefront curvature [14, 40, 41] was in controversy with the observation that the transmural fiber arrangement, including the range of transmural change in fiber angle in ventricular wall, although varied between species [42, p. 173], was consistent within a species. So that the question was that, if the pro-arrhythmic mechanism of cardiac re-entry initiation by the anisotropic discontinuities in a heart [14, 40, 41] was correct, what would then have been a reason for the consistent structure [42, p. 173] of the anisotropic discontinuities in healthy mammalian hearts. The combination of the High Performance Computing with the high-resolution DT-MRI based anatomy models of the heart allows anatomically realistic *in silico* testing of the effects of individual heart anatomy and anisotropy on the cardiac re-entry dynamics [34, 43, 44, 49, 56]. In this paper, for the first time, we present the anatomy and myofiber structure realistic computer simulation study of the cardiac re-entry dynamics in the DT-MRI based model of the human fetal heart [45].

The human fetal heart single anisotropic geometry dataset used in these simulations needs to be a typical and accurate representation of the cardiac structure and tissue architecture, with a spatial resolution suitable for numerical solution of the excitation equations. For a smoothly changing anisotropic geometry the imaged dataset may be interpolated to provide sufficient spatial resolution. DT-MRI has provided 17–200 cubic voxel datasets of human fetal heart [45, 48, 57, 58]. Finite difference numerical solutions of propagation in biophysically detailed models of adult cardiac tissue need $\sim 100\,\mu$m space steps in a Cartesian coordinate system. During fetal development the

	Original MRI		"Edited" MRI	
Isotropic	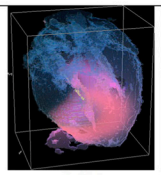	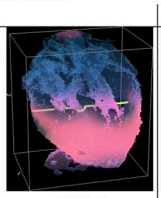	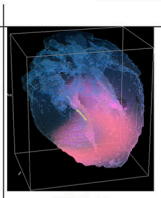	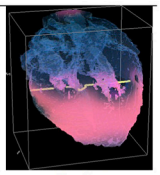
Simulation FIG.	FIG.3	FIG.5	FIG.7	FIG.9
Filaments Termination time (t.u)	t=∞	t=4.0	t=16.9	t=4.0
Recovery time (t.u)	t=∞	t=7.5	t=17.5	t=7.5
Average $\#\ of\ filaments$	3.4	4.7	3.2	4.7
Average *total length*	29.3	80.5	28.7	82.9
$max(\#\ of\ filaments)(t_{max(\#\ of\ filaments)})$	9 (t=1.0)	12 (t=1.4)	9 (t=0.2)	12 (t=0.5)
$max(total\ length)\ (t_{max(total\ length)})$	127.1 (t=1.6)	188.0 (t=1.5)	122.3 (t=0.7)	190.7 (t=1.5)
Anisotropic	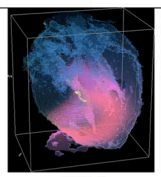	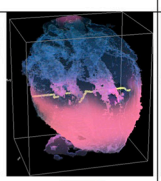	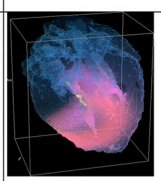	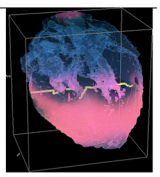
Simulation FIG.	FIG.4	FIG.6	FIG.8	FIG.10
Filaments Termination time (t.u)	t=5.3	t=2.6	t=4.8	t=2.3
Recovery time (t.u)	t=10.0	t=4.0	t=6.0	t=3.0
Average $\#\ of\ filaments$	6.5	9.5	6.3	10.3
Average *total length*	91.2	152.6	95.4	177.0
$max(\#\ of\ filaments)(t_{max(\#\ of\ filaments)})$	13 (t=0.8)	17 (t=0.5)	17 (t=0.4)	16 (t=0.7)
$max(total\ length)\ (t_{max(total\ length)})$	179.7 (t=1.8)	278.6 (t=0.9)	180.3 (t=0.7)	290.2 (t=1.0)

FIGURE 11 | Whole heart simulation: re-entry termination times. The translucent fetal heart is shown in blue, excitation front shown in red (see the color box in **Figure 3**), the yellow lines are the instant organizing filaments of the excitation vortices. Re-entry self-termination time in time units of Equations (1, 2) is shown under each simulation **Figures 3**–**10** initiation panel. Comparison of the respective isotropic (top row) vs. anisotropic (bottom row) simulations shows that, regardless of with or without the "leftover" piece, anisotropy results in faster termination of re-entry, and at least twice shorter recovery time. Respective comparison of the original MRI with the corresponding "edited out leftover" simulations shows that the leftover "incidental capacitor" effect, depending of the re-entry location/orientation with respect to the "incidental capacitor" own location/orientation, might significantly prolongate cardiac re-entry life time. The bigger number and the total length of the filaments tend to correlate with the faster termination of re-entry, though these fail to identify persistent re-entry in **Figure 3** simulation.

structure of the heart changes, the ventricular wall is compactified and trabeculated, and the size of the heart increases. Any atlas of the developing human fetal heart would need to come from longitudinal studies (which are impractical and potentially unethical), or from a large number of hearts obtained and imaged at different gestational ages. Here, all simulations are done on a single cardiac geometry that was selected as the transmural changes in fiber helix angle had developed. The results illustrated are specific for this particular anisotropic cardiac geometry, which is critically determined by how it was imaged and reconstructed. The fiber orientation angles of the heart were obtained from the orientation of the DT-MRI primary eigenvectors. Propagation velocity was twice as fast along the fibers than across the fibers. In all the simulations on this DT-MRI based cardiac geometry, the anisotropy of the myocardial tissue shortens the duration of re-entry by several fold. The numerical simulations depend on the validity of the DT-MRI dataset used. The ventricular wall showed the characteristic transmural rotation of the helix angle of the developed mammalian heart, while the fiber orientation in the atria was irregular. We expect the results be subsequently verified on other anatomy data, including different technique data e.g., MRI vs. DT-MRI vs. micro-CT vs. serial section histology, etc.

The comparative isotropic vs. anisotropic simulation of the otherwise homogeneous model of the fetal heart shows that, in the 2D slice of the heart, the fiber anisotropy might change the re-entry dynamics from the re-entry pinned at the sharp end of the septum cuneiform opening, **Figure 2A**, into the fast anatomical re-entry around the opening, **Figure 2B**. Note that, despite of the only basic segmentation of the MRI model into the tissue/not tissue points, and the ventricles not being isolated from the atria, because of the 2D re-entry pinning to either the sharp end of the septum opening, as in the isotropic simulation shown in **Figure 2A**, or to the whole septum opening, as in the case of anatomical re-entry in the anisotropic simulation shown in **Figure 2B**, the tip of the re-entry never penetrated from the ventricles into the atria.

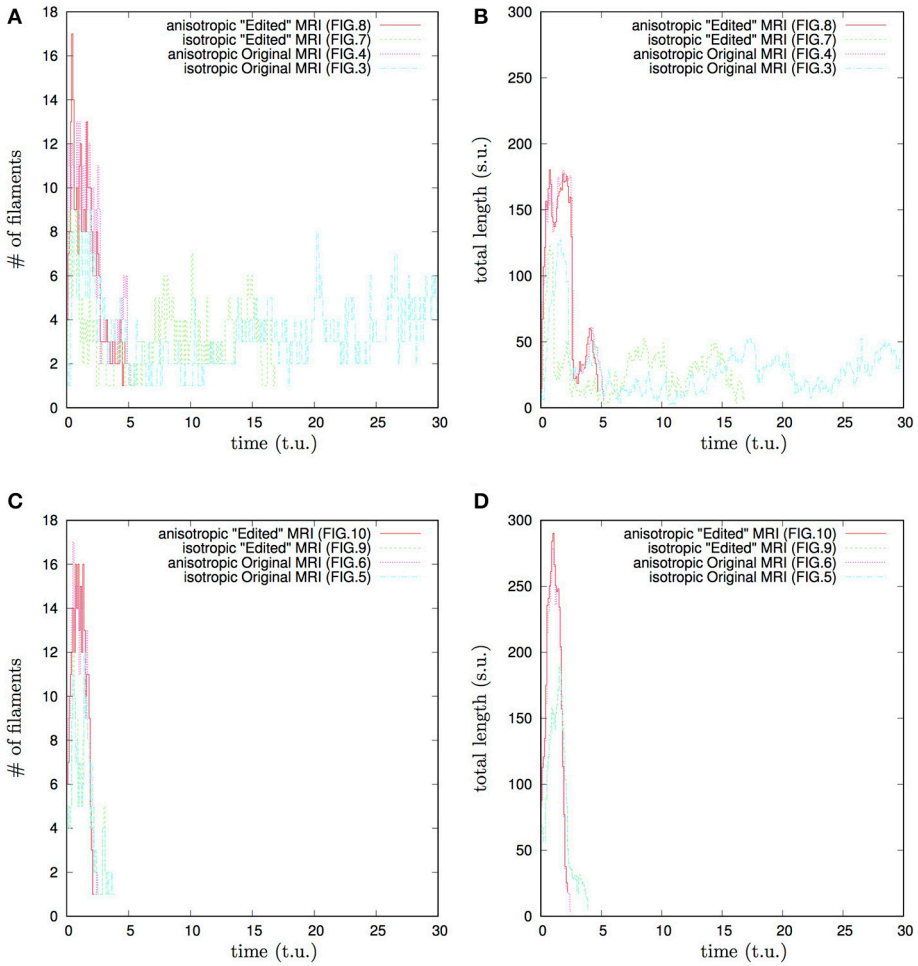

FIGURE 12 | Whole heart simulation: time course of the number of filaments #, and of the total length of the filaments, time and the total length of the filaments shown in the time and space units of Equations (1, 2). Initial position of the vortex filament *along the x axis*, **Figures 3**, **4**, **7**, **8** simulations: **(A)** time course of the number of filaments # ; **(B)** time course of the total length of the filaments. Initial position of the vortex filament *along the y axis*, **Figures 5**, **6**, **9**, **10** simulations: **(C)** time course of the number of filaments # ; **(D)** time course of the total length of the filaments. Anisotropy increases the transient number and the transient total length of the filaments. The bigger transient number and the total length of the filaments tend to correlate with the faster termination of re-entry. The biggest transient total lengths of the filaments was in case of the re-entry initiated *along the y axis*, **(D)**, which ensured its fastest termination. It can be seen from **Figures 5**, **6**, **9**, **10**, that the initial position of the filament *along the y axis* allowed it to grow intramurally, thus maximally increasing the transient total length of the filaments, and speeding up their termination.

Although, from the cardiac physiology point of view, the only basic segmentation of the raw DT-MRI data [45] into the tissue/non-tissue pixels might be seen as a major limitation of the study, from the non-linear science point of view, the use of the raw MRI data, as an example of a nature provided medium to study a re-entry dynamics, gives an important insight into the pure anatomy induced drift in an otherwise homogeneous 2D medium, and into the possibility of pinning of the re-entry not to a major blood vessel but to a sharp end of an anatomical opening [20]; and into that a real fiber anisotropy is capable to turn the pinned re-entry into an anatomical one. Importantly though, the 2D simulations in **Figure 2** are an important step to highlight the role and the necessity of the whole heart structure in the re-entry dynamics and self-termination.

In the 3D DT-MRI based *isotropic* model of the fetal heart, depending on the initial location/orientation of the re-entry organizing filament, the geometry of the fetal heart might sustain perpetual cardiac re-entry even with a positive filament tension, see **Figures 3**, **12A,B**. However, if the same positive filament tension vortex is initiated at the exactly same location/orientation in the *anisotropic* DT-MRI based model, the fiber structure of the fetal heart facilitates fast self-termination of cardiac re-entry, see **Figures 4**, **12A,B**.

From the respective comparison of the "isotropic vs. anisotropic" simulations in **Figure 3** vs. **Figure 4**, and **Figure 7** vs. **Figure 8**, it can be seen that, whereas the re-entry organizing filaments were capable to penetrate from the ventricles to atria in the isotropic simulations shown in **Figures 3**, **7,** the abrupt change in the fiber angles between the atria and the ventricles,

which one can see in **Figure 1**, did not allow the organizing filaments to penetrate from ventricles into atria in the anisotropic simulations shown in **Figures 4**, **8**, so that the anisotropy of ventricles could complete the speedy elimination of the re-entry within a single rotation.

The comparison of re-entry termination times in the whole heart raw DT-MRI simulations shown in **Figures 3–6**, with the corresponding "edited" MRI simulations shown in **Figures 7–10** showed that, although the filament of cardiac re-entry never got through into the tiny piece of the "leftover" tissue adjacent to the apex of the heart in the raw DT-MRI , the "not heart" excitable tissue served as an accidental "capacitor," significantly prolongating the life time of cardiac re-entry initiated at a particular location/orientation respective to the "leftover" piece location/orientation. The comparison of the re-entry termination times in **Figures 11**, **12** shows that the higher maximum number of the filaments and the bigger total length of the filaments tend to correlate with the faster termination of re-entry. However, the usual transient increase in both the number of the filaments and in the total length of the filaments, still failed to identify and terminate the persistent re-entry shown in **Figures 3**, **12A,B**.

The "isotropic vs. anisotropic" comparison of self-termination time, both in the raw and in the "edited" MRI whole heart simulations, confirmed that, regardless of with or without the "leftover" piece adjacent to the apex, anisotropy of the heart shortens re-entry self-termination time several folds, see **Figures 11**, **12**. **Figure 12** shows that anisotropy increases the maximum number and the maximum total length of the filaments. The bigger maximum number and the maximum total length of the filaments tend to correlate with the faster termination of re-entry. The biggest transient total lengths of the filaments was in the anisotropic case of re-entry initiated *along the y axis*, see the corresponding dotted pink and solid red lines in **Figure 12D**, which ensured the re-entry fastest termination. It can be seen from **Figures 5**, **6**, **9**, **10**, that the initial position of the filament *along the y axis* allowed the filament to grow intramurally, thus maximally increasing the transient total length of the filaments, and shortening their termination time.

The comparison of the "edited" MRI simulations of thus completely isolated heart shown in **Figures 7–10,** with the raw DT-MRI simulations shown in **Figures 3–6**, provide an important new insight into cardiac re-entry dynamics. Namely, that an excitable tissue accidentally adjacent to the heart might serve a capacitor capable to extend re-entry self-termination time, see for the respective comparison **Figure 3** vs. **Figure 7**, **Figure 4** vs. **Figure 8**, **Figure 5** vs. **Figure 9**, and **Figure 6** vs. **Figure 10**, summarized in **Figures 11**, **12**. The latter suggests a possible new mechanism for a persistent cardiac re-entry. That is if, apart from the major blood vessels normally adjacent to the heart *in vivo*, and affecting cardiac re-entry dynamics, there were also an accidental "touching" of the heart by an adjacent excitable tissue, for example, due to a change of posture in the night [59], the "incidental capacitor" effect could have extended re-entry self-termination time, up to the failure to self-terminate. The "incidental capacitor" hypothesis could be an additional explanation to the circadian rhythm [60], for the elusive and difficult to reproduce longer arrhythmia episodes reported in the night ECGs as opposed to the on average shorter arrhythmias in the day time ECGs. Although the raw DT-MRI simulations with the "leftover" piece of tissue might have been seen a limitation of the study, the real heart *in vivo* does not exist in complete isolation from the main blood vessels and other neighboring tissues. So, we believe that our "incidental" leftover tissue results only once more confirm the importance and the necessity of taking into account of the real anatomical settings and surrounding of the heart for the full appreciation of cardiac re-entry dynamics.

The BeatBox DT-MRI based *in silico* comparative study confirms the heart anatomy and anisotropy functional effect on cardiac re-entry self-termination as opposed to its sustainability, pinning to anatomical features, transformation from pinned to anatomical re-entry, while the anisotropy of the tissue facilitates re-entry self-termination.

One of the limitations of the present study is the use of the simplified FitzHugh-Nagumo [50] excitation model, chosen for this study in order to eliminate the effects of realistic cell excitation kinetics, such as e.g., meander [50], alternans [52], negative filament tension [51], etc., and enhance and highlight the pure effects of the heart anatomy and anisotropy on the re-entry. The realistic cell excitation models should be used in the future studies, in order to clarify specific interplay of the cell kinetics with the heart anatomy and anisotropy.

As it can be seen from **Figure 1**[for the color-encoded fractional anisotropy (FA) and for the color-encoded all the three components of the fiber angles see also Figure 4 in Pervolaraki et al. [45, p. 5]], formation of the fetal heart fiber structure at the epicardium and endocardium is not completed yet, so that only the already formed intramural laminar myofibers affect dynamics of the re-entry. Although the use of the not fully formed fetal heart can be seen as a limitation of the study, on the other hand, the irregular epicardium and endocardium fibers seem to prevent a re-entry from pinning to the fine endocardium features, which were yet to be developed [45] later on. We appreciate that the anatomy and fiber structure differences in the fetal and in a fully formed adult heart might alter the re-entry dynamics, such as in e.g., the reported case of re-entry pinning to the junction of pectinate muscles with crystae terminalis in adult human atrium [31, 33, 49]. That is, although it is possible to initiate a cardiac re-entry in the tiny 1.4*g* (at 143 DGA) fetal heart [45], the already formed intramural laminar anisotropy of the fetal heart facilitates the re-entry self-termination, **Figure 11**. With the hindsight of the present study, in an adult heart, because of the pinning opportunities provided by the endocardium anatomical features [31, 33, 49], there must exist additional mechanisms to facilitate cardiac re-entry self-termination [61].

The most serious limitation of the study is that only the basic segmentation of the raw DT-MRI data [45] into the tissue/non-tissue pixels based on the MRI luminosity threshold, and only the primary eigenvalues of fibers orientation, were taken into account in the BeatBox [44] computer simulations of cardiac re-entry dynamics. Further levels of DT-MRI segmentation, in order to take into account e.g., the heart collagen skeleton, isolation of ventricles from atria, etc., will inevitably change the outcome of

the re-entry, by adding the electrically impermeable barriers to cardiac re-entry. Currently, this further segmentation is added into DT-MRI based models via complex rule based image post-processing [62, 63], which brings in artificial assumptions, as well as limits the number of available segmented data sets. From the non-linear science point of view we pursued in this initial study, the rationale was to use the raw DT-MRI as an example of a nature provided medium to study a re-entry dynamics. In the future, the multichannel computer tomography might offer automatic tissue segmentation, so that multi-level segmented DT-MRI based models become more available, and be used in the BeatBox [44] anatomically and biophysically realistic simulations.

Finally, we believe that a simple "mechanistic" explanation, although often craved for, might be rather inadequate/premature here, and will require better theoretical understanding of the demonstrated potential effect of the heart anatomy and anisotropy on cardiac re-entry dynamics, for it is not a particular feature, or a sequence of features, but rather the whole complex of the shape, anisotropy, and position of the heart within the body, which affects the re-entry dynamics in a particular way, and which seems to have evolved in order to ensure the fastest self-termination of cardiac re-entry. If our hypothesis is correct, it might explain the difficulties with reproducibility of the arrhythmia *in vivo* and in an isolated heart. A general role of fiber anisotropy in the genesis and sustenance of arrhythmias could be and has been addressed by numerics on idealized and simplified geometries with different spatial distributions of anisotropy [14]. The biomedical question addressed in the manuscript is whether self-terminating ventricular arrhythmias can occur in a developing fetal heart, as has inferred from fECG data in Benson et al. [46]. The most important novel finding of the paper is that, contrary to what currently seems to be a commonly accepted view of the pro-arrhythmic nature of cardiac anisotropy, the point of view based on the mainly theoretical and simplified anatomy models studies, for the first time ever, and for the first time in a real whole heart DT-MRI based model, we have demonstrated that anisotropy of the heart might have rather anti-arrhythmic effect, as it facilitates the fastest self-termination of cardiac re-entry.

5. RESOURCE IDENTIFICATION INITIATIVE

BeatBox, RRID:SCR_015780.

AUTHOR CONTRIBUTIONS

IB, AH, EP, and FW contributed conception and design of the study; RA, AH, and EP contributed the human fetal heart DT-MRI data sets; IB and FW converted the DT-MRI data sets into BeatBox geometry format and ran the simulations; IB performed visualization of the simulations and analysis, and wrote the first draft of the manuscript. FW approved submission of the paper. IB, RA, AH, and EP contributed to manuscript revision, read and approved the submitted version.

FUNDING

We acknowledge the support of the UK Medical Research Council grant G1100357 for the human fetal heart DT-MRI data sets. We also wish to acknowledge the support of the BeatBox software development project by EPSRC (UK) grants EP/I029664 and EP/P008690/1.

ACKNOWLEDGMENTS

We thank all the developers of the BeatBox HPC Simulation Environment for Biophysically and Anatomically Realistic Cardiac Electrophysiology. We are grateful to Professor V. N. Biktashev for much appreciated advice and discussion.

SUPPLEMENTARY MATERIAL

The Supplementary Material for this article can be found online at: https://www.frontiersin.org/articles/10.3389/fphy.2018.00015/full#supplementary-material

Supplementary Video 1 | 2D slice simulation, Isotropic Conduction: slow excitation re-entry pins to the sharp end of the septum cuneiform opening in the fetal heart.

Supplementary Video 2 | 2D slice simulation, Anisotropic Conduction: anisotropy of the fetal heart turns initial spiral wave into fast anatomical re-entry around the septum cuneiform opening.

Supplementary Video 3 | Isotropic whole heart simulation. After a short transient of the vortex initiated along the x-axis, the organizing filament breaks into the two short pieces each of which finds its own synchronous perpetual pathway, resulting in the perpetual cardiac re-entry in the fetal heart.

Supplementary Video 4 | Anisotropic whole heart simulation. The anisotropy of the heart causes the fast transient distortion of the organizing filament of the vortex initiated along the x-axis, and drift toward the inexcitable boundary of the heart, resulting in the very fast self-termination of the excitation vortex.

Supplementary Video 5 | Isotropic whole heart simulation. After a short transient of the vortex initiated along the y-axis, the organizing filament breaks into two pieces each of which fast terminates: one at the base and another at the apex of the heart.

Supplementary Video 6 | Anisotropic whole heart simulation. The anisotropy of the heart causes the fast transient distortion of the organizing filament of the vortex initiated along the y-axis, followed by the fast drift and self-termination at the apex of the heart.

Supplementary Video 7 | Isotropic "edited" whole heart simulation. After a short transient of the vortex initiated along the x-axis, the organizing filament breaks into two short pieces, each of which finds its own synchronous pathway, resulting after a few rotations in the synchronous termination of the filaments in the base of the fetal heart.

Supplementary Video 8 | Anisotropic "edited" whole heart simulation. The anisotropy of the heart causes the significant transient distortion of the organizing filament of the vortex initiated along the x-axis, followed by its fast drift toward the apex, and the ultimate termination before completing a single rotation.

Supplementary Video 9 | Isotropic "edited" whole heart simulation. After a short transient of the vortex initiated along the y-axis, the organizing filament breaks into two pieces, each of which fast terminates: one at the base and another at the apex of the heart.

Supplementary Video 10 | Anisotropic "edited" whole heart simulation. The anisotropy of the heart causes the fast significant transient distortion of the organizing filament of the vortex initiated along the y-axis, followed by the fast drift toward the apex and termination before the first rotation has ever started.

REFERENCES

1. Mines GR. On dynamic equilibrium in the heart. *J Physiol.* (1913) **46**:349–83. doi: 10.1113/jphysiol.1913.sp001596
2. Garey WE. The nature of fibrillatory contraction of the heart – its relation to tissue mass and form. *Am J Physiol.* (1914) **33**:397–414. doi: 10.1152/ajplegacy.1914.33.3.397
3. Allessie MA, Bonke FIM, Schopman FJ. Circus movement in rabbit atrial muscle as a mechanism of tachycardia. *Circ Res.* (1973) **32**:54–62. doi: 10.1161/01.RES.33.1.54
4. Pertsov AM, Davidenko JM, Salomonsz R, Baxter JWT. Spiral waves of excitation underlie reentrant activity in isolated cardiac muscle. *Circ Res.* (1993) **72**:631–50. doi: 10.1161/01.RES.72.3.631
5. Wiener N, Rosenblueth A. The mathematical formulation of the problem of conduction of impulses in a network of connected excitable elements, specifically in cardiac muscle. *Arch Inst Cardiologia de Mexico.* (1946) **16**:205–65.
6. Balakhovsky IS. Some regimes of excitation movement in an ideal excitable tissue. *Biofizika* (1965) **9**:1–63.
7. Krinsky VI. Fibrillation in the excitable media. *Problemy Kibernetiki.* (1968) **2**:59–80.
8. Panfilov AV, Rudenko AN, Pertsov AM. Twisted scroll waves in active 3-dimensional media. *Doklady AN SSSR.* (1984) **279**:1000–2. doi: 10.1007/978-3-642-70210-5_18
9. Davydov VA, Zykov VS, Mikhailov AS, Brazhnik PK. Drift and resonance of spiral waves in active media. *Radiofizika* (1988) **31**:574–82.
10. Keener JP. The dynamics of three-dimensionsional scroll waves in excitable media. *Physica D.* (1988) **31**:269–76. doi: 10.1016/0167-2789(88)90080-2
11. Ermakova EA, Pertsov AM, Shnol EE. On the interaction of vortices in 2-dimensional active media. *Physica D.* (1989) **40**:185–95. doi: 10.1016/0167-2789(89)90062-6
12. Biktashev VN, Holden AV. Design principles of a low-voltage cardiac defibrillator based on the effect of feed-back resonant drift. *J Theor Biol.* (1994) **169**:101–13. doi: 10.1006/jtbi.1994.1132
13. Biktashev VN. A three-dimensional autowave turbulence. *Int J Bifurcation Chaos* (1998) **8**:677–84. doi: 10.1142/S0218127498000474
14. Fenton F, Karma A. Vortex dynamics in three-dimensional continuous myocardium with fiber rotation: filament instability and fibrillation. *Chaos* (1998) **8**:20–47. doi: 10.1063/1.166311
15. Pertsov AM, Wellner M, Vinson M, Jalife J. Topological constraint on scroll wave pinning. *Phys Rev Lett.* (2000) **84**:2738–41. doi: 10.1103/PhysRevLett.84.2738
16. Wellner M, Berenfeld O, Jalife J, Pertsov AM. Minimal principle for rotor filaments. *Proc Natl Acad Sci USA.* (2002) **99**:8015–8. doi: 10.1073/pnas.112026199
17. Biktasheva IV, Biktashev VN. Wave-particle dualism of spiral waves dynamics. *Phys Rev E* (2003) **67**:026221. doi: 10.1103/PhysRevE.67.026221
18. Biktashev VN, Barkley D, Biktasheva IV. Orbital motion of spiral waves in excitable media. *Phys Rev Lett.* (2010) **104**:058302. doi: 10.1103/PhysRevLett.104.058302
19. Biktashev VN, Biktasheva IV, Sarvazyan NA. Evolution of spiral and scroll waves of excitation in a mathematical model of ischaemic border zone. *PLoS ONE* (2011) **6**:e24388. doi: 10.1371/journal.pone.0024388
20. Biktasheva IV, Dierckx H, Biktashev VN. Drift of scroll waves in thin layers caused by thickness features: asymptotic theory and numerical simulations. *Phys Rev Lett.* (2015) **114**:068302. doi: 10.1103/PhysRevLett.114.068302
21. Bosch RF, Nattel S. Cellular electrophysiology of atrial fibrillation. *Cardiovasc. Res.* (2002) **54**:259–69. doi: 10.1016/S0008-6363(01)00529-6
22. Workman AJ, Kane KA, Rankin AC. Cellular bases for human atrial fibrillation. *Heart Rhythm* (2008) **5**:S1–6. doi: 10.1016/j.hrthm.2008.01.016
23. Kushiyama Y, Honjo H, Niwa R, Takanari H, Yamazaki M, Takemoto Y, et al. Partial I-K1 blockade destabilizes spiral wave rotation center without inducing wave breakup and facilitates termination of reentrant arrhythmias in ventricles. *Am J Physiol Heart Circul Physiol.* (2016) **311**:H750–75. doi: 10.1152/ajpheart.00228.2016
24. Pellman J, Lyon RC, Sheikh F. Extracellular matrix remodeling in atrial fibrosis: mechanisms and implications in atrial fibrillation. *J Mol Cell Cardiol.* (2010) **48**:461–7. doi: 10.1016/j.yjmcc.2009.09.001
25. Eckstein J, Maesen B, Linz D, Zeemering S, van Hunnik A, Verheule S, et al. Time course and mechanisms of endo-epicardial electrical dissociation during atrial fibrillation in the goat. *Cardiovasc Res.* (2011) **89**:816–24. doi: 10.1093/cvr/cvq336
26. Takemoto Y, Takanari H, Honjo H, Ueda N, Harada M, Kato S, et al. Inhibition of intercellular coupling stabilizes spiral-wave reentry, whereas enhancement of the coupling destabilizes the reentry in favor of early termination. *Am J Physiol Heart Circ Physiol.* (2012) **303**:H578–86. doi: 10.1152/ajpheart.00355.2012
27. Eckstein J, Zeemering S, Linz D, Maesen B, Verheule S, van Hunnik A, et al. Transmural conduction is the predominant mechanism of breakthrough during atrial fibrillation: evidence from simultaneous endo-epicardial high-density activation mapping. *Circ Arrhyth Electrophysiol.* (2013) **6**:334–41. doi: 10.1161/CIRCEP.113.000342
28. MacEdo PG, Kapa S, Mears JA, Fratianni A, Asirvatham SJ. Correlative anatomy for the electrophysiologist: ablation for atrial fibrillation. Part II: regional anatomy of the atria and relevance to damage of adjacent structures during AF ablation. *J Cardiovasc Electrophysiol.* (2010) **21**: 829–36.
29. Anselmino M, Blandino A, Beninati S, Rovera C, Boffano C, Belletti M, et al. Morphologic analysis of left atrial anatomy by magnetic resonance angiography in patients with atrial fibrillation: a large single center experience. *J Cardiovasc Electrophysiol.* (2011) **22**:1–7. doi: 10.1111/j.1540-8167.2010.01853.x
30. Gray RA, Pertsov AM, Jalife J. Incomplete reentry and epicardial breakthrough patterns during atrial fibrillation in the sheep heart. *Circulation* (1996) **94**:2649–61. doi: 10.1161/01.CIR.94.10.2649
31. Wu TJ, Yashima M, Xie F, Athill CA, Kim YH, Fishbein MC, et al. Role of pectinate muscle bundles in the generation and maintenance of intra-atrial reentry. Potential implications for the mechanism of conversion between atrial fibrillation and atrial flutter. *Circ Res.* (1998) **83**:448–62. doi: 10.1161/01.RES.83.4.448
32. Nattel S. New ideas about atrial fibrillation 50 years on. *Nature* (2002) **415**:219–26. doi: 10.1038/415219a
33. Yamazaki M, Mironov S, Taravant C, Brec J, Vaquero LM, Bandaru K, et al. Heterogeneous atrial wall thickness and stretch promote scroll waves anchoring during atrial fibrillation. *Cardiovasc Res.* (2012) **94**:48–57. doi: 10.1093/cvr/cvr357
34. Bishop MJ, Plank G, Burton RAB, Schneider JE, Gavaghan DJ, Grau V, et al. Development of an anatomically detailed MRI-derived rabbit ventricular model and assessment of its impact on simulations of electrophysiological function. *Am J Physiol Heart Circ Physiol.* (2010) **298**:H699–718. doi: 10.1152/ajpheart.00606.2009
35. Bishop MJ, Vigmond E, Plank G. Cardiac bidomain bath-loading effects during arrhythmias: interaction with anatomical heterogeneity. *Biophys J.* (2011) **101**:2871–81. doi: 10.1016/j.bpj.2011.10.052
36. Bishop MJ, Plank G. The role of fine-scale anatomical structure in the dynamics of reentry in computational models of the rabbit ventricles. *J Physiol.* (2012) **590**:4515–35. doi: 10.1113/jphysiol.2012.229062
37. Fukumoto K, Habibi M, Ipek SEG, Khurram IM, Zimmerman SL, Zipunnikov V, et al. Association of left atrial local conduction velocity with late gadolinium enhancement on cardiac magnetic resonance in patients with atrial fibrillation. *Circ Arrhyt Electrophysiol.* (2016) **9**:e002897. doi: 10.1161/CIRCEP.115.002897
38. Rodriguez B, Eason JC, Trayanova N. Differences between left and right ventricular anatomy determine the types of reentrant circuits induced by an external electric shock. A rabbit heart simulation study. *Prog Biophys Mol Biol.* (2006) **90**:399–413. doi: 10.1016/j.pbiomolbio.2005.06.008
39. Dierckx H, Brisard E, Verschelde H, Panfilov AV. Drift laws for spiral waves on curved anisotropic surfaces. *Phys Rev E* (2013) **88**:012908. doi: 10.1103/PhysRevE.88.012908
40. Spach M. Mechanisms of the dynamics of reentry in a fibrillating myocardium - Developing a genes-to-rotors paradigm. *Circ Res.* (2001) **88**:753–5. doi: 10.1161/hh0801.090538
41. Smaill BH, LeGrice IJ, Hooks DA, Pullan AJ, Caldwell BJ, Hunter PJ. Cardiac structure and electrical activation: models and measurement. *Clin Exp Pharmacol Physiol.* (2004) **31**:913–9. doi: 10.1111/j.1440-1681.2004.04131.x

42. Hunter PJ, Smaill BH, Nielsen PMF, Le Grice IJ. A mathematical model of cardiac anatomy. In: Holden AV, Panfilov AV, editors. *Computational Biology of the Heart*. Chichester: Wiley (1997). p. 171–215.
43. Vigmond E, Vadakkumpadan F, Gurev V, Arevalo H, Deo M, Plank G, et al. Towards predictive modelling of the electrophysiology of the heart. *Exp Physiol.* (2009) **94**:563–77. doi: 10.1113/expphysiol.2008.044073
44. Antonioletti M, Biktashev VN, Jackson A, Kharche SR, Stary T, Biktasheva IV. BeatBox - HPC simulation environment for biophysically and anatomically realistic cardiac electrophysiology. *PLoS ONE* (2017) **12**:e0172292. doi: 10.1371/journal.pone.0172292
45. Pervolaraki E, Anderson RA, Benson AP, Hays-Gill B, Holden AV, Moore BJR, et al. Antenatal architecture and activity of the human heart. *Interf Focus* (2013) **3**:20120065. doi: 10.1098/rsfs.2012.0065
46. Benson AP, Hayes-Gill B, Holden AV, Matthews R, Naz A, Page S, et al. Self-terminating re-entrant cardiac arrhythmias: quantitative characterization. *Comput Cardiol.* (2015) **42**:641–4. doi: 10.1109/CIC.2015.7410992
47. Mekkaoui C, Porayette P, Jackowski MP, Kostis WJ, Dai G, Sanders S, et al. Diffusion MRI tractography of the developing human fetal heart. *PLoS ONE* (2013) **8**:e72795. doi: 10.1371/journal.pone.0072795
48. Pervolaraki E, Dachtler J, Anderson RA, Holden AV. Ventricular myocardium development and the role of connexins in the human fetal heart. *Sci Rep.* (2017) **7**:12272. doi: 10.1038/s41598-017-11129-9
49. Kharche SR, Biktasheva IV, Seeman G, Zhang H, Biktashev VN. A computer simulation study of anatomy induced drift of spiral waves in the human atrium. *BioMed Res Int.* (2015) **2015**:731386. doi: 10.1155/2015/731386
50. Winfree AT. Varieties of spiral wave behaviour — an experimentalist's approach to the theory of excitable media. *Chaos* (1991) **1**:303–34. doi: 10.1063/1.165844
51. Biktashev VN, Holden AV, Zhang H. Tension of organizing filaments of scroll waves. *Phil Trans Roy Soc Lond A* (1994) **347**:611–30. doi: 10.1098/rsta.1994.0070
52. Karma A. Electrical alternans and spiral wave breakup in cardiac tissue. *Chaos* (1994) **4**:461–72. doi: 10.1063/1.166024
53. Biktashev VN, Holden AV. Re-entrant waves and their elimination in a model of mammalian ventricular tissue. *Chaos* (1998) **8**:48–56. doi: 10.1063/1.166307
54. Zhu RJ, Millrod MA, Zambidis ET, Tung L. Variability of action potentials within and among cardiac cell clusters derived from human embryonic stem cells. *Sci Rep.* (2016) **6**:18544. doi: 10.1038/srep18544
55. Pervolaraki E, Hodgson S, Holden AV, Benson AP. Towards computational modelling of the human fetal electrocardiogram: normal sinus rhythm and congenital heart block. *Europace* (2014) **16**:758–65. doi: 10.1093/europace/eut377
56. Kharche SR, Biktasheva IV, Seemann G, Zhang H, Zhao J, Biktashev VN. Computational modelling of low voltage resonant drift of scroll waves in the realistic human atria. *Lect Notes Comput Sci.* (2015) **9126**:421–9. doi: 10.1007/978-3-319-20309-6_48
57. Pervolaraki E, Anderson RA, Benson AP, Moore BJ, Zhang H, Holden AV. Diffusion tensor magnetic resonance imaging of anisotropic and orthotropic architecture of the human fetal ventricular myocardium. *Proc Physiol Soc.* (2012) **28**:PC26. Available online at: http://www.physoc.org/proceedings/abstract/Proc%20Physiol%20Soc%2028PC26
58. Tang M, Holden AV, Anderson RA, Pervolaraki E. Contrast-enhanced magnetic resonance imaging of the human foetal heart reveals its myocardial architecture. *Proc Physiol Soc.* (2016) **37**:PCA060. Available online at: http://www.physoc.org/proceedings/abstract/Proc%20Physiol%20Soc%2037PCA060
59. Hu K, Scheer FAJL, Laker M, Smales C, Shea SA. Endogenous circadian rhythm in vasovagal response to head-up tilt. *Circulation* (2011) **123**:961–U85. doi: 10.1161/CIRCULATIONAHA.110.943019
60. Jeyaraj D, Haldar SM, Wan XP, McCauley MD, Ripperger JA, Hu K, et al. Circadian rhythms govern cardiac repolarization and arrhythmogenesis. *Nature* (2012) **483**:96–U141. doi: 10.1038/nature10852
61. Clayton RH, Murray A, Higham PD, Campbell RWF. Self-terminating ventricular tachyarrhythmias - a diagnostic dilemma. *Lancet* (1993) **341**:93–5. doi: 10.1016/0140-6736(93)92567-D
62. Lombaert H, Peyrat JM, Croisille P, Rapacchi S, Fanton L, Cheriet F, et al. Human atlas of the cardiac fiber architecture: study on a healthy population. *IEEE Tran Med Imaging* (2012) **31**:1436–47. doi: 10.1109/TMI.2012.2192743
63. Gahm JK, Kung GL, Ennis DB. Weighted component-based tensor distance applied to graph-based segmentation of cardiac DT-MRI. In: *2013 IEEE 10th International Symposium on Biomedical Imaging (ISBI)*. San Francisco, CA (2013). p. 504–7.

Conflict of Interest Statement: The authors declare that the research was conducted in the absence of any commercial or financial relationships that could be construed as a potential conflict of interest.

frontiers in Physiology

REVIEW
published: 15 February 2018
doi: 10.3389/fphys.2018.00106

Validation and Trustworthiness of Multiscale Models of Cardiac Electrophysiology

Pras Pathmanathan and Richard A. Gray*

Office of Science and Engineering Laboratories, Center for Devices and Radiological Health, U.S. Food and Drug Administration, Silver Spring, MD, United States

Computational models of cardiac electrophysiology have a long history in basic science applications and device design and evaluation, but have significant potential for clinical applications in all areas of cardiovascular medicine, including functional imaging and mapping, drug safety evaluation, disease diagnosis, patient selection, and therapy optimisation or personalisation. For all stakeholders to be confident in model-based clinical decisions, cardiac electrophysiological (CEP) models must be demonstrated to be trustworthy and reliable. Credibility, that is, the belief in the predictive capability, of a computational model is primarily established by performing validation, in which model predictions are compared to experimental or clinical data. However, there are numerous challenges to performing validation for highly complex multi-scale physiological models such as CEP models. As a result, credibility of CEP model predictions is usually founded upon a wide range of distinct factors, including various types of validation results, underlying theory, evidence supporting model assumptions, evidence from model calibration, all at a variety of scales from ion channel to cell to organ. Consequently, it is often unclear, or a matter for debate, the extent to which a CEP model can be trusted for a given application. The aim of this article is to clarify potential rationale for the trustworthiness of CEP models by reviewing evidence that has been (or could be) presented to support their credibility. We specifically address the complexity and multi-scale nature of CEP models which makes traditional model evaluation difficult. In addition, we make explicit some of the credibility justification that we believe is implicitly embedded in the CEP modeling literature. Overall, we provide a fresh perspective to CEP model credibility, and build a depiction and categorisation of the wide-ranging body of credibility evidence for CEP models. This paper also represents a step toward the extension of model evaluation methodologies that are currently being developed by the medical device community, to physiological models.

Keywords: credibility, calibration, validation, computational modeling, cardiac models

OPEN ACCESS

Edited by:
Ruben Coronel,
University of Amsterdam, Netherlands

Reviewed by:
Maxime Sermesant,
Institut National de Recherche en Informatique et en Automatique (INRIA), France
Wayne Rodney Giles,
University of Calgary, Canada

****Correspondence:***
Pras Pathmanathan
pras.pathmanathan@fda.hhs.gov

Specialty section:
This article was submitted to Cardiac Electrophysiology, a section of the journal Frontiers in Physiology

Received: *01 November 2017*
Accepted: *31 January 2018*
Published: *15 February 2018*

Citation:
Pathmanathan P and Gray RA (2018) Validation and Trustworthiness of Multiscale Models of Cardiac Electrophysiology. Front. Physiol. 9:106. doi: 10.3389/fphys.2018.00106

INTRODUCTION

One of the most remarkable properties of the natural world is that is it can be understood using mathematical equations—a property described by Eugene Wigner as "the unreasonable effectiveness of mathematics in the natural sciences." Once the appropriate mathematical groundwork had been developed, it became possible to describe intricate and multi-faceted physical

phenomena using relatively simple mathematical equations, e.g., fluid flow, deformation of solid bodies, electromagnetic wave propagation, and phenomena at widely different scales from atoms to galaxies. Computational models, which are mathematical models solved by means of a computer, can be used to solve governing equations underlying complex systems and simulate their behavior. The remarkable predictive capability of computational models based on the fundamental laws of physics has enabled such models to be routinely used in a multitude of engineering applications.

Biology, in contrast to physics, is less easily characterized by simple or small numbers of mathematical equations. Primarily, this is due to the complexity and variability in biological processes which makes them inherently non-linear, multi-disciplinary and multi-scale. While computational models of human physiological processes have been developed and refined for decades, they are not as predictive as computational models in engineering, and likely never will be. Nevertheless, biomedical computational models have without doubt the potential for revolutionizing medicine just as physics-based models have forever changed research, design, and evaluation in engineering.

One field which holds considerable promise for clinical applications is cardiac modeling, owing to the maturity of the field (Trayanova, 2011) (Winslow et al., 2012) and the fact that heart disease is the leading cause of the death in the industrialized world. Computational cardiac models can simulate the electrophysiology and/or mechanical deformation of cardiac myocytes, tissue, or the whole heart. This paper is focused on cardiac electrophysiological (CEP) models. **Figure 1** illustrates the typical components to a CEP model, which are usually multi-scale, containing as a fundamental unit a cellular model of myocyte EP activity. Such "cell models," of which over a 100 have been published of varying complexity and for a range of mammalian species, are typically sets of ordinary differential equations (ODEs), and predict the action potential (AP) and many other cellular and sub-cellular quantities. Notable recent human cell models include (Iyer et al., 2004; ten Tusscher et al., 2004; ten Tusscher and Panfilov, 2006; Grandi et al., 2010) and (O'Hara et al., 2011). For reviews of single cell models, see (Fink et al., 2011; Noble, 2011; Noble et al., 2012). Cell models are often composed of multiple sub-models, for different ion channels, pumps and exchangers or representing subcellular processes such as calcium handling. These sub-models are usually also systems of ODEs. To simulate electrical wave propagation, including arrhythmic activity, in tissue or the whole heart, cell models are coupled to partial differential equations (PDEs) known as the "bidomain" or "monodomain" equations (Clayton et al., 2011; Franzone et al., 2014; Lopez-Perez et al., 2015); see **Figure 1**. A further extension is to model the heart embedded in the torso, which allows for simulation of the electrocardiogram (ECG) (Richards et al., 2013; Zemzemi et al., 2013). In recent years various imaging, modeling and computational advances have enabled *patient-specific* heart models to be generated using clinical data (see e.g., Smith et al., 2011; Chabiniok et al., 2016 for discussions). Anatomical personalisation using clinical imaging data is most common (e.g., Arevalo et al., 2016), although personalisation of functional (Chen et al., 2016) or material (Aguado-Sierra et al., 2011) parameters using clinical data has also been performed. Patient-specific models can be used to make patient-specific clinical predictions and represent an important step forward toward precision medicine.

All types of CEP model—ion channel or subcellular models, cell models, tissue, and organ-level models—have proved to be powerful tools complementing experiment in basic cardiac electrophysiological research (Plank et al., 2009), for understanding mechanisms behind both normal rhythm and cardiac arrhythmias. However, CEP models also have potential applications in all aspects of cardiovascular medicine, including device design and evaluation, functional imaging and mapping, drug safety evaluation, disease diagnosis, patient selection, and therapy optimisation or personalisation. There are numerous reviews covering the current and potential applications of CEP models; (see e.g., Trayanova and Boyle, 2014; Davies et al., 2016; Niederer and Smith, 2016). However, one aspect of the modeling which has been inadequately covered in the current cardiac modeling literature is rationale for when and why cardiac models can be *trusted*.

The **credibility** of a computational model has been defined as the belief in the predictive capability of the model for a given intended use (ASME, 2017) or the willingness of people to trust a model's predictions (Patterson and Whelan, 2017). Typically, credibility of a computational model is founded upon **validation** results. Validation is the process of testing a model by comparing model predictions to experimental or clinical data. (A more precise definition is provided below). However, other types of evidence (non-validation evidence) can also be used to argue that a model is sufficiently credible for its intended use. As we explain below, the credibility of CEP models is typically founded upon a wide range of factors, and consequently it can be very unclear, or a matter for debate, the extent to which a cardiac model can be trusted for a given application. In fact, many papers in the literature leave implicit why, and to what extent, the model predictions can be considered credible.

The aim of this article is to clarify and discuss reasons that could support the trustworthiness of CEP models. We will do so by reviewing different types of evidence that have been presented to support CEP model credibility, or are otherwise relevant to the assessment of credibility, hereafter referred to as CEP model **credibility evidence**. The review will include: (i) discussion of common practice regarding CEP model validation; (ii) examples of strategies taken for performing CEP model validation; and (iii) discussion of other credibility evidence for CEP models, including historical evidence that often *implicitly* supports simulation studies. The review will *not* aim to evaluate specific cardiac models or in any way judge the *quality* of any validation results or other evidence. Such decisions require difficult judgements based on careful consideration of all available evidence, in the context of the precise application that model is to be used for (including assessment of the risks associated with inaccurate predictions NASA, 2009) and are therefore beyond the scope of this review. In other words, we are *not* claiming or implying that any CEP model "is" or "is not trustworthy"; nor do we argue that any modeling approach or process is or is not trustworthy. Instead, our focus will be on *types*

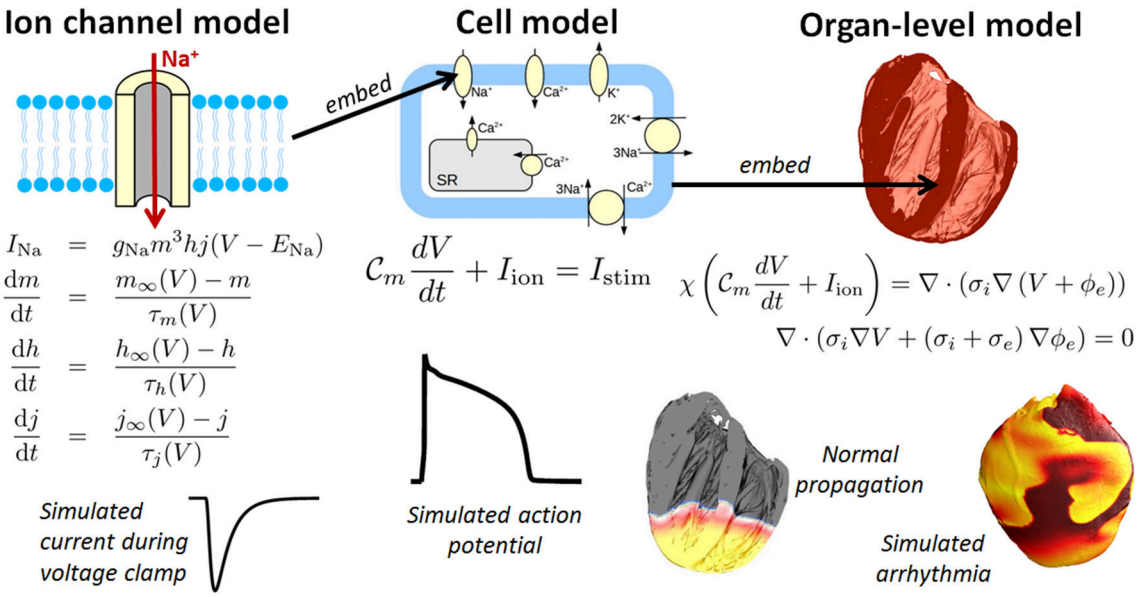

FIGURE 1 | Components of a multiscale cardiac electrophysiology (CEP) model. **(Left)**: equations and sample output for a Hodgkin-Huxley formulation of the rapid sodium current. Multiple such sub-cellular models can be used to define a cell model. **(Center)**: schematic of sub-cellular processes included in a hypothetical cell model, together with the differential equation governing the transmembrane voltage, and sample output. Cell models differ in their formulation of the ionic current I_{ion} and can be made up of dozens of ordinary differential equations. **(Right)**: Cell models can be incorporated into the bidomain equations and solved on a computational mesh of the heart [top right: high-resolution rabbit biventricular mesh of Bishop et al. (2010)], to simulate normal or arrhythmic cardiac activity (bottom right).

of evidence that could, in principle, support the trustworthiness of a model for a given intended use.

In previous work we advocated that engineering model assessment approaches known as verification, validation, and uncertainty quantification (VVUQ) could be important in the advancement of cardiac CEP modeling (Pathmanathan and Gray, 2013) and explored verification (Pathmanathan and Gray, 2014) and uncertainty quantification (UQ) for CEP models (Pathmanathan et al., 2015). This paper continues this line of work by focusing on validation-related activities. Only activities related to comparison of the model to the real world are within the scope of this review. Therefore, activities such as code verification, calculation verification, and sensitivity analysis, while important for overall assessment of credibility and receiving increasing interest in the field (Sobie, 2009; Niederer et al., 2011; Chang et al., 2015) are outside the scope of this paper. Additionally, while uncertainty quantification is related to validation as will be described in section Why Trust a Computational Model?, research on the process of performing uncertainty quantification with CEP models is also outside the scope of the review, though this is also receiving increasing recent interest in CEP; (see e.g., Konukoglu et al., 2011; Johnstone et al., 2016; Chang et al., 2017).

In fact, there is enormous current interest across computational science in methods and best practices for demonstrating or evaluating the reliability of computational models (National Research Council, 2012). The medical device community is collaborating on a Standard for assessing credibility of computational models for medical device applications (ASME, 2017). However, this Standard and related medical device Guidances (Food and Drug Administration, 2016) are motivated by traditional "physics-based" engineering models in biomedical applications [e.g., models based on solid mechanics (Pelton et al., 2008), fluid dynamics (Stewart et al., 2012), or electromagnetism (Angelone et al., 2010)]. The relevance of such approaches to the evaluation of complex physiological models such as CEP models is limited. In particular, while both (Food and Drug Administration, 2016) and (ASME, 2017) address validation, they do not account for the possibility of multiple sources of different types of validation evidence, or other evidence which could support credibility. In this paper, we demonstrate how a large body of evidence will generally support a CEP model. By exposing and discussing this wide range of potential credibility evidence for CEP models, this paper is a necessary first step toward the extension of the above approaches to cardiac and other physiological models.

The paper is organized as follows. In section Why Trust a Computational Model? we categorize and discuss different types of credibility evidence, and discuss validation in detail. Section Credibility of CEP Models at Different Spatial Scales then reviews credibility evidence for CEP models organized by spatial scale. Section Discussion summarizes and discusses our conclusions.

WHY TRUST A COMPUTATIONAL MODEL?

Figure 2 provides an overview of the concepts discussed throughout this section. Various types of rationale could be used to argue for the credibility of a computational model. The following are three distinct categories of evidence that could support *some* level of confidence in a model:

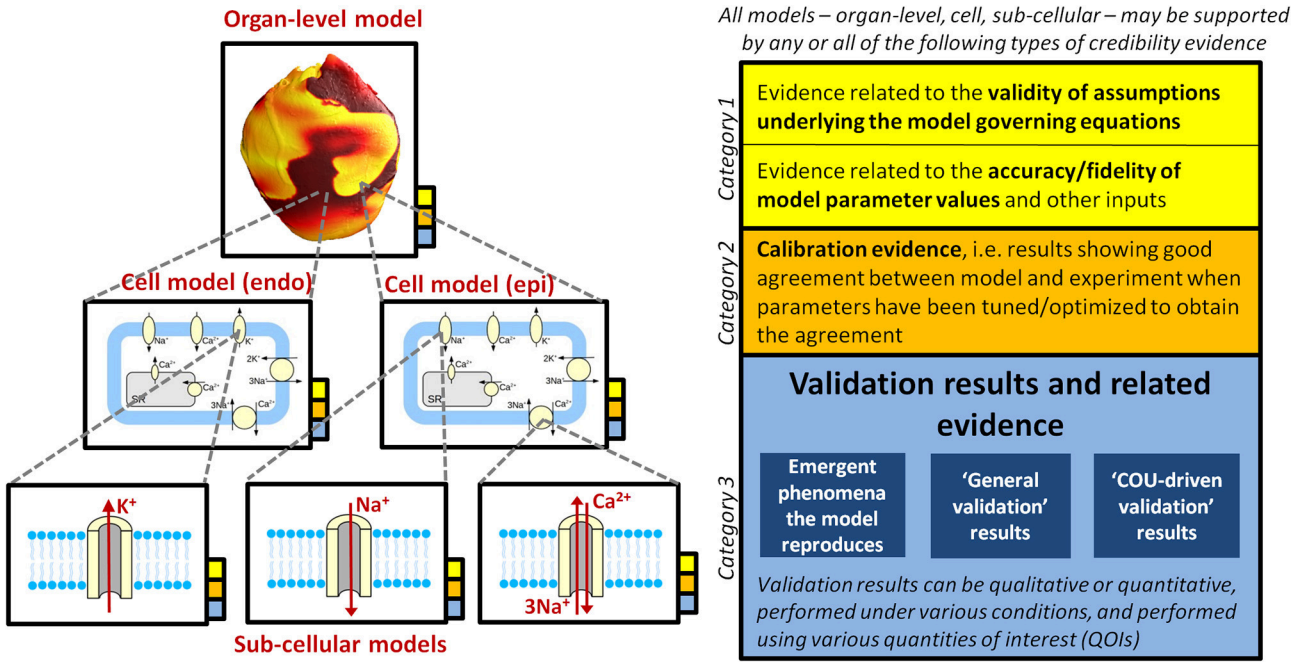

FIGURE 2 | Illustration of how a multiscale CEP model may be supported by multiple sources of credibility evidence (that is, evidence relevant when assessing the credibility of the model), taken from model evaluation at multiple scales. The overall model (i.e., organ-level model), the underlying cell models (here it is assumed that the organ-level model incorporates two different cell models, one for epicardial tissue, one for endocardial), and all underlying sub-cellular models may all be supported by the different types of evidence presented in the right of the figure. See section Why Trust a Computational Model? for full discussion.

Category 1: Evidence related to the **validity of assumptions underlying the model governing equations**, together with evidence related to the **accuracy/fidelity of model parameter values** and other inputs. These are grouped together because if the equations are considered appropriate, but there is no confidence that the parameters are accurate, then there will be little confidence in model predictions, and vice versa.

Category 2: **Calibration evidence**. Calibration is the process of tuning, fitting or optimizing parameters in a model so that the model results match experimental or clinical data. Calibration is primarily performed to determine model parameter values that cannot be directly measured. However, if the results from calibration demonstrate a good match between model and the experimental/clinical data, the results could potentially *also* be used as evidence for credibility of the model.

Category 3: Evidence generated from testing the predictive capability of the *completed* model. This includes **validation evidence**, that is, comparison of model predictions to independent real-world data *not used* in the construction of the model (Roache, 2009). Validation is discussed in detail later in this section.

These are distinct types of evidence and may provide very different levels of confidence in a model. The first category is based on model equations, assumptions and parameter values, but not on actual model outputs or results, with no actual testing of the model. This category includes historical evidence supporting the governing equations that were used in the model. It also includes evidence regarding the quality of data used to determine model parameters. The second category is based on comparing model outputs with experimental/clinical data, but allows for model parameters to be altered for the model to match the data. Calibration results are regularly used, either implicitly and explicitly, as evidence for credibility of biological computational models. If a model's parameters can be chosen so that the model reproduces certain experimental data, this ability to fit the data or to reproduce phenomena could be used in support of the model—especially when a complex phenomenon is reproduced using a model with only a few parameters. The last category—validation and related evidence—is obviously the strongest test of the model: it assumes the model has been completely defined and *then* its ability to reproduce the real world is tested.

For many applications—in particular the basic science applications of hypothesis generation and mechanistic insight—use of a model that has no supporting validation evidence may be perfectly appropriate. Mathematical models in biology can be thought of a means in which existing knowledge or hypotheses are integrated (Brodland, 2015), in which case running a simulation is simply an efficient means of determining the logical consequences of those knowledge/hypotheses, impossible through mental deduction alone for complex systems. This is one of the reasons why mathematical modeling has proven a successful complement to experiments in understanding biological processes (Noble, 2011). However, when a model is to be used in decision-making, and in particular for

high-risk applications such as safety-critical clinical applications, validation becomes very important. (Carusi et al., 2012) provide a discussion on the meaning of CEP models as representations. Patterson and Whelan (2017) provide an excellent general discussion on models as representations vs. as predictive tools, and propose a high-level framework for deciding how to evaluate models along this spectrum.

Validation

Validation has been described as "*the assessment of the accuracy of a computational simulation by comparison with experimental data*" (Oberkampf et al., 2004). One definition initially proposed by the Department of Defense (DoD) and commonly used by the engineering community and elsewhere (Oberkampf et al., 2004; Roache, 2009; National Research Council, 2012), including increasingly within the medical devices community (Food and Drug Administration, 2016), (ASME, 2017), is: "*the process of determining the degree to which a model is an accurate representation of the real world from the perspective of the intended uses of the model.*" This definition emphasizes that the validation process is dependent on the specific "intended use" of the model, also referred to as the "model application" or the "**context of use**" **(COU)**. (Roache, 2009) provide a good discussion of the DoD definition of validation, and explains how many different interpretations of it are made even within the engineering community. Moreover, there is no inter-disciplinary consensus on a precise definition of validation, and different communities may have very different understandings of what constitutes model validation. (Bellocchi et al., 2010) list 20 definitions of model validation proposed between 1960 and 2010. (Eddy et al., 2012) describe a categorisation of validation used in the health economics and outcomes community. (Patterson and Whelan, 2017) describe a broad concept of validation of biological models, which includes but is more expansive than the engineering/DoD understanding of validation. (Viceconti, 2011) refer to model "falsification," rather than validation, based on the contention that models can only be invalidated (falsified). One common feature of most of the different interpretations of validation is that validation must involve new data not used in the construction of the model, i.e., "calibration is not validation" (Roache, 2009).

The DoD definition arguably presents a contradiction regarding validation of CEP models—especially *cellular* models—because they are typically developed as **general-purpose models**, i.e., without a specific COU in mind. When novel cell models are published, predictions of model outputs and derived quantities—for example, action potential shape, action potential duration (APD) restitution, ionic concentration transients and others—are usually compared to experimental data. This arguably does not constitute validation according to the DoD definition since no COU (intended use) has been prescribed. Incidentally, this could be considered a limitation of the DoD definition; see (Roache, 2009) for a discussion. Note though that regardless of the definition of validation, it is vital to recognize the importance of the COU in evaluation of a computational model. In particular, the COU must be specified for the "final" evaluation of a model, and any claim that a general-purpose model is a "validated model" cannot be justified, since it is the COU that determines what level of agreement between model and experiment can be deemed acceptable (Roache, 2009; National Research Council, 2012).

To distinguish between different types of evidence, we introduce the terminology **general validation evidence** to describe scientific evidence obtained by comparing model predictions with real world data *when no particular COU has been specified*. This could also have been called "baseline validation." Examples of general validation for CEP models include initial validation of a novel general-purpose cell model (discussed in detail in section Cell Models), general testing vs. experimental/clinical data of previously published cell models (regularly carried out in the cardiac modeling community), and the comparison against data of activation patterns predicted by general-purpose ventricular, atrial or whole-heart models (discussed in section Organ-Level Models). There is almost unlimited scope for such evaluation, since modern CEP cell models are very complex, and therefore there is an ever-growing volume of literature incorporating general validation of CEP models.

We define **COU-driven validation evidence** using the DoD definition, as scientific evidence obtained by comparing model predictions with real world data for the purposes of evaluating the predictive capability of the model for a specific, prescribed, application (COU) of the model. A simple example of this would be comparing APDs of a model to experimental values, when the COU is prediction of drug effects on APD. Another example is comparison of whole-heart model predictions of number of phase singularities during ventricular fibrillation, against clinical data, when the COU is to use the model to understand mechanisms behind ventricular fibrillation (see section Organ-Level Models). We include in this category validation of model-derived quantities, including: drug pro-arrhythmic risk indices (see sections Cell Models and Organ-Level Models); sudden cardiac death (SCD) risk indices (see section Organ-Level Models); and ablation targets (see section Organ-Level Models).

Note that a terminology complication can arise when considering validation of patient-specific models, which are often generated using a workflow that may be mostly or fully automated. One could distinguish between validation of the simulation software *only*, and validation of model predictions using the full *workflow*; there is therefore a potential for different interpretations of what constitutes "model validation" in this context. In this paper, we will include validation of the full workflow (for example, evaluation of the predictive ability of a workflow that takes in patient imaging data and outputs a clinical prediction) within our broad interpretation of model validation.

Comparator, Quantities of Interest, and Method of Comparison

Validation involves comparison of model predictions with real world data of some form. (Note that comparison against results of a *different* computational model is generally not considered validation, but see Roache, 2009 for a discussion). The **comparator** is defined as the source of the real world data. For CEP models this is usually experimental or clinical data.

Important aspects of experimental comparators in CEP model validation include species, experimental conditions including temperature, and whether the data is historical (taken from the literature) or obtained from new experiments performed for the purpose of model validation. Important aspects of clinical comparators include patient demographics, patient cardiac myopathies, and co-morbidities. For patient specific CEP models that make patient specific clinical predictions, the validation comparator has to be clinical data taken from the same patient (distinct to the data used for personalisation of the model). Regardless of whether the comparator is experimental or clinical data, there are often significant challenges to obtaining high quality data, especially *in vivo* data under physiological conditions, which can impose severe constraints on the ability to perform high quality validation. These experimental/clinical challenges are covered elsewhere in the CEP literature, and therefore will not be a main focus of the present review.

Another important aspect of validation is which outputs of the model, or derived quantities—here referred to as **quantities of interest (QOIs)**—are compared to the real-world data. Commonly validated QOIs for cell models include transmembrane voltage and the APD restitution curve. For whole-heart models, validation QOIs can be global (e.g., the ECG) or local (e.g., activation patterns). Validation using global QOIs only provides indirect evidence on the credibility of local QOIs.

There are various possibilities for the **method of comparison** between the model and comparator. (Oberkampf et al., 2004) provide a good introduction to this topic; here we only provide a very brief overview. The comparison can be qualitative (often the case in physiological modeling) or quantitative. If quantitative, the comparison could take into account experimental error, model uncertainty, both, or neither. Model uncertainty is accounted for by performing uncertainty quantification (UQ), where uncertainty in model parameters (due to, for example, measurement uncertainty or inherent physiological variability) is quantified using probability distributions, and then the resultant uncertainty in the QOI(s) are computed (Smith, 2013; Mirams et al., 2016). Various validation metrics for quantifying the difference between experimental data and model predictions taking into account error estimates and simulation uncertainty have been proposed in the engineering literature; (see e.g., Oberkampf and Barone, 2006). For some CEP model-derived outputs such as risk indices or model-based biomarkers, other analytic or statistical comparison methods (different to those used in traditional model validation) may be appropriate, such as measures of specificity and specificity, receiver operating characteristic (ROC) curves, biomarker validation methods, etc.

Sometimes a CEP model is stated as matching known physiological phenomena, for example in statements such as "the AP shows the characteristic spike notch dome architecture found for epicardial cells" (ten Tusscher et al., 2004) or discussion of re-entrant waves breaking up into sustained fibrillation under pro-arrhythmic conditions (Krishnamoorthi et al., 2014). This is perhaps not validation *per se*, as there is no explicit comparator—or more precisely, arguably not validation according to the engineering/DoD understanding of validation; it is arguably "epistemic validation" using the broader definition of Patterson and Whelan (2017). Nevertheless, it is important and relevant evidence for assessing the model's predictive ability for a COU. This type of evidence, which we will refer to as **reproduced phenomena**, may be especially important in evaluation of biological models since biological systems exhibit emergent phenomena, and therefore a powerful test of a model is whether such it predicts such phenomena.

Validation of Multiscale Models

For multiscale models we can distinguish between evidence at different spatial scales, and in particular at which scales validation was performed (see **Figure 2**). For a multiscale model of the whole-heart, there may be validation evidence available for model sub-components (i.e., all sub-cellular models and the cell model), and/or for the system-as-a-whole (whole-heart model). If validation is only performed for sub-models but *not* the overall system, credibility of system-level predictions is founded (perhaps implicitly) on the sub-model validation results *and* belief in the theory underlying how sub-models interact. For example, most cardiac cell models assume that ionic currents are independent and can therefore simply be added together. System-level validation may be especially important with physiological models, since physiological systems exhibit emergent behavior that cannot be predicted from understanding all sub-system behavior. "Hierarchical validation," in which validation is performed for all model sub-components, sub-systems *and* the entire system, is recommended in the engineering validation literature so that the model provides the "right answer for the right reasons" (Hills et al., 2008).

Often, validation is performed at one scale to provide confidence that the model is sufficiently credible for it to be used as a sub-model in a larger scale (e.g., develop a cell model, perform validation of cell model, and then proceed to tissue model if validation results are favorable). Even if this is the case, the sub-model validation results may be relevant in evaluation of the final model for a COU.

It should now be clear how a CEP model may be supported by **multiple sources of credibility evidence, taken from model evaluation at multiple scales** (see **Figure 2**). **Table 1** lists different sources of evidence and provides examples for ion channel, cell and organ-level models. We reiterate that we are not making any assertions regarding what evidence is *necessary* when assessing cardiac models for a COU. Our motivation is simply to describe how multiple sources of evidence may exist and be relevant when assessing the credibility of a CEP model for a specific COU. Confidence in a model tends to increase with the body of evidence available to support it (Patterson and Whelan, 2017). Therefore, when a complex model is evaluated, ideally the model should be treated as a "glass box" (the opposite of a "black box"), so that the most informed decision is made. Any or all of the types of evidence in **Table 1** may be relevant in glass box cardiac model evaluation. The most important source of evidence for a whole-heart model will likely be organ-level COU-driven validation evidence, if available. Strong validation results of the full model, if highly "applicable" (Pathmanathan et al., 2017) to the COU, reduce the relative importance of the other factors

TABLE 1 | Different types of evidence relevant to the credibility of a cardiac EP model, with ion channel, cell, and organ-level examples.

Category	Type of credibility evidence	Examples		
		Ion channel	**Cell model**	**Organ-level model**
Category 1	Evidence regarding validity of model assumptions or supporting the model formulation	Successes of Hodgkin-Huxley formulation for modeling ion channels—see section Ion channel models	Evidence supporting the formulation of cell membrane as a parallel resistor-capacitor electric circuit	The successes of the bidomain equations, in particular predictions made that were later experimentally observed—see section Organ-level models
	Evidence regarding accuracy/fidelity of model parameters/inputs	Evidence supporting accuracy of steady-state inactivation parameters—see section Ion Channel Models	Rationale behind standard choice of membrane capacitance equal to 1 uF/cm^2.	Evidence on fidelity of geometry used and on fidelity of fiber/sheet specification—discussed in section Organ-Level Models.
Category 2	Calibration results	Results showing agreement between ion channel model and experimentally recorded current-voltage relationship when ion channel parameters are calibrated using this data	Results showing agreement between the model action potential and experimental recordings when maximal conductances are tuned to achieve the match	Results showing activation patterns match experiment if fast sodium current maximal conductance (which controls conduction velocity) chosen to maximize agreement
Category 3	Reproduced (emergent) phenomena	Simulation results demonstrating that a rapid sodium current model can exhibit damped oscillations	Simulation results demonstrating that a cell model reproduces action potential spike and dome morphology	Simulation results demonstrating that ECG predicted by a heart and torso model exhibits realistic-looking QRS complex and T wave
	General validation results	Comparison of a general-purpose ion channel model predictions to new voltage-clamp data not used in the construction of the model.	Comparisons of model results with experimental data for a novel general-purpose cell model, e.g., all such results in O'Hara et al. (2011). Discussed in detail in section Cell Models	Excitation patterns of general purpose bi-ventricular model compared to experimental/clinical data. ECG of general-purpose heart and torso model compared to experimental/clinical data.
	COU-driven validation results	Evaluation of a hERG model to predict pharmaceutical pro-arrhythmic risk	Evaluation of a cell model-based biomarker to predict pharmaceutical pro-arrhythmic risk (e.g., CiPA, discussed in section Cell Models)	Number of phase singularities during ventricular fibrillation (VF) compared to clinical data, when the model will be used to understand mechanisms behind VF—see section Organ-Level Models. Clinical evaluation of a whole-heart model which uses patient-specific information to predict optimal ablation targets to terminate arrhythmias—see section Organ-Level Models

(including reducing the need for evidence supporting model assumptions (Patterson and Whelan, 2017).

CREDIBILITY OF CEP MODELS AT DIFFERENT SPATIAL SCALES

We now discuss credibility evidence of CEP models at each of the spatial scales. The scope of the following review is limited to the most common types of CEP model: zero-dimensional models (i.e., systems of ODEs) of ionic channels and of the cell, and tissue/organ models that utilize the monodomain or bidomain formulation. Therefore, models that explicitly represent the spatial structure of ion channels or cardiac myocytes are out of scope of the review, including molecular dynamics models. Due to space limitations, we will only discuss ion channel models; other types of sub-cellular model such as calcium handling models are not included. We only consider models which are at least partially motivated by biophysical understanding, excluding phenomenological models, or statistical models such as those developed using neural networks or machine learning techniques. We re-iterate that this paper is focused on electrophysiology only; models of cardiac mechanics or hemodynamics are out of scope, although similar principles are expected to apply. Note that the scope of the following review is still quite broad and it is therefore not possible to describe or cite all publications that have performed validation of CEP models. The papers cited below were chosen to provide selected examples of approaches to CEP model validation.

Ion Channel Models

There is a long history of modeling the dynamics of transmembrane ion channels using the Hodgkin-Huxley (HH) formulation (Hodgkin and Huxley, 1952). In the HH formulation, transmembrane current is taken to be the product of

a maximum conductance, dynamic gating variables representing probabilities of channels gates being in an open state, and a driving force. Gating variable dynamics are modeled using ODEs, with dynamics determined by the voltage-dependent steady-state activation/inactivation and voltage-dependent "time constant" relationships for each gating variable (see **Figure 1**, which includes the equations for a HH formulation of the rapid sodium current with three gating variables m, h, and j). The HH formulation has in fact become so integral to cardiac electrophysiology that experimentalists regularly present data by publishing HH-based model parameters. Markov models of ionic currents are a more general formulation. For more details (see e.g., Fink et al., 2011).

Generally speaking, validation of novel ion channel models is *not* common practice (Fink et al., 2011). Here, we are referring to validation of the novel channel in isolation, not as part of a larger cell model. While voltage clamp data is used to develop and calibrate the models, those calibrated models are typically not then tested to new data. In fact, generally simulations are not even performed to show that the models predict the voltage-clamp results that they were based on, and surprisingly, simulations of voltage clamp protocols from which parameters are derived do not necessarily match the original data (Carro et al., 2017). (This can happen for a variety of reasons, such as the assumption of inactivation being much faster than activation not holding). Such observations demonstrate the value of ion channel model evaluation including validation. It can be difficult to determine in publications if results presented correspond to validation, because calibration and validation are often not clearly separated in presentation of results. An example of genuine validation is (Yang et al., 2015), in which validation of a new model of the late sodium current I_{NaL} is performed by comparing model predictions of the I_{NaL} current-voltage relationship under a slow depolarising voltage ramp, against experimental recordings under the same protocol. Another is the L-type calcium current model in O'Hara et al. (2011). As shown in **Figure 3**, validation of the calibrated I_{CaL} model was performed by comparing model with experimental data using an action potential clamp protocol. (Beattie et al., 2017) proposes a novel approach to developing cell-specific models of the rapid delayed rectifier potassium current I_{Kr}. Eight seconds of data using a novel sinusoidal voltage clamp protocol was used to calibrate the cell-specific I_{Kr} models, which were then validated against 5 min of data taken from the same cell, covering a range of voltage clamp protocols.

When no validation evidence is presented, the credibility of novel ion channel models is essentially founded—often implicitly—on a range of other factors, including the maturity of the HH formulation and related historical evidence, calibration evidence, and evidence regarding the accuracy of identified parameters. We discuss these in the remainder of this section.

The model of squid giant axon excitability proposed by Hodgkin and Huxley (Hodgkin and Huxley, 1952) is considered one of the greatest successes in twentieth century biophysics (Häusser, 2000; Schwiening, 2012). This is due to the ability of the relatively simple set of equations to reproduce a variety of phenomena (Häusser, 2000) and the fact that the HH modeling approach was then successfully applied to a wide range of excitable cells, including cardiac cells (Noble, 1962). The ideas and equations behind the HH model are now standard building blocks in electrophysiology (Schwiening, 2012). HH-based cardiac models have contributed greatly to understanding of cardiac electrophysiology, with various predictions made using cardiac models that were later experimentally verified. Examples include the existence of non-sodium inward currents and stoichiometry of the Na^+/Ca^{2+} exchanger; see (Noble, 2011) for a detailed review. However, despite these successes, there are several caveats that should be stated regarding use of a general HH formulation for a given ion channel. First, for some ion channels and some applications, such as the rapid delayed rectifier potassium current I_{Kr} and drug-binding applications, a Markov model based approach may be more appropriate (Clancy and Rudy, 1999). Additionally, there is still a lack of consensus and ongoing research into a variety of details of specific formulations. For example, for the fast sodium current I_{Na}, while the originally-proposed (Hodgkin and Huxley, 1952) and commonly-used m^3 formulation of activation can be argued to have a justification at the molecular level (Armstrong, 2006), it is unclear how to simultaneously represent the various modes of I_{Na} inactivation (fast, slow, and persistent; Nesterenko et al., 2011). Similarly, for the L-type calcium channel I_{CaL}, there is not a unique approach to simultaneously quantifying both voltage- and calcium-dependent inactivation (Grandi et al., 2010).

Once a HH-based model formulation is proposed and justified, model parameters need to be estimated. This includes parameters representing the voltage-dependent steady-state activation/inactivation and time-constant functions for each gate, which are estimated using voltage clamp data. Evidence on the accuracy of these parameters is important in evaluating model credibility, especially if no validation is performed. However, before asking about the accuracy of parameter values, one can ask if ion channel model parameters are uniquely identifiable from experimental data in the first place. A parameter cannot be claimed to be accurate if it is provably unidentifiable given the data. Although the methodology for nonlinear model identifiability has been extensively studied (Rothenberg, 1971; Jacquez and Greif, 1985; Walter and Pronzato, 1996), their utilization in the field of CEP modeling has been limited. The conditions under which model parameters can be identified has been studied in the context of single current sub-models (Beaumont et al., 1993; Wang and Beaumont, 2004; Lee et al., 2006; Csercsik et al., 2012; Raba et al., 2013) and more recently incorporated into a multi-scale framework using a simplified action potential model (Shotwell and Gray, 2016).

Returning to parameter estimation, voltage-dependant *steady-state* (in)activation relationships for many currents are typically well-approximated using sigmoidal functions using standard voltage clamp protocols, however obtaining data for accurate characterisation of voltage-dependent time constants is considerably more difficult. Assumptions underlying voltage clamp protocols should be well understood by model developers and may be questionable for protocols used to identify certain parameters (e.g., the assumption that inactivation is much faster than activation for protocols used to identify I_{Na} steady state

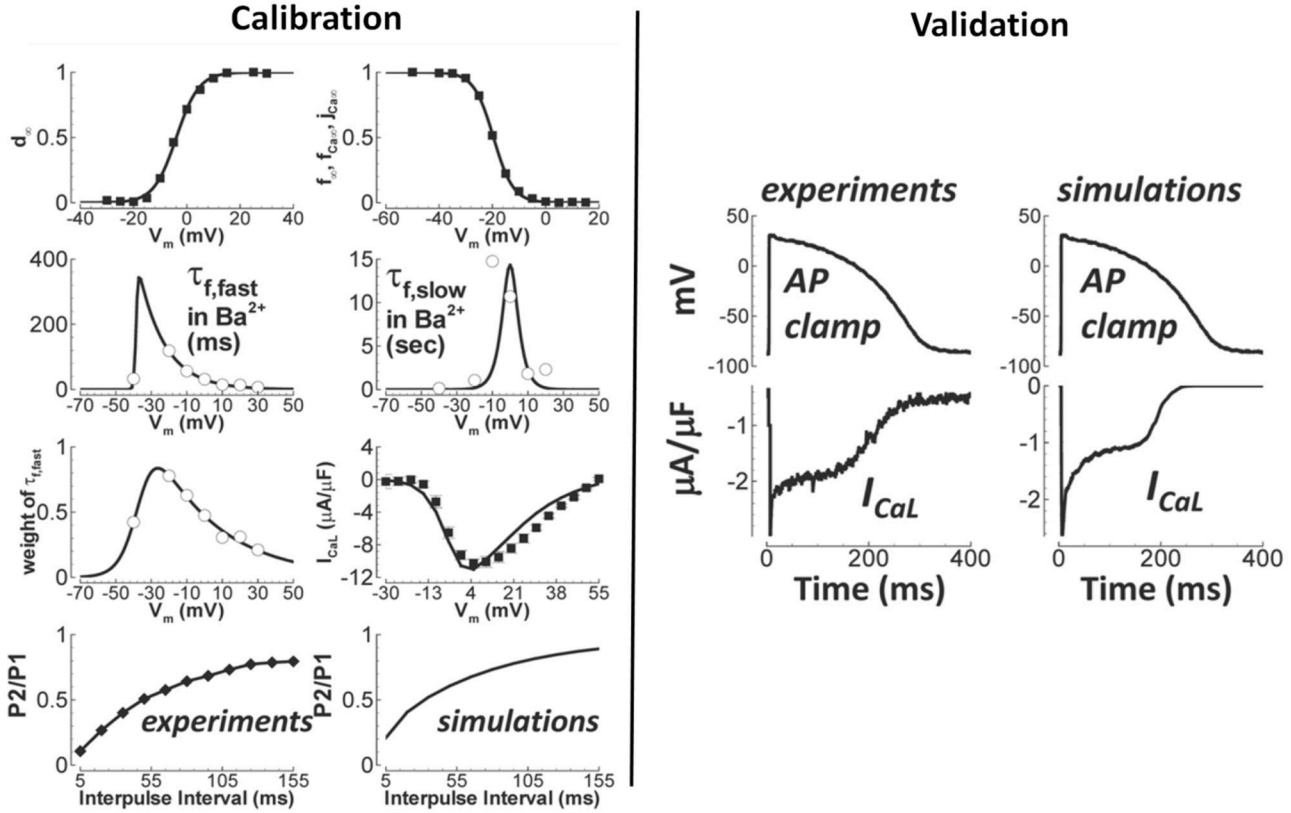

FIGURE 3 | Calibration and validation of the L-type Ca^{2+} current of O'Hara et al. (2011). Left figures show calibration results (circles/squares/diamonds—experiment; solid lines—simulation), including fitting of steady-state activation and inactivation (top row) and time constants (second row). Right figures are qualitative validation of the formulated I_{CaL} model by comparison of simulation and experiment under an identical action potential clamp. Quantitative validation of peak current is also provided in original paper. (Adapted from Figure 1 of O'Hara et al. (2011) with permission under Creative Commons license).

gating activation parameters Csercsik et al., 2012). Manual recording from single cells using well-established voltage clamp protocols remains the gold standard for obtaining high-quality current-voltage relationships (Elkins et al., 2013). Nevertheless, there are numerous (often "hidden") details regarding the specific procedures and protocols in the laboratory to isolate individual currents and to minimize recording artifacts (e.g., accounting for liquid junction potentials and capacitive compensation). Technical advances has improved the ability to measure rapid transients, however, it is still not possible to characterize activation for the fast sodium current steady-state activation from adult myocytes under physiological conditions (Berecki et al., 2010). Experimental reproducibility and variability between cells also present challenges (Pathmanathan et al., 2015). Regarding the voltage dependence of time constants, there is not even consensus on the appropriate functional forms, unlike steady state parameters. In general, fits to time constant data are much poorer than to steady-state (in)activation data [compare steady state and time constant fits in (e.g., ten Tusscher et al., 2004) or (O'Hara et al., 2011); also see **Figure 3**]. The quality of such fits is rarely quantified.

Overall, if a novel ion channel model is developed but no validation is performed, given the numerous issues described above there may be significant uncertainty regarding the true predictive capability of the ion channel model. This is especially true for simulations using conditions that are quite different to the conditions used for model calibration. Often, however, novel ion channel models are developed as one component of a cell model, and validation is instead performed at that level, as described in the next section.

Cell Models

Regarding validation of cardiac cell models, we first make two remarks. First, it should be noted that the majority of cell models are developed as general-purpose tools, as opposed to for a specific COU. Any initial testing against experimental data of a general purpose cell model therefore falls under the category of "general validation." Second, it can be especially difficult to determine in publications whether results presented are obtained by calibration or are genuinely validation evidence. For example, simulated and experimental action potentials may be presented in papers to demonstrate a close match between simulation and experiment, but it can be unclear if any parameters (e.g., ion channel maximal conductances) were tuned to obtain the match.

There is an enormous range in the extent of general validation performed when novel cell models are published.

They can vary in terms of which model outputs are compared to experiment, which pacing protocols are applied, the source of the experimental/clinical data, and the type of comparison between model and experiment (e.g., qualitative vs. quantitative). As an example, for validation of their human cell model, (ten Tusscher et al., 2004) first present action potential and calcium transient time courses under 1 Hz pacing, stating how the AP reproduces the characteristic spike notch dome of epicardial cells and the calcium transient reproduces the experimentally observed rounded-off triangular shape ("reproduced phenomena" evidence as discussed in section Why Trust a Computational Model?). They then semi-quantitatively compare several AP properties and diastolic/systolic calcium concentration with experiment, qualitatively compare APD restitution and conduction velocity restitution results with experiment, as well as present several other validation-related results, including at the tissue level (after coupling the cell model with the monodomain equations). This is arguably more extensive validation than presented for *most* other cell models. The most comprehensive set of validation tests for a new cell model is, as far as we aware, that presented in the original O'Hara-Rudy-dynamic (ORd) model paper O'Hara et al. (2011), in which validation was performed for all of the following QOIs: AP shape under multiple pacing rates, resting voltage, maximum voltage, maximum upstroke velocity, APD restitution properties (steady state; dynamic; with and without channel-specific blockers; single cell and in tissue), APD alternans and accommodation, AP shape with induced early after-depolarisation (EAD), peak intracellular sodium and calcium ion concentrations at multiple rates, calcium transient at multiple rates, and various current voltage relationships under various voltage/potassium/sodium/calcium clamps. This extensive validation, together with the use of human data for model development, are reasons why the ORd model is one of the most highly regarded of modern cell models, although we emphasize that even this model should not be considered a "validated cell model," both because of the issues with such terminology (see section Validation and Roache, 2009), and also because of certain ways it does not match clinical observations (Mann et al., 2016; Dutta et al., 2017).

In general it is important to note that modern cell models may simulate dozens of quantities (i.e., have dozens of state variables), of which usually only a handful have been directly compared to experimental data; this is certainly true even of the ORd model. Credibility in QOIs not compared to experiment is therefore based on "indirect" validation. It should also be appreciated that most cell models are typically *not* validated using data directly related to the initiation and maintenance of arrhythmias, although there are notable exceptions such as the validation involving EADs in O'Hara et al. (2011) or Nordin and Ming (1995) and involving reentrant waves in ten Tusscher et al. (2004).

The above are all examples of general validation; next we consider validation of cell models for a prescribed COU, i.e., COU-driven validation. For single cell cardiac models, the application (i.e., COU) with the greatest current research interest is prediction of proarrhythmic risk of novel pharmaceutical compounds (Davies et al., 2016). (Davies et al., 2012) develop an ensemble of 19 cell models calibrated to data from 19 dogs for this COU. For validation, they first compare model predictions of drug effect on action potential shape against experimental data (using various compounds). They then test the ability of the model ensemble to predict—blinded—whether a drug will cause AP shortening, prolongation, or have no effect, on a test set of 53 compounds and using measures of sensitivity, specificity and predictivity. Other CEP model-based biomarkers have also been recently proposed (Mirams et al., 2011; Passini et al., 2017), and have been evaluated against risk classifications scores using test sets of compounds. This application area has matured rapidly, and recently regulators, academia and the pharmaceutical industry have come together in the Cardiac *in vitro* Proarrhythmia Assay (CiPA) program (Cavero and Holzgrefe, 2014; Colatsky et al., 2016). The aim of the CiPA program is to develop a novel framework for assessing proarrhythmic risk. The proposed framework involves a series of predominantly nonclinical assays, one of which utilizes a cardiac cell model to integrate drug ion channel effects to the action potential level. The ORd model is being modified for this purpose, and the ultimate aim is to develop a model-based metric that converts drug ion channel effects into a predictive risk index (Dutta et al., 2017). Twelve drugs with well-characterized risk are being used for model and metric development, and the final metric will be validated (in a blinded fashion) using 16 different drugs with well-characterized proarrhythmic risk.

When no validation evidence is available for a cell model, which may be the case for a novel—or considerably modified—cell model, credibility of model predictions is essentially founded, perhaps implicitly, upon multiple factors. This includes the consensus view that the cell membrane can be modeled as a parallel resistor-capacitor electric circuit (Cole and Moore, 1960; Mauro et al., 1970), together with any evidence supporting credibility of each of the sub-cellular models incorporated (i.e., as discussed in section Ion Channel Models), and any calibration evidence (e.g., ability to reproduce AP shape or characteristics when model parameters are selected accordingly). In this case a lot of subject matter expertise may be required to interpret and to judge reliability of predictions.

Organ-Level Models

Tissue- and organ-level simulations have been used for many years and with great success in basic science applications (Trayanova et al., 2006; Bishop et al., 2009). These models involve the solution of the bidomain or monodomain equations (Tung, 1978; Henriquez, 1993; Neu and Krassowska, 1993; Bourgault et al., 2009), incorporating one or more specific cell models, on a computational mesh that approximates the geometry of interest (which can be a 2D monolayer (ten Tusscher et al., 2004), 3D slab of tissue, the atria (Seemann et al., 2006; Zhao et al., 2013), the ventricles (Plank et al., 2009) or the whole heart (Deng et al., 2012; Baillargeon et al., 2014). It is also possible to model the heart in a conductive medium, such as saline bath or the torso, which allows the electrocardiogram and defibrillation to be simulated (Aguel et al., 1999; Richards et al., 2013; Zemzemi et al., 2013; Okada et al., 2015). Tissue-level parameters that need to be prescribed include intra- and extra-cellular conductivities

(dependent on the local fiber and sheet directions Legrice et al., 1995). For more details (see, e.g., Lopez-Perez et al., 2015), which reviews 60 3D cardiac models developed over the past fifty years.

In fact, the methodology for tissue- and organ-level simulation studies is so well-established that simulation studies are routinely published in which a model is used for EP research but no validation results are presented, and no other rationale for credibility is explicitly presented. For such studies, the credibility of the model predictions is essentially based—implicitly—on the following: (i) confidence in the model governing equations (including historical evidence supporting the bidomain formulation); (ii) confidence in the cell model used; and (iii) the accuracy/fidelity of model parameters and geometrical inputs. We discuss each of these below.

First, we note that bidomain equations have a strong biophysical basis, being mathematically derived through a formal homogenisation of an underlying set of governing equations derived from Maxwell's equations (Neu and Krassowska, 1993). The underlying anatomical and physiological assumptions are mostly considered reasonable, although there remains ongoing research into alternative formulations that may better represent electrical propagation through myocardium, for example the fractional diffusion model of Bueno-Orovio et al. (2014), the alternative homogenisation derived by Richardson and Chapman (2011), or the hyperbolic bidomain model of Rossi and Griffith (2017). The bidomain equations reduce to the monodomain equations under the assumption that the intracellular and extracellular conductivity tensors are aligned. While this is known to not be the case in cardiac tissue, in the absence of extracellular stimuli (such as defibrillatory shocks) solutions of the monodomain equations can be very similar to those of the bidomain (Potse et al., 2006; Clayton et al., 2011). Perhaps the strongest evidence supporting the use of the bidomain equations are the numerous historical examples of quantitative predictions from bidomain simulations that have been reproduced experimentally, including complex phenomena that were predicted by simulation studies and only later observed experimentally. The most famous example regards specific virtual electrode patterns: simulations preceded experiment in predicting that unipolar excitation can result in a "dog-bone" shaped virtual cathode with regions of hyperpolarisation (virtual anode) in the vicinity of the virtual cathode (Sepulveda et al., 1989; Wikswo et al., 1991, 1995). This unexpected phenomenon is the result of the unequal anisotropy ratios of the intracellular and extracellular conductivity tensors. (Wikswo and Roth, 2009) provide a detailed review and numerous other examples of bidomain simulations matching experiment.

Credibility of tissue-level predictions is also dependent on the specific cell model used in the simulations. Credibility of cell models was discussed in section Cell Models. However, note that validation at the cell level does not necessarily imply that simulations will reproduce tissue-level phenomena. For example, (Gray et al., 2013) measured the action potential upstroke shape during propagation and found that it differed from that predicted in tissue simulations using a variety of cell models. (Uzelac et al., 2017) show that current cell models when incorporated into tissue level models do not reproduce the voltage and calcium dynamics of alternans. In addition, it is fairly common to adjust cell model parameters in tissue simulations (e.g., to shorten APD when simulating fibrillation Bishop and Plank, 2012), without any "re-validation" of the modified cell model; for such cases, it is unclear how much the previous cell model validation results can be relied upon. It is also increasingly common to re-calibrate cell model parameters in an organ-level model using data taken from intact tissue, including clinical data (e.g., Keldermann et al., 2008); again, it is unclear the extent that the body of previous validation results holds. We will return to this subject in the discussion.

The third factor especially relevant to model credibility when no validation results are available is the accuracy/fidelity of model parameters and other inputs. In regards to parameters we refer to Clayton et al. (2011), which provides a review of the challenges of estimating parameters in the bidomain equations. Note though that when estimating personalized parameters from clinical data for patient specific models, questions can be raised on the identifiability and accuracy those parameters; see (Chabiniok et al., 2016) for a general discussion. Here we focus on geometrical inputs. In organ-level simulations, an important factor that may require consideration when evaluating credibility is the anatomical fidelity of the computational mesh. There are a range of possibilities, from use of simple truncated ellipsoids (Vetter and McCulloch, 1998) to image-based meshes. Meshes vary in terms of the anatomical detail included. For example, they may include ventricular endocardial structures such as papillary muscles and trabeculae (Bishop et al., 2010); atrial endocardial structures such as fossa ovalis (Seemann et al., 2006); myocardial blood vessels (Bishop et al., 2010); and/or the Purkinje system (Romero et al., 2010; Bordas et al., 2011). The appropriate level of detail for specific applications is not yet clear; in particular there is ongoing research into the role of microstructure on the initiation, maintenance and termination of fibrillation (Bishop and Plank, 2012; Connolly et al., 2017). As well as geometry, there is a question on the fidelity of the prescribed fiber and sheet orientations. This can be estimated using DT-MRI imaging data (Mekkaoui et al., 2012); however DT-MRI data can be noisy due to partial volume effects and sensitive to motion artifacts (Bishop et al., 2009; Dierckx et al., 2009). An alternative approach is to use a "rule-based" method (see **Figure 5**, later, for an example), in which a mathematical algorithm is used to generate fiber and sheet architectures [see e.g., (Potse et al., 2006; Bishop et al., 2010; Bayer et al., 2012) for ventricles or (Krueger et al., 2011; McDowell et al., 2012) for atria], and has been shown to provide results that are very similar to those based on DT-MRI (Bishop et al., 2009; Bayer et al., 2012), but may not correctly capture fine-scale details such as fiber direction near the apex, around vessels or near infarcts. Therefore, either way, there may be considerable uncertainty about the true fidelity of the prescribed fiber/sheet directions, which may impact credibility of predictions of quantities expected to be sensitive to anisotropy.

Next, we move on to validation of organ-level models. The ability to perform validation of such models is of

course heavily constrained by difficulties in obtaining the necessary experimental or clinical data for model validation, and therefore the vast majority of validation of organ-level models has been limited to heart surface potentials. Heart surface potential data can be obtained from a variety of measurement modalities, including transmembrane voltage recorded from glass microelectrodes or using fluorescent dyes (e.g., optical mapping), or extracellular electrograms using electrode plaques, socks, baskets, or other mapping systems (contact and non-contact). These measurements vary in their spatial resolution from a single site to hundreds or thousands of sites. Each modality has its advantages and disadvantages; for example optical mapping provides very high spatial resolution but low voltage fidelity, and is always *ex vivo* for human tissue and only *in vivo* with great difficulty for animal experiments (Dillon et al., 1998). In contrast, extracellular electrograms can be used to obtain *in vivo* data but at lower spatial resolution. With the exception of the transmembrane microelectrodes, all modalities do not directly measure transmembrane voltage, which can lead to difficulties in achieving a like-for-like comparison between simulation and experiment. This can be remedied in the computational model. For example, fluorescent signals from optical mapping are different than transmembrane signals in that they have a longer upstroke (Gray, 1999), which was determined to be a result of photon scattering (Hyatt et al., 2003), which led to the development of CEP models that also simulated fluorescence with scattering to enable like-for-like comparisons (Bishop et al., 2007; Roth and Pertsov, 2009).

Many groups have performed validation of organ-level CEP models using data obtained from these modalities. Here we will provide a few representative examples, to give a flavor of the possibilities for validation of surface potentials or derived quantities. (Relan et al., 2011) describe a framework for the functional personalisation of a porcine biventricular model using *ex vivo* porcine optical mapping data. As shown in **Figure 4A**, following calibration using optical recordings under one pacing protocol, they quantitatively validated predictions of epicardial APD and activation time, using optical recordings from the same heart under various different pacing scenarios. (Rodriguez et al., 2005) investigated the role of structural differences between right and left ventricles in vulnerability to electric shocks in the rabbit heart. The study used a combination of biventicular bidomain simulations and optical recordings from an experimental Langendorff-perfused rabbit heart. The setup enabled various QOIs to be qualitatively compared between simulation and experiment (to support the credibility of simulation-based results of the study), including post-shock transmembrane potential distributions on the epicardial surface, and the probability of tachyarrhythmia induction as a function of shock strength and coupling interval. (Muzikant and Henriquez, 1998) and (Muzikant et al., 2002) compare bidomain predictions with experimental results from the paced *in vivo* canine heart measured using a 528 channel electrode plaque. This study is notable because of the quantitative approach to the validation of spatial patterns, analyzing the root mean squared (RMS) error and Pearson's correlation

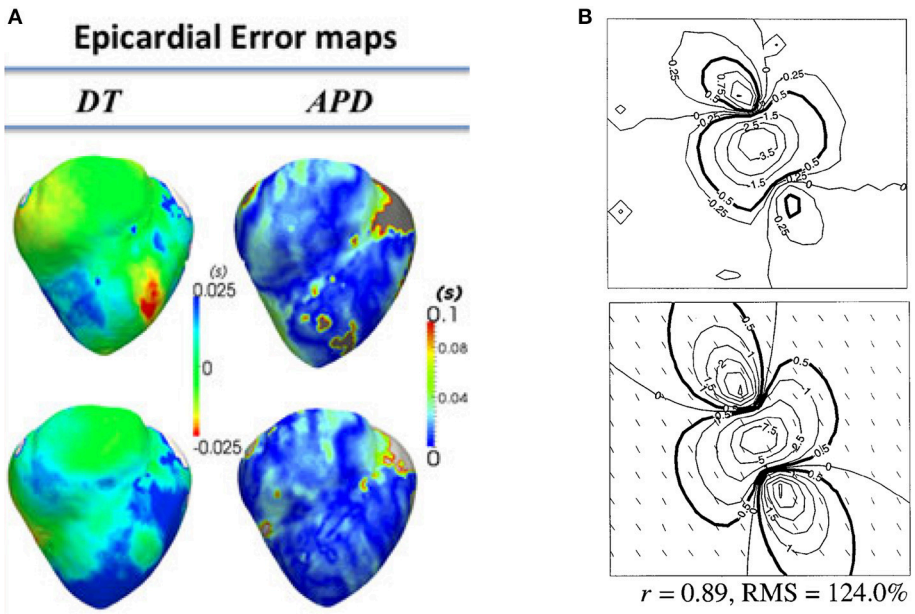

FIGURE 4 | Examples of quantitative validation of organ-level models. **(A)** Error maps (i.e., difference between model and experiment; here optical mapping-derived experimental data) for depolarisation time (DT) and APD (top row—pacing on left ventricle epicardium; bottom row—pacing on right ventricular endocardium) (Reproduced with permission from Relan et al., 2011). **(B)** Experimentally measured extracellular potential in mV using electrode plaque (top) compared to predictions of extracellular potential from bidomain simulations (bottom), with difference quantified using Pearson's correlation coefficient (r) and root mean squared (RMS) error. (Reproduced with permission from Muzikant et al., 2002).

coefficient between simulation and experiment, for extracellular potential and conduction velocity; see **Figure 4B**. (Niederer et al., 2010) use patient-specific biventricular electro*mechanical* models to investigate the relationship between the Frank-Starling mechanism and cardiac resynchronisation therapy (CRT) efficacy. To calibrate and validate the electrophysiological part of the electromechanical model, they use patient-specific clinical endocardial data obtaining using the EnSite™ cardiac mapping system. Clinical activation maps during sinus rhythm were used for model calibration, and activation maps under left ventricular pacing were used for validation of the calibrated model. (ten Tusscher et al., 2009) is a combined modeling and clinical study on the organization of ventricular fibrillation (VF) in the human heart. To support the credibility of the model used, epicardial excitation patterns are compared between model and clinical recordings obtained using a sock electrode, as is the time series of electrical activity at a fixed location. Dominant frequency of the time series is used for quantitative comparison between model and experiment. In addition, numbers of wavefronts and number of phase singularities over time are also compared. These quantities are convenient for condensing the complex spatio-temporal behavior of VF into simple time-series, useful for potential quantitative validation of very complex behavior.

Finally, we consider validation of organ-level CEP models with a specific clinical application; in particular, where a model is proposed to be used in clinical decision-making. One proposed application of CEP models is to use patient-specific simulations for risk stratification of patients with myocardial infarction, to determine which patients are at risk of SCD and therefore should receive prophylactic implantable cardioverter defibrillator (ICD) implant, as described in Arevalo et al. (2016). As illustrated in **Figure 5**, the software developed for this application uses patient-specific MR data to generate a biventricular mesh which includes regions of scar tissue and border zone. Electrical activity is simulated using the monodomain equations with the cell model of ten Tusscher et al. (2004). Various pacing protocols are virtually applied to determine if ventricular tachycardia (VT) is inducible, and if so the patient is classified as being at risk of SCD. We highlight two sets of validation results relevant to this model. The first, presented in Deng et al. (2015), is validation of epicardial excitation maps, for a swine version of the model, against swine data obtained using sock electrodes. The second, presented in Arevalo et al. (2016), describes a retrospective clinical study performed to test the risk index. In this study, the workflow described above was applied on a number of patients who had had ICD implant, and the risk classification as predicted by the model was compared to the clinical endpoint of ICD appropriately firing (or cardiac death). This is another form of (COU-driven) model validation, and of course it is a very strong form of validation because the QOI that is evaluated is the final QOI to be used in decision-making (i.e., risk index). Since it involves a clinical study, for this type of validation the appropriate quantitative analysis method is statistical; see (Arevalo et al., 2016) for details.

Other studies have proposed that related model-based tools could be used for prediction of ablation targets for patients affected by atrial fibrillation (AF) (McDowell et al., 2015), left atrial flutter (LAFL) (Zahid et al., 2016), or VT (Ashikaga et al., 2013). The proposed process for predicting ablation targets for all three arrhythmias is very similar to the process described above: an anatomically patient-specific model of the atria or ventricles is generated using MR data, and virtually interrogated to determine if AF/LAFL/VT is inducible. If so, ablation sites can be predicted that render AF/LAFL/VT non-inducible (a method for doing so is described in Zahid et al., 2016). (Zahid et al., 2016) presents a retrospective clinical study in which predicted LAFL ablation sites using the patient-specific atrial models are compared to the clinically ablated sites. (Chen et al., 2016) present a related workflow for developing patient-specific cardiac models, with personalisation of some functional parameters as well as anatomical personalisation. They perform validation by comparing model predictions of VT inducibility and re-entrant circuits to results from clinical VT stimulation studies.

Finally, similarly to cell models as discussed in section Cell Models, whole heart models have also been proposed to be used to predict drug-induced arrhythmogenic risk. (Okada et al., 2015) proposed that a heart and torso model which simulates the ECG can be used to integrate *in vitro* ion channel assays. The drug concentration at which Torsades de Pointes is induced in the simulated ECG is the proposed biomarker, and the predictive ability of this biomarker is tested using data for 12 drugs with well-characterized risk.

DISCUSSION

In this paper, we have categorized and discussed different types of evidence that could be used as a basis for the credibility of a CEP model. Our aim was to provide clarity on the body of evidence that typically is relevant (and often implied) in the evaluation of CEP models. As we transition into the era of Digital Health, there is a need for a systematic, rigorous and well-established methodology for justifying and assessing the credibility of computational models with biomedical applications. Current efforts toward these goals (ASME, 2017) are focused on "physics-based" models that have so far had most impact in medical devices applications (Pelton et al., 2008; Angelone et al., 2010; Stewart et al., 2012). However, these modeling fields are very different to physiological modeling in terms of model complexity, multi-scale nature, feasible validation, and inherent variability. In a previous publication we advocated that engineering model assessment methodologies of verification, validation and uncertainty quantification (VVUQ) could be used to improve credibility of models (Pathmanathan and Gray, 2013). However, while verification and uncertainty quantification methods are certainly relevant to CEP model assessment, best practices and quantitative methods in the engineering literature regarding validation appear less relevant to CEP models and other physiological models, due in part to the unique challenges in obtaining data for validation of physiological models. In general, the types of evidence supporting the credibility of physiological models will likely be very different to that for engineering models. Therefore, this paper is motivated by the need for a clear understanding of potential credibility evidence for CEP models, which can guide future efforts toward systematic

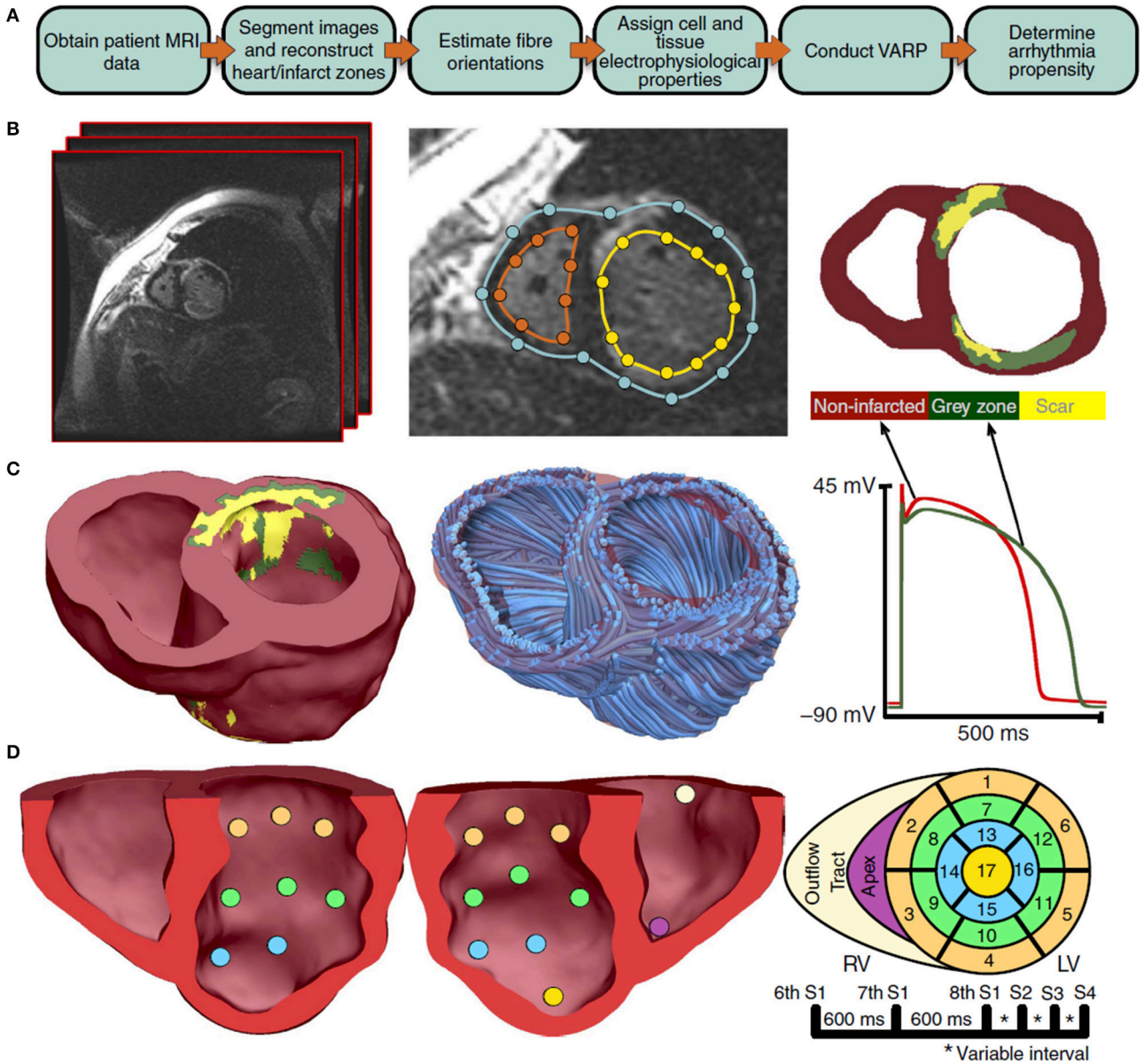

FIGURE 5 | Overview of process used to predict sudden cardiac death risk in Arevalo et al. (2016). A flowchart of the pipeline is shown in sub-figure **(A)**. MR images are segmented [sub-figure **(B)**] to develop a patient-specific computational model which includes regions of scar tissue and border zone ("gray zone") [sub-figure **(C)**]. A rule-based approach is used to specify fiber directions. The model is paced from 19 sites [sub-figure **(D)**] and with various pacing protocols and assessed for whether ventricular tachycardia is inducible. (Reproduced from Arevalo et al., 2016 with permission under Creative Commons license).

approaches for credibility assessment/justification which are relevant to physiological models.

We specifically highlighted validation of general-purpose CEP models not performed for any prescribed COU, and defined this as "general validation" evidence. As discussed in section Why Trust a Computational Model? the ever-increasing complexity of CEP cell models means that there are almost unlimited possibilities for such evaluation, and there is a large and ever-growing body of general validation results in the CEP modeling literature—in particular regarding cell models. Note that in this review we described several examples of general validation but we did not discuss the "quality" of any general validation results. For example, we avoided subjective statements such as "validation results showed good agreement between model and experiment." This is because the level of agreement needed between model and experiment is determined by the COU, and when no COU is specified, a statement that a model shows "good agreement" without any context could potentially lead to inappropriate use of a model. In general, while general validation can provide important preliminary information about a computational

model, it may not be advisable to convert general validation results into binary "good"/"bad" or "acceptable"/"unacceptable" statements. However, when a COU of a model is chosen, previous general validation results can certainly be (re-)evaluated to determine how supportive they are of the model in the COU. This will likely require assessment of both the level of agreement between model and simulation, and also the relevance or "applicability" of the validation conditions to the COU; discussed in detail in Pathmanathan et al. (2017).

Currently, general validation results for cell models that are published in the literature are not collected, curated, or made available in one place. One resource that could potentially be useful for the cardiac modeling community is a resource on credibility evidence for cell models. The CEP modeling community already leads the way in model sharing and reproduction through the CellML repository and related software (Lloyd et al., 2008). The CellML language is a XML-based language for defining CEP cell (and other) models, allowing models to be defined unambiguously and easily shared, and the CellML repository serves as the starting point when using a cell model published in the literature. However, the repository does not include information regarding model validation results or other credibility evidence, and there is no way to easily look up such information. A sister repository containing model credibility evidence could therefore be useful to CEP model developers/users when deciding on which cell model to use for a particular COU. Examples of information that could be stored in such as repository include which emergent phenomena the model reproduces (and does not reproduce), and general validation results under a wide range of precisely prescribed protocols. One resource that provides a path toward such a repository is the Cardiac Electrophysiology Web Lab (Cooper et al., 2016). This is an online tool for easy comparison of multiple CellML-defined cell models under a wide range of protocols (which required the development of an XML-based language for specifying protocols Cooper et al., 2011). Being able to easily compare models is important because even models of the same species and heart region can behave quite differently; (see e.g., Cherry and Fenton, 2007). While the Web Lab does not currently provide explicit comparison to experimental data, it already serves as a potential tool for identifying which phenomena models can reproduce, and one can imagine an extension in which experimental data (from a wide range of sources and with full details on experimental conditions and protocols) are also included and comparison to model predictions are provided, both visually for qualitative comparison and perhaps quantitatively with appropriate validation metrics. In fact, inclusion of experimental data is one of the future plans of the Web Lab developers (personal communications). As stated above, we believe such results should not be converted into binary good/bad or acceptable/unacceptable judgements, or used to rank models. Instead, such a repository would serve as a rich resource by providing information needed for selecting between competing models for a particular COU, as well as providing validation results that could serve as a starting point for justification of model credibility for the COU. Moreover, if users were able to upload models and automatically run all protocols (already possible in Web Lab) and then compare against the experimental data, this would be a powerful tool for validation of *modified* cell models (examples of which were provided in section Organ-Level Models), i.e., for comprehensive "re-validation." Note that we are *not* stating that an altered model should only be used if it "passes all validation tests." Indeed, for many COUs, a model not reproducing given phenomena could be argued to be acceptable given the COU. The point is that trust in cardiac models can be improved by collection of evidence, glass box evaluation, and explicit justification that the model is sufficiently credible for the COU despite its limitations.

It can be difficult to determine whether results presented in publications are calibration or validation results, as we mentioned in section Credibility of CEP Models at Different Spatial Scales. Specifically, while figures may be provided in which simulation and experimental results can be visually (and qualitatively) compared, it is often unclear whether any model parameters were tuned, optimized or tweaked to obtain the agreement with the experimental data. When that is the case, the results are calibration results, which is fundamentally weaker credibility evidence than validation of the *completed* model. Therefore, ideally calibration and validation results should be presented separately. While we believe that the examples of validation discussed in this paper are genuine validation results, it is certainly possible that some are actually calibration results. We also mentioned how simulation studies using CEP models are often performed in which no validation results or discussion of model credibility is presented. Such studies essentially implicitly rely—not unreasonably—on the maturity of the field and the various sources of historical evidence that we discussed in sections Ion Channel Models, Cell Models, and Organ-Level Models. The problem with this approach is it can contribute to a lack of clarity in the literature about the trustworthiness of CEP models, which can potentially lead to overconfidence in CEP models by non-experts who are unfamiliar with model subtleties (see initial discussion in Gong et al., 2017) as well as under-confidence in simulation-based conclusions by those who are skeptical of computational models in medicine. Such skepticism may be one of the biggest hurdles that needs to be overcome for computational models to achieve their potential in medical applications. These issues could be addressed by a clear and explicit presentation of the rationales for credibility of models used in simulation studies, referring as appropriate to the different sources of credibility evidence that support the use of the model for the COU as shown in **Table 1** (and/or appealing to the idea of models as representations, as discussed in section Why Trust a Computational Model?, when appropriate). As stated above, one aim is to argue that the model is sufficiently credible for the COU, despite model limitations. While there is no standardized method for determining what constitutes "sufficient credibility," the risk-informed strategy of (NASA, 2009; ASME, 2017) provides one method. The basic idea is that the credibility that needs to be demonstrated for a model should be related to the risk associated with incorrect predictions. Two factors are used to determine model risk. The first is model *influence*, which is the extent to which the model predictions will influence the decision to be made or conclusions of the study, compared

to other sources of information. The second is the *consequence* of incorrect decisions. For example, if a model is proposed to be used as the sole source of information in a safety-critical clinical decision, both influence and consequence are high, and the overall risk will be considered to be very high. Therefore, high credibility will be required of the model. In simulation studies, influence will often be high but consequence may be judged to be low, and overall risk may also be judged to be low, which means the credibility requirements are lower. Ultimately, we believe that routine and explicit justification of credibility will enable CEP models to have even greater impact in cardiac EP research, and facilitate their passage into clinical applications.

DISCLAIMER

The mention of commercial products, their sources, or their use in connection with material reported herein is not to be construed as either an actual or implied endorsement of such products by the Department of Health and Human Services.

AUTHOR CONTRIBUTIONS

PP: Devised the paper, performed review of literature, and wrote the paper; RG: Provided feedback and edits on all aspects of paper.

REFERENCES

Aguado-Sierra, J., Krishnamurthy, A., Villongco, C., Chuang, J., Howard, E., Gonzales, M. J., et al. (2011). Patient-specific modeling of dyssynchronous heart failure: a case study. *Prog. Biophys. Mol. Biol.* 107, 147–155. doi: 10.1016/j.pbiomolbio.2011.06.014

Aguel, F., Eason, J., Trayanova, N., Iekas, G., and Fishler, M. (1999). Impact of transvenous lead position on active-Can ICD defibrillation: a computer simulation study. *Pacing Clin. Electrophysiol.* 22, 158–164. doi: 10.1111/j.1540-8159.1999.tb00324.x

Angelone, L. M., Ahveninen, J., Belliveau, J. W., and Bonmassar, G. (2010). Analysis of the role of lead resistivity in specific absorption rate for deep brain stimulator leads at 3T MRI. *IEEE Trans. Med. Imaging* 29, 1029–1038. doi: 10.1109/TMI.2010.2040624

Arevalo, H. J., Vadakkumpadan, F., Guallar, E., Jebb, A., Malamas, P., Wu, K. C., et al. (2016). Arrhythmia risk stratification of patients after myocardial infarction using personalized heart models. *Nat. Commun.* 7:11437. doi: 10.1038/ncomms11437

Armstrong, C. M. (2006). Na channel inactivation from open and closed states. *Proc. Natl. Acad. Sci. U.S.A.* 103, 17991–17996. doi: 10.1073/pnas.0607603103

Ashikaga, H., Arevalo, H., Vadakkumpadan, F., Blake, R.C. III., Bayer, J.D., Nazarian, S., et al. (2013). Feasibility of image-based simulation to estimate ablation target in human ventricular arrhythmia. *Heart Rhythm* 10, 1109–1116. doi: 10.1016/j.hrthm.2013.04.015

ASME, S. (2017). *Draft V&V 40 - Standard for Verification and Validation in Computational Methods for Medical Devices*. (New York, NY: American Society of Mechanical Engineers).

Baillargeon, B., Rebelo, N., Fox, D.D., Taylor, R.L., and Kuhl, E. (2014). The living heart project: a robust and integrative simulator for human heart function. *Eur. J. Mech. A Solids* 48, 38–47. doi: 10.1016/j.euromechsol.2014.04.001

Bayer, J. D., Blake, R. C., Plank, G., and Trayanova, N. A. (2012). A novel rule-based algorithm for assigning myocardial fiber orientation to computational heart models. *Ann. Biomed. Eng.* 40, 2243–2254. doi: 10.1007/s10439-012-0593-5

Beattie, K.A., Hill, A.P., Bardenet, R., Cui, Y., Vandenberg, J.I., Gavaghan, D.J., et al. (2017). Sinusoidal voltage protocols for rapid characterization of ion channel kinetics. *bioRxiv*. doi: 10.1101/100677

Beaumont, J., Roberge, F., and Leon, L. (1993). On the interpretation of voltage-clamp data using the Hodgkin-Huxley model. *Math. Biosci.* 115, 65–101. doi: 10.1016/0025-5564(93)90047-E

Bellocchi, G., Rivington, M., Donatelli, M., and Matthews, K. (2010). Validation of biophysical models: issues and methodologies. A review. *Agron. Sustain. Dev.* 30, 109–130. doi: 10.1051/agro/2009001

Berecki, G., Wilders, R., De Jonge, B., Van Ginneken, A. C., and Verkerk, A. O. (2010). Re-evaluation of the action potential upstroke velocity as a measure of the Na+ current in cardiac myocytes at physiological conditions. *PLoS ONE* 5:e15772. doi: 10.1371/journal.pone.0015772

Bishop, M. J., and Plank, G. (2012). The role of fine-scale anatomical structure in the dynamics of reentry in computational models of the rabbit ventricles. *J. Physiol.* 590, 4515–4535. doi: 10.1113/jphysiol.2012.229062

Bishop, M. J., Hales, P., Plank, G., Gavaghan, D. J., Scheider, J., and Grau, V. (2009). "Comparison of Rule-Based and DTMRI-Derived Fibre Architecture in a whole rat ventricular computational model," in *Functional Imaging and Modeling of the Heart: 5th International Conference, FIMH 2009, Nice, France, Proceedings* eds. N. Ayache, H. Delingette, and M. Sermesant. (Berlin; Heidelberg: Springer Berlin Heidelberg), 87–96.

Bishop, M. J., Plank, G., Burton, R. A., Schneider, J. E., Gavaghan, D. J., Grau, V., et al. (2010). Development of an anatomically detailed MRI-derived rabbit ventricular model and assessment of its impact on simulations of electrophysiological function. *Am. J. Physiol. Heart Circ. Physiol.* 298, H699–H718. doi: 10.1152/ajpheart.00606.2009

Bishop, M. J., Rodriguez, B., Qu, F., Efimov, I. R., Gavaghan, D. J., and Trayanova, N. A. (2007). The role of photon scattering in optical signal distortion during arrhythmia and defibrillation. *Biophys. J.* 93, 3714–3726. doi: 10.1529/biophysj.107.110981

Bordas, R., Gillow, K., Lou, Q., Efimov, I., Gavaghan, D., Kohl, P., et al. (2011). Rabbit-specific ventricular model of cardiac electrophysiological function including specialized conduction system. *Prog. Biophys. Mol. Biol.* 107, 90–100. doi: 10.1016/j.pbiomolbio.2011.05.002

Bourgault, Y., Coudiere, Y., and Pierre, C. (2009). Existence and uniqueness of the solution for the bidomain model used in cardiac electrophysiology. *Nonlinear Anal. Real World Appl.* 10, 458–482. doi: 10.1016/j.nonrwa.2007.10.007

Brodland, G. W. (2015). How computational models can help unlock biological systems. *Semin. Cell Dev. Biol.* 47, 62–73. doi: 10.1016/j.semcdb.2015.07.001

Bueno-Orovio, A., Kay, D., Grau, V., Rodriguez, B., and Burrage, K. (2014). Fractional diffusion models of cardiac electrical propagation: role of structural heterogeneity in dispersion of repolarization. *J. R. Soc. Interface* 11:20140352. doi: 10.1098/rsif.2014.0352

Carro, J., Rodríguez-Matas, J. F., Monasterio, V., and Pueyo, E. (2017). Limitations in electrophysiological model development and validation caused by differences between simulations and experimental protocols. *Prog. Biophys. Mol. Biol.* 129, 53–64. doi: 10.1016/j.pbiomolbio.2016.11.006

Carusi, A., Burrage, K., and Rodríguez, B. (2012). Bridging experiments, models and simulations: an integrative approach to validation in computational cardiac electrophysiology. *Am. J. Physiol. Heart Circ. Physiol.* 303, H144–H155. doi: 10.1152/ajpheart.01151.2011

Cavero, I., and Holzgrefe, H. (2014). Comprehensive *in vitro* proarrhythmia assay, a novel *in vitro*/*in silico* paradigm to detect ventricular proarrhythmic liability: a visionary 21st century initiative. *Expert Opin. Drug Saf.* 13, 745–758. doi: 10.1517/14740338.2014.915311

Chabiniok, R., Wang, V. Y., Hadjicharalambous, M., Asner, L., Lee, J., Sermesant, M., et al. (2016). Multiphysics and multiscale modelling, data–model fusion and integration of organ physiology in the clinic: ventricular cardiac mechanics. *Interface Focus* 6:20150083. doi: 10.1098/rsfs.2015.0083

Chang, E. T., Strong, M., and Clayton, R. H. (2015). Bayesian sensitivity analysis of a cardiac cell model using a Gaussian process emulator. *PLoS ONE* 10:e0130252. doi: 10.1371/journal.pone.0130252

Chang, K. C., Dutta, S., Mirams, G. R., Beattie, K. A., Sheng, J., Tran, P. N., et al. (2017). Uncertainty quantification reveals the importance of data

variability and experimental design considerations for *in silico* proarrhythmia risk assessment. *Front. Physiol.* 8:917. doi: 10.3389/fphys.2017.00917

Chen, Z., Cabrera-Lozoya, R., Relan, J., Sohal, M., Shetty, A., Karim, R., et al. (2016). Biophysical modeling predicts ventricular tachycardia inducibility and circuit morphology: a combined clinical validation and computer modeling approach. *J. Cardiovasc. Electrophysiol.* 27, 851–860. doi: 10.1111/jce.12991

Cherry, E. M., and Fenton, F. H. (2007). A tale of two dogs: analyzing two models of canine ventricular electrophysiology. *Am. J. Physiol. Heart Circ. Physiol.* 292, H43–H55. doi: 10.1152/ajpheart.00955.2006

Clancy, C. E., and Rudy, Y. (1999). Linking a genetic defect to its cellular phenotype in a cardiac arrhythmia. *Nature* 400, 566. doi: 10.1038/23034

Clayton, R., Bernus, O., Cherry, E., Dierckx, H., Fenton, F., Mirabella, L., et al. (2011). Models of cardiac tissue electrophysiology: progress, challenges and open questions. *Prog. Biophys. Mol. Biol.* 104, 22–48. doi: 10.1016/j.pbiomolbio.2010.05.008

Colatsky, T., Fermini, B., Gintant, G., Pierson, J. B., Sager, P., Sekino, Y., et al. (2016). The comprehensive *in vitro* proarrhythmia assay (CiPA) initiative—Update on progress. *J. Pharmacol. Toxicol. Methods* 81, 15–20. doi: 10.1016/j.vascn.2016.06.002

Cole, K. S., and Moore, J. W. (1960). Ionic current measurements in the squid giant axon membrane. *J. Gen. Physiol.* 44, 123–167. doi: 10.1085/jgp.44.1.123

Connolly, A., Vigmond, E., and Bishop, M. (2017). Virtual electrodes around anatomical structures and their roles in defibrillation. *PLoS ONE* 12:e0173324. doi: 10.1371/journal.pone.0173324

Cooper, J., Mirams, G. R., and Niederer, S. A. (2011). High-throughput functional curation of cellular electrophysiology models. *Prog. Biophys. Mol. Biol.* 107, 11–20. doi: 10.1016/j.pbiomolbio.2011.06.003

Cooper, J., Scharm, M., and Mirams, G. R. (2016). The cardiac electrophysiology web lab. *Biophys. J.* 110, 292–300. doi: 10.1016/j.bpj.2015.12.012

Csercsik, D., Hangos, K. M., and Szederkényi, G. (2012). Identifiability analysis and parameter estimation of a single Hodgkin–Huxley type voltage dependent ion channel under voltage step measurement conditions. *Neurocomputing* 77, 178–188. doi: 10.1016/j.neucom.2011.09.006

Davies, M. R., Mistry, H. B., Hussein, L., Pollard, C. E., Valentin, J.-P., Swinton, J., et al. (2012). An *in silico* canine cardiac midmyocardial action potential duration model as a tool for early drug safety assessment. *Am. J. Physiol. Heart Circ. Physiol.* 303, H497–H498. doi: 10.1152/ajpheart.00808.2011

Davies, M. R., Wang, K., Mirams, G. R., Caruso, A., Noble, D., Walz, A., et al. (2016). Recent developments in using mechanistic cardiac modelling for drug safety evaluation. *Drug Discov. Today* 21, 924–938. doi: 10.1016/j.drudis.2016.02.003

Deng, D., Arevalo, H., Pashakhanloo, F., Prakosa, A., Ashikaga, H., McVeigh, E., et al. (2015). Accuracy of prediction of infarct-related arrhythmic circuits from image-based models reconstructed from low and high resolution MRI. *Front. Physiol.* 6:282. doi: 10.3389/fphys.2015.00282

Deng, D., Jiao, P., Ye, X., and Xia, L. (2012). An image-based model of the whole human heart with detailed anatomical structure and fiber orientation. *Comput. Math. Methods Med.* 2012:891070. doi: 10.1155/2012/891070

Dierckx, H., Benson, A. P., Gilbert, S. H., Ries, M. E., Holden, A. V., Verschelde, H., et al. (2009). "Intravoxel fibre structure of the left ventricular free wall and posterior left-right ventricular insertion site in canine myocardium using Q-Ball imaging," in *International Conference on Functional Imaging and Modeling of the Heart* (Springer), 495–504. doi: 10.1007/978-3-642-01932-6_53

Dillon, S. M., Kerner, T. E., Hoffman, J., Menz, V., Li, K., and Michele, J. (1998). A system for *in-vivo* cardiac optical mapping. *IEEE Eng. Med. Biol. Mag.* 17, 95–108. doi: 10.1109/51.646226

Dutta, S., Chang, K. C., Beattie, K. A., Sheng, J., Tran, P. N., Wu, W. W., et al. (2017). Optimization of an *in silico* cardiac cell model for proarrhythmia risk assessment. *Front. Physiol.* 8:616. doi: 10.3389/fphys.2017.00616

Eddy, D. M., Hollingworth, W., Caro, J. J., Tsevat, J., McDonald, K. M., and Wong, J. B. (2012). Model transparency and validation a report of the ISPOR-SMDM modeling good research practices task force−7. *Med. Decis. Making* 32, 733–743. doi: 10.1177/0272989X12454579

Elkins, R.C., Davies, M.R., Brough, S.J., Gavaghan, D.J., Cui, Y., Abi-Gerges, N., et al. (2013). Variability in high-throughput ion-channel screening data and consequences for cardiac safety assessment. *J. Pharmacol. Toxicol. Methods* 68, 112–122. doi: 10.1016/j.vascn.2013.04.007

Fink, M., Niederer, S. A., Cherry, E. M., Fenton, F. H., Koivumäki, J. T., Seemann, G., et al. (2011). Cardiac cell modelling: observations from the heart of the cardiac physiome project. *Prog. Biophys. Mol. Biol.* 104, 2–21. doi: 10.1016/j.pbiomolbio.2010.03.002

Food and Drug Administration, (2016). *Reporting of Computational Modeling Studies in Medical Device Submissions—Guidance for Industry and Food and Drug Administration Staff*. (Washington, DC: Food and Drug Administration).

Franzone, P. C., Pavarino, L. F., and Scacchi, S. (2014). *Mathematical Cardiac Electrophysiology*. New York, NY: Springer.

Gong, J. Q., Shim, J. V., Nú-ez-Acosta, E., and Sobie, E. A. (2017). I love it when a plan comes together: insight gained through convergence of competing mathematical models. *J. Mol. Cell. Cardiol.* 102, 31–33. doi: 10.1016/j.yjmcc.2016.10.015

Grandi, E., Morotti, S., Ginsburg, K. S., Severi, S., and Bers, D. M. (2010). Interplay of voltage and Ca-dependent inactivation of L-type Ca current. *Prog. Biophys. Mol. Biol.* 103, 44–50. doi: 10.1016/j.pbiomolbio.2010.02.001

Gray, R. A. (1999). What exactly are optically recorded "action potentials"? *J. Cardiovasc. Electrophysiol.* 10, 1463–1466. doi: 10.1111/j.1540-8167.1999.tb00205.x

Gray, R. A., Mashburn, D. N., Sidorov, V. Y., and Wikswo, J. P. (2013). Quantification of transmembrane currents during action potential propagation in the heart. *Biophys. J.* 104, 268–278. doi: 10.1016/j.bpj.2012.11.007

Häusser, M. (2000). The Hodgkin-Huxley theory of the action potential. *Nat. Neurosci.* 3, 1165–1165. doi: 10.1038/81426

Henriquez, C. S. (1993). Simulating the electrical behavior of cardiac tissue using the bidomain model. *Crit. Rev. Biomed. Eng.* 21, 1–77.

Hills, R. G., Pilch, M., Dowding, K. J., Red-Horse, J., Paez, T. L., Babuška, I., et al. (2008). Validation challenge workshop. *Comput. Methods Appl. Mech. Eng.* 197, 2375–2380. doi: 10.1016/j.cma.2007.10.016

Hodgkin, A. L., and Huxley, A. F. (1952). A quantitative description of membrane current and its application to conduction and excitation in nerve. *J. Physiol.* 117, 500–544. doi: 10.1113/jphysiol.1952.sp004764

Hyatt, C. J., Mironov, S. F., Wellner, M., Berenfeld, O., Popp, A. K., Weitz, D. A., et al. (2003). Synthesis of voltage-sensitive fluorescence signals from three-dimensional myocardial activation patterns. *Biophys. J.* 85, 2673–2683. doi: 10.1016/S0006-3495(03)74690-6

Iyer, V., Mazhari, R., and Winslow, R.L. (2004). A computational model of the human left-ventricular epicardial myocyte. *Biophys. J.* 87, 1507–1525. doi: 10.1529/biophysj.104.043299

Jacquez, J. A., and Greif, P. (1985). Numerical parameter identifiability and estimability: integrating identifiability, estimability, and optimal sampling design. *Math. Biosci.* 77, 201–227. doi: 10.1016/0025-5564(85)90098-7

Johnstone, R. H., Chang, E. T., Bardenet, R., De Boer, T. P., Gavaghan, D. J., Pathmanathan, P., et al. (2016). Uncertainty and variability in models of the cardiac action potential: can we build trustworthy models? *J. Mol. Cell. Cardiol.* 96, 49–62. doi: 10.1016/j.yjmcc.2015.11.018

Keldermann, R. H., Ten Tusscher, K. H. W. J., Nash, M. P., Hren, R., Taggart, P., and Panfilov, A. V. (2008). Effect of heterogeneous APD restitution on VF organization in a model of the human ventricles. *Am. J. Physiol. Heart Circ. Physiol.* 294, H764–H774. doi: 10.1152/ajpheart.00906.2007

Konukoglu, E., Relan, J., Cilingir, U., Menze, B. H., Chinchapatnam, P., Jadidi, A., et al. (2011). Efficient probabilistic model personalization integrating uncertainty on data and parameters: application to eikonal-diffusion models in cardiac electrophysiology. *Prog. Biophys. Mol. Biol.* 107, 134–146. doi: 10.1016/j.pbiomolbio.2011.07.002

Krishnamoorthi, S., Perotti, L. E., Borgstrom, N. P., Ajijola, O. A., Frid, A., Ponnaluri, A. V., et al. (2014). Simulation methods and validation criteria for modeling cardiac ventricular electrophysiology. *PLoS ONE* 9:e114494. doi: 10.1371/journal.pone.0114494

Krueger, M. W., Schmidt, V., Tobón, C., Weber, F. M., Lorenz, C., Keller, D. U. J., et al. (2011). "Modeling atrial fiber orientation in patient-specific geometries: a semi-automatic rule-based approach," in *Functional Imaging and Modeling of the Heart: 6th International Conference, FIMH 2011, New York City, NY, USA Proceedings,* eds D. N. Metaxas and L. Axel (Berlin; Heidelberg: Springer Berlin Heidelberg), 223–232. doi: 10.1007/978-3-642-21028-0_28

Lee, J., Smaill, B., and Smith, N. (2006). Hodgkin-Huxley type ion channel characterization: an improved method of voltage clamp experiment parameter estimation. *J. Theor. Biol.* 242, 123–134. doi: 10.1016/j.jtbi.2006.02.006

Legrice, I. J., Smaill, B., Chai, L., Edgar, S., Gavin, J., and Hunter, P. J. (1995). Laminar structure of the heart: ventricular myocyte arrangement and connective tissue architecture in the dog. *Am. J. Physiol. Heart Circ. Physiol.* 269, H571–H582. doi: 10.1152/ajpheart.1995.269.2.H571

Lloyd, C. M., Lawson, J. R., Hunter, P. J., and Nielsen, P. F. (2008). The CellML model repository. *Bioinformatics* 24, 2122–2123. doi: 10.1093/bioinformatics/btn390

Lopez-Perez, A., Sebastian, R., and Ferrero, J. M. (2015). Three-dimensional cardiac computational modelling: methods, features and applications. *Biomed. Eng. Online* 14:35. doi: 10.1186/s12938-015-0033-5

Mann, S. A., Imtiaz, M., Winbo, A., Rydberg, A., Perry, M. D., Couderc, J.-P., et al. (2016). Convergence of models of human ventricular myocyte electrophysiology after global optimization to recapitulate clinical long QT phenotypes. *J. Mol. Cell. Cardiol.* 100, 25–34. doi: 10.1016/j.yjmcc.2016.09.011

Mauro, A., Conti, F., Dodge, F., and Schor, R. (1970). Subthreshold behavior and phenomenological impedance of the squid giant axon. *J. Gen. Physiol.* 55, 497–523. doi: 10.1085/jgp.55.4.497

McDowell, K. S., Vadakkumpadan, F., Blake, R., Blauer, J., Plank, G., Macleod, R. S., et al. (2012). Methodology for patient-specific modeling of atrial fibrosis as a substrate for atrial fibrillation. *J. Electrocardiol.* 45, 640–645. doi: 10.1016/j.jelectrocard.2012.08.005

McDowell, K. S., Zahid, S., Vadakkumpadan, F., Blauer, J., Macleod, R. S., and Trayanova, N. A. (2015). Virtual electrophysiological study of atrial fibrillation in fibrotic remodeling. *PLoS ONE* 10:e0117110. doi: 10.1371/journal.pone.0117110

Mekkaoui, C., Huang, S., Chen, H. H., Dai, G., Reese, T. G., Kostis, W. J., et al. (2012). Fiber architecture in remodeled myocardium revealed with a quantitative diffusion CMR tractography framework and histological validation. *J. Cardiovasc. Magn. Reson.* 14:70. doi: 10.1186/1532-429X-14-70

Mirams, G. R., Cui, Y., Sher, A., Fink, M., Cooper, J., Heath, B. M., et al. (2011). Simulation of multiple ion channel block provides improved early prediction of compounds' clinical torsadogenic risk. *Cardiovasc. Res.* 91, 53–61. doi: 10.1093/cvr/cvr044

Mirams, G. R., Pathmanathan, P., Gray, R. A., Challenor, P., and Clayton, R. H. (2016). Uncertainty and variability in computational and mathematical models of cardiac physiology. *J. Physiol.* 594, 6833–6847. doi: 10.1113/JP271671

Muzikant, A., and Henriquez, C. (1998). Validation of three-dimensional conduction models using experimental mapping: are we getting closer? *Prog. Biophys. Mol. Biol.* 69, 205–223. doi: 10.1016/S0079-6107(98)00008-X

Muzikant, A. L., Hsu, E. W., Wolf, P. D., and Henriquez, C. S. (2002). Region specific modeling of cardiac muscle: comparison of simulated and experimental potentials. *Ann. Biomed. Eng.* 30, 867–883. doi: 10.1114/1.1509453

NASA (2009). *7009: Standard for Models and Simulation*. Washington, DC: NASA.

National Research Council (2012). *Assessing the Reliability of Complex Models: Mathematical and Statistical Foundations of Verification, Validation, and Uncertainty Quantification*. Washington, DC: National Academies Press.

Nesterenko, V. V., Zygmunt, A. C., Rajamani, S., Belardinelli, L., and Antzelevitch, C. (2011). Mechanisms of atrial-selective block of Na+ channels by ranolazine: II. Insights from a mathematical model. *Am. J. Physiol. Heart Circ. Physiol.* 301, H1615–H1624. doi: 10.1152/ajpheart.00243.2011

Neu, J., and Krassowska, W. (1993). Homogenization of syncytial tissues. *Crit. Rev. Biomed. Eng.* 21, 137–199.

Niederer, S. A., and Smith, N. P. (2016). Using physiologically based models for clinical translation: predictive modelling, data interpretation or something in-between? *J. Physiol.* 594, 6849–6863. doi: 10.1113/JP272003

Niederer, S. A., Kerfoot, E., Benson, A. P., Bernabeu, M. O., Bernus, O., Bradley, C., et al. (2011). Verification of cardiac tissue electrophysiology simulators using an N-version benchmark. *Phil. Trans. R. Soc. A* 369, 4331–4351. doi: 10.1098/rsta.2011.0139

Niederer, S. A., Plank, G., Chinchapatnam, P., Ginks, M., Lamata, P., Rhode, K. S., et al. (2010). Length-dependent tension in the failing heart and the efficacy of cardiac resynchronization therapy. *Cardiovasc. Res.* 89, 336–343. doi: 10.1093/cvr/cvq318

Noble, D. (1962). A modification of the Hodgkin—Huxley equations applicable to Purkinje fibre action and pacemaker potentials. *J. Physiol.* 160, 317–352. doi: 10.1113/jphysiol.1962.sp006849

Noble, D. (2011). Successes and failures in modeling heart cell electrophysiology. *Heart Rhythm* 8, 1798–1803. doi: 10.1016/j.hrthm.2011.06.014

Noble, D., Garny, A., and Noble, P. J. (2012). How the Hodgkin–Huxley equations inspired the cardiac physiome project. *J. Physiol.* 590, 2613–2628. doi: 10.1113/jphysiol.2011.224238

Nordin, C., and Ming, Z. (1995). Computer model of current-induced early afterdepolarizations in guinea pig ventricular myocytes. *Am. J. Physiol. Heart Circ. Physiol.* 268, H2440–H2459. doi: 10.1152/ajpheart.1995.268.6.H2440

Oberkampf, W. L., and Barone, M. F. (2006). Measures of agreement between computation and experiment: validation metrics. *J. Comput. Phys.* 217, 5–36. doi: 10.1016/j.jcp.2006.03.037

Oberkampf, W. L., Trucano, T. G., and Hirsch, C. (2004). Verification, validation, and predictive capability in computational engineering and physics. *Appl. Mech. Rev.* 57:345. doi: 10.1115/1.1767847

O'Hara, T., Virág, L., Varró, A., and Rudy, Y. (2011). Simulation of the undiseased human cardiac ventricular action potential: model formulation and experimental validation. *PLoS Comput. Biol.* 7:e1002061. doi: 10.1371/journal.pcbi.1002061

Okada, J.-I., Yoshinaga, T., Kurokawa, J., Washio, T., Furukawa, T., Sawada, K., et al. (2015). Screening system for drug-induced arrhythmogenic risk combining a patch clamp and heart simulator. *Sci. Adv.* 1:e1400142. doi: 10.1126/sciadv.1400142

Passini, E., Britton, O. J., Lu, H. R., Rohrbacher, J., Hermans, A. N., Gallacher, D. J., et al. (2017). Human *in silico* drug trials demonstrate higher accuracy than animal models in predicting clinical pro-arrhythmic cardiotoxicity. *Front. Physiol.* 8:668. doi: 10.3389/fphys.2017.00668

Pathmanathan, P., and Gray, R. A. (2013). Ensuring reliability of safety-critical clinical applications of computational cardiac models. *Front. Physiol.* 4:358. doi: 10.3389/fphys.2013.00358

Pathmanathan, P., and Gray, R. A. (2014). Verification of computational models of cardiac electro-physiology. *Int. J. Numer. Methods Biomed. Eng.* 30, 525–544. doi: 10.1002/cnm.2615

Pathmanathan, P., Gray, R. A., Romero, V. J., and Morrison, T. M. (2017). Applicability analysis of validation evidence for biomedical computational models. *J. Verif. Valid. Uncert. Quantification* 2, 021005–021005-11. doi: 10.1115/1.4037671

Pathmanathan, P., Shotwell, M. S., Gavaghan, D. J., Cordeiro, J. M., and Gray, R. A. (2015). Uncertainty quantification of fast sodium current steady-state inactivation for multi-scale models of cardiac electrophysiology. *Prog. Biophys. Mol. Biol.* 117, 4–18. doi: 10.1016/j.pbiomolbio.2015.01.008

Patterson, E. A., and Whelan, M. P. (2017). A framework to establish credibility of computational models in biology. *Prog. Biophys. Mol. Biol.* 129, 13–19. doi: 10.1016/j.pbiomolbio.2016.08.007

Pelton, A., Schroeder, V., Mitchell, M., Gong, X.-Y., Barney, M., and Robertson, S. (2008). Fatigue and durability of Nitinol stents. *J. Mech. Behav. Biomed. Mater.* 1, 153–164. doi: 10.1016/j.jmbbm.2007.08.001

Plank, G., Burton, R. A., Hales, P., Bishop, M., Mansoori, T., Bernabeu, M. O., et al. (2009). Generation of histo-anatomically representative models of the individual heart: tools and application. *Philos. Trans. R. Soc. Lond. A Math. Phys. Eng. Sci.* 367, 2257–2292. doi: 10.1098/rsta.2009.0056

Potse, M., Dubé, B., Richer, J., Vinet, A., and Gulrajani, R. M. (2006). A comparison of monodomain and bidomain reaction-diffusion models for action potential propagation in the human heart. *IEEE Trans. Biomed. Eng.* 53, 2425–2435. doi: 10.1109/TBME.2006.880875

Raba, A. E., Cordeiro, J. M., Antzelevitch, C., and Beaumont, J. (2013). Extending the conditions of application of an inversion of the Hodgkin–Huxley Gating model. *Bull. Math. Biol.* 75, 752–773. doi: 10.1007/s11538-013-9832-7

Relan, J., Pop, M., Delingette, H., Wright, G. A., Ayache, N., and Sermesant, M. (2011). Personalization of a cardiac electrophysiology model using optical mapping and MRI for prediction of changes with pacing. *IEEE Trans. Biomed. Eng.* 58, 3339–3349. doi: 10.1109/TBME.2011.2107513

Richards, D. F., Glosli, J. N., Draeger, E. W., Mirin, A. A., Chan, B., Fattebert, J.-L., et al. (2013). Towards real-time simulation of cardiac electrophysiology in a human heart at high resolution. *Comput. Methods Biomech. Biomed. Eng.* 16, 802–805. doi: 10.1080/10255842.2013.795556

Richardson, G., and Chapman, S. J. (2011). Derivation of the bidomain equations for a beating heart with a general microstructure. *SIAM J. Appl. Math.* 71, 657–675. doi: 10.1137/090777165

Roache, P. J. (2009). Perspective: validation—What does it mean? *J. Fluids Eng.* 131:034503. doi: 10.1115/1.3077134

Rodriguez, B., Li, L., Eason, J. C., Efimov, I. R., and Trayanova, N. A. (2005). Differences between left and right ventricular chamber geometry affect cardiac vulnerability to electric shocks. *Circ. Res.* 97, 168–175. doi: 10.1161/01.RES.0000174429.00987.17

Romero, D., Sebastian, R., Bijnens, B. H., Zimmerman, V., Boyle, P. M., Vigmond, E. J., et al. (2010). Effects of the purkinje system and cardiac geometry on biventricular pacing: a model study. *Ann. Biomed. Eng.* 38, 1388–1398. doi: 10.1007/s10439-010-9926-4

Rossi, S., and Griffith, B. E. (2017). Incorporating inductances in tissue-scale models of cardiac electrophysiology. *Chaos* 27, 093926. doi: 10.1063/1.5000706

Roth, B. J., and Pertsov, A. M. (2009). Hybrid modeling of electrical and optical behavior in the heart. *Physica D Nonlinear Phenomena* 238, 1019–1027. doi: 10.1016/j.physd.2009.01.014

Rothenberg, T. J. (1971). Identification in parametric models. *Econometrica* 577–591. doi: 10.2307/1913267

Schwiening, C. J. (2012). A brief historical perspective: Hodgkin and Huxley. *J. Physiol.* 590, 2571–2575. doi: 10.1113/jphysiol.2012.230458

Seemann, G., Höper, C., Sachse, F. B., Dössel, O., Holden, A. V., and Zhang, H. (2006). Heterogeneous three-dimensional anatomical and electrophysiological model of human atria. *Philos. Trans. R. Soc. Lond. A Math. Phys. Eng. Sci.* 364, 1465–1481. doi: 10.1098/rsta.2006.1781

Sepulveda, N. G., Roth, B. J., and Wikswo, J. (1989). Current injection into a two-dimensional anisotropic bidomain. *Biophys. J.* 55, 987–999. doi: 10.1016/S0006-3495(89)82897-8

Shotwell, M. S., and Gray, R. A. (2016). Estimability analysis and optimal design in dynamic multi-scale models of cardiac electrophysiology. *J. Agric. Biol. Environ. Stat.* 21, 261–276. doi: 10.1007/s13253-016-0244-7

Smith, N., De Vecchi, A., McCormick, M., Nordsletten, D., Camara, O., Frangi, A. F., et al. (2011). euHeart: personalized and integrated cardiac care using patient-specific cardiovascular modelling. *Interface Focus* 1, 349–364. doi: 10.1098/rsfs.2010.0048

Smith, R. C. (2013). *Uncertainty Quantification: Theory, Implementation, and Applications*. Philadelphia, PA: SIAM.

Sobie, E. A. (2009). Parameter sensitivity analysis in electrophysiological models using multivariable regression. *Biophys. J.* 96, 1264–1274. doi: 10.1016/j.bpj.2008.10.056

Stewart, S. F., Paterson, E. G., Burgreen, G. W., Hariharan, P., Giarra, M., Reddy, V., et al. (2012). Assessment of CFD performance in simulations of an idealized medical device: results of FDA's first computational interlaboratory study. *Cardiovasc. Eng. Technol.* 3, 139–160. doi: 10.1007/s13239-012-0087-5

ten Tusscher, K. H., and Panfilov, A. V. (2006). Cell model for efficient simulation of wave propagation in human ventricular tissue under normal and pathological conditions. *Phys. Med. Biol.* 51, 6141–6156. doi: 10.1088/0031-9155/51/23/014

ten Tusscher, K. H., Mourad, A., Nash, M., Clayton, R. H., Bradley, C. P., Paterson, D. J., et al. (2009). Organization of ventricular fibrillation in the human heart: experiments and models. *Exp. Physiol.* 94, 553–562. doi: 10.1113/expphysiol.2008.044065

ten Tusscher, K. H., Noble, D., Noble, P. J., and Panfilov, A. V. (2004). A model for human ventricular tissue. *Am. J. Physiol. Heart Circ. Physiol.* 286, H1573–H1589. doi: 10.1152/ajpheart.00794.2003

Trayanova, N., Plank, G., and Rodríguez, B. (2006). What have we learned from mathematical models of defibrillation and postshock arrhythmogenesis? Application of bidomain simulations. *Heart Rhythm* 3, 1232. doi: 10.1016/j.hrthm.2006.04.015

Trayanova, N. A. (2011). Whole-heart modeling. *Circ. Res.* 108, 113–128. doi: 10.1161/CIRCRESAHA.110.223610

Trayanova, N. A., and Boyle, P. M. (2014). Advances in modeling ventricular arrhythmias: from mechanisms to the clinic. *Wiley Interdiscipl. Rev. Syst. Biol. Med.* 6, 209–224. doi: 10.1002/wsbm.1256

Tung, L. (1978). *A bi-Domain Model for Describing Ischemic Myocardial dc Potentials*. Massachusetts Institute of Technology.

Uzelac, I., Ji, Y.C., Hornung, D., Schröder-Scheteling, J., Luther, S., Gray, R. A., et al. (2017). Simultaneous quantification of spatially discordant alternans in voltage and intracellular calcium in langendorff-perfused rabbit hearts and inconsistencies with models of cardiac action potentials and Ca transients. *Front. Physiol.* 8:819. doi: 10.3389/fphys.2017.00819

Vetter, F. J., and McCulloch, A. D. (1998). Three-dimensional analysis of regional cardiac function: a model of rabbit ventricular anatomy. *Prog. Biophys. Mol. Biol.* 69, 157–183. doi: 10.1016/S0079-6107(98)00006-6

Viceconti, M. (2011). A tentative taxonomy for predictive models in relation to their falsifiability. *Phil. Trans. R. Soc. A* 369, 4149–4161. doi: 10.1098/rsta.2011.0227

Walter, E., and Pronzato, L. (1996). On the identifiability and distinguishability of nonlinear parametric models. *Math. Comput. Simul.* 42, 125–134. doi: 10.1016/0378-4754(95)00123-9

Wang, G. J., and Beaumont, J. (2004). Parameter Estimation of the Hodgkin–Huxley gating model: an inversion procedure. *SIAM J. Appl. Math.* 64, 1249–1267. doi: 10.1137/S0036139902419826

Wikswo, J. P., Lin, S.-F., and Abbas, R. A. (1995). Virtual electrodes in cardiac tissue: a common mechanism for anodal and cathodal stimulation. *Biophys. J.* 69, 2195–2210. doi: 10.1016/S0006-3495(95)80115-3

Wikswo, J. P., and Roth, B. J. (2009). "Virtual electrode theory of pacing," in *Cardiac Bioelectric Therapy,* eds I. R. Efimov, M. W. Kroll, and P. J. Tchou (Boston, MA: Springer), 283–330.

Wikswo, J. P., Wisialowski, T. A., Altemeier, W. A., Balser, J. R., Kopelman, H. A., and Roden, D. M. (1991). Virtual cathode effects during stimulation of cardiac muscle. Two-dimensional *in vivo* experiments. *Circulation Res.* 68, 513–530. doi: 10.1161/01.RES.68.2.513

Winslow, R. L., Trayanova, N., Geman, D., and Miller, M. I. (2012). Computational medicine: translating models to clinical care. *Sci. Transl. Med.* 4, 158rv111. doi: 10.1126/scitranslmed.3003528

Yang, P. C., Song, Y., Giles, W. R., Horvath, B., Chen-Izu, Y., Belardinelli, L., et al. (2015). A computational modelling approach combined with cellular electrophysiology data provides insights into the therapeutic benefit of targeting the late Na+ current. *J. Physiol.* 593, 1429–1442. doi: 10.1113/jphysiol.2014.279554

Zahid, S., Whyte, K. N., Schwarz, E. L., Blake, R. C., Boyle, P. M., Chrispin, J., et al. (2016). Feasibility of using patient-specific models and the "minimum cut" algorithm to predict optimal ablation targets for left atrial flutter. *Heart Rhythm* 13, 1687–1698. doi: 10.1016/j.hrthm.2016.04.009

Zemzemi, N., Bernabeu, M. O., Saiz, J., Cooper, J., Pathmanathan, P., Mirams, G. R., et al. (2013). Computational assessment of drug-induced effects on the electrocardiogram: from ion channel to body surface potentials. *Br. J. Pharmacol.* 168, 718–733. doi: 10.1111/j.1476-5381.2012.02200.x

Zhao, J., Butters, T. D., Zhang, H., Legrice, I. J., Sands, G. B., and Smaill, B. H. (2013). Image-based model of atrial anatomy and electrical activation: a computational platform for investigating atrial arrhythmia. *IEEE Trans. Med. Imaging* 32, 18–27. doi: 10.1109/TMI.2012.2227776

Conflict of Interest Statement: The authors declare that the research was conducted in the absence of any commercial or financial relationships that could be construed as a potential conflict of interest.

frontiers in Physics

ORIGINAL RESEARCH
published: 13 February 2018
doi: 10.3389/fphy.2018.00008

Initiation of Rotors by Fast Propagation Regions in Excitable Media: A Theoretical Study

Xiang Gao[1,2], *Alexei Krekhov*[1], *Vladimir Zykov*[1]* *and Eberhard Bodenschatz*[1,3,4,5]

[1] Max-Planck-Institute for Dynamics and Self-Organization, Göttingen, Germany, [2] School of Physics and Information Technology, Shaanxi Normal University, Xi'an, China, [3] German Center for Cardiovascular Research, Göttingen, Germany, [4] Institute for Nonlinear Dynamics, University of Göttingen, Göttingen, Germany, [5] Cornell University, Ithaca, NY, United States

We study the effect of geometry of a fast propagation region (FPR) in an excitable medium on the rotor initiation using a generic two-dimensional reaction-diffusion model. We find that, while the flat boundary of a rectangularly shaped FPR may block the propagation of the excitation wave, a large local curvature at the rounded corners of the FPR would prevent the blockage and thus initiate a rotor. Our simulations demonstrate that the prerequisites for the rotor initiation are the degree of the heterogeneity, its shape and size. These results may explain the incidence of arrhythmias by local heterogeneities induced, for example, by a cardiac tissue remodeling.

Keywords: excitable media, rotor initiation, arrhythmia, source-sink mismatch, fast propagation region

OPEN ACCESS

Edited by:
Simonetta Filippi,
Università Campus Bio-Medico, Italy

Reviewed by:
Alfonso Bueno-Orovio,
University of Oxford, United Kingdom
Winfried Mayr,
Medizinische Universität Wien, Austria

***Correspondence:**
Vladimir Zykov
vladimir.zykov@ds.mpg.de

Specialty section:
This article was submitted to Biomedical Physics, a section of the journal Frontiers in Physics

Received: *01 November 2017*
Accepted: *26 January 2018*
Published: *13 February 2018*

Citation:
Gao X, Krekhov A, Zykov V and Bodenschatz E (2018) Initiation of Rotors by Fast Propagation Regions in Excitable Media: A Theoretical Study. Front. Phys. 6:8. doi: 10.3389/fphy.2018.00008

1. INTRODUCTION

Rotors, also known as spiral waves, are observed in many systems, including the Belousov-Zhabotinsky chemical reactions [1–4], autocatalytic reactions of carbon monoxide on a platinum surface [5], aggregations of *Dictyostelium discoideum* amoebae [6], Xenopus oocytes [7], disinhibited mammalian neocortex [8], chicken retina [9], and especially cardiac tissue [10, 11]. Rotors, resulting in reentries in heart tissue, are known to cause cardiac arrhythmias and even sudden death [12–14]. To understand the mechanism of the rotor initiation and to eliminate the consequential malignant arrhythmias, the effects of the electrophysiological heterogeneity are thought to be one of the major causes and have attracted much attention [15–20].

Destabilization of wave fronts and the subsequent initiation of reentrant excitation can result from both intrinsic and dynamical heterogeneity. For example, a possible result of a multiple pacing of cardiac tissue is a dynamically induced heterogeneities of repolarization leading to a destabilization of a propagating wave and initiation of a self-sustained activity [21–25]. The heterogeneities of the electrical coupling and automaticity also might lead to the appearance of fragmented ectopic waves [26]. Furthermore, the boundary layer between the well-coupled and uncoupled cardiac tissues would create a rich set of phenomena associated with self-organized spiral waves and ectopic waves [27]. Transient rotors could be also initiated in complicated and rare situations [28, 29]. An abrupt transition of the coupling gradient would block the wave propagation, but nearby parts with a smooth transition would not and therefore cause a reentry. The wave blockage was also found in a model of human ventricular tissue due to an abrupt transition of the anisotropic coupling [30].

As exemplary mentioned above, there are many situations, which can lead to the initiation of a self-sustained excitation wave. One novel scenario, which was found recently in a generic model for the excitable system, is that a region with the fast propagation of an excitation wave might cause

a unidirectional block of the wave propagation [31]. This unidirectional block is realized based on a phenomenon termed source-sink mismatch in the cardiology literature [32]. The further study demonstrated that rotors could be nucleated in the presence of a localized fast propagation region (FPR) after application of one stimulus only [33]. It was shown also that various geometrical factors play an important role in rotor initiation [34].

Here we show that in the two-dimensional medium the flat boundary of a rectangularly shaped FPR may block the propagation of the outside excitation wave. However, a large local curvature at the rounded corner of the FPR would prevent the blockage and thus let the outside excitation penetrate into the FPR causing a rotor initiation. We demonstrate that the rotor initiation critically depends on the size of the FPR and the degree of the heterogeneity. If the FPR size is below a certain threshold, the initiated rotor would vanish eventually when it approaches the medium's boundary. The critical size of the FPR depends on the degree of the heterogeneity.

2. MODEL AND METHOD

Although some aspects of the complex electrical activity in the cardiac tissue need to be studied using the reaction-diffusion equations with the detailed ionic channel model, many general spatiotemporal features of cardiac dynamics can be reproduced by a relatively simple but universal two-component system as follows

$$\frac{\partial u}{\partial t} = \nabla \cdot (D\nabla u) - AF(u,v), \tag{1}$$

$$\frac{\partial v}{\partial t} = \epsilon G(u,v), \tag{2}$$

where u and v are the activator and inhibitor, respectively. The local kinetics of u and v are specified by the nonlinear functions $F(u,v)$ and $G(u,v)$. Let us consider a widely-used computationally-efficient model proposed by Barkley [35]. In this generic model, the two nonlinear functions read as

$$F(u,v) = u(u-1)\left(u - \frac{v+b}{a}\right), \tag{3}$$

$$G(u,v) = \begin{cases} (u-v) & u \geq v, \\ k_\epsilon(u-v) & u < v. \end{cases} \tag{4}$$

To simulate a relatively quick recovery of the excitability after a pulse generation, the original Barkley model is slightly modified by introducing an additional parameter $k_\epsilon > 1$.

The propagation wave velocity in the Barkley model is proportional to $\sqrt{DA}$. Spatial heterogeneity of the parameters D and A can result in creation of FPR capable to initiate spiral waves [33, 34].

Below a FPR is considered to be a rounded rectangular region of the length L with two rounded corners of the radius R, as illustrated in **Figure 1A**. Inside this region, the values of D and/or A are larger than outside. It is inserted into a square shaped medium of size 450×450 in space unit, and the no-flux boundary conditions at the boundaries are implied. The parameters $a = 1$, $b = 0.44$, $\epsilon = 0.00011$ and $k_\epsilon = 10$ are fixed in our simulations. We use the explicit finite difference method in the Cartesian coordinates. The staircase approximation is used at the rounded corner. The spatial step $dx = 0.3$, and the time step $dt = 0.01$, when $R \geq 15$. The finer spatial and time steps are used for smaller R. For instance, $dx = 0.2$ and $dt = 4.44 \times 10^{-3}$, when $R = 10$, and $dx = 0.1$ and $dt = 1.11 \times 10^{-3}$, when $R = 5$.

The variables u and v in Equations (1)-(4) are vary within the range $0 < u < 1$ and $0 < v < a - 2b$. The spatiotemporal dynamics of u and v is represented in **Figures 1–4**, **6**, **7** by color-coded distribution of the excitation phase ϕ, where $-\pi < \phi < \pi$. The phase is defined as $\phi = \alpha + 3\pi/4$, in which an angle α is determined by the direction of the vector with components $(u - 1/2)$ and $(v - a/2 + b)/(a - 2b)$ on the (u, v) phase plane. According to this definition, $\phi = 0$ corresponds to the resting state of the medium (green areas in **Figures 1–4**, **6**, **7**), narrow yellow (dark blue) regions represent the wave front (wave back), and red areas correspond to a wave plateau, whereas blue ones represent the refractory regions.

3. RESULTS

3.1. Rotor Initiated from a Rectangularly Shaped FPR

To illustrate the phenomenon of the rotor initiation from a rounded rectangular heterogeneous region, we set $L = 300$, $R = 15$, as shown in **Figure 1**. Inside this region $D = 1$ and $A = 2$, while outside $D = 1$ and $A = 1$. Due to an increased value of A, this rounded rectangular region could be considered as a FPR since the propagation velocity inside it is larger than outside. For such parameter choice, the flat boundary of the FPR would unidirectionally block a plane wave propagating through the medium outside FPR. However, the local curvature at the rounded corner of the FPR $1/R \approx 0.067$ is large enough to prevent the blockage and let the excitation penetrate into the FPR. Then, a phase change point (PCP) emerges, and a self-sustained rotor is initiated. The process is similar to the scenario described in Zykov et al. [33, 34].

However, if the local curvature at the rounded corner of the FPR is below some critical value, as illustrated in **Figure 2**, there would be no penetration into the FPR at the corner. Thus, the FPR would act for propagating waves as an obstacle. The transient rotor starts to circulate around the FPR and vanishes eventually when it approaches the medium boundary. The critical value of the corner curvature depends on D and A within the FPR.

Another scenario appears when the values of D and/or A within the FPR are below some critical values. As illustrated in **Figure 3**, in this case, the flat boundary of the FPR would not block the propagating wave. The plane wave would become curved, propagates through the FPR, and vanishes eventually

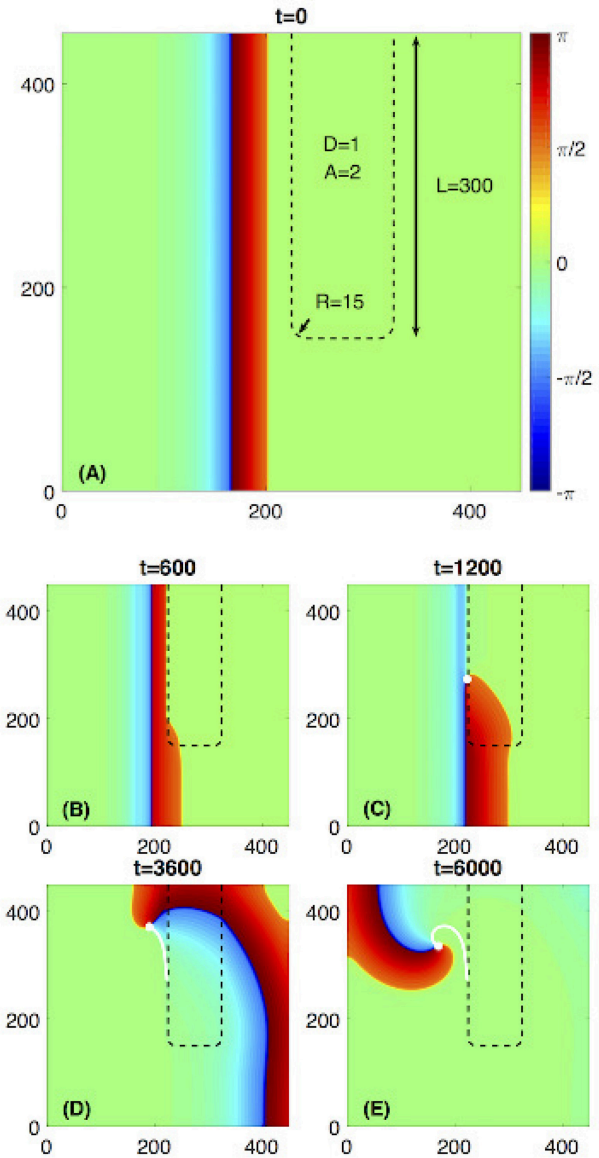

FIGURE 1 | Rotor initiated due to a rectangularly shaped fast propagation region (FPR). **(A)** The FPR marked by a black dashed line has length $L = 300$ and two rounded corners with the radius of $R = 15$. Within the FPR $D = 1$, $A = 2$ and outside the FPR $D = 1$ and $A = 1$. A plane wave propagates from the left toward the FPR. **(B)** The wave is blocked at the flat boundary of the FPR but penetrates into it at the rounded corner. **(C–E)** A rotor is initiated and stably rotates. The white dot and line are the rotors phase change point (PCP) and its trajectory, respectively.

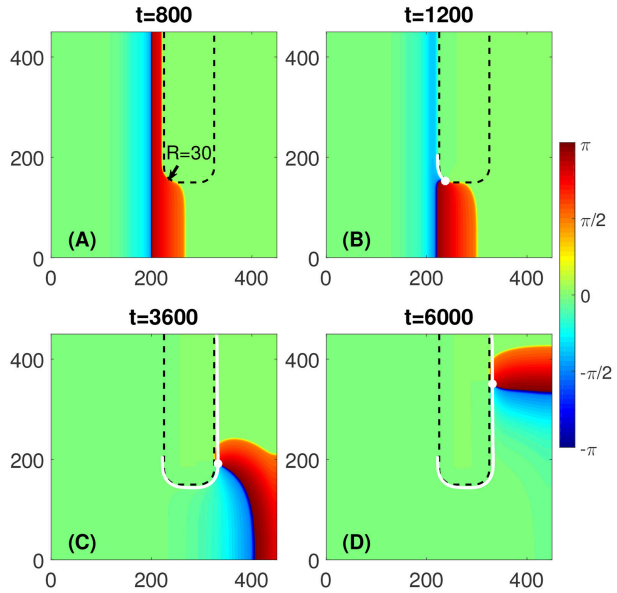

FIGURE 2 | No wave penetration occurs at the rounded corner of a FPR if R is above some critical value. **(A)** No penetration is observed at the corner of radius $R = 30$, as an example. **(B–D)** The PCP (white dot) would travel along the FPR boundary and vanishes eventually, as shown by its trajectory (white line). Other parameters are the same as in **Figure 1**.

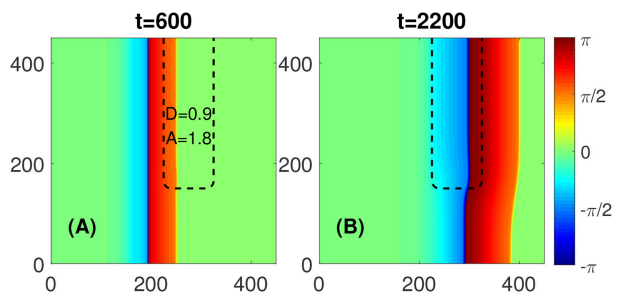

FIGURE 3 | No blockage occurs at the flat boundary of a FPR if D and/or A inside it are below some critical values. **(A)** No PCP would emerge for $D = 0.9$ and $A = 1.8$, as an example. **(B)** A slightly deformed plane wave propagates through the FPR and disappears at the right boundary of the medium. Other parameters are the same as in **Figure 1**.

when it reaches the medium's boundary. No self-sustained rotors are initiated.

3.2. Critical Length of a Rectangularly Shaped FPR

For a given D and A within the FPR, its length L is also a critical parameter to initiate a self-sustained rotor. If L is shorter than a certain critical length, as illustrated in **Figure 4**, the PCP would approach the medium boundary and vanishes eventually. After the PCP has disappeared, a curved wave propagates through the medium and vanishes at its boundary. Thus, no rotors are initiated.

We investigate in detail the critical length of the FPR needed to initiate a self-sustained rotor and determine the boundaries of the non-penetration and non-blockage regions for various A and D, as shown in **Figure 5**. Here the radius of the rounded corner is fixed as $R = 15$. As shown in **Figure 5A**, the non-penetration occurs when D and/or A are above some critical values, and the non-blockage occurs when D and/or A are below other critical values. Between these two boundaries, the initiation of a self-sustained rotor is possible with the color-coded critical length L_c

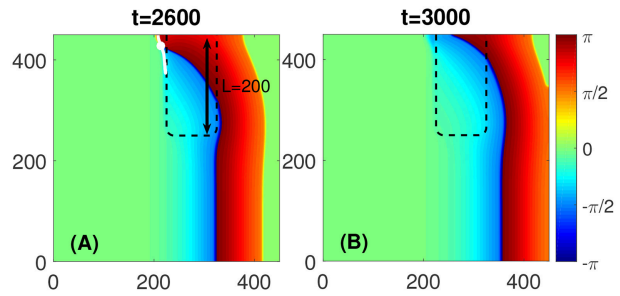

FIGURE 4 | No stably rotating rotor appears if L is shorter than a critical length. **(A)** Although a PCP would be initiated like in the case shown in **Figures 1A–C**, the PCP (white dot) would be too close to the medium boundary and vanishes eventually, as shown by its trajectory (white line). **(B)** After the PCP vanishing the curved wave would propagate to the right boundary of the medium, and no stably rotating rotor would exist. The FPR length $L = 200$ and other parameters are the same as in **Figure 1**.

of the rounded rectangular FPR. The larger D and/or A are, the shorter L_c would be.

This dependence of L_c on D and A is further confirmed in **Figures 5B,C**, where we show how L_c shrinks as D or A increases for different corner radius R. **Figures 5B,C** also demonstrate how L_c changes as R increases.

We also investigate the impact of the width of the rectangular FPR. The simulation results show that the FPR width has no significant effect on the rotor initiation if it is larger than $2R$.

4. ANALYSIS

To analyze the conditions for the rotor initiation by a rounded rectangular FPR, we simplify the two-component reaction-diffusion equations by taking $\epsilon = 0$ and setting $v = 0$. In this limiting case, the initial Equations (1)–(4) can be reduced to

$$\frac{\partial u}{\partial t} = \nabla \cdot (D\nabla u) - Au(u-1)\left(u - \frac{b}{a}\right). \tag{5}$$

This equation describes a bistable extended system, where the resting state $u = 0$, the excited state $u = 1$, and the unstable steady state $u = b/a$ exist. The value $\beta = b/a$ is the excitation threshold. The bistable equation has been widely used to analyze the propagation of the wave front when $\epsilon \ll 1$ [36]. It is also useful to establish fundamental mechanism behind the blockage and penetration at the FPR boundary.

4.1. Analysis of the Non-blockage and Non-penetration Boundary

To analyze the conditions for the blockage of the initial plane wave at the flat boundary of the FPR, we could further simplify Equation (5) to consider a stationary wave profile for a one-dimensional bistable system as follows

$$\frac{d}{dx}\left(D(x)\frac{du}{dx}\right) - A(x)u(u-1)(u-\beta) = 0, \tag{6}$$

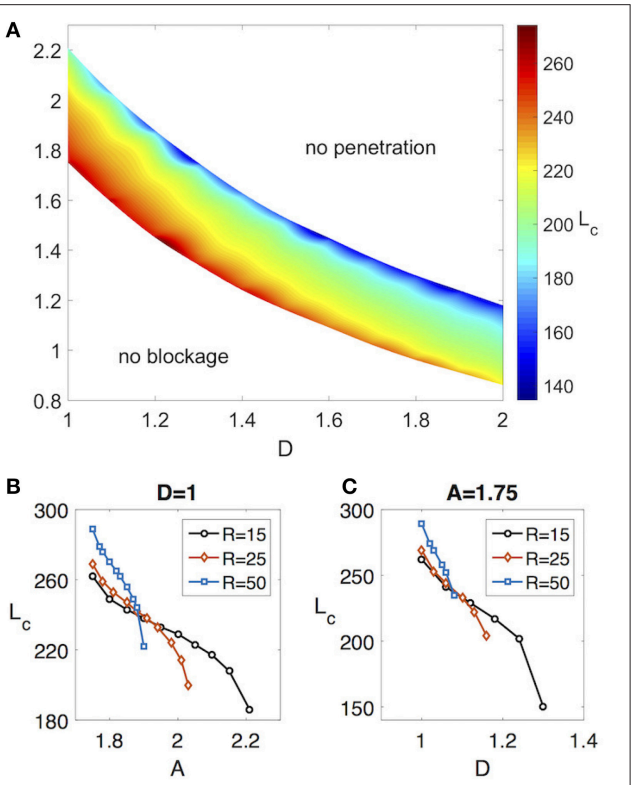

FIGURE 5 | (A) The phase diagram shows the regions of non-penetration, non-blockage, and rotor initiation due to the FPR with critical length L_c for different values of D and A but fixed $R = 15$. **(B)** The detailed dependence of L_c on A for fixed $D = 1$ and different R. **(C)** The detailed dependence of L_c on D for fixed $A = 2$ and different R.

where $A(x) = 1, D(x) = 1$ for $x \leq 0$ and $A(x) = A, D(x) = D$ for $x > 0$. The boundary conditions and the continuity conditions at $x = 0$ read as

$$u|_{x=-\infty} = 1,\ u|_{x=\infty} = 0,$$
$$\left.\frac{du}{dx}\right|_{x=-\infty} = \left.\frac{du}{dx}\right|_{x=\infty} = 0, \tag{7}$$
$$\left.\frac{du}{dx}\right|_{x=-0} = D\left.\frac{du}{dx}\right|_{x=+0}. \tag{8}$$

Multiplying Equation (6) by du/dx, integrating over x from $-\infty$ to 0 and from 0 to ∞, using Equations (7) and (8), we obtain the following equation

$$\int_1^{u(0)} u(u-1)(u-\beta)du = DA\int_0^{u(0)} u(u-1)(u-\beta)du, \tag{9}$$

which determines the value of $u(0)$ at the point of the parameter jump as a function of the product DA. Note that the front could be stopped only if $u(0) < \beta$. Thus, the Equation (9) for $u(0) = \beta$ gives the critical value of the product DA, above which the propagation blockage could be observed. Therefore, the non-blockage boundary in the phase diagram has an analytical form

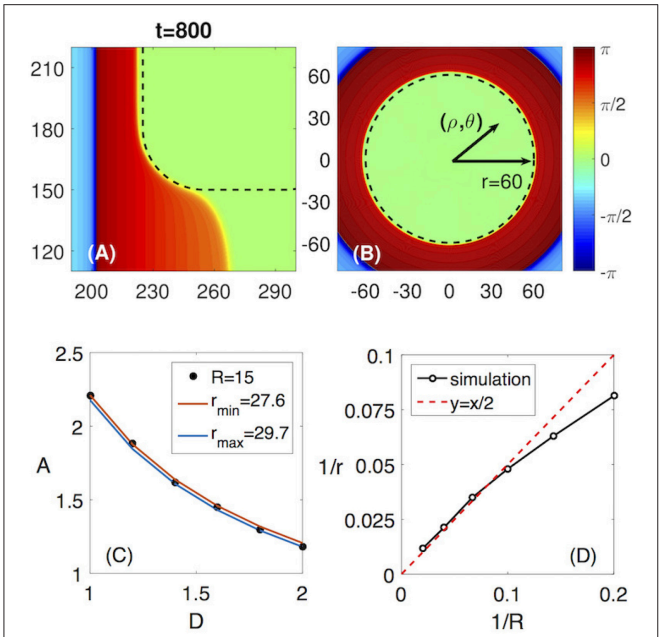

FIGURE 6 | Analogy between the non-penetration at the corner of a rectangularly shaped FPR and the non-penetration of a circular wave into a circular shaped FPR. **(A)** The non-penetration at the rounded corner of the FPR (zoomed from **Figure 2A**). **(B)** A circular wave blocked by the circular shaped FPR of the radius $r = 60$. **(C)** The non-penetration boundaries for the rectangularly shaped FPR for $R = 15$ (black dots) and for the circular wave and the circular shaped FPR with the radii $r_{min} = 27.6$ (red line) and $r_{max} = 29.7$ (blue line). **(D)** The dependence of $1/r = 1/(2R)$ is proofed to be valid for a large range of R.

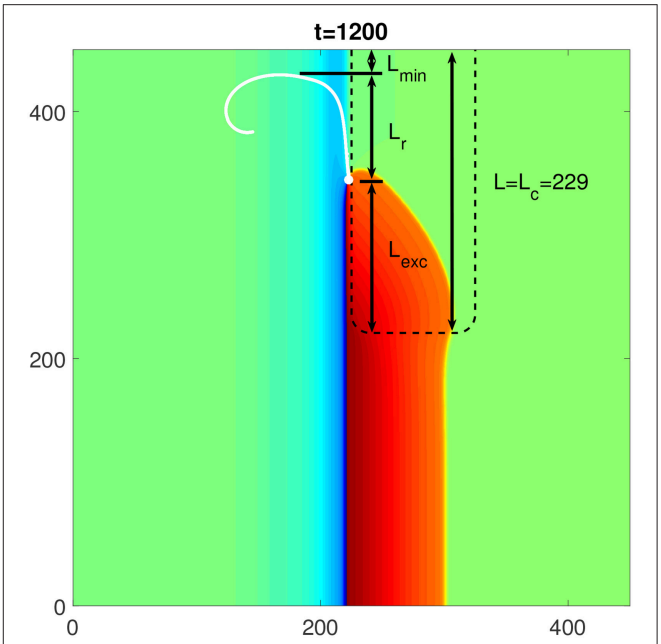

FIGURE 7 | The composition of the critical length L_c of a rectangularly shaped FPR to initiate a rotor. The white dot and line are the initial location and the following trajectory of the PCP, respectively. Three components of L_c are: L_{min} which describes the minimum distance of a persistent PCP from the top medium boundary, L_r which describes the vertical range of the PCP trajectory in the medium outside the FPR, and L_{exc} which describes the propagation of the penetrated excitation within the FPR. The FPR length $L = L_c = 229$ and other parameters are the same as in **Figure 1**.

as follows

$$DA < \frac{(1-\beta^2)(1-\beta)^2}{\beta^3(2-\beta)}. \tag{10}$$

This expression represents a modification of another one mentioned already in Zykov et al. [33, 34]. It looks more simple because of the normalized values of the parameters $A = 1$ and $D = 1$ in the part of the medium outside an FPR. This normalization performed by rescaling of time and space variables in Equation (5) is made without loss of generality. It is worth to note also that this expression generalizes a similar analysis for the case of a steep rise of the parameter D under constant value of A performed earlier in Pauwelussen [37] and Mornev [38].

It is important to stress that the obtained analytical expression (10) gives a very precise estimate of the non-blockage boundary obtained by numerical computations illustrated by **Figure 5A**. The deviations do not exceed one percent.

To analyze the conditions to prevent wave penetration at the rounded corner of the FPR, we look in detail into the process of the (non-)penetration, as illustrated in **Figure 6A**. The initial plane wave would become curved at the rounded corner of the FPR. It is analogous to a circular wave penetrating into a circular FPR with a radius r, as shown in **Figure 6B**.

To verify the analogy, we compare the non-penetration boundaries for the rounded rectangular FPR with the circular FPR in a $A - D$ diagram. As shown in **Figure 6C**, the non-penetration boundary for the rectangularly shaped FPR with the corner radius of R is located between two curves corresponding to non-penetration boundaries for the circular FPR with the radius r_{min} and r_{max}, as shown in **Figure 6C**. Note, that in a vicinity of the rounded corner the boundary curvature jumps from zero to $1/R$. Hence, it is natural to assume that the non-penetration boundaries for the circular FPR with the curvature about an averaged curvature of the rounded corner, $1/r \approx 1/(2R)$, will approximate the non-penetration boundary for the rounded rectangular FPR. This approximation is working well for $10 \leq R \leq 50$, as demonstrated in **Figure 6D**.

Therefore, we can use the results of the simulations for the circular FPR and the radius relation $r \approx 2R$ to approximate the non-penetration boundary for the rounded rectangular FPR. Since the circular FPR in the polar coordinates (ρ, θ) has a rotational symmetry, this allows us to transform the two-dimensional Equations (1) and (2) to the one-dimensional ones as follows

$$\frac{\partial u}{\partial t} = \frac{1}{\rho}\frac{\partial}{\partial \rho}\left(D(\rho)\rho\frac{\partial u}{\partial \rho}\right) - A(\rho)F(u,v), \tag{11}$$

$$\frac{\partial v}{\partial t} = \epsilon G(u,v). \tag{12}$$

This one-dimensional equations considerably simplifies the analysis. The corresponding computations have been performed by use of the explicit finite difference method with the spatial step $d\rho = 0.3$ and the time step $dt = 0.005$. In order to simulate a circular wave approaching a circular shaped FPR, a part of the medium with $\rho > \rho_{ext}$ is assumed to be in the excited state at $t = 0$, as illustrated in **Figure 6B**.

4.2. Analysis of the Critical Length L_c of a Rounded Rectangular FPR

To understand the mechanism behind the dependence of L_c on the characteristics of the FPR, i.e., D, A and R, we separate L_c into three parts, as shown in **Figure 7**. The first part is the distance from the rounded corner of the FPR, where the penetration of the excitation starts, to the position where the PCP emerges for the first time. This part, named L_{exc}, should be determined by the characteristics of the FPR since it describes the propagation of the excitation inside the FPR. The second part is the distance from the initial position of the PCP to the highest position in its trajectory. This part, named L_r, describes the range of the PCP trajectory along the FPR but located outside the FPR. This trajectory part should be practically independent of the FPR characteristics. The third part is the distance from the highest PCP position in its trajectory to the top medium boundary. This part, named L_{min}, should be above some minimum distance toward the top medium's boundary. Otherwise, the PCP would be too close to the boundary and vanishes eventually. The value of L_{min} should only depend on the given characteristics of the medium outside the FPR, and thus is fixed in our simulations. Therefore, the value of L_c is the sum of L_{min} and L_r, which are fixed, and L_{exc}, which is determined by D and A inside the FPR, and R at the FPR corner.

Hence, L_{exc} is the only part which is varied and depends on D, A, and R. Its value may read as

$$L_{exc} = \int_{t_p}^{t_r} c_v dt, \tag{13}$$

where t_p is the time when the penetration of the excitation at the rounded corner of the FPR starts, t_r is the time when the PCP initially emerges, and c_v is the propagation velocity of the excitation along the flat border of the FPR. As shown in **Figure 8**, t_r remains constant for different sets of D, A, and R, while t_p varies. The velocity c_v changes with time and also depends on D, A, and R.

Based on these results, three conclusions can be made. First, larger D, A, or R would delay t_p. Second, t_r is nearly the same in all cases since it is determined by the time when the wave back of the plane wave reaches the left flat boundary of the FPR. Therefore, it is determined by the fixed characteristics of the medium outside the FPR. Third, for the most part of the trajectory, c_v is larger than the plane wave velocity c_p in a homogeneous medium where the parameters D and A are the same as inside the FPR, as shown in the subfigure of **Figure 8**. Obviously, c_v is accelerated since the value of the activator $u > 0$ in the vicinity of the left flat boundary of the FPR due to a diffusive influence of the blocked plane wave. Such

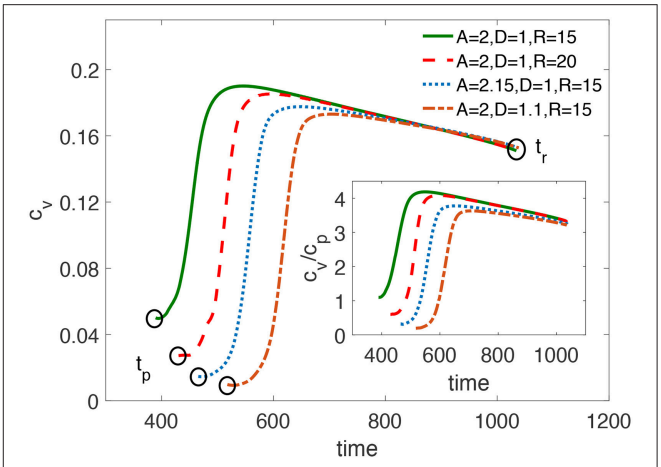

FIGURE 8 | The propagation speed c_v of the penetrated excitation along the vertical flat boundary of a FPR over time. t_p is the time when the penetration at the FPR corner starts. t_r is the time when the PCP initially emerges. Larger D, A, or R lead to a delayed t_p, but nearly the same t_r. The subfigure shows the change of the ratio between c_v and c_p over time, where c_p is the plane wave velocity for the medium's parameters established inside the FPR.

increase of the propagation velocity is a general effect in bistable models of one-dimensional excitable media if ahead of the wave front the activator value exceeds the resting state [39]. In the context of a flame propagation, which also can be described by Equation (6), this phenomenon is named as preheating effect [40].

4.2.1. Mechanism of Delay of t_p

The delay of t_p occurs at the rounded corner of a FPR. As shown above, the penetration of the plane wave into the rounded corner with the radius of R is analogous to the penetration of a circular wave into a circular FPR with the radius $r \approx 2R$. Thus, considering the analogy and just focusing on the propagation of the excitation wave front, we could use the bistable version of Equations (11) and (12) to investigate the variation of u at the rounded FPR corner with time. The bistable equation for the circular FPR expressed in the polar coordinates (ρ, θ) reads as

$$\frac{\partial u}{\partial t} = \frac{1}{\rho}\frac{\partial}{\partial \rho}\left(D(\rho)\rho\frac{\partial u}{\partial \rho}\right) - A(\rho)u(u-1)(u-\beta). \tag{14}$$

Using the finite difference method with space step $\Delta\rho$, at the circular FPR boundary $r = 2R$, Equation (14) could be expanded as

$$\begin{aligned}\frac{\partial u|_r}{\partial t} = \frac{1}{r\Delta\rho^2}\big[& D|_{r+\Delta\rho/2}\,(r+\Delta\rho/2)\,\big(u|_{r+\Delta\rho} - u|_r\big) \\ & - D|_{r-\Delta\rho/2}\,(r-\Delta\rho/2)\,\big(u|_r - u|_{r-\Delta\rho}\big)\big] \\ & - A|_r\,u|_r\,(u|_r - 1)\,(u|_r - \beta)\,,\end{aligned} \tag{15}$$

where

$$D|_{r+\Delta\rho/2} = \frac{1}{2}\left(D|_{r+\Delta\rho} + D|_r\right) = \frac{1}{2}(1+D),$$
$$D|_{r-\Delta\rho/2} = \frac{1}{2}\left(D|_r + D|_{r-\Delta\rho}\right) = \frac{1}{2}(D+D) = D,$$
$$A|_r = A.$$

When the circular wave reaches the circular FPR boundary at r, we have $u|_{r-\Delta\rho} < u|_r < u|_{r+\Delta\rho}$, and $u|_r$ is still smaller than the excitation threshold β. Thus, $u|_r(u|_r - 1)(u|_r - \beta) > 0$. Then we can divide the right hand side of Equation (15) into two terms. The term which would cause an increase of $u|_r$ with time is named as the source term. It reads as

$$\frac{1}{\Delta\rho^2}\frac{1+D}{2}\left(1+\frac{\Delta\rho}{2r}\right)\left(u|_{r+\Delta\rho} - u|_r\right). \tag{16}$$

The other term which would cause a decrease of $u|_r$ with time is named the sink term. It reads as

$$-\frac{1}{\Delta\rho^2}D\left(1-\frac{\Delta\rho}{2r}\right)\left(u|_r - u|_{r-\Delta\rho}\right)$$
$$-A\,u|_r\left(u|_r - 1\right)\left(u|_r - \beta\right). \tag{17}$$

From the above expressions of two terms, we find that larger D would enhance the source term (Equation 16) but enhances the sink term (Equation 17) even more. Larger A would not affect the source term but enhance the sink term. Larger r, i.e., $2R$ in the analogy, would reduce the source term, but enhance the sink term.

Therefore, the conclusion is that the larger D, A and R are, the stronger the sink term would be, and the later $u|_r$ reaches the excitation threshold. This is the cause of the delay of the start time of the excitation penetration near the corner of the rounded rectangular FPR, i.e., t_p in Equation (13).

As shown in **Figure 9**, the numerical simulation results prove our explanation of the delay effect by plotting the value of u at the corner of the rounded rectangular FPR with time.

4.2.2. Influence of "Preheating" on c_v

Inside the rounded rectangular FPR, the accelerating effect on the propagation velocity c_v occurs near its vertical flat boundary. When the initial plane wave is blocked at the flat boundary, although it does not penetrate inside the FPR, it yet increases the value of u in a vicinity of the FPR boundary. This is quite similar to a preheating effect in the flame propagation when the fuel temperature ahead of the flame front is increased [39, 40]. This "preheated" medium would accelerate the propagation velocity c_v of the excitation wave front along the vertical flat boundary of the FPR.

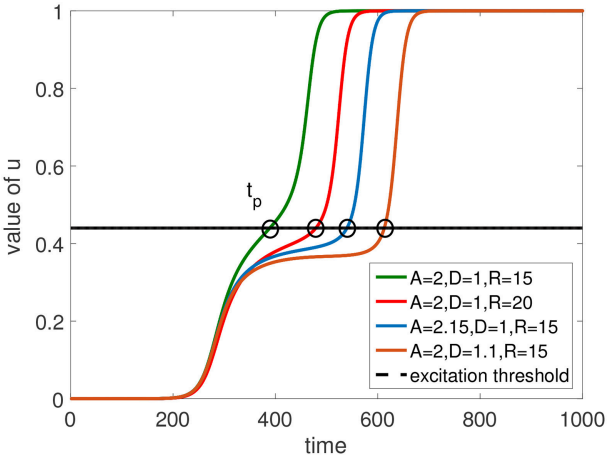

FIGURE 9 | Temporal dynamics of the value of u at the junction point between the flat boundary and the corner of a rectangularly shaped FPR. An increase of D, A, or R inside the FPR delays the time t_p when the excitation threshold is reached.

The mechanism of the accelerated wave front could be analytically understood from Equation (5) for the bistable distributed system. If a preheated part of the FPR near its flat boundary is assumed as a nearly one-dimensional medium, we can establish a comoving frame as $z = x + ct$, where c is the propagation velocity of the wave front. Thus, Equation (5) would be simplified as

$$Du_{zz} - cu_z - Au(u-1)(u-\beta) = 0. \tag{18}$$

The preheating effect increases the value of u to some preheated state u_p, and makes the excitation start from $u_p > 0$ instead of the resting state $u = 0$. Based on the theory described in Keener and Sneyd [36], the propagation velocity of the excitation wave front could be expressed as

$$c(u_p) = \frac{\int_{u_p}^{1} Au(1-u)(u-\beta)du}{\int_{-\infty}^{\infty} u_z^2 dz} = \frac{\int_{u_p}^{\beta} Au(1-u)(u-\beta)du + \int_{\beta}^{1} Au(1-u)(u-\beta)du}{\int_{-\infty}^{\infty} u_z^2 dz}. \tag{19}$$

The analytical expressions of Equation (19) would be obtained for two limiting cases. The first one is the unpreheated case at which u_p is equal to the resting state. That gives

$$c(0) = \sqrt{DA/2}(1-2\beta). \tag{20}$$

The second is the fully preheated case at which u_p is equal to the excitation threshold β. This gives

$$c(\beta) = \sqrt{DA/2}(1+\beta). \tag{21}$$

The above two analytical expressions apparently demonstrate that $c(\beta) > c(0)$, since $\beta > 0$.

We also investigate the preheated propagation velocity in the numerical simulations of Equation (5). As shown in **Figure 10**, the numerical results elucidate the acceleration of the propagation velocity $c(u_p)$ as a function of the preheated state

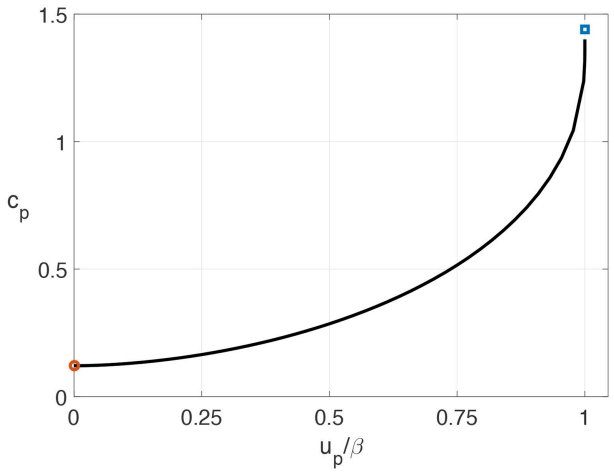

FIGURE 10 | The propagation speed c_p corresponding to the preheated state $u = u_p$. The values of $D = 1$ and $A = 2$ are taken as an example. The solid line represents the numerical simulation results in a one-dimensional medium described by Equation (5). The value of u ahead of the wave front is set to be u_p. The open circle and square are the analytic results from Equations (20) and (21) at the limiting cases of $u_p = 0$ and $u_p = \beta$, i.e., the resting state and the excitation threshold, respectively.

u_p. The analytical results from Equations (20) and (21) perfectly describe both limiting cases following from these numerical data.

5. CONCLUSIONS AND APPLICATIONS

Our results demonstrate that a self-sustained rotor could be initiated from the spatial heterogeneity, i.e., a rectangularly shaped FPR. We use a generic model to parameterize the heterogeneity with three parameters D, A, and R. In the $D - A$ diagram at a given R, the region of the rotor initiation is located between the non-blockage and non-penetration regions. The two boundaries of the rotor initiation region could be estimated by the analytical equation for the bistable distributed system and the simulations in a one-dimensional medium for a circular FPR, respectively. We also show that to initiate the self-sustained rotor the length of the rounded rectangular FPR should be larger than the critical L_c. The critical value L_c depends on the parameters D and A, within the FPR, as well as on the radius R of a rounded corner.

Our findings in the generic model might be applicable to describe the electrophysiological dynamics of cardiac tissue. Indeed, the distribution of transmembrane potential V in a two-dimensional tissue could be described by the reaction-diffusion equation as follows [41]

$$\frac{\partial V}{\partial t} = \frac{1}{\chi C_m}\nabla\,(\boldsymbol{\sigma}\cdot\nabla V) - \frac{I_{ion}(V,\vec{h})}{C_m}, \tag{22}$$

$$\frac{\partial \vec{h}}{\partial t} = g(V,\vec{h}), \tag{23}$$

where χ is the surface-to-volume ratio of the cardiac cells, C_m is the membrane capacitance, $\boldsymbol{\sigma}$ is the tensor of electric conductivity, and I_{ion} is the sum of ion channel currents. Intensity of each separate current is determined by corresponding component of the vector $\vec{h}$. Equations (22) and (23) can be generalized into a two-component reaction-diffusion system as follows

$$\frac{\partial V}{\partial t} = \nabla\,(D\cdot\nabla V) - \frac{I_{ion}(V,h)}{C_m}, \tag{24}$$

$$\frac{\partial h}{\partial t} = g(V,h), \tag{25}$$

where the effective diffusion coefficient tensor $D = \sigma/\chi C_m$ and the description of the ion currents is reduced to a scalar value h. In an isotropic tissue, we can simplify the tensors σ and thus D to be scalars. Thus, the reduced system which describes electrophysiological properties of the cardiac tissue looks similar to the reaction-diffusion model we use.

Nowadays many detailed models of human atria incorporate both structural and electrophysiological heterogeneities leading to differences in conduction velocity between the neighboring regions [42–44]. It is also well known that atrial fibrosis in the aging heart can result in spatial variations in the electrical conductivity of a part of the cardiac muscle [45]. If some regions within this part remain unchanged, they can resemble fast propagation regions introduced in our model. Note, that a similar nonhomogeneity in the electrical conductivity can appear, for instance, when fresh stem cells aggregates implanted in strongly remodeled cardiac tissue form gap junctions with adult cardiac myocytes [46]. Moreover, some cardiac diseases cause ion channel remodeling [47]. This remodeling can be represented as a variation of the term I_{ion} in Equation (22). This is to some extent equivalent to a variation of the parameter A in our model. If this remodeling occurs non-uniformly in space, one can expect the creation of some spots with a negligible variation of this parameter in comparison to its strong decrease in the surrounding regions. Thus, nonhomogeneous remodeling can results in a creation of fast propagation regions considered in this study.

Of course, the model used above is aimed to reproduce only most generic features of electrical activity in myocardial tissue. Investigation of specific dynamical features can be done by application of more detailed models widely used in the literature [48–50]. It is important to note that our recent results based on the Fenton-Karma model [48] indicate that all scenarios of rotor initiation obtained with the Barkley model are perfectly reproducible [33]. An obvious reason for this is that the restitution of action potential duration in detail reproduced in the Fenton-Karma model plays only a restricted role in the described scenarios, where spiral waves are generated after application of a single excitation stimulus. Of course, the following dynamics of the initiated rotors is strongly influenced by many other factors and specific features of cardiac tissue, which are not reproduced in the framework of the generic model used in the study.

Therefore, computer simulations of a real tissue in the framework of much more detailed models and most importantly

experimental investigations definitely can help to verify the role of the observed scenario for generation of cardiac arrhythmias.

AUTHOR CONTRIBUTIONS

All authors conceived of the presented idea. XG, AK, VZ performed the computations. All authors discussed the results and contributed to the final manuscript.

FUNDING

This work was supported by the National Natural Science Foundation of China under Grants No. 11447026 and No. 11705114, the Max Planck Society, the German Center for Cardiovascular Research (DZHK), and Grant DFG-SFB937 Collective Behavior of Soft and Biological Matter.

REFERENCES

1. Winfree AT. Spiral waves of chemical activity. *Science* (1972) **175**:634–6. doi: 10.1126/science.175.4022.634
2. Agladze KI, Krinsky VI. Multi-armed vortices in an active-chemical medium. *Nature* (1982) **296**:424–6. doi: 10.1038/296424a0
3. Ouyang Q, Flesselles JM. Transition from spirals to defect turbulence driven by a convective instability. *Nature* (1996) **379**:143–6. doi: 10.1038/379143a0
4. Vanag VK, Epstein IR. Inwardly rotating spiral waves in a reaction-diffusion system. *Science* (2001) **294**:835–7. doi: 10.1126/science.1064167
5. Jakubith S, Rotermund HH, Engel W, Vonoertzen A, Ertl G. Spatiotemporal concentration patterns in a surface-reaction - propagating and standing waves, rotating spirals, and turbulence. *Phys Rev Lett.* (1990) **65**:3013–6. doi: 10.1103/PhysRevLett.65.3013
6. Sawai S, Thomason PA, Cox EC. An autoregulatory circuit for long-range self-organization in Dictyostelium cell populations. *Nature* (2005) **433**:323–6. doi: 10.1038/nature03228
7. Lechleiter J, Girard S, Peralta E, Clapham D. Spiral calcium wave-propagation and annihilation in xenopus-laevis oocytes. *Science* (1991) **252**:123–6. doi: 10.1126/science.2011747
8. Huang XY, Troy WC, Yang Q, Ma HT, Laing CR, Schiff SJ, et al. Spiral waves in disinhibited mammalian neocortex. *J Neurosci.* (2004) **24**:9897–902. doi: 10.1523/JNEUROSCI.2705-04.2004
9. Yu Y, Santos LM, Mattiace LA, Costa ML, Ferreira LC, Benabou K, et al. Reentrant spiral waves of spreading depression cause macular degeneration in hypoglycemic chicken retina. *Proc Natl Acad Sci USA* (2012) **109**:2585–9. doi: 10.1073/pnas.1121111109
10. Davidenko JM, Pertsov AV, Salomonsz R, Baxter W, Jalife J. Stationary and drifting spiral waves of excitation in isolated cardiac-muscle. *Nature* (1992) **355**:349–51. doi: 10.1038/355349a0
11. Gray RA, Pertsov AM, Jalife J. Spatial and temporal organization during cardiac fibrillation. *Nature* (1998) **392**:75–8.
12. Carmelite E, Vereecke J. *Cardiac Cellular Electrophysiology*. New York, NY: Springer (2002).
13. Jalife J. Ventricular fibrillation: mechanisms of initiation and maintenance. *Annu Rev Physiol.* (2000) **62**:25–50. doi: 10.1146/annurev.physiol.62.1.25
14. Karma A. Physics of cardiac arrhythmogenesis. *Annu Rev Condens Matt Phys.* (2013) **4**:313–37. doi: 10.1146/annurev-conmatphys-020911-125112
15. Luther S, Fenton FH, Kornreich BG, Squires A, Bittihn P, Hornung D, et al. Low-energy control of electrical turbulence in the heart. *Nature* (2011) **475**:235–9. doi: 10.1038/nature10216
16. Alonso S, Bar M. Reentry near the percolation threshold in a heterogeneous discrete model for cardiac tissue. *Phys Rev Lett.* (2013) **110**:158101. doi: 10.1103/PhysRevLett.110.158101
17. Gao X, Zhang H. Mechanism of unpinning spirals by a series of stimuli. *Phys Rev E* (2014) **89**:062928–32. doi: 10.1103/PhysRevE.89.062928
18. Quail T, Shrier A, Glass L. Spiral symmetry breaking determines spiral wave chilarity. *Phys Rev Lett.* (2014) **113**:158101. doi: 10.1103/PhysRevLett.113.158101
19. Feng X, Gao X, Tang JM, Pan JT, Zhang H. Wave trains induced by circularly polarized electric fields in cardiac tissues. *Sci Rep.* (2015) **5**:13349–57. doi: 10.1038/srep13349
20. Kazbanov IV, ten Tusscher KHWJ, Panfilov AV. Effects of heterogeneous diffuse fibrosis on arrhythmia dynamics and mechanism. *Sci Rep.* (2016) **6**:20835. doi: 10.1038/srep20835
21. Fenton FH, Cherry EM, Hastings HM, Evans SJ. Multiple mechanisms of spiral wave breakup in a model of cardiac electrical activity. *Chaos* (2002) **12**:852–92. doi: 10.1063/1.1504242
22. Cherry EM, Fenton FH. Suppression on alternans and conduction blocks despite steep APD restitution: electrotonic, memory, and conduction velocity restitution effects. *Am J Physiol Heart Circ Physiol.* (2004) **286**:H2332–41. doi: 10.1152/ajpheart.00747.2003
23. Gelzer ARM, Koller ML, Otani NF, Fox JJ, Enyeart MW, Hooker GJ, et al. Dynamic mechanism for initiation of ventricular fibrillation *in vivo*. *Circulation* (2008) **118**:1123–9. doi: 10.1161/CIRCULATIONAHA.107.738013
24. Bueno-Orovio A, Hanson BM, Gill JS, Taggart P, Rodriguez B. *In vivo* human left-to-right ventricular differences in rate adaptation transiently increase pro-arrhythmic risk following rate acceleration. *PLoS ONE* (2012) **7**:e52234. doi: 10.1371/journal.pone.0052234
25. Bueno-Orovio A, Cherry EM, Evans SJ, Fenton FH. Basis for the unduction of tissue-level phase-2 reentry as a repolarization disorder in the Brugada syndrome. *BioMed Res Int.* (2015) **2015**:197586. doi: 10.1155/2015/197586
26. Pumir A, Arutunyan A, Krinsky V, Sarvazyan N. Genesis of ectopic waves: role of coupling, automaticity, and heterogeneity. *Biophys J.* (2005) **89**:2332–49. doi: 10.1529/biophysj.105.061820
27. Biktashev VN, Arutunyan A, Sarvazyan NA. Generation and escape of local waves from the boundary of uncoupled cardiac tissue. *Biophys J.* (2008) **94**:3726–38. doi: 10.1529/biophysj.107.117630
28. Zemlin CW, Pertsov AM. Bradycardic onset of spiral wave re-entry: structural substrates. *Europace* (2007) **9**:59–63. doi: 10.1093/europace/eum205
29. Zemlin CW, Mitrea GB, Pertsov AM. Spontaneous onset of atrial fibrillation. *Physica D* (2009) **238**:969–75. doi: 10.1016/j.physd.2008.12.004
30. Kudryashova NN, Kazbanov IV, Panfilov AV, Agladze KI. Conditions for waveblock due to anisotropy in a model of human ventricular tissue. *PLoS ONE* (2015) **10**:e0141832–849. doi: 10.1371/journal.pone.0141832
31. Gao X, Zhang H, Zykov VS, Bodenschatz E. Stationary propagation of a wave segment along an inhomogeneous excitable stripe. *New J Phys.* (2014) **16**:033012–28. doi: 10.1088/1367-2630/16/3/033012
32. Rudy Y. Reentry-insights from theoretical simulations in a fixed pathway. *J Cardiovasc Electrophysiol.* (1995) **6**:294–312. doi: 10.1111/j.1540-8167.1995.tb00402.x
33. Zykov V, Krekhov A, Bodenschatz E. Fast propagation regions cause self-sustained reentry in excitable media. *Proc Natl Acad Sci USA* (2017) **114**:1281–6. doi: 10.1073/pnas.1611475114
34. Zykov V, Krekhov A, Bodenschatz E. Geometrical factors in propagation block and spiral wave initiation. *Chaos* (2017) **27**:093923. doi: 10.1063/1.4999473
35. Barkley D. A model for fast computer-simulation of waves in excitable media. *Physica D* (1991) **49**:61–70. doi: 10.1016/0167-2789(91)90194-E
36. Keener J, Sneyd J. *Mathematical Physiology*. New York, NY: Springer Science+Business Media (2009).
37. Pauwelussen JP. Nerve impulse propagation in a branching nerve system: a simple model. *Physica* (1981) **4D**:67–88. doi: 10.1016/0167-2789(81)90005-1
38. Mornev OA. Elements of optics of autowaves. In: Krinsky VI, editor. *Self-Organization: Autowaves and Structures Far from Equilibrium Springer Series in Synergetics*, Vol. 28, Berlin; Heidelberg: Springer (1984). p. 111–8.
39. Zykov VS. *Simulation of Wave Processes in Excitable Media*. New York, NY: Manchester University Press (1987).

40. Dikici B, Pantoya ML, Levitas V. The effect of pre-heating on flame propagation in nanocomposite thermites. *Combustion Flame* (2010) **157**:1581–5. doi: 10.1016/j.combustflame.2010.04.014
41. Qu ZL, Hu G, Garfinkel A, Weiss JN. Nonlinear and stochastic dynamics in the heart. *Phys Rep*. (2014) **543**:61–162. doi: 10.1016/j.physrep.2014.05.002
42. Seemann G, Höper C, Sachse FB, Dössel O, Holden AV, Zhang H. Heterogeneous three-dimensional anatomical and electrophysiological model of human atria. *Philos Trans R Soc A* (2006) **364**:1465–81. doi: 10.1098/rsta.2006.1781
43. Xie Y, Garfinkel A, Camelliti P, Kohl P, Weiss JN. Effects of fibroblast-myocyte coupling on cardiac conduction and vulnerability to reentry: a computational study. *Heart Rhythm* (2009) **6**:1641–9. doi: 10.1016/j.hrthm.2009.08.003
44. Sanchez C, Bueno-Orovio A, Pueyo E, Rodriguez B. Atrial fibrillation dynamics and ionic block effects in six heterogeneous human 3D virtual atria with distinct repolarization dynamics. *Front Bioeng Biotechnol.* (2017) **5**:29. doi: 10.3389/fbioe.2017.00029
45. Rother J, Richter C, Turco L, Knocj F, Mey I, Luther S, et al. Crosstalk of cardiomyocytes and fibroblasts in co-cultures. *Open Biol*. (2015) **5**:150038. doi: 10.1098/rsob.150038
46. Smit NW, Coronel R. Stem cells can form gap junctions with cardiac myocytes and exert pro-arrhythmic effects. *Front Physiol*. (2014) **5**:419–26. doi: 10.3389/fphys.2014.00419
47. Nattel S. Effects of heart disease on cardiac ion current density versus current amplitude: important conceptual subtleties in the language of arrhythmogenic ion channel remodeling. *Circul Res*. (2008) **102**:1298–300. doi: 10.1161/CIRCRESAHA.108.178087
48. Fenton F, Karma A. Vortex dynamics in three-dimensional continuous myocardium with fiber rotation: filament instability and fibrillation. *Chaos* (1998) **8**:20–47. doi: 10.1063/1.166311
49. Faber GM, Rudy Y. Action potential and contractility changes in [Na(+)](i) overloaded cardiac myocytes: a simulation study. *Biophys J*. (2000) **78**:2392–404. doi: 10.1016/S0006-3495(00)76783-X
50. Bueno-Orovio A, Cherry E, Fenton F. Minimal model for human ventricular action potentials in tissue. *J Theor Biol*. (2008) **253**:544–60. doi: 10.1016/j.jtbi.2008.03.029

Conflict of Interest Statement: The authors declare that the research was conducted in the absence of any commercial or financial relationships that could be construed as a potential conflict of interest.

frontiers in Physiology

REVIEW
published: 15 January 2018
doi: 10.3389/fphys.2017.01136

Progress in Mathematical Modeling of Gastrointestinal Slow Wave Abnormalities

Peng Du[1]*, *Stefan Calder*[1], *Timothy R. Angeli*[1], *Shameer Sathar*[1], *Niranchan Paskaranandavadivel*[1], *Gregory O'Grady*[1,2] and *Leo K. Cheng*[1,3]

[1] Auckland Bioengineering Institute, University of Auckland, Auckland, New Zealand, [2] Department of Surgery, University of Auckland, Auckland, New Zealand, [3] Department of Surgery, Vanderbilt University, Nashville, TN, United States

Gastrointestinal (GI) motility is regulated in part by electrophysiological events called slow waves, which are generated by the interstitial cells of Cajal (ICC). Slow waves propagate by a process of "entrainment," which occurs over a decreasing gradient of intrinsic frequencies in the antegrade direction across much of the GI tract. Abnormal initiation and conduction of slow waves have been demonstrated in, and linked to, a number of GI motility disorders. A range of mathematical models have been developed to study abnormal slow waves and applied to propose novel methods for non-invasive detection and therapy. This review provides a general outline of GI slow wave abnormalities and their recent classification using multi-electrode (high-resolution) mapping methods, with a particular emphasis on the spatial patterns of these abnormal activities. The recently-developed mathematical models are introduced in order of their biophysical scale from cellular to whole-organ levels. The modeling techniques, main findings from the simulations, and potential future directions arising from notable studies are discussed.

Keywords: slow wave, GI, multi-scale modeling, arrhythmias, Electrophysiology

OPEN ACCESS

Edited by:
S. Sridhar,
Robert Bosch Centre for Cyber- Physical Systems, Indian Institute of Science, India

Reviewed by:
Arun V. Holden,
University of Leeds, United Kingdom
Alok Ranjan Nayak,
International Institute of Information Technology, India
Martin Buist,
National University of Singapore, Singapore

***Correspondence:**
Peng Du
peng.du@auckland.ac.nz

Specialty section:
This article was submitted to Computational Physiology and Medicine, a section of the journal Frontiers in Physiology

Received: *03 October 2017*
Accepted: *22 December 2017*
Published: *15 January 2018*

Citation:
Du P, Calder S, Angeli TR, Sathar S, Paskaranandavadivel N, O'Grady G and Cheng LK (2018) Progress in Mathematical Modeling of Gastrointestinal Slow Wave Abnormalities. Front. Physiol. 8:1136. doi: 10.3389/fphys.2017.01136

GASTROINTESTINAL ELECTROPHYSIOLOGICAL DEFINITIONS AND DISORDERS

Cyclical contractions of the gastrointestinal (GI) tract are initiated and coordinated by rhythmic, propagating bioelectrical events, termed slow waves (Szurszewski, 1998). Abnormal slow wave activity has long been observed to occur in the gut, and their putative causation of gastrointestinal symptoms and disorders remains an area of significant interest (Lammers, 2013; O'Grady et al., 2014). In the healthy stomach, slow waves normally originate from a single pacemaker located in the proximal stomach along the greater-curvature, rapidly establishing ring wavefronts that propagate antegrade toward the distal stomach, terminating at the pylorus (O'Grady et al., 2010a). A number of mathematical models have been developed to study both normal slow wave activity, and a wide range of slow wave abnormalities observed in functional disorders and animal models (Lammers et al., 2012, 2015; O'Grady et al., 2012a; Angeli et al., 2015). This review presents the current state of mathematical modeling of these slow wave abnormalities, and also discusses the methods for validating these models.

Terminology

Several terminologies have been applied to describe abnormal GI slow wave activities. While some of these terms have been adopted from cardiac electrophysiology, where they have been

well-defined, it is worthwhile to also review these terms in the context of their usage in the GI field. Earlier cardiac electrophysiologists pointed out the granular difference between arrhythmias, i.e., absence of rhythm, and dysrhythmias, i.e., abnormalities of rhythm (Trommer, 1982), but usages in practice over the years have converged the two terms to become synonyms (Marriott, 1984). Conventionally in the GI field, dysrhythmias, and arrhythmias have also been used interchangeably to represent any abnormal slow waves (Lammers, 2013; O'Grady et al., 2014). Nelsen et al., used both arrhythmias and dysrhythmias to describe abnormal slow waves as early as 1968 (Nelsen and Kohatsu, 1968), while other investigators have maintained both usages to describe abnormal slow wave events (Code and Marlett, 1974).

Dysrhythmias can either be defined in terms of frequency, or in terms of spatial pattern. In the stomach, frequency abnormalities have typically been defined as either quiescence, bradygastria, or tachygastria (Code and Marlett, 1974; Stern et al., 1987); while spatial abnormalities have been subjected to a growing list of classifications by various researchers and in various animal models (**Table 1**). Furthermore, following cardiac conventions, spatial dysrhythmias could also be defined as either abnormal initiation, e.g., ectopic pacemaker, or abnormal conduction, e.g., retrograde propagation. It is worth noting that each of these terms typically describes a single aspect of a dysrhythmia, but in practice dysrhythmic episodes may not occur in isolation. For example, an ectopic initiation event could occur simultaneously with conduction block and collision (**Figure 1C**), and a conduction block could lead to an aberrant focus of initiation, or a re-entrant conduction abnormality could give rise to secondary conduction abnormalities (O'Grady et al., 2014).

Dysrhythmias and GI Functional Disorders

Several GI functional disorders have been associated with slow wave dysrhythmias (O'Grady et al., 2014), as detailed in **Table 2**, with examples of the types of dysrhythmias that have been reported with each disorder. The majority of previous studies of slow wave activity have utilized low-resolution recording methods, where a sparse number of electrodes were placed on the body-surface (electrogastrography/EGG) or directly on the serosal or mucosal surfaces of the GI organs (Familoni et al., 1987; Lin et al., 1998; Lin and Chen, 2001; Coleski and Hasler, 2009). These studies established foundational discoveries of normal and dysrhythmic slow wave activation, but analysis was largely restricted to the frequency domain, although propagation analysis was also attempted (Simonian et al., 2004; Coleski and Hasler, 2009). The results of these EGG and low-resolution electrode studies thereby focused primarily on ectopic activation as a mechanism of slow wave dysrhythmias (Lin et al., 1998; Lin and Chen, 2001; Simonian et al., 2004).

More recently, high-resolution GI mapping has emerged as a key methodological advance, where spatially-dense arrays of hundreds of electrodes are placed directly on the GI organ, enabling analysis of slow wave propagation in spatiotemporal detail (Lammers et al., 2008a; Du et al., 2009a). Recent high-resolution mapping studies in patients with diabetic and idiopathic gastroparesis, and chronic unexplained nausea and vomiting, have now demonstrated that spatially-complex dysrhythmias are prevalent in these functional GI disorders (O'Grady et al., 2012a; Angeli et al., 2015). Importantly, many of these spatial dysrhythmias (**Table 1**) are now known to occur within the normal slow wave frequency range, such that they may likely have gone undiagnosed with previous frequency-reliant methods. Furthermore, it has also been reported that the slow wave dysrhythmias were correlated with loss of the interstitials cells of Cajal (ICC) (O'Grady et al., 2012a; Angeli et al., 2015), which could result in ICC network remodeling (Ordog et al., 2000).

CURRENT STATE OF GI ELECTROPHYSIOLOGICAL MODELING

Mathematical modeling uses equations to formulate relationships between parameters of a biophysical process. Additional analyses can then be performed on the equations to infer the causal relationship between the parameters over a large parameter space *in silico*, complementary to experimental data, which are needed to validate the model in some capacity. It is worth noting that although a goal is to develop models capable of predictive simulations of physiological functions, no model in its current state can realistically accomplish this ambitious aim in a way that mimics real biological events. Instead, mathematical models are developed to represent electrophysiological mechanisms at discrete biophysical scales as simply and accurately as possible, with input from experimental data at each scale, and attempts are then made to link mechanisms together across these scales.

One particularly significant approach of mathematical modeling is thus to develop a system of equations by following the hierarchy of biological systems across multiple spatiotemporal scales. Such an approach is also called multi-scale modeling, which has been increasingly applied with great effect to study normal and dysrhythmic GI slow waves and dysmotility (Cheng et al., 2013; Du et al., 2013, 2016b). Generally, in a multi-scale model of dysrhythmias the lowest scale relates to the kinetics of the ion channels, which are usually collected into individual ion conductances, with Hill-type activation and inactivation parameters fitted to experimental data (Lees-Green et al., 2011). The dependence of an ion conductance on membrane potential can be modeled using a Hodgkin & Huxley approach, and applied over multiple types of conductance to model the change in slow waves. It is worth noting that the conductance modeled presents an averaged activity of all the same type of conductance in the cell, rather than individual ion channels. As our knowledge of the subcellular processes becomes increasingly clear, more sophisticated techniques such as stochastic modeling and subcellular domain diffusion have also been incorporated to cell models (Lees-Green et al., 2011).

Tissue models require connecting multiple cell models together in a continuum, i.e., spatially averaged, sense has typically been achieved using a reaction-diffusion technique, either in the form of monodomain, bidomain, or tridomain

TABLE 1 | Definitions of gastric dysrhythmias. Spatial information was obtained from HR mapping taken directly from the gastric serosal surface.

Terms	Definitions
Arrhythmias/Dysrhythmias (temporal or spatio-temporal)	Abnormal slow wave frequency and/or propagation. Normal human gastric frequency range is typically defined as 2–4 cycle per minute (cpm) (**Figure 1**) (Owyang and Hasler, 2002).
Quiescent (temporal)	No slow waves (Angeli et al., 2015).
Bradygastria (temporal)	<2 cpm (Parkman et al., 2003; Lim et al., 2012).
Tachygastria (temporal)	> 4 cpm (Parkman et al., 2003; Lim et al., 2012).
Uncoupling (spatio-temporal)	Loss of entrainment leading to two distinct slow wave frequencies in adjacent tissues (Somarajan et al., 2015; Wei et al., 2017).
Anatomical re-entry (spatial)	Self-perpetuating propagation around the circumference of the gut lumen (Angeli et al., 2013b; Du et al., 2017).
Functional re-entry/rotor (spatial)	A rotating wavefront propagating in a single-direction around in a circuit around a central "core" region that acts as a functional conduction block (Lammers et al., 2008b; Angeli et al., 2013b, 2015).
Figure-of-eight/double rotor (spatial)	A single common wavefront that breaks into two rotors propagating in opposite directions (clockwise and anticlockwise) around a core, forming a repeated "figure-of-eight" continuous pattern of activations (Angeli et al., 2013b; Du et al., 2016a).
Conduction block (spatial)	Either a partial or complete block to propagation of normal slow waves (Lammers et al., 2012; O'Grady et al., 2012a; Angeli et al., 2013b).
Retrograde propagation (spatial)	A slow wave event propagating abnormally in the orad direction (O'Grady et al., 2012a; Angeli et al., 2015).
Ectopic activation (spatial)	An ectopic activation was defined as an aberrant initiation of slow waves from a location other than the natural pacemaker (proximal greater curvature) (Lammers et al., 2008b; O'Grady et al., 2012a).
Wave Collision (spatial)	Meeting and termination of two independent wavefronts propagating in opposite directions, e.g., retrograde and antegrade or circumferentially (Lammers et al., 2012, 2015; O'Grady et al., 2012a; Angeli et al., 2015).
Merging wavefronts (spatial)	Joining of two independent wavefronts propagating in the same direction (Angeli et al., 2013b).

Temporal information was obtained from HR mapping, low resolution serosal recording, and non-invasive recording techniques such EGG and MGG.

(extended bidomain) equations (Equations 1–6) (Buist and Poh, 2010; Corrias et al., 2012; Du et al., 2013, 2016b; Sathar et al., 2015). The number of domains typically represents the predominant avenues through which the cells are coupled to each other. In the monodomain representation, ICC are assumed to be predominantly coupled via the intracellular domain, whereas in the bidomain representation, the current flow through the extracellular space is also modeled. In contrast to cardiac applications of the tridomain model, which is used to model an additional phase due to non-excitable elements such as fibroblasts (Sachse et al., 2009), the more recently proposed tridomain model represents the coupling between the intracellular spaces of ICC and smooth muscle cells (SMC) and a shared extracellular space (Corrias et al., 2012; Sathar et al., 2015). In each of these cases, under certain assumptions, the higher-order domain models could be reduced to the monodomain model, and extracellular potentials could then be estimated based on the membrane potentials.

Monodomain:

$$\nabla \cdot (\sigma \nabla V_m) = A_m \left(C_m \frac{\partial V_m}{\partial_t} + I_{ion} \right) \tag{1}$$

Bidomain:

$$\nabla \cdot ((\sigma_i + \sigma_e)\, \nabla \phi_e) = -\nabla \cdot (\sigma_i \nabla V_{\mathrm{m}}) \tag{2}$$

$$\nabla \cdot (\sigma_i \nabla V_{\mathrm{m}}) + \nabla \cdot (\sigma_i \nabla \phi_e) = A_m \left(C_m \frac{\partial V_m}{\partial t} + I_{ion} \right) \tag{3}$$

Tridomain:

$$\nabla \cdot \left(\sigma_i^{(1)} \nabla V_m^{(1)} + \phi_e \right) = A_1 \left(C_m^1 \left(\frac{\partial \phi_i^{(1)}}{\partial t} + \frac{\partial \phi_c}{\partial t} \right) + I_{ion}^{(1)} \right) + A_{gap} I_{gap} \tag{4}$$

$$\nabla \cdot \left(\sigma_i^{(2)} \nabla V_m^{(2)} + \phi_e \right) = A_2 \left(C_m^2 \left(\frac{\partial \phi_i^{(2)}}{\partial t} + \frac{\partial \phi_c}{\partial t} \right) + I_{ion}^{(2)} \right) - A_{gap} I_{gap} \tag{5}$$

$$\nabla \cdot \left(\sigma_e + \sigma_i^{(1)} + \sigma_i^{(2)} \right) \nabla \phi_e = -\nabla \cdot \left(\sigma_i^{(1)} \nabla V_m^{(1)} \right) - \nabla \cdot \left(\sigma_i^{(2)} \nabla V_m^{(2)} \right) \tag{6}$$

where σ represents the tissue conductivity, which could be further characterized as intracellular conductivity (σ_i; [S m^{-1}]) or extracellular conductivity (σ_e; [S m^{-1}]). Membrane potential (V_m; [V]) can also be expressed as the difference between intracellular potential and extracellular potential, i.e., $\phi_i - \phi_e$. The total current is denoted by I_{ion} [A]. A_m [m^{-1}] denotes the surface-to-volume ratio and C_m [F m^{-2}] denotes the membrane capacitance. In the case of the tridomain equations, conductivities, surface-to-volume ratio, membrane capacitance and intracellular potentials are further distinguished between two cell types, with an added coupling current (I_{couple}) between the two cell types. One of the intracellular domains (Equation 4) represents the cytoplasm of ICC, while the other intracellular

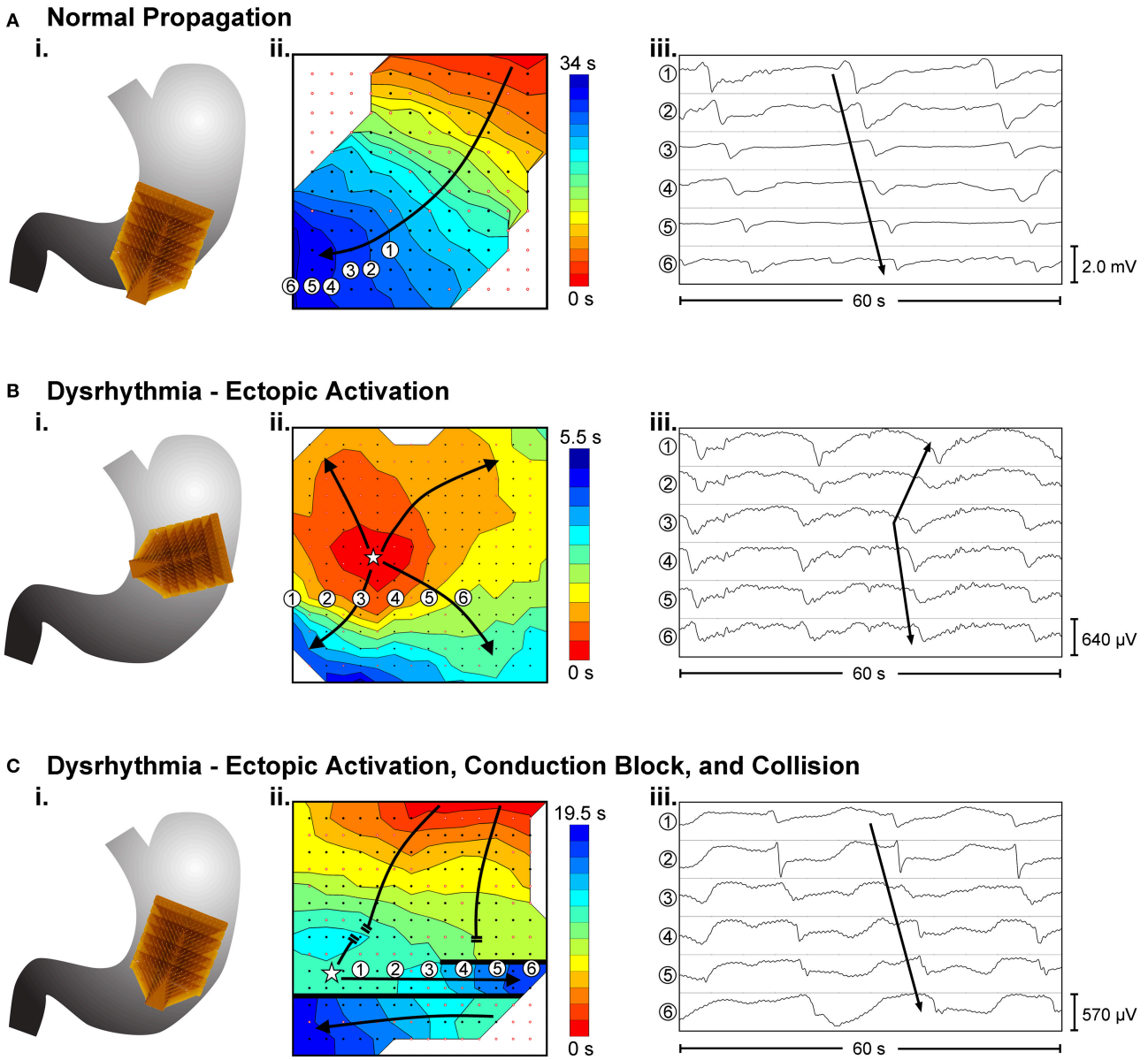

FIGURE 1 | Examples of high-resolution mapping of *in-vivo* gastric slow waves. (i) An array of 16 × 16 electrodes (brown patch) were placed on the serosal surface of the stomach. (ii) Activation times of slow waves were identified and reconstructed into activation maps with red representing early activation and blue presenting late activation. (iii) Example slow wave recordings from six electrodes are shown in each case. **(A)** Normal antegrade propagation pattern of gastric slow wave activation (Angeli et al., 2015). **(B)** An ectopic activation (star) in the proximal stomach. **(C)** Simultaneous ectopic activation, conduction block and collision of slow waves in the gastric corpus. Adapted from (Angeli et al., 2015).

domain (Equation 5) represents the cytoplasm of SMC. The two intracellular domains share a common extracellular domain (Equation 6).

The choice of the governing equations in the continuum model typically depends on the specific applications. For example, in the absence of detailed measurements of conductivity parameters, applications involving entrainment modeling would typically only require the monodomain model (Du et al., 2015b, 2017), whereas simulations involving an extracellular stimulus would typically require a bidomain/tridomain approach (Sathar et al., 2015). On the other hand, the higher-domain approach would require more computational power due to the increased complexity of formulation. Though direct comparisons between computational times of GI models are difficult to ascertain with varying parameters and numerical solvers involved in the process, on average the computational time of cardiac bidomain models can be an order of magnitude longer than monodmain models (Plank et al., 2009).

TABLE 2 | Examples of GI functional disorders associated with slow wave dysrhythmias.

Disorders	Recording method(s)	Slow wave dysrhythmias reported
Chronic unexplained nausea and vomiting (Angeli et al., 2015)	HR mapping	Spatiotemporal dysrhythmias occurring across all frequency bands.
Surgical manipulations (Kelly and Code, 1971; Schaap et al., 1990; Du et al., 2015a; Berry et al., 2017)	Low resolution recording, HR mapping	Uncoupling of slow waves across surgical GI bisections; Excisions/incisions led to emergence of rapid circumferential propagation; Frequency abnormalities after gastric resections and anastomoses.
Diabetic dysfunction (intestine) (Lammers et al., 2012, 2015)	HR mapping	Re-entry, ectopic activation with collisions (rodent data).
Mesenteric ischemia (Lammers et al., 1997; Somarajan et al., 2015)	HR mapping, MGG	Uncoupling, with significant decrease in postprandial intestinal slow wave frequency.
Gastroparesis (Lin et al., 1998; O'Grady et al., 2012a)	HR mapping, EGG	Spatiotemporal dysrhythmias occurring across all frequency bands.
Gastroesophageal reflux disease (Leahy et al., 2001; Chen et al., 2004)	EGG	Unstable slow waves, with increased tachygastria in patients with regurgitation.
Systemic sclerosis (McNearney et al., 2009)	EGG	Bradygastria correlated with nausea.
Hyperglycaemia (Hasler et al., 1995; Gonlachanvit et al., 2003; Lien et al., 2003)	EGG	Tachygastria following dextrose infusion.
Chronic intestinal pseudo-obstruction (Debinski et al., 1996)	EGG	Tachygastria, irregular activities, mixture of bradygastria and tachygastria.
Motion sickness (Kim et al., 1997)	EGG	Increase in tachygastria due to vection.
Hyperemesis gravidarum (Koch et al., 1990)	EGG	Mainly tachygastria, with some bradygastria and flat-line activities.
Functional dyspepsia (Pfaffenbach et al., 1997; Leahy et al., 1999; Lin and Chen, 2001; Simonian et al., 2004)	EGG	Increased episodes of tachygastria compared to patients with normal gastric emptying.

Relating the slow wave activity at the whole-organ level to specific individual cells is a challenging, if not impossible, aspect to resolve. Conceptually, the multi-scale models represent slow waves in a spatially-averaged sense, meaning the "continuum" represents an averaged activity of a group of the same cell types within the immediate vicinity in the underlying tissue (Angeli et al., 2013a). A similar loss of spatial information occurs when whole-organ activity is inferred electromagnetically from the body-surface (Kim et al., 2013; Bradshaw et al., 2016b). In this case, the electrophysiological activation of the organ is approximated using dipole(s), which represent the net activation state of the organ at an instance in time. Despite the loss of specificity in the electrical information when upscaling, the higher-level spatial scales also remain a particularly useful approximation of slow waves in the *in vivo* state. The appropriate scale of models should be considered according to the level of mechanisms and specific research questions of interest.

Cell Models

The two main types of biophysically-based cell models being developed over recent years are SMC and ICC, which have been covered extensively in previous reviews (Lees-Green et al., 2011). In general, ICC models incorporate self-excitatory intracellular calcium-based mechanisms to generate slow waves at a specific intrinsic frequency, whereas SMC models require an input stimulus to drive the membrane potentials. Key conductance and/or intracellular calcium dynamics in these cell models are generally fitted to experimental data and validated by reproducing membrane potentials and response to perturbations such as electrical stimuli and drugs. The number of SMC models is limited, including a gastric SMC model derived from animal experimental data (Corrias and Buist, 2007), and uterine SMC derived from uterine human smooth muscle cells (Atia et al., 2016). A list of biophysically-based SMC models is presented in **Table 3**.

TABLE 3 | A list of biophysically-based smooth muscle cell models.

Smooth Muscle Models	Number of ion conductances
Human colonic smooth muscle cells (Yeoh et al., 2017)	8
Gastric smooth muscle cells (Corrias and Buist, 2007)	8
Human uterine smooth muscle cells (Atia et al., 2016)	27

A recent example of ICC model development is the finite-state machine based biophysical model by Sathar et al. (2014). In this model, the cellular activity of the model was represented by an active state and passive state, whereby the active state corresponded to the ionic dynamics of the ICC model developed by Corrias and Buist (2008). The transition between the states was modeled using a finite-state machine approach that was dependent on membrane potential, calcium dynamics, and the refractory/non-refractory period parameters defining the intrinsic frequency of the slow wave pacemaker activity (**Figure 2A**; Sathar et al., 2014). The finite-state machine approach enabled modeling the effects of external current on the cellular activity and has successfully reproduced experimentally observations of gastric pacing. The finite-state machine model is governed by two important rules: (i) if the cellular activity is "active," it remains active until the calcium dynamics returns to a quiescent state—after which, it changes to a "passive" state; (ii) on the other hand, if the current cellular activity is "passive," it remains "passive" until the membrane potential exceeds an excitation potential or until the cellular activity has passed the non-refractory period (**Figure 2B**).

In addition to ICC and SMC, other types of cells have also been proposed to play a role in the electrophysiology

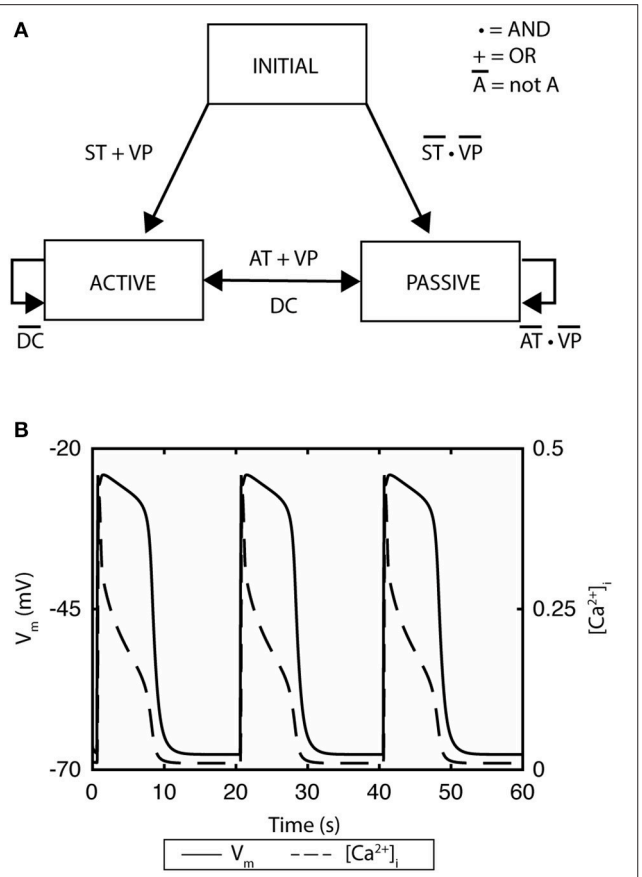

FIGURE 2 | A finite state machine cell model of gastric interstitial cells of Cajal. **(A)** The model consists of an active state and a passive state. ST indicates if time has passed the startTime, which is set as a parameter and which determines initial excitation when there is no threshold voltage. AT indicates if the non-refractory period has been passed and signals transition from passive state to active state. DC identifies if the change in concentration of intracellular Ca^{2+} has returned to quiescent state. VP variable is set to true if there is a voltage which is greater than the threshold of the cell. **(B)** Simulated gastric slow waves and the associated intracellular calcium. Adapted from (Sathar et al., 2014).

and neurotransmission of the GI tract. One such cell is the fibroblast-like cell (FLC), which form discrete networks in the myenteric plexus and are widely distributed within the muscular layer of the colon (Kurahashi et al., 2012). One specific FLC positive for platelet-derived growth factor receptor ($PDGFR\alpha^+$) is of particular interest because they are involved in purinergic inhibitory neurotransmissions (Yeoh et al., 2016). Purines released by enteric motor neurons bind to the G-protein coupled receptors in the membrane of the $PDGFR\alpha^+$ cells. The binding initiates a series of intracellular processes resulting in the release of Ca^{2+} due to inositol 1,4,5-triphosphate (IP_3) entering the cytoplasm. The elevation of intracellular Ca^{2+} in turns activates small Ca^{2+}-activated K^+ (SK3) conductance, leading to hyperpolarization of the membrane potential, and potentially also neighboring SMC. Yeoh et al. developed a $PDGFR\alpha^+$ cell model by modifying a spatially-independent version of the model proposed by Bennett et al. (2005) and Yeoh et al. (2016), and with their specific description of the SK3 conductance. The authors were able to demonstrate ATP-induced hyperpolarisation and inhibitory effects of MRS2500 and apamin (SK3 channel blocker) (Bennett et al., 2005). The potential applications of this model may be significant in future, as it may be coupled with existing ICC and SMC models to simulate the effects of neural innervation and feedback on slow wave generations and smooth muscle membrane potentials.

Biophysically-based mathematical models of GI cells have been developed at a steady pace, mainly governed by the availability of experimental data and convergence of evidence regarding key electrophysiological mechanisms. However, nearly all GI cell models have been developed as an "after thought" based on published data that were not originally designed with the potential for modeling in mind. The models were generally only able to reproduce the cellular responses over a set of specific interventions that had already been demonstrated experimentally, although some interesting and clinically-relevant applications have already been demonstrated through the predictive modeling of GI channelopathies (Poh et al., 2012). While this is not a unique problem to the GI field, the true predictive power of cell models could be better realized if investigators would consider modeling when developing their experimental design, as has been done in the cardiac field (Maltsev et al., 2017).

Tissue Models

Propagation of slow waves has typically been modeled as a series of coupled phenomenologically-based oscillators, or by employing biophysically-based ICC models. While there are many ways to formulate the specific coupling between ICC models, the ability of an ICC with a higher intrinsic frequency to "entrain" another coupled ICC with lower intrinsic frequency is fundamental (van Helden et al., 2010). The process of entrainment is a key point of distinction between GI and cardiac electrophysiological models. Whereas the cardiac models represent myocytes as single-event active potentials in response to a pacemaker (often modeled as a stimulus), GI models require an interconnected network of pacemakers, where every point in the network is potentially capable of intrinsically generating slow wave activation (Cheng et al., 2013; Du et al., 2013, 2016b). Previous reviews have covered models that have successfully simulated propagation of gastric and intestinal slow waves at the tissue levels (Du et al., 2013, 2016b). This review covers recent work on the simulation of GI slow wave dysrhythmias.

Most recent tissue-level investigations have focused predominantly on the effects of perturbations on the organization of slow waves. Weakly-coupled oscillators have been used to model both intestinal and colonic slow waves (Linkens, 1978; Linkens and Mhone, 1979). This concept was explored further in a recent study to explore the effects of spatial noise in the intrinsic frequency gradient on intestinal slow wave propagation (Parsons and Huizinga, 2016). The study demonstrated that as the coupling (modeled as a gap junction) between the oscillators decreased over a segment of intestine, more slow wave frequency plateaus appeared (Parsons and Huizinga, 2016). One of the conclusions of this study points to the role of a spatial noise on

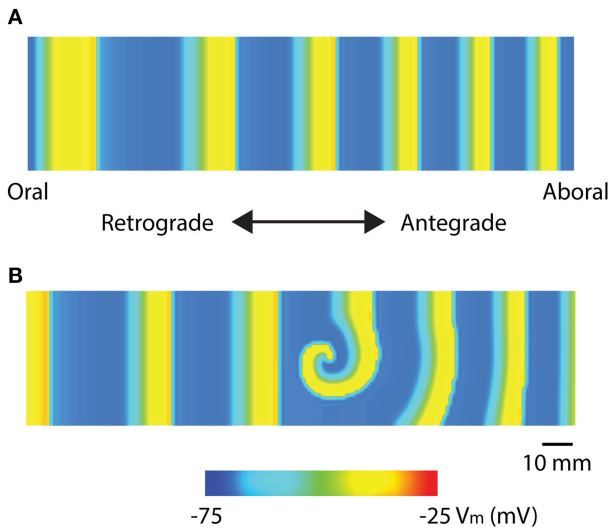

FIGURE 3 | Mathematical models of intestinal slow wave propagation. **(A)** Entrained slow waves over an intrinsic frequency gradient of 17–14.6 cpm (entrained to 17 cpm) were simulated over a 2D model. **(B)** A functional rotor was invoked in the middle of the 2D model using a 30 s long prolonged temporary conduction block. The rotor could be sustained with entrained waves propagating in both antegrade and retrograde directions, with an elevated frequency of 21 cpm. Adapted from (Du et al., 2017).

the organization of slow wave propagation and motor patterns in the intestine. As a limitation of the model, the authors pointed out that the intestinal "waxing and waning" phenomenon was not reproduced by the model, but could be explained by a phase-amplitude modulation mechanism (Huizinga et al., 2014). The dynamic interactions between intestinal slow waves in response to a field-stimulus were later quantified using a phase response curve (Parsons and Huizinga, 2017). The weakly-coupled oscillator was extended to a 2D model to reproduce intestinal slow waves in a number of species, as well as the effects of circumferential ICC loss on partitioning of slow waves (Wei et al., 2017).

Recent high-resolution mapping studies have reported re-entry activities in the stomach and intestine (**Table 1**). Two specific re-entry activities were discovered: *functional re-entry* (Du et al., 2015b), where slow waves propagate in a sustained manner around a core either as in a rotor (**Figure 3**), or figure-of-eight pattern; and *anatomical re-entry*, where slow wave propagation occurs in continuity around the lumen of the intestine (Angeli et al., 2013b). These re-entry activities were recently modeled in two-dimensional models using a simplified ICC model and the monodomain equation, using a stimulus-driven protocol to invoke the re-entry (Du et al., 2015b, 2017). In order to invoke a rotor in a short segment intestinal tissue, single-pulse stimulus (100 μA mm^{-2}; 100 ms) was used to initiate the re-entry next to a temporary conduction block prescribed by the refractory period in the middle of the model (Plank et al., 2009). In particular, it was demonstrated that there was a relatively narrow parameter space in terms of the timing relative to the refractory tail of the previous wavefronts, during which a sustained functional re-entry could be invoked; otherwise, the prescribed intrinsic frequency gradient in the models was essentially able to correct the wavefront over time (Du et al., 2015b, 2017). Anatomical re-entry around the circumference of a 3D lumen was also demonstrated to occur under a similar set of constraints to the functional re-entry, with the added consideration of the geometry of the lumen (Du et al., 2017). One of the features of a sustained re-entry is the elevated frequency associated with the entrainment of slow waves in the core, as demonstrated experimentally (Lammers et al., 2008b). This elevated frequency serves to sustain the re-entry and can lead to entrainment of a substantial section of adjacent intestine. A secondary observation was a frequency-conduction restitution type of relationship where the elevated frequency induces a local reduction in conduction velocity of slow waves (Du et al., 2015b, 2017). Other investigators have modeled the effects of temperature on intestinal slow waves and the formation of re-entry activities (Gizzi et al., 2010).

A bi-directionally coupled model of ICC networks, achieved through coupling of myenteric and intramuscular ICC populations, has been proposed as a homeostatic mechanism in the gut (O'Grady et al., 2012b). Gastric slow waves demonstrate a high degree of anisotropy, whereby slow waves propagate 2.5 times faster in the circumferential axis than the longitudinal axis (O'Grady et al., 2012b; Du et al., 2016a). Similar anisotropy also exists in the small intestine of some species, albeit to a much lesser extent (Angeli et al., 2013b). During normal gastric slow wave propagation, this anisotropy is only observed in the region of the normal pacemaker; thereafter, ring wavefronts are rapidly formed that propagate solely in the longitudinal axis without the need for circumferential spread (O'Grady et al., 2010a). However, during dysrhythmias, the rapid circumferential propagation is routinely observed to emerge in regions adjacent to dysrhythmic sources, due to either aberrant foci of initiation or conduction abnormalities interrupting the normal longitudinal pattern (O'Grady et al., 2012b; Cheng et al., 2013).

The impact of conduction anisotropy was further explored in a simulation where a small full-thickness segment of gastric tissue was excised as part of a biopsy (Du et al., 2015a). Gastric slow wave propagation around this type of excisional biopsy was also mapped experimentally from human subjects. The results demonstrated that area of rapid circumferential conduction was dependent on the orientation of the excision. At all orientations, the slow waves began to normalize in the longitudinal direction at a distance distal to the stapled wound within the field of mapping (60×60 mm^2). It is notable that there is no standard guideline on the dimensions and orientations of gastric excisional procedures in practice (Du et al., 2015a), and these findings could theoretically provide novel insights to minimize post-operative motility changes associated with gastric incisions in future.

In contrast to cell modeling work, recent GI tissue models were generally designed with specific experimental protocols to explore key physiological questions, and/or to provide predictions of potential protocols to invoke sustained dysrhythmia behaviors. Particular efforts have been invested by multiple groups to investigate the organization of intestinal slow waves over extended tissue scales and the formation of

re-entry in the stomach and intestine (Gizzi et al., 2010; Du et al., 2015b, 2017; Parsons and Huizinga, 2016). Experimentally, one of the next steps is to attempt to invoke sustained periods of re-entry to thoroughly explore the conditions under which these dysrhythmias occur and possible ways to eliminate them. The proposed relationship between the timing of stimulus and the refractory tail of the preceding wave in invoking re-entry already suggests the potential requirement for monitoring slow wave propagation in real-time experimentally (Bull et al., 2011). Another important avenue of tissue modeling studies has been to explore the structure-function relationship between the ICC network, slow wave propagation and other GI cells, such as the FLC. One potential approach is to reconstruct the structural distributions of these cells from immunofluorescence images and develop a continuum framework in which the interactions between multiple cell types could be taken into account. The structural networks and cellular functions could then be perturbed to explore the effects of ion chancel inhibition and/or cell loss on GI slow waves. Effects of non-electrically active tissues could be modeled by detailed description of the extracellular tissue conductivities in the higher domain models.

Organ Models

The techniques of simulating slow waves over the whole-organ are similar to the tissue models, with a few added considerations (Du et al., 2013, 2016b). First, gastric slow wave propagation has been shown to exhibit significant inter-regional variations within the stomach (Kelly and Code, 1971; Lammers and Stephen, 2008; Egbuji et al., 2010; O'Grady et al., 2010a). *In vivo* high-resolution mapping data have demonstrated that the fundus is generally quiescent in large monogastric species, and a pacemaker region exists in the proximal corpus along the greater curvature, from which gastric slow waves rapidly form ring wavefronts that propagate distally toward the antrum (Lammers and Stephen, 2008; Egbuji et al., 2010; O'Grady et al., 2010a). In humans, a marked acceleration of slow wave activation is then seen in the region of the terminal antrum, just proximal to the pylorus, which constitutes the basis of the terminal antral contraction (Berry et al., 2016). Second, a resting membrane potential gradient due to the action of ICC-derived carbon monoxide as a hyperpolarizing agent exists from the proximal to the distal stomach, as well as across the gastric and small intestinal wall (Farrugia et al., 2003). In the colon, the direction of the resting membrane potential gradient across the colonic wall is reversed compared to the stomach and intestine (Szurszewski and Farrugia, 2004). Finally, gastric slow waves entrain to a singular frequency in the healthy stomach, whereas in the intestine slow waves occur at multiple frequencies organized into plateaus along the length of the organ, each governed by an independent pacemaker, effectively forming a step-wise gradient of decreasing frequency along the intestine (Diamant and Bortoff, 1969; Lammers and Stephen, 2008; Angeli et al., 2013c). Previous reviews have covered studies that have attempted to unify all three aspects in a single model by prescribing parameters in the cell model to reproduce the intrinsic frequency, resting membrane potential gradients, and the conduction velocities in each region of the stomach (Du et al., 2010a, 2013). Recent modeling studies have now expanded on the whole-organ model to investigate the mechanisms of slow wave recovery and gastric dysrhythmias (Calder et al., 2016; Paskaranandavadivel et al., 2017).

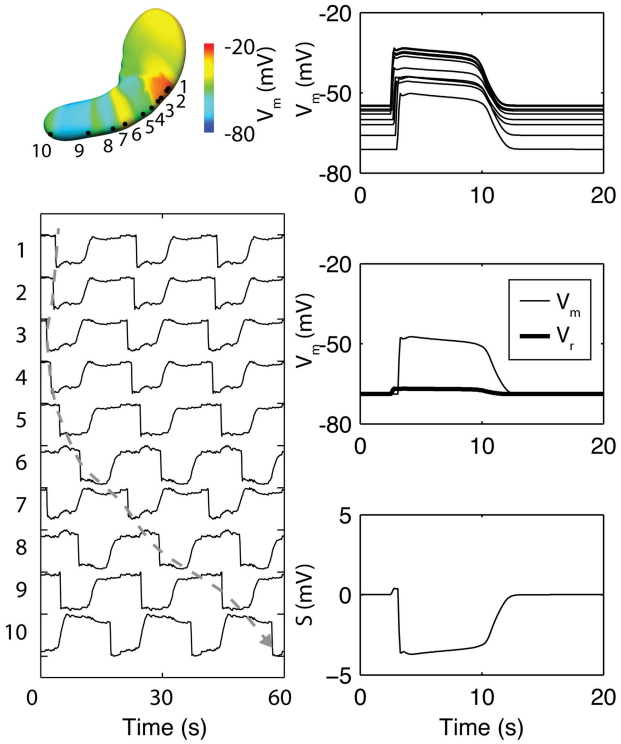

FIGURE 4 | Simulation of whole-organ gastric slow waves. **(A)** Gastric slow waves originate from a pacemaker region along the greater curvature in the proximal stomach. Simultaneous and multiple wavefronts occur in the stomach, with each propagating wavefront taking up to 60 s to reach to the terminal antrum. **(B)** The existence of resting membrane potential gradient in the stomach plays a key role to the recovery component in the extracellular signals, when calculated as a difference between membrane potential (V_m) and a spatially invariant term (V_r). Adapted from (Paskaranandavadivel et al., 2017).

In a notable recent study, the basis of the slow wave refractory/recovery was explored by sampling simulated slow waves from 96 solution points sampled over a whole-organ model (Paskaranandavadivel et al., 2017). The unipolar potential recorded in standard extracellular mapping techniques was simulated as a combination of a local component, i.e., membrane potential, and a spatially-independent component based on a scaled average of the residuals between the local component and the extracellular potentials from the whole-organ (**Figure 4**; Paskaranandavadivel et al., 2017). The simulations demonstrated that the resting membrane potential gradient may be a significant contributor to the recovery phase of the gastric slow wave extracellular potential. Specifically focusing on the spatially-independent component (**Figure 4B**), the gradient of resting membrane potentials had the effect of "averaging out" the defined profile of the spatially-independent component, as also seen in the cardiac simulations (Potse et al., 2009). The result

was a pronounced recovery phase in the extracellular potential (**Figure 4B**).

Whole-organ gastric dysrhythmias were simulated by adding a stimulus driven protocol and/or conduction block based on the tissue models (Calder et al., 2016). Three dysrhythmias have been reproduced to date: re-entry, conduction block and ectopic pacemaker (**Figure 5**; see **Table 1** for definitions). Gastric re-entry was successfully invoked in the corpus where the distance between the refractory-depolarization of two subsequent waves is the longest, allowing more time for re-entry to develop. Both conduction blocks and ectopic pacemakers (of equal frequency to the entrainment frequency) were prescribed to the antrum, where the two dysrhythmias have been most commonly identified. The potential applications of these whole-organ gastric dysrhythmia models include investigations of forward and inverse modeling techniques, relating the effects of dysrhythmias with motility through computational fluid dynamic studies, and in identifying enhanced methods of gastric pacing (Berry et al., 2016).

Whole-organ modeling studies of slow waves have mainly focused on the stomach, where both *in vivo* and *in vitro* data are most abundant. With the development of a foundational gastric model, recent investigations have utilized this model to investigate detailed mechanisms for physiological recordings, as well as simulations of dynamic dysrhythmias over the entire organ. Similar intestinal models will likely be developed in idealized geometry segments, as the overall intestinal length of multiple meters poses a significant computational challenge to the current models that rely on a high spatial resolution of solution points (<0.3 mm). Furthermore, there is also uncertainty in whether some of the "abnormal" intestinal slow waves are truly dysrhythmic, or rather occur as stochastic behaviors as part of the natural pacemaking and/or dynamic interactions between intestinal slow wave plateaus (Parsons and Huizinga, 2016, 2017).

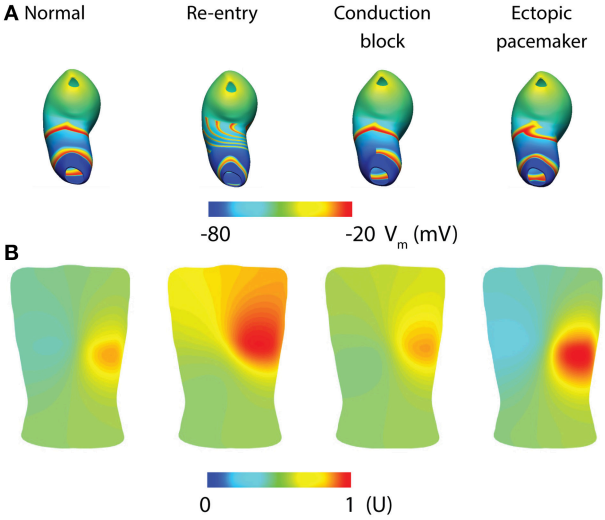

FIGURE 5 | Whole-organ gastric slow wave dysrhythmias and electrogastrography (EGG) simulations (Calder et al., 2016). **(A)** Four instance of gastric slow wave activation (normal, re-entry, conduction block in the antrum and ectopic pacemaker in the proximal stomach). **(B)** Corresponding EGG simulations are calculated using a forward approach over an anatomically realistic torso, with the EGG potentials normalized (U).

Non-Invasive Recordings

One of the ultimate aims of GI slow wave recordings is the ability to more reliably interpret slow wave activities non-invasively from the body surface. For gastric slow waves, the interpretation has principally been done through cutaneous recordings known as electrogastrography (EGG) (Bortolotti, 1998). It is also possible to detect the magnetic fields associated with the generation of slow waves with a superconducting quantum interference device (SQUID) using a technique called magnetogastrography (MGG) (Somarajan et al., 2015; Bradshaw et al., 2016b). Modeling investigations on both techniques have been ongoing as our understanding of the detailed activation sequence of gastric slow waves has improved. In particular, investigators are increasingly focusing on multi-channel/high-resolution EGG for detecting the underlying gastric slow wave propagation (Gharibans et al., 2016).

Given the relatively low signal-to-noise ratio of EGG, and the complexity of the underlying sources, investigators have long struggled with reliably separating the EGG signal component from other sources, e.g., respiration interference and cardiac electrical activity, though signal processing techniques have recently been developed to minimize these contaminants (Komorowski and Tkacz, 2015; Komorowski and Pietraszek, 2016). As a result, the sensitivity and specificity of the EGG has remained suboptimal, limiting clinical uptake. Mathematical modeling offers an attractive platform to assist in further development, because it can provide a "noise free" environment in which simulated EGG can be directly matched with gastric slow waves, provided that the correct slow wave behaviors are reproduced. A recent modeling investigation studied the EGG associated with normal and dysrhythmias gastric slow waves as demonstrated by high-resolution mapping (Calder et al., 2016). The whole-organ simulations were conducted as outlined in the whole-organ section of this review above (**Figure 5A**). The network activation of the whole-organ slow waves was represented using a dipole, which was placed inside an anatomically-realistic model of the adult torso with 192 cutaneous EGG electrodes (**Figure 5B**; Calder et al., 2016). EGG was modeled using the boundary-element method with the assumption of homogeneity inside the torso. The main finding was that, in addition to detecting the frequency of slow waves, it is also theoretically possible to detect and reliably distinguish spatial dysrhythmias (re-entry, conduction block, and ectopic pacemaker) using multi-channel (HR) EGG. Alternatively, slow wave activation has also been modeled as a 1D propagation source, and EGG calculated as a weighted summation of slow waves at every instance in time (Gharibans et al., 2016). Crucially, this study also used surface Laplacian and wave estimation techniques to determine the direction and propagation of slow waves from EGG recorded from eight human subjects (Gharibans et al., 2016). The clinical significance of these interesting recent developments will be more clear once the ability to interpret clinical EGG recordings improves.

The relationship between slow wave dysrhythmias and MGG has been validated experimentally with gastric disease

models and intestinal ischemia (Bradshaw et al., 2007, 2016a; Somarajan et al., 2015). Investigators have resolved the theoretical relationship of MGG to normal gastric slow wave activation. One recent study compared the surface current density method and a second-order blind source separation method to the theoretical prediction of the source location based on a dipole, and found close agreement with the measurements and the predicted data (Bradshaw et al., 2016b). This study also raised the question of whether gastric slow waves can be well captured using a single dipole, or better represented by multiple dipoles to track the simultaneous propagating wavefronts.

The current progress in non-invasive recording techniques is mirrored with the improved understanding of the underlying gastric slow wave activation. The technical capabilities of inferring data from multiple channels are allowing more quantifiable techniques to be applied to EGG and MGG. Most simulation studies in this field have updated their source to represent a more realistic activation pattern based on experimental data. However, questions will always remain regarding the sensitivity of the EGG and MGG until experimental studies can definitively prove that the EGG and MGG can be related to specific spatial activation states of gastric slow waves, beyond just a frequency correlation, which will require simultaneous HR recordings from the stomach and body-surface. In addition, reliable protocols for invoking specific types of dysrhythmias in a consistent manner are also still needed to determine the relationship between EGG/MGG and dysrhythmias. One potential such method, for example, is through high-energy gastric pacing to create a stable ectopic activation (Du et al., 2009b; O'Grady et al., 2010b; Sathar et al., 2015).

SIMULATION ENVIRONMENTS AND STANDARDS

As models increase in scale there is an associated increase in the computational cost in order to solve these models. This is especially important in GI modeling because the time-scale is typically orders of magnitudes higher than neural and cardiac simulations (milliseconds to minutes vs. milliseconds). Furthermore, as models gain sophistication it is ever more important to develop a standard by which these models can be encoded and reproduced in a consistent manner, as well as for encapsulation of meta-data. To this end, a number of standards and simulation tools have been developed (**Table 4**). The list of tools in **Table 4** is by no means exhaustive, but is listed to highlight some examples of the available modeling standards and tools. One important reason for adopting similar standards is to allow rapid exchange of information and reproducibility of simulation results.

TABLE 4 | Examples of markup standards for encoding models and simulation environments.

Name	Programming language	Purpose
CellML (Lloyd et al., 2004) www.cellml.org	XML	Encoding subcellular and cellular processes
SBML (Chaouiya et al., 2013) http://sbml.org	XML	Systems Biology Markup Language for encoding subcellular and cellular processes
FieldML (Christie et al., 2009) www.fieldml.org	XML	Modeling and interchanging spatially-varying field parameters.
CMISS www.cmiss.org	Fortran	A multi-scale simulation tool.
OpenCMISS (Bradley et al., 2011) http://opencmiss.org/	Fortran	A distributed parallel mathematical modeling environment for multi-scale simulations.
Chaste (Pitt-Francis et al., 2008) http://www.cs.ox.ac.uk/chaste/	C/C++	A distributed parallel mathematical modeling environment for multi-scale simulations.
Continuity http://www.continuity.ucsd.edu	Python	Multi-scale modeling and data analysis

FINAL REMARKS AND FUTURE DIRECTION

Mathematical modeling of GI electrophysiology has seen remarkable progress in recent years. While still lacking the depth of detailed understanding in physiological and pathological mechanisms that exists in the cardiac and neural fields, the recent advance in cellular slow wave mechanisms and the detailed spatiotemporal descriptions of gastric spatial dysrhythmias have enabled a new focus and level of impact for many GI modeling studies. As new knowledge of cellular ion channelopathies and tissue degradation in diseases becomes available (Beyder and Farrugia, 2016), existing models can be updated with improved specificity to understand a particular pathology, infer its influence on the organ through multi-scale modeling, and determine detectability through non-invasive recording methodologies.

As biological modeling is often informed by experimental data, the focus on technical setup in experiments is becoming increasingly important. For example, EGG and MGG at the body surface have different signal characteristics compared to the signals recorded by direct contact on the serosal surface. Therefore, more consideration needs to be given to the choice of amplifiers and signal processing techniques. Inappropriate applications of recording and/or processing techniques could lead to incorrect interpretation of signals (Paskaranandavadivel et al., 2013). Furthermore, there is a danger of relying on recordings at one scale to interpret recordings obtained at a different scale. For example, some investigators have incorrectly discussed how the slow wave signals recorded using extracellular mapping do not appear to have the same rate of change as the intracellular recordings obtained from individual cells (Sanders et al., 2016). This interpretation relies on the false presumption that the extracellular serosal recordings directly accord with the activation of an individual cell, which is not

the case in practice (Angeli et al., 2013a; O'Grady et al., 2017).

The role of the structure-function relationship of ICC and smooth muscles in GI dysrhythmias is a critical current question in clinical GI motility. Structural imaging and calcium functional recordings have both pointed to a strong relationship between the spatial distribution of ICC/cellular manipulations and loss of synchronicity of calcium activities and motility (Singh et al., 2014; Malysz et al., 2017), which are associated with slow wave dysrhythmias. At present, imaging and functional recording techniques are applied in isolation. It would be of great value to develop a foundational modeling framework that can integrate the experimental data from different modalities using biophysically-based models. Previous modeling investigations have attempted simulating slow wave propagation over a small-scale ICC network, either obtained from imaging data or using network generation algorithms (Du et al., 2010b; Gao et al., 2015). Validation for these studies was difficult because functional recording of the tissue-specific networks was not available at the time. With the advent of ratiometric Ca^{2+} imaging in live GI tissues (Singh et al., 2014; Malysz et al., 2017), it is now possible to compare the simulated intracellular Ca^{2+} activities that accompany slow wave generation to experimental data under varied physiological conditions.

The capability of recording Ca^{2+} transients at the tissue level could also lead to the development of new electromechanical models (Du et al., 2011; Singh et al., 2014; Malysz et al., 2017). This is critical because motility is a functional consequence of slow wave activation, and ICC have been shown to exhibit significant mechano-sensitivity (Beyder et al., 2010), which has been studied using a mathematical cell model (Poh et al., 2012). Both a passive constitutive model and an active tension model should be developed in order to translate the electromechanical coupling to the tissue level. Experiments based on biaxial stretch of the GI tissues are needed to quantify the parameters for the constitutive models, while a steady-state tension–length–calcium relationship could be adapted to define the active tension model. Perturbations to ion channel and tissue conductances could then be prescribed to the electrometrical models to simulate dysmotility. When translated to the whole-organ level, the simulated deformation of the GI wall could be used as a boundary condition input to computational fluid dynamic simulations of the mixing and breakdown of luminal contents due to different motility patterns (Fullard et al., 2014).

In summary, recent GI mathematical models have increased in sophistication and their ability to simulate key physiological mechanisms. These models have been applied in a predictive manner, across multiple biophysical scales, to begin to address some of the long-standing questions in the GI field, including the mechanisms, significance, and non-invasive diagnostics of gastric dysrhythmias. The progress of models relating to slow wave dysrhythmias is encouraging to date. However, as both experimental and technical capabilities within the field continue to improve, models will be better informed and validated by additional types of data. In turn, mathematical models of GI slow wave activity will continue to provide an ever-expanding platform for an integrative understanding of experimental data across multiple modalities.

AUTHOR CONTRIBUTIONS

PD: manuscript preparation, study design. SC, TA, GO, NP, SS and LC: manuscript preparation. SS and NP contributed to drafting and preparation of the manuscript.

ACKNOWLEDGMENTS

This work was funded in part by grants from the National Institutes of Health (R01 DK64775), Health Research Council of New Zealand, New Zealand Medical Technologies Center of Research Excellence (MedTech CoRE), and the Riddet Institute. PD is supported by a Rutherford Discovery Fellowship administered by the Royal Society of New Zealand. SC is supported by the Andrew Pullan Doctoral Scholarship. TA is supported by an Edith C. Coan Postdoctoral Fellowship from the Auckland Medical Research Foundation.

REFERENCES

Angeli, T. R., Cheng, L. K., Du, P., Wang, T. H., Bernard, C. E., Vannucchi, M. G., et al. (2015). Loss of interstitial cells of cajal and patterns of gastric dysrhythmia in patients with chronic unexplained nausea and vomiting. *Gastroenterology 149*, 56-66 e5. doi: 10.1053/j.gastro.2015.04.003

Angeli, T. R., Du, P., Paskaranandavadivel, N., Janssen, P. W., Beyder, A., Lentle, R. G., et al. (2013a). The bioelectrical basis and validity of gastrointestinal extracellular slow wave recordings. *J. Physiol.* 591, 4567–479. doi: 10.1113/jphysiol.2013.254292

Angeli, T. R., O'Grady, G., Du, P., Paskaranandavadivel, N., Pullan, A. J., Bissett, I. P., et al. (2013c). Circumferential and functional re-entry of *in vivo* slow-wave activity in the porcine small intestine. *Neurogastroenterol. Motil.* 25, e304–e314. doi: 10.1111/nmo.12085

Angeli, T. R., O'Grady, G., Paskaranandavadivel, N., Erickson, J. C., Du, P., Pullan, A. J., et al. (2013b). Experimental and automated analysis techniques for high resolution electrical mapping of small intestine slow wave activity. *J. Neurogastroenterol. Motil.* 19, 179–191. doi: 10.5056/jnm.2013.19.2.179

Atia, J., McCloskey, C., Shmygol, A. S., Rand, D. A., H. A., van den Berg, and Blanks, A. M. (2016). Reconstruction of cell surface densities of ion pumps, exchangers, and channels from mRNA expression, conductance kinetics, whole-cell calcium, and current-clamp voltage recordings, with an application to human uterine smooth muscle cells. *PLoS Comput. Biol.* 12:e1004828. doi: 10.1371/journal.pcbi.1004828

Bennett, M. R., Farnell, L., and Gibson, W. G. (2005). A quantitative model of purinergic junctional transmission of calcium waves in astrocyte networks. *Biophys. J.* 89, 2235–2250. doi: 10.1529/biophysj.105.062968

Berry, R., Cheng, L. K., Du, P., Paskaranandavadivel, N., Angeli, T. R., Mayne, T., et al. (2017). Patterns of abnormal gastric pacemaking after sleeve gastrectomy defined by laparoscopic high-resolution electrical mapping. *Obes. Surg.* 27, 1929–1937. doi: 10.1007/s11695-017-2597-6

Berry, R., Miyagawa, T., Paskaranandavadivel, N., Du, P., Angeli, T. R., Trew, M. L., et al. (2016). Functional physiology of the human terminal antrum defined by high-resolution electrical mapping and computational modeling. *Am. J. Physiol. Gastrointest. Liver Physiol.* 311, G895–G902. doi: 10.1152/ajpgi.00255.2016

Beyder, A., and Farrugia, G. (2016). Ion channelopathies in functional GI disorders. *Am. J. Physiol. Gastrointest. Liver Physiol.* 311, G581–G586. doi: 10.1152/ajpgi.00237.2016

Beyder, A., Rae, J. L., Bernard, C., Strege, P. R., Sachs, F., and Farrugia, G. (2010). Mechanosensitivity of Nav1.5, a voltage-sensitive sodium channel. *J. Physiol.* 588, 4969–4985. doi: 10.1113/jphysiol.2010.199034

Bortolotti, M. (1998). Electrogastrography: a seductive promise, only partially kept. *Am. J. Gastroenterol.* 93, 1791–1794. doi: 10.1111/j.1572-0241.1998.01791.x

Bradley, C., Bowery, A., Britten, R., Budelmann, V., Camara, O., Christie, R., et al. (2011). OpenCMISS: a multi-physics & multi-scale computational infrastructure for the VPH/Physiome project. *Prog. Biophys. Mol. Biol.* 107, 32–47. doi: 10.1016/j.pbiomolbio.2011.06.015

Bradshaw, L. A., Cheng, L. K., Chung, E., Obioha, C. B., Erickson, J. C., Gorman, B. L., et al. (2016a). Diabetic gastroparesis alters the biomagnetic signature of the gastric slow wave. *Neurogastroenterol. Motil.* 28, 837–848. doi: 10.1111/nmo.12780

Bradshaw, L. A., Kim, J. H., Somarajan, S., Richards, W. O., and Cheng, L. K. (2016b). Characterization of electrophysiological propagation by multichannel sensors. *IEEE Trans. Biomed. Eng.* 63, 1751–1759. doi: 10.1109/TBME.2015.2502065

Bradshaw, L. A., Sims, J. A., and Richards, W. O. (2007). Noninvasive assessment of the effects of glucagon on the gastric slow wave. *Am. J. Physiol. Gastrointest. Liver Physiol.* 293, G1029–G1038. doi: 10.1152/ajpgi.00054.2007

Buist, M. L., and Poh, Y. C. (2010). An extended bidomain framework incorporating multiple cell types. *Biophys. J.* 99, 13–18. doi: 10.1016/j.bpj.2010.03.054

Bull, S. H., O'Grady, G., Cheng, L. K., and Pullan, A. J. (2011). A framework for the online analysis of multi-electrode gastric slow wave recordings. *Conf. Proc. IEEE Eng. Med. Biol. Soc.* 2011, 1741–1744. doi: 10.1109/IEMBS.2011.6090498

Calder, S., O'Grady, G., Cheng, L., and Du, P. (2016). A theoretical analysis of electrogastrography (EGG) signatures associated with gastric dysrhythmias. *IEEE Trans. Biomed. Eng.* 64, 1592–1601. doi: 10.1109/TBME.2016.2614277

Chaouiya, C., Berenguier, D., Keating, S. M., Naldi, A., van Iersel, M. P., Rodriguez, N., et al. (2013). SBML qualitative models: a model representation format and infrastructure to foster interactions between qualitative modelling formalisms and tools. *BMC Syst. Biol.* 7:135. doi: 10.1186/1752-0509-7-135

Chen, C. L., Lin, H. H., Huang, L. C., Huang, S. C., and Liu, T. T. (2004). Electrogastrography differentiates reflux disease with or without dyspeptic symptoms. *Dig. Dis. Sci.* 49, 715–719. doi: 10.1023/B:DDAS.0000030079.20501.62

Cheng, L. K., Du, P., and O'Grady, G. (2013). Mapping and modeling gastrointestinal bioelectricity: from engineering bench to bedside. *Physiology* 28, 310–317. doi: 10.1152/physiol.00022.2013

Christie, G. R., Nielsen, P. M., Blackett, S. A., Bradley, C. P., and Hunter, P. J. (2009). FieldML: concepts and implementation. *Philos. Trans. A Math. Phys. Eng. Sci.* 367, 1869–1884. doi: 10.1098/rsta.2009.0025

Code, C. F., and Marlett, J. A. (1974). Canine tachygastria. *Mayo Clin. Proc.* 49, 325–332.

Coleski, R., and Hasler, W. L. (2009). Coupling and propagation of normal and dysrhythmic gastric slow waves during acute hyperglycaemia in healthy humans. *Neurogastroenterol Motil* 21, 492-9, e1–2. doi: 10.1111/j.1365-2982.2008.01235.x

Corrias, A., and Buist, M. L. (2007). A quantitative model of gastric smooth muscle cellular activation. *Ann. Biomed. Eng.* 35, 1595–1607. doi: 10.1007/s10439-007-9324-8

Corrias, A., and Buist, M. L. (2008). Quantitative cellular description of gastric slow wave activity. *Am. J. Physiol. Gastrointest. Liver Physiol.* 294, G989–G995. doi: 10.1152/ajpgi.00528.2007

Corrias, A., Pathmanathan, P., Gavaghan, D. J., and Buist, M. L. (2012). Modelling tissue electrophysiology with multiple cell types: applications of the extended bidomain framework. *Integr. Biol.* 4, 192–201. doi: 10.1039/c2ib00100d

Debinski, H. S., Ahmed, S., Milla, P. J., and Kamm, M. A. (1996). Electrogastrography in chronic intestinal pseudoobstruction. *Dig. Dis. Sci.* 41, 1292–1297. doi: 10.1007/BF02088549

Diamant, N. E., and Bortoff, A. (1969). Nature of the intestinal slow-wave frequency gradient. *Am. J. Physiol.* 216, 301–307.

Du, P., Hameed, A., Angeli, T. R., Lahr, C., Abell, T. L., Cheng, L. K., et al. (2015a). The impact of surgical excisions on human gastric slow wave conduction, defined by high-resolution electrical mapping and in silico modeling. *Neurogastroenterol. Motil.* 27, 1409–1422. doi: 10.1111/nmo.12637

Du, P., O'Grady, G., and Cheng, L. K. (2017). A theoretical analysis of anatomical and functional intestinal slow wave re-entry. *J. Theor. Biol.* 425, 72–79. doi: 10.1016/j.jtbi.2017.04.021

Du, P., O'Grady, G., Cheng, L. K., and Pullan, A. J. (2010a). A multiscale model of the electrophysiological basis of the human electrogastrogram. *Biophys. J.* 99, 2784–2792. doi: 10.1016/j.bpj.2010.08.067

Du, P., O'Grady, G., Egbuji, J. U., Lammers, W. J., Budgett, D., Nielsen, P., et al. (2009a). High-resolution mapping of *in vivo* gastrointestinal slow wave activity using flexible printed circuit board electrodes: methodology and validation. *Ann. Biomed. Eng.* 37, 839–846. doi: 10.1007/s10439-009-9654-9

Du, P., O'Grady, G., Gao, J., Sathar, S., and Cheng, L. K. (2013). Toward the virtual stomach: progress in multiscale modeling of gastric electrophysiology and motility. *Wiley Interdiscip. Rev. Syst. Biol. Med.* 5, 481–493. doi: 10.1002/wsbm.1218

Du, P., O'Grady, G., Gibbons, S. J., Yassi, R., Lees-Green, R., Farrugia, G., et al. (2010b). Tissue-specific mathematical models of slow wave entrainment in wild-type and 5-HT(2B) knockout mice with altered interstitial cells of Cajal networks. *Biophys. J.* 98, 1772–1781. doi: 10.1016/j.bpj.2010.01.009

Du, P., O'Grady, G., Paskaranandavadivel, N., Tang, S. J., Abell, T., and Cheng, L. K. (2016a). Simultaneous anterior and posterior serosal mapping of gastric slow-wave dysrhythmias induced by vasopressin. *Exp. Physiol.* 101, 1206–1217. doi: 10.1113/EP085697

Du, P., O'Grady, G., Windsor, J. A., Cheng, L. K., and Pullan, A. J. (2009b). A tissue framework for simulating the effects of gastric electrical stimulation and *in vivo* validation. *IEEE Trans. Biomed. Eng.* 56, 2755–2761. doi: 10.1109/TBME.2009.2027690

Du, P., Paskaranandavadivel, N., Angeli, T. R., Cheng, L. K., and O'Grady, G. (2016b). The virtual intestine: *in silico* modeling of small intestinal electrophysiology and motility and the applications. *Wiley Interdiscip. Rev. Syst. Biol. Med.* 8, 69–85. doi: 10.1002/wsbm.1324

Du, P., Paskaranandavadivel, N., O'Grady, G., Tang, S. J., and Cheng, L. K. (2015b). A theoretical study of the initiation, maintenance and termination of gastric slow wave re-entry. *Math. Med. Biol.* 32, 405–423. doi: 10.1093/imammb/dqu023

Du, P., Poh, Y. C., Lim, J. L., Gajendiran, V., O'Grady, G., Buist, M. L., et al. (2011). A preliminary model of gastrointestinal electromechanical coupling. *IEEE Trans. Biomed. Eng.* 58, 3491–3495. doi: 10.1109/TBME.2011.2166155

Egbuji, J. U., G., O'grady, Du, P., Cheng, L. K., Lammers, W. J., Windsor, J. A., et al. (2010). Origin, propagation and regional characteristics of porcine gastric slow wave activity determined by high-resolution mapping. *Neurogastroenterol. Motil.* 22, e292–300. doi: 10.1111/j.1365-2982.2010.01538.x

Familoni, B. O., Kingma, Y. J., and Bowes, K. L. (1987). Study of transcutaneous and intraluminal measurement of gastric electrical activity in humans. *Med. Biol. Eng. Comput.* 25, 397–402. doi: 10.1007/BF02443360

Farrugia, G., Lei, S., Lin, X., Miller, S. M., Nath, K. A., Ferris, C. D., et al. (2003). A major role for carbon monoxide as an endogenous hyperpolarizing factor in the gastrointestinal tract. *Proc. Natl. Acad. Sci. U.S.A.* 100, 8567–8570. doi: 10.1073/pnas.1431233100

Fullard, L., Lammers, W., Wake, G. C., and Ferrua, M. J. (2014). Propagating longitudinal contractions in the ileum of the rabbit–efficiency of advective mixing. *Food Funct.* 5, 2731–2742. doi: 10.1039/C4FO00487F

Gao, J., Sathar, S., O'Grady, G., Archer, R., and Cheng, L. K. (2015). A Stochastic algorithm for generating realistic virtual interstitial cell of Cajal networks. *IEEE Trans. Biomed. Eng.* 62, 2070–2078. doi: 10.1109/TBME.2015.2412533

Gharibans, A. A., Kim, S., Kunkel, D., and Coleman, T. P. (2016). High-resolution electrogastrogram: *a* novel, noninvasive method for determining gastric slow-wave direction and speed. *IEEE Trans. Biomed. Eng.* 64, 807–815. doi: 10.1109/TBME.2016.2579310

Gizzi, A., Cherubini, C., Migliori, S., Alloni, R., Portuesi, R., and Filippi, S. (2010). On the electrical intestine turbulence induced by temperature changes. *Phys. Biol.* 7:16011. doi: 10.1088/1478-3975/7/1/016011

Gonlachanvit, S., Chen, Y. H., Hasler, W. L., Sun, W. M., and Owyang, C. (2003). Ginger reduces hyperglycemia-evoked gastric dysrhythmias in healthy humans: possible role of endogenous prostaglandins. *J. Pharmacol. Exp. Ther.* 307, 1098–1103. doi: 10.1124/jpet.103.053421

Hasler, W. L., Soudah, H. C., Dulai, G., and Owyang, C. (1995). Mediation of hyperglycemia-evoked gastric slow-wave dysrhythmias by endogenous prostaglandins. *Gastroenterology* 108, 727–736. doi: 10.1016/0016-5085(95)90445-X

Huizinga, J. D., Chen, J. H., Zhu, Y. F., Pawelka, A., McGinn, R. J., Bardakjian, B. L., et al. (2014). The origin of segmentation motor activity in the intestine. *Nat. Commun.* 5, 3326. doi: 10.1038/ncomms4326

Kelly, K. A., and Code, C. F. (1971). Canine gastric pacemaker. *Am. J. Physiol.* 220, 112–118. doi: 10.1152/ajplegacy.1971.220.1.112

Kim, J. H., Du, P., and Cheng, L. K. (2013). Reconstruction of normal and abnormal gastric electrical sources using a potential based inverse method. *Physiol. Meas.* 34, 1193–1206. doi: 10.1088/0967-3334/34/9/1193

Kim, M. S., Chey, W. D., Owyang, C., and Hasler, W. L. (1997). Role of plasma vasopressin as a mediator of nausea and gastric slow wave dysrhythmias in motion sickness. *Am. J. Physiol.* 272, G853–G862. doi: 10.1152/ajpgi.1997.272.4.G853

Koch, K. L., Stern, R. M., Vasey, M., Botti, J. J., Creasy, G. W., and Dwyer, A. (1990). Gastric dysrhythmias and nausea of pregnancy. *Dig. Dis. Sci.* 35, 961–968. doi: 10.1007/BF01537244

Komorowski, D., and Pietraszek, S. (2016). The Use of Continuous wavelet transform based on the fast fourier transform in the analysis of multi-channel electrogastrography recordings. *J. Med. Syst.* 40, 10. doi: 10.1007/s10916-015-0358-4

Komorowski, D., and Tkacz, E. (2015). A new method for attenuation of respiration artifacts in electrogastrographic (EGG) signals. *Conf. Proc. IEEE Eng. Med. Biol. Soc.* 2015, 6006–6009. doi: 10.1109/EMBC.2015.7319760

Kurahashi, M., Nakano, Y., Hennig, G. W., Ward, S. M., and Sanders, K. M. (2012). Platelet-derived growth factor receptor alpha-positive cells in the tunica muscularis of human colon. *J. Cell. Mol. Med.* 16, 1397–1404. doi: 10.1111/j.1582-4934.2011.01510.x

Lammers, W. J. (2013). Arrhythmias in the gut. *Neurogastroenterol. Motil.* 25, 353–357. doi: 10.1111/nmo.12116

Lammers, W. J., el-Kays, A., Manefield, G. W., Arafat, K., and el-Sharkawy, T. Y. (1997). Disturbances in the propagation of the slow wave during acute local ischaemia in the feline small intestine. *Eur. J. Gastroenterol. Hepatol.* 9, 381–388. doi: 10.1097/00042737-199704000-00012

Lammers, W. J., Michiels, B., Voeten, J., Ver Donck, L., and Schuurkes, J. A. (2008a). Mapping slow waves and spikes in chronically instrumented conscious dogs: automated on-line electrogram analysis. *Med. Biol. Eng. Comput.* 46, 121–129. doi: 10.1007/s11517-007-0294-7

Lammers, W. J., and Stephen, B. (2008). Origin and propagation of individual slow waves along the intact feline small intestine. *Exp. Physiol.* 93, 334–346. doi: 10.1113/expphysiol.2007.039180

Lammers, W. J., Stephen, B., and Karam, S. M. (2012). Functional reentry and circus movement arrhythmias in the small intestine of normal and diabetic rats. *Am. J. Physiol. Gastrointest. Liver Physiol.* 302, G684–G689. doi: 10.1152/ajpgi.00332.2011

Lammers, W. J., Stephen, B. S., and Karam, S. M. (2015). Slow wave dysrhythmias in the diabetic small intestine. *Neurogastroenterol. Motil.* 27, 1344. doi: 10.1111/nmo.12608

Lammers, W. J., Ver Donck, L., Stephen, B., Smets, D., and Schuurkes, J. A. (2008b). Focal activities and re-entrant propagations as mechanisms of gastric tachyarrhythmias. *Gastroenterology* 135, 1601–1611. doi: 10.1053/j.gastro.2008.07.020

Leahy, A., Besherdas, K., Clayman, C., Mason, I., and Epstein, O. (1999). Abnormalities of the electrogastrogram in functional gastrointestinal disorders. *Am. J. Gastroenterol.* 94, 1023–1028. doi: 10.1111/j.1572-0241.1999.01007.x

Leahy, A., Besherdas, K., Clayman, C., Mason, I., and Epstein, O. (2001). Gastric dysrhythmias occur in gastro-oesophageal reflux disease complicated by food regurgitation but not in uncomplicated reflux. *Gut* 48, 212–215. doi: 10.1136/gut.48.2.212

Lees-Green, R., Du, P., O'Grady, G., Beyder, A., Farrugia, G., and Pullan, A. J. (2011). Biophysically based modeling of the interstitial cells of cajal: current status and future perspectives. *Front. Physiol.* 2:29. doi: 10.3389/fphys.2011.00029

Lien, H. C., Sun, W. M., Chen, Y. H., Kim, H., Hasler, W., and Owyang, C. (2003). Effects of ginger on motion sickness and gastric slow-wave dysrhythmias induced by circular vection. *Am. J. Physiol. Gastrointest. Liver Physiol.* 284, G481–G489. doi: 10.1152/ajpgi.00164.2002

Lim, H. C., Lee, S. I., Chen, J. D., and Park, H. (2012). Electrogastrography associated with symptomatic changes after prokinetic drug treatment for functional dyspepsia. *World J. Gastroenterol.* 18, 5948–5956. doi: 10.3748/wjg.v18.i41.5948

Lin, X., and Chen, J. Z. (2001). Abnormal gastric slow waves in patients with functional dyspepsia assessed by multichannel electrogastrography. *Am. J. Physiol. Gastrointest. Liver Physiol.* 280, G1370–G1375. doi: 10.1152/ajpgi.2001.280.6.G1370

Lin, Z. Y., McCallum, R. W., Schirmer, B. D., and Chen, J. D. (1998). Effects of pacing parameters on entrainment of gastric slow waves in patients with gastroparesis. *Am. J. Physiol.* 274, G186–G191. doi: 10.1152/ajpgi.1998.274.1.G186

Linkens, D. A. (1978). Canine colonic pacing and coupled oscillator synchronization [proceedings]. *J. Physiol.* 278, 26P-27P.

Linkens, D. A., and Mhone, P. G. (1979). Frequency transients in a coupled oscillator model of intestinal myoelectrical activity. *Comput. Biol. Med.* 9, 131–144. doi: 10.1016/0010-4825(79)90029-5

Lloyd, C. M., Halstead, M. D., and Nielsen, P. F. (2004). CellML: its future, present and past. *Prog. Biophys. Mol. Biol.* 85, 433–450. doi: 10.1016/j.pbiomolbio.2004.01.004

Maltsev, A. V., Maltsev, V. A., and Stern, M. D. (2017). Clusters of calcium release channels harness the Ising phase transition to confine their elementary intracellular signals. *Proc. Natl. Acad. Sci. U.S.A.* 114, 7525–7530. doi: 10.1073/pnas.1701409114

Malysz, J., Gibbons, S. J., Saravanaperumal, S. A., Du, P., Eisenman, S. T., Cao, C., et al. (2017). Conditional genetic deletion of Ano1 in interstitial cells of Cajal impairs Ca^{2+} transients and slow waves in adult mouse small intestine. *Am. J. Physiol. Gastrointest. Liver Physiol.* 312, G228–G245. doi: 10.1152/ajpgi.00363.2016

Marriott, H. J. (1984). Arrhythmia versus dysrhythmia. *Am. J. Cardiol.* 53, 628. doi: 10.1016/0002-9149(84)90043-2

McNearney, T. A., Sallam, H. S., Hunnicutt, S. E., Doshi, D., Wollaston, D. E., Mayes, M. D., et al. (2009). Gastric slow waves, gastrointestinal symptoms and peptides in systemic sclerosis patients. *Neurogastroenterol. Motil.* 21, 1269–e120. doi: 10.1111/j.1365-2982.2009.01350.x

Nelsen, T. S., and Kohatsu, S. (1968). Clinical electrogastrography and its relationship to gastric surgery. *Am. J. Surg.* 116, 215–222. doi: 10.1016/0002-9610(68)90496-0

O'Grady, G., Angeli, T. R., Du, P., Lahr, C., Lammers, W. J., Windsor, J. A., et al. (2012a). Abnormal initiation and conduction of slow-wave activity in gastroparesis, defined by high-resolution electrical mapping. *Gastroenterology* 143, 589-98 e1–e3. doi: 10.1053/j.gastro.2012.05.036

O'Grady, G., Du, P., Cheng, L. K., Egbuji, J. U., Lammers, W. J., Windsor, J. A., et al. (2010a). Origin and propagation of human gastric slow-wave activity defined by high-resolution mapping. *Am. J. Physiol. Gastrointest. Liver Physiol.* 299, G585–G592. doi: 10.1152/ajpgi.00125.2010

O'Grady, G., Du, P., Lammers, W. J., Egbuji, J. U., Mithraratne, P., Chen, J. D., et al. (2010b). High-resolution entrainment mapping of gastric pacing: a new analytical tool. *Am. J. Physiol. Gastrointest. Liver Physiol.* 298, G314–G321. doi: 10.1152/ajpgi.00389.2009

O'Grady, G., Du, P., Paskaranandavadivel, N., Angeli, T. R., Lammers, W. J., Asirvatham, S. J., et al. (2012b). Rapid high-amplitude circumferential slow wave propagation during normal gastric pacemaking and dysrhythmias. *Neurogastroenterol. Motil.* 24, e299–e312. doi: 10.1111/j.1365-2982.2012.01932.x

O'Grady, G., Paskaranandavadivel, N., Du, P., Angeli, T., Erickson, J. C., and Cheng, L. K. (2017). Correct techniques for extracellular recordings of electrical activity in gastrointestinal muscle. *Nat. Rev. Gastroenterol. Hepatol.* 14, 372. doi: 10.1038/nrgastro.2017.15

O'Grady, G., Wang, T. H., Du, P., Angeli, T., Lammers, W. J., and Cheng, L. K. (2014). Recent progress in gastric arrhythmia: pathophysiology, clinical significance and future horizons. *Clin. Exp. Pharmacol. Physiol.* 41, 854–862. doi: 10.1111/1440-1681.12288

Ordog, T., Takayama, I., Cheung, W. K., Ward, S. M., and Sanders, K. M. (2000). Remodeling of networks of interstitial cells of Cajal

in a murine model of diabetic gastroparesis. *Diabetes* 49, 1731–1739. doi: 10.2337/diabetes.49.10.1731

Owyang, C., and Hasler, W. L. (2002). Physiology and pathophysiology of the interstitial cells of Cajal: from bench to bedside. VPathogenesis, I and therapeutic approaches to human gastric dysrhythmias. *Am. J. Physiol. Gastrointest. Liver Physiol.* 283, G8–G15. doi: 10.1152/ajpgi.00095.2002

Parkman, H. P., Hasler, W. L., Barnett, J. L., and Eaker, E. Y. (2003). Electrogastrography: a document prepared by the gastric section of the American motility society clinical GI motility testing task force. *Neurogastroenterol. Motil.* 15, 89–102. doi: 10.1046/j.1365-2982.2003.00396.x

Parsons, S. P., and Huizinga, J. D. (2016). Spatial noise in coupling strength and natural frequency within a pacemaker network; consequences for development of intestinal motor patterns according to a weakly coupled phase oscillator model. *Front. Neurosci.* 10:19. doi: 10.3389/fnins.2016.00019

Parsons, S. P., and Huizinga, J. D. (2017). The phase response and state space of slow wave contractions in the small intestine. *Exp. Physiol.* 102, 1118–1132. doi: 10.1113/EP086373

Paskaranandavadivel, N., Cheng, L. K., Du, P., Rogers, J. M., and O'Grady, G. (2017). High-resolution mapping of gastric slow wave recovery profiles: biophysical model, methodology and demonstration of applications. *Am. J. Physiol. Gastrointest. Liver Physiol.* 313, G265–G276. doi: 10.1152/ajpgi.00127.2017

Paskaranandavadivel, N., O'Grady, G., and Du, P. (2013). Comparison of filtering methods for extracellular gastric slow wave recordings. *Neurogastroenterol. Motil.* 25, 79–83. doi: 10.1111/nmo.12012

Pfaffenbach, B., Adamek, R. J., Bartholomaus, C., and Wegener, M. (1997). Gastric dysrhythmias and delayed gastric emptying in patients with functional dyspepsia. *Dig. Dis. Sci.* 42, 2094–2099. doi: 10.1023/A:1018826719628

Pitt-Francis, J., Bernabeu, M. O., Cooper, J., Garny, A., Momtahan, L., Osborne, J., et al. (2008). Chaste: using agile programming techniques to develop computational biology software. *Philos. Trans. A Math. Phys. Eng. Sci.* 366, 3111–3136. doi: 10.1098/rsta.2008.0096

Plank, G., Burton, R. A., Hales, P., Bishop, M., Mansoori, T., Bernabeu, M. O., et al. (2009). Generation of histo-anatomically representative models of the individual heart: tools and application. *Philos. Trans. A Math. Phys. Eng. Sci.* 367, 2257–2292. doi: 10.1098/rsta.2009.0056

Poh, Y. C., Beyder, A., Strege, P. R., Farrugia, G., and Buist, M. L. (2012). Quantification of gastrointestinal sodium channelopathy. *J. Theor. Biol.* 293, 41–48. doi: 10.1016/j.jtbi.2011.09.014

Potse, M., Vinet, A., Opthof, T., and Coronel, R. (2009). Validation of a simple model for the morphology of the T wave in unipolar electrograms. *Am. J. Physiol. Heart Circ. Physiol.* 297, H792–801. doi: 10.1152/ajpheart.00064.2009

Sachse, F. B., Moreno, A. P., Seemann, G., and Abildskov, J. A. (2009). A model of electrical conduction in cardiac tissue including fibroblasts. *Ann. Biomed. Eng.* 37, 874–889. doi: 10.1007/s10439-009-9667-4

Sanders, K. M., Ward, S. M., and Hennig, G. W. (2016). Problems with extracellular recording of electrical activity in gastrointestinal muscle. *Nat. Rev. Gastroenterol. Hepatol.* 13, 731–774. doi: 10.1038/nrgastro.2016.161

Sathar, S., Trew, M. L., Du, P., O'Grady, G., and Cheng, L. K. (2014). A biophysically based finite-state machine model for analyzing gastric experimental entrainment and pacing recordings. *Ann. Biomed. Eng.* 42, 858–870. doi: 10.1007/s10439-013-0949-5

Sathar, S., Trew, M. L., O. G. G., and Cheng, L. K. (2015). A Multiscale tridomain model for simulating bioelectric gastric pacing. *IEEE Trans. Biomed. Eng.* 62, 2685–2692. doi: 10.1109/TBME.2015.2444384

Schaap, H. M., Smout, A. J., and Akkermans, L. M. (1990). Myoelectrical activity of the Billroth II gastric remnant. *Gut* 31, 984–988. doi: 10.1136/gut.31.9.984

Simonian, H. P., Panganamamula, K., Chen, J. Z., Fisher, R. S., and Parkman, H. P. (2004). Multichannel electrogastrography (EGG) in symptomatic patients: a single center study. *Am. J. Gastroenterol.* 99, 478–485. doi: 10.1111/j.1572-0241.2004.04103.x

Singh, R. D., Gibbons, S. J., Saravanaperumal, S. A., Du, P., Hennig, G. W., Eisenman, S. T., et al. (2014). Ano1, a Ca^{2+}-activated Cl- channel, coordinates contractility in mouse intestine by Ca^{2+} transient coordination between interstitial cells of Cajal. *J. Physiol.* 592, 4051–4068. doi: 10.1113/jphysiol.2014.277152

Somarajan, S., Muszynski, N. D., Cheng, L. K., Bradshaw, L. A., Naslund, T. C., and Richards, W. O. (2015). Noninvasive biomagnetic detection of intestinal slow wave dysrhythmias in chronic mesenteric ischemia. *Am. J. Physiol. Gastrointest. Liver Physiol.* 309, G52–G58. doi: 10.1152/ajpgi.00466.2014

Stern, R. M., Koch, K. L., Stewart, W. R., and Lindblad, I. M. (1987). Spectral analysis of tachygastria recorded during motion sickness. *Gastroenterology* 92, 92–97. doi: 10.1016/0016-5085(87)90843-2

Szurszewski, J. H. (1998). A 100-year perspective on gastrointestinal motility. *Am. J. Physiol.* 274, G447–G453. doi: 10.1152/ajpgi.1998.274.3.G447

Szurszewski, J. H., and Farrugia, G. (2004). Carbon monoxide is an endogenous hyperpolarizing factor in the gastrointestinal tract. *Neurogastroenterol. Motil.* 16(Suppl. 1), 81–85. doi: 10.1111/j.1743-3150.2004.00480.x

Trommer, P. R. (1982). Cardiolocution and dysrhythmia. *Am. J. Cardiol.* 50, 1198. doi: 10.1016/0002-9149(82)90445-3

van Helden, D. F., Laver, D. R., Holdsworth, J., and Imtiaz, M. S. (2010). Generation and propagation of gastric slow waves. *Clin. Exp. Pharmacol. Physiol.* 37, 516–524. doi: 10.1111/j.1440-1681.2009.05331.x

Wei, R., Parsons, S. P., and Huizinga, J. D. (2017). Network properties of interstitial cells of Cajal affect intestinal pacemaker activity and motor patterns, according to a mathematical model of weakly coupled oscillators. *Exp. Physiol.* 102, 329–346. doi: 10.1113/EP086077

Yeoh, J. W., Corrias, A., and Buist, M. L. (2016). A mechanistic model of a PDGFRalpha(+) cell. *J. Theor. Biol.* 408, 127–136. doi: 10.1016/j.jtbi.2016.08.004

Yeoh, J. W., Corrias, A., and Buist, M. L. (2017). Modelling human colonic smooth muscle cell electrophysiology. *Cell. Mol. Bioeng.* 10, 186–197. doi: 10.1007/s12195-017-0479-6

Conflict of Interest Statement: PD, TA, NP, GO, and LC hold intellectual property/patent applications in the field of mapping gastrointestinal electrophysiology. PD, TA, NP, SS, GO, LC are shareholders in FlexiMap. No commercial or industry funding was provided for this work.

frontiers in Physics

ORIGINAL RESEARCH
published: 10 October 2017
doi: 10.3389/fphy.2017.00048

A Cell-Based Framework for Numerical Modeling of Electrical Conduction in Cardiac Tissue

Aslak Tveito[1,2]*, *Karoline H. Jæger*[1], *Miroslav Kuchta*[1,3], *Kent-Andre Mardal*[1,3] *and Marie E. Rognes*[1]

[1] Simula Research Laboratory, Center for Biomedical Computing, Lysaker, Norway, [2] Department of Informatics, University of Oslo, Oslo, Norway, [3] Department of Mathematics, University of Oslo, Oslo, Norway

In this paper, we study a mathematical model of cardiac tissue based on explicit representation of individual cells. In this EMI model, the extracellular (E) space, the cell membrane (M), and the intracellular (I) space are represented as separate geometrical domains. This representation introduces modeling flexibility needed for detailed representation of the properties of cardiac cells including their membrane. In particular, we will show that the model allows ion channels to be non-uniformly distributed along the membrane of the cell. Such features are difficult to include in classical homogenized models like the monodomain and bidomain models frequently used in computational analyses of cardiac electrophysiology. The EMI model is solved using a finite difference method (FDM) and two variants of the finite element method (FEM). We compare the three schemes numerically, reporting on CPU-efforts and convergence rates. Finally, we illustrate the distinctive capabilities of the EMI model compared to classical models by simulating monolayers of cardiac cells with heterogeneous distributions of ionic channels along the cell membrane. Because of the detailed representation of every cell, the computational problems that result from using the EMI model are much larger than for the classical homogenized models, and thus represent a computational challenge. However, our numerical simulations indicate that the FDM scheme is optimal in the sense that the computational complexity increases proportionally to the number of cardiac cells in the model. Moreover, we present simulations, based on systems of equations involving ∼117 million unknowns, representing up to ∼16,000 cells. We conclude that collections of cardiac cells can be simulated using the EMI model, and that the EMI model enable greater modeling flexibility than the classical monodomain and bidomain models.

Keywords: transmembrane potential, finite difference method, finite element method, cell modeling, conduction velocity

OPEN ACCESS

Edited by:
Christian F. Klingenberg, University of Würzburg, Germany

Reviewed by:
Edward Joseph Vigmond, Université de Bordeaux, France
Edoardo Milotti, University of Trieste, Italy

***Correspondence:**
Aslak Tveito
aslak@simula.no

Specialty section:
This article was submitted to Computational Physics, a section of the journal Frontiers in Physics

Received: *21 June 2017*
Accepted: *25 September 2017*
Published: *10 October 2017*

Citation:
Tveito A, Jæger KH, Kuchta M, Mardal K-A and Rognes ME (2017) A Cell-Based Framework for Numerical Modeling of Electrical Conduction in Cardiac Tissue. Front. Phys. 5:48. doi: 10.3389/fphy.2017.00048

1. INTRODUCTION

The pumping function of the heart is governed by an electrochemical wave traversing the entire cardiac muscle resulting in the muscle's synchronized contraction. This electrochemical wave has been subject to intense study over many decades and mathematical models have played an essential role in understanding its properties. However, these models are based on homogenization of the

cardiac tissue, which imposes limitations on the level of detail that can be studied by the models. For instance, the details of the dynamics surrounding a single cell are difficult to study using classical homogenized models simply because the single cell is not present in such models.

In this paper, we consider an emerging mathematical modeling framework for representing and simulating excitable cells in general and cardiac cells in particular. In this framework, the extracellular space, the cell membranes, and the intracellular spaces are explicitly represented as separate physical and geometrical objects. The state variables are the extracellular, membrane, and intracellular potentials defined over the corresponding domains. We refer to this framework as the EMI (Extracellular-Membrane-Intracellular) model. This approach has been applied in several earlier papers (e.g., [1–7]), which used the EMI framework (or related approaches) for detailed simulations of a single cell or a small number of cells. Indeed, the presentation here is very much motivated by the formulation presented by Stinstra et al. [5] and by Agudelo-Toro and Neef [4]. Furthermore, the EMI approach was used to study the effect of the ephaptic coupling of neurons in Tveito et al. [8].

The EMI framework represents an alternative to the classical and more common bidomain or monodomain models. These latter models are based on homogenization of the cardiac tissue and the extracellular space, the intracellular space, and the cell membrane are all assumed to exist everywhere (e.g., [9–13]). In the following, when we refer to homogenized models, we will refer to models of the monodomain or bidomain type. In contrast, the EMI approach avoids this full homogenization at the tissue level. Note however, that homogenization is also used in the EMI approach to formulate equations for the intracellular domain and the extracellular domain.

The classical models (monodomain, bidomain) have been successfully used to study the propagation of the electrochemical wave in cardiac tissue (e.g., [14–16]), the initiation of excitation waves (e.g., [17–21]), the development of cardiac arrhythmias (e.g., [14, 17, 18]), the effect of defibrillation (e.g., [22–28]), and the effect of various drugs (e.g., [29–32]).

Despite the many successful applications of the monodomain and bidomain models, there are a number of motivating factors for introducing a more explicit, more accurate, and more detailed framework for modeling cardiac tissue. We address some of these factors in the following paragraphs.

1.1. Homogenized Models May Be Insufficient to Represent Details of the Remodeling of the Heart

Although, classical models represent the big picture of the electrochemical wave traversing cardiac tissue well, they may fail to reveal the finer details of cardiac conduction. For example, it is well-established that local perturbations to the conduction velocity may be arrhythmogenic; in particular, slowed conduction will increase the risk of arrhythmias [33]. It is therefore essential to understand how various remodelings of the heart affect the conduction velocity. Individual perturbations of the size and shape of the cardiac cells clearly affect the conduction velocity (e.g., [34]), but such changes are very hard to represent in a classical homogenized model, since a detailed representation of the individual cells in the tissue is needed. Furthermore, local density distributions of ion channels on the cell membrane will affect local conduction properties and such effects are also very hard, if even possible, to represent in the classical models.

1.2. Homogenized Models Are Unsuitable for Addressing the Ephaptic Coupling of Cardiac Cells

The electrical conduction of the heart is believed to depend on direct cell-to-cell contact realized in terms of gap junctions (e.g., [35–37]). These connections are reduced under heart failure, resulting in impaired conduction velocity that may in turn increase the probability of arrhythmias (e.g., [37, 38]). However, even when conduction through gap junctions is significantly reduced, electrical signals are still conducted (e.g., [39]). This conduction is believed to rely on ephaptic coupling between neighboring cells via the extracellular space. The effect depends on the shape and size of the extracellular space and is thus not directly amenable to analysis via the homogenized bidomain or monodomain models.

1.3. Simulating Cell Monolayers is of Increasing Significance

The number of cardiomyocytes in the human ventricles can be estimated to be around 8 billion (e.g., [40]), and the number is close to 4 million for the mouse heart (e.g., [41]). In both cases, a homogenized model may be justified by the large number of cells involved. However, for experimental setups with monolayers of cardiac cells, the number of cells is much lower (hundreds or a few thousands) and the validity of the homogenized continuum approach becomes questionable. The EMI model, on the other hand, is very well suited, since it represents every individual cell. The ability to faithfully simulate monolayers of cardiac cells has become very important since it has become possible to simultaneously measure the transmembrane potential and the intracellular calcium concentration (e.g., [42]). Therefore, at least in principle, the inversion of spatial models of monolayers may be applied to characterize properties of single cells using monolayer experiments. This is particularly important because of the development of human induced pluripotent stem cells (hi-PSC). Based on skin samples, such cells can be used to derive cardiac cells with certain properties identical to a patient's cardiac cells. Therefore, this technology is believed to have great potential in the development of personalized drugs for rare diseases (e.g., [43–45]).

1.4. Available Computational Power Allows for Cell Size Resolution

Twenty-five years ago, the best mathematical model of cardiac tissue was solved using 257 computational nodes [12, 46]. At that time, an accurate representation of cardiac tissue in terms of the representation of individual cells was inconceivable for reasons of both storage and computing time. This has changed dramatically; in recent computational studies, 29 million computational nodes

were used to represent cardiac tissue [27, 47]. The computational mesh size in these simulations was about 59 μm, which should be compared with 100 μm, the typical length of a cardiac cell. This means that current simulators of the electrophysiology of the heart are, at least in principle, able to resolve features at the individual cell level.

The main purpose of the present paper is to assess the computational challenges of the EMI modeling framework. We will show how the model's complexity increases as the number of cardiac cells in the simulations increases and how the complexity of the membrane model affects the overall CPU demands.Furthermore, we will demonstrate that the EMI framework opens the possibility of simulating local properties of the cell that are hard to represent in homogenized models.

We introduce an operator splitting scheme for the EMI model and propose and compare three numerical schemes for the discretization of the resulting partial differential equations (PDEs): one finite difference-based (FDM) and two finite element-based (FEM) schemes of various degrees of complexity, computational cost, and accuracy. We compare the three schemes numerically in terms of convergence rates and computational cost. Moreover, to illustrate the distinctive capabilities of the EMI model, we present new results for simulating monolayers of cardiac cells with spatially heterogeneous distributions of ionic channels across the cell membrane.

Our results demonstrate that the EMI approach is computationally feasible: We can solve systems relevant for simulating monolayers of cardiac cells with sufficient resolution. Moreover, we show, using numerical computations based on the FDM code, that the computational effort per cell is bounded independently of the number of cardiac cells, and thus that the effort increases at most linearly with the number of cells.

1.5. Outline

In the next section, we will present the EMI model and three numerical methods used to solve the model. Next, we will discuss the numerical accuracy of the solutions, show convergence under mesh refinements, and assess the methods' CPU demands. To illustrate the ability to model local properties of individual cells, we present an example showing the difference in the conduction velocity of cells with uniform and non-uniform distributions of sodium channels. In the final sections, the results will be summarized and discussed.

2. MODELS AND METHODS

In this section, we present the EMI model and numerical methods for solving the corresponding set of equations.

2.1. The EMI Model

We will use the EMI model to simulate collections of cardiac cells. However, to present the model, it is sufficient to consider the case of two coupled cells.

We assume that the complete computational domain consists of intracellular spaces Ω_i^k, with $k = 1, 2$ in the case of two cells, that are connected by gap junctions $\Gamma_{1,2}$ and surrounded by a connected extracellular space Ω_e. The membrane is defined to be the intersection between each intracellular domain Ω_i^k and the extracellular domain and is denoted by Γ_k, while the remaining boundary of the extracellular domain is denoted by $\partial\Omega_e$. **Figure 1** illustrates a two-dimensional (2D) version of this setup, showing two connected cells surrounded by extracellular space. In our computations (except in the first simple test case with an analytical solution) all cells are 3D and the cells can be connected in one-, two-, or three-dimensional collections. In one-dimensional strands of cells, the cell coupling is as illustrated in **Figure 1**; for two and three-dimensional collections of cells, the coupling in the y- and z-directions are similar to the x-coupling illustrated in the figure.

For the case illustrated in **Figure 1**, the EMI model can be formulated as follows: Find the extracellular potential u_e defined over Ω_e, the intracellular potentials u_i^k defined over Ω_i^k, and the transmembrane potentials v^k defined over Γ_k for $k = 1, 2$ and w defined over $\Gamma_{1,2}$ satisfying

$$\nabla \cdot \sigma_e \nabla u_e = 0 \qquad \text{in } \Omega_e, \tag{1}$$

$$\nabla \cdot \sigma_i \nabla u_i^k = 0 \qquad \text{in } \Omega_i^k, \tag{2}$$

$$u_e = 0 \qquad \text{at } \partial\Omega_e, \tag{3}$$

$$n_e \cdot \sigma_e \nabla u_e = -n_i^k \cdot \sigma_i \nabla u_i^k \equiv I_m^k \qquad \text{at } \Gamma_k, \tag{4}$$

$$u_i^k - u_e = v^k \qquad \text{at } \Gamma_k, \tag{5}$$

$$v_t^k = \frac{1}{C_m}(I_m^k - I_{\text{ion}}^k) \qquad \text{at } \Gamma_k, \tag{6}$$

$$n_i^2 \cdot \sigma_i \nabla u_i^2 = -n_i^1 \cdot \sigma_i \nabla u_i^1 \equiv I_{1,2} \qquad \text{at } \Gamma_{1,2}, \tag{7}$$

$$u_i^1 - u_i^2 = w \qquad \text{at } \Gamma_{1,2}, \tag{8}$$

$$w_t = \frac{1}{C_{1,2}}(I_{1,2} - I_{\text{gap}}) \qquad \text{at } \Gamma_{1,2}, \tag{9}$$

for $k = 1, 2$. Here, n_e is the normal pointing out from Ω_e and n_i^k is the (outward) normal pointing out from Ω_i^k for $k = 1, 2$; σ_i and σ_e are the intracellular and extracellular conductivities, respectively; I_{ion}^k represents the ionic current density, which typically depends on additional state variables such as ionic concentrations; and I_{gap} represents the gap junction current density. In terms of units, the potentials u_e, u_i^k, v^k, and w are given in mV; the current densities I_m^k, I_{ion}^k, $I_{1,2}$, and I_{gap} are given in μA/cm^2; the conductivities σ_i and σ_e are given in mS/cm; the capacitances C_m and $C_{1,2}$ are given in μF/cm^2; length is given in cm; and time is given in ms. In the following, we will refer to (1–9) as the EMI model. For brevity, we will write u_i in place of u_i^k, v in place of v^k, I_{ion} in place of I_{ion}^k and Γ in place of Γ_k for $k = 1, 2$ when context allows.

2.2. Membrane Model

In our computations, we will consider both a passive and an active model for the dynamics on the cell membrane between the intracellular and extracellular spaces. In the passive model, I_{ion} is given by the linear model

$$I_{\text{ion}}(v) = \frac{1}{R_m}(v - v_{\text{rest}}), \tag{10}$$

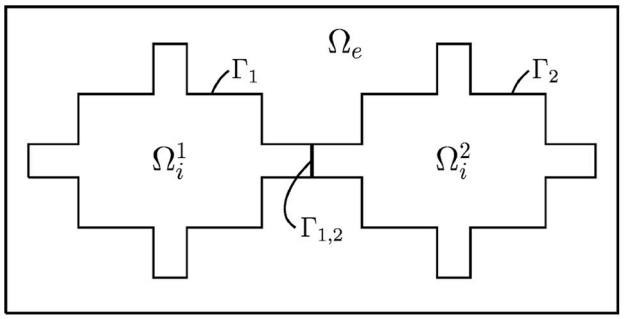

FIGURE 1 | Illustration of an idealized computational domain: two idealized cells Ω_i^1 and Ω_i^2 connected by a gap junction $\Gamma_{1,2}$ and the surrounding extracellular domain Ω_e.

where R_m represents the resistance of the passive membrane (in kΩcm^2) and v_{rest} denotes the resting potential of the membrane. In the active model, we let I_{ion} be represented by the action potential (AP) model of Grandi et al. [48]. In this case, Equation (6) is replaced by a system of the form

$$v_t = \frac{1}{C_m}(I_m - I_{\text{ion}}(v, s)), \tag{11}$$

$$s_t = F(v, s), \tag{12}$$

where v represents the membrane potential and s represents a collection of additional state variables introduced in the AP model. Furthermore, I_{ion} represents the sum of the ionic current densities across the membrane through a number of different types of ion channels, pumps, and exchangers and $F(v, s)$ represents the ordinary differential equations (ODEs) describing the dynamics of the additional state variables. The Grandi model is implemented by defining a membrane potential v and a set of state variables s for each of the membrane nodes of the mesh. We let all state variables of the Grandi model, including the intracellular ionic concentrations, be defined only on the mesh nodes located on the cell membrane, and we allow the value of these variables to vary for different membrane nodes located on the same cell. The values of the state variables are updated in each time step using an operator splitting scheme described below. Intracellular and extracellular gradients of the ionic concentrations are ignored (see comment in section 4).

Finally, we represent the gap junction between neighboring cells by a passive membrane:

$$I_{\text{gap}}(w) = \frac{1}{R_{\text{gap}}} w, \tag{13}$$

where R_{gap} represents the resistance of the passive membrane (in kΩcm^2). A discussion of the modeling of the gap-junctions is given in Hogues et al. [1] where a boundary element method is used to solve a model similar to the system (1–9).

2.3. Operator Splitting Scheme

The ionic current density I_{ion} entering the EMI model through (6) typically introduce a significant number of additional states [e.g., as in (11)]. For this reason, we consider an operator splitting approach to solve the EMI model defined by (1–9).

The system (1–9) is solved by first applying given initial conditions for v and w. Then, for each time step n, we assume that the solutions v^{n-1} and w^{n-1} are known for $t = t_{n-1}$ on Γ and $\Gamma_{1,2}$ respectively. We then find the solutions at $t = t_n$ using a two-step (first-order) operator splitting procedure, but note that a three-step (second-order) operator splitting could equally well be used (e.g., [11]).

In the first step, we update the solutions for the membrane potential by solving a system of ODEs of the form (11) and (12) over Γ with I_m set equal to zero. In the following numerical experiments, the ODE system (11) and (12) is solved by taking m forward Euler steps of size $\Delta t^* = \Delta t/m$ for each global time step, though any other suitable ODE scheme could be used.

In the second (PDE) step of the operator splitting procedure, we solve the linear system arising from an implicit discretization in time and space of (1–9) with I_{ion}^1 and I_{ion}^2 set to zero. For the discretization in time of (6) and (9), we use an implicit Euler scheme using the solution from the first (ODE) step of the operator splitting scheme as the previous state.

When a linear model for I_{ion} is considered, the first (ODE) step of the splitting scheme is redundant and thus omitted, and I_{ion}^k for $k = 1, 2$ is kept in the PDE step, altering the linear system to be solved.

We propose and compare three different approaches for the spatial discretization of the PDE step in this study, each presented in the following sections. For the numerical experiments, the finite difference method (FDM) was implemented directly in MATLAB, while the finite element methods (FEMs) were implemented using the FEniCS finite element library [49, 50]. All computations were run on a Dell PowerEdge R430 with dual Intel Xeon processors (E5-2623 v4 2.60 GHz) and 12 x 32 GB RDIMM; each processor runs four kernels with two threads each.

2.3.1. Finite Difference Method for Solving the EMI PDEs

We first consider a finite difference scheme for solving the PDE step of the EMI model as defined above. To simplify the notation, we describe here the 2D case only; the extension to three dimensions is immediate. The spatial discretization employed here is taken from Tveito et al. [8].

Figure 2 shows the four different types of nodes used in the computations. Nodes marked by $\times$ represent the extracellular domain. In these nodes, we define a single unknown, u_e. Similarly, nodes marked by $\circ$ represent the intracellular domain (either Ω_i^1 or Ω_i^2) and we define a single unknown u_i for these nodes. Nodes marked by $\otimes$ represent the membrane between the intracellular and the extracellular space ($\Gamma = \Gamma_1 \cup \Gamma_2$). For these nodes, we define three unknowns: u_e, u_i, and v, with $v = u_i - u_e$. Similarly, nodes marked by $\bullet$ represent the membrane between two cells and, for these nodes, we define the three unknowns u_i^1, u_i^2, and w, with $w = u_i^1 - u_i^2$.

We use the notation $u_e^{n,j,k}$ for the numerical solution of the extracellular potential, u_e, at the point $(x_j, y_k) = (j\Delta x, k\Delta y)$ at

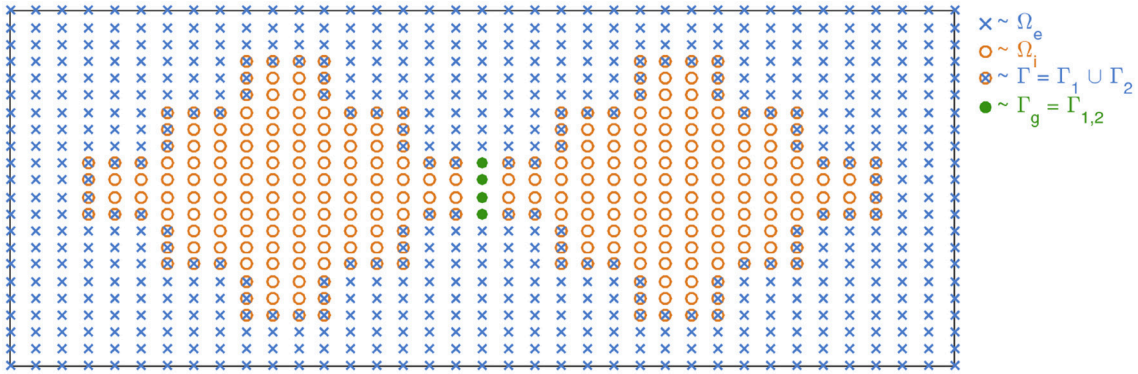

FIGURE 2 | Sketch of the computational mesh used for the FDM. Nodes in Ω_e are marked by ×, nodes in $\Omega_i = \Omega_i^1 \cup \Omega_i^2$ are marked by ○, nodes on the membrane between the intracellular and the extracellular space ($\Gamma = \Gamma_1 \cup \Gamma_2$) are marked by ⊗, and nodes on the membrane between two cells ($\Gamma_{1,2}$) are marked by ●.

time $t_n = n\Delta t$ and use an analogous notation for the numerical solution of the remaining variables.

We discretize (1) using the finite difference scheme

$$\frac{\sigma_e^{j+1/2,k}(u_e^{n,j+1,k} - u_e^{n,j,k}) - \sigma_e^{j-1/2,k}(u_e^{n,j,k} - u_e^{n,j-1,k})}{\Delta x^2} + \frac{\sigma_e^{j,k+1/2}(u_e^{n,j,k+1} - u_e^{n,j,k}) - \sigma_e^{j,k-1/2}(u_e^{n,j,k} - u_e^{n,j,k-1})}{\Delta y^2} = 0, \tag{14}$$

where $\sigma_e^{j+1/2,k} = \sigma_e((j+1/2)\Delta x, k\Delta y)$. Equation (2) is discretized similarly, with σ_e replaced by σ_i and u_e replaced by u_i.

On the membrane between the intracellular and extracellular domains, there are three unknowns and three equations. The first equation is given directly by (5) and the second equation is given by a first-order finite difference discretization of (4). Finally, the third equation is given by an implicit discretization of (6) of the form

$$\frac{v^{n,j,k} - v^{n-1/2,j,k}}{\Delta t} = \frac{1}{C_m} I_m^{n,j,k}, \tag{15}$$

where $I_m^{n,j,k}$ is a discrete version of the term $n_e \cdot \sigma_e \nabla u_e$ from (4) and $v^{n-1/2,j,k}$ is the solution of the membrane potential from the first step of the operator splitting procedure.

Similarly, for the nodes on the membrane between the cells, there are three unknowns and three equations. The first equation is given directly by (8), the second is a first-order finite difference discretization of (7), and the third is an implicit discretization of (9) of the form

$$\frac{w^{n,j,k} - w^{n-1,j,k}}{\Delta t} = \frac{1}{C_{1,2}} \left(I_{1,2}^{n,j,k} - I_{\text{gap}}(w^{n,j,k}) \right), \tag{16}$$

where $I_{1,2}^{n,j,k}$ is a discrete version of the term $n_i^2 \cdot \sigma_i \nabla u_i^2$ from (7) and $I_{\text{gap}}(w^{n,j,k})$ is a linear function of $w^{n,j,k}$ given by (13). It is worth mentioning here that if the gap junction dynamics is modeled using a non-linear model, operator splitting can be applied as was done for the membrane model.

Two special types of nodes require some special treatment. The first type is the nodes on the corners of the membrane. For these nodes, we define two flux terms $I_m^{n,j,k} = n_e \cdot \sigma_e \nabla u_e$, one for the normal derivative in the x direction and one for the normal derivative in the y direction, and we use the mean of these two terms in the equation of the form (15). Furthermore, in the flux equality Equation (4), we also define two intracellular flux terms, one for each direction, and let the sum of the two intracellular flux terms equal the sum of the two extracellular flux terms.

The second special node type is the extracellular nodes located next to a node on the membrane between two cells. In **Figure 2**, these are the two extracellular nodes just above or below $\Gamma_{1,2}$. For these nodes, we define a no-flux boundary condition between the extracellular node and the adjacent node on $\Gamma_{1,2}$. This is implemented by defining an extracellular potential for the node on the end of $\Gamma_{1,2}$ with a value equal to the extracellular potential in the node just outside $\Gamma_{1,2}$.

When considering a linear model for I_{ion}, we skip the first step of the operator splitting procedure and replace the equation of the form (15) in the finite difference scheme by

$$\frac{v^{n,j,k} - v^{n-1,j,k}}{\Delta t} = \frac{1}{C_m} \left(I_m^{n,j,k} - I_{\text{ion}}(v^{n,j,k}) \right). \tag{17}$$

A major drawback of the finite difference discretization is the fact that actual cell geometries are quite complex and virtually impossible to handle with this method. However, complex geometries can be resolved by the finite element method. In the following, we shall propose two different FEM formulations of the EMI Equations (1–9): the mortar finite element formulation, where the primary unknowns are the intra/extracellular potentials, and the H(div)-based finite element formulation, where the currents are the primary unknowns in the cells/tissue.

2.3.2. Mortar Finite Element Method for Solving the EMI PDEs

Mortar finite element methods ([51]; see also [4] for the application of the method in simulations of cell membranes)

allow for the coupling of different types of variational problems posed over non-overlapping domains by weakly (in an integral sense) enforcing interface conditions on common boundaries. For the EMI system, the Poisson problems (1) and (2) are coupled by the conditions (4) and (5) and the conditions (7) and (8).

Let V_e and V_i^k be spaces of functions over Ω_e and Ω_i^k for $k = 1, 2$, and let Q be a function space defined over $\Gamma = \Gamma_1 \cup \Gamma_2 \cup \Gamma_{1,2}$, to be precisely defined below. For any $\psi \in Q$, we denote by ψ^1, ψ^2 and $\psi^{1,2}$ the restriction of ψ to Γ_1, Γ_2, and $\Gamma_{1,2}$, respectively. With this notation, given $(v^k)^n$ and w^n at time level n, at each time level $n+1$ of the temporal discretization, we aim to find the membrane current density $J \in Q$, defined such that $J^k = I_m^k$ and $J^{1,2} = I_{1,2}$ and the extracellular and intracellular potentials $u_e \in V_e$ and $u_i^i \in V_i^k$ such that:

$$
\begin{aligned}
\int_{\Omega_i^1} \sigma_i \nabla u_i^1 \cdot \nabla \phi_i^1 \, \mathrm{d}x + \int_{\Gamma_1} J^1 \phi_i^1 \, \mathrm{d}s + \int_{\Gamma_{1,2}} J^{1,2} \phi_i^1 \, \mathrm{d}s = 0 \qquad & \forall \phi_i^1 \in V_i^1, \\
\int_{\Omega_i^2} \sigma_i \nabla u_i^2 \cdot \nabla \phi_i^2 \, \mathrm{d}x + \int_{\Gamma_2} J^2 \phi_i^2 \, \mathrm{d}s - \int_{\Gamma_{1,2}} J^{1,2} \phi_i^2 \, \mathrm{d}s = 0 \qquad & \forall \phi_i^2 \in V_i^2, \\
\int_{\Omega_e} \sigma_e \nabla u_e \cdot \nabla \phi_e \, \mathrm{d}x - \int_{\Gamma_1} J^1 \phi_e \, \mathrm{d}s - \int_{\Gamma_2} J^2 \phi_e \, \mathrm{d}s = 0 \qquad & \forall \phi_e \in V_e, \\
\int_{\Gamma_1} (u_i^1 - u_e) \psi^1 \, \mathrm{d}s - \frac{\Delta t}{C_m} \int_{\Gamma_1} J^1 \psi^1 \, \mathrm{d}s = \int_{\Gamma_1} (v^1)^n \psi^1 \, \mathrm{d}s \qquad & \forall \psi \in Q, \\
\int_{\Gamma_2} (u_i^2 - u_e) \psi^2 \, \mathrm{d}s - \frac{\Delta t}{C_m} \int_{\Gamma_2} J^2 \psi^2 \, \mathrm{d}s = \int_{\Gamma_1} (v^2)^n \psi^2 \, \mathrm{d}s \qquad & \forall \psi \in Q, \\
\int_{\Gamma_{1,2}} (u_i^1 - u_i^2) \psi^{1,2} \, \mathrm{d}s - \frac{\Delta t}{C_{1,2}} \int_{\Gamma_{1,2}} J^{1,2} \psi^{1,2} \, \mathrm{d}s = \int_{\Gamma_{1,2}} w^n \psi^{1,2} \, \mathrm{d}s \qquad & \forall \psi \in Q.
\end{aligned}
\tag{18}
$$

Here, the first three equations of the variational problem are obtained by multiplying (1) and (2) by test functions ϕ_e and ϕ_i^k and integrating over the associated domains while using conditions (4) and (7) in the integration by parts. The final three equations are then weakly enforcing the constraints

$$
u_i^k - u_e - \frac{\Delta t}{C_m} I_m^k = (v^k)^n \text{ on } \Gamma_i^k, \quad u_i^1 - u_i^2 - \frac{\Delta t}{C_{1,2}} I_{1,2} = w^n \text{ on } \Gamma_{1,2} \tag{19}
$$

which are obtained by a backward Euler discretization of (6) and (9) (cf. Equations 15 and 16) while expanding the transmembrane potentials of Γ_i^k and $\Gamma_{1,2}$ at the $(n+1)$th temporal level using definitions (5) and (8), respectively. We note that the definitions of the transmembrane potentials enter the variational problem only via (19). Moreover, the membrane current density J can be interpreted as the multiplier of the augmented Lagrangian associated with these constraints.

System (18) is the linear part of the operator splitting procedure described above. The well-posedness of the system (18) was established in Belgacem [52] or Lamichhane [53] for the stationary case, where it was shown that a unique solution exists in the Sobolev spaces $V_e = H^1_{0,\partial\Omega_e}(\Omega_e)$, $V_i^k = H^1(\Omega_i^k)$ and $Q = H^{-1/2}(\Gamma)$.

To discuss the finite element discretization of the well-posed problem (18), we denote by $\mathcal{T}_{e,h}$ and $\mathcal{T}_{i,h}^k$ simplicial meshes of the domains Ω_e and Ω_i^k, respectively. Generally, the mortar finite element approach allows the tessellations to be independent of one another and the elements of Γ_h, the triangulation of Γ, are defined in terms of facets of one of the sharing tessellations. For simplicity, we opt here for meshes such that they share facets on Γ (see **Figure 3**). In particular, the neighboring tessellations define identical meshes Γ_h.

In the following, the discrete finite element subspaces of V_e, V_i^k, and Q will be constructed from continuous piecewise linear Lagrange elements. More precisely, we let

$$
\begin{aligned}
V_{e,h} &= \left\{ v \in C(\mathcal{T}_{e,h});\, v|_K = P^1(K) \, \forall K \in \mathcal{T}_{e,h} \right\}, \\
V_{i,h}^k &= \left\{ v \in C(\mathcal{T}_{i,h}^k);\, v|_K = P^1(K) \, \forall K \in \mathcal{T}_{i,h}^k \right\}, \\
Q_h &= \left\{ v \in C(\Gamma_h);\, v|_K = P^1(K) \, \forall K \in \Gamma_h \right\}
\end{aligned}
$$

and thus the space Q_h is the trace space of the functions in $V_{e,h}$ and $V_{i,h}^k$. We refer to Wohlmuth [54] and references therein for proof of the numerical stability of this choice of discretization. We also note that the choice of element for the space Q_h simplifies the implementation, however, dual Lagrange multipliers (see [53, 54]), though more involved, are more suitable if static condensation is employed to solve the linear system arising from (18). Finally, in the numerical experiments, the scheme was implemented using the FEniCS$_{ii}$ extension [55] of the FEniCS finite element library [49, 50].

2.3.3. H(div)-Based Finite Element Method for Solving the EMI PDEs

The mortar finite element formulation defined above introduces separate function spaces for each of the intracellular domains Ω_i^k, which adds implementational complexity. As an alternative approach, we also consider an H(div)-based finite element method (e.g., [56]) for solving the PDE step of the operator splitting scheme. This scheme relaxes the continuity constraint for the potentials throughout the domain Ω and introduces *potential gradients* as additional variables with the appropriate normal continuity regularity for the associated currents. Therefore, the interface continuity conditions for the currents can be handled seamlessly.

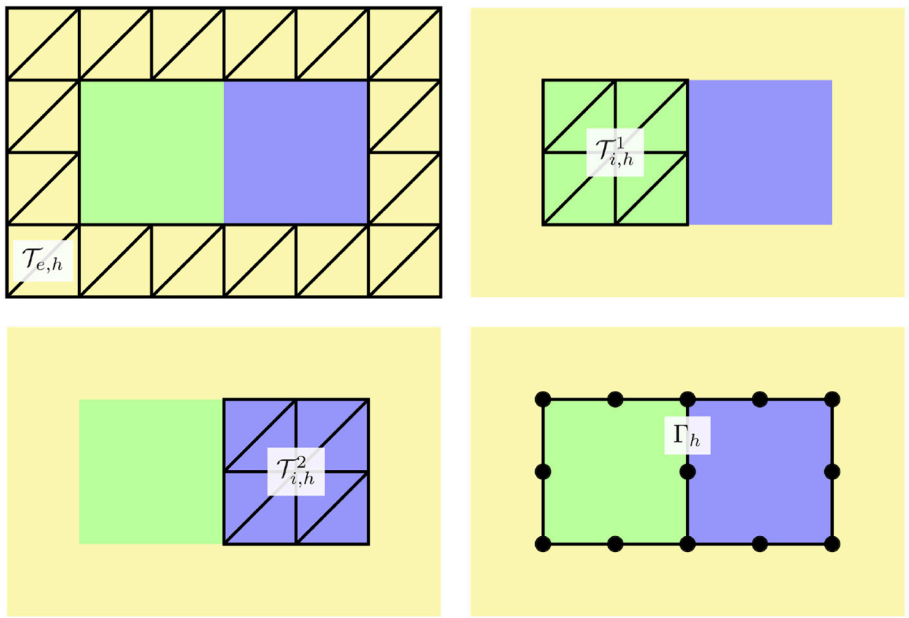

FIGURE 3 | Schematic representation of finite element meshes considered with the mortar element method: **(upper left)** the tesselation $\mathcal{T}_{e,h}$ of the extracellular domain, **(upper right and bottom left)** the tessellations $\mathcal{T}^1_{i,h}$ and $\mathcal{T}^2_{i,h}$ of the intracellular domains, and **(bottom right)** the membrane discretization Γ_h. In our implementation, $\mathcal{T}_{e,h}$ and $\mathcal{T}^k_{i,h}$ have identical facets on Γ and the facets define the finite element cells of Γ_h, see the location of the vertices of the 1D mesh depicted by black circles.

To this end, we use the intracellular current density vector $\hat{J}_i$ and the extracellular current density vector $\hat{J}_e$ as additional vector fields defined over Ω_i and Ω_e, respectively:

$$\hat{J}_i = -\sigma_i \nabla u_i, \quad \hat{J}_e = -\sigma_e \nabla u_e. \tag{20}$$

We let $\hat{J}$ denote the extension of $\hat{J}_i$ and $\hat{J}_e$ to Ω, and assume that $\hat{J}$ is in the space H(div, Ω), that is, $\hat{J}$ is a square-integrable vector field with square-integrable divergence. Furthermore, denote by u the extension of u_i and u_e to Ω, and analogously for σ. In addition, we define $\hat{v}$ as the extension of the transmembrane potential v and the transcellular potential w and we let $\hat{I}$ denote the extension of I_{ion} and I_{gap}. Thus the variable u is defined over Ω while $\hat{v}$ and $\hat{I}$ are defined over the whole interior membrane $\hat{\Gamma} = \Gamma_1 \cup \Gamma_2 \cup \Gamma_{1,2}$.

Let n_i denote the outward normal, from the intracellular domains to the extracellular domain, on Γ_k for $k = 1, 2$ and from Ω_i^1 to Ω_i^2 on $\Gamma_{1,2}$ and, analogously, let n_e denote the outward normal from the extracellular to the intracellular domains. By the flux continuity conditions (4) and (7), we require that $\hat{J}_i \cdot n_i = -\hat{J}_e \cdot n_e$ on Γ_k $(k = 1, 2)$ and analogously on $\Gamma_{1,2}$. Let $\hat{v}^{n,*}$ denote the membrane potential solution from the ODE step in the nonlinear case or the membrane solution $\hat{v}^{n,*} = \hat{v}_h^{n-1}$ at the previous time in the linear (no ODE) case.

With this notation and after an implicit Euler discretization in time, our H(div)-based finite element scheme at each time step n reads as follows: For given $v^{n,*}$, f^n, and g^n, find $u_h^n \in U_h$, $\hat{J}_h^n \in S_h$ and $\hat{v}_h^n \in V_h$ such that

$$-\int_\Omega \nabla \cdot \hat{J}_h^n \phi \, \mathrm{d}x = \int_\Omega f^n \phi \, \mathrm{d}x \; \forall \, \phi \in U_h, \tag{21}$$

$$\int_\Omega \left(\sigma^{-1} \hat{J}_h^n \cdot \tau - \nabla \cdot \tau \, u_h^n \right) \mathrm{d}x + \int_{\hat{\Gamma}} \tau \cdot n_i \, \hat{v}_h^n \, \mathrm{d}s = \int_\Omega g^n \cdot \tau \, \mathrm{d}x \; \forall \, \tau \in S_h, \tag{22}$$

$$\int_{\hat{\Gamma}} \left(C_m \hat{v}_h^n + \Delta t(-\hat{J}_h^n \cdot n_i + \alpha \hat{I}(\hat{v}_h^n)) \right) \beta \, \mathrm{d}s = \int_{\hat{\Gamma}} C_m \hat{v}^{n,*} \beta \, \mathrm{d}s \; \forall \, \beta \in V_h. \tag{23}$$

In the case of a nonlinear I_{ion}, we set $\alpha = 0$ and treat the non-linear term by operator splitting as outlined above.

In the numerical experiments, as for the mortar finite element method described in section 2.3.2, we let $\mathcal{T}_h$ denote a simplicial mesh of Ω conforming to Ω_i^k $(k = 1, 2)$ and Ω_e such that $\hat{\Gamma}_h$, the restriction of $\mathcal{T}_h$ to $\hat{\Gamma}$, defines a conforming mesh of $\hat{\Gamma}$ (of one topological dimension lower). Relative to these meshes, we define the spaces S_h as the lowest-order Raviart–Thomas elements defined over $\mathcal{T}_h$ and U_h as the space of (discontinuous) piecewise constants defined over $\mathcal{T}_h$, and V_h as the space of (discontinuous) piecewise constants defined over $\hat{\Gamma}_h$. The Raviart–Thomas elements are, by definition, such that the normal components of the vector fields are continuous across cell facets (edges in 2D, faces in 3D) and thus the flux continuity conditions (4) and (7) hold by construction [56].

This mixed finite element combination is conforming and our numerical experiments indicate that the element pairing is stable and convergent. The scheme can also be compared to the schemes discussed by Sacco [57]. Based on the interpolation properties of the lowest-order finite element spaces as described above, we expect to observe first-order convergence for u, $\hat{J}$, and $\hat{v}$ in the respective L^2 norms, and first-order convergence for $\hat{J}$ in the H(div) norm. Higher-order convergence in the L^2 norm of $\hat{J}$ can be recovered by using the Brezzi–Douglas–Marini [58] H(div) elements instead of the Raviart–Thomas family.

In the numerical experiments, this scheme was implemented using the FEniCS finite element library [49, 50].

2.4. Optimal Solvers

A common problem in scientific computing is to solve a linear PDE defined on a certain geometry. After applying some sort of discretization characterized by a mesh parameter h, the remaining problem is to solve a linear system of algebraic equations. The linear solution process is usually said to be order optimal provided that the number of floating point operations (FLOPs) required to solve the problem grows linearly in the number of unknowns as h decreases. For self-adjoint, linear PDEs, optimal solvers are well understood (e.g., see the review papers [59, 60] for the theory of saddle point problems). In simulating cardiac tissue, optimal solvers exist for both the monodomain model and the bidomain model (e.g., [11, 61, 62]).

Feynman [63] suggested an alternative, but related, definition of order optimality: Suppose a numerical method is used to simulate a small space–time volume of a physical process and the mesh is refined to convergence. Then computational complexity should only grow linearly as the space–time volume is increased. For our application, this definition is very well suited; we consider a single cell surrounded by an extracellular space, and we carry out numerical simulations to find the mesh resolution in time and space necessary to obtain convergence. Then we define a numerical solution as being order optimal provided that the CPU efforts only increase linearly in the number of biological cells in the computation.

3. RESULTS

In this section, we present applications of the methods introduced above. We start by assessing the accuracy of the numerical methods for a very simple unitless test problem where an analytical solution can be enforced using the method of manufactured solutions. For non-linear membrane dynamics, we explore convergence under mesh refinements. Next, we consider the CPU efforts needed to solve the numerical problems arising from the EMI model and we are particularly interested in the CPU effort per physical cell to understand the scalability of the EMI approach. For the FEM, we also show results for cylindrical geometries. Finally, we investigate the effect of non-uniform distributions of sodium channels along the cell membrane.

3.1. Model Parameters

In the first unitless test problem we consider a 2D domain consisting of an extracellular domain and a single cell. In the remaining simulations, we consider 3D domains consisting of a number of connected cells and the surrounding extracellular space. The coupled cells are organized as a single layer where the cells are connected to each other in a grid in the x and y directions by gap junctions. The shape and size of the cells and the extracellular domain will be specified for each simulation below. We primarily consider cells of the shape illustrated in **Figure 4**, where each part of the intracellular domain, Ω_O, Ω_W, Ω_E, Ω_S, and Ω_N, is shaped as a rectangular cuboid.

The parameter values used in the simulations are given in **Table 1** unless otherwise specified. Moreover, we use the initial condition $w = 0$ in all the simulations of connected cells. When the Grandi model is used to model I_{ion}, we mainly use the default initial conditions of the Grandi model for v and the remaining state variables. When a passive model is used for I_{ion}, we primarily use the initial condition $v = v_{\text{rest}}$.

3.2. Numerical Verification and Accuracy

3.2.1. Linear Ionic Current: Method of Manufactured Solutions

To evaluate the accuracy of the numerical methods, we construct an analytical solution for a 2D single-cell version of the EMI

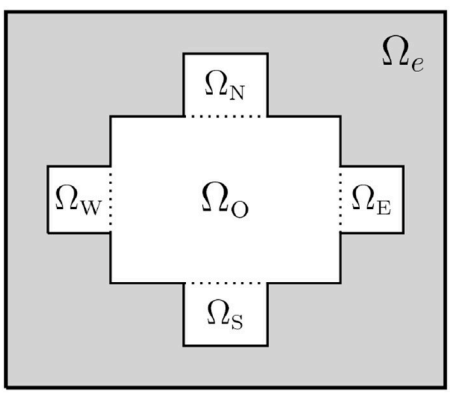

FIGURE 4 | Sketch of the 2D version of a domain in the case of a single cell. Here, $\Omega_i = \Omega_O \cup \Omega_W \cup \Omega_E \cup \Omega_S \cup \Omega_N$.

TABLE 1 | Default parameter values used in the simulations.

Parameter	Value	References
C_m	1 μF/cm^2	[64]
$C_{1,2}$	1 μF/cm^2	
σ_i	5 mS/cm	[65]
σ_e	20 mS/cm	[7]
v_{rest}	−85 mV	[66]
R_m	10 kΩcm^2	[64]
R_g	0.0015 kΩcm^2	[7]
Δx, Δy, Δz	2 μm	
Δt (PDE part)	0.1 ms	
Δt^* (ODE part)	0.001 ms	

For the parameters used in the Grandi model, we refer to Grandi et al. [48].

model with the passive model $I_{\text{ion}} = v$. The analytical solution of this simple example is constructed using the method of manufactured solutions (e.g., [67]). We consider a single cell surrounded by extracellular space:

$$\nabla \cdot \sigma_i \nabla u_i = f, \text{ in } \Omega_i, \tag{24}$$

$$\nabla \cdot \sigma_e \nabla u_e = g, \text{ in } \Omega_e, \tag{25}$$

$$u_e = 0, \text{ at } \partial\Omega_e, \tag{26}$$

$$n_e \cdot \sigma_e \nabla u_e = -n_i \cdot \sigma_i \nabla u_i, \text{ at } \Gamma, \tag{27}$$

$$u_i - u_e = v, \text{ at } \Gamma, \tag{28}$$

$$I_m = -n_i \cdot \sigma_i \nabla u_i, \text{ at } \Gamma, \tag{29}$$

$$v_t = \frac{1}{C_m}(I_m - I_{\text{ion}}), \text{ at } \Gamma. \tag{30}$$

For this case, we assume that the model is unitless with parameters $\sigma_i = \sigma_e = C_m = 1$, and we define the domain $\Omega = \Omega_i \cup \Omega_e = [0,1] \times [0,1]$, where $\Omega_i = [0.25, 0.75] \times [0.25, 0.75]$.

We let

$$f = f(x,y,t) = -8\pi^2 \sin(2\pi x)\sin(2\pi y)(1 + e^{-t}), \tag{31}$$

$$g = g(x,y,t) = -8\pi^2 \sin(2\pi x)\sin(2\pi y) \tag{32}$$

and the analytical solution of (24–30) is then given by

$$u_i(x,y,t) = (1 + e^{-t})\sin(2\pi x)\sin(2\pi y), \tag{33}$$

$$u_e(x,y,t) = \sin(2\pi x)\sin(2\pi y), \tag{34}$$

$$v(x,y,t) = e^{-t}\sin(2\pi x)\sin(2\pi y). \tag{35}$$

In the numerical experiments of this test case, we use $\Delta t = 0.01/n$, where for the FDM, n equals the number of intervals in each direction of the spatial discretization of the domain. In the FEM case, $2n^2$ is the number of triangles that constitute the uniformly discretized mesh. We note that the chosen time step criterion is not necessary for numerical stability of any of the methods. Rather, it was selected to yield more stable convergence rates. For this test case, the linear systems arising in the experiments are solved by direct solvers (LU factorization), and the errors are computed at time $t = 0.1$.

Table 2 shows the maximum error of the finite difference method as the discretization parameters are refined. We observe that the convergence rates of the intracellular and extracellular potentials u_h and the membrane potential v_h are both close to one, indicating that the maximum (L^∞) error of the FDM is $O(h)$.

In **Table 3**, we report the results obtained with the mortar FEM. The error of the potentials u_h is reported in the broken H^1 norm $\|u - u_h\|_1$, which is natural for the problem [53], the L^2 norm $\|u - u_h\|_0$ to enable comparison with the H(div) FEM, and the supremum norm $\|u - u_h\|_\infty$ to allow for comparison across different numerical methods. The error in the current density J_h is measured in the L^2 norm rather than the natural but more involved $H^{-1/2}$ norm. Finally, we report convergence of the membrane potential difference $\|v - v_h\|_\infty$, where v_h is obtained from the definition $u_{i,h} - u_{e,h} = v_h$ using the computed potentials. We note that the integral norms are evaluated by first interpolating the error in the space of discontinuous fourth-order polynomials. The supremum norms are then computed using linear polynomials.

TABLE 2 | Convergence of the finite difference method for the manufactured test problem with convergence rates in parentheses.

n	$\|u - u_h\|_\infty$	$\|v - v_h\|_\infty$
16	3.24E−01 (--)	1.21E−01 (--)
32	1.73E−01 (0.91)	7.24E−02 (0.75)
64	9.32E−02 (0.89)	3.98E−02 (0.86)
128	4.80E−02 (0.96)	2.09E−02 (0.93)
256	2.43E−02 (0.98)	1.07E−02 (0.96)
512	1.22E−02 (0.99)	5.44E−03 (0.98)

The convergence rates in row i are computed by $r = \frac{\log(E_i/E_{i-1})}{\log(h_i/h_{i-1})}$, *where* E_i *is the maximum error of u or v in row i and* h_i *is the value of* $h = \Delta x = \Delta y = 100\Delta t$ *used in the simulation in row i.*

Using piecewise linear elements, the observed convergence rates in the integral norms (see the first three columns of **Table 3**), are 1.0 (optimal) and 1.73 (slightly suboptimal) for the broken H^1 norm and the L^2 norm of potentials, respectively, while order 2 can be seen in the L^2 norm of the current density. We note that the suboptimal rate of convergence is due to the error being dominated by the temporal discretization and decreasing the time step restores the optimal quadratic convergence. Let us also note that the quadratic convergence of the current density is likely related to the fact that $I_m = 0$ in the test case. The observed order of convergence in the supremum norms is 1.59 and 1.56 for u_h and v_h, respectively. However, the error here seems again to be dominated by temporal discretization, since using $\Delta t = 10^{-3}/n$ improves the rates toward 2.0.

Table 4 reports the errors and convergence rates for the H(div)-based FEM. The error in the computed intracellular and extracellular potentials u_h and the error in the membrane potential v_h are reported in the L^2 norm and in the supremum norm. Furthermore, the error in the computed potential gradient $\hat{J}_h$ is reported in the L^2 and H(div) norms. We observe that the convergence rate is one both for the error in the L^2 norm for u_h and v_h and for the H(div) and L^2 norms for $\hat{J}_h$. These rates are in complete agreement with the theoretical expectations. In addition, we observe that the convergence of the supremum norm of u_h and v_h, computed after a projection onto continuous piecewise linears, appears to be close to quadratic.

3.2.2. Nonlinear Ionic Current: Mesh Refinement

To investigate the accuracy of the numerical methods using the Grandi AP model, we compare the solutions obtained from the numerical methods using different spatial resolutions.

Figure 5 shows the solution of the membrane potential in a single point on the membrane for the FDM and the H(div)-based FEM for a number of resolutions. We consider the solution for two connected cells; and the sizes of the cells and the domain used in the simulations are given in **Table 5**.

In the upper panel of **Figure 5**, the solutions for different resolutions are almost indistinguishable, but in the lower panel we focus on a small part of the solution and a difference is visible for the different resolutions of the FDM. The H(div) FEM

TABLE 3 | Convergence of the mortar finite element method for the manufactured test problem, with convergence rates in parentheses.

n	$\|u-u_h\|_1$	$\|u-u_h\|_0$	$\|J-J_h\|_0$	$\|u-u_h\|_\infty$	$\|v-v_h\|_\infty$
16	1.11E+00 (--)	2.85E−02 (--)	1.45E−01 (--)	6.36E−02 (--)	5.03E−02 (--)
32	5.59E−01 (0.98)	7.37E−03 (1.95)	4.01E−02 (1.86)	2.09E−02 (1.60)	1.82E−02 (1.47)
64	2.80E−01 (1.00)	1.90E−03 (1.96)	1.05E−02 (1.94)	6.73E−03 (1.64)	6.22E−03 (1.54)
128	1.40E−01 (1.00)	4.99E−04 (1.93)	2.65E−03 (1.98)	2.15E−03 (1.65)	2.08E−03 (1.58)
256	7.02E−02 (1.00)	1.38E−04 (1.86)	6.66E−04 (1.99)	6.93E−04 (1.63)	6.90E−04 (1.59)
512	3.51E−02 (1.00)	4.16E−05 (1.73)	1.66E−04 (2.00)	2.31E−04 (1.59)	2.34E−04 (1.56)

TABLE 4 | Convergence of the H(div) finite element method for the manufactured test problem, with convergence rates in parentheses.

n	$\|u-u_h\|_0$	$\|\hat{J}-\hat{J}_h\|_0$	$\|\hat{J}-\hat{J}_h\|_{\text{div}}$	$\|v-v_h\|_0$	$\|u-u_h\|_\infty$	$\|v-v_h\|_\infty$
16	8.41E−02 (--)	6.49E−01 (--)	6.62E+00 (--)	1.02E−01 (--)	2.73E−02 (--)	2.53E−03 (--)
32	4.21E−02 (1.00)	3.24E−01 (1.00)	3.32E+00 (0.99)	5.13E−02 (1.00)	6.87E−03 (1.99)	6.36E−04 (1.99)
64	2.11E−02 (1.00)	1.62E−01 (1.00)	1.66E+00 (1.00)	2.56E−02 (1.00)	1.72E−03 (2.00)	1.57E−04 (2.02)
128	1.05E−02 (1.00)	8.10E−02 (1.00)	8.31E−01 (1.00)	1.28E−02 (1.00)	4.30E−04 (2.00)	3.76E−05 (2.06)
256	5.27E−03 (1.00)	4.05E−02 (1.00)	4.16E−01 (1.00)	6.41E−03 (1.00)	1.08E−04 (2.00)	8.63E−06 (2.12)
512	2.63E−03 (1.00)	2.03E−02 (1.00)	2.08E−01 (1.00)	3.21E−03 (1.00)	2.69E−05 (2.00)	1.77E−06 (2.29)

solutions are very similar for different resolutions, indicating that the method is more accurate than the FDM in this case as well.

3.3. CPU Requirements

As mentioned in the section 1, simulation of the electrophysiology of cardiac tissue is usually based on homogenized models such as the monodomain model or the bidomain model. The motivation for this is certainly that it requires considerably less computing power than the EMI approach considered here. Therefore, it is very important to understand the computational complexity of the EMI model to appreciate the applications in which this approach can be used.

3.3.1. Finite Difference Method

Tables 7, **8** report the CPU times, number of iterations, and system size for the FDM as the number of cells included in the simulation is increased. In **Table 7**, we use the passive model (10) for I_{ion}, and in **Table 8**, we use the Grandi AP model. The linear systems are solved using the BiCGStab method (see [68, 69]) with an incomplete LU preconditioner (e.g., [68]) and relative tolerance of 10^{-5} for the *true/unpreconditioned* (l^2) norm of the residuum. The computations are performed using MATLAB. The last column of the tables reports the simulation time per cell for a single time step and we observe that the simulation time *per physical cell* appears to be bounded as the number of cells is increased.

3.3.2. Finite Element Method

Because of the complexity of the mortar FEM, which introduces a separate function space for the potential of each cell[1] Ω_i^k, we shall focus on the H(div) FEM in the following.

[1]The space for intracellular potentials for the case considered with FDM in the section 3.3.1 would be $V_i^1 \times V_i^2 \times \cdots \times V_i^n$ where $n = 16,384$.

Table 9 shows the CPU time, the number of iterations, and the dimensions of the finite element spaces for a number of simulations using the H(div) FEM described in section 2.3.3 with an increasing number of cells and a passive membrane model. The linear systems are again solved using the biconjugate gradient stabilized method with an incomplete LU preconditioner and a convergence criterion as in the FDM case. The linear solver and the preconditioner were provided by the PETSc library [70], while the system was assembled using FEniCS [49, 50].

Since the definition of the H(div)-based variational problem (21) in FEniCS is not immediately obvious, we briefly comment on some implementational aspects. Recall that the solution is sought in the space $U_h \times S_h \times V_h$, where the functions in V_h are defined over $\hat{\Gamma}_h$, the discretization of the cell mebranes Γ. However, FEniCS (version 2017.1) does not currently support mixed spaces with components defined over different meshes, such as over $\mathcal{T}_h$ and $\hat{\Gamma}_h$. To bypass this restriction, we construct the space V_h over all the facets of $\mathcal{T}_h$ and the excess degrees of freedom are set to zero in the assembled linear system. As illustrated above the construction yields the correct numerical solution. However, the additional degrees of freedom naturally affect the performance of the linear solvers, since they increase the computational cost of the matrix–vector product significantly. FEniCS support for mixed finite element spaces with components defined over different meshes is currently under development and we thus expect this issue to be resolved in future FEniCS releases.

Comparing the results of **Table 9** with those of the FDM (see **Table 7**), we observe that the CPU times for the FEM are considerably larger (by a factor of ∼70). While the longer solution times for the FEM are expected due to the larger linear systems stemming from the method (with factors of ∼23 and ∼14 for the system with or without the additional degrees of freedom

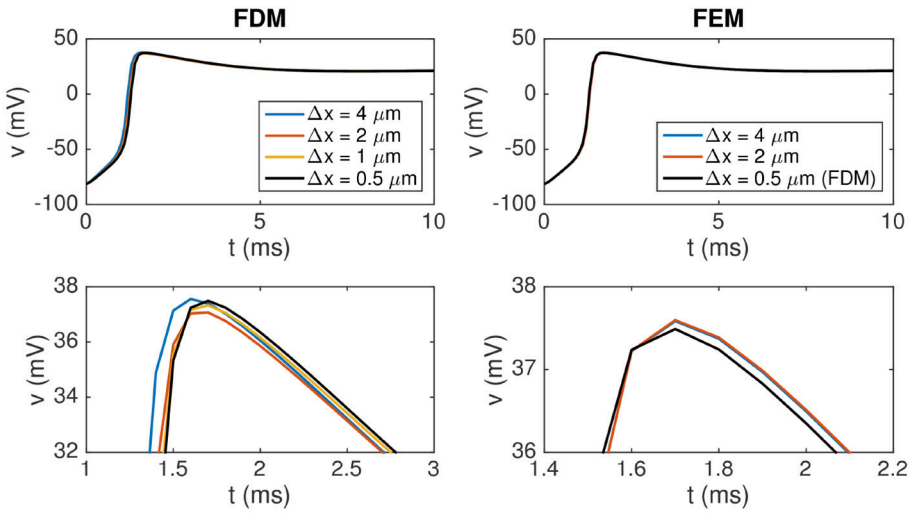

FIGURE 5 | Membrane potential at the point (112, 24, 16 μm) for the finite difference and the finite element methods for two connected cells for some different values of $\Delta x = \Delta y = \Delta z$. The **upper panel** shows the solution from $t = 0$ ms to $t = 10$ ms. In the **lower panel**, we zoom in on the peak to observe a difference between the solutions. Note that the scaling of the y axis is different for the two plots in the **lower panel** and that the FEM solutions for $\Delta x = 4$ μm and $\Delta x = 2$ μm are almost indistinguishable in the lower right plot. The parameter values used in the simulations are given in **Tables 1**, **5**, and we apply a 1-ms-long stimulus current of 120 μA/μF for the first 24 μm of the first cell.

TABLE 5 | The cell and domain sizes used in the simulations reported in **Figure 5**.

Domain	Size
Ω_O	36 × 16 × 16 μm
Ω_W, Ω_E	8 × 8 × 8 μm
Ω_S, Ω_N	20 × 8 × 8 μm
$\Omega_i \cup \Omega_e$	120 × 48 × 32 μm

*The intracellular domain consists of two connected cells, where each cell is a composition of the domains $\Omega_O, \Omega_W, \Omega_E, \Omega_S$, and Ω_N (see **Figure 4**). Note that the geometry used in the remaining 3D simulations is specified in **Tables 6**, **10**.*

TABLE 6 | Cell sizes used in the simulations reported in **Figures 7**–**9** and **Tables 7**–**9**.

Domain	Size
Ω_O	100 × 12 × 12 μm
Ω_W, Ω_E	4 × 8 × 8 μm
Ω_S, Ω_N	60 × 4 × 8 μm

*The intracellular domain consists of a number of connected cells where each cell is a composition of the domains $\Omega_O, \Omega_W, \Omega_E, \Omega_S$, and Ω_N (see **Figure 4**). The size of $\Omega = \Omega_i \cup \Omega_e$ is $L_x \times L_y \times L_z$, where $L_z = 20$ μm and L_x and L_y depend on the number of cells in the simulation. The minimal distance between the intracellular domain and the boundary of the extracellular domain is 8 μm in both the x and y directions.*

introduced in V_h, respectively), the results also point out that the iterative solver does not perform as well as in the FDM case. More efficient solution strategies for the system are currently being investigated.

3.4. Cylindrical Geometry

The somewhat clunky geometry of the cells used above does not reflect reality very well. Indeed, cardiac cells have cylindrical shapes, but such shapes are inconvenient to address using FDMs, and we therefore apply the FEM. **Figure 6** shows the membrane potential and surrounding extracellular potential for a simulation of two connected cylinders using the parameters given in **Tables 1**, **10**. We note that the FEM is well suited for handling cylindrical geometry, and we expect that the method can also be used to handle the even more complex geometries that will arise when the T-tubules of ventricular cells (e.g., [71]) are incorporated in the model.

TABLE 7 | CPU times for the finite difference method for a passive membrane model.

Cells	Grid points	System size	n_{it}	T (s)	T/cell (s)
1	13,167	14,609	44	0.5	0.5
4	37,323	42,563	122	3.9	1.0
16	121,275	141,179	146	7.2	0.5
64	431,739	509,243	198	24.3	0.4
256	1,622,907	1,928,699	256	86.4	0.3
1,024	6,286,203	7,500,923	258	328.7	0.3
4,096	24,736,635	29,578,619	250	1,195.9	0.3
16,384	98,132,859	117,467,003	209	3,696.8	0.2

*Here, n_{it} is the number of iterations in the fourth time step of size $\Delta t = 0.1$ ms and T is the solution time for the fourth time step. The parameters used in the computations are given in **Table 1** and the domain sizes are specified in **Table 6**. For the 25% of the cells at the center of the domain, we use the initial condition $v = 10$ mV and, for the remaining cells, we use the initial condition $v = v_{\text{rest}}$.*

3.5. Ion Channel Density Distribution Affects Conduction Velocity

As mentioned in the section 1, it is difficult to represent a non-uniform distribution of ion channels along the cell

TABLE 8 | CPU times for the finite difference method using the Grandi membrane model for I_{ion}.

Cells	Grid points	System size	n_{it}	T_{ODE} (s)	T_{PDE} (s)	T (s)	T/cell (s)
1	13,167	14,609	64	2.9	0.7	3.6	3.6
4	37,23	42,563	150	7.6	4.5	12.1	3.0
16	121,275	141,179	210	23.9	12.7	36.5	2.3
64	431,739	509,243	260	85.1	41.5	126.6	2.0
256	1,622,907	1,928,699	318	351.9	109.8	461.7	1.8
1,024	6,286,203	7,500,923	338	1,256.0	442.6	1698.6	1.7
4,096	24,736,635	29,578,619	322	4,512.8	1,515.8	6028.6	1.5
16,384	98,132,859	117,467,003	360	1,7594.6	6,171.9	23,766.5	1.5

*Here, $T = T_{ODE} + T_{PDE}$ is the solution time for the fourth time step of size $\Delta t = 0.1$ ms, where T_{ODE} is the solution time for the first (ODE) part of the operator splitting procedure and T_{PDE} is the solution time for the second (PDE) part of the procedure. Furthermore, n_{it} is the number of iterations needed to achieve convergence of the BiCGStab method used in the PDE part of the procedure. The parameters used in the computations are given in **Tables 1**, **6**. For the 25% of the cells at the center of the domain, we replace the default initial conditions of the Grandi model with the values of the state variables obtained when the membrane potential first reached $v = -10$ mV during the upstroke of the AP in a single-cell simulation of the model. For the remaining cells, we use the default initial conditions of the Grandi model.*

TABLE 9 | CPU times for the H(div) finite element method for a passive membrane model.

Cells	dim(S_h)	dim(U_h)	dim($V_h\|\Gamma_h$)	dim(M_h)	n_{it}	T (s)	T/cell (s)
1	137,752	66,960	3,216	342,464	74	6.1	6.1
4	399,136	194,880	12,320	993,152	220	49.8	12.5
16	1,317,184	645,120	48,192	3,279,488	458	337.6	21.1
64	4,734,400	2,323,200	190,592	11,792,000	637	1,684.8	26.3

*Here, n_{it} is the number of iterations in the fourth time step of size $\Delta t = 0.1$ ms and T is the solution time for the fourth time step. Furthermore, T/cell is the solution time per cell for the fourth time step. The second to fifth columns give the dimensions of the various finite element spaces (see section 2.3.3). Note that $V_h|\Gamma_h$ refers to the space V_h restricted to the membrane Γ_h but that V_h is defined in the entire domain in the computations reported in the table. Note also that dim(M_h) refers to the dimension of the total mixed space $U_h \times S_h \times V_h$. The parameters used in the computations are given in **Tables 1**, **6**. For the 25% of the cells at the center of the domain, we use the initial condition $v = 10$ mV and, for the remaining cells, we use the initial condition $v = v_{rest}$.*

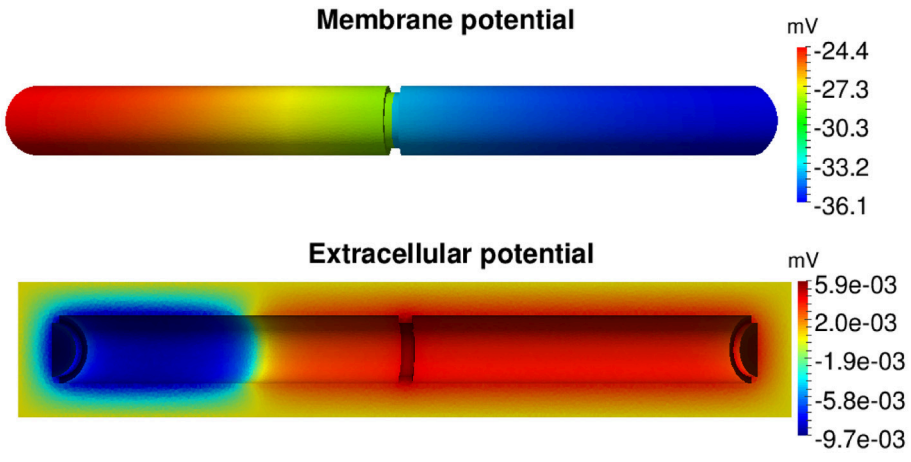

FIGURE 6 | Membrane potential and the surrounding extracellular potential of two connected cylinders at time $t = 1$ ms computed by the H(div) FEM. The parameters used in the simulations are given in **Tables 1**, **10** and we apply a stimulus current of 120 μA/μF for the first half of the first cell in the x direction.

membrane using classical homogenized models. This is an important shortcoming of the classical methods, because a non-uniform distribution of sodium channels is believed to affect the conduction velocity. In the EMI modeling framework, the representation of non-uniform distributions of ion channels is straightforward.

Figure 7 shows the solutions of two simulations of a collection of 30 × 5 cells with different distributions of the sodium channel conductance, g_{Na}. In the left panel the value of g_{Na} is constant on the entire membrane, while, in the right panel, g_{Na} is zero over a large part of the membrane and only non-zero on Ω_W and Ω_E, that is, near the ends of the cell in the x

direction. The mean value of g_{Na} over the cells is the same in the two simulations. We observe that the conduction velocity is increased for the case with a varying value of g_{Na} compared to the case with a constant value. The conduction velocities reported in the figure are computed from the 10th and 20th cells in the third row in the y direction, and are defined as the distance between the cell centers divided by the time between each of the two cell centers reaches a membrane potential of $v = 0$ mV.

TABLE 10 | Cell and domain sizes used in the simulations of the two connected cylinders in **Figure 6**.

Length of Ω_O	100 μm
Radius of Ω_O	10 μm
Length of Ω_W and Ω_E	4 μm
Radius of Ω_W and Ω_E	8 μm
Domain ($\Omega_i \cup \Omega_e$)	228 × 40 × 40 μm

The intracellular domain consists of two cells, where each cell is a composition of three cylinders Ω_W, Ω_O, and Ω_E.

Figure 8 shows a more detailed view of the two cells at the center of the domain. Here, we observe that the conduction velocity across the first part of the cell appears to be higher for the case with a constant value of g_{Na} than for the varying case, but that the traveling wave moves faster across the gap junction for the case with a varying g_{Na} than for the constant case, leading to an overall increased conduction velocity for the varying case.

This effect is studied more closely in **Figure 9**, which shows the activation times and conduction velocities along the length of two cells in a similar pair of simulations. The gap junction between the two cells is located at $x = 548$ μm, and we observe that there is a delay of about 0.1 ms between when the membrane on each side of the gap junction is activated. The delay appears to be slightly longer for the case with a constant g_{Na} compared to the varying case. We also observe that, overall, the wave uses less time to activate the two cells for the case with a varying g_{Na} than for the constant case, consistent with the results of **Figures 7**, **8**. In addition, we observe that the shape of the activation curve is different in the two cases. In the case with a constant g_{Na}

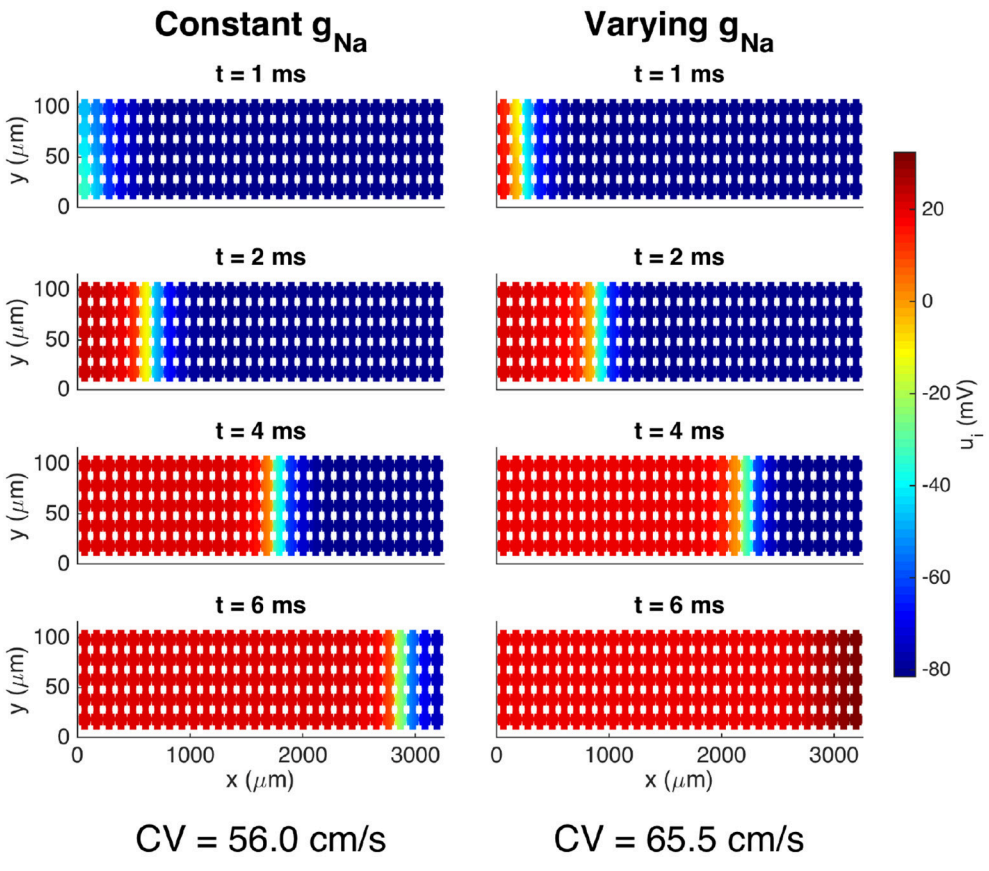

FIGURE 7 | Intracellular potential at four points in time for a collection of cells with two different distributions of the sodium channel conductance. In the case of a constant g_{Na}, the value is $g_{\text{Na}} = 23$ mS/μF on the entire membrane, and in the case of a varying g_{Na}, the value is $g_{\text{Na}} = 783$ mS/μF on Ω_W and Ω_E and zero elsewhere. The solutions are obtained using the FDM and the parameters used in the simulations are given in **Tables 1**, **6**, except that we use $\Delta t = 0.01$ ms. We apply a 1-ms-long stimulus current of 120 μA/μF for the 2 × 2 cells in the lower left corner of the domain.

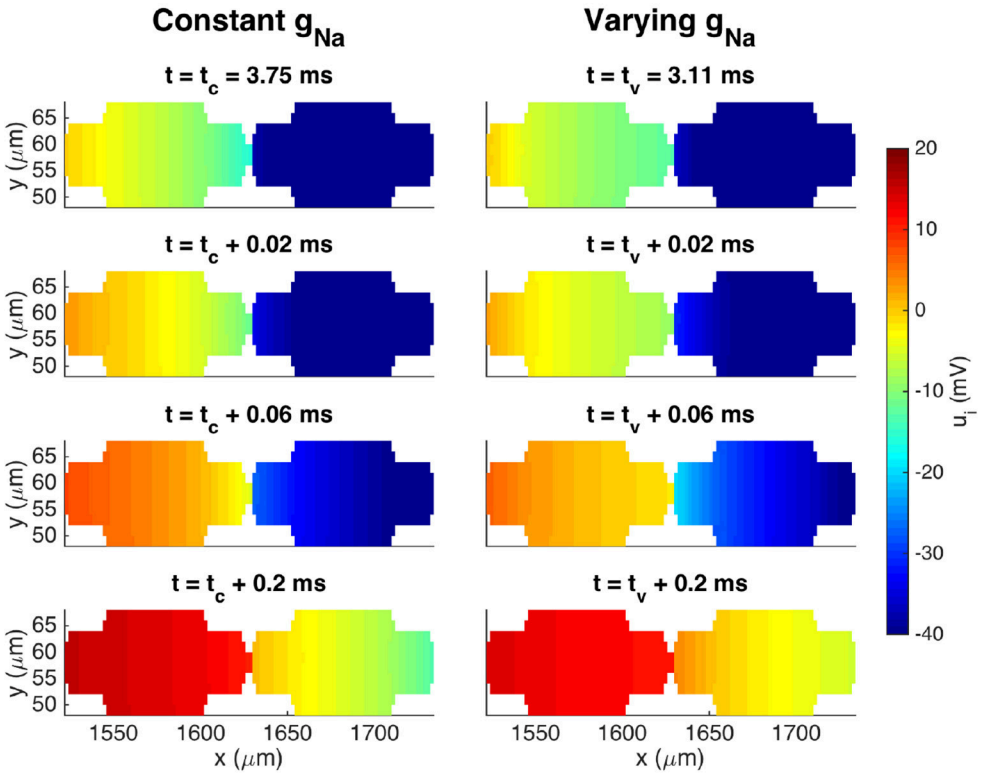

FIGURE 8 | Intracellular potentials at four points in time for the two cells at the center of the domain from the simulation in **Figure 7**. The plots in the upper panel show the solutions at the last point in time before the intracellular potential at the start of the first cell is first positive. Because the conduction velocity is different in the two cases, this occurs at two different points in time, t_C and t_V, for the cases with a constant g_{Na} and a varying g_{Na}, respectively. The next plots show the solutions at times 0.02, 0.06, and 0.2 ms after t_C and t_V.

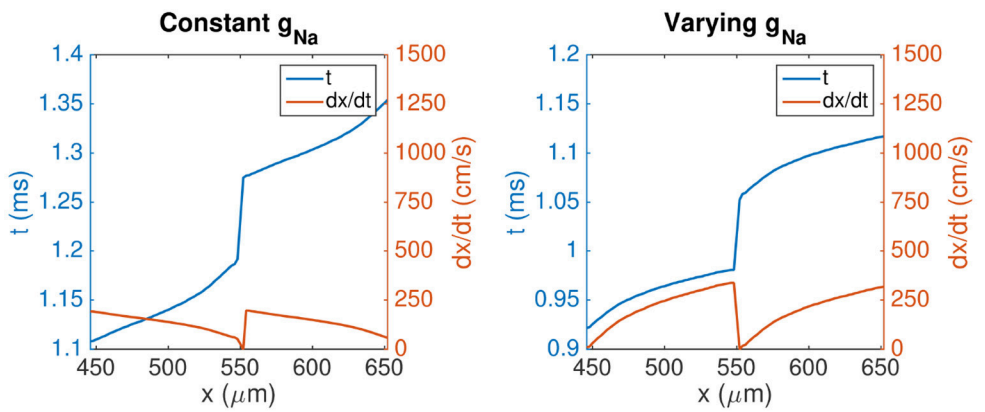

FIGURE 9 | Activation times and conduction velocities along the length of two cells in a simulation of 10 × 1 cells with different distributions of g_{Na}, similar to the simulations shown in **Figure 7**. The blue line shows the points in time when the membrane nodes corresponding to each x-value along cells number five and six first reach a membrane potential of 0 mV. The orange line shows the corresponding conduction velocity along the two cells, computed from a piecewise second order polynomial approximation of the activation curves. The parameters used in the simulations are given in **Tables 1**, **6**, except that we use $\Delta t = 0.0005$ ms. Note that the values of the left y-axis (representing activation time) is different in the two plots, but that the scaling of the axis is the same in both plots.

distribution, the activation curve becomes steeper toward the end of the cells, corresponding to a decreasing conduction velocity along the cell lengths. For the varying case, however, the activation curve flattens out toward the end of the cells, corresponding to an increased conduction velocity toward the cell ends.

4. DISCUSSION

As described above, the classical models of cardiac tissue are founded on homogenization of the tissue and the resulting models therefore assume that the extracellular space, the cell membrane, and the intracellular space exist everywhere. This leads to tractable computing problems that have provided insights into important applications such as the propagation of an electrochemical wave, cardiac arrhythmias, the effect of defibrillation, the onset of cardiac waves, and the effect of diverse drugs. However, in some cases, it is of interest to see the dynamics surrounding individual cells as part of the tissue, which is hard to do using homogenized models. It is also of interest to be able to change local properties of the tissue that are difficult to represent in homogenized models.

In the present report, we focused on the computational challenges of a different approach in which separate geometrical domains for the extracellular space, the cell membrane, and the intracellular domain represent the tissue; we refer to this as the EMI model. Clearly, the computational problems arising from the EMI model are much more challenging than for traditional models, but we have shown that, for some applications, the more detailed model is feasible. In particular, we have shown that the EMI model is suitable for monolayers of cells. Furthermore, we have demonstrated that the EMI framework allows the representation of local properties of cells that are hard to represent in classical homogenized models of cardiac tissue.

4.1. Membrane Dynamics

The dynamics of the cell membrane are absolutely critical for the functioning of the cell and have been subject to intense studies for centuries. A wide variety of models are available through the open CellML library [72]. In our computations, we have used the ventricular cell model by Grandi et al. [48]. That model consists of a system of 39 ODEs defined on every computational node of the cell membrane and is believed to provide an accurate representation of the cell's action potential. From a computational point of view, we could have used numerous other models (e.g., [73–80]) with comparable complexity of the membrane computations. Common to all these models is that the ion currents are represented using models where the ion channel density must be specified. When the models are used as part of a monodomain or bidomain model, the channel density is most conveniently treated as a constant for each cell, but in the EMI model, the ion channel density associated with any of the currents can be specified as a function of space on the cell membrane. We noted in **Figure 7** that a non-uniform distribution of sodium channels significantly affects the tissue's conduction velocity.

4.2. Numerical Accuracy

The numerical accuracy of the discretizations considered was assessed using a single-cell problem (24–30) and the method of manufactured solutions. As seen in **Tables 2**–**4**, all the discretizations provide converging numerical solutions. However, taking the L^∞ norms of the computed potentials for comparison, there are considerable differences in the convergence properties of the methods.

The convergence of the FDM discretization is linear and this method is the least accurate. The first order convergence of the FDM is to be expected, since all internal boundary conditions are approximated using first-order finite differences. Compared to the FDM, the mortar FEM yields solutions with considerably smaller error and the observed rates are about 1.5. It should be noted that, on a given grid, the methods lead to identical numbers of unknowns. The H(div) FEM is the most accurate among the methods considered with errors much smaller than those of the mortar FEM. As noted in section 3.3, the H(div) FEM leads to larger linear systems than the other two methods do (see **Tables 7**, **9**). Finally, let us note that the manufactured solution employed was particularly simple and thus the numerical results obtained may not be universally valid.

4.3. CPU Requirements

The CPU efforts needed to solve the system (1–9) using the FDM or the FEM are given in **Table 7** (FDM, passive membrane dynamics), **Table 8** (FDM, membrane dynamics given by the Grandi model), and **Table 9** (H(div) FEM, passive membrane dynamics). We observe that, for the FDM, the CPU efforts per cell seem to be bounded independently of the number of cardiac cells. This result implies that the solver is optimal in the sense defined above. When the Grandi model is used for the membrane dynamics, the CPU efforts per time step per cell are around 1.5 s. This enables us to simulate 16,384 cells, which defines a linear system with over 117 million unknowns. Since the CPU efforts per cell seem to be bounded independent of the number of cells, the CPU efforts will not explode as more cells are added to the computations. With proper parallelization strategies, it should be possible to simulate huge numbers of cells. In fact, the mouse heart, with around 4 million cells, may be within reach; with a computer that is 1,000 times faster (for large problems) than the one we used, it would require about one week to perform 100 time steps for 4 million cardiac cells.

We observe from **Tables 8**, **9** that the FDM method in the current implementation is significantly faster than the FEM code even though the FDM code is implemented in Matlab. It has proven to be difficult to derive optimal preconditioners to be used for the FEM, but we hope to be able to improve this part of the code in the future.

4.4. Cell Geometry

In the present report, we have used very simple geometries to represent the cells. We have assumed that the geometries are simple rectangular cuboids or have cylindrical shapes. However, real cardiac cells have much more complex geometries and future work will investigate the effect of the geometry on the solutions. Of particular importance is the effect of T-tubules in ventricular cells and how they change during illness (e.g., [71, 81]). The diameter of the T-tubules ranges from 20 to 450 nm (see [82]) and therefore a very fine computational mesh would be needed to represent these invaginations. Presently, we have run the FDM code with spatial resolution of 5 nm (in the case of only three coupled cells), so including T-tubules is within reach for the FDM code but not for the FEM code.

4.5. Intracellular Calcium Dynamics

The focus of the present report has been to show that it is possible to simulate the electrical potential of cardiac cells based on explicit representation of the cells. We have focused on models that represent the membrane dynamics in terms of interchange over the cell membrane and we have ignored the spatial gradients of the ionic concentrations away from the cell membrane. Certainly, this is a major simplification; the intracellular concentration of calcium is essential and can be modeled using partial differential equations defined in the intracellular domain, see e.g. [83–86]. In Nivala et al. [83], a model based on Calcium released units (CRUs) is presented and the number of CRUs for a single cell used in the computations is typically ∼20,000. In our model, a cardiac cell with a volume of 30 pL and a typical mesh length of 1 μm would consist of 30,000 computational blocks within each cell. A reasonable representation of the CRUs in the EMI model is therefore within reach.

4.6. Conduction Velocity

As mentioned above, the conduction velocity is essential for the stability of the electrochemical wave underpinning the rhythmic contraction of the cardiac muscle. In numerical computations, the distribution of ion channels is usually assumed to be constant, but experimental evidence suggests that the ion channel density is non-uniform along the cell membrane. For instance, the density of sodium channels is believed to be much higher closer to the intercalated discs separating individual cells (e.g., [87]). The difference between uniform and non-uniform distributions of sodium channels was addressed in **Figures 7–9**. We observed that the conduction velocity was significantly lower in the case of a constant distribution of the sodium channels compared to the case of a non-uniform distribution. Interestingly, we also observed (**Figure 9**) that for the uniform case, the conduction velocity decreased along the cell, whereas it increased in the case of non-uniform distribution. Again, such effects are difficult to observe in the classical models (monodomain, bidomain). This effect deserves closer scrutiny and the EMI model provides a suitable framework for such studies.

5. CONCLUSION

Local properties of cells and cell membranes are difficult to represent in standard (bidomain, monodomain) models of excitable tissue. In this paper, we have demonstrated that a more accurate model and method can be used. In our approach, every cell is represented in terms of its surrounding extracellular space, the cell membrane, and the intracellular space. The extracellular and intracellular spaces are represented using a mesh of length of 2 μm and the membrane is represented as the intersection of the extracellular and intracellular meshes. We have seen that, with a finite difference method using a very simple geometry, the computations are quite efficient and the computational demands increase linearly in the number of physical cells. We have solved for up to 16,384 cells using this method. More complex geometries must be represented using a method allowing flexible grids and, in the present paper, we have shown the results for two variants of the finite element method. Although, the solution process of the finite element equations is much more time-consuming, the results indicate that more complex cell geometries can, in fact, be handled.

AUTHOR CONTRIBUTIONS

Numerical methods: AT, KJ, MK, KM, MR. Software development: KJ, MK, MR. Simulations: AT, KJ, MK. Writing paper: AT, KJ, MK, KM, MR.

FUNDING

The research was supported by The Research Council of Norway through the grant 145739/F20.

REFERENCES

1. Hogues H, Leon L, Roberge F. A model study of electric field interactions between cardiac myocytes. *IEEE Trans Biomed Eng.* (1992) **39**:1232–43.
2. Krassowska W, Neu JC. Response of a single cell to an external electric field. *Biophys J.* (1994) **66**:1768.
3. Ying W, Henriquez CS. Hybrid finite element method for describing the electrical response of biological cells to applied fields. *IEEE Trans Biomed Eng.* (2007) **54**:611–20. doi: 10.1109/TBME.2006.889172
4. Agudelo-Toro A, Neef A. Computationally efficient simulation of electrical activity at cell membranes interacting with self-generated and externally imposed electric fields. *J Neural Eng.* (2013) **10**:026019. doi: 10.1088/1741-2560/10/2/026019
5. Stinstra JG, Henriquez CS, MacLeod RS. Comparison of microscopic and bidomain models of anisotropic conduction. In: Murray A, editor. *Computers in Cardiology*. IEEE (2009). p. 657–60.
6. Stinstra JG, MacLeod RS, Henriquez CS. Incorporating histology into a 3D microscopic computer model of myocardium to study propagation at a cellular level. *Ann Biomed Eng.* (2010) **38**:1399–414. doi: 10.1007/s10439-009-9883-y
7. Stinstra JG, Hopenfeld B, MacLeod RS. On the passive cardiac conductivity. *Ann Biomed Eng.* (2005) **33**:1743–51. doi: 10.1007/s10439-005-7257-7
8. Tveito A, Jæger KH, Lines GT, Paszkowski Ł, Sundnes J, Edwards AG, et al. An evaluation of the accuracy of classical models for computing the membrane potential and extracellular potential for neurons. *Front Comput Neurosci.* (2017) **11**:27. doi: 10.3389/fncom.2017.00027
9. Keener JP, Sneyd J. *Mathematical Physiology*. New York, NY: Springer (2009).
10. Franzone PC, Pavarino LF, Scacchi S. *Mathematical Cardiac Electrophysiology*. Cham; Heidelberg; New York, NY; Dordrecht; London: Springer International Publishing (2014).
11. Sundnes J, Nielsen BF, Mardal KA, Cai X, Lines GT, Tveito A. On the computational complexity of the bidomain and the monodomain models of electrophysiology. *Ann Biomed Eng.* (2006) **34**:1088–97. doi: 10.1007/s10439-006-9082-z
12. Roth BJ. Bidomain simulations of defibrillation: 20 years of progress. *Heart Rhythm* (2013) **10**:1218–9. doi: 10.1016/j.hrthm.2013.05.002
13. Trayanova NA. Whole-heart modeling: applications to cardiac electrophysiology and electromechanics. *Circ Res.* (2011) **108**:113–28. doi: 10.1161/CIRCRESAHA.110.223610

14. Vigmond E, Vadakkumpadan F, Gurev V, Arevalo H, Deo M, Plank G, et al. Towards predictive modelling of the electrophysiology of the heart. *Exp Physiol*. (2009) **94**:563–77. doi: 10.1113/expphysiol.2008.044073
15. Tveito A, Lines GT, Artebrant R, Skavhaug O, Maleckar MM. Existence of excitation waves for a collection of cardiomyocytes electrically coupled to fibroblasts. *Math Biosci*. (2011) **230**:79–86. doi: 10.1016/j.mbs.2011.01.004
16. Tveito A, Lines GT, Edwards AG, Maleckar MM, Michailova A, Hake J, et al. Slow Calcium–Depolarization–Calcium waves may initiate fast local depolarization waves in ventricular tissue. *Prog Biophys Mol Biol*. (2012) **110**:295–304. doi: 10.1016/j.pbiomolbio.2012.07.005
17. Xie Y, Sato D, Garfinkel A, Qu Z, Weiss JN. So little source, so much sink: requirements for afterdepolarizations to propagate in tissue. *Biophys J*. (2010) **99**:1408–15. doi: 10.1016/j.bpj.2010.06.042
18. Xie Y, Garfinkel A, Weiss JN, Qu Z. Cardiac alternans induced by fibroblast-myocyte coupling: mechanistic insights from computational models. *Am J Physiol Heart Circ Physiol*. (2009) **297**:H775–84. doi: 10.1152/ajpheart.00341.2009
19. Qu Z, Nivala M. Multiscale nonlinear dynamics in cardiac electrophysiology: from sparks to sudden death. In: Pesenson MZ, editor. *Multiscale Analysis and Nonlinear Dynamics: From Genes to the Brain*. Weinheim: Wiley-VCH Verlag (2013). p. 257–75.
20. Qu Z, Hu G, Garfinkel A, Weiss JN. Nonlinear and stochastic dynamics in the heart. *Physics Rep*. (2014) **543**:61–162. doi: 10.1016/j.physrep.2014.05.002
21. Tveito A, Lines GT. A condition for setting off ectopic waves in computational models of excitable cells. *Math Biosci*. (2008) **213**:141–50. doi: 10.1016/j.mbs.2008.04.001
22. Keener JP, Panfilov AV. A biophysical model for defibrillation. *Biophys J*. (1996) **71**:1335–45.
23. Plank G, Vigmond EJ, Leon LJ. Shock energy for successful defibrillation of atrial tissue during vagal stimulation. In: *Proceedings of the 25th annual International Conference of the IEEE EMBS* (2003). p. 167–70.
24. Plank G, Leon LJ, Kimber S, Vigmond EJ. Defibrillation depends on conductivity fluctuations and the degree of disorganization in reentry patterns. *J Electrophysiol*. (2005) **16**:205–16. doi: 10.1046/j.1540-8167.2005.40140.x
25. Trayanova N, Gernot Plank EJJ. Modeling cardiac defibrillation. In: Saunders WB, editor. *Cardiac Electrophysiology: From Cell to Bedside*. Philadelphia (2009). p. 361–72.
26. Tveito A, Lines G, Rognes ME, Maleckar MM. An analysis of the shock strength needed to achieve defibrillation in a simplified mathematical model of cardiac tissue. *Int J Numer Anal Model*. (2012) **9**:644–57. Available online at: http://www.math.ualberta.ca/ijnam/
27. Rantner LJ, Tice BM, Trayanova NA. Terminating ventricular tachyarrhythmias using far-field low-voltage stimuli: mechanisms and delivery protocols. *Heart Rhythm* (2013) **10**:1209–17. doi: 10.1016/j.hrthm.2013.04.027
28. Trayanova NA, Rantner LJ. New insights into defibrillation of the heart from realistic simulation studies. *Europace* (2014) **16**:705–13. doi: 10.1093/europace/eut330
29. Moreno JD, Zhu ZI, Yang PC, Bankston JR, Jeng MT, Kang C, et al. A computational model to predict the effects of class I anti-arrhythmic drugs on ventricular rhythms. *Sci Transl Med*. (2011) **3**:1–8. doi: 10.1126/scitranslmed.3002588
30. Rodriguez B, Burrage K, Gavaghan D, Grau V, Kohl P, Noble D. The systems biology approach to drug development: application to toxicity assessment of cardiac drugs. *Clin Pharmacol Ther*. (2010) **88**:130–4. doi: 10.1038/clpt.2010.95
31. Tveito A, Lines GT, Maleckar MM. Note on a possible proarrhythmic property of antiarrhythmic drugs aimed at improving gap-junction coupling. *Biophys J*. (2012) **102**:231–7. doi: 10.1016/j.bpj.2011.11.4015
32. Tveito A, Lines GT. A note on a method for determining advantageous properties of an anti-arrhythmic drug based on a mathematical model of cardiac cells. *Math Biosci*. (2009) **217**:167–73. doi: 10.1016/j.mbs.2008.12.001
33. Veeraraghavan R, Gourdie RG, Poelzing S. Mechanisms of cardiac conduction: a history of revisions. *Am J Physiol Heart Circ Physiol*. (2014) **306**:H619–27. doi: 10.1152/ajpheart.00760.2013
34. Spach MS, Heidlage JF, Barr RC, Dolber PC. Cell size and communication: role in structural and electrical development and remodeling of the heart. *Heart Rhythm* (2004) **1**:500–15. doi: 10.1016/j.hrthm.2004.06.010
35. Rudy Y, Quan W. A model study of the effects of the discrete cellular structure on electrical propagation in cardiac tissue. *Circ Res*. (1987) **61**:815–23.
36. Shaw RM, Rudy Y. Ionic mechanisms of propagation in cardiac tissue. *Circ Res*. (1997) **81**:727–41.
37. Wei N, Mori Y, Tolkacheva EG. The dual effect of ephaptic coupling on cardiac conduction with heterogeneous expression of connexin 43. *J Theor Biol*. (2016) **397**:103–14. doi: 10.1016/j.jtbi.2016.02.029
38. Poelzing S, Rosenbaum DS. Altered connexin43 expression produces arrhythmia substrate in heart failure. *Am J Physiol Heart Circ Physiol*. (2004) **287**:H1762–70. doi: 10.1152/ajpheart.00346.2004
39. Lin J, Keener JP. Ephaptic coupling in cardiac myocytes. *IEEE Trans Biomed Eng*. (2013) **60**:576–82. doi: 10.1109/TBME.2012.2226720
40. Olivetti G, Melissari M, Capasso JM, Anversa P. Cardiomyopathy of the aging human heart. Myocyte loss and reactive cellular hypertrophy. *Circ Res*. (1991) **68**:1560–8.
41. Doevendans PA, Daemen MJ, de Muinck ED, Smits JF. Cardiovascular phenotyping in mice. *Cardiovasc Res*. (1998) **39**:34–49.
42. Lee P, Klos M, Bollensdorff C, Hou L, Ewart P, Kamp TJ, et al. Simultaneous voltage and calcium mapping of genetically purified human induced pluripotent stem cell–derived cardiac myocyte monolayers novelty and significance. *Circ Res*. (2012) **110**:1556–63. doi: 10.1161/CIRCRESAHA.111.262535
43. Grskovic M, Javaherian A, Strulovici B, Daley GQ. Induced pluripotent stem cells – opportunities for disease modelling and drug discovery. *Nat Rev Drug Discov*. (2011) **10**:915–29. doi: 10.1038/nrd3577
44. Matsa E, Burridge PW, Wu JC. Human stem cells for modeling heart disease and for drug discovery. *Sci Transl Med*. (2014) **6**:239ps6. doi: 10.1126/scitranslmed.3008921
45. Strauss DG, Blinova K. Clinical trials in a dish. *Trends Pharmacol Sci*. (2017) **38**:4–7. doi: 10.1016/j.tips.2016.10.009
46. Trayanova NA, Roth BJ, Malden LJ. The response of a spherical heart to a uniform electric field: a bidomain analysis of cardiac stimulation. *IEEE Trans Biomed Eng*. (1993) **40**:899–908.
47. Niederer S, Mitchell L, Smith N, Plank G. Simulating human cardiac electrophysiology on clinical time-scales. *Front Physiol*. (2011) **2**:14. doi: 10.3389/fphys.2011.00014
48. Grandi E, Pasqualini FS, Bers DM. A novel computational model of the human ventricular action potential and Ca transient. *J Mol Cell Cardiol*. (2010) **48**:112–21. doi: 10.1016/j.yjmcc.2009.09.019
49. Alnæs MS, Blechta J, Hake J, Johansson A, Kehlet B, Logg A, et al. The FEniCS project version 1.5. *Arch Numer Softw*. (2015) **3**. doi: 10.11588/ans.2015.100.20553
50. Logg A, Mardal KA, Wells GN. *Automated Solution of Differential Equations by the Finite Element Method: The FEniCS Book, Vol. 84*. Heidelberg; Dordrecht; London; New York, NY: Springer Science & Business Media (2012).
51. Bernardi C, Maday Y, Patera AT. Domain decomposition by the mortar element method. In: Kaper HG, Garbey M, Pieper GW, editors. *Asymptotic and Numerical Methods for Partial Differential Equations with Critical Parameters*. Dordrecht: Springer Netherlands. (1993). p. 269–86.
52. Belgacem FB. The mortar finite element method with Lagrange multipliers. *Numer Math*. (1999) **84**:173–97.
53. Lamichhane BP, Wohlmuth BI. Mortar finite elements for interface problems. *Computing* (2004) **72**:333–48. doi: 10.1007/s00607-003-0062-y
54. Wohlmuth BI. A mortar finite element method using dual spaces for the Lagrange multiplier. *SIAM J Numer Anal*. (2000) **38**:989–1012. doi: 10.1137/S0036142999350929
55. Holter KE, Kuchta M, Mardal KA. Trace Constrained Problems in FEniCS. In: Hale JS, editor. *Proceedings of the FEniCS Conference 2017*. (2017). doi: 10.6084/m9.figshare.5086369
56. Raviart PA, Thomas JM, (Editors). A mixed finite element method for 2-nd order elliptic problems. In: *Mathematical Aspects of Finite Element Methods*. Berlin; Heidelberg: Springer (1977). p. 292–315.

57. Sacco R. *Multiscale Modeling of Interface Phenomena in Biology*. Available online at: http://www1.mate.polimi.it/~ricsac/NotesCMElBioMath.pdf
58. Brezzi F, Douglas J, Marini L. Two families of mixed finite elements for second order elliptic problems. *Numer Math*. (1985) **47**:217–35.
59. Benzi M, Golub GH, Liesen J. Numerical solution of saddle point problems. *Acta Numer*. (2005) **14**:1–137. doi: 10.1017/S0962492904000212
60. Mardal KA, Winther R. Preconditioning discretizations of systems of partial differential equations. *Numer Linear Algeb Appl*. (2011) **18**:1–40. doi: 10.1002/nla.716
61. Mardal KA, Nielsen BF, Cai X, Tveito A. An Order Optimal Solver for the Discretized Bidomain Equations. *Numer Linear Algeb Appl*. (2007) **14**:83–98. doi: 10.1002/nla.501
62. Linge S, Sundnes J, Hanslien M, Lines GT, Tveito A. Numerical solution of the bidomain equations. *Philos Trans R Soc Lond A* (2009) **367**:1931–50. doi: 10.1098/rsta.2008.0306
63. Feynman RP. Simulating physics with computers. *Int J Theor Phys*. (1982) **21**:467–88.
64. Weidmann S. Electrical constants of trabecular muscle from mammalian heart. *J Physiol*. (1970) **210**:1041.
65. Cascio WE, Yan GX, Kleber AG. Passive electrical properties, mechanical activity, and extracellular potassium in arterially perfused and ischemic rabbit ventricular muscle. Effects of calcium entry blockade or hypocalcemia. *Circ Res*. (1990) **66**:1461–73.
66. Jaye DA, Xiao YF, Sigg DC. Basic cardiac electrophysiology: excitable membranes. In: Sigg D, Iaizzo P, Xiao YF, He B, editors. *Cardiac Electrophysiology Methods and Models*. Boston, MA: Springer (2010). p. 41–51.
67. Roache PJ. *Verification and Validation in Computational Science and Engineering*. Hermosa, CA: Albuquerque, NM (1998).
68. Axelsson O. *Iterative Solution Methods*. Cambridge University Press (1996).
69. Van der Vorst HA. Bi-CGSTAB: A fast and smoothly converging variant of Bi-CG for the solution of nonsymmetric linear systems. *SIAM J Sci Stat Comput*. (1992) **13**:631–44.
70. Balay S, Abhyankar S, Adams MF, Brown J, Brune P, Buschelman K, et al. *PETSc Web page*. (2017). Available online at: http://www.mcs.anl.gov/petsc
71. Lyon AR, MacLeod KT, Zhang Y, Garcia E, Kanda GK, Korchev YE, et al. Loss of T-tubules and other changes to surface topography in ventricular myocytes from failing human and rat heart. *Proc Natl Acad Sci USA*. (2009) **106**:6854–9. doi: 10.1073/pnas.0809777106
72. Cuellar AA, Lloyd CM, Nielsen PF, Bullivant DP, Nickerson DP. Hunter PJ. An overview of CellML 1.1, a biological model description language. *Simulation* (2003) **79**:740–7. doi: 10.1177/0037549703040939
73. Noble D. Cardiac action and pace-maker potentials based on the Hodgkin–Huxley equations. *Nature* (1960) **188**:495–7.
74. Luo CH, Rudy Y. A model of the ventricular cardiac action potential. Depolarization, repolarization, and their interaction. *Circ Res*. (1991) **68**:1501–26.
75. Luo CH, Rudy Y. A dynamic model of the cardiac ventricular action potential. I. Simulations of ionic currents and concentration changes. *Circ Res*. (1994) **74**:1071–96.
76. Hund TJ, Kucera JP, Otani NF, Rudy Y. Ionic charge conservation and long-term steady state in the Luo–Rudy dynamic cell model. *Biophys J*. (2001) **81**:3324–31. doi: 10.1016/S0006-3495(01)75965-6
77. Rudy Y, Silva JR. Computational biology in the study of cardiac ion channels and cell electrophysiology. *Q Rev Biophys*. (2006) **39**:57–116. doi: 10.1017/S0033583506004227
78. Maleckar MM, Greenstein JL, Giles WR, Trayanova NA. K+ current changes account for the rate dependence of the action potential in the human atrial myocyte. *Am J Physiol Heart Circ Physiol*. (2009) **297**:H1398–410. doi: 10.1152/ajpheart.00411.2009
79. Rudy Y, Weinstein H. From genes and molecules to organs and organisms: heart. *Compr Biophys*. (2012) **2**:268–327. doi: 10.1016/B978-0-12-374920-8.00924-3
80. Tveito A, Lines GT. *Computing Characterizations of Drugs for Ion Channels and Receptors Using Markov Models, Vol. 111*. Heidelberg: Springer-Verlag (2016).
81. Louch WE, Sejersted OM, Swift F. There goes the neighborhood: pathological alterations in T-tubule morphology and consequences for cardiomyocyte Ca^{2+} handling. *J Biomed Biotechnol*. (2010) **2010**:503906. doi: 10.1155/2010/503906
82. Soeller C, Cannell M. Examination of the transverse tubular system in living cardiac rat myocytes by 2-photon microscopy and digital image–processing techniques. *Circ Res*. (1999) **84**:266–75.
83. Nivala M, de Lange E, Rovetti R, Qu Z. Computational modeling and numerical methods for spatiotemporal calcium cycling in ventricular myocytes. *Front Physiol*. (2012) **3**:114. doi: 10.3389/fphys.2012.00114
84. Cheng Y, Yu Z, Hoshijima M, Holst MJ, McCulloch AD, McCammon JA, et al. Numerical analysis of Ca^{2+} signaling in rat ventricular myocytes with realistic transverse-axial tubular geometry and inhibited sarcoplasmic reticulum. *PLoS Comput Biol*. (2010) **6**:e1000972. doi: 10.1371/journal.pcbi.1000972
85. Swietach P, Spitzer KW, Vaughan-Jones RD. Modeling calcium waves in cardiac myocytes: importance of calcium diffusion. *Front Biosci*. (2010) **15**:661.
86. Tveito A, Lines GT, Hake J, Edwards AG. Instabilities of the resting state in a mathematical model of calcium handling in cardiac myocytes. *Math Biosci*. (2012) **236**:97–107. doi: 10.1016/j.mbs.2012.02.005
87. Kucera JP, Rohr S, Rudy Y. Localization of sodium channels in intercalated disks modulates cardiac conduction. *Circ Res*. (2002) **91**:1176–82. doi: 10.1161/01.RES.0000046237.54156.0A

Conflict of Interest Statement: The authors declare that the research was conducted in the absence of any commercial or financial relationships that could be construed as a potential conflict of interest.

Advantages of publishing in Frontiers

OPEN ACCESS
Articles are free to read for greatest visibility and readership

FAST PUBLICATION
Around 90 days from submission to decision

HIGH QUALITY PEER-REVIEW
Rigorous, collaborative, and constructive peer-review

TRANSPARENT PEER-REVIEW
Editors and reviewers acknowledged by name on published articles

Frontiers
Avenue du Tribunal-Fédéral 34
1005 Lausanne | Switzerland

Visit us: www.frontiersin.org
Contact us: info@frontiersin.org | +41 21 510 17 00

REPRODUCIBILITY OF RESEARCH
Support open data and methods to enhance research reproducibility

DIGITAL PUBLISHING
Articles designed for optimal readership across devices

FOLLOW US
@frontiersin

IMPACT METRICS
Advanced article metrics track visibility across digital media

EXTENSIVE PROMOTION
Marketing and promotion of impactful research

LOOP RESEARCH NETWORK
Our network increases your article's readership